

**MOLECULAR ENGINEERING STRATEGIES FOR THE DEVELOPMENT
OF ENERGY-TRANSPORTING CONJUGATED SYSTEMS
TOWARDS BIOELECTRONICS**

by

Herdeline Ann Mallari Ardoña

A dissertation submitted to Johns Hopkins University in conformity with the requirements
for the degree of Doctor of Philosophy in Chemistry

Baltimore, Maryland

June 2017

© 2017 Herdeline Ann Mallari Ardoña
All Rights Reserved

ABSTRACT

Peptidic nanostructures appended with π -electron units present a powerful class of biomaterials that merges the chemical versatility of self-assembling peptides and the optoelectronic function of organic π -electron units. This dissertation spans research efforts from understanding some rational design concepts to the bioelectronic utility of π -conjugated peptides. Chapter 1 describes the progress in the field of peptidic nanomaterials bearing π -electron systems and how this relates to advances in bioelectronics. In Chapters 2 and 3, key properties and aspects of molecular design that can be utilized to rationally tune optoelectronic and mechanical properties of oligothiophene-peptide hybrid hydrogelators are discussed. Chapter 2 focuses on the effect of varied amino acid size and hydrophobicity on material properties at different length scales. Chapter 3 investigates the photophysical effects of confining individual π -units within nanostructures and how the coassembly behavior is affected by local fields imparted by the peptide moieties. The next two chapters introduce a multicomponent strategy to create and characterize the nanostructure of different functional materials, either with the co-incorporation of bioactive epitopes within peptide nanostructures or showing energy and/or electron transfer events among π -electron systems that are spatially engineered within peptidic constructs. Chapter 4 presents energy-transporting nanomaterials comprised of donor-acceptor peptide pairs existing in either solution or hydrogel phase. Chapter 5 aims to shed light on the local structure formed upon supramolecular coassembly in both solution and hydrogel phases using solid state NMR and small-angle neutron scattering techniques.

Finally, Chapter 6 presents the developmental efforts towards creating biological scaffolds out of these peptidic nanostructures with tunable physicochemical properties that can potentially facilitate nanostructural energy transport upon electrical or light stimulation. These peptide nanomaterials offer a platform for scaffolds that can mimic the natural environment of electrosensitive tissues such as nerves. Much of the progress accomplished towards this application is to establish a stable system against material degradation during long periods under cell culture conditions. We show that aligned constructs that are pre-assembled by an external trigger followed by covalent crosslinking were successful in imparting topographical guidance to human neural stem cells or dorsal root ganglion neuron explants. The latter part of this Chapter reports the extension of these efforts towards developing known electroactive organic polymers that can be processed as aligned soft materials for neural stem cells and neonatal rat ventricular cardiomyocytes. This dissertation aims to bridge the understanding of chemical design and self-assembly principles with the biomaterial applications of peptide-based optoelectronic assemblies and related conjugated polymers.

Advisor:

Professor John D. Tovar

Co-Advisor:

Professor Hai-Quan Mao

Thesis Readers:

Professor Marc M. Greenberg and Professor Craig A. Townsend

PREFACE

Beyond exploring new functional soft materials and efficient synthetic routes to produce their molecular components, achieving success in their development towards practical applications requires the utmost understanding of the material properties at different length scales. For organic materials with extended π -conjugation, the development of organic light-emitting diodes, organic photovoltaics, wearable electronics, and other such technological advancements would not be possible if not for the fundamental concepts such as charge transport, doping process or structure-property correlations for conductive organic polymers.

For the past few years in the Tovar Group, exploration of synthetic methodologies for supramolecular peptidic monomers merged with π -systems has paved the way for the construction of self-assembling peptides with unique optoelectronic properties that are processable under aqueous or physiological conditions. Along with detailed photophysical investigations and new material processing techniques to create hydrogels with fiber alignment and anisotropic optoelectronic properties, this novel class of material is envisioned to create an innovative platform for biological interfacing applications.

Despite the promising advances contributed by the group over the years, there are several design aspects of this peptidic nanomaterial that are left unexplored. Such supramolecular polymers often present a complex system—its dynamic structure and assembly behavior make it challenging to engineer its function based on chemical design. But with such complexity, we aim to achieve unique material functionalities that can potentially match the complex engineering requirements towards its biological applications. Highly interdisciplinary approaches were taken together with our collaborators to realize different molecular engineering strategies for the development of these peptides. This dissertation provides insights on rationally designing peptide-based optoelectronic assemblies to contribute to the continuously growing field of bioelectronics.

ACKNOWLEDGEMENTS

*For the past five years, I had a wonderful time pursuing graduate school mainly because of the **long** list of people that have been part of this journey:*

First and foremost, I would like to express my sincerest gratitude to my Ph. D. advisor, Prof. J. D. Tovar. Every student in the Tovar Group can attest, without a doubt, as to how much J. D. supports our scientific growth and independence in research. I will always be thankful to J. D. for supporting me in all the endeavors that I have pursued while in graduate school, as well as for creating a research environment where learning trumps failed experiments. I believe that he has set a great example for leading a research group that emphasizes on the scientific development of his students. He is truly a vital part of my development as a scientist and I will always be grateful for that.

I am also deeply indebted to my co-advisor, Prof. Hai-Quan Mao. My unique graduate school experience would not have been the same if not for the opportunity to work in Dr. Mao's group. This experience, despite a challenging project, has expanded my scientific horizons beyond what I can learn from my Chemistry classes and from J. D.'s lab. I would especially like to thank Dr. Mao for being appreciative of every small research milestone and for being equally supportive towards my scientific endeavors. With J. D. and Dr. Mao, I am fortunate to have mentors in my graduate career who are always encouraging and sincerely cares about of their students, and I hope to do the same if given the chance.

I would also like to thank Prof. Marc Greenberg and Prof. Craig Townsend for being in my thesis committee, as well as in my committee for my departmental oral exam and graduate board oral exam.

Accomplishing the experiments and the writing tasks for this dissertation would not be possible without the help and daily support from my labmates. From sharing our day-to-day updates about research (whether it is for having a nice result, guessing an unknown by-product, or agonizing over a broken instrument...) to randomly talking about stuff outside of science, these have made it easier to move forward in grad school and I am lucky to have found friends in the lab to have these great conversations with every day. I would first like to thank Dr. Brian Wall, Dr. Allix Sanders and Ashley Zacca for the guidance and training when I was starting in the group. Brian has been tremendously helpful by giving suggestions for synthetic routes or setups and providing advice even when he already left the group. Allix trained me for most of the lab techniques useful in the Tovar lab and has always been there for me to pass on her knowledge about the project or to simply share her daily stories! I also thank Dr. Ben Streifel and Dr. Dave Levine, who were the other senior graduate students when I joined the Tovar Group and have willingly extended their help even though

they were working on a different project. It has also been a pleasure to work with Dr. Teju Kale and Dr. Wathsala Liyanage, giving the lab a different perspective from a postdoc standpoint. And of course, my sincerest thanks to the current members...that have and are currently dealing with all my stories of excitement and frustration as I am transitioning out of grad school—Justin DeFrancisco, Reid Messersmith, Garvin Peters, Jessie Dibble and Sayak Panda. I can't be more thankful to have built such great memories with all these people and I will always remember those, as well as their contributions in shaping me as a scientist. I am very happy to have been part of the Tovar Group!

In Dr. Mao's Lab, I especially want to thank Brian Ginn for very patiently training me from the beginning (having no background at all on cell work prior to coming to Hopkins!) up to answering some of my questions until now, Dr. Xiaowei Li for always extending his help and guidance despite being in a completely different project, Dr. Markus Tammia for his helpful insights, Dr. Jose Roman for training me on doing primary cell isolations from rats, and to Dr. Shuming Zhang, for all of his experimental suggestions when I started. I also thank the rest of the Mao Lab-Regenerative Medicine Subgroup: Dr. Kellin Krick, Dr. Russ Martin, Dr. Xuesong Jiang, Dr. Jisuk Choi, Dr. Huanhuan Liu and Calvin Chang, who for sure, have individually helped me at some point. Whether it is for asking suggestions about an experiment, finding an antibody buried somewhere in our freezer, or simply changing a CO₂ tank, I thank these people for always helping me willingly, particularly when I was starting in the group and the learning curve was so steep from being a Chemistry student to doing all the biomaterial work. The same goes for all the past and current members of the Mao Research Group, thank you!

I would also like to thank our collaborators that have made several experiments possible for this dissertation. Prof. Howard Katz, more than supervising our collaboration on the device fabrication with our peptidic nanomaterials, has provided me support and advice for fellowship applications as well as for my postdoctoral hunt. I sincerely thank him for extending his help on those. Dr. Kalpana Besar was an important part of Chapter 2 and has been a pleasure to work with. I also want to acknowledge Jennifer Dailey for our discussions about impedance spectroscopy, figuring out the correct setup together and her efforts to even make it better.

I thank Prof. Dave Adams for providing me a wonderful opportunity to work in his lab in Liverpool (and for J. D. for allowing me to do so despite my failed proposal application for a travel grant!), as well as for welcoming me there and even sharing some career advice. Indeed, I had a great time there and learned new things with the help of Dr. Emily Draper, Matthew Wallace, Dr. Laura Mears, and the rest of the Adams Lab. This short research experience turned into a nice collaborative work, also with Prof. Louise Serpell and Dr. Francesca Citossi whom I am thankful for performing fXRD on my samples.

Chapter 5 of this dissertation was made possible with the help of Prof. Christopher Jaroniec, Dr. Zhe Qi, and Dr. Chris Stanley. I am thankful for Zhe and Prof. Jaroniec for accommodating our samples, and even showing me their facility and explaining their work. Many thanks to Chris for providing significant help for all the neutron scattering experiments—from providing feedback on my beamtime proposals (and again to J. D., for allowing me to apply!), planning out the experiments and data analyses. I also want to thank Prof. Art Bragg and Tim Magnanelli for accommodating our samples for transient absorption measurements.

I should thank Markus (Mao Lab) for directing me to people in Prof. Ahmet Höke's group such as Dr. Chris Cashman and Dr. Jeremy Sullivan. Chris has been extremely helpful for figuring out the appropriate setups for electrical stimulation and calcium imaging experiments. In my attempts to do calcium imaging and find the correct experimental conditions for my samples and cell lines, I should thank Dr. Scot Kuo for directing me to Prof. Ivy Dick who has been enormously helpful in the calcium imaging and cardiomyocyte experiments. Ivy, together with our collaboration with Grayson Lab, have opened another avenue for me to explore the utility of the hydrogel scaffolds that I'm working with: towards cardiomyocytes and not just for neurons. If not for these collaborations, I probably would not have read about cardiac mechanotransduction and would have not even considered applying for a postdoctoral position in Prof. Kit Parker's group.

I am also thankful to be surrounded by people here at Hopkins who are very helpful and accommodating. To my friends in the Chemistry department, thanks for making every Chemistry happy hour more fun to go to. Special thanks to my roommates (Suzanne Adam and Miranda Gallagher) and other Chemistry friends in the neighborhood (Darcie Long, Julie Messersmith, Ron Lankone, Saghar Nourian, Dellwood people, etc.). It makes me more excited to go to lab and accomplish things in the most efficient way to spend more time hanging out with these people after work. I must especially thank Suz for always accommodating us in her old apartment since we were in our 1st year, which became an ongoing tradition, and she has since then become one of the most supportive and thoughtful friends of mine. Lastly, my most sincere *'salamat'* to the other Filipino graduate students and postdocs here at Hopkins—Dr. Joanna San Pedro (who has been like a big sister to me since I first moved here to U.S.), Paulo Zaragoza (who dealt with me the longest, especially with my repeating stories!), Miguel Sulangi, Michelle Acoba, Jireh Sacramento, Marco Jacinto, Jayson Pagaduan and Rico Gamuyao, for easing homesickness and making me feel that Baltimore is closer to home for these past years! It's nice to have people whom you can share stories with in your own native language. I also thank my other friends doing grad school in the U.S. (especially Daben Libardo!). Most of them I met in my work at U.P. Diliman or during my undergrad years, and they have shared with me the memories of reviewing for GRE, having to take a 7-hour bus ride from Manila for the GRE Chem when

we ran out of slots in Manila to take this exam, sending applications to schools, and even periodically spending short vacations together which always makes me feel refreshed. In addition to my other friends from home and those who are doing graduate school in other parts of the world/ U.S. who have constantly supported me from far away, all of these friends that I met at Hopkins are very important in my survival in graduate school and I will always consider them as my lifelong friends.

My sincerest thanks also to Tita Chit, Tito Rey and Tito Eval for being my family here in Baltimore; especially to Tita Chit for cooking Filipino dishes and teaching me some of her recipes! To the Carlos Family, especially to my Aunts (Titas Jay, Joy, Jolly and Jenny)—thank you for always welcoming me in CA and for being the family I can spend my Christmas and New Year with during the times that I can't go home. I especially thank Tita Jay for her support, advice and care since my undergraduate years up to this point. This journey in pursuing a career in Chemistry would also not have been possible without Ninang Melody, my mom's longest friend, for the help that she has given throughout my undergraduate years.

I was about to go to medical school and apply for M.D.-Ph.D. programs after finishing my Chemistry degree in the Philippines, but I have to thank one person for putting me back on the right track—Maxx Arguilla, who have inspired me to pursue a Ph.D. in Chemistry. I am infinitely thankful to you for staying beside me throughout these years and am I very fortunate to have someone who can listen to whatever I am talking about, whether about science or not. I have no regrets to have always considered you in making my career options and I know that everything will always be better if we are together in our adventures, now and in the near future.

Finally, I would like to thank my family who have showered me with unconditional love and happiness at all times. My grandmother, who I grew up with and was a chemical engineer, has always been my great role model as a woman pursuing a career in STEM. My father, who is my first Math tutor, will always be in our hearts and is an inspiration to always keep moving forward instead of quitting. My mother and my sister have always been my source of strength since my father passed away, and I will be always proud of the challenges we've been through together. I am very happy to have been raised by a family who is very supportive of pursuing opportunities that I genuinely want. I humbly dedicate this work to them, and the future discoveries that this journey will lead me to...

*Dedicated to my family,
especially to my parents—Hernando and Adelina.*

TABLE OF CONTENTS

CHAPTER 1	Introduction—Merging Organic Electronics and Peptide-Based Supramolecular Systems.....	1
CHAPTER 2	Structure-Function Correlation Studies for π -Conjugated Peptide Hydrogelators	
	Introduction.....	48
	Results and Discussion.....	54
	Conclusions.....	81
	Experimental Details.....	82
	References.....	92
CHAPTER 3	Non-Resonant Effects in Peptidic Nanostructures Bearing π -Conjugated Oligomers	
	Introduction.....	101
	Results and Discussion.....	105
	Conclusions.....	136
	Experimental Details.....	138
	References.....	145
CHAPTER 4	Establishing Energy Gradients within Multicomponent Optoelectronic Peptide Nanostructures Under Aqueous Conditions	
	Introduction.....	152
	Results and Discussion.....	156
	Conclusions.....	193
	Experimental Details.....	196
	References.....	205
CHAPTER 5	Probing the Local Nanostructure of π -Conjugated Peptide Coassemblies	
	Introduction.....	214
	Results and Discussion.....	218
	Conclusions.....	232
	Experimental Details.....	233
	References.....	238

CHAPTER 6	Aligned Bioscaffolds with π-Conjugated Systems for Electrosensitive Cells	
	Introduction.....	242
	Results and Discussion.....	252
	Conclusions.....	274
	Experimental Details.....	275
	References.....	285
CHAPTER 7	Future Directions and Concluding Remarks.....	292
APPENDIX	Characterization Data and Supporting Information.....	304
BIOGRAPHICAL SKETCH.....		390
CURRICULUM VITAE.....		391

LIST OF TABLES

Table 2.1. Relative quantum yields (Φ_{PL}) and absorption maximum (λ_{max}) of <i>DXX</i> peptides (*normalized to DVV peptide in acidic solutions)	68
Table 2.2. Mobility values for different OT4-containing π -conjugated peptides.	76
Table 3.1. Photoluminescence lifetimes of DDD- and DVV-OPV3 peptides, their co-assemblies with C10 peptides and mixtures of pre-assembled nanostructures.....	127
Table 3.2. Fluorescence lifetimes of DDD- and DVV-OT4 and solutions co-mixed with C10 peptides.....	130
Table 3.3. Fluorescence lifetimes of DDD- and DVV-OT4dM and solutions co-mixed with C10 peptides.....	131
Table 4.1. Fluorescence lifetimes of DFAA-OPV3, DFAA-OT4, and their coassemblies	167
Table 5.1. List of EAA- and VAVKIEAA-OT4 coassembled hydrogel components. ..	219
Table 5.2. Different R_g values calculated from Guinier-Porod model fits at different temperatures; all under acidic conditions.	232
Table 6.1. Common electrically conducting polymers used in tissue engineering	245
Table A3.1. Relative quantum yields for co-assemblies of DDD OPV3/ DDD C10 and DVV OPV3/ DVV C10 with respect to the respective pure, acidic OPV3 peptide.	349
Table A5.1. List peaks in the NCO spectrum of A1- ¹³ C-A2- ¹⁵ N-EAA-OT4.	375
Table A5.2. List peaks in the NCO spectrum of A1- ¹³ C-A2- ¹⁵ N-DFAA-OPV3.....	375
Table A5.3. Nominal and actual* ratios for EAA-OT4 control samples.....	376
Table A5.4. Nominal and actual* ratios for the mixed samples.	376
Table A5.5. Calculated parameters from parallelepiped model fits for SANS data for one-component samples; the longest axis dimension was fixed to 4000 Å (a and b represent the shorter dimensions).....	379

LIST OF FIGURES

- Figure 1.1.** Structure, schematic of assembly morphology and nanoscale structure of 1D-materials based on π -conjugated units. 3
- Figure 1.2.** The proposed model for stepwise self-organization of oligopeptides, from single beta-sheet tapes to higher-order fibrillar structures.. 5
- Figure 1.3.** A schematic representation of the energy landscapes for peptide amphiphile self-assembly and the different conditions and pathways that the favor β -sheet formation of thermodynamic, kinetic and metastable fibrillar products..... 7
- Figure 1.4.** Self-assembling peptides functionalized with pyrene via lysine appendages. Variation of the functional groups at the N-termini results in different morphological outcomes. 9
- Figure 1.5.** General synthetic strategies used for the construction of peptide- π system hybrids..... 10
- Figure 1.6.** Computational self-assembly models for a) poly(ethylene oxide)-peptide-oligothiophene; b) poly(isoprene)-peptide-polydiacetylene; and c) peptide-oligothiophene conjugates.. 11
- Figure 1.7.** Molecular structures (a-c) and the corresponding nanostructural morphologies (d-f) observed upon self-assembly of different thiophene-based peptide units..... 14
- Figure 1.8.** Molecular structures of a) photoswitchable azobenzene-peptide conjugates (and diagram for the superposition of structures for the two isomers); and (b, c, d) some examples of water-soluble peptide-based oligophenyl assemblies. 15
- Figure 1.9.** Different depictions of self-assembly for peptide- π conjugates containing phenylene vinylene units: (a) a molecular image of Schenning and Meijer's peptide-OPV diblock molecules and (b) the associated STM image, (c) TEM image of peptide-OPV-peptide by Maggini and co-workers, (d) Ferguson's molecular dynamics simulations of the Tovar OPV nanomaterials before (left) and after (right) relaxation, and (e) the observed nanostructures imaged with TEM. 16
- Figure 1.10.** Molecular structures of different peptide-diacetylene hybrids..... 18
- Figure 1.11.** (a) Diagram showing the strategy to magnetically align peptide amphiphile assemblies. (green= polymerizable peptide-polydiacetylene amphiphile; blue= polymerized nanofibers; red= direction of the magnetic field); SEM images of (b) unaligned and (c) aligned peptide-diacetylene amphiphiles.. 19

Figure 1.12. Illustration of the different self-assembly patterns reported for NDI-containing peptides.....	21
Figure 1.13. Molecular structures of different aromatic dye-peptide hybrid gelators; ^{84,85} a) optical images of pyrene-peptide gels in o-dichlorobenzene; c) example of a peptide-exTTF conjugate.....	24
Figure 1.14. Schematic diagram of complexation between a HBC stack and lysine-rich oligopeptides.....	25
Figure 1.15. a) Scope of a systematic study of amino acid variation for OPV-containing π -conjugated peptides; b) absorption profiles of DFAX-OPV peptides under acidic conditions, with X residues being varied; c) synthesis of helical peptides conjugated with oxadiazole-containing phenylenevinylene units; d) absorption profiles for peptide-chromophore conjugates with varied distances among oxadiazole-containing phenylenevinylene units (6-17 Å).....	27
Figure 1.16. a) Utilizing the differential pK_a in a two-component system to promote self-sorting via slow pH drop, utilizing GdL hydrolysis; b) incorporation of self-assembled exTTF-peptide units around a CNT.....	30
Figure 1.17. Schematic representation of the ionic interactions in a silicon inorganic semiconductor and poly(3,4-ethylenedioxythiophene) (PEDOT) organic semiconductor in an electrolytic environment.....	34
Figure 2.1. Molecular structures of the quaterthiophene-peptide (DXX) hydrogelators studied herein.....	52
Figure 2.2. Schematic diagram of the proposed self-assembly process for π -conjugated peptides.....	54
Figure 2.3. Representative energy-minimized models for the supramolecular assembly of DGG, DVV and DFF peptides showing the hydrogen bonding interactions (---).....	55
Figure 2.4. TEM micrographs of peptide nanostructures prepared from 0.1 wt% of DXX peptides.....	56
Figure 2.5. TEM images of the acid-assembled 1wt% DXX peptide hydrogels.....	57
Figure 2.6. AFM image of 0.1 mg/mL dropcast film of assembled EAA-OT4 peptide, (a) height and (b) phase profiles; (c) TEM image of 1 mg/mL solution of acidified EAA-OT4 solution; (d) surface profile of a 10 mg/mL dropcast film of EAA-OT4 under a laser microscope.....	58
Figure 2.7. 3D surface profiles of 1 wt% DXX- and EXX-OT4 peptide films used for FET measurements.....	60

Figure 2.8. Representative SEM images of critical point-dried, acid-assembled, DXX hydrogels (1 wt%).....	61
Figure 2.9. Storage and loss moduli data (at 1 Hz) taken from frequency sweep experiments at 0.3% strain (25°C), for DXX hydrogelators (left); frequency sweeps (0.1-10 Hz; 0.3% strain; 25°C) for 1 wt% DXX peptide hydrogels (right).....	63
Figure 2.10. Strain sweeps (left, including cyclic sweeps) and temperature sweeps (right) for DAA-, DII-, and DFF-OT4 1 wt% peptide hydrogels.	64
Figure 2.11. Representative strain sweeps for DVV; (a) 0.1% to 100%; (b) 0.1 to 500% strain; *indicates reverse strain sweeps, 100% to 0.1% for (a) and 500% to 0.1% for (b); (c) representative temperature sweep for DVV, showing the stable G' and G'' values from 4°C to 40°C.	65
Figure 2.12. (a) UV-Vis, (b) PL (λ_{exc} = 410 nm), and (c) CD spectra of DXX peptides (~14 μ M) in basic (ca. pH 10, ---) and acidic solutions (ca. pH 2, —).	67
Figure 2.13. (a) Absorption, (b) emission (λ_{exc} = nm) (~14 μ M), and (c) circular dichroism spectra (~6 μ M) of OT4-peptides in basic (ca. pH 10, ---) and acidic solutions (ca. pH 2, —). For the emission spectra, peptides were normalized with respect to EVV and the basic spectrum was arbitrarily set to the same intensity as EVV.....	70
Figure 2.14. Representative sheet resistance vs. current plots for the dried, acid-assembled DGG peptide films under light and dark conditions.	71
Figure 2.15. Representative sheet resistance vs. current plots for the dried, acid-assembled DGG peptide films under light and dark conditions.	73
Figure 2.16. (a) Schematic of the FET architecture used to measure the hole mobilities within the peptide nanostructures; (b,c) control compounds used as the active layer replacing OT4-peptides in the configuration shown in (a).	74
Figure 2.17. Output curves for OFET devices with the OT4 bis(peptides) as the semiconductor active layers.....	75
Figure 2.18. (a) Schematic diagram of the FET devices with peptide nanostructures as the gate; output curves for (b) control peptide 2 and (c) DAA-OT4 used as a gate layer in the configuration shown in (a).	79
Figure 2.19. Output curves showing the effect of varying the dielectric thickness of an OFET configuration with (a-c) DAA-OT4 and (d-f) EAA-OT4 as the gate, pentacene as the semiconductor, and C ₄₄ H ₉₀ as the dielectric layer.	80

Figure 3.1. Molecular structures of peptides used in this study.....	106
Figure 3.2. An illustration representing the possible structural outcomes of the co-assembled peptides that conform in a 1-D nanostructural geometry	107
Figure 3.3. TEM images for DDD- (left panel) and DVV- (right panel) C10 assemblies and their respective co-assemblies (5 and 20 mol%) with OPV3.	109
Figure 3.4. TEM images for 5 mol% DDD- (left panel) and DVV- (right panel) OT4 and OT4dM/ co-assemblies with C10 peptides.....	110
Figure 3.5. UV-vis absorption spectra of DDD-OPV3 (a-c) and DVV-OPV3 (d-f); homo-assemblies (a, d), co-assemblies (b, e) and separately assembled mixtures (c, f) with their respective C10 peptide equivalents.....	113
Figure 3.6. PL spectra of DDD-OPV3 (a-c) and DVV-OPV3 (d-f); homo-assemblies (a, d), co-assemblies (b, e) and separately assembled mixtures (c, f) with their respective C10 peptide equivalents.....	115
Figure 3.7. Absorption (a,b) and PL spectra of DDD-OT4/OT4dM homoassemblies and co-assemblies with their respective C10 peptide equivalents.....	120
Figure 3.8. Absorption (a,b) and PL (c,d) spectra of DVV-OT4/OT4dM homo-assemblies, and co-assemblies with their respective C10 peptide equivalents	121
Figure 3.9. Comparison of emission spectra of pure assemblies, co-assembled and self-sorted DDD- (a, b) and DVV- (c, d) OT4/OT4dM peptides and their C10 coassemblies.	122
Figure 3.10. Circular dichroism spectra of DDD-OPV3 (a) and DVV-OPV3 (b) homo-assemblies, and co-assemblies with their respective C10 peptide equivalents.....	124
Figure 3.11. Circular dichroism spectra of DDD-OT4/OT4dM (a, c) and DVV-OT4/OT4dM (b, d) assemblies, and co-assemblies with their respective C10 peptide equivalents	126
Figure 3.12. PL (a, c) and CD (b, d) spectra of acidic DDD-OPV3 homo-assemblies and co-assemblies at 5 mol% and 20 mol% with DDD-C10; spectra taken at (a,b) 5 °C and (c, d) 60 °C in comparison to room temperature (RT).....	133
Figure 3.13. PL (a, c) and CD (b, d) spectra of acidic DVV-OPV3 homo-assemblies and co-assemblies at 5 mol% and 20 mol% with DVV-C10; spectra taken at (a, b) 5 °C and (c, d) 60 °C in comparison to room temperature (RT)	135
Figure 4.1. Molecular structures of some multichromophoric systems reported in the literature.	153

Figure 4.2. Molecular structures the DFAA-OPV3 and -OT4 peptides.	157
Figure 4.3. (a) Energy-minimized assembly model for a hypothetical portion of an DFAA-OPV3/-OT4 heterostructure with a single isolated DFAA-OT4 unit within the DFAA-OPV3 majority aggregate. TEM images (stained with 2% uranyl acetate) along with the observed widths of nanostructures formed from 0.1 wt% acidic, coassembled DFAA-OPV3/-OT4 solutions: (b) 1 mol% (5.6 ± 0.64 nm) and (c) 9 mol% DFAA-OT4 (13.6 ± 2.3 nm).	159
Figure 4.4. Absorption spectra of DFAA-OPV3, DFAA-OT4, and their co-mixtures under basic (a) and acidic (b) conditions. Emission spectra (c) recorded at pH=10 (---, λ_{exc} = 320 nm) and pH=2 (—, λ_{exc} = 330 nm). For comparison, a direct excitation of OT4 molecules and assemblies at 450 nm is shown in (c). [DFAA-OPV3]= 3.2 μ M, [DFAA-OT4]= 0.03-3.2 μ M; arrows show trends as mol% DFAA-OT4 is increased. Relative* quantum yields (d) of the DFAA-OPV3/-OT4 mixtures at pH=2 (λ_{exc} = 330 nm), reported as the ratio of sample absorption \times PL peak area of DFAA-OPV3/-OT4 mixtures with respect to DFAA-OPV3.....	161
Figure 4.5. PL spectra for DFAA-OPV3 and DFAA-OT4 coassemblies (arrows indicate increasing mol% DFAA-OT4) at different excitation wavelengths	164
Figure 4.6. Space-filling, energy-minimized model of DFAA-OT4 coassembled within 1D-stacks of DFAA-OPV3, illustrating the possible energy transfer processes (resonance energy transfer (RET) and carrier migration).	165
Figure 4.7. Transient absorption spectra (λ_{ex} = 400 nm) of DFAA-OT4 under basic and acidic conditions.	168
Figure 4.8. Transient absorption spectra (λ_{ex} = 400 nm) of DFAA-OPV3/-OT4 (10 mol% OT4) under basic and acidic conditions, with the samples sparged with N ₂	169
Figure 4.9. Transient absorption spectra (top) (λ_{ex} = 330 nm) of DFAA-OPV3/-OT4 (10 mol% OT4) under basic and acidic conditions and broadband polarization anisotropy spectra (bottom).	170
Figure 4.10. (a) PL spectra (λ_{exc} =330 nm) of resulting solutions from titrating DFAA-OT4 to a pre-assembled DFAA-OPV3 acidic solution (arrows indicate increasing mol% DFAA-OT4) and (b) their corresponding relative* quantum yields, reported as the ratio of sample absorption \times PL peak area of DFAA-OPV3/-OT4 mixtures with respect to DFAA-OPV3.	172
Figure 4.11. UV-Vis (a,b) and PL (c,d) spectra of (a,c) re-basified (λ_{exc} =320 nm) and (b,d) re-acidified solutions used in Figure 4.3a and 4.3c	173
Figure 4.12. Monitoring the emission λ_{exc} =330 nm during the thermal cycling process for acidic samples of (a) DFAA-OPV3 and (b) 9 mol% DFAA-OT4 solutions.	176

Figure 4.13. CD spectra of (a) acidic (—; pH 2), basic (---; pH 10), and (b) annealed DFAA-OPV3/-OT4 coassembled solutions [OPV3]= 3.2 μ M; arrows indicate increasing mol % DFAA-OT4 (4.8%, 50% to 100%). 178

Figure 4.14. (a) Molecular structures of the peptides studied herein and (b,c) diagrams of the potential energy (e.g., resonance energy transfer, RET) and electron transfer events occurring within a two-component peptidic nanostructure with three π -electron units for b) self-sorted and c) randomly coassembled systems. 180

Figure 4.15. Monitoring of peptide assembly and hydrogel formation for 1:1 OPV3 and OT4-Ac solutions prepared with 30 mg/mL GdL via a) 1 H NMR and b) rheology (G' = solid circles; G'' =smaller circles). Each peptide component is at 5 mg/mL (total of 10 mg/mL peptides for the 1:1 mixed sample). 183

Figure 4.16. Fiber X-ray diffraction data for hydrogels prepared with 30 mg/mL GdL, comprised of one peptide component (a, OPV3 only; b, OT4-Ac only) and two peptide components (c, OPV3:OT4-NDI; d, OPV3:OT4-Ac; both 1:1). Each peptide component is at 5 mg/mL (total of 10 mg/mL peptides for the 1:1 mixed samples). 184

Figure 4.17. TEM images of 1:1 mixed assemblies (3 μ M peptide concentration for each component) of OPV3 with (a,b) OT4-NDI or (c,d) OT4-Ac (1:1) assembled via (a,c) HCl addition and (b,d) GdL (10 mg/mL) hydrolysis..... 185

Figure 4.18. Solution phase UV-vis absorption (a-c) and steady-state emission (d-f) spectra for GdL- (10 mg/mL) or HCl-assembled peptide homoassemblies of (a) OPV3 (blue), (b) OT4-Ac (red), and (c) OT4-NDI (black); solutions measured under different conditions: molecularly dissolved samples (---), (a, d) with GdL (empty circles), (b, e) with HCl (—), and (c, f) with HCl, aged (...); [peptide] = 3 μ M; X= Raman scatter of water. 187

Figure 4.19. Solution phase steady-state PL spectra for mixed peptide structures of OPV3 with OT4-Ac (red) and with OT4-NDI (black) prepared with GdL- (10 mg/mL) or HCl; measured under different conditions: (a, b, c) λ_{exc} = 350 nm; (d, e, f) λ_{exc} = 430 nm; a) with GdL (empty circles), b) with HCl (—), and c) with HCl, aged (...); [OPV3] = 3 μ M.... 191

Figure 5.1. Schematic representation of narcissistic self-sorting and social coassembly under thermodynamic equilibrium..... 214

Figure 5.2. Schematic representation of an ideally coassembled 1D-structure that can be formed by EAA- and VAVKIEAA OT4 binary peptide system. 217

Figure 5.3. Molecular structures of the symmetrical π -conjugated compounds used in these studies. 218

Figure 5.4. 2-D NCO spectra of 1 wt% hydrogels from (a) Sample 2, A1-1- 13 C-A2- 15 N-EAA-OT4, and (b) Sample 10, A1-1- 13 C-A2- 15 N-DFAA-OPV3..... 220

Figure 5.5. A generalized stacking scheme between peptide-OT4 monomer units with labeled ^{13}C and ^{15}N pairs interacting for the TEDOR experiment.....	221
Figure 5.6. DRAWS and TEDOR curves for EAA-OT4.....	222
Figure 5.7. DRAWS curves for DFAA-OPV3 and -OT4.....	223
Figure 5.8. DRAWS and TEDOR curves of mixed EAA- and VAVKIEAA-OT4.....	224
Figure 5.9. DRAWS and TEDOR curves of mixed DFAA-OPV3 and -OT4	225
Figure 5.10. Schematic representation of structural contributors for mixed two-component π -conjugated peptides with different (a) and similar (b) monomer lengths, as assessed from the ssNMR experiments.....	226
Figure 5.11. SANS curves for DFAA-OPV3 and DFAA-OT4 (H) at 0.2 wt% and 1 wt% solutions in D_2O . Data fitting was done with a parallelepiped model.	229
Figure 5.12. An idealized parallelepiped model for the assembly of DFAA- π peptides; correlated with a representative TEM image for DFAA-OPV3 whereby the longest axis for the fitting curves was fixed to 4000 Å.	230
Figure 5.13. Histogram of atomic correlations from pair-distribution analysis for peptide samples in 40% D_2O	231
Figure 6.1. Schematic diagrams summarizing a) the progress in the field of tissue engineering for the past decade, b) its future, and the different ongoing challenges	243
Figure 6.2. Schematic illustration of photocurrent stimulation of cells and how it affects intracellular signaling.....	246
Figure 6.3. General structure of a peptide- π -peptide monomer with bioactive segment (top); making an aligned hydrogel by shear-flow assembly, with a representative SEM image ¹⁸ showing the aligned nanostructures and an idealized molecular model of a coassembled π -conjugated peptide (bottom).	250
Figure 6.4. Molecular structures of previously studied π -conjugated peptide monomers that are crosslinkable by guest molecules upon hydrogelation (left). The right panel shows an image of a self-supporting, crosslinked gel and the confocal microscopy images of human neural stem cells on a crosslinked gel and on tissue culture polystyrene.	251
Figure 6.5. Molecular structures of the π -conjugated systems used for electrospun fiber scaffolds.	252

Figure 6.6. Representative images of mechanically-robust HO-DVV-peptide hydrogels with a) OT4 and b) polydiacetylene core; c) representative SEM image of the peptide system in (a).	253
Figure 6.7. SEM images showing the alignment within shear-assembled hydrogels comprised of different ratios (v/v) of 1 wt% aqueous solutions of EAA-OT4: VAVKIEAA-OT4; a) 100:0; b) 90:10; c, d) 75:25; e) 50:50.	254
Figure 6.8. (a) SEM image showing the macroscopic alignment between the bundled hydrogel fibers formed by electrospinning 1.5 wt% alginate with 1.5 wt% VAVKIEAA-OT4; (b) epifluorescence image showing the distribution of OT4 units within the spun fibers; (c-e) birefringence due to alignment as observed under a polarized optical microscope.	255
Figure 6.9. SEM images of Schwann cells adhered on the alginate: VAVKIEAA-OT4 (1:1) composite hydrogel.	256
Figure 6.10. Dependence of the 1,4-polymerization of diacetylene on the molecular packing of monomers.	257
Figure 6.11. Molecular structures of the peptide-diacetylene monomers used for the hydrogel bioscaffolds used; (a) DK(Alloc)VV-diacetylene; (b) DK(biotin)VV-diacetylene. After assembling the peptides in a solution with high ionic strength (~200 mM CaCl ₂) or adding GdL, the hydrogels that formed were exposed to a 254 nm 4-W light source to yield the polydiacetylenes.	258
Figure 6.12. a) Human neural stem cells at Day 4 under a brightfield microscope, seeded on top on 2 wt% DK(biotin)VV-polydiacetylene; agarose channels with the peptide hydrogel b) before and c) after exposure to cell culture medium and depositing the aligned peptide hydrogel.	260
Figure 6.13. Topographical guidance provided by peptide-polydiacetylene hydrogels to human NSCs (7 days in culture on DK(biotin)VV-diacetylene gels) and DRG explant (8 days in culture on DK(Alloc)VV-diacetylene gels).	260
Figure 6.14. Control setups for the human neural stem cells (Tuj1+; 7 days in culture) on DK(biotin)VV-diacetylene “random gels” (left) and in Matrigel-coated TCPS (right).	261
Figure 6.15. (a) Comparison of neurite outgrowth lengths under different imposed conditions (with electrical stimulation: 150 mV/mm; with BDNF: hydrogels were soaked in 5 ng/mL BDNF in room temperature for 1 h); (b-d) representative DRG explants on polydiacetylene peptide gels after 10 days (immunostained against neurofilament).	262
Figure 6.16. Comparing the Tuj+ vs. GFAP+ cells (12 days in culture) seeded on 2 wt% DK(Alloc)VV-diacetylene “random” hydrogels, with (100 mV/mm) or without stimulation.	263

- Figure 6.17.** (a-c) Representative images of tissue-culture plate grown samples (7 days in culture), with and without irradiation. 265
- Figure 6.18.** (a) Spectral responsivity curve of a 1:1 P3HT/PCBM film blend (from Ref. 72); (b) representative optical images of P3HT/PCBM films (I, II) and spun fibers (III); films before (I) and after (II) annealing are shown. 266
- Figure 6.19.** Human neural stem cells (10 days in culture) on top of spin-coated P3HT:PCBM films. 268
- Figure 6.20.** Human neural stem cell spheroids (10 days in culture) on top of P3HT:PCBM aligned, electrospun fibers under (a,c) irradiated (10-W 528 nm LED source) and (b) non-irradiated conditions; (a) fibers with an insulating poly(vinylpyrrolidone) coating. 269
- Figure 6.21.** Representative SEM images for electrospun fiber bundles of fibrin (a,c) and fibrin-PPy composite (b,d); inset: optical image of the actual fibrin-PPy composite. ... 271
- Figure 6.22.** Representative optical microscopy images of fibrin and fibrin-PPy bundles (before and after plasmin treatment) and the results of the dynamic mechanical analysis for these aligned bundles. 272
- Figure 6.23.** (a) Current response over time of fibrin-PPy bundles exposed in an electrolytic cell culture medium, with 10% strain applied every 10 s using a bioreactor setup; (b) sheet resistance curve obtained using van der Pauw method. 273
- Figure 6.24.** Representative images of neonatal rat ventricular myocytes seeded on top of aligned, electrospun (a) fibrin and (b) fibrin-PPy bundles. 274
- Figure 7.1.** Schematic diagram of an AFM nanoindentation setup. The Hertz model relates the force (F) of indentation to the indentation distance (δ), and to the elastic modulus (E) of a material with a specific Poisson ratio (ν). 294
- Figure 7.2.** a) Proposed components for the active layers of an all-peptide transistor; b) image of the layers showing a clear interface between EAA-OT4 and FF-Fmoc without dissolution. 295
- Figure 7.3.** (a) DRAWS curve of A1-¹³C-EAA-OT4 under dynamic nuclear polarization conditions (inset: structure of AMUPol, the biradical agent used for these DNP runs); (b,c) AFM images (in peak force error mode) of EAA-OT4 nanostructures in (b) 70 mM HCl solution and in (c) 3:2 glycerol:70 mM HCl solution. 296
- Figure 7.4.** (left) SAV units bound to PDA-peptide 1-D nanostructures; (right) PDA-peptide solutions at 10^{-3} M. (A) acidified/polymerized gel; (B) heated/acidified/polymerized, without and with SAV; (C) acidified/ polymerized solution, without and with SAV; (D) after addition of base to C; (E) after addition of acid to D; (F) 20 minutes after E. 297

Figure A2.1. ^1H (400 MHz, d_6 -DMSO) NMR spectrum of DGG OT4 peptide.	310
Figure A2.2. ^1H (400 MHz, d_6 -DMSO) NMR spectrum of DVV OT4 peptide.	310
Figure A2.3. ^1H (400 MHz, d_6 -DMSO) NMR spectrum (top) and ^1H (600 MHz, D_2O) NMR spectrum (bottom) of DAA OT4 peptide.	311
Figure A2.4. ^1H (400 MHz, d_6 -DMSO) NMR spectrum of DII OT4 peptide.	312
Figure A2.5. ^1H (400 MHz, d_6 -DMSO) NMR spectrum of DFF OT4 peptide.	312
Figure A2.6. ^1H (600 MHz, D_2O) NMR spectrum of EGG OT4 peptide.	313
Figure A2.7. ^1H (400 MHz, d_6 -DMSO) NMR spectrum of EAA OT4 peptide.	313
Figure A2.8. ^1H (600 MHz, D_2O) NMR spectrum of EVV OT4 peptide.	314
Figure A2.9. ^1H (400 MHz, d_6 -DMSO) NMR spectrum of EII OT4 peptide.	314
Figure A2.10. ^1H (400 MHz, d_6 -DMSO) NMR spectrum of DVV C10 peptide.	315
Figure A2.11. Analytical HPLC trace of DGG OT4, monitoring at 400 nm.	315
Figure A2.12. Analytical HPLC trace of DAA OT4, monitoring at 400 nm.	315
Figure A2.13. Analytical HPLC trace of DVV OT4, monitoring at 400 nm.	316
Figure A2.14. Analytical HPLC trace of DII OT4, monitoring at 400 nm.	316
Figure A2.15. Analytical HPLC trace of DFF OT4, monitoring at 400 nm.	316
Figure A2.16. Analytical HPLC trace of EGG OT4 peptide, monitoring at 400 nm. ...	316
Figure A2.17. Analytical HPLC trace of EAA OT4 peptide, monitoring at 400 nm. ...	317
Figure A2.18. Analytical HPLC trace of EVV OT4 peptide, monitoring at 400 nm. ...	317
Figure A2.19. Analytical HPLC trace of EII OT4 peptide, monitoring at 400 nm.	317
Figure A2.20. Analytical HPLC trace of DVV C10 peptide, monitoring at 220 nm. ...	317
Figure A2.21. ESI-MS spectrum of DGG OT4 peptide.	318
Figure A2.22. ESI-MS spectrum of DAA OT4 peptide.	318

Figure A2.23. ESI-MS spectrum of DVV OT4 peptide.	319
Figure A2.24. ESI-MS spectrum of DII OT4 peptide.....	319
Figure A2.25. ESI-MS spectrum of DFF OT4 peptide.....	320
Figure A2.26. ESI-MS spectrum of EGG OT4 peptide.....	320
Figure A2.27. ESI-MS spectrum of EAA OT4 peptide.....	321
Figure A2.28. ESI-MS spectrum of EVV OT4 peptide.....	321
Figure A2.29. ESI-MS spectrum of EII OT4 peptide.....	322
Figure A2.30. ESI-MS spectrum of DVV-C10 peptide.....	322
Figure A2.31. Attenuated total reflectance IR spectra of DGG, DAA, DVV, DII, and DFF OT4 peptides in solid state.....	323
Figure A2.32. Attenuated total reflectance IR spectra of DAA, DVV, DII and DFF OT4 peptides in gel state.....	324
Figure A2.33. TEM images of 1 wt% DGG-OT4 peptide gel.....	324
Figure A2.34. TEM images of 1 wt% DAA-OT4 peptide gel.....	325
Figure A2.35. TEM images of 1 wt% DVV-OT4 peptide gel.....	325
Figure A2.36. TEM images of 1 wt% DII-OT4 peptide gel.....	326
Figure A2.37. TEM images of 1 wt% EGG-OT4 peptide gel.	326
Figure A2.38. TEM images of 1 wt% EAA-OT4 peptide gel.	327
Figure A2.39. TEM images of 1 wt% EVV-OT4 peptide gel.	327
Figure A2.40. TEM images of 1 wt% EII-OT4 peptide gel.	328
Figure A2.41. Absorption (left) and photoluminescence (right) spectra for HOOC-(quaterthiophene)-COOH (OT4) under basic (---) and acidic (—) conditions, for reference; λ_{exc} = 380 and 340 for PL, respectively.	328
Figure A3.1. ^1H NMR (D_2O) spectrum of peptide DDD C10.	329
Figure A3.2. ^1H NMR (D_2O) spectrum of peptide DDD OPV3.....	329

Figure A3.3. ^1H NMR (D_2O) spectrum of peptide DDD OT4.	330
Figure A3.4. ^1H NMR (D_2O) spectrum of peptide DDD OT4dM.	330
Figure A3.5. ^1H NMR (D_2O) spectrum of peptide DVV OPV3.....	331
Figure A3.6. ^1H NMR (D_2O) spectrum of peptide DVV OT4dM.	331
Figure A3.7. Analytical HPLC trace of DDD C10 peptide, monitoring at 220 nm.	332
Figure A3.8. Analytical HPLC trace of DDD OPV3 peptide, monitoring at 400 nm. ..	332
Figure A3.9. Analytical HPLC trace of DDD OT4 peptide, monitoring at 400 nm.....	332
Figure A3.10. Analytical HPLC trace of DDD OT4dM peptide, monitoring at 400 nm..	332
Figure A3.11. Analytical HPLC trace of DVV C10 peptide, monitoring at 220 nm. ...	333
Figure A3.12. Analytical HPLC trace of DVV OPV3 peptide, monitoring at 365 nm. 333	
Figure A3.13. Analytical HPLC trace of DVV OT4 peptide, monitoring at 400 nm....	333
Figure A3.14. Analytical HPLC trace of DVV OT4dM peptide, monitoring at 400 nm..	333
Figure A3.15. ESI-MS spectrum of peptide DDD C10.	334
Figure A3.16. ESI-MS spectrum of peptide DDD OPV3.....	334
Figure A3.17. ESI-MS spectrum of peptide DDD OT4.	335
Figure A3.18. ESI-MS spectrum of peptide DDD OT4dM.	335
Figure A3.19. ESI-MS spectrum of peptide DVV C10.	336
Figure A3.20. ESI-MS spectrum of peptide DVV OPV3.....	336
Figure A3.21. ESI-MS spectrum of peptide DVV OT4.	337
Figure A3.22. ESI-MS spectrum of peptide DVV OT4dM.	337
Figure A3.23. FT-IR spectra of DDD peptides (top, left) and co-assemblies thereof with DDD C10 peptide (top, right) and DVV peptides (bottom, left) and co-assemblies thereof with DVV C10 peptide (bottom, right).....	338

Figure A3.24. TEM images of DDD OPV3/ DDD C10 co-assembled nanostructures obtained at 5 °C (top) and 60 °C (bottom). All scale bars are 200 nm.	339
Figure A3.25. TEM images of DVV OPV3/ DVV C10 co-assembled nanostructures obtained at 5 °C (top) and 60 °C (bottom).	340
Figure A3.26. TEM images of DDD OT4/ DDD-C10 co-assembled nanostructures obtained at 5 °C (top) and 60 °C (bottom). All scale bars are 200 nm.	341
Figure A3.27. TEM images of DDD OT4dM/ DDD C10 co-assembled nanostructures obtained at 5 °C (top) and 60 °C (bottom). All scale bars are 200 nm.	342
Figure A3.28. TEM images of DVV OT4/ DVV C10 co-assembled nanostructures obtained at 5 °C (top) and 60 °C (bottom).	343
Figure A3.29. TEM images of DVV OT4dM/ DVV C10 co-assembled nanostructures obtained at 5 °C (top) and 60 °C (bottom).	344
Figure A3.30. UV-Vis absorption (top) and PL (bottom) data of different concentrations of DDD OPV3 peptide homo-assemblies in aqueous media; recorded at room temperature.	345
Figure A3.31. UV-Vis absorption (top) and PL (bottom) data of different concentrations of DVV OPV3 peptide homo-assemblies in aqueous media; recorded at room temperature.	346
Figure A3.32. DLS data of DDD OPV3/ DDD C10 co-assembled nanostructures generated at 25 °C displayed as intensity (left), number (center) and volume (right) averages.	347
Figure A3.33. DLS data of DVV OPV3/ DVV C10 co-assembled nanostructures generated at 25 °C displayed as intensity (left), number (center) and volume (right) averages.	348
Figure A3.34. PL lifetime measurements recorded for DDD peptides.	349
Figure A3.35. PL lifetime measurements recorded at room temperature for DVV peptides.	350
Figure A3.36. Normalized PL spectra of (a) DDD OPV3 and (b) DVV OPV3 peptides in molecularly dissolved state (pH 10) at various temperatures; [OPV3]= 8 μM.	350
Figure A3.37. Absorption spectra recorded at 5 °C (a,c) and 60 °C (b,d) spectra of DDD OPV3 (a,b) and DVV OPV3 (c,d) homo-assemblies, and co-assemblies with their respective C10 peptide equivalents.	351
Figure A4.1. ¹ H (400 MHz, d ₆ -DMSO) NMR of DFAA-OPV3 peptide.	352

Figure A4.2. ^1H (400 MHz, $\text{d}_6\text{-DMSO}$) NMR of DFAA-OT4 peptide.	352
Figure A4.3. ESI-MS spectrum of DFAA-OPV3 peptide.	353
Figure A4.4. Analytical HPLC trace of DFAA-OPV3, monitoring at 365 nm.	353
Figure A4.5. ESI-MS spectrum of DFAA-OT4 peptide.	354
Figure A4.6. Analytical HPLC trace of DFAA-OT4, monitoring at 400 nm.	354
Figure A4.7. Attenuated total reflectance (ATR)-IR spectra of DFAA-OPV3 (left) and DFAA-OT4 (right) in solid state.	355
Figure A4.8. ATR-IR spectra of lyophilized acidic solutions of DFAA- (a) OPV3, OT4, and (b,c) coassemblies.	355
Figure A4.9. Representative TEM images showing the nanostructures from a 0.1 wt% acidic solution of DFAA-OT4.	356
Figure A4.10. Representative TEM images of the nanostructures from a 0.1 wt% acidic solution of coassembled DFAA-OPV3/-OT4 at different mol% DFAA-OT4.	356
Figure A4.11. Representative TEM images of the nanostructures from a 0.1 wt% acidic solution of (a) coassembled DFAA-OPV3/-OT4 (1:1) and a solution wherein (b) DFAA-OT4 was added to pre-assembled DFAA-OPV3 solution (1:1).	356
Figure A4.12. Plots showing the spectral overlap between the DFAA-OPV3 donor emission and DFAA-OT4 acceptor absorbance for basic (left) and (right) acidic solutions.	357
Figure A4.13. Lifetime decay profiles ($\lambda_{\text{exc}} = 375$ nm) of pure donor and coassemblies under (a) basic (ca. pH 10) and (b,c) acidic (ca. pH 2) conditions.	357
Figure A4.14. Lifetime decay profiles ($\lambda_{\text{exc}} = 340$ nm) of pure donor and coassemblies under acidic (ca. pH 2) conditions.	357
Figure A4.15. ^1H (400 MHz, D_2O) NMR spectrum of OT4-Ac peptide.	358
Figure A4.16. ^1H (400 MHz, D_2O) NMR spectrum of OT4-NDI peptide. Peak broadness can be attributed to the aggregation of the material even at high pH. A presaturation pulse was applied during spectrum acquisition to suppress water.	358
Figure A4.17. ESI-MS spectrum of OT4-Ac peptide.	359
Figure A4.18. Analytical HPLC trace of OT4-Ac, monitoring at 400 nm.	359
Figure A4.19. ESI-MS spectrum of OT4-NDI peptide.	360

Figure A4.20. Analytical HPLC trace of OT4-NDI, monitoring at 400 nm.....	360
Figure A4.21. pH titration curves for the homoassemblies of OPV3, OT4-NDI and OT4-Ac, and co-assemblies of OPV3 with OT4-Ac and with OT4-NDI (1:1 mixture). Plateaus on the curve indicate the apparent pK_a of the gelators.....	361
Figure A4.22. Monitoring of GdL-triggered gelation via ^1H NMR for OT4-NDI and OPV3 mixed sample; final concentration of each peptide component is 5 mg/mL; prepared with 30 mg/mL GdL [no resonances were observed for pure OT4-NDI solutions even at high pH].	361
Figure A4.23. Rheology plots (G' = solid circles; G'' =smaller circles) for peptide homoassemblies and mixed assemblies prepared with 30 mg/mL of GdL. Each peptide component is at 5 mg/mL (total of 10 mg/mL peptides for the 1:1 mixed samples; 5 mg/mL for the pure peptide samples).....	362
Figure A4.24. TEM images of OPV3, OT4-Ac, OT4-NDI homoassemblies ([peptide]= 3 μM) prepared with HCl addition and GdL (10 mg/mL).	362
Figure A4.25. UV-vis absorption spectra for GdL- (10 mg/mL) and HCl-coassembled peptide structures of OPV3 with OT4-Ac (red) and with OT4-NDI (black); measured under different conditions: a) with GdL empty circles), b) with HCl (—), and c) with HCl, aged (...); [OPV3]= 3 μM	363
Figure A4.26. Circular dichroism spectra for GdL- (10 mg/mL) and HCl- assembled peptide structures with a,b) one-component/ homo-assemblies, [peptide]= 3 μM ; c) 10 mol% and d) 50 mol% OT4-Ac and OT4-NDI in OPV3, [OPV3]= 3 μM	363
Figure A4.27. Dynode voltage vs. wavelength plots for the CD spectra in Figure A4.26; GdL- (10 mg/mL) and HCl- assembled peptide structures with a,b) one-component/ homo-assemblies; c) 10 mol% and d) 50 mol% OT4-Ac and OT4-NDI in OPV3; [OPV3]= 3 μM	364
Figure A5.1. ESI-MS spectrum of HO-(A1- ^{13}C -VAVKIEAA) $_2$ -OT4.	365
Figure A5.2. Analytical HPLC trace of HO-(A1- ^{13}C -VAVKIEAA) $_2$ -OT4, monitoring at 400 nm.	365
Figure A5.3. ESI-MS spectrum of HO-(A1- ^{13}C -A2- ^{15}N -EAA) $_2$ -OT4.	366
Figure A5.4. Analytical HPLC trace of HO-(A1- ^{13}C -A2- ^{15}N -EAA) $_2$ -OT4, monitoring at 400 nm.	366
Figure A5.5. ESI-MS spectrum of HO-(A1- ^{13}C -EAA) $_2$ -OT4.	367

Figure A5.6. Analytical HPLC trace of HO-(A1- ¹³ C-EAA) ₂ -OT4, monitoring at 400 nm.	367
Figure A5.7. ESI-MS spectrum of HO-(A2- ¹⁵ N-EAA) ₂ -OT4.	368
Figure A5.8. Analytical HPLC trace of HO-(A2- ¹⁵ N-EAA) ₂ -OT4, monitoring at 400 nm.	368
Figure A5.9. ESI-MS spectrum of HO-(A1- ¹³ C-A2- ¹⁵ N-DFAA) ₂ -OPV3.	369
Figure A5.10. Analytical HPLC trace of HO-(A1- ¹³ C-A2- ¹⁵ N-DFAA) ₂ -OPV3, monitoring at 365 nm.....	369
Figure A5.11. ESI-MS spectrum of HO-(A1- ¹³ C-DFAA) ₂ -OT4.....	370
Figure A5.12. Analytical HPLC trace of HO-(A1- ¹³ C-DFAA) ₂ -OT4, monitoring at 400 nm.	370
Figure A5.13. ESI-MS spectrum of HO-(A2- ¹⁵ N-DFAA) ₂ -OPV3.....	371
Figure A5.14. Analytical HPLC trace of HO-(A2- ¹⁵ N-DFAA) ₂ -OPV3, monitoring at 365 nm.	371
Figure A5.15. ESI-MS spectrum of HO-(DFAA-d ₄) ₂ -OT4.....	372
Figure A5.16. Analytical HPLC trace of HO-(DFAA-d ₄) ₂ -OT4, monitoring at 400 nm..	372
Figure A5.17. ¹³ C (400 MHz, CDCl ₃) NMR spectrum of 2,5-dibromothiophene (d ₂)..	373
Figure A5.18. ¹³ C (400 MHz, d ₆ -DMSO) NMR spectrum of 5-bromothiophene-2- carboxylic acid (d ₂); peaks at 56 and 19 ppm are from tetrahydrofuran.	373
Figure A5.19. ¹ H (400 MHz, D ₂ O) NMR spectrum of DFAA-OT4 (d ₄) peptide.....	374
Figure A5.20. 1-D ¹³ C cross polarization spectra of N. A. EAA-OT4. (a) N. A. EAA-OT4 on 500 MHz spectrometer; (b) N. A. EAA-OT4 on 800 MHz spectrometer.; (c) A2- ¹⁵ N- EAA-OT4 on 500 MHz spectrometer.....	374
Figure A5.21. 1-D ¹³ C cross polarization of N.A. DFAA-OPV3.	375
Figure A5.22. Mapping of DRAWS signal contribution. Red: ¹³ C nucleus; Gray: ¹² C nucleus. Considering three neighboring carbon nuclei in a row, if the middle one is ¹³ C, the two peripheral ones can be both ¹³ C (case a, 25% probability), one ¹³ C and one ¹² C (cases b and c, 25% probability each), or both ¹² C (case d, 25% probability)	376

Figure A5.23. Representative images of 1 wt% peptide solutions and hydrogels. (a) EAA-OT4 in basic solution; (b) self-supporting EAA-OT4 hydrogel after HCl addition; (c) DFAA-OPV3 in basic solution; and (d) self-supporting DFAA-OPV3 hydrogel after HCl addition	376
Figure A5.24. SANS curves for DFAA-OPV3 and DFAA-OT4 at 0.2 wt% solutions in D ₂ O. Data fitting was done with a Guinier-Porod model.	377
Figure A5.25. SANS curves for mixed DFAA (d ₄) OT4 and OPV3 (mol% of OT4 indicated) in 40% D ₂ O in H ₂ O. Data fitting was done with a parallelepiped model.	378
Figure A5.26. SANS curves for 10:90 (DFAA OT4 d ₄ : DFAA OPV3) at 0.2 wt% and 1 wt%, in different temperatures.	379
Figure A6.1. ¹ H (600 MHz, D ₂ O) NMR spectrum of VAVKIEAA-OT4 peptide	380
Figure A6.2. ¹ H (400 MHz, D ₂ O) NMR spectrum of DK(Alloc)VV-diacetylene peptide.	381
Figure A6.3. ¹ H (400 MHz, D ₂ O) NMR spectrum of DK(biotin)VV-diacetylene peptide.	381
Figure A6.4. ESI-MS spectrum of HO-(VAVKIEAA) ₂ -OT4.	382
Figure A6.5. Analytical HPLC trace of HO-(VAVKIEAA) ₂ -OT4, monitoring at 400 nm.	382
Figure A6.6. ESI-MS spectrum of HO-(DK(Alloc)) ₂ -diacetylene peptide.	383
Figure A6.7. Analytical HPLC trace of HO-(DK(Alloc)) ₂ -diacetylene peptide, monitoring at 260 nm.	383
Figure A6.8. ESI-MS spectrum of HO-(DK(biotin)) ₂ -diacetylene peptide.	384
Figure A6.9. Analytical HPLC trace of HO-(DK(biotin)) ₂ -diacetylene peptide, monitoring at 260 nm.	384
Figure A6.10. Modified electrospinning setup for fiber hydrogel processing.	385
Figure A6.11. WST-1 proliferation assay, data within five days of Schwann cell culture with the hybrid fiber (alginate + VAVKIEAA-OT4).	385
Figure A6.12. Representative rheology plot for co-spun fiber bundles of alginate and VAVKIEAA-OT4 at 1 Hz and 5% oscillation strain.	386

Figure A6.13. Bulk rheology measurements (dynamic oscillatory frequency sweep) for 2 wt% DK(bio)VV-diacetylene hydrogels under different irradiation times with a 4-W 254 nm source. Solid and empty shapes represent storage (G') and loss moduli (G''), respectively. 386

Figure A6.14. (a) Stitched images showing a Day 8-DRG explant in culture on TCPS substrate and (b) a Day 1-DRG explant on DK(Alloc)VV-polydiacetylene; The stitched region is indicated by the dashed lines in (a); immunostained images against neurofilament. 387

Figure A6.15. Relative mRNA expression of hNSCs seeded on P3HT/PCBM films after 11 days in culture. All results were normalized with respect to non-irradiated TCPS samples. 387

Figure A6.16. Bioreactor setup used to apply 10% strain to fibrin and fibrin-PPy for current vs. time recordings and in vitro NRVM culture.. 388

Figure A6.17. Current response over time for fibrin-PPy bundles. The material was strained manually (~10%), for every 10 s. 388

CHAPTER ONE:

Introduction—Merging Organic Electronics and
Peptide-Based Supramolecular Systems

π -Conjugated Systems for Organic Electronics

Since the groundbreaking reports on conjugated conducting polymers from 1970s, to the Nobel Prize recognition for Heeger, MacDiarmid and Shirakawa in 2000 for the discovery of iodine-doped polyacetylene as a conductive polymer,¹ a broad range of potential applications—from semiconductors, to energy storage applications, and to biomedical applications—has been realized for π -conjugated polymeric materials. Driven by the general motivation to develop solution processable or printable, flexible, and low-cost components for large scale electronic circuits, several of these organic π -conjugated systems have been incorporated for device applications as active semiconductor components. Despite the variety of applications possible for these materials, tuning the charge transport properties *via* precise ordering of π -units (*e.g.*, carrier generation and propagation) remains to be a challenge.²⁻⁴ This is a critical aspect to consider when developing functional optoelectronic elements such as light-emitting diodes, photorefractive materials, sensors, field-effect transistors and photovoltaics.⁵⁻¹⁰

Supramolecular engineering has since then received tremendous attention as a key strategy to build functional π -conjugated organic materials in a bottom-up manner with controllable ordering pattern for gels, liquid crystals, nanoribbon, nanotubes, nanorods or nanowires. This also allows the incorporation of multicomponent systems (*e.g.*, for bulk heterojunction systems) to provide different functionalities in rationally engineered supramolecular materials.^{6,11-13} For this bottom-up strategy, the material processing technique and the design of the monomers both play a crucial role in the final structure and material function. Functionalization of π -units with groups bearing supramolecular synthons has been a widely used strategy to encourage supramolecular polymerization with

tunable nano- to microscale morphologies. This requires the synthesis of monomeric units that can exhibit long-range order which can be controlled by the molecular structure.¹⁰ Non-covalent interactions between hierarchically ordered structures are prevalent in Nature and can serve as an inspiration for synthetic systems that exhibit controllable self-assembly.^{10,14,15} Among the different groups used to assist in the ordering of π -systems, biologically-relevant macromolecules offers the potential to construct diverse bioelectronic nanomaterials.^{5,8,16} Shown in Figure 1.1 are some examples of functional supramolecular polymers derived from organic monomers, some of which are appended with active π -units or with bioinspired hydrogen-bonding moieties such as peptides.

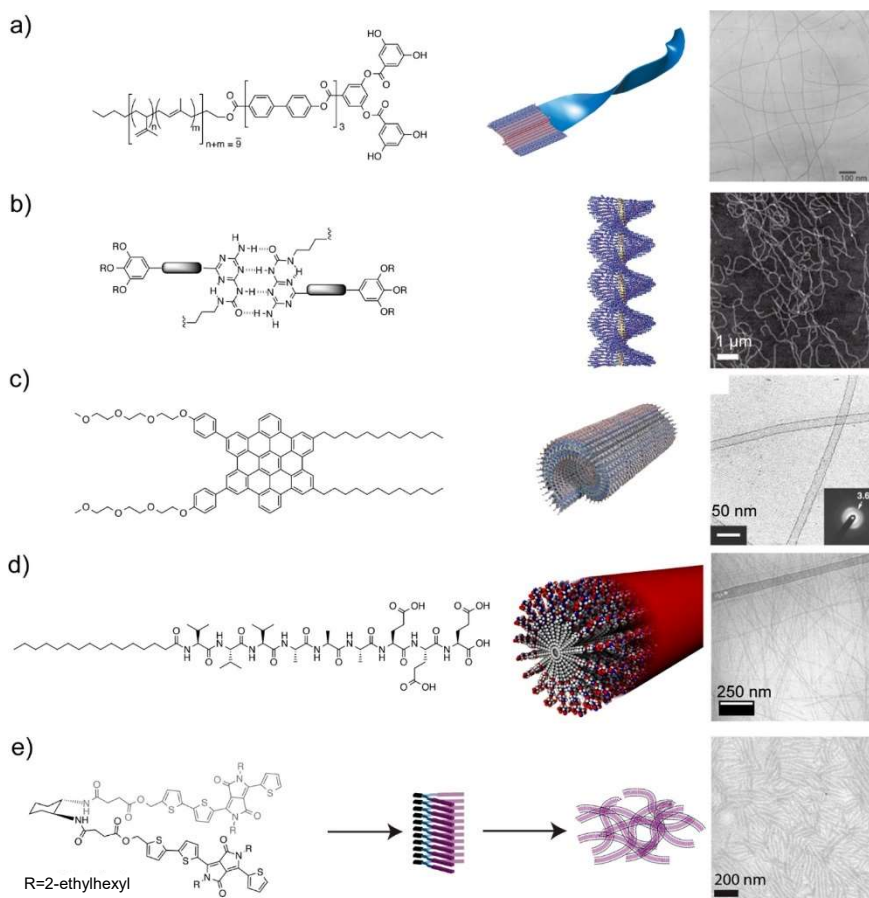


Figure 1.1. Structure, schematic of assembly morphology and nanoscale structure of 1D-materials based on π -conjugated units¹⁶ (Copyright 2014 American Chemical Society).

Figure 1.1a shows a pioneering example from Stupp and co-workers involving a dendron rod-coil compound that assembles into nanoribbons. Within the blocked architecture of each monomer consisting of a rod-like, coil-like and dendron segments, the assembly is driven by hydrogen-bonding between the hydroxyl groups of the dendron segment and the π - π stacking between the biphenyl groups. Figure 1.1b is a self-assembling system reported by Schenning, Meijer and co-workers with a unique quadruplex hydrogen-bonding scheme and involves an oligo(*p*-phenylenevinylene) units on the monomer that assembles into twisted ribbons. Figure 1.1c-e show other self-assembling systems driven by non-covalent interactions reported by the Stupp group, with nanotube-forming amphiphilic hexabenzocoronene in Figure 1.1c, peptide amphiphile nanofibers in Figure 1.1d, and a hairpin-shaped monomer with diketopyrrolopyrrole that can act as an electron donor for organic photovoltaics in Figure 1.1d.

Peptide- π Electron Conjugates

The molecular design of self-assembling π -conjugated peptide units requires careful consideration of the enthalpic stabilization derived from π -electron-centered quadrupolar interactions and peptide-centered intermolecular hydrogen bonds balanced with entropic/solvation factors. The intermolecular forces in these systems allow for aqueous assembly into supramolecular structures that are responsive to environmental conditions depending on the functional groups attached. This mechanism of self-assembly is akin to peptide fibrillization associated with the formation of insoluble deposits such as protein amyloid plaques. Figure 1.2 shows the stepwise organization of oligopeptide assembly as described by Boden and co-workers, with peptide units that assemble as β -

sheet tapes with left-handed twists along the long axis of the tape based on the chirality of *L*-amino acids.^{17,18} This then leads to chemically anisotropic lateral association of tapes into ribbons, whereby the attraction energy between the ribbons stabilizes the higher order fibrillar assemblies. Furthermore, the resulting twists determine the thickness of the nanostructures because they impose geometric packing constraints.¹⁷

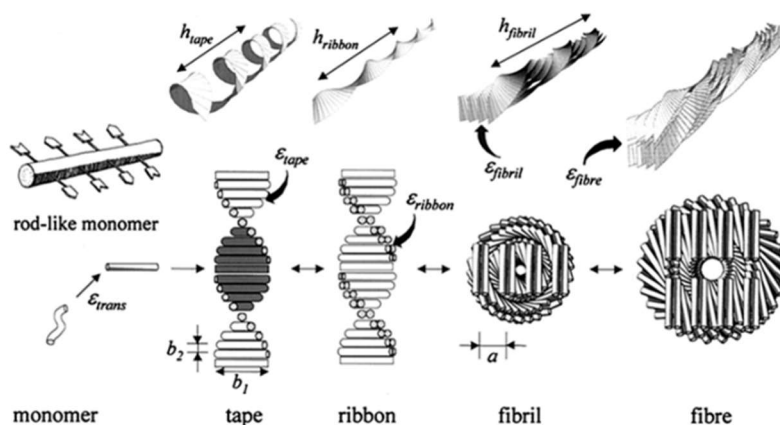


Figure 1.2. The proposed model for stepwise self-organization of oligopeptides, from single beta-sheet tapes to higher-order fibrillar structures.¹⁷ Copyright (2001) National Academy of Sciences, U.S.A.

It is also highly important to consider the assembly dynamics of such self-assembling peptides, as well as the thermodynamic and kinetic parameters involved in supramolecular polymerization.^{19,20} There are several studies reported about the theoretical foundations of covalent polymerization, however, the mechanistic framework for non-covalent assemblies is less established. It is specifically challenging to perform computational studies on water due to the size and complexity of systems, as well as solvation effects from water.¹⁹ The most recent computational work focused on peptidic systems used (coarse-grained) molecular dynamics or Monte Carlo simulation.²¹⁻²³ Although there are continuous advancements in the computational methods which can

provide more mechanistic insights about noncovalent polymer synthesis, it is still important to show evidence in actual experimental setups and establish correlations between the structural design of the monomer to its assembly behavior and performance as a material. Ashkenasy and co-workers demonstrated the dependence of conductivity on the morphology of peptide fibrils.²⁴ Meijer and co-workers took inspiration from the different aggregation pathways in protein, and studied the competing pathways for the assembly of hydrogen-bonded oligo(*p*-phenylenevinylene) oligomers under kinetic conditions.²⁵ Two parallel pathways, one kinetic and the other thermodynamic, produce assemblies with opposite helicity that have final structures affected by the metastable structures during the process of aggregation. Stupp and co-workers reported that peptide amphiphiles, which are of high interest as artificial extracellular matrices for regenerative medicine, have assembly and hydrogelation behaviors that are dependent on concentration, temperature and salt content of the environment (Figure 1.3).²⁶ When used as a substrate for the growth of myoblast progenitor cells, the rate of filopodia spreading and cell spreading was found to be highly dependent on the length of individual hydrogel fibers. Thus, the thermodynamic state is correlated to cytotoxicity. In a related study for these amphiphilic materials, they have shown the presence of a “good” solvent such as hexafluoroisopropanol destabilizes the formation of β -sheet structures and that such structures show high kinetic stability.²⁷ Therefore, the pathway selected for the preparation of such peptide fibers affect the final morphology and even the cytotoxicity of the fibrous material.

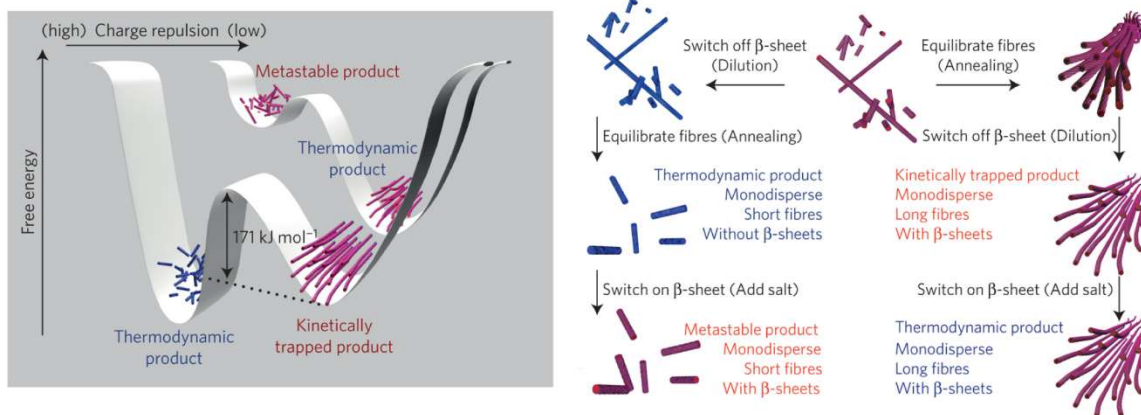


Figure 1.3. A schematic representation of the energy landscapes for peptide amphiphile self-assembly and the different conditions and pathways that favor β -sheet formation of thermodynamic, kinetic and metastable fibrillar products (Adapted from Ref. 26).

For peptide-bound π -electron constructs, the geometrical constraints imposed by peptide stacking/hydrogen-bonding force the π -units to interact more cofacially which is not entirely favorable in terms of electrostatics. The balance between these enthalpic factors contribute to the high reliability of peptides in forming well-defined structures. Because of the importance of electrostatic considerations, one of the most common stimuli to initiate self-assembly is pH. This aspect is very relevant to peptides, considering that the relevant pK_{as} can be tuned according to the choice of amino acid sequence.²⁸ The presence of multiple charged residues would cause Coulombic repulsion at certain pH conditions, causing the self-assembly process to be less favored, while multiple hydrophobic units present insolubility issues.

In selecting the π -electron system and amino acid sequence, the formal nature of the intermolecular hydrogen-bonding patterns expected to form among the constituent peptides must be considered. This is very important for the functional outcome of the peptide aggregates because the nature of the intermolecular hydrogen bonding network

(*e.g.*, parallel or antiparallel β -sheet) is expected to have a direct influence on the geometries of the intermolecular π -electron interactions, thus influencing energy transport efficiency.²⁹ Furthermore, the individual peptide sequences affect the structural motif formed during assembly because each amino acid has different inherent propensities to form different motifs.³⁰⁻³³ For example, β -sheet forming sequences are known to lead to tape-like structures while α -helices favor coiled-coil motifs, both of which can also result in distinct nanostructural assemblies.³⁴ The ability of alkyl groups to foster van der Waals interactions can result in the formation of lamellar superstructures and other higher-order assemblies such as those found in peptide amphiphiles. This provides another design component in addition to the π - π interactions.^{27,35-37} There are several reports illustrating the morphological effects of peptide sequence such as the fluorenylmethoxycarbonyl (Fmoc)-protected peptide-based hydrogelators studied by Ulijn and co-workers. These studies highlight that antiparallel β -sheet and antiparallel π -stacking of the fluorenyl groups are required to satisfy the formation of a cylindrical nanostructure.³⁸ Lee and co-workers reported a rational way of tuning the nanostructural output by controlling the hydrogen bonding interactions between pyrene-functionalized tripeptide units.³⁹ By simply changing the end functional groups at the *N*-termini (Figure 1.4), the morphological outcomes ranged from spherical hollow capsules to linear nanoribbons.

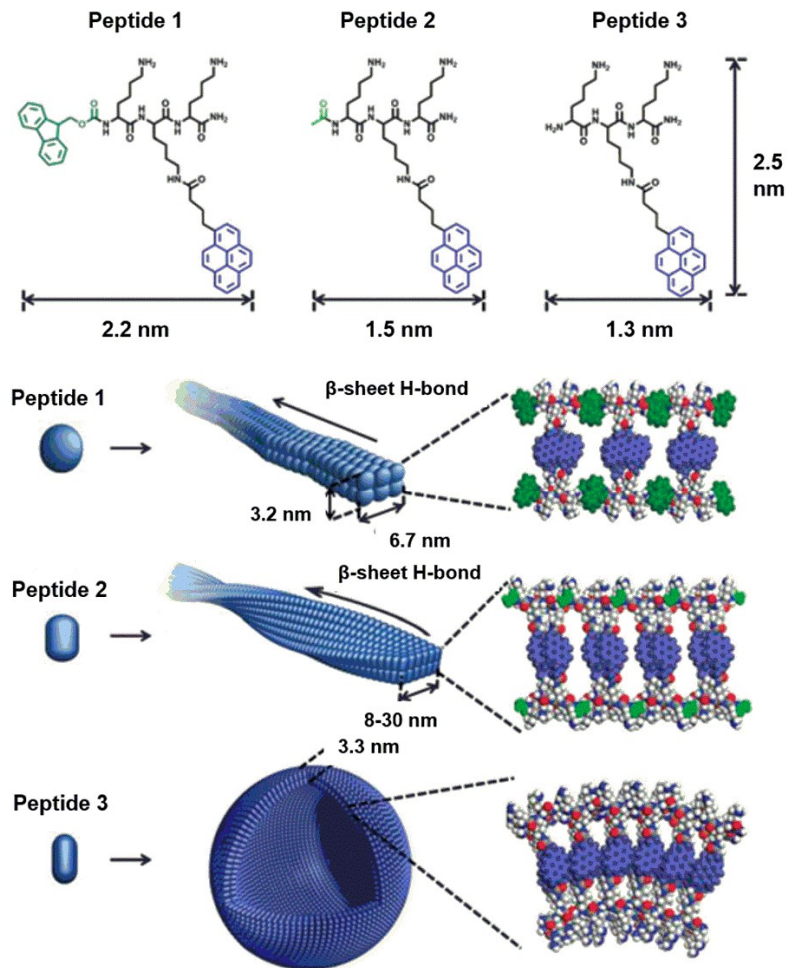


Figure 1.4. Self-assembling peptides functionalized with pyrene *via* lysine appendages. Variation of the functional groups at the *N*-termini results in different morphological outcomes.³⁹

New extensions towards synthesis of π -conjugated peptides require efficient ways of incorporating π -electron systems into or onto peptide backbones while considering synthetic hurdles such as insolubility. Several π -electron units can be attached to peptides *via* classical amide-bond forming chemistries akin to amino acid couplings. Early examples employed synthetic routes that utilized π -conjugated “amino acid” precursors, which often required lengthy synthetic procedures in order to functionalize the π -electron systems and enable their solid-phase coupling within a peptide backbone.⁴⁰⁻⁴² Other examples of peptide- π hybrids were synthesized using solution-based reactions that couple the π -system

within or at the end of the main peptide chain (or the side chains).^{37,43,44} Although solution-phase synthesis gives better yields, solid-phase synthesis enables the construction of longer peptides and coupling with longer, insoluble π -electron systems.^{43,45} Solid-phase synthetic approaches that are generally applicable to a wide variety of π -electron units were developed by Tovar and co-workers.^{45,46} This is important because the isolated early examples of peptide π -electron conjugates were limited to specific chromophore compositions. For example, solid-phase amidations and Pd-catalyzed reactions were used to initiate “dimerization” reactions between π -electron units and resin-bound peptides that after cleavage from the resin resulted in peptide- π -peptide triblock molecules.⁴⁵ The Pd-catalyzed route has been especially applicable to longer oligothiophene units because the inherent insolubility of the requisite building blocks (*e.g.*, quaterthiophene to sexithiophene diacids, which contain enough thiophene repeat units required to initiate charge transport) limited reasonable synthetic preparation.⁴⁴ Figure 1.5 shows some of these solid-phase synthetic routes.

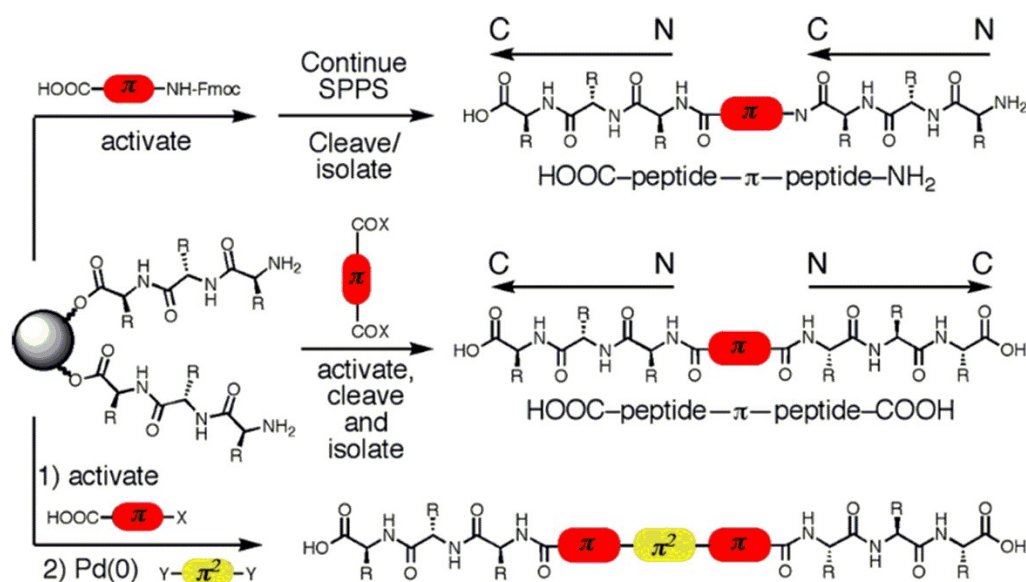


Figure 1.5. General synthetic strategies used for the construction of peptide- π system hybrids.^{31,45,46} Adapted from Ref. 8.

Several examples of π -conjugated systems bound to peptide moieties utilize chromophores that have semiconducting capabilities or unique photophysical properties. The field of peptide self-assembly itself is very rich and well-studied, and it provides multiple insights for the construction of hierarchically ordered electronic materials based on peptides. Utilizing common intermolecular interactions such as hydrogen-bonding and π -stacking, a very impressive array of peptide- π conjugates has been synthesized in order to have peptide-mediated assembly that allows for electronic delocalization between the π -units (Figure 1.6). In addition to the diversity of oligopeptide sequences and π -electron systems that can be installed, there are several other design iterations of peptide and π -electron system hybrids that are reported in the literature such as peptide with π -groups as side chains, peptide- π -peptide units, π -peptide- π units—all of which lead to engineered nanostructures with distinct morphologies. The following sections will discuss some of the key examples of π -conjugated peptides from the current literature.

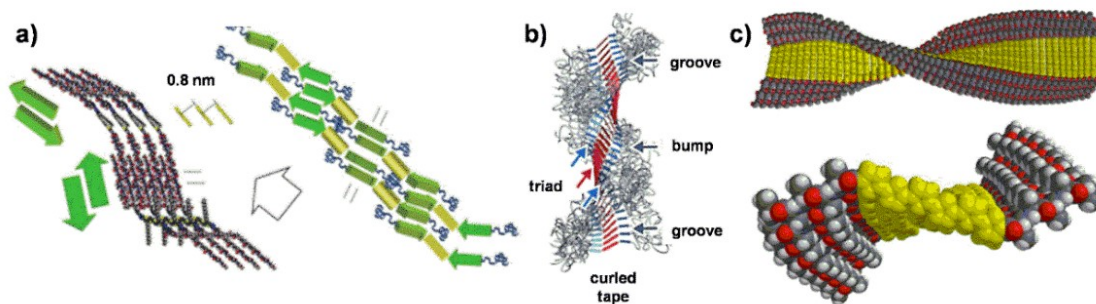


Figure 1.6. Computational self-assembly models for a) poly(ethylene oxide)-peptide-oligothiophene; b) poly(isoprene)-peptide-polydiacetylene; and c) peptide-oligothiophene conjugates. Adapted from Ref. 37,47,48.

Polythiophenes represent a powerful class of semiconducting materials, the archetype being poly(3-hexylthiophene) (P3HT), which is now widely employed in organic electronic devices such as in solar cell prototypes and field effect transistors (FET).

Bäuerle and co-workers reported the first example of a peptide-oligothiophene conjugate, derived from a quater(3-hexylthiophene) coupled to a silk-inspired oligopeptide sequence, whose optical and electrochemical properties are similar to the parent quaterthiophene.⁴⁹ Based on this initial report, Bäuerle and co-workers presented another peptide-oligothiophene derivative that contains PEO block segments in order to facilitate solubility.³⁷ Alternating valine and threonine residues were incorporated in order to have high propensities towards β -sheet formation, while pseudoproline “switch ester” moieties served to frustrate aggregation. Fibrillar structures resulting from self-assembly were successfully observed in dichloromethane and methanol mixture (Figure 1.7a,d).

Stupp and co-workers have studied several oligothiophene-conjugated peptide diblock assemblies. An initial report on terthiophene peptide lipids showed that they assemble into one-dimensional nanostructures (Figure 1.7.b,e).⁵⁰ They also reported a triblock variant whereby β -sheet tetrapeptides were substituted onto a center quinquethiophene.⁴⁴ This peptide- π -peptide triblock design incorporates examples with alkyl spacers to promote solubility and add more flexibility to the structure in organic media. Spectroscopic investigations support the π - π overlap driven by the hydrogen-bonding moieties, resulting in observed conductivities. The observed nanostructures showed helical twists as supported by AFM and TEM. Frauenrath and co-workers also utilized quaterthiophene-peptide conjugates with alkyl moieties, having poly(isobutylene)s units at the termini of peptide-quaterthiophene-peptide triblocks.⁴⁷

A series of oligothiophene-embedded peptides that self-assemble in completely aqueous environments was also previously reported from the Tovar group (Figure 1.7c,f). The initial example was a peptide-bithiophene-peptide molecule by Stephen Diegelmann

in Tovar group, wherein the central bithiophene was attached *via* solid-phase amidation of a bithiophene “amino acid” to the free amine termini of the resin-bound oligopeptide.⁴⁰ The assembled structures that formed under acidic conditions were observed using AFM to reveal one-dimensional structures (2-6 nm heights) reminiscent of the early thermodynamic sinks in the process of amyloid-like fibril formation. Peptide-oligothiophene-peptide triblocks were also afforded by solid-phase amidation/”dimerization” between diacid-functionalized ter- and quaterthiophenes and the free amine termini of the resin-bound oligopeptides, a synthetic route jointly developed by Geeta Vadehra, Brian Wall and Stephen Diegelmann in the Tovar group.⁴⁶ More recently, the scope of π -conjugation length that can be attached was broadened *via* Pd-catalyzed cross coupling as developed by Allix Sanders in the Tovar group.⁴⁵ From bithiophene to sexithiophene, all of the resulting peptide-oligothiophene-peptide triblock molecules showed pH-triggered self-assembly as confirmed by the observation of spectroscopic signatures consistent with H-aggregates only under acidic conditions.

In addition to targeting β -sheet motifs, Holmes and co-workers⁵¹ reported sexithiophenes attached to α -helical poly-*L*-lysine which forms organogels at 2 wt% in cyclohexane. Organic photovoltaic and field-effect transistors (FET) were fabricated out of these materials, wherein the semiconductor peptide was blended with phenyl-C₆₀-butyric acid methyl ester (PCBM) to form a donor-acceptor system that was used for the photovoltaic device and as an active semiconducting unit for the FET. Although the hole mobilities measured for their active material were low, and the performance of photovoltaic devices were lower than with P3HT, this example still presented bioinspired devices

utilizing α -helical peptide-based semiconductors that can potentially operate under biologically-relevant environments.

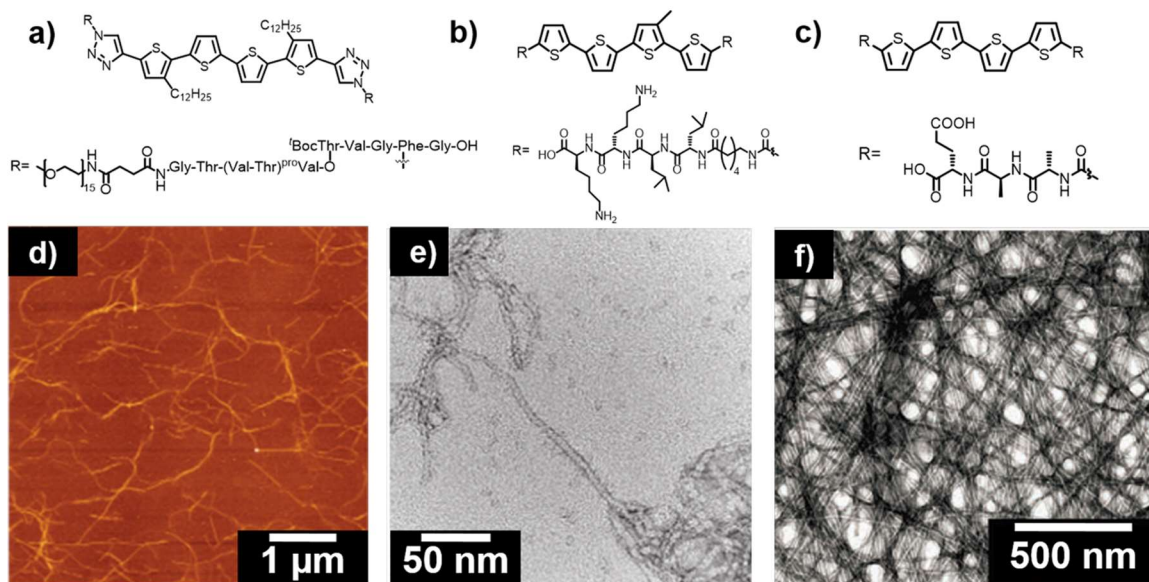


Figure 1.7. Molecular structures (a-c) and the corresponding nanostructural morphologies (d-f) observed upon self-assembly of different thiophene-based peptide units.^{37,44,48}

There were also several reports on oligophenyls appended to peptide moieties. One of the earliest incorporations of an extended π -electron system within an oligopeptide backbone was reported by Chmielewski and co-workers,⁴¹ which involved a cyclic peptide with an internal azobenzene amino acid that functioned as a conformational switch (Figure 1.8a). Although no self-assembly between the cyclic peptide monomers was presented, the azo linkage provides a photoregulated switch from a *cis* to a *trans* linkage that controlled the extent that monomers adopted a β -turn conformation. Likewise, Nowick and co-workers used non-natural amino acids to form water-soluble molecular rods (Figure 1.8b).⁴² Using 4'-amino-[1,1'-biphenyl]-4-carboxylic acid, they reported peptide- π -peptide triblocks with biphenyl groups at the core. These building blocks were later on utilized for the construction of water-soluble macrocycles with well-defined shapes.⁵² The

Tovar group have also shown self-assembling peptide- π -peptide hydrogelators with biphenyl, terphenyl, (Figure 1.8c-d) and alternating thiophene and phenyl units as the central π -electron core using either solid-phase amidation of a pre-formed chromophore or on-resin Pd-catalyzed cross coupling to build complex π -electron cores.^{45,46}

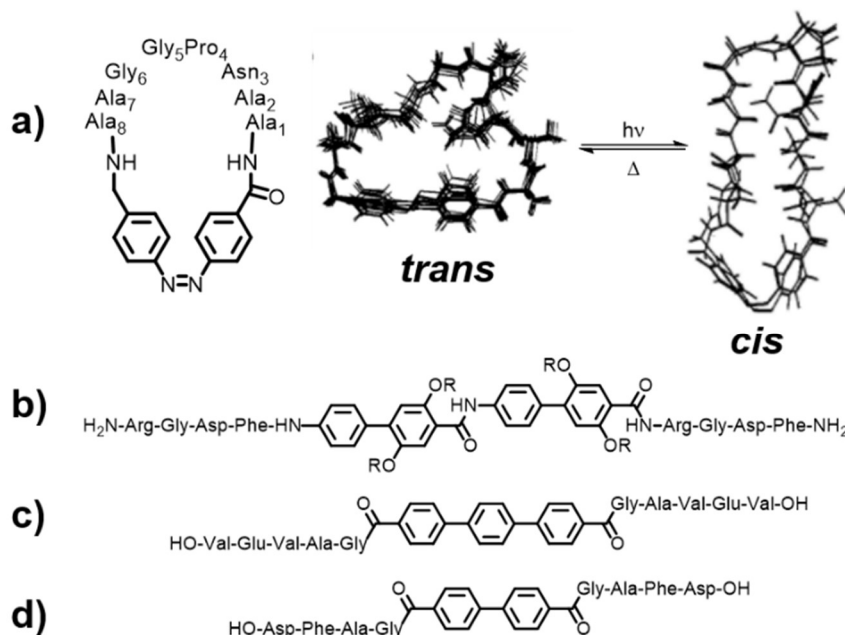


Figure 1.8. Molecular structures of a) photoswitchable azobenzene-peptide conjugates (and diagram for the superposition of structures for the two isomers)⁴¹; and (b,⁴² c,⁴⁵ d⁴⁶) some examples of water-soluble peptide-based oligophenyl assemblies.

Oligo(*p*-phenylenevinylene)s (OPV) are another well-studied class of organic semiconductors with notable fluorescence properties. One of the pioneering examples of OPV-peptide conjugates from Stupp and co-workers involves multiple *L*-lysine segments attached to a dendritic OPV unit that self-assembles in water.⁵³ Thin films from these peptide-OPV conjugates were used as a surface for 3T3 fibroblasts adhesion and the fluorescent amphiphiles were gradually taken up by the cells *via* an endocytic pathway, and thus accumulated in the lysosomes. This was notable because the nanomaterials survive the acidic conditions and proteolytic enzymes within the lysosome without a

substantial loss in fluorescence, thus showing the potential of these materials for biosensing and tracking of molecular delivery to cellular targets.

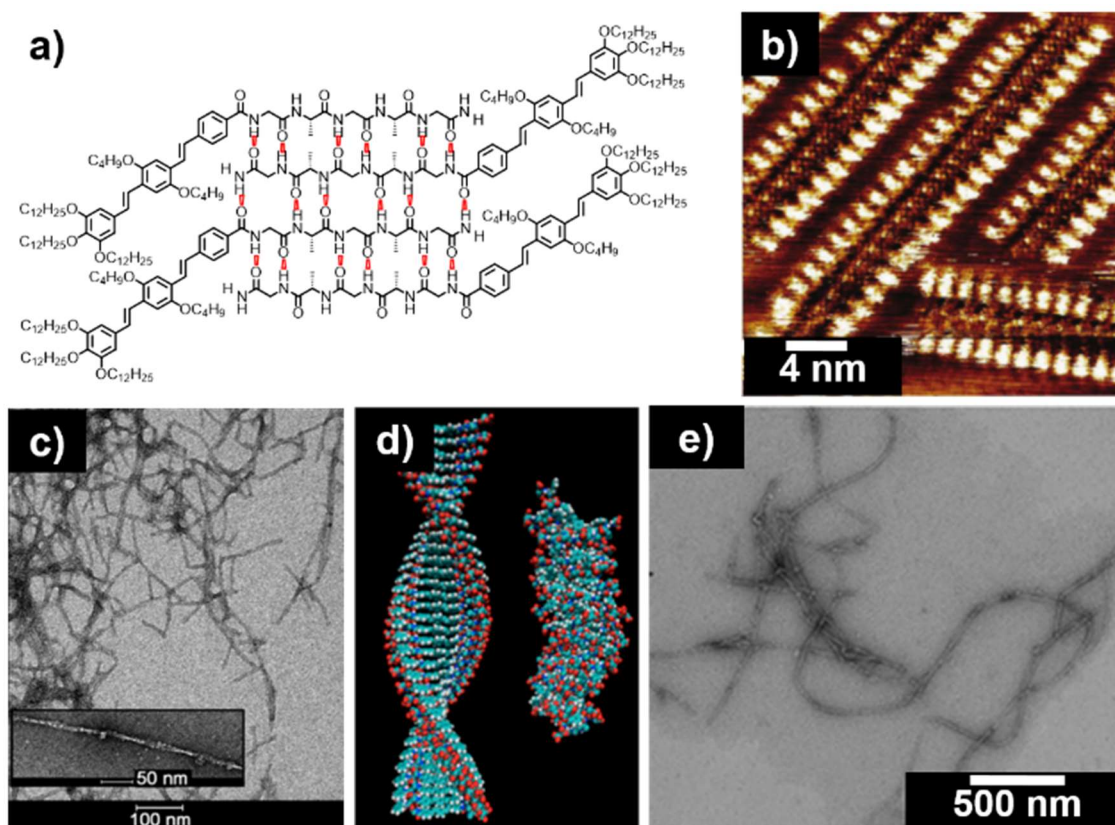


Figure 1.9. Different depictions of self-assembly for peptide-pi conjugates containing phenylene vinylene units: (a) a molecular image of Schenning and Meijer's peptide-OPV diblock molecules and (b) the associated STM image,⁴³ (c) TEM image of peptide-OPV-peptide by Maggini and co-workers,⁵⁶ (d) Ferguson's molecular dynamics simulations of the Tovar OPV nanomaterials before (left) and after (right) relaxation, and (e) the observed nanostructures imaged with TEM.³⁰

Meijer, Schenning and co-workers reported diblock OPV-peptide systems that show amphiphilic behavior and form cylindrical micelles in aqueous and organic solvents (Figure 1.9a-b).⁴⁵ The formation of nanofibers and assembly of OPV units was shown to be dependent on the peptide sequence for system. Further investigations on the incorporation of OPV into peptide backbones led to more molecular designs that can form supramolecular assembly under completely aqueous solution environments, which became one of the most studied π -conjugated peptides in our group in terms of photophysical

properties (Figure 1.9d-e).^{30,31} Later, Maggini and co-workers showed that related materials can be tailored to form gels in both acidic and basic conditions (Figure 1.9c).⁵⁶ Certain peptides were also shown to bind to poly(phenylene vinylene) surfaces via π - π interactions, having potential use for novel bioimaging and biosensing methods.⁵⁷

Polydiacetylenes (PDA) are also π -systems that have attracted attention because of their distinct chromic and sensing properties.⁵⁴ This is because their polymerized forms result in two distinct conformational extremes: a blue phase (~640 nm maximum absorption), which is reported to be nonfluorescent and under certain environmental stimuli, and a fluorescent red phase (~550 nm maximum absorption).^{55,56} The monomeric diacetylene precursor is known to undergo topochemical polymerization *via* 1,4-addition, provided that strict geometric requirements are achieved by the precursor crystal.⁵⁷ Frauenrath and co-workers developed a powerful system that uses hydrogen-bonded peptide regions to promote order among the diacetylene units and drives the polymerization within hydrogel or organogel networks. Their first generation peptide-PDA conjugates had poly(isoprene) units on one end which promotes solubility in organic solvents, tetra-*L*-alanine for anisotropic β -sheet formation, and the diacetylene unit on the other end (Figure 1.10a).⁵⁸ Upon polymerization, flat ribbon and tape-like nanostructures were observed. More recent structural interrogations of the assembly and how it depends on the molecular structure of supramolecular synthons involved peptide-diacetylene-peptide triblocks containing non-natural amino acids. For example, Wang and co-workers studied peptide-polydiacetylene conjugates bearing alkyl units that form aqueous cylindrical nanostructures. These structures can be maintained even under dry states.⁵⁹ However due to the steric bulk imposed by the phenyl group directly adjacent to the diacetylene group, the

blue-red transition is not as distinctly observed in this system as in others. The first report of a peptide-polydiacetylene conjugate from Tovar group demonstrated such reversible blue-red transition driven by pH changes in a self-assembled peptide- π -peptide triblock system with diphenyl butadiyne as the polymerizable unit rather than the traditional dialkyl butadiene monomers (Figure 1.10b).⁶⁰ This can be attributed to Coulombic repulsions among peptide chains at basic pH that caused the PDA backbone to twist out of planarity. Stupp and co-workers reported peptide amphiphile structures where the diacetylene unit was embedded within the hydrocarbon tail (Figure 1.10c). These molecules assembled into fibrous structures that formed PDA hydrogels in the blue phase, and the resulting nanomaterials had temperature-dependent chiroptical properties.⁶¹

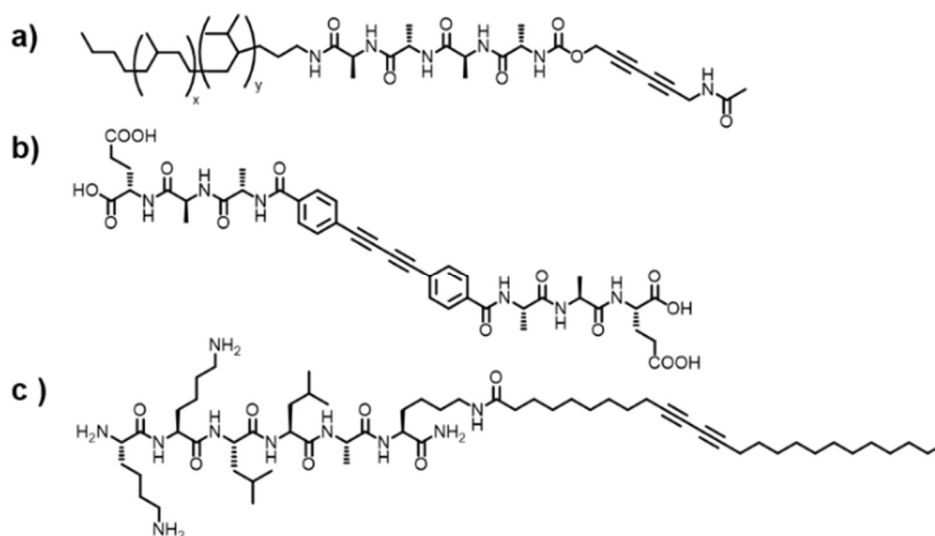


Figure 1.10. Molecular structures of different peptide-diacetylene hybrids.^{58,60,61}

The temperature and pH dependence of nanostructure formation and the effect of alkyl tail chain length was systematically studied by van Hest, Löwik, and co-workers for related peptide-diacetylene conjugates, showing that alkyl chain length affects the assembly and disassembly temperature while pH did not have a large influence on the assembly structure.⁶² Their group also reported another peptide-diacetylene amphiphile

whose assembled structures were able to be aligned under the influence of applied magnetic fields (Figure 1.11).⁶³

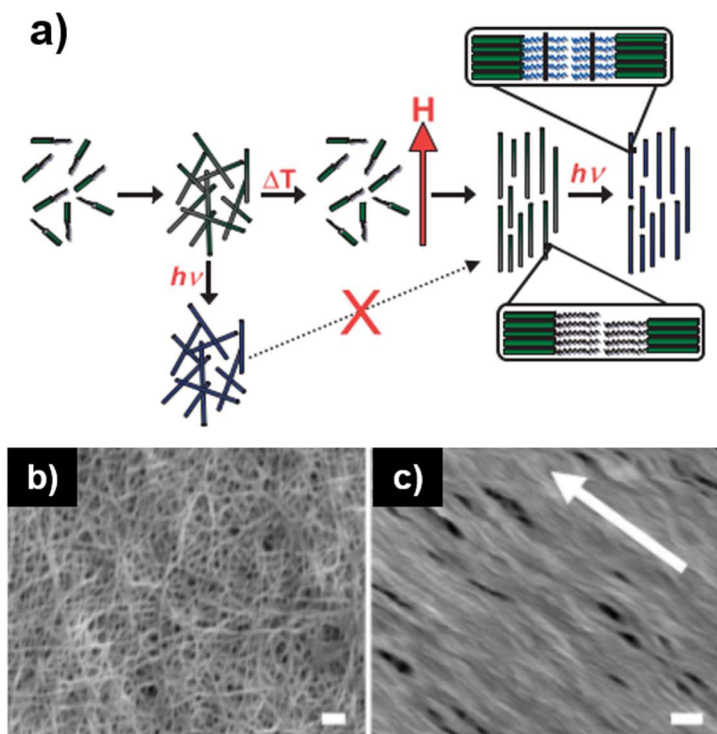


Figure 1.11. (a) Diagram showing the strategy to magnetically align peptide amphiphile assemblies. (green= polymerizable peptide-polydiacetylene amphiphile; blue= polymerized nanofibers; red= direction of the magnetic field); SEM images of (b) unaligned and (c) aligned peptide-diacetylene amphiphiles (scale bars= 500 nm). Adapted from Ref. 63.

In addition to the list of π -electron systems for creating functional peptide conjugates, aromatic diimides such as perylene diimide (PDI) and naphthalene diimides (NDI) are well-studied *n*-channel semiconductors that are considered as promising electron acceptors for solar energy conversion and molecular electronics.²⁹ Several studies on multichromophoric systems involved PDI as one of the building blocks.^{47,64,65} Ghadiri and co-workers explored cyclic peptides comprised of alternating *D*- and *L*-peptides as a template to promote ring stacking and charge transfer between NDI side chains.⁶⁶ With the

aim of improving the electronic conductivity of peptide nanotubes, they further investigated an eight-residue cyclic *D,L*-peptide with four NDI chains which has an overall self-assembly process that is redox-triggered.⁶⁷ Parquette and co-workers reported an interesting type of peptide-NDI conjugate (Figure 1.12), having dilysine peptides functionalized with NDI at the ϵ -amino position.⁶⁸ They synthesized a series of groups with varying hydrophobicities (H-, acetyl-, or Fmoc-protecting group) on the *N*-terminus of the peptide main chain.^{17,72} These types of molecules formed nanobelts in water and also led to self-supporting hydrogels. Their group also reported the self-assembly of NDI units with *L*-lysine headgroups and lysine-NDI-butyl amphiphilic conjugates that resulted in nanotube structures that were characterized by TEM and more atomistically by solid state NMR.^{69,70} Ashkenasy and co-workers reported fibril-forming short amphiphilic peptides with multiple lysines substituted with NDI units. In order to modulate the number of NDI units present in each fibril, NDI-containing peptides were coassembled with peptide units with similar sequence but the NDI-lysine positions were replaced with phenylalanines. They induced anion radical formation on the NDI units using sodium dithionite under anaerobic reduction conditions, resulting in fibril formation with less helical inter-NDI arrangement as shown by the disappearance of Cotton effect in the CD spectra.⁷¹

Other diimide examples involve direct embedding within the peptide backbone. Early reports of peptide-NDI and peptide-PDI 1-D nanostructures (< 10 nm in width) from the Tovar group showed pH-responsive that exhibited a conventional H-type aggregation under acidic environments similar to other dimerized peptide- π units.⁴⁶ Related peptide-PDI-peptide triblocks were also investigated by Hodgkiss and co-workers, who explored ionic effects and solvatochromism in the aggregation of the peptide-PDI units.⁷² The H-

aggregate character was significantly enhanced in the presence of divalent cation-containing salts (more specifically with Zn^{2+}). This is due to their strong ability to coordinate two glutamates between neighboring peptide-PDI conjugate units, which results in screening of charges and crosslinking of the PDI cores into more cofacial geometries. Frauenrath and co-workers presented a very detailed structural investigation of peptide-PDI-conjugates with flexible poly(isobutylene) units at the exterior.⁴⁷ Morphological investigations and molecular dynamics simulations support tight π - π stacking that can facilitate one-dimensional charge transport along the long axis of stacking irrespective of the electronic nature of chromophores. The poly(isobutylene)s at the exterior enhances the tight π - π stacking and also provides an insulating shell that can be relevant for utilizing these nanofibrils in organic electronic devices.

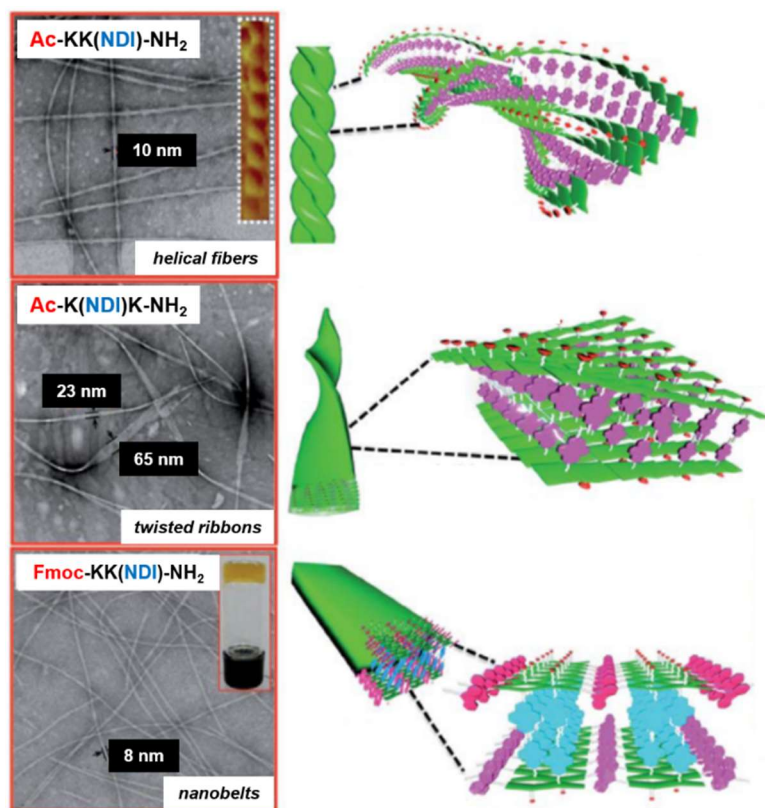


Figure 1.12. Illustration of the different self-assembly patterns reported for NDI-containing peptides. Adapted from Ref. 29 and 68.

Self-assembling peptides coupled with the fluorenyl-9-methoxycarbonyl (Fmoc) group and/or with multiple phenylalanine units also offer additional π - π interactions that can guide supramolecular interactions, inspiring a lot of π -conjugated peptides with optoelectronic activity. Indeed, several studies led independently by the groups of Ulijn, Gazit and Xu have provided extensive details on the properties and mechanisms of Fmoc- and oligophenylalanine-containing assemblies that effectively form self-supporting gels.^{38,73-77} Fmoc-diphenylalanine hydrogels have now found applications in biological sensing⁷⁸ and cell culture^{79,803-881,82} due to their ability to form hydrogels under physiological conditions. In addition, naphthalene, pyrene, and other small aromatic compounds have found applications to create low molecular weight peptide gelators.⁸³ Banerjee and co-workers reported the self-assembly of a pyrene-peptide conjugate that results in the formation of a transparent, self-supporting gel in various organic solvents and is specifically fluorescent in *o*-dichlorobenzene (Figure 1.13a).⁸⁴ However, since fluorene (in Fmoc) and pyrene are potentially carcinogenic, there is a need to look for other reliable aromatic units for hydrogelation such as naphthalene groups which are quite common fragments of clinically approved drug molecules.⁸³ Peptide-naphthalene conjugates are found to have high gelation efficiency (as low as 0.07 wt%) and cytocompatible based on cell toxicity assays (Figure 1.13b).⁸⁵ The biostability of naphthalene-diphenylalanine against proteinase K was also investigated.⁸⁶

Non-natural thienyl alanine units (either the 2- or 3-thienyl isomers),^{87,88} were also used to synthesize thienyl-containing oligopeptides that led to nanostructure formation. These nanomaterials are poised to facilitate charge delocalization as supported by quantum mechanical/molecular dynamics simulations. Hamley, Ashkenasy and co-workers found

that both electrons and protons (1:2 current ratio) contribute to the conduction of peptide functionalized with 2-thienyl units under low humidity conditions while protonic conduction dominates at high humidity.⁸⁹ This hybrid conductivity behavior was explained to be a function of peptide folding behavior which is highly dependent on the humidity range. New electroactive supramolecular fibers have also been formed by Kato and co-workers from tetrathiafulvalene (TTF) bound to an oligopeptide scaffold in aromatic liquid crystals.⁹⁰ Fibrous aggregates were observed under AFM, representing the first example of hydrogen-bonded one-dimensional aggregates having electroactive moieties whose electrical conductivities were measured after doping. Aligned fibers from this system were also studied, along with the exponential temperature dependence of conductivity of the fibers which is consistent with the behavior of a semiconductor. Moreover, partial oxidization of the TTF moieties upon exposure to iodine leads to an apparent enhancement in stacking and more thermally stable fibers. Guldi, Martin, and co-workers have synthesized peptides bearing concave 9,10-di(1,3-dithiol-2ylidene)-9,10-dihydroanthracene (exTTF) units, resulting in multilamellar supramolecular helical assemblies (Figure 1.13c).^{91,92} Twisted flat ribbon-like structures in CHCl₃ and methylcyclohexane form as a result of 3D-supramolecular ordering at the mesoscale due to solvophobic collapse. This was the first report where a concave π -electron system contributes to the effective supramolecular ordering of 3D helical fibers at mesoscopic length scales.⁹¹

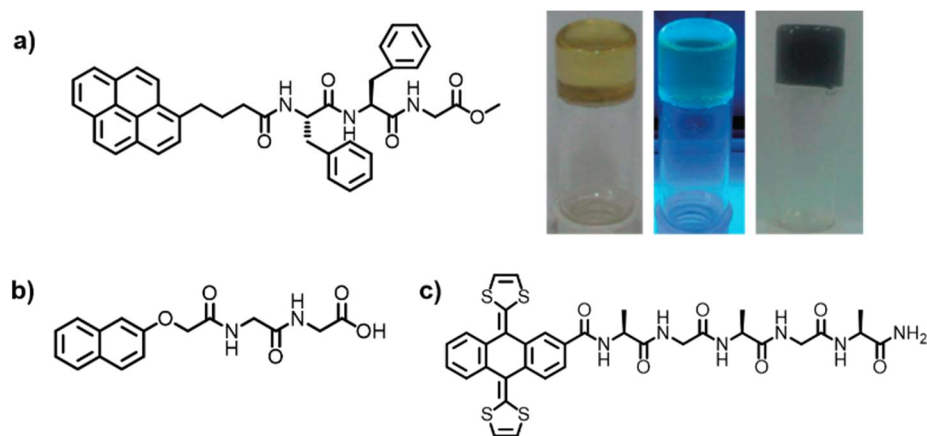


Figure 1.13. Molecular structures of different aromatic dye-peptide hybrid gelators;^{84,85} a) optical images of pyrene-peptide gels in *o*-dichlorobenzene;⁸⁴ c) example of a peptide-exTTF conjugate.⁹¹

Considering larger aromatic systems, hexa-*peri*-hexabenzocoronenes (HBC) are known for their self-assembling capabilities and are well-studied because of their possible applications in organic electronic devices. To further direct their self-assembly processes and enhance columnar stacking, Müllen and co-workers developed peptide-HBC hybrids where ionized HBCs were complexed with charged peptides via electrostatic interactions (*i.e.* negatively charged HBC and positively charged poly(ethylene oxide)-*block*-poly(*L*-lysine)).⁹³ This was the first example of a coassembly process wherein HBC nanostructures served as a template for the subsequent assembly of biomolecules (Figure 1.14). A similar strategy was employed by Fairman and co-workers with an anionic porphyrin (mesotetrakis(4-sulfonatophenyl)porphine) that induces a coiled-coil structure in an oligopeptide.⁹⁴ The binding was supported by the porphyrin Soret band at 413 nm which decreases with increasing peptide concentration. Zinc phthalocyanine-peptide conjugates synthesized *via* Sonogashira cross coupling of an iodinated zinc phthalocyanine with acetylenic bombesin protein or arginine-glycine-aspartic acid (RGD) tripeptide were also recently investigated photosensitizers for the photodynamic therapy for cancer.⁹⁵

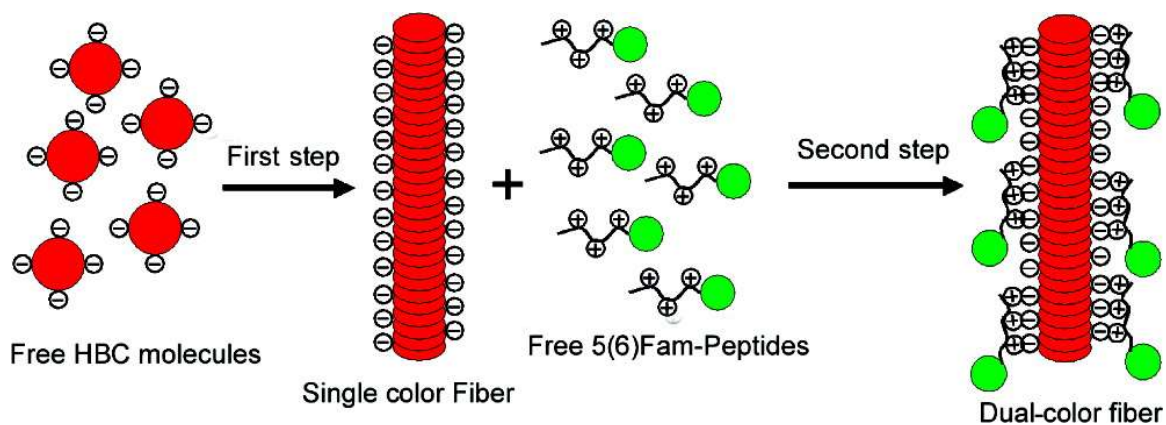


Figure 1.14. Schematic diagram of complexation between a HBC stack and lysine-rich oligopeptides.⁹³

As a consequence of supramolecular polymerization, π -electron systems confined within peptide assemblies such as those aforementioned exhibit optoelectronic properties that deviate from their molecularly dissolved counterparts. The new environments around the chromophores upon self-assembly present the possibility for different exciton coupling among the transition dipoles of the π -electron units confined within the nanostructures. Therefore, UV-Vis absorption and fluorescence are typically used to provide evidence for supramolecular polymerization. The aggregation among the chromophores typically leads to unique spatial arrangements of the transition dipoles that has apparent consequences in the optical response of the material.⁹⁶⁻⁹⁸ For a series of tetrapeptide OPV and tripeptide quaterthiophene conjugates, extensive studies on the optoelectronic effects of amino acid sequence^{30,99} and formal hydrogen bonding networks³¹ were reported for π -conjugated peptides that generally result in H-type aggregates (blue-shifted absorption and red-shifted, quenched emission of assemblies as compared to the molecularly dissolved units). These amino acid sequence or formal hydrogen bonding directionality variations did not result in any dramatic perturbations in the ability of the molecules to self-assemble, but the photophysical responses varied from long-lived excimeric to short-lived excitonic (Figure

1.15a-b) which could be of interest for light emission applications or energy transport, respectively.¹⁰⁰ Exciton-coupling variations were also reported by Kiick and co-workers who systematically varied the distances between the π -electron units placed along an α -helical peptide. Oxadiazole-containing phenylenevinylene units were conjugated onto *p*-brominated phenylalanine (*p*-BrPhe) units in helical peptides, and varying the position of *p*-BrPhe groups (Figure 1.15c).^{101,102} In addition to varied absorption spectral profiles (Figure 1.15d), the nature of the exciton-coupled CD spectra dramatically changed due to distance and dihedral angles between the chromophores.¹⁰¹ Variation in the peptide location (*i.e.*, peptide- π -peptide vs. π -peptide- π) was also investigated by Guo and workers,³³ showing that H-aggregation is supported in both motifs but there is a stronger π - π packing in the peptide- π -peptide motif as interpreted from the absorption and emission spectra.

Circular dichroism is also a widely employed technique used to examine the secondary structures of peptide sequences based on the collective orientation of the amide bond transition dipoles. CD spectra in the amide bond region often are interpreted in conjunction with FT-IR spectra to confirm the existence specific secondary structure motifs within the self-assembled structures. Likewise, the orientations of the π -electron transition dipoles can give very strong bisignate signals (Cotton effects) in cases where π -electron systems are held in chiral local environments. Bäuerle and co-workers reported proline-oligothiophene conjugates that have assembly behaviors that depend on the stereochemistry of the proline residue as supported by optical and CD spectroscopy.¹⁰³ Frauenrath and co-workers utilized CD, along with UV-Vis absorptions, in order establish design rules in peptide-PDI conjugates with polymeric alkyl side chains.¹⁰⁴

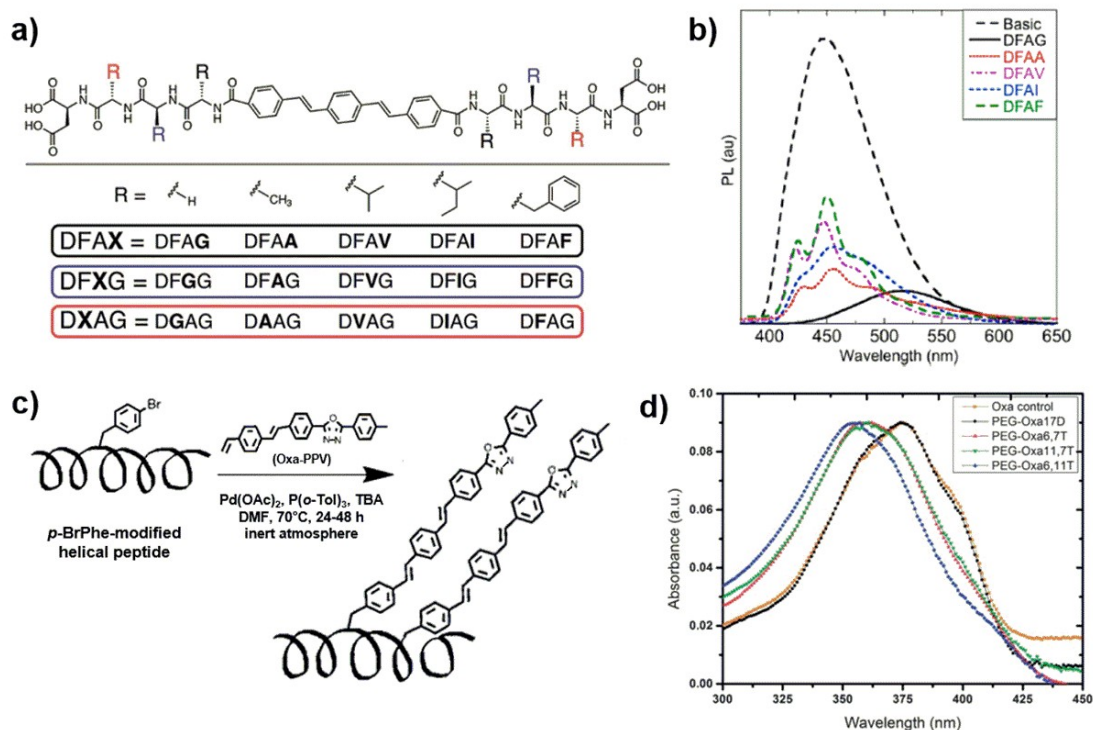


Figure 1.15. a) Scope of a systematic study of amino acid variation for OPV-containing π -conjugated peptides; b) absorption profiles of DFAX-OPV peptides under acidic conditions, with X residues being varied;³⁰ c) synthesis of helical peptides conjugated with oxadiazole-containing phenylenevinylene units; d) absorption profiles for peptide-chromophore conjugates with varied distances among oxadiazole-containing phenylenevinylene units (6-17 Å).¹⁰¹

Although there are reports regarding the inherent conductivity (ionic or electronic) of proteins and even peptide chains,¹⁰⁹⁻¹¹² the discussions in the succeeding Chapters will focus on conductive properties due to the installed π -systems within the peptide scaffold of these materials. The electrical properties of certain π -conjugated peptides were shown to be correlated to the specific peptide sequence attached and the consequent structural motif. For example, the investigation of bulk electrical properties of conductive films comprised of peptide-oligothiophene nanostructures and its dependence on the amino acid sequence showed how the inherent aggregation into films could vary simply through peptide substitutions, and hence affect the surface roughness of the films that are correlated

to the sheet resistance of the material.⁹⁹ This coincides with the findings for pure peptide conductance wherein the morphology and peptide content (i.e., more aromatic residues for electron transport) are crucial in improving the conductance of peptide nanostructures.¹⁰⁵ Peptide-oligothiophene hydrogelators have been incorporated as active layers of FET, resulting in hole mobilities ranging from 10^{-5} to $0.03 \text{ cm}^2 \text{ V}^{-1} \text{ s}^{-1}$.^{45,48} These values are higher as compared to the performance of hairpin-shaped sexithiophene self-assemblies ($\mu_{\text{h}} = \sim 10^{-7}$ - $10^{-6} \text{ cm}^2 \text{ V}^{-1} \text{ s}^{-1}$) with amide hydrogen-bonding groups as reported by Stupp and co-workers or the OFET devices reported by Holmes and co-workers with α -helical peptide-based oligothiophenes as the semiconductor ($\mu_{\text{h}} = \sim 10^{-8}$ - $10^{-7} \text{ cm}^2 \text{ V}^{-1} \text{ s}^{-1}$).^{51,106} Electrostatic force microscopy has also been used to qualitatively prove the ability of peptide-polydiacetylene conjugates to facilitate the movement of charge carriers, showing an innovative way to look at electrical conductivity without requiring the physical deposition of electrodes.^{8,60}

Several groups have also extensively studied the rational engineering of the molecular design and its impact on the hydrogelation process and the corresponding mechanical properties of the hydrogels formed. Ulijn and co-workers have studied the significance of aromatic groups in Fmoc-peptide assembly,¹⁰⁷ the impact of simple amino acid residue substitutions,²⁸ and developed molecular models of assembly based on X-ray scattering experiments and theoretical simulations.³⁸ Zukoski and co-workers followed up on these studies by constructing a phase diagram for the liquid-gel transition and correlating this and gelation kinetics to the dimethyl sulfoxide to water ratio in the gelation solvent.¹⁰⁸ The mechanical properties of tripeptide-oligothiophene conjugates were also found to be dependent of the amino acid bulk and hydrophobicity presented adjacent to the

π -electron core.⁹⁹ Such research efforts for the Tovar group peptide nanomaterials will be discussed in detail in Chapter 2.

Different strategies of improving the control over self-assembly have been demonstrated for peptide- π conjugates. In order to control the gelation time of naphthalene-peptide conjugates, Adams and co-workers used glucono- δ -lactone (GdL) which upon hydrolysis triggers a slow assembly of bromonaphthalene-Ala-Val dipeptide hydrogelator (Figure 1.16a).¹¹ Further investigations on the gelation behavior of naphthalene-dipeptide systems were conducted by Jamart-Grégoire and co-workers, looking at different amino acid derivatives and different solvents.¹⁰⁹ Another interesting strategy was presented by Martin and co-workers,¹¹⁰ wherein carbon nanotubes (CNT) were used as a template for peptide-based exTTF supramolecular assembly. The self-assembly was initiated upon the addition of CaCl₂, which resulted in a lamellar packing with a periodical *d*-spacing of 4.56 nm as supported by the results from small-angle X-ray scattering (SAXS) experiments (Figure 1.16b). Another approach to explore the stimuli-responsiveness aspect of peptide- π hybrids is to utilize enzyme-triggered self-assembly coupled with ionic effects. Alkaline phosphatase,^{74,111} esterase,¹¹² hydrolase¹¹³ and even protein clusters such as bovine serum albumin and β -lactoglobulin¹¹⁴ have been used to trigger and/or affect the assembly and mechanical properties of peptide-based hydrogelators bearing π -units. This strategy has led to a cooperative manner of self-assembly due to the thermodynamic influence of biocatalysis, leading to controllable self-assembly behavior that can be used to tune hydrogel properties.

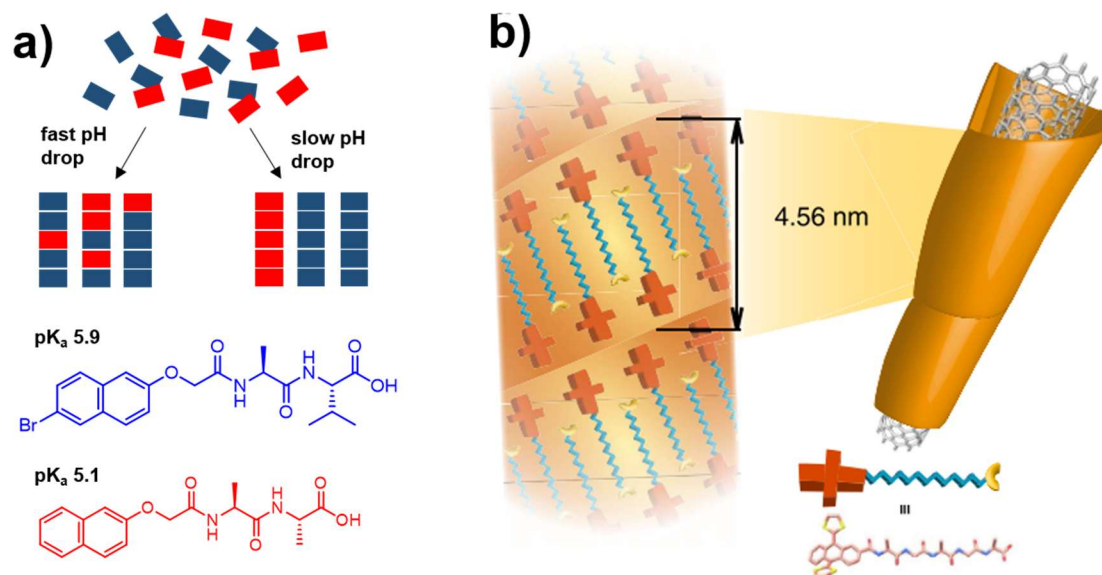


Figure 1.16. a) Utilizing the differential pK_a in a two-component system to promote self-sorting *via* slow pH drop, utilizing GdL hydrolysis; b) incorporation of self-assembled exTTF-peptide units around a CNT. Modified from Ref. 11, 73 and 110.

Towards Organic Bioelectronics

The merger of peptide segments and π -electron systems does not only support intermolecular interactions, but also serves as a means to incorporate bioactive epitopes such as the arginine-glycine-aspartic acid (RGD) peptide as a cell adhesion cue in hydrogels, or exotic energy transfer pathways. A few of these materials have already reached application in electronic device such as in field effect transistors, while some are underway for future energy harvesting applications.¹¹⁵⁻¹¹⁸ As an example of biomaterial applications of peptide- π systems, Bäuerle and co-workers used oligothiophene-bolamphiphiles for the loading of doxorubicin (an anti-cancer drug) to cells.¹¹⁹ This peptidic material presents a fluorescent biomaterial for membrane probing and drug delivery monitoring. Even for pure fluorescent peptides, such as dipeptide nanoparticles with tryptophan/phenylalanine, Zhang and co-workers used these as materials for real-time

cancer cell imaging and monitoring of drug release.¹²⁰ Although the field of nanobioelectronics has always been dominated by inorganic-based materials such as Si nanowires,¹²¹ the development of organic semiconductors coupled with biomolecules or organic coatings with “softer” properties is highly encouraging in terms of mimicking the native biological tissue. Lieber and co-workers reported Si nanowires coated with trans-activating transcriptional activator peptide to facilitate the internalization of nanowires in cells.¹²² This eases the recording of intracellular events by the Si nanowires because having this specific peptide at the material interface can prevent any disruption of cellular integrity or metabolic activity. On the other hand, Schmidt and co-workers recently presented a microelectronic neuronal cuff based on indium gallium zinc oxide supported by polyimide to guide the growth of neuronal cells during regeneration. This is an example of integrated microelectronics, wherein an external stimuli is sent to the biological tissue via a bridging material directly attached to the biotic interface.¹²³ With the highlighted examples of self-assembling peptide- π conjugates provided above, as well as the current insights about the design, synthesis, and application of this powerful class of materials, the introduction of electronic conductivity in peptide conduits in water presents a remarkable advancement that could be applicable towards the development of new functional biomaterials—particularly, for future bioelectronics materials. The ease of synthesis and established procedures for functionalization also adds to the significance of these systems. The variety of peptides, π -electron systems, and the different design strategies for their hybridization that has developed in recent years opens several opportunities for these peptide- π hybrid materials to contribute in the advancement of organic bioelectronics.

Organic bioelectronics is an emerging field that drives the next generation of biomedical devices towards materials with optoelectronic functions originating from organic systems.^{16,124-127} Compared to their inorganic counterparts, organic materials are viewed to have superior potential for bioelectronic applications mainly due to the ability of these “soft” materials to better facilitate ionic conduction in biological environments.¹²⁸ Figure 1.17 emphasizes on the difference between forces that hold the inorganic or organic semiconductor network. Covalent interactions are prevalent for inorganic networks while organic materials rely on non-covalent (van der Waals or electrostatic) interactions. Both examples shown above function as p-type semiconductors with boron and poly(styrene sulfonate) (PSS) as the dopants, but due to the non-covalent nature of interactions within organic materials, there is a better possibility for a hydrated ion to traverse further within the material and therefore lead to better ionic conduction. Furthermore, organic electronic materials offer much simpler processing conditions (*e.g.* solution processable, lower temperature of processing than inorganics, and cost-effective), easier molecular structure modification (*i.e.*, *via* side chain engineering) for tuning of the properties, generally have oxide-free interfaces, and favorable ionic transport as mentioned above.

Along with the tremendous advancements in the field of organic electronics, such as in organic light emitting diodes for display applications and organic photovoltaics for solar energy harvesting, the use of organic materials towards bioelectronic applications has been recently emerging as proven by the increasing number of literature reports in organic-based materials for biosensing¹²⁹ and electrophysiological recording or stimulation.¹²⁶ For interfacing with neural environments, it is crucial that the impedance across the electrode and the cerebrospinal fluid is kept as low as possible in order to facilitate a better

communication between ionic current flow in the biotic environment and electronic current from the electrode during electrical recording or stimulation.^{121,128,130,131} Conducting polymers have shown great potential not only in terms of reducing the material impedance, but also enhancing the implant or electrode lifetime, making these favorable coatings or main material for bioelectronic systems.¹³² Among the most predominant geometries employed for neural recording using organic materials are in the form of organic electrochemical transistors (OECT). Martin and co-workers presented early reports on organic electrochemical electrodes with polypyrrole:PSS coated onto gold electrodes via electrochemical deposition, having a 13 μm -thick coating that resulted in the lowest possible impedance that is 26 times lower than a bare Au electrode.^{133,134} More recent electrodes utilized PEDOT:PSS as the material of choice, leading to more OECTs that use PEDOT:PSS due to the combined high electronic and ionic mobilities.¹³⁵ Despite the advancements, the standard organic materials used for organic bioelectronic applications still face numerous challenges including the lower carrier mobilities of organic than that of inorganic semiconductors (PEDOT:PSS, $\sim 1 \text{ cm}^2 \text{ V}^{-1} \text{ s}^{-1}$ while III-IV group and graphene can be as high as $104 \text{ cm}^2 \text{ V}^{-1} \text{ s}^{-1}$), noise characteristics in an electrolytic environment, and the lack of high-performing devices that has been evaluated for clinical implantation in patients.¹²⁸ Despite these challenges, from implantable devices to wearable electronics, organic π -conjugated polymers have emerged as a class of material that can provide the flexibility and mechanical properties that would match the requirements for biological applications which are not currently found in silicon microelectronics.¹³⁶

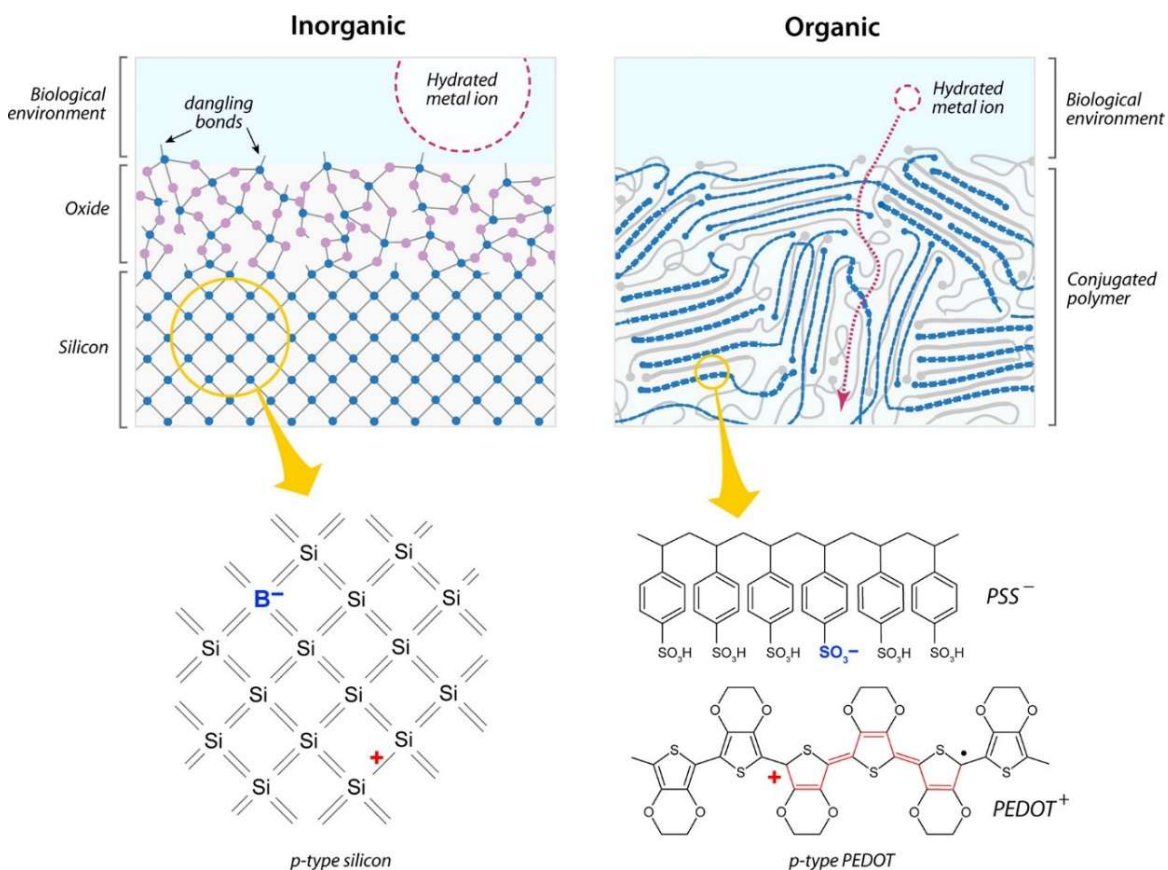


Figure 1.17. Schematic representation of the ionic interactions in a silicon inorganic semiconductor and poly(3,4-ethylenedioxythiophene) (PEDOT) organic semiconductor in an electrolytic environment¹²⁸ (Copyright 2013 American Chemical Society).

In this dissertation, the overarching goal is to develop π -conjugated peptide nanomaterials that can be utilized towards bioelectronic scaffolding for electrosensitive cells while understanding their assembly behavior and exploring different strategies to impart electronic and biological function. Considering that the success of a conductive biomaterial as a scaffold for the regrowth of an electrosensitive tissue depends if the electrical properties can be harnessed within the size regimes comparable to extracellular matrix (ECM) components, the development of new bioelectronic materials requires tunability of physicochemical properties at different size regimes. In addition, it is important that the material consequently exhibits nanostructural energy transport under

physiological conditions and also provides good integration with cells. Utilizing peptide self-assembly and the ability of peptides to mimic the components of extracellular matrix (ECM), we conjugate semiconducting π -units to peptide moieties for the formation of functional nanowires in aqueous environments. Four of the described π -electron systems in the earlier sections: quaterthiophene, oligo(*p*-phenylenevinylene), polydiacetylene, naphthalene diimide, and their peptide-conjugated equivalents will be discussed in Chapters 2 to 6. With peptide- π -peptide monomers that are found to self-assemble in aqueous environments in response to external stimuli, the electronic functionality carried by π -stacked units is buried within the peptide moiety that “communicates” with the biotic environment. The energy transport within these molecularly engineered nanostructures can be useful for modulating cellular response and behavior at the nanoscale which relies on the semiconductive properties of the system rather than the conventional macroscopic scales utilized in previously reported conducting polymers. With the lack of tunable bioelectronic nanomaterials and the high demand for minimally invasive techniques for bridging the challenges of nerve regeneration, the implication of the results from the studies discussed in the subsequent Chapters has the potential to impact the current state-of-the-art methods for modulating cellular responses and tissue engineering approaches in regenerating electrosensitive tissues by using nanoscale-controlled electrical and photonic stimulation within peptide-based scaffolds.

Portions of this chapter were adapted (with permission) in part from:

Ardoña, H. A. M. and Tovar, J. D. “Peptide π -electron conjugates: organic electronics for biology?” *Bioconjugate Chem.* 2015, 26, 2290–2302. Copyright 2015 American Chemical Society.

References

- (1) Chiang, C. K., Fincher, C. R., Park, Y. W., Heeger, A. J., Shirakawa, H., Louis, E. J., Gau, S. C., and MacDiarmid, A. G. (1977) Electrical conductivity in doped polyacetylene. *Phys. Rev. Lett.* *39*, 1098-1101.
- (2) Noriega, R., Rivnay, J., Vandewal, K., Koch, F. P. V., Stingelin, N., Smith, P., Toney, M. F., and Salleo, A. (2013) A general relationship between disorder, aggregation and charge transport in conjugated polymers. *Nat. Mater.* *12*, 1038-1044.
- (3) Zhang, R., Li, B., Iovu, M. C., Jeffries-EL, M., Sauv e, G., Cooper, J., Jia, S., Tristram-Nagle, S., Smilgies, D. M., Lambeth, D. N., McCullough, R. D., and Kowalewski, T. (2006) Nanostructure dependence of field-effect mobility in regioregular poly(3-hexylthiophene) thin film field-effect transistors. *J. Am. Chem. Soc.* *128*, 3480–3481.
- (4) Kim, F. S., Ren, G., and Jenekhe, S. A. (2011) One-dimensional nanostructures of π -conjugated molecular systems: assembly, properties, and applications from photovoltaics, sensors, and nanophotonics to nanoelectronics. *Chem. Mater.* *23*, 682–732.
- (5) Aida, T., Meijer, E. W., and Stupp, S. I. (2012) Functional supramolecular polymers. *Science* *335*, 813–817.
- (6) Li, X.-Q., Stepanenko, V., Chen, Z., Prins, P., Siebbeles, L. D. A., and W urthner, F. (2006) Functional organogels from highly efficient organogelator based on perylene bisimide semiconductor. *Chem. Commun.* 3871-3873.
- (7) Liu, H., Br emond,  . E., Prlj, A., Gonthier, J. F., and Corminboeuf, C. (2014) Adjusting the local arrangement of π -stacked oligothiophenes through hydrogen bonds: a viable route to promote charge transfer. *J. Phys. Chem. Lett.* *5*, 2320-2324.
- (8) Tovar, J. D. (2013) Supramolecular construction of optoelectronic biomaterials. *Acc. Chem. Res.* *46*, 1527-1537.
- (9) Facchetti, A. (2011) π -Conjugated polymers for organic electronics and photovoltaic cell applications. *Chem. Mater.* *23*, 733-758.
- (10) Gonz alez-Rodr iguez, D. and Schenning, A. P. H. J. (2011) Hydrogen-bonded supramolecular π -functional materials. *Chem. Mater.* *23*, 310-325.
- (11) Morris, K. L., Chen, L., Raeburn, J., Sellick, O. R., Cotanda, P., Paul, A., Griffiths, P. C., King, S. M., O'Reilly, R. K., Serpell, L. C., et al. (2013) Chemically programmed self-sorting of gelator networks. *Nat. Commun.* *4*, 1480
- (12) Sakakibara, K., Chithra, P., Das, B., Mori, T., Akada, M., Labuta, J., Tsuruoka, T., Maji, S., Furumi, S., Shrestha, L. K., et al. (2014) Aligned 1-D nanorods of a π -gelator exhibit molecular orientation and excitation energy transport different from entangled fiber networks. *J. Am. Chem. Soc.* *136*, 8548-8551.

- (13) Sugiyasu, K., Kawano, S., Fujita, N., and Shinkai, S. (2008) Self-sorting organogels with p–n heterojunction points. *Chem. Mater.* 20, 2863-2865.
- (14) Ajayaghosh, A., George, S. J. and Schenning, A. P. H. J. (2005) Hydrogen-bonded assemblies of dyes and extended pi-conjugated systems. *Top. Curr. Chem.* 258, 83-118.
- (15) Jatsch, A., Schillinger, E. -K., Schmid, S., and B auerle, P. (2010) Biomolecule assisted self-assembly of pi-conjugated oligomers. *J. Mater. Chem.* 20, 3563-3578.
- (16) Stupp, S. I., and Palmer, L. C. (2014) Supramolecular chemistry and self-assembly in organic materials design. *Chem. Mater.* 26, 507-518.
- (17) Aggeli, A., Nyrkova, I. A., Bell, M., Harding, R., Carrick, L., McLeish, T. C. B., Semenov, A. N., and Boden, N. (2001) Hierarchical self-assembly of chiral rod-like molecules as a model for peptide β -sheet tapes, ribbons, fibrils, and fibers. *Proc. Natl. Acad. Sci. U. S. A.* 98, 11857-11862.
- (18) Frauenrath, H., and Jahnke, E. (2008) A general concept for the preparation of hierarchically structured pi-conjugated polymers. *Chem.-Eur. J.* 14, 2942-2955.
- (19) Krieg, E., Bastings, M. M. C., Besenius, P., and Rybtchinski, B. (2016) Supramolecular polymers in aqueous media. *Chem. Rev.* 116, 2414-2477.
- (20) Eakins, G. L., Gallaher, J. K., Keyzers, R. A., Falber, A., Webb, J. E. A., Laos, A., Tidhar, Y., Weissman, H., Rybtchinski, B., Thordarson, P., and Hodgkiss, J. M. (2014) Thermodynamic factors impacting the peptide-driven self-assembly of perylene diimide nanofibers. *J. Phys. Chem. B* 118, 8642–8651.
- (21) Thurston, B. A., Tovar, J. D., Ferguson, A. L. (2015) Thermodynamics, morphology, and kinetics of early-stage self-assembly of π -conjugated oligopeptides. *Mol. Simul.* 42, 955-975.
- (22) Tuttle, T. (2015) Computational approaches to understanding the self-assembly of peptide-based nanostructures. *Isr. J. Chem.* 55, 724-734.
- (23) Saracino, G. A. A., Cigognini, D., Silva, D., Caprini, A., and Gelain, F. (2013) Nanomaterials design and tests for neural tissue engineering. *Chem. Soc. Rev.* 42, 225-262.
- (24) Ivnitski, D., Amit, M., Silberbush, O., Atsmon-Raz, Y., Nanda, J., Cohen-Luria, R., Miller, Y., Ashkenasy, G., and Ashkenasy, N. (2016) The strong influence of structure polymorphism on the conductivity of peptide fibrils. *Angew. Chem. Int. Ed.* 55, 9988-9992.
- (25) Korevaar, P. A., George, S. J., Markvoort, A. J., Smulders, M. M. J., Hilbers, P. A. J., Schenning, A. P. H. J., De Greef, T. F. A., and Meijer, E. W. (2012) Pathway complexity in supramolecular polymerization. *Nature* 481, 492-496.
- (26) Tantakitti, F., Boekhoven, J., Wang, X., Kazantsev, R. V., Yu, T., Li, J., Zhuang, E., Zandi, R., Ortony, J. H., Newcomb, C. J., Palmer, L. C., Shekhawat, G. S., la Cruz, de, M. O., Schatz, G. C., and Stupp, S. I. (2016) Energy landscapes and functions of supramolecular systems. *Nat. Mater.* 15, 469-476.

- (27) Korevaar, P. A., Newcomb, C. J., Meijer, E. W., and Stupp, S. I. (2014) Pathway selection in peptide amphiphile assembly. *J. Am. Chem. Soc.* *136*, 8540-8543.
- (28) Tang, C., Ulijn, R. V., and Saiani, A. (2011) Effect of glycine substitution on Fmoc-diphenylalanine self-assembly and gelation properties. *Langmuir* *27*, 14438-14449.
- (29) Kim, S. H., and Parquette, J. R. (2012) A model for the controlled assembly of semiconductor peptides. *Nanoscale* *4*, 6940-6947.
- (30) Wall, B. D., Zacca, A. E., Sanders, A. M., Wilson, W. L., Ferguson, A. L., and Tovar, J. D. (2014) Supramolecular polymorphism: tunable electronic interactions within pi-conjugated peptide nanostructures dictated by primary amino acid sequence. *Langmuir* *30*, 5946-5956.
- (31) Wall, B. D., Zhou, Y., Mei, S., Ardoña, H. A. M., Ferguson, A. L., and Tovar, J. D. (2014) Variation of formal hydrogen-bonding networks within electronically delocalized π -conjugated oligopeptide nanostructures. *Langmuir* *30*, 11375-11385.
- (32) Zhao, Y., Wang, J., Deng, L., Zhou, P., Wang, S., Wang, Y., Xu, H., and Lu, J. R. (2013) Tuning the self-assembly of short peptides via sequence variations. *Langmuir* *29*, 13457-13464.
- (33) Guo, Z., Song, Y., Gong, R., Mu, Y., Jiang, Y., Li, M., and Wan, X. (2013) Assembly of peptide-thiophene conjugates: the influence of peptide content and location. *Supramol. Chem.* *26*, 383-391.
- (34) Woolfson, D. N., and Mahmoud, Z. N. (2010) More than just bare scaffolds: towards multi-component and decorated fibrous biomaterials. *Chem. Soc. Rev.* *39*, 3464-3479.
- (35) Jun, H. W., Paramonov, S. E., and Hartgerink, J. D. (2006) Biomimetic self-assembled nanofibers. *Soft Matter* *2*, 177-181.
- (36) Hartgerink, J. D., Beniash, E., and Stupp, S. I. (2002) Peptide-amphiphile nanofibers: A versatile scaffold for the preparation of self-assembling materials. *Proc. Natl. Acad. Sci. U. S. A.* *99*, 5133-5138.
- (37) Schillinger, E., Mena-Osteritz, E., Hentschel, J., Börner, H. G., and Bäuerle, P. (2009) Oligothiophene versus beta-sheet peptide: synthesis and self-assembly of an organic semiconductor-peptide hybrid. *Adv. Mater.* *21*, 1562-1567.
- (38) Smith, A. M., Williams, R. J., Tang, C., Coppo, P., Collins, R. F., Turner, M. L., Saiani, A., and Ulijn, R. V. (2008) Fmoc-diphenylalanine self assembles to a hydrogel via a novel architecture based on pi-pi interlocked beta-sheets. *Adv. Mater.* *20*, 37-41.
- (39) Choi, I., Park, I., Ryu, J., and Lee, M. (2012) Control of peptide assembly through directional interactions. *Chem. Commun.* *48*, 8481-8483.
- (40) Diegelmann, S. R., Gorham, J. M., and Tovar, J. D. (2008) One-dimensional optoelectronic nanostructures derived from the aqueous self-assembly of π -conjugated oligopeptides. *J. Am. Chem. Soc.* *130*, 13840-13841.

- (41) Ulysse, L., Cubillos, J., and Chmielewski, J. (1995) Photoregulation of cyclic peptide conformation. *J. Am. Chem. Soc.* *117*, 8466-8467.
- (42) Gothard, C. M., Rao, N. A., and Nowick, J. S. (2007) Nanometer-sized amino acids for the synthesis of nanometer-scale water-soluble molecular rods of precise length. *J. Am. Chem. Soc.* *129*, 7272-7273.
- (43) Matmour, R., De Cat, I., George, S. J., Adriaens, W., Leclère, P., Bomans, P. H. H., Sommerdijk, N. A. J. M., Gielen, J. C., Christianen, P. C. M., Heldens, J. T., et al. (2008) Oligo(*p*-phenylenevinylene)-peptide conjugates: synthesis and self-assembly in solution and at the solid-liquid interface. *J. Am. Chem. Soc.* *130*, 14576-14583.
- (44) Stone, D. A., Hsu, L., and Stupp, S. I. (2009) Self-assembling quinquethiophene-oligopeptide hydrogelators. *Soft Matter* *5*, 1990-1993.
- (45) Sanders, A. M., Dawidczyk, T. J., Katz, H. E., and Tovar, J. D. (2012) Peptide-based supramolecular semiconductor nanomaterials via Pd-catalyzed solid-phase "dimerizations." *ACS Macro Lett.* *1*, 1326-1329.
- (46) Vadehra, G. S., Wall, B. D., Diegelmann, S. R., and Tovar, J. D. (2010) On-resin dimerization incorporates a diverse array of pi-conjugated functionality within aqueous self-assembling peptide backbones. *Chem. Commun.* *46*, 3947-3949.
- (47) Marty, R., Szilluweit, R., Sánchez-Ferrer, A., Bolisetty, S., Adamcik, J., Mezzenga, R., Spitzner, E., Feifer, M., Steinmann, S. N., Corminboeuf, C., et al. (2013) Hierarchically structured microfibers of "single stack" perylene bisimide and quaterthiophene nanowires. *ACS Nano* *7*, 8498-8505.
- (48) Wall, B. D., Diegelmann, S. R., Zhang, S., Dawidczyk, T. J., Wilson, W. L., Katz, H. E., Mao, H.-Q., and Tovar, J. D. (2011) Aligned macroscopic domains of optoelectronic nanostructures prepared via shear-flow assembly of peptide hydrogels. *Adv. Mater.* *23*, 5009-5014.
- (49) Klok, H., Rösler, A., Götz, G., Mena-Osteritz, E., and Bäuerle, P. (2004) Synthesis of a silk-inspired peptide-oligothiophene conjugate. *Org. Biomol. Chem.* *2*, 3541-3544.
- (50) Tsai, W., Li, L., Cui, H., Jiang, H., and Stupp, S. I. (2008) Self-assembly of amphiphiles with terthiophene and tripeptide segments into helical nanostructures. *Tetrahedron* *64*, 8504-8514.
- (51) Kumar, R. J., MacDonald, J. M., Singh, T. B., Waddington, L. J., and Holmes, A. B. (2011) Hierarchical self-assembly of semiconductor functionalized peptide alpha-helices and optoelectronic properties. *J. Am. Chem. Soc.* *133*, 8564-8573.
- (52) Gothard, C. M., and Nowick, J. S. (2010) Nanometer-scale water-soluble macrocycles from nanometer-sized amino acids. *J. Org. Chem.* *75*, 1822-1830.
- (53) Harrington, D. A., Behanna, H. A., Tew, G. N., Claussen, R. C., and Stupp, S. I. (2005) Supramolecular fluorophores for biological studies: phenylene vinylene-amino acid amphiphiles. *Chem. Biol.* *12*, 1085-1091.

- (54) Sun, X., Chen, T., Huang, S., Li, L., and Peng, H. (2010) Chromatic polydiacetylene with novel sensitivity. *Chem. Soc. Rev.* 39, 4244-4257.
- (55) Carpick, R. W., Sasaki, D. Y., Marcus, M. S., Eriksson, M. A., and Burns, A. R. (2004) Polydiacetylene films: a review of recent investigations into chromogenic transitions and nanomechanical properties. *J. Phys-Condens. Mat.* 16, R679-R697.
- (56) Jelinek, R., and Ritenberg, M. (2013) Polydiacetylenes—recent molecular advances and applications. *RSC Adv.* 3, 21192-21201.
- (57) Diegelmann, S. R., and Tovar, J. D. (2013) Polydiacetylene-peptide 1D nanomaterials. *Macromol. Rapid Comm.* 34, 1343-1350.
- (58) Jahnke, E., Lieberwirth, I., Severin, N., Rabe, J. P., and Frauenrath, H. (2006) Topochemical polymerization in supramolecular polymers of oligopeptide-functionalized diacetylenes. *Angew. Chem. Int. Ed.* 45, 5383-5386.
- (59) Yin, S., Wang, C., Song, B., Chen, S., and Wang, Z. (2009) Self-organization of a polymerizable bolaamphiphile bearing a diacetylene group and *L*-aspartic acid group. *Langmuir* 25, 8968-8973.
- (60) Diegelmann, S. R., Hartman, N., Markovic, N., and Tovar, J. D. (2012) Synthesis and alignment of discrete polydiacetylene-peptide nanostructures. *J. Am. Chem. Soc.* 134, 2028-2031.
- (61) Hsu, L., Cvetanovich, G. L., and Stupp, S. I. (2008) Peptide amphiphile nanofibers with conjugated polydiacetylene backbones in their core. *J. Am. Chem. Soc.* 130, 3892-3899.
- (62) van den Heuvel, M., Löwik, D. W. P. M., and van Hest, J. C. M. (2008) Self-assembly and polymerization of diacetylene-containing peptide amphiphiles in aqueous solution. *Biomacromolecules* 9, 2727-2734.
- (63) Löwik, D. W. P. M., Shklyarevskiy, I. O., Ruizendaal, L., Christianen, P. C. M., Maan, J. C., and van Hest, J. C. M. (2007) A highly ordered material from magnetically aligned peptide amphiphile nanofiber assemblies. *Adv. Mater.* 19, 1191-1195.
- (64) Neuteboom, E. E., Meskers, S., van Hal, P. A., van Duren, J. K. J., Meijer, E. W., Janssen, R. A. J., Dupin, H., Pourtois, G., Cornil, J., Lazzaroni, R., et al. (2003) Alternating oligo (p-phenylene vinylene)-perylene bisimide copolymers: Synthesis, photophysics, and photovoltaic properties of a new class of donor-acceptor. *J. Am. Chem. Soc.* 125, 8625-8638.
- (65) López-Andarias, J., Rodriguez, M. J., Atienza, C., López, J. L., Mikie, T., Casado, S., Seki, S., Carrascosa, J. L., and Martín, N. (2015) Highly ordered *n/p*-co-assembled materials with remarkable charge mobilities. *J. Am. Chem. Soc.* 137, 893-897.
- (66) Ashkenasy, N., and Ghadiri, M. R. (2005) Modulating charge transfer through cyclic *D, L*-alpha-peptide self-assembly. *Chem. Eur. J.* 11, 1137-1144.

- (67) Ashkenasy, N., Horne, W. S., and Ghadiri, M. R. (2006) Design of self-assembling peptide nanotubes with delocalized electronic states. *Small* 2, 99-102.
- (68) Shao, H., Nguyen, T., Romano, N. C., Modarelli, D. A. and Parquette, J. R. (2009) Self-assembly of 1-D *n*-type nanostructures based on naphthalene diimide-appended dipeptides. *J. Am. Chem. Soc.* 131, 16374-16376.
- (69) Shao, H., Gao, M., Kim, S. H., Jaroniec, C. P., and Parquette, J. R. (2011) Aqueous self-assembly of *L*-lysine-based amphiphiles into 1D *n*-type nanotubes. *Chem- Eur. J.* 17, 12882-12885.
- (70) Shao, H., Seifert, J., Romano, N. C., Gao, M., Helmus, J. J., Jaroniec, C. P., Modarelli, D. A., and Parquette, J. R. (2010) Amphiphilic self-assembly of an *n*-type nanotube. *Angew. Chem. Int. Ed.* 122, 7854-7857.
- (71) Ivnitski, D., Amit, M., Rubinov, B., Cohen-Luria, R., Ashkenasy, N., and Ashkenasy, G. (2014) Introducing charge transfer functionality into prebiotically relevant beta-sheet peptide fibrils. *Chem. Commun.* 50, 6733-6736.
- (72) Gallaher, J. K., Aitken, E. J., Keyzers, R. A., and Hodgkiss, J. M. (2012) Controlled aggregation of peptide-substituted perylene-bisimides. *Chem. Commun.* 48, 7961-7963.
- (73) Fleming, S., and Ulijn, R. V. (2014) Design of nanostructures based on aromatic peptide amphiphiles. *Chem. Soc. Rev.* 43, 8150-8177.
- (74) Zhou, J., Du, X., Gao, Y., Shi, J., and Xu, B. (2014) Aromatic–aromatic interactions enhance interfiber contacts for enzymatic formation of a spontaneously aligned supramolecular hydrogel. *J. Am. Chem. Soc.* 136, 2970-2973.
- (75) Tang, C., Smith, A. M., Collins, R. F., Ulijn, R. V., and Saiani, A. (2009) Fmoc-diphenylalanine self-assembly mechanism induces apparent pK_a shifts. *Langmuir*, 25, 9447-9453.
- (76) Orbach, R., Adler-Abramovich, L., Zigerson, S., Mironi-Harpaz, I., Seliktar, D., and Gazit, E. (2009) Self-assembled Fmoc-peptides as a platform for the formation of nanostructures and hydrogels. *Biomacromolecules* 10, 2646-2651.
- (77) Raeburn, J., Pont, G., Chen, L., Cesbron, Y., Lévy, R., and Adams, D. J. (2012) Fmoc-diphenylalanine hydrogels: understanding the variability in reported mechanical properties. *Soft Matter* 8, 1168-1174.
- (78) Zhang, Y., Gu, H., Yang, Z., and Xu, B. (2003) Supramolecular hydrogels respond to ligand-receptor interaction. *J. Am. Chem. Soc.* 125, 13680-13681.
- (79) Jayawarna, V., Ali, M., Jowitt, T. A., Miller, A. F., Saiani, A., Gough, J. E., Ulijn, R. V. (2006) Nanostructured hydrogels for three-dimensional cell culture through self-assembly of fluorenylmethoxycarbonyl–dipeptides. *Adv. Mater.* 18, 611-614.

- (80) Liyanage, W., Vats, K., Rajbhandary, A., Benoit, D. S. W., and Nilsson, B. L. (2015) Multicomponent dipeptide hydrogels as extracellular matrix-mimetic scaffolds for cell culture applications. *Chem. Commun.* 51, 11260-11263.
- (81) Jayawarna, V., Richardson, S. M., Hirst, A. R., Hodson, N. W., Saiani, A., Gough, J. E., and Ulijn, R. V. (2009) Introducing chemical functionality in Fmoc-peptide gels for cell culture. *Acta Biomater.* 5, 934-943.
- (82) Cheng, G., Castelletto, V., Jones, R. R., Connon, C. J., and Hamley, I. W. (2011) Hydrogelation of self-assembling RGD-based peptides. *Soft Matter* 7, 1326-1333.
- (83) Tomasini, C., and Castellucci, N. (2013) Peptides and peptidomimetics that behave as low molecular weight gelators. *Chem. Soc. Rev.* 42, 156-172.
- (84) Adhikari, B., Nanda, J., and Banerjee, A. (2011) Pyrene-containing peptide-based fluorescent organogels: inclusion of graphene into the organogel. *Chem. Eur. J.* 17, 11488-11496.
- (85) Yang, Z., Liang, G., Ma, M., Gao, Y., and Xu, B. (2007) Conjugates of naphthalene and dipeptides produce molecular hydrogelators with high efficiency of hydrogelation and superhelical nanofibers. *J. Mater. Chem.* 17, 850-854.
- (86) Liang, G., Yang, Z., Zhang, R., Li, L., Fan, Y., Kuang, Y., Gao, Y., Wang, T., Lu, W. W., and Xu, B. (2009) Supramolecular hydrogel of a *D*-amino acid dipeptide for controlled drug release in vivo. *Langmuir* 25, 8419-8422.
- (87) Rodríguez-Ropero, F., Zanuy, D., Assfeld, X., and Alemán, C. (2009) Modeling an electronic conductor based on natural peptide sequences. *Biomacromolecules* 10, 2338-2343.
- (88) Hamley, I. W., Brown, G. D., Castelletto, V., Cheng, G., Venanzi, M., Caruso, M., Placidi, E., Aleman, C., Revilla-López, G., Zanuy, D. (2010) Self-assembly of a designed amyloid peptide containing the functional thienylalanine unit. *J. Phys. Chem. B* 114, 10674-10683.
- (89) Amit, M., Appel, S., Cohen, R., Cheng, G., Hamley, I. W., and Ashkenasy, N. (2014) Hybrid proton and electron transport in peptide fibrils. *Adv. Funct. Mater.* 24, 5873-5880.
- (90) Kitamura, T., Nakaso, S., Mizoshita, N., Tochigi, Y., Shimomura, T., Moriyama, M., Ito, K., and Kato, T. (2005) Electroactive supramolecular self-assembled fibers comprised of doped tetrathiafulvalene-based gelators. *J. Am. Chem. Soc.* 127, 14769-14777.
- (91) López, J. L., Atienza, C., Insuasty, A., López-Andarias, J., Romero-Nieto, C., Guldi, D. M., and Martín, N. (2012) Concave versus planar geometries for the hierarchical organization of mesoscopic 3D helical fibers. *Angew. Chem. Int. Ed.* 51, 3857-3861.
- (92) López, J. L., Atienza, C., Seitz, W., Guldi, D. M., and Martín, N. (2010) Controlling the transformation of primary into quaternary structures: towards hierarchically built-up twisted fibers. *Angew. Chem. Int. Ed.* 49, 9876-9880.

- (93) Yin, M., Shen, J., Pisula, W., Liang, M., Zhi, L., and Müllen, K. (2009) Functionalization of self-assembled hexa-peri-hexabenzocoronene fibers with peptides for bioprobng. *J. Am. Chem. Soc.* *131*, 14618-14619.
- (94) Kovaric, B. C., Kokona, B., Schwab, A. D., Twomey, M. A., de Paula, J. C., Fairman, R. (2006) Self-assembly of peptide porphyrin complexes: toward the development of smart biomaterials. *J. Am. Chem. Soc.* *128*, 4166-4167.
- (95) Ranyuk, E., Cauchon, N., Klarskov, K., Guérin, B., and van Lier, J. E. (2013) Phthalocyanine-peptide conjugates: receptor-targeting bifunctional agents for imaging and photodynamic therapy. *J. Med. Chem.* *56*, 1520-1534.
- (96) Spano, F. C., and Silva, C. (2014) H-and J-aggregate behavior in polymeric semiconductors. *Annu. Rev. Phys. Chem.* *65*, 477-500.
- (97) Spano, F. C. (2010) The spectral signatures of Frenkel polarons in H- and J-aggregates. *Acc. Chem. Res.* *43*, 429-439.
- (98) Kasha, M. Rawls, H. R. and Ashraf El-Bayoumi, M. (1965) The exciton model in molecular spectroscopy. *Pure. Appl. Chem.* *11*, 371-392.
- (99) Ardoña, H. A. M., Besar, K., Tovar, J. D., Togninalli, M., Katz, H. E., and Tovar, J. D. (2015) Sequence-dependent mechanical, photophysical and electrical properties of pi-conjugated peptide hydrogelators. *J. Mater. Chem. C* *3*, 6505-6514.
- (100) Tovar, J. D. (2015) Peptide nanostructures with pi-ways: photophysical consequences of peptide/pi-electron molecular self-assembly. *Isr. J. Chem* *55*, 622-627
- (101) Bhagwat, N. and Kiick, K. (2013) Polymer-peptide templates for controlling electronic interactions of organic chromophores. *J. Mater. Chem. C* *1*, 4836-4845.
- (102) Kas, O. Y., Charati, M. B., Kiick, K. L., and Galvin, M. E. (2006) Manipulating association of electroactive chromophores via the use of peptidic templates. *Chem. Mater.* *18*, 4238-4245.
- (103) Schillinger, E., Kümin, M., Digennaro, A., Mena-Osteritz, E., Schmid, S., Wennemers, H., and Bäuerle, P. (2013) Guiding suprastructure chirality of an oligothiophene by a single amino acid. *Chem. Mater.* *25*, 4511-4521.
- (104) Marty, R., Nigon, R., Leite, D., and Frauenrath, H. (2014) Two-fold odd-even effect in self-assembled nanowires from oligopeptide-polymer-substituted perylene bisimides. *J. Am. Chem. Soc.* *136*, 3919-3927.
- (105) Amit, M., Cheng, G., Hamley, I. W., and Ashkenasy, N. (2012) Conductance of amyloid β based peptide filaments: structure-function relations. *Soft Matter* *8*, 8690-8696.
- (106) Tsai, W., Tevis, I. D., Tayi, A. S., Cui, H., and Stupp, S. I. (2010) Semiconducting nanowires from hairpin-shaped self-sssembling sexithiophenes. *J. Phys. Chem. B* *114*, 14778-14786.

- (107) Fleming, S., Debnath, S., Frederix, P. W. J. M., Tuttle, T., and Ulijn, R. V. (2013) Aromatic peptide amphiphiles: significance of the Fmoc moiety. *Chem. Commun.* *49*, 10587-10589.
- (108) Dudukovic, N. A., and Zukoski, C. F. (2014) Mechanical properties of self-assembled Fmoc-diphenylalanine molecular gels. *Langmuir* *30*, 4493-4500.
- (109) Curcio, P., Allix, F., Pickaert, G., and Jamart-Grégoire, B. (2011) A favorable, narrow, δ_h Hansen-parameter domain for gelation of low-molecular-weight amino acid derivatives. *Chem. Eur. J.* *17*, 13603-13612.
- (110) López-Andarias, J., López, J. L., Atienza, C., Romero-Nieto, C., and Martín, N. (2014) Controlling the crystalline three-dimensional order in bulk materials by single-wall carbon nanotubes. *Nat. Commun.* *5*, 3763.
- (111) Thornton, K., Abul-Haija, Y. M., Hodson, N., and Ulijn, R. V. (2013) Mechanistic insights into phosphatase triggered self-assembly including enhancement of biocatalytic conversion rate. *Soft Matter* *9*, 9430-9439.
- (112) Roy, S., Javid, N., Sefcik, J., Halling, P. J., and Ulijn, R. V. (2012) Salt-induced control of supramolecular order in biocatalytic hydrogelation. *Langmuir* *28*, 16664-16670.
- (113) Huang, Z., Guan, S., Wang, Y., Shi, G., Cao, L., Gao, Y., Dong, Z., Xu, J., Luo, Q., and Liu, J. (2013) Self-assembly of amphiphilic peptides into bio-functionalized nanotubes: a novel hydrolase model. *J. Mater. Chem. B* *1*, 2297-2304.
- (114) Javid, N., Roy, S., Zelzer, M., Yang, Z., Sefcik, J., and Ulijn, R. V. (2013) Cooperative self-assembly of peptide gelators and proteins. *Biomacromolecules* *14*, 4368-4376.
- (115) Chen, L., Revel, S., Morris, K., and Adams, D. J. (2010) Energy transfer in self-assembled dipeptide hydrogels. *Chem. Commun.* *46*, 4267-4269.
- (116) Ardoña, H. A. M., and Tovar, J. D. (2015) Energy transfer within responsive pi-conjugated coassembled peptide-based nanostructures in aqueous environments. *Chem. Sci.* *6*, 1474-1484.
- (117) Nalluri, S. K. M., and Ulijn, R. V. (2013) Discovery of energy transfer nanostructures using gelation-driven dynamic combinatorial libraries. *Chem. Sci.* *4*, 3699-3705,
- (118) Javid, N., Frederix, P., and Ulijn, R. V. (2014) Biocatalytic self-assembly of supramolecular charge-transfer nanostructures based on n-type semiconductor-appended peptides. *Angew. Chem. Int. Ed.* *126*, 5992-5997.
- (119) Schmid, S., Ng, D. Y. W., Mena-Osteritz, E., Wu, Y., Weil, T., and Bäuerle, P. (2016) Self-assembling oligothiophene-bolaamphiphiles for loading and controlled release of doxorubicin into living cells. *Chem Commun.* *52*, 3235-3238.

- (120) Fan, Z., Sun, L., Huang, Y., Wang, Y., and Zhang, M. (2016) Bioinspired fluorescent dipeptide nanoparticles for targeted cancer cell imaging and real-time monitoring of drug release. *Nat. Nanotech.* 11, 388-394.
- (121) Zhang, A., and Lieber, C. M. (2016) Nano-bioelectronics. *Chem. Rev.* 116, 215-257.
- (122) Lee, J.-H., Zhang, A., You, S. S., and Lieber, C. M. (2016) Spontaneous internalization of cell penetrating peptide-modified nanowires into primary neurons. *Nano Lett.* 16, 1509-1513.
- (123) Karnaushenko, D., Münzenrieder, N., Karnaushenko, D. D., Koch, B., Meyer, A. K., Baunack, S., Petti, L., Tröster, G., Makarov, D. and Schmidt, O. G. (2015) Biomimetic microelectronics for regenerative neuronal cuff implants. *Adv. Mater.* 27, 6797-6805.
- (124) Hammock, M. L., Chortos, A., Tee, B. C.-K., Tok, J. B.-H. and Bao, Z. (2013) The evolution of electronic skin (E-Skin): a brief history, design considerations, and recent progress. *Adv. Mater.* 25, 5997-6038.
- (125) Boekhoven, J., and Stupp, S. I. (2014) Supramolecular materials for regenerative medicine. *Adv. Mater.* 26, 1642-1659.
- (126) Berggren, M. and Richter-Dahlfors, A. (2007) Organic bioelectronics. *Adv. Mater.* 19, 3201-3213.
- (127) Lanzani, G. (2014) Materials for bioelectronics: organic electronics meets biology. *Nat. Mater.* 13, 775-776.
- (128) Rivnay, J., Owens, R. M., and Malliaras, G. G. (2014) The rise of organic bioelectronics. *Chem. Mater.* 26, 679-685.
- (129) Huang, W., Diallo, A. K., Dailey, J. L., Besar, K., and Katz, H. E. (2015) Electrochemical processes and mechanistic aspects of field-effect sensors for biomolecules. *J. Mater. Chem. C* 3, 6445–6470.
- (130) Jonsson, A., Inal, S., Uguz, L., Williamson, A. J., Kergoat, L., Rivnay, J., Khodagholy, D., Berggren, M., Bernard, C., Malliaras, G. G., and Simon, D. T. (2016) Bioelectronic neural pixel: chemical stimulation and electrical sensing at the same site. *Proc. Natl. Acad. Sci. U. S. A.* 113, 9440-9445.
- (131) Khodagholy, D., Rivnay, J., Sessolo, M., Gurfinkel, M., Leleux, P., Jimison, L. H., Stavriniidou, E., Herve, T., Sanaur, S., Owens, R. M., and Malliaras, G. G. (2013) High transconductance organic electrochemical transistors. *Nat. Commun.* 4, 2133.
- (132) Fang, Y., Li, X., and Fang, Y. (2015) Organic bioelectronics for neural interfaces. *J. Mater. Chem. C* 3, 6424-6430.
- (133) Cui, X., Hetke, J. F., Wiler, J. A., Anderson, D. J., and Martin, D. C. (2001) Electrochemical deposition and characterization of conducting polymer polypyrrole/PSS on multichannel neural probes. *Sensor. Actuat. A-Phys.* 93, 8-18.

- (134) Cui, X., and Martin, D. C. (2003) Electrochemical deposition and characterization of poly(3,4-ethylenedioxythiophene) on neural microelectrode arrays. *Sensor. Actuat. B-Chem.* 89, 92-102.
- (135) Stavriniidou, E., Leleux, P., Rajaona, H., Khodagholy, D., Rivnay, J., Lindau, M., Sanaur, S., and Malliaras, G. G. (2013) Direct measurement of ion mobility in a conducting polymer. *Adv. Mater.* 25, 4488-4493.
- (136) Someya, T., Bao, Z., and Malliaras, G. G. (2016) The rise of plastic bioelectronics. *Nature* 540, 379-385.

CHAPTER TWO:

Structure-Function Correlation Studies for
 π -Conjugated Peptide Hydrogelators

Introduction

Perturbations on the π -system ordering of organic polymers such as fluctuations in local packing, distribution of torsion angles or conformational freedom in flexible molecules or chains can lead to energetic disorder that affects transport efficiency.¹ Several strategies have been reported to solubilize π -compounds in appropriate solvents and promote crystalline structures in the solid state that could organize the π -units in a way that maximizes charge transport efficiencies and minimizes structural defects. For most oligopeptide- π assemblies described in Chapter 1, the large fraction of peptide moieties acts as a solubilizing group for aqueous environments but limits the charge transport properties due to their “insulating” nature, and therefore presents a challenge when used to build electronic devices as well as for the direct characterization of their conductivity.^{2,3}

Currently, functional self-assembling peptides with rationally engineered properties and morphologies are generally considered of high importance in applications towards drug delivery, membrane protein stabilization, 3D tissue engineering and supramolecular electronics.⁴⁻⁶ In the context of tissue engineering, natural and synthetic peptides that can form functional hydrogels⁷ are considered as good extracellular matrix (ECM) mimics which can provide a more *in vivo*-like environment for the cells or tissues⁷⁻⁹ due to their unique biocompatibility, flexible methods of synthesis, range of constituents, and tunable physical characteristics¹⁰⁻¹² such as water content, topography and porosity. Most peptide-based hydrogels rely on non-covalent interactions such as hydrogen-bonding to form fibrous networks,¹³ which presents an advantage over polymeric crosslinked gels as this allows the material to rebuild strength and elasticity upon cessation of shear¹⁴ as well as to respond rapidly towards chemical or physical stimuli such as pH or

temperature.¹⁵ Numerous examples of peptide- π hybrid hydrogelators and their corresponding synthetic methodology and applications were described in Chapter 1.

In an effort to replicate the mechanical and viscoelastic properties of biological tissues,¹⁶⁻¹⁹ several studies were done that present strategies to tune the mechanical properties of peptide hydrogels^{16,20-24} such as monitoring the effects of changing the temperature,²⁵ ionic strength,²⁶ pH,²⁷ chirality,²⁸ or even the use of alternative self-assembly pathways that utilize enzymatic reactions^{20,29} or charge of the peptide sequence³⁰ to manipulate the extent of self-assembly. Most molecular-based peptide hydrogels have properties that can be tuned by controlling intermolecular interactions by the molecular design.^{15,31} For example, in Fmoc-dipeptides, the main driving force of assembly is a combination of both hydrophobic and π - π interactions of fluorenyl moieties with secondary effects from hydrogen-bonding of the peptidic components.²⁷ In peptide amphiphiles (PA), the choice of gelling agent (HCl or CaCl₂) substantially affects the gel behavior and stiffness due to the ionic bridges establishing stronger fiber crosslinks than the hydrogen bonds.³² The stiffness of PA gels was also correlated to the extent of β -sheet formation, hydrogen bonding alignment with respect to fiber long axis, twisting and disorder.³³ To further mimic the environment *in vivo*, embedding electronically-active units within a biomaterial³⁴⁻³⁷ such as in electrically conducting hydrogels is being explored because electrical signals are known to play an important role in the function of cardiac tissues and neurons, as well as for cell growth, organization, and stimulation of stem cells towards a specific lineage.³⁸⁻⁴¹

For the self-assembly and hydrogelation process of π -conjugated peptides, it is important to consider that these often occur under non-equilibrium conditions with

contributions from reaction-dominated and diffusion-controlled processes, such that rate of transport of the assembly trigger (*i.e.*, acid) within the monomer solution can dictate the homogeneity of the peptide network within the hydrogel.⁴² To further understand the hydrogelation process, it is equally important to understand the bottom-up self-assembly process to form the fibrillar network that comprise the hydrogel structures. For peptide- π -peptide triblock systems, atomistic molecular dynamics simulations for a prototypical tetrapeptide (DFAG) oligo(*p*-phenylenevinylene) (OPV3) unit indicate that the monomers coalesce into small clusters *via* structural ripening, followed by diffusion-limited aggregation to initiate the 1-D nanostructure formation.⁴³ In the simulation studies by Thurston and Ferguson, early-stage assembly process was found to be dependent on the intramolecular interactions that dictate the monomer peptide collapse or extension, and intermolecular interactions dictate the dimerization kinetics between extended peptide monomers. Similar to amyloid fibril formation, these early stages form micelle-like structures depending on the monomer hydrophobicity. Successive monomeric additions were compared to the aggregation of dimers to form longer oligomeric assemblies, and the latter pathway whereby smaller clusters coalesce to form larger assemblies is more favored. As such, aggregates smaller than a pentamer undergo internal structural rearrangement to form β -sheet-like clusters that act as the nuclei for the 1-D assembly with a linear stacking arrangement. In a related study by Tovar, Ferguson and co-workers,⁴⁴ the symmetry of the monomer was correlated to the photophysical behavior of the assembly as well as to the intermolecular distances. The symmetric DFAG OPV3 (C- to C- termini) showed an excimeric emission behavior and was simulated to have favorable parallel β -sheet motif formation. On the other hand, the nonsymmetric DFAG (C- to N- termini) showed an

excitonic emission behavior with more favorable antiparallel β -sheet structure formation. Taken together with the simulation findings that the DFAG OPV3 antiparallel homodimer units have smaller intermolecular spacings than the parallel/symmetric counterpart, these results were consistent with a previous report for these peptide-OPV3 assemblies where the assemblies with smaller π - π distances exhibited excitonic emission while those with larger spacings showed excimeric states.⁴⁵ The findings from these molecular dynamics simulation highlight the importance of the monomer design that dictate the extent of intra- and intermolecular interactions that consequentially affect the kinetics and thermodynamics of the self-assembly process.

This Chapter will discuss the effect of varying the amino acid bulk adjacent to the central quaterthiophene (OT4) unit, a hole-transporting organic semiconductor, on the material properties of peptide- π -peptide triblock constructs.⁴⁶ Because the enthalpic origin of many self-assembled structures in water is the intermolecular interactions between the hydrophilic and hydrophobic segments among the constituent molecules, we varied the hydrophobicity and the size of the amino acids adjacent to the π -core, changing from glycine (G), alanine (A), valine (V), isoleucine (I) to phenylalanine (F), while keeping the terminal negatively charged residue, aspartic acid (D) or glutamic acid (E), constant (Figure 2.1). Here, the discussion of the sequence-dependence of photophysical, rheological and bulk electrical properties will focus on five *DXX* OT4 peptides ($X=$ G, A, V, I, F) while the device measurements will include eight *DXX* and *EXX* OT4 peptides ($X=$ G, A, V, I). This reports the findings for the first attempts towards a comprehensive study of the hydrogelation mechanics aspect of these materials. We chose a tripeptide sequence to emphasize the effect of the dipeptide variation on the π -stacking behavior. Glycine

residues are known to induce flexibility within peptide chains²⁷ and are the smallest residues among the 20 natural amino acids. Alanine is known for being a weak β -sheet former with a higher preference for α -helices.⁴⁷ On the other hand, valine, isoleucine, and phenylalanine were reported to have high propensities towards β -sheet formation, with valine having the strongest preference in forming such motifs.^{47,48} Phenylalanine is also widely employed as a dipeptide hydrogelator when conjugated to a *N*-fluorenylmethoxycarbonyl (Fmoc) group,²⁷ as discussed in Chapter 1. The variations between these amino acids involve steric bulk and differences in the nature of their hydrophobicity. It is proposed that this systematic molecular design variation affects the supramolecular assembly and the fibrillization process, and thus propagates to influence bulk hydrogel characteristics.

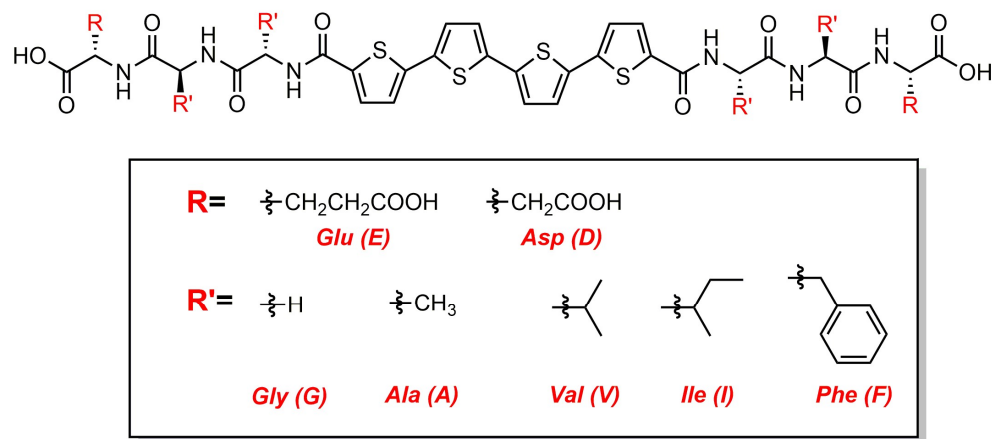


Figure 2.1. Molecular structures of the quaterthiophene-peptide (DXX) hydrogelators studied herein.

In earlier studies from the Tovar group, these peptide- π -peptide constructs were incorporated as active layers of OFETs, with hole mobility values of 1.4×10^{-3} to $0.03 \text{ cm}^2 \text{ V}^{-1} \text{ s}^{-1}$ for an OT4 core with different macroscopic orientations.⁴⁹ The previous study with

Glu-Ala-Ala peptides conjugated to a OT4 core is the first report of gate field conductance modulation for nanostructured π -conjugated units embedded within insulating peptide moieties assembled under aqueous conditions. Other seminal studies on π -conjugated peptides support that peptidic segments offer a way to vary the associated electronic properties of self-assembled systems.^{45,50-55} An earlier work by Brian Wall in the Tovar group for the investigation of structure-property correlations for peptide- π nanomaterials showed that single amino acid substitutions within π -conjugated tetrapeptide scaffolds resulted in significant changes in electronic interactions and in the nature of excited states due to the influence of intermolecular forces imparted by the peptide segments on the core π -orbital overlap.⁴⁵ Studying the effect of amino acid substitutions on the macroscale electrical transport and mechanical properties of these π -conjugated peptides is also important in understanding the structure-property correlation for these materials. The findings from these studies provide insights on the rational design strategies for the construction of soft, biologically-relevant and optoelectronic hydrogels for future tissue engineering applications. Moreover, the following sections will discuss the incorporation of various sequences of OT4-bound tripeptide nanomaterials as both the active semiconducting layer and, for the first time, as a gate contact in an OFET device. The utility of these optoelectronically-active peptide hydrogelators as a gate or semiconductor in an FET geometry allows the fundamental understanding of carrier transport and voltage equilibration within these materials for future biological applications.

Results and Discussion

Previous reports on the spectroscopic properties of several peptide- π -peptide triblock molecules with semiconducting properties verify the formation of 1-D nanostructures triggered by either increasing the ionic strength or decreasing the pH of the solution.⁴⁹ The assembly process (Figure 2.2) ideally results in intimate π -system contact and electronic delocalization among the embedded chromophores. Assemblies formed from the DXX peptides upon acidification should ideally contain β -sheet-rich structures such as those found in natural amyloid fibrils, but such ordered internal structures are not crucial in forming nanostructures with or without delocalized electronic states.^{45,56} It was previously reported that these assembled peptide networks can aggregate into higher-order fibrillar superstructures with local disorder while maintaining electronic delocalization among the embedded π -electron units.^{57,58}

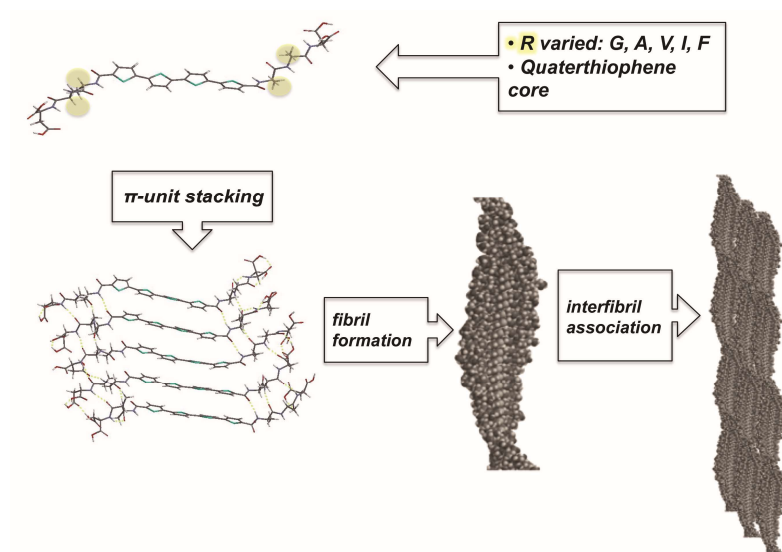


Figure 2.2. Schematic diagram of the proposed self-assembly process for π -conjugated peptides (The π -stacked units are low-level energy-minimized models while the space-filling models are not energy-minimized and are only constructed for illustration purposes).

Based on energy-minimized models generated from pentameric stacks of each peptide (Figure 2.3), there are apparent differences in the organization of the hydrogen bonds between the peptide monomers along with differences in the distance between the π -units of the central π -system. The employed geometry optimization method shows DVV and DII having the least deviation from ideal β -sheet peptide motifs due to the strong β -sheet preference of valine and isoleucine residues. The DGG sequence, which places the non-chiral glycine residues nearest to the π -core, has sufficient conformation flexibility to significantly deviate from the ideal β -sheet peptide motif. However, the FT-IR spectra taken from lyophilized peptides suggest that comparable hydrogen-bonding interactions and secondary structures are adopted in the solid state within all peptide nanostructures. All five examples show Amide I ($\sim 1630\text{ cm}^{-1}$) and Amide II ($\sim 1530\text{ cm}^{-1}$) IR bands within the range for a typical peptide with a β -sheet motif (Figure A2.31-32).

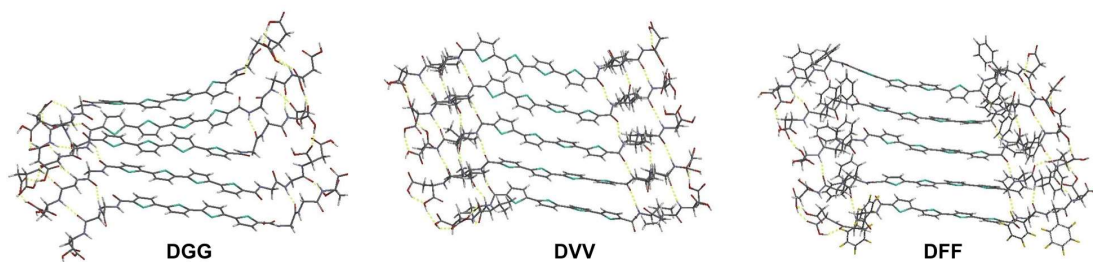


Figure 2.3. Representative energy-minimized models for the supramolecular assembly of DGG, DVV and DFF peptides showing the hydrogen bonding interactions (---).

The formation of 1-D nanostructures from 0.01 to 1 wt% peptide solutions under acidic conditions were consistently observed for all the nine OT4 peptides (DFF, DXX and EXX, X= G, A, V, I) studied in solution and in dropcast films, with the alanine-containing peptides having the largest nanostructure widths (Figure 2.4). All the peptides formed 1-D

nanostructures that span up to micrometers in length but with varying fiber widths and persistence lengths as expected from these polydisperse supramolecular polymers. The DGG peptide shows more entangled networks and seemingly flexible fibrils with relatively shorter persistence lengths, while the DAA peptide shows apparent twists within each nanostructure and is the thickest among the five peptides with approximately three-times the width of the other four peptide nanostructures. This relatively thicker nanostructure width was also observed for a previously reported tripeptide variant, EAA-OT4 peptide (13 ± 1.6 nm).⁴⁹ The peptides DVV, DII and DFF showed comparable nanostructure dimensions and also led to higher aspect ratio nanostructures as compared to DGG but with smaller nanostructure widths than DAA. The fiber widths for DFF are approximately the same as those observed previously for Fmoc-FF fibrils (~ 3.0 nm).^{27,59}

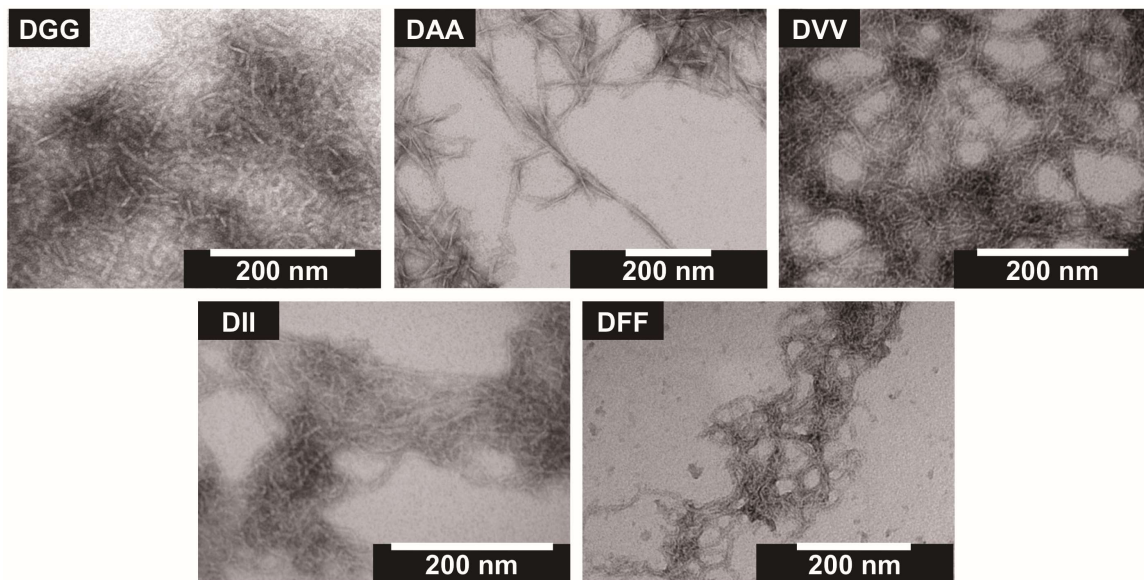


Figure 2.4. TEM micrographs of peptide nanostructures prepared from 0.1 wt% of DXX peptides (fiber widths in parentheses): DGG (4.4 ± 0.6 nm), DAA (12.3 ± 1.8 nm), DVV (3.0 ± 0.5 nm), DII (3.6 ± 0.4 nm), and DFF (4.1 ± 0.7 nm).

The differences in fiber widths suggest that these molecular variations led to different lateral interfibril associations, which arises from the fact as the surface composition of each stack is varied and the lateral electrostatic and solvation preferences are significantly affected.^{60,61} The nanomaterial topology associated with the more concentrated 1 wt% hydrogels were also characterized using TEM, consistently showing 1-D nanostructure formation in the hydrogel state comparable to those found in the 0.1 wt% acidic nanostructure solutions (Figure 2.5). All peptide sequences show well connected nanostructures in the gel form, as shown in the TEM images (Figure A2.34-40). The VV- and II-containing peptide hydrogels seem to have regions with local alignment, which could be attributed to high β -sheet propensities within the peptide backbones based upon these sequences. Even though nanostructure bundling is evident for these cases, the hydrogel fiber network seems to be less dense than for GG- and AA-containing peptides in the gel state.

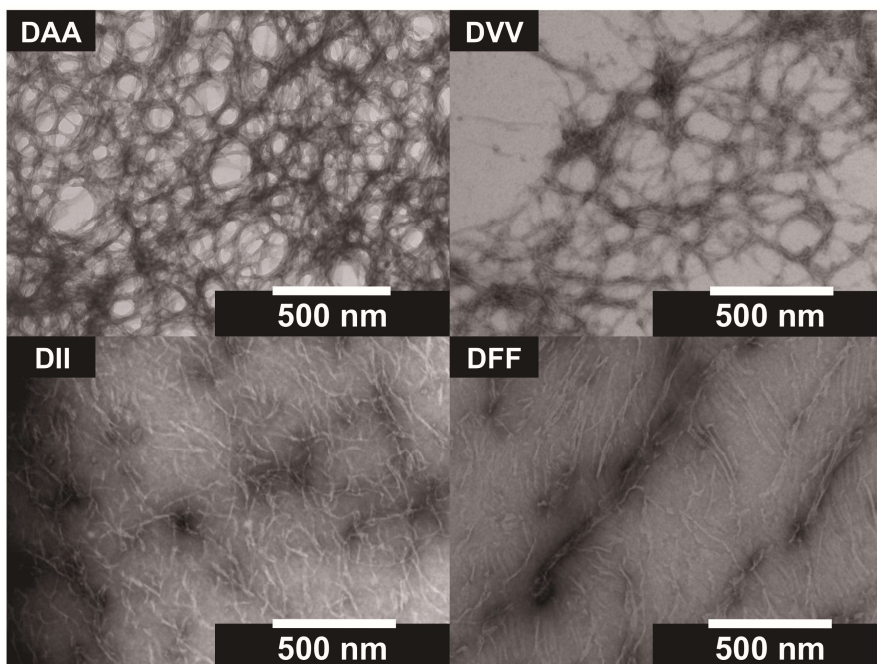


Figure 2.5. TEM images of the acid-assembled 1 wt% DXX peptide hydrogels.

For the dropcast films created from the nine OT4 peptides, the film topography was studied using AFM and laser profilometry. The representative AFM images for EAA-OT4 peptides show that the 1-D nanostructures are still microns in length in the dropcast films that were used for device fabrication. (Figure 2.6) These are consistent with the observed morphologies in the solution-state as shown in Figure 2.4.

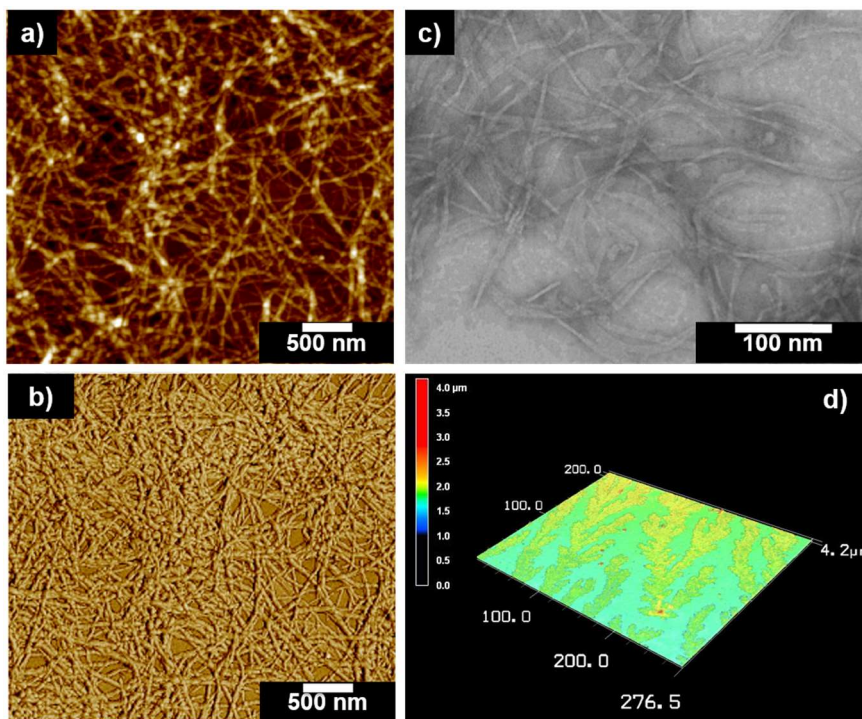


Figure 2.6. AFM image of 0.1 mg/mL dropcast film of assembled EAA-OT4 peptide, (a) height and (b) phase profiles; (c) TEM image of 1 mg/mL solution of acidified EAA-OT4 solution (width= 8.9 ± 2.4 nm); (d) surface profile of a 10 mg/mL dropcast film of EAA-OT4 under a laser microscope.

The microscopic surface profiles show varied surface roughness among the OT4 peptides that can be attributed to the different nanostructure aggregation behaviors upon drying of dropcast films of the peptides with different hydrophobicities (Figure 2.7). Due to the observed variations in the surface roughness and local aggregation patterns of the

films of the sequence-varied peptides, we expect that this would have implications for the macroscopic connectivity of the semiconducting units, and thus, the currents passing through the films in device structures, as discussed later. These surface profiles for the dropcast films of the eight *DXX* and *EXX* peptides (< 10 μm -thick) support the network characteristics observed in hydrogel TEM, wherein GG- and AA-containing peptides show islands of dense networks of assembled nanostructures while VV- and II-containing peptides show more uniform films. Both AFM and surface profile characterizations were conducted on silicon surfaces and therefore can be reasonably extrapolated to the surfaces upon which these nanomaterials would be deposited for device fabrication.

On the other hand, among the five *DXX* peptides, only DGG did not form a hydrogel and instead resulted in precipitation from a 1 wt% acidic solution. This was also observed in analogous Fmoc-GG hydrogels that exhibit entangled fibrillar networks and were reported to be particularly susceptible to precipitation within the range of 4 to 25°C, at pH conditions below its apparent pK_a .²⁷ We qualitatively assessed the density of each *DXX* hydrogel fiber network by taking SEM images of critical point-dried hydrogels. Among the four, the DII hydrogel had the highest crosslinking network density, with tightly packed mesh and smaller pores as supported by the SEM images. The images shown in Figure 2.8 are representative of the major topography of critical point-dried gels that were consistently observed with at least three independently formed gels for each peptide sequence.

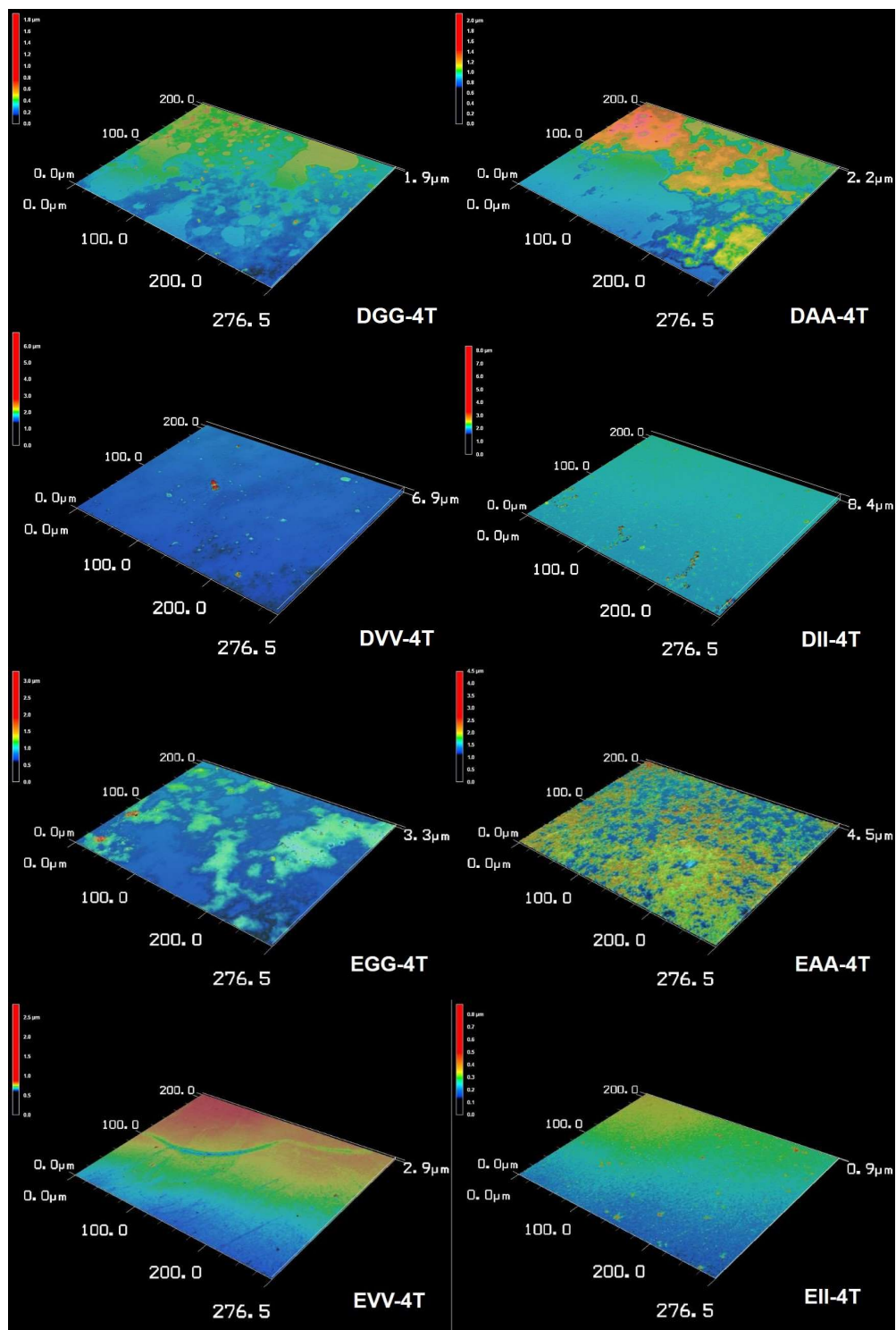


Figure 2.7. 3-D surface profiles of 1 wt% DXX- and EXX-OT4 peptide films used for FET measurements.

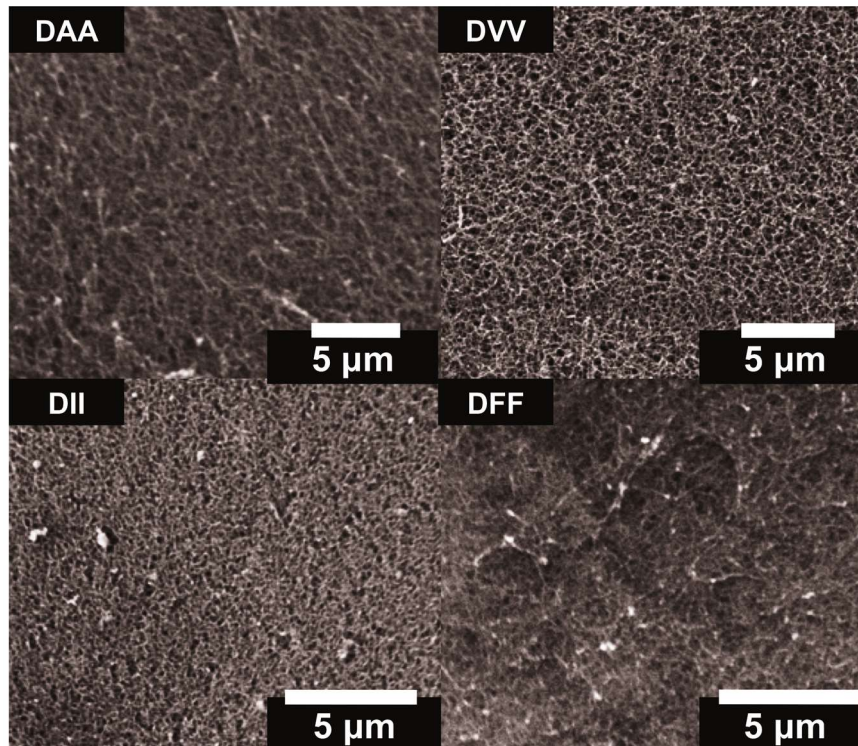


Figure 2.8. Representative SEM images of critical point-dried, acid-assembled, *DXX* hydrogels (1 wt%).

The rheological properties of the *DXX* π -conjugated peptides were determined by dynamic oscillatory rheometry with varied frequency (Figure 2.9), strain (Figure 2.10 and 2.11) and temperature (Figure 2.10 and 2.11), providing a dynamic mechanical analysis of the storage (G') and loss (G'') moduli that characterize the elastic and viscous properties of a material, respectively. The bulk rheology measurements indicate that all of the four *DXX* hydrogelators have $G' > G''$, suggesting more elastic or solid-like character rather than viscous or fluid-like character, which is indicative of gel formation. In general, a gel with $G' \geq 10$ Pa is considered stable, while those with $G' \leq 1$ Pa is would be too soft to process and handle for practical use.⁶² The DVV and DII hydrogels both have the highest G' (~20 kPa), which is almost an order of magnitude higher than the DAA hydrogel (~3 kPa).

Although there are no definitive trends that can be directly correlated to molecular structures, the DVV and DII hydrogels both contain residues that have strong preferences for β -sheet formation, similar to other peptide-based hydrogels such as peptide amphiphiles and Fmoc-dipeptides that are also comprised of residues that favor β -sheet formation ($G' \sim 1-60$ kPa).^{27,33} The weaker mechanical properties of the DAA hydrogel can be attributed to the high amount of twisting within the assemblies as suggested by a large red-shift of the high-energy CD signal with respect to an ideal β -sheet signal that would increase the hydrogen bond length between amino acids and would thus weaken the bonding within the supramolecular polymer.^{33,63} The phenylalanine residues within the DFF sequence presumably should offer strong β -sheet propensity, but a weaker gel is also obtained. The mechanical properties of Fmoc-FF hydrogels^{14,27,59} under different conditions (*e.g.*, pH, concentration, temperature) are highly dependent on the Fmoc and Phe π - π interactions that are maximized when the peptide moieties can associate in anti-parallel β -sheet orientations.⁵⁹ It could then be deduced that the DFF symmetrical peptide- π -peptide construct, which requires peptide moieties to associate in a parallel β -sheet arrangement, yields weaker mechanical properties than its Fmoc-FF equivalent hydrogels (G' up to ~ 10 kPa).⁵⁹ The G' values of the hydrogels studied herein match the mechanical properties of adipose tissues and muscle, thus suggesting some relevance for the future use of these hydrogels as scaffolds for these tissues.⁶⁴ Tuning of the gelation conditions such as lowering the peptide concentration within the hydrogel, a strategy used for other peptide-based hydrogelators,³² can extend the range of mechanical properties towards the lower end (100 to 1000 Pa) for future use with “softer” electrosensitive biological systems.

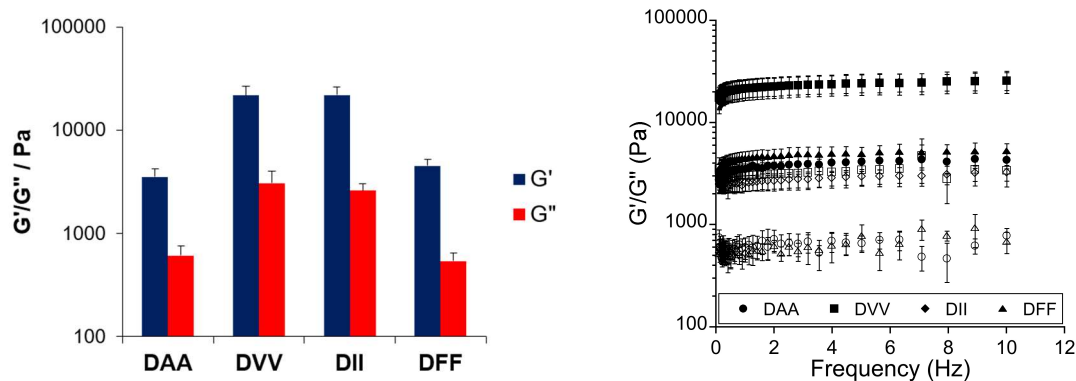


Figure 2.9. Storage and loss moduli data (at 1 Hz) taken from frequency sweep experiments at 0.3% strain (25 °C), for DXX hydrogelators (*left*); frequency sweeps (0.1-10 Hz; 0.3% strain; 25 °C) for 1 wt% DXX peptide hydrogels (*right*).

In order to classify these materials in the context of soft matter and complex fluids, we analyzed the strain sweep profiles acquired from dynamic oscillatory shear tests. The strain sweep curves generated from DXX hydrogels generally show constant moduli up to 1% strain, with varying limiting strain values (γ_L , which is the transition between the linear and non-linear viscoelastic regimes); hence, all the frequency and temperature sweeps are carried out below 1% strain to ensure that all measurements are within the linear regime. From the strain sweep experiments, we observed that all the four hydrogels follow the curve characteristic to a polymeric solution with *weak-strain overshoot behavior*.⁶⁵ This is less commonly observed for polymeric solutions than the *strain thinning behavior*, wherein the polymer chains disentangle and align with the local field as the strain increases. The weak-strain overshoot behavior has been previously observed for xanthan gum solutions, dough (flour/water/salt), oil-in-water emulsions, and polyisoprene containing carbon black, among many others. Having this type of behavior is suggestive of complex structures comprising the bulk gel, which have components that interact differently upon varying the strain but is susceptible to the disassembly of the complex structure past beyond a certain

strain deformation limit wherein the components would follow a local alignment along with the flow field. The behavior of the gels were further assessed as a function of strain by extending the strain sweeps to higher strain values (up to 500%) and did a cyclic strain sweep, wherein the strain was increased and then swept back to both 100% and 500% strain.

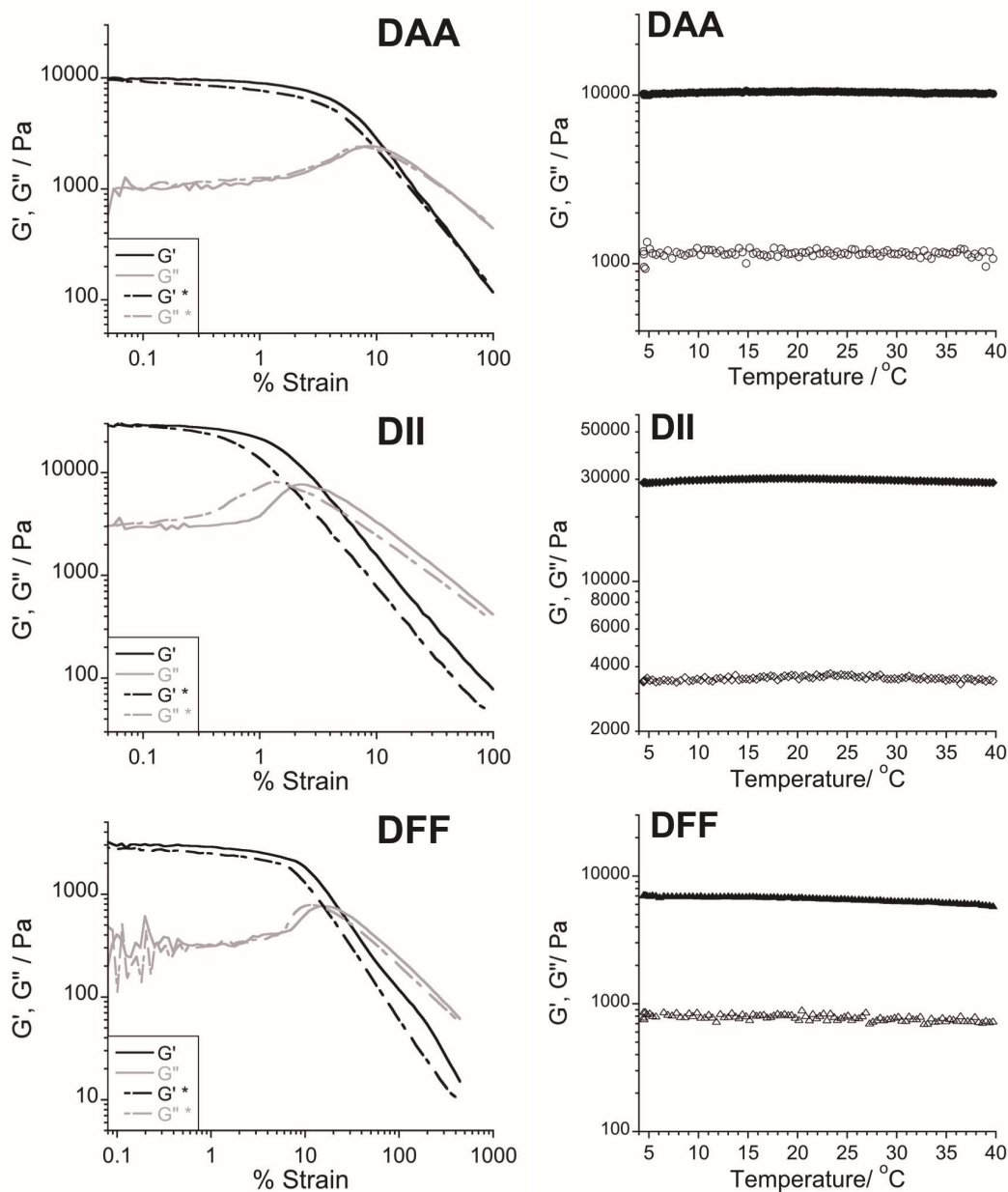


Figure 2.10. Strain sweeps (*left*, including cyclic sweeps) and temperature sweeps (*right*) for DAA-, DII-, and DFF-OT4 1 wt% peptide hydrogels.

For DVV, even at 500%, the gel had an almost complete recovery of the G' and G'' values. The observations from these cyclic strain sweep experiments suggest the reversibility of the mechanical properties of these hydrogels upon subjecting to different strain conditions. To see whether there are any drastic changes in the gel stiffness upon approaching the physiological temperature (37 °C), a temperature sweep was conducted for all four gels from 4 °C to 40 °C. All four gels showed constant G' and G'' values within the temperature window, showing that any changes in the supramolecular ordering within the 1-D structures as a function of temperature increase are very minimal and do not impact the bulk rheological properties of the gels.

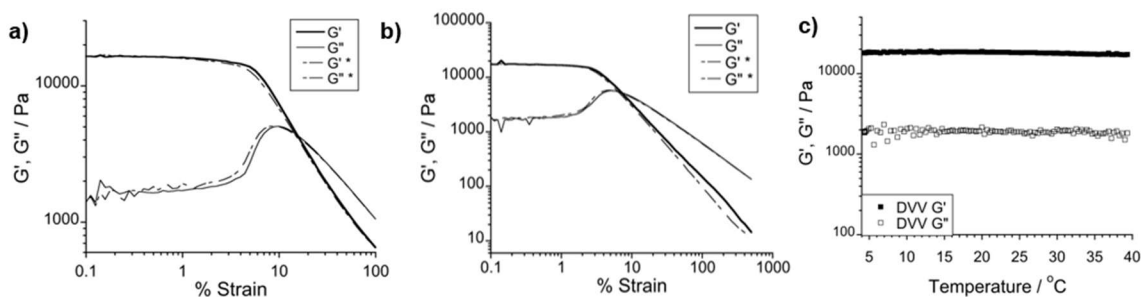


Figure 2.11. Representative strain sweeps for DVV; (a) 0.1% to 100%; (b) 0.1 to 500% strain; * indicates reverse strain sweeps, 100% to 0.1% for (a) and 500% to 0.1% for (b); (c) representative temperature sweep for DVV, showing the stable G' and G'' values from 4 °C to 40 °C.

In principle, the intermolecular geometries within each peptide- π -peptide nanostructure can be differentiated based on the resulting photophysical behaviors. However, these types of peptidic nanomaterials form rather polydisperse structures with local disorder, so spectroscopic measurements should be interpreted as a representation of the ensemble average of different local chromophore orientations within the supramolecular networks. Because the absorbing chromophore is essentially the same (quaterthiophene- α,ω -bis(carboxamide)), it is reasonable to relate photophysical

differences to different internal chromophore orientations. Figure 2.12 and 2.13 shows the region of quaterthiophene absorption (*a*) and emission (*b*) for both the dissolved and assembled DXX and EXX OT4 peptides under basic and acidic conditions, respectively. The absorption and emission spectra for dissolved peptides under basic conditions (*ca.* pH 10) did not significantly vary between the amino acid substitutions showing that the residues did not significantly affect the photophysics of the isolated chromophores. Upon acidification, the general assembly model in Figure 2.2 would suggest an “H-like” aggregation, wherein the peptide hydrogen-bonding networks support near-cofacial interactions between the quaterthiophene units. This is consistently observed in other self-assembled oligothiophene systems such as nucleotide-bound quaterthiophenes in water,⁶⁶ bis(trialkoxymethyl)-functionalized quaterthiophene derivatives in non-polar solvents (e.g., cyclohexane, *n*-pentane),⁶⁷ and perfect crystalline and orientationally disordered domains of quaterthiophene in films.⁶⁸ The absorption profiles of the acidic peptide solutions all show a blue-shift in absorbance with respect to the spectra at basic conditions. In addition, a progressive blue-shift in absorption maxima as the amino acid bulk adjacent to the π -core unit decreases was also observed (Figure 2.12a), with the nanostructures derived from the less hydrophobic DGG and DAA peptides being the most distinctively blue-shifted by *ca.* 50 nm with respect to the basic (dissolved) OT4 peptides. In contrast, the nanomaterials derived from the larger DVV, DII and DFF peptides show much less pronounced shifts (*ca.* 8 nm). In addition to the blue-shifted absorption peaks due to an “H-like” aggregation, the observed shoulders in the absorption spectra (\sim 440, \sim 470 nm) for the five peptides can be attributed to the increase in local conformational order within the assembly.⁶⁷

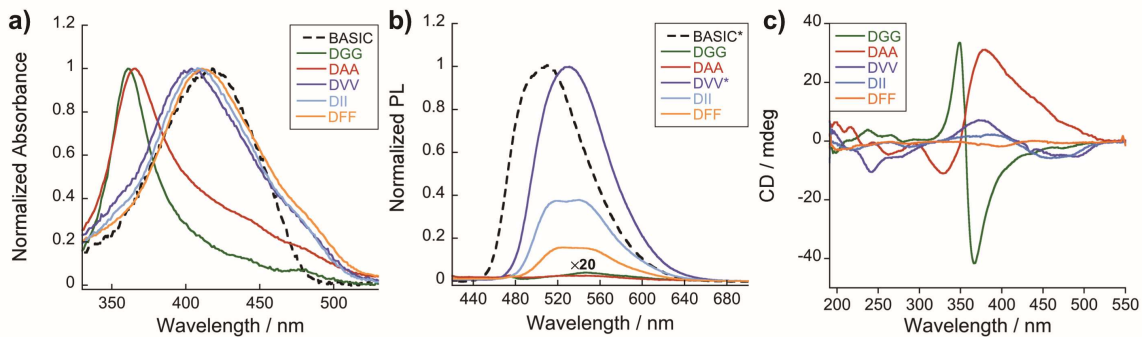


Figure 2.12. (a) UV-Vis, (b) PL ($\lambda_{\text{exc}}=410$ nm), and (c) CD spectra of DXX peptides (~ 14 μM) in basic (*ca.* pH 10, ---) and acidic solutions (*ca.* pH 2, —). For PL spectra, all peptides were normalized with respect to DVV and the basic spectrum was arbitrarily set to the same intensity as DVV; DGG and DAA spectra, $\times 20$.

The emission profiles of the nanostructures also showed varied spectral signatures and extents of quenching with respect to the molecular emission profile (Table 2.1). Nanostructures composed of the less hydrophobic DGG and DAA peptides had almost completely quenched, featureless, red-shifted emission profile relative to that of the basic, molecular solution. On the other hand, nanostructures derived from the more hydrophobic DVV, DII and DFF sequences also have red-shifted, quenched emission spectra with respect to the molecular spectrum but with higher intensities as compared to DGG and DAA. The two bulkiest dipeptides, -II and -FF, showed a bimodal emission profile similar to the reported emission profiles of longer oligothiophenes and quaterthiophenes in less polar solvents.^{67,69,70}

Table 2.1. Relative quantum yields (Φ_{PL}) and absorption maximum (λ_{max}) of DXX peptides (*normalized to DVV peptide in acidic solutions).

	Relative* Φ_{PL}	λ_{max} / nm
DGG	0.008	362
DAA	0.002	366
DVV, <i>pH 2</i>	1.00	403
DII	0.39	408
DFF	0.16	412
DVV, <i>pH 10</i>	8.40	416

The circular dichroism (CD) spectra of the assembled (acidic) peptide solutions (Figure 2.12c) reveal a diversity of locally chiral chromophore environments. In all cases, the existence of an exciton-coupled Cotton band that has a crossover near the absorption maximum of the peptides indicates that the chromophores are held in local chiral environments. The intensity and the sign of Cotton effect varied among the peptide nanostructures, which also indicates the differences in the extent of interactions between the chromophores within the respective 1-D π -stacks. Moreover, the distinct difference in the handedness of the CD signals (DGG vs. DAA; DVV/DII vs. DFF) supports the influence of these simple dipeptide substitutions on the resulting aggregate internal structure that varies the collective ensemble orientation of the transition dipoles. The peptide hydrogen-bonding networks can also be analyzed from the CD spectra, wherein DVV shows the most intense minimum (246 nm) within peptide absorption region among the five peptides. A standard β -sheet signal has a maximum at \sim 195-210 nm and minimum at 216 nm; observed red-shifts with respect to these standard signals, such as that observed in DVV, have been associated to twisting of the β -sheet. An increase in the extent of red-shift of this high energy CD peak is associated with more twisting.^{71,72} For the structures studied here, the hydrogen bonding networks may not directly correlate to that of the

natural systems not bound to π -conjugated units *via* carbonyl or carboxamide linkages. Therefore, the information regarding the peptide hydrogen bonding networks extracted from CD and IR spectroscopy may present some ambiguity but does not discredit the formation of one-dimensional nanostructures assisted by peptide hydrogen bonds. The CD spectra collected here show predominant nanostructure handedness that places the quaterthiophenes in globally chiral electronic environments within each of the peptide hydrogen-bonding networks.

In general, these spectroscopic measurements performed for the assembled π -conjugated peptides studied herein showed two distinct spectral responses corresponding to the *smaller* DGG and DAA peptides and the *larger* DVV, DII and DFF peptides. The DGG and DAA peptides showed dramatic blue-shifts in absorbance, quenched and red-shifted emission profiles, and more pronounced bisignate Cotton effect CD signatures, which all support the H-like aggregation of quaterthiophene buried within these peptide moieties. On the other hand, the more hydrophobic DVV, DII and DFF peptides also show emission red-shifts with respect to the dissolved spectrum but with higher intensities (i.e., less quenching) than DGG and DAA, and they are also minimally blue-shifted relative to the absorbance of the basic solution. The steric bulk presented by the relatively larger aliphatic (valine, isoleucine) and aromatic (phenylalanine) residues potentially contributes to a significantly varied chromophore planarization and intermolecular electronic coupling within the nanostructures, leading to the less blue-shifted absorption and more intense PL signals than DGG/DAA. These trends regarding the steric bulk of the residues adjacent to the π -core were previously observed in a systematic investigation of the effect of single amino acid substitutions on the chromophore photophysics of tetrapeptide bound to an

oligo(*p*-phenylenevinylene) core with the same peptide- π -peptide motif.⁴⁵ The CD signatures corresponding to the DVV, DII and DFF peptides are also less intense (with the aromatic side chain-containing DFF peptide having the least intensity) than the DGG and DAA peptides, showing the difference in the extent of exciton-coupling of quaterthiophene units within each specific chiral peptide environment.

The spectroscopic trends found for DXX-OT4 peptides were consistent with the findings for EXX-OT4 peptides (Figure 2.13). The maximum absorption of EXX OT4 ranges from \sim 360 nm to 410 nm as the amino acid bulk adjacent to the chromophore increases while the PL at basic conditions also have a maximum at 510 nm, which red-shifts to \sim 540 nm under acidic conditions. The CD spectra also shows varied bisignate exciton-coupled π - π^* signal intensity and handedness. Overall, varying the amino acid termini from glutamic acid residues to aspartic acid residues does not dramatically change the observed spectral profiles.

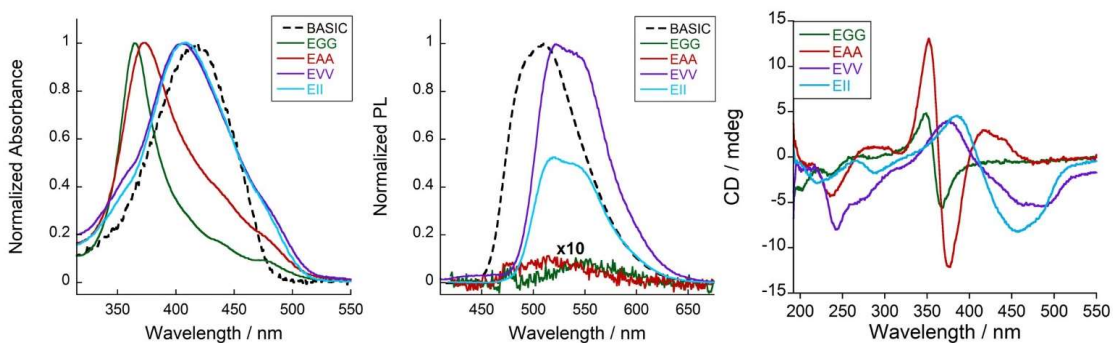


Figure 2.13. (a) Absorption, (b) emission ($\lambda_{\text{exc}} = \text{nm}$) ($\sim 14 \mu\text{M}$), and (c) circular dichroism spectra ($\sim 6 \mu\text{M}$) of OT4-peptides in basic (*ca.* pH 10, ---) and acidic solutions (*ca.* pH 2, —). For the emission spectra, peptides were normalized with respect to EVV and the basic spectrum was arbitrarily set to the same intensity as EVV.

In order to characterize and compare the electrical properties of these different peptide nanomaterials, we first measured the resistivity of dried, acid-assembled peptides using four-point probe measurements and then calculated the sheet resistance (R_s) values using the van der Pauw method (Figure 2.14). The microscopic surface profiles obtained for each dropcast film sample showed that all peptides formed continuous films but differed in surface roughness (Figure 2.7). The trends suggest that the roughness of a peptide film appears to play a more crucial role in determining the bulk resistivity value rather than the geometry or persistence length of each nanostructure.

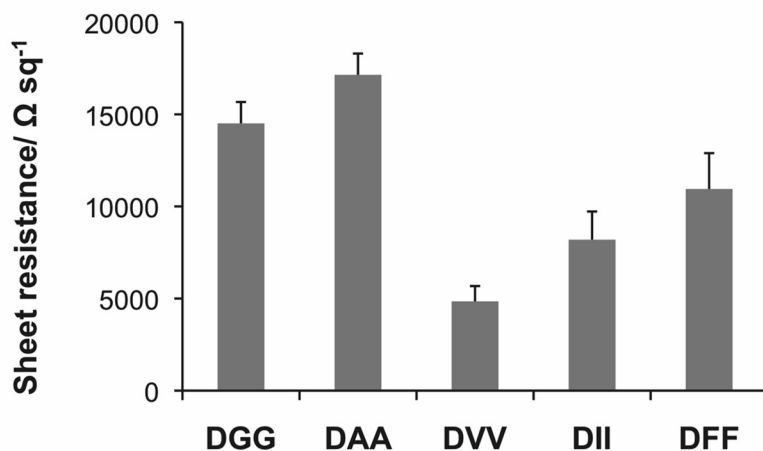


Figure 2.14. Representative sheet resistance vs. current plots for the dried, acid-assembled DGG peptide films under light and dark conditions.

The DAA peptide, which formed nanostructures with the greatest fibril thickness (implying a highly favored interfibril association) but had the roughest surface features, showed the highest R_s . Although the favorability of interfibril bundling translates to the formation of thicker nanostructures such that the interpenetrating networks between the nanostructures provide more efficient pathways for carriers, this aspect is of higher significance in determining the carrier mobility within or among the nanostructures but

does not take into account the other factors that affect bulk electrical properties such as resistivity. Theoretically, the higher surface roughness of films leads to higher material resistance due to increased electron scattering effects.⁷³ The trend observed here does not directly correlate to the hydrophobicity or the amino acid bulk adjacent to the central π -core; however, the final surface roughness of the films can be correlated to the gelation properties of each peptide. During the slow acidification process (*i.e.*, exposure of molecular peptide solutions to acid vapors), the 1 wt% solutions pass through a gel state prior to drying. Due to the dynamic nature of bonds of supramolecular polymers such as these, softer gels are more susceptible to the rearrangement of features as water is being eliminated from the hydrogel architecture during the drying process of the films. On the other hand, the stiffer gels potentially lock the nanofibril network in a more efficient manner than the softer gels, and thus lead to a more uniform dried film that resembles the initial hydrogel network. Hence, this electrical property is still dependent on the inherent aggregation behavior of a specific peptide- π -peptide monomer. Only the DGG peptide film exhibited considerable photoconductive response (Figure 2.15), resulting in a decrease in sheet resistance by $6.6 \pm 1.6 \text{ k}\Omega \text{ sq}^{-1}$ after illumination with a 150-W halogen lamp source. These measurements then provide an insight on how the sheet resistance of a conductive material can be altered by simple side chain substitutions even though the buried semiconducting unit within peptide moieties, quaterthiophene, is kept constant across the peptide series.

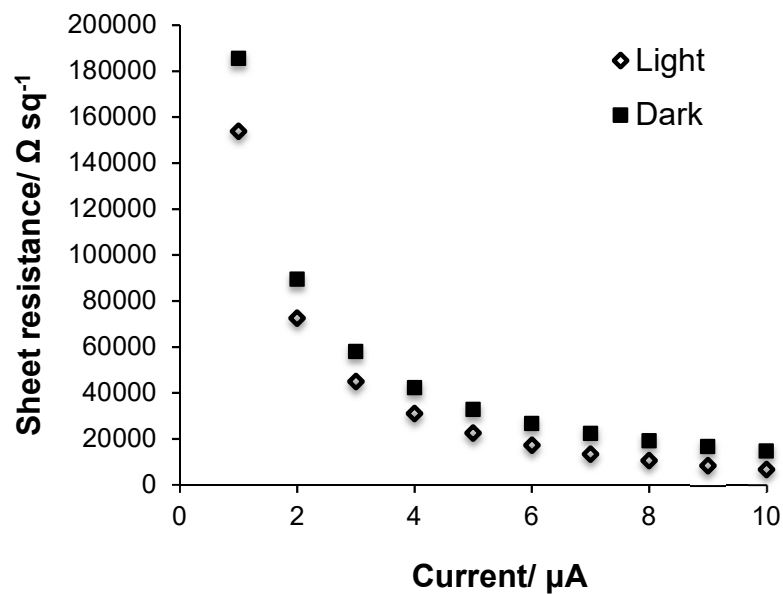


Figure 2.15. Representative sheet resistance vs. current plots for the dried, acid-assembled DGG peptide films under light and dark conditions.

To measure the charge transport properties, the eight OT4 peptides (DXX and EXX; X= G, A, V, I) were used as active semiconductor layers in an OFET. OFET geometries are the foundational structure for technical applications like RFID (radio frequency detection), roll-up light emitting displays and different sensor platforms that possess attractive attributes such as printability, low cost production, and mechanical flexibility,^{74,75} whereby film morphologies are closely related to device output currents.⁷⁶⁻⁸¹ Here, we are using the OFET architecture as an analytical tool to indicate effects of different nanostructure assembly morphologies on charge carrier mobility and electrical conductivity. Specific morphological factors include grain size, connectivity, orientation or packing disorder and traps (chemical or interfacial) in the films.⁸² All eight peptides studied herein form 1-D nanostructures that are microns in length, 3-12 nm in width, varied network connectivities in gel and solution state, and varied film surface roughness in the microscale (Figure 2.6-2.7).

There have been a few isolated reports on the carrier mobilities of biomolecule-containing oligothiophene nanomaterials with π -electron function, revealing mobilities on the order of 10^{-8} - 10^{-4} $\text{cm}^2 \text{V}^{-1} \text{s}^{-1}$.^{66,83,84} One goal of the present work is to reveal how molecular variation impacts nanostructure-dependent transport properties. Peptides without the semiconducting unit were used as controls (Figure 2.16b-c).⁸⁵ These two peptide nanomaterials were chosen as the control samples because they form similar one-dimensional nanostructures under aqueous conditions that would be geometrically relevant as a comparison for the π -conjugated peptides studied herein. Control sample **1** is a direct analog of peptide-OT4-peptide, with the OT4 substituted by $-(\text{CH}_2)_{10}$ units, while control sample **2** has an amphiphilic design with more charged residues in the peptide backbone than **1**. When the controls were used as the semiconducting layer, no apparent gating effects were observed. This supports the premise that the OT4-containing nanostructures in the film are providing to charge transport pathways that do not merely rely on ionic effects and in fact require the presence of hole-transporting OT4 subunits.

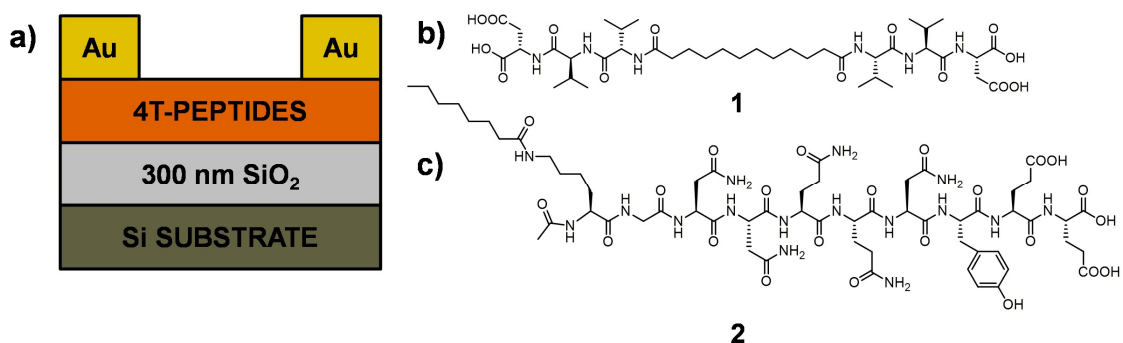


Figure 2.16. (a) Schematic of the FET architecture used to measure the hole mobilities within the peptide nanostructures; (b,c) control compounds used as the active layer replacing OT4-peptides in the configuration shown in (a).

All the peptide-OT4 nanowires gave semiconductor characteristics but the mobility values (Table 2.2) were observed to vary by three orders of magnitude upon varying the amino acids adjacent to the OT4 semiconductor. The corresponding output curves (Figure 2.17) show the gate-modulated field conductance for all the peptides.

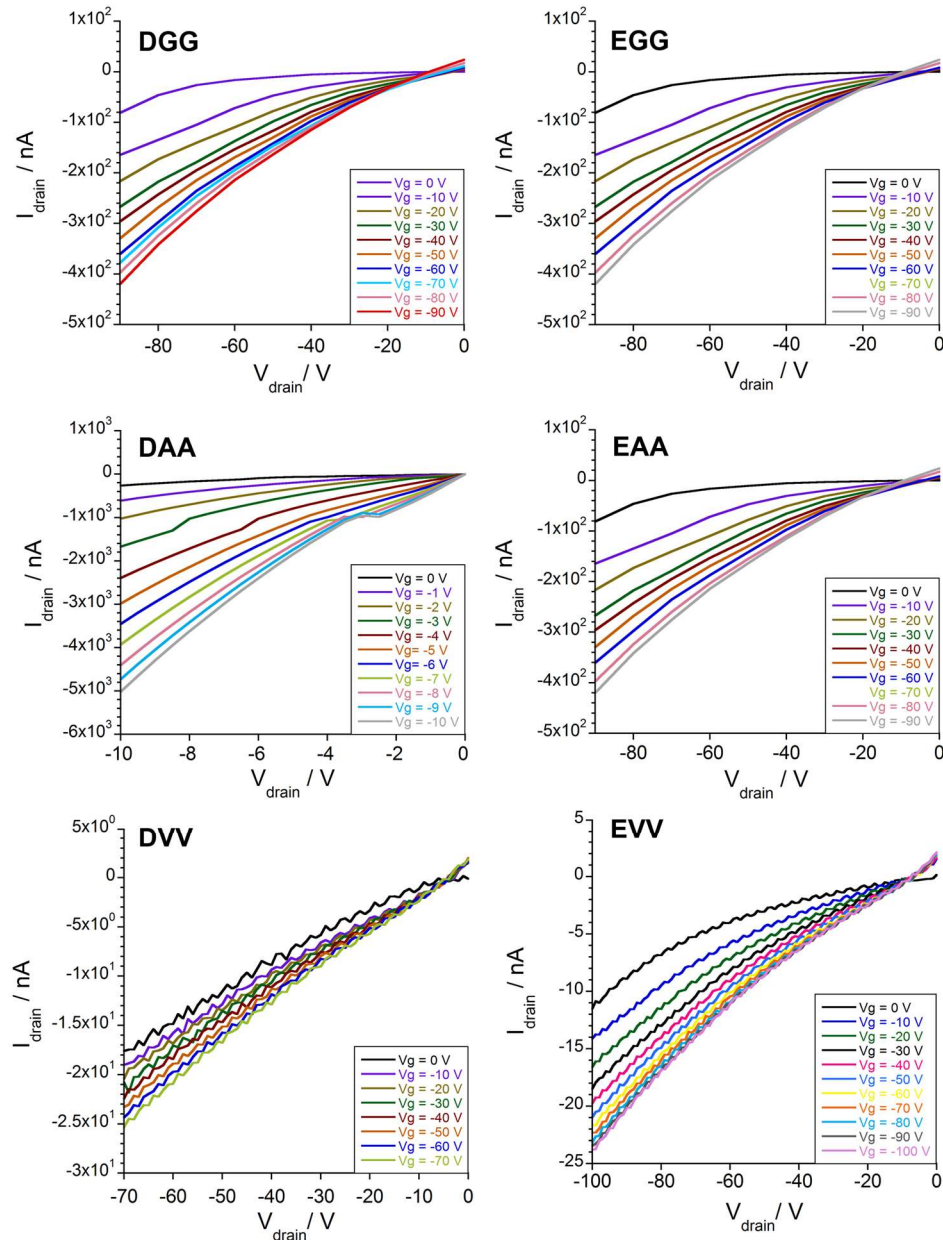


Figure 2.17. Output curves for OFET devices with the OT4 bis(peptides) as the semiconductor active layers.

Table 2.2. Mobility values for different OT4-containing π -conjugated peptides.

Peptide -OT4	$\mu_h / \text{cm}^2 \text{V}^{-1} \text{s}^{-1}$
DGG	0.017 ± 0.006
DAA	0.004 ± 0.003
DVV	$6.9 \times 10^{-5} \pm 2.1 \times 10^{-5}$
EGG	0.002 ± 0.0006
EAA	0.005 ± 0.004
EVV	$4.7 \times 10^{-5} \pm 6.2 \times 10^{-5}$

* *DII and EII are not included because no measurable hole mobility was obtained.*

Although we cannot directly compare the mobility values between devices constructed using different protocols, it is worth noting that the better performing -Gly and -Ala based peptides are within the order of magnitude or higher than the mobility values ($\sim 10^{-3} \text{ cm}^2 \text{V}^{-1} \text{s}^{-1}$) reported for unsubstituted quaterthiophenes unbound to peptide moieties.^{86,87} Those peptide nanostructures with the bulky -VV sequences, which have photophysical properties for the assembly that are least shifted from the dissolved π -conjugated peptide under basic conditions, showed the lowest mobility values. Apparently, even bulkier hydrophobic isoleucine residues perturb the assembly such that the charge-transporting properties within the assembly (as represented by hole mobilities) are inferior to the other peptides studied herein. This trend for the hole transport properties of these peptide nanostructures is a manifestation of the photophysical properties observed in solution state (Figure 2.12 and 2.13), wherein the -GG and -AA peptides that have the strongest intermolecular electronic couplings with the most blue-shifted absorption spectra and most quenched emission yielded higher mobility values. Such a trend can also be correlated to the importance of local packing order (nanostructure helicity, packing homogeneity, propensity to form ordered structures) and intermolecular distances of the semiconducting oligomers within the self-assembled nanostructures on the charge

transport behavior of the resulting films; both of which affect intermolecular π -electron delocalization.

The DAA and EAA peptides show ~three times greater nanostructure width than the six other peptides. While this suggests a general correlation of nanostructure width and mobility, DGG is an exception, where the intermolecular interactions leading to the blue-shifted spectra are apparently dominant. The DVV and EVV samples, on the other hand, were observed to have more dispersed nanostructures within their dropcast films or in their gel state. With the mobility data presented in Table 2.2 and the nanostructure characteristics that comprise the dropcast films, it could be deduced that nanostructure connectivity (*i.e.*, network formation) and the individual nanostructure morphology are the major factors to be considered for performance of these devices. Another factor that might be affecting the huge variations of mobility values between the devices of same peptide is the local alignment of nanowires within the device. It was previously reported that having the electrodes parallel to the alignment of the nanostructures led to better charge transport as compared to when the electrodes are perpendicular to the direction of material alignment.⁴⁹ Ideally, the films reported here should have randomly aligned nanostructures distributed within the layer. However, it is possible that there are areas with local alignment where the probes are directed, and hence leading to higher mobility values as compared to other area. Moreover, the different chemical and interfacial traps could also be unevenly distributed within the semiconducting film that is mainly comprised of non-conducting peptide moieties, leading to variations for the calculated mobility values per device. When these devices are tested over a period of time, a continuous increase in drain current was observed with or without light irradiation which indicates that there are low-lying traps being filled.

No photoconductive response was observed in this geometry, although there are reports about photoconductive effects for other semiconductor-containing peptide gels.⁸⁸ The two effects (field effect and photoconductivity) likely target the same energy level, so they are very closely intertwined and, in this particular device structure, we are not able to decouple these effects. It was also observed that there is a significant off-current—free ionic current in the material that is not related to gate leakage.

Because the –AA sequences yielded the nanostructures with the largest widths and resulted in films with apparently good connectivities between nanostructures, these nanostructures were chosen to function as gates for OFET devices (Figure 2.18) in order to assess the capability for these nanomaterials to support voltage transmission from an electrode contact and thus serve as an electrical extension of this contact. In this configuration, pentacene was used as the semiconductor while C₄₄H₉₀ (tetratetracontane) and pentaerythritol were chosen as the materials for gate dielectric layers because they form continuous films and bracket the extremes of hydrophobicity and hydrophilicity. The hydrocarbon has a dielectric constant of about 2.5.⁸⁹ Pentaerythritol will have a dielectric constant on the order of 10, depending on the degree of hydration, by analogy to dextran, a solid with similar density of polar oxy- functional groups.⁹⁰ With its high density of OH groups, pentaerythritol begins to model the OH-rich environment around cells. To determine whether the conjugated core and the nanowire self-assembly were necessary for gate voltage equilibration, we also fabricated devices with control samples **1** and **2** (Figure 2.16b-c) as the gate material. Control sample **2** gave very similar results to the DAA sample, although the drain current in the pentacene channel was slightly lower **2** than for DAA, while **1** does not give any working OFET data. This indicates that the free ions present in

the materials are partially responsible for the voltage transmission properties regardless of the composition of the internal cores (the hydrogels formed from peptides with and without π -electron cores are acidic).

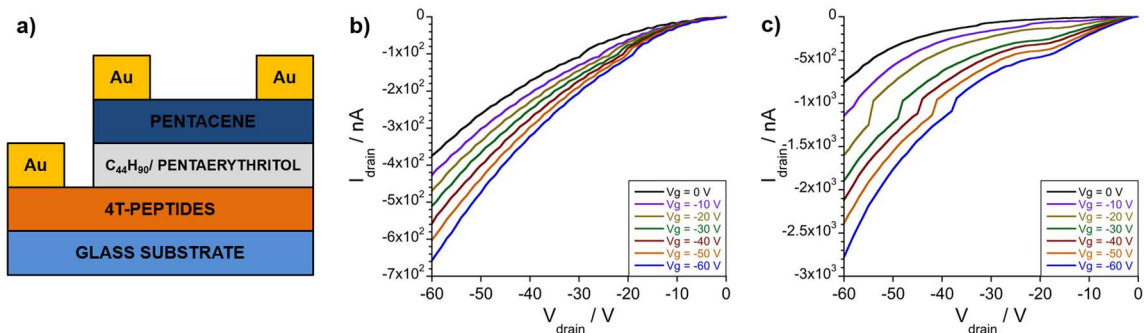


Figure 2.18. (a) Schematic diagram of the FET devices with peptide nanostructures as the gate; output curves for (b) control peptide 2 and (c) **DAA-OT4** used as a gate layer in the configuration shown in (a).

The thickness of the dielectric layer was varied between 20 nm and 100 nm in order to establish the maximum thickness through which the nanowire materials can transmit modest voltage that could be needed to stimulate a bilipical structure across cell membranes (*i.e.*, < 10 nm). Theoretically, it is expected that by increasing the dielectric thickness over which the voltage has to be transmitted, the gating effect would be weaker as interfacial dipole could compensate the voltage applied through the dielectric. It was observed that 35-40 nm dielectric allows the maximum electric field to drop across the dielectric layer without undue leakage current (Figure 2.19). Consistent with previous observation we found that 20 nm was too low thickness for forming well connected films because of island growth morphology of tetratetracontane.⁸⁹ Related π -conjugated peptides have been previously found to have both protons and electrons as contributors to the conduction, with the dominating carrier being dependent on the humidity because of its effect on peptide folding.⁹¹

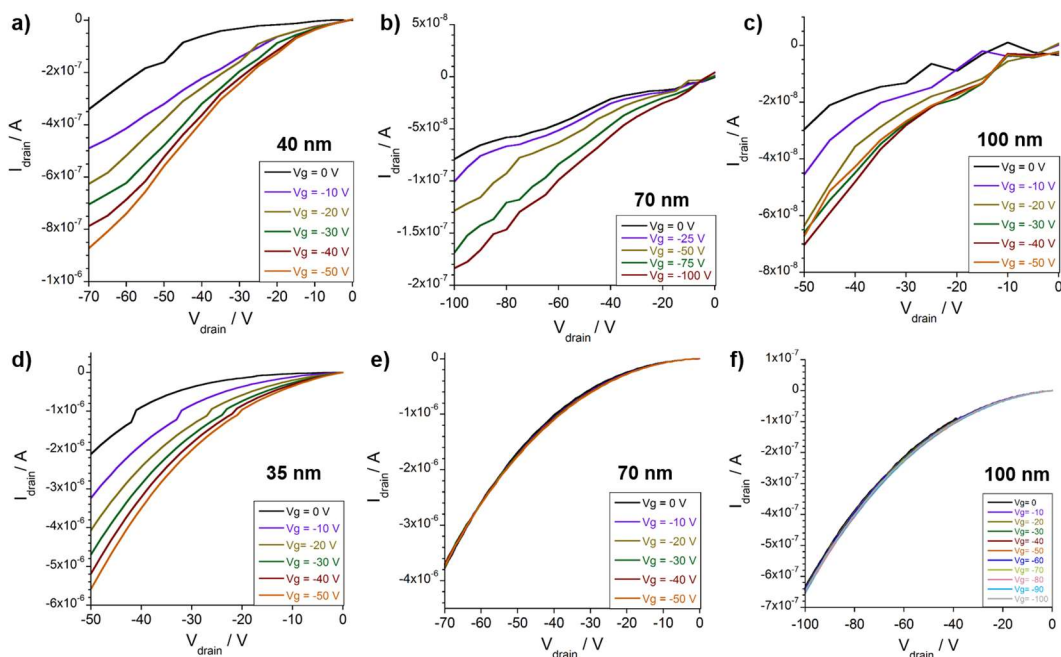


Figure 2.19. Output curves showing the effect of varying the dielectric thickness of an OFET configuration with (a-c) **DAA-OT4** and (d-f) **EAA-OT4** as the gate, pentacene as the semiconductor, and $C_{44}H_{90}$ as the dielectric layer.

These results imply that the materials studied herein can impart an electrical field over approximately 35-40 nm effectively. We noticed that DAA does demonstrate the expected trend with the increasing dielectric thickness but the gating behavior is still apparent, while in EAA, the gating behavior almost ceases to exist above 70 nm dielectric thickness. Upon testing control sample **1**, with less charged residues and is mainly comprised of hydrophobic valine residues, no gating effect was observed for this geometry. Together, these results strengthen our claim that terminal charged groups indeed have a contribution in the overall gating effect.

Conclusions

This Chapter presents the sequence-dependence of mechanical, photophysical and electrical transport properties of peptide- π -peptide supramolecular hydrogelators and the utility of these peptides as an active layer in an OFET geometry to measure their charge transport properties. The effect of increasing the steric bulk adjacent to the π -core and altering the relative hydrophobicity of each monomer does not solely dictate the final nanostructure and mechanical properties of the hydrogel; other intermolecular forces such as hydrogen bonding and π - π interactions also contribute to the overall dynamics of hydrogel network construction. Variation of the amino acid side chains adjacent to the π -core resulted in perturbed electronic interactions (which can be attributed to the altered stacking behavior) and varied 1-D nanostructure dimensions (which can be correlated to different interfibril associations). With the design presented here, utilizing a tripeptide sequence and varying the side-chain bulk adjacent to the chromophore core, the storage modulus values range from ~ 3 to 20 kPa. The sheet resistance measurements provided insights on how the microscopic roughness of the film, which resulted from specific peptide aggregation behavior, dictates the efficiency of electrical conduction. From these studies, it was found that varying the relative size and hydrophobicity of the amino acids adjacent to the π -system core allows for the tuning of the mechanical properties of the resulting hydrogels and dictate the microscale aggregation behavior of films that is related to the resistivity of the material. Investigating the properties of OT4 bis(tripeptide)-based nanostructure OFETs show that this type of material can show mobility values as high as $\sim 0.02 \text{ cm}^2 \text{ V}^{-1} \text{ s}^{-1}$ and can be tuned within a range of three orders of magnitude by simply changing the amino acid sequence while keeping the same semiconducting unit. The

materials were also sufficiently ionically conductive to serve as OFET gate electrodes. The success in incorporating assembled nanostructures in OFETs with clearly observable field-effect modulation when serving both as OFET semiconductors and gates for pentacene semiconductors is the key finding of this study. The modulation of nanostructures as semiconductors required the presence of the conjugated core, even though it was a small fraction of the total nanostructure mass. This demonstration of hole transport, beyond ionic conductivity, is crucial for our ultimate goal of electronically or photonically stimulating these materials to influence cell growth and behavior. These results contribute towards the understanding on how nanostructure and macroscale properties correlate to the molecular design of peptide- π -peptide constructs. The findings in this Chapter are expected to serve as a future guide to design bioelectronic hydrogelators and optimize their electronic and mechanical functions.

Experimental Details

Peptide synthesis. All π -conjugated peptides were synthesized and purified according to our previous reports. Peptide segments were synthesized *via* standard solid phase peptide synthesis procedures and quaterthiophene was covalently attached to the peptides *via* Pd-catalyzed cross coupling between the resin bound peptides terminally *N*-acylated with a thienyl bromide and *bis*-stannylated bithiophene. Details of the synthesis and purification methods can be found in the Appendix.

DGG OT4. Solid-supported Wang-DGG-NH₂ peptide *N*-acylated with 5-bromothiophene-2-carboxylic acid was prepared (0.5 mmol). The peptide was coupled with 5,5'-bis-tributylstannyl-[2,2']-bithiophene (0.25 mmol, 0.186 g) in the presence of

Pd(PPh₃)₄ (0.02 mmol, 0.023 g) using the general on-resin Stille coupling procedure for 15 hours. Resin was then subjected to the general cleavage procedure. Crude peptide obtained was observed as an orange powder (λ_{\max} =418 nm, pH=8, 0.066 g, 30%). MS (ESI-) m/z 897.1 (M-2H⁺+Na⁺) (calc. 897.1), m/z 875.2 (M-H⁺) (calc. 875.1), m/z 437.2 (M-2H⁺) (calc. 437.6). ¹H NMR (400 MHz, d₆-DMSO) δ , ppm: 8.91 (m, 1H), 8.26 (m, 1H), 7.78 (d, 2H, J = 4.0 Hz), 7.44 (d, 1H, J = 4.0 Hz), 7.40 (m, 2H), 7.01 (br s, H), 4.15 (m, 1H), 3.90 (d, 2H, J = 6.0 Hz), 3.74 (d, 2H, J = 5.7 Hz), 2.47 (s, 1H), 2.45 (s, 1H), 2.35 (d, 1H, J = 2.4 Hz), 2.31 (d, 1H, J = 2.4 Hz).

DAA OT4. Solid-supported Wang-DAA-NH₂ peptide *N*-acylated with 5-bromothiophene-2-carboxylic acid was prepared (0.5 mmol). The peptide was coupled with 5,5'-bis-tributylstannyl-[2,2']-bithiophene (0.25 mmol, 0.186 g) in the presence of Pd(PPh₃)₄ (0.02 mmol, 0.023 g) using the general on-resin Stille coupling procedure for 15 hours. Resin was then subjected to the general cleavage procedure. Crude peptide obtained was observed as an orange powder (λ_{\max} =418 nm, pH=8, 0.045 g, 19%). MS (ESI-) m/z 953.2 (M-2H⁺+Na⁺) (calc. 953.2), m/z 931.3 (M-H⁺) (calc. 931.2), m/z 465.3 (M-2H⁺) (calc. 465.1). ¹H NMR (400 MHz, d₆-DMSO) δ , ppm: 8.64 (m, H), 7.87 (d, H, J = 4.1 Hz), 7.43 (d, H, J = 3.8 Hz), 7.39 (d, 4H, J = 3.8 Hz) 4.50-4.30 (m, 6H), 4.25 (br s, 2H), 2.65 (m, 2H), 2.32 (m, 2H), 1.37 (d, 6H, J = 6.8 Hz), 1.23 (d, 6H, J = 6.8 Hz).

DVV OT4. Solid-supported Wang-DVV-NH₂ peptide *N*-acylated with 5-bromothiophene-2-carboxylic acid was prepared (0.5 mmol). The peptide was coupled with 5,5'-bis-tributylstannyl-[2,2']-bithiophene (0.25 mmol, 0.186 g) in the presence of Pd(PPh₃)₄ (0.02 mmol, 0.023 g) using the general on-resin Stille coupling procedure for 15 hours. Resin was then subjected to the general cleavage procedure. Crude peptide

obtained was observed as an orange powder (λ_{\max} =418 nm, pH=8, 0.048 g, 18%). MS (ESI-) m/z 1065.3 (M-2H⁺+Na⁺) (calc. 1065.3), m/z 1043.4 (M-H⁺) (calc. 1043.4), m/z 521.4 (M-2H⁺) (calc. 521.1). ¹H NMR (400 MHz, d₆-DMSO) δ , ppm: 8.43 (d, 2H, J = 8.8 Hz), 8.38 (s, 1H), 8.07 (d, 2H, J = 8.8 Hz), 7.95 (d, 2H, J = 4.0 Hz), 7.63 (d, 2H, J = 6.4 Hz), 7.43 (d, 2H, J = 4.0 Hz), 7.38 (dd, 4H, J = 3.8 Hz, 1.2 Hz), 4.35 (t, 4H, J = 8.4 Hz), 4.16-4.08 (m, 4H), 2.45-2.30 (m, 6H), 2.14 (q, 2H, J = 6.4 Hz), 2.04 (q, 4H, J = 6.4 Hz), 0.91 (m, 12H), 0.85 (d, 12H, J = 6.8 Hz).

DII OT4. Solid-supported Wang-DII-NH₂ peptide *N*-acylated with 5-bromothiophene-2-carboxylic acid was prepared (0.5 mmol). The peptide was coupled with 5,5'-bis-tributylstannyl-[2,2']-bithiophene (0.25 mmol, 0.186 g) in the presence of Pd(PPh₃)₄ (0.02 mmol, 0.023 g) using the general on-resin Stille coupling procedure for 16 hours. Resin was then subjected to the general cleavage procedure. Crude peptide obtained was observed as a yellow powder (λ_{\max} =416 nm, pH=8, 0.055 g, 20%). MS (ESI-) m/z 1099.6 (M-H⁺)⁻ (calc. 1099.3), m/z 549.5 (M-2H⁺)⁻² (calc. 549.2). ¹H NMR (400 MHz, d₆-DMSO) δ , ppm: 8.46 (d, 1H, J = 8.3 Hz), 8.09 (d, 1H, J = 9.2 Hz), 7.93 (d, 1H, J = 4.0 Hz), 7.65 (br s, 1H), 7.43 (d, 1H, J = 4.0 Hz), 7.38 (m, 2H), 4.37 (t, 2H, J = 9.0 Hz), 4.16 (t, 2H, J = 7.8 Hz), 2.43-2.30 (m, 2H), 1.92, (m, 1H), 1.76 (m, 1H), 1.45 (m, 2H), 1.13 (m, 3H), 0.88 (d, 3H, J = 6.8 Hz), 0.83 (m, 9H).

DFE OT4. Solid-supported Wang-DFE-NH₂ peptide *N*-acylated with 5-bromothiophene-2-carboxylic acid was prepared (0.5 mmol). The peptide was coupled with 5,5'-bis-tributylstannyl-[2,2']-bithiophene (0.25 mmol, 0.186 g) in the presence of Pd(PPh₃)₄ (0.02 mmol, 0.023 g) using the general on-resin Stille coupling procedure for 18 hours. Resin was then subjected to the general cleavage procedure. Crude peptide

obtained was observed as an orange powder ($\lambda_{\max}=418$ nm, pH=8, 0.017 g, 6%). MS (ESI-) m/z 1257.3 (M-2H⁺+Na⁺) (calc. 1257.3), m/z 1235.4 (M-H⁺) (calc. 1235.3), m/z 628.3 (M-3H⁺+Na⁺) (calc. 628.7), m/z 617.4 (M-2H⁺) (calc. 617.2) m/z 411.4 (M-3H⁺) (calc. 411.1). ¹H NMR (400 MHz, d₆-DMSO) δ , ppm: 8.42 (d, 1H, $J=7.6$ Hz), 7.82 (d, 1H, $J=6.8$ Hz), 7.80 (d, 1H, $J=4.0$ Hz), 7.40 (d, 1H, $J=3.6$ Hz), 7.36-7.33 (m, 3H), 7.28-7.15 (m, 6H), 4.68 (m, 1H), 4.51 (m, 1H), 4.09 (m, 1H), 3.18-3.06 (m, 4H), 2.96-2.85 (m, 4H), 2.46-2.33 (m, 2H).

EGG OT4. Solid-supported Wang-EGG-NH₂ peptide *N*-acylated with 5-bromothiophene-2-carboxylic acid was prepared (0.5 mmol). The peptide was coupled with 5,5'-bis-tributylstannyl-[2,2']-bithiophene (0.25 mmol, 0.186 g) in the presence of Pd(PPh₃)₄ (0.02 mmol, 0.023 g) using the general on-resin Stille coupling procedure for 14 hours. Resin was then subjected to the general cleavage procedure. Crude peptide obtained was observed as an orange powder (0.077 g, 34%). MS (ESI-) m/z 925.3 (M-2H⁺+Na⁺) (calc. 925.1), m/z 903.3 (M-H⁺) (calc. 903.1), m/z 451.3 (M-2H⁺) (calc. 451.1). ¹H NMR (600 MHz, D₂O) δ , ppm: 8.37 (d, 1H, $J=3.6$ Hz), 7.53 (s, 1H), 7.21 (s, 1H), 7.14 (d, 2H, $J=15.6$ Hz), 4.11-4.08 (m, 1H), 4.05 (d, 1H, $J=3.0$ Hz), 3.93 (d, 1H, $J=3.0$ Hz), 2.20-2.17 (m, 1H), 2.05-2.00 (m, 1H), 1.89-1.84 (m, 1H).

EAA OT4. The synthesis for **EAA-OT4** peptide was adapted from Ref. 49, with the exception that the resin was washed with NMP, methanol and DCM instead of DMF, isopropanol, water, THF, acetonitrile, ether and hexanes prior to cleavage. Crude peptide obtained was observed as an orange powder; characterization matched that of literature.

EVV OT4. Solid-supported Wang-EVV-NH₂ peptide *N*-acylated with 5-bromothiophene-2-carboxylic acid was prepared (0.5 mmol). The peptide was coupled

with 5,5'-bis-tributylstannyl-[2,2']-bithiophene (0.25 mmol, 0.186 g) in the presence of Pd(PPh₃)₄ (0.02 mmol, 0.023 g) using the general on-resin Stille coupling procedure for 15 hours. Resin was then subjected to the general cleavage procedure. Crude peptide obtained was observed as an orange powder (0.102 g, 38%). MS (ESI-) *m/z* 1109.5 (M-2H⁺+K⁺) (calc. 1109.3), *m/z* 1071.7 (M-H⁺) (calc. 1071.3), *m/z* 535.5 (M-2H⁺) (calc. 535.2). ¹H NMR (600 MHz, D₂O) δ, ppm: 8.37 (dd, 1H, *J*= 1.2 Hz), 7.59 (d, 1H, *J*= 3.6 Hz), 7.25 (s, 1H), 7.19 (m, 2H), 4.20 (dd, 2H, *J*= 8.4 Hz, 2.7 Hz), 4.13 (dd, 2H, *J*= 7.8 Hz, 2.7 Hz), 4.09-4.07 (m, 2H), 2.12 (t, 6H, *J*= 8.1 Hz), 2.07-2.03 (m, 5H), 1.96-1.94 (m, 3H), 1.84-1.80 (m, 3H), 0.95 (d, 8H, *J*= 3.0 Hz), 2.12 (t, 24H, *J*= 6.6 Hz).

EII OT4. Solid-supported Wang-EII-NH₂ peptide *N*-acylated with 5-bromothiophene-2-carboxylic acid was prepared (0.5 mmol). The peptide was coupled with 5,5'-bis-tributylstannyl-[2,2']-bithiophene (0.25 mmol, 0.186 g) in the presence of Pd(PPh₃)₄ (0.02 mmol, 0.023 g) using the general on-resin Stille coupling procedure for 16 hours. Resin was then subjected to the general cleavage procedure. Crude peptide obtained was observed as yellow/orange powder (0.055 g, 19%). MS (ESI-) *m/z* 1149.6 (M-2H⁺+Na⁺) (calc. 1150.4), *m/z* 1127.7 (M-H⁺) (calc. 1127.4), *m/z* 563.5 (M-2H⁺) (calc. 563.2). ¹H NMR (400 MHz, d₆-DMSO) δ, ppm: 8.48 (d, 1H, *J*= 8.8 Hz), 8.00 (d, 1H, *J*= 8.8 Hz), 7.96 (d, 1H, *J*= 7.2 Hz), 7.92 (d, 1H, *J*= 4.0 Hz), 7.42 (d, 1H, *J*= 4.0 Hz), 7.38 (dd, 2H, *J*= 4.0 Hz, 2.6 Hz), 4.35 (t, 1H, *J*= 9.0 Hz), 4.20-4.14 (m, 2H), 2.28-2.23 (m, 2H), 1.91-1.74 (m, 4H), 1.49-1.44 (m, 2H), 1.23-1.04 (m, 2H), 0.87-0.78 (m, 12H).

DVV C10. 0.0288 g (0.125 mmol) of dodecanedioic acid and 0.0650 g (0.125 mmol) of PyBOP was dissolved in 10-mL of 2:1 NMP:DCM solution, after which 0.522 mL of DIPEA was gradually added then mixed for one minute. This solution was added to

the solid-supported Wang-DVV-NH₂ (0.25 mmol) in a peptide chamber and mixed for 12 h. Resin was rinsed using the standard wash cycle. The general cleavage procedure was followed, only that the cleavage cocktail was diluted in a 1:1 ratio DCM and was mixed with the resin for 2 h. Crude peptide was obtained as a white powder (0.0565 g, 53%). MS (ESI-) m/z 893.5 (M-2H⁺+K⁺) (calc. 893.6), m/z 427.2 (M-2H⁺) (calc. 427.3). ¹H NMR (400 MHz, d₆-DMSO) δ , ppm: 7.83 (m, 2H), 7.72 (br), 7.71 (br), 4.24-4.12 (ddd, 4H, J = 32.4 Hz, 8.8 Hz, 7.2 Hz), 2.17-2.10 (m, 2H), 2.03-1.97 (m, 2H), 1.47 (t, 2H, J = 9.2 Hz), 1.22 (s, 6H), 0.85-0.81 (m, 12H).

UV-Vis and photoluminescence (PL). All samples for absorption and emission scans were prepared by dissolving lyophilized peptides in Milli-Q water (~14 μ M final peptide concentration). The pH of the samples was adjusted accordingly (acidic: ~pH 2; basic: ~pH 10) using aliquots of 1 M HCl or 1 M KOH. UV-Vis spectra were collected using a Varian Cary 50 Bio UV-vis spectrophotometer. PL data were collected using a PTi Photon Technology International Fluorometer (QuantaMaster 40) with a 75-W Ushio Xenon short arc lamp and operated with Felix32 Version 1.2 software; ($\lambda_{\text{exc}} = \lambda_{\text{max, abs}}$).

Circular dichroism (CD). CD spectra (all at 20 °C) were acquired using a Jasco J-810 spectropolarimeter. The basic samples (*ca.* pH 10) were prepared by adding 10 μ L of 1 M KOH to 3 mL of 14 μ M stock peptide solution prepared as above while acidic samples were prepared by adding 20 μ L of 1 M HCl (*ca.* pH 2) to the basic samples.

Transmission electron microscopy (TEM). The nanostructure samples in solution were prepared by acidifying 0.1 wt% (*ca.* 1 mM) solutions of peptides in Milli-Q water. The samples were adsorbed for 5 minutes (at 25 °C) onto 200 mesh copper grids coated with Formvar film (Electron Microscopy Sciences). The hydrogel samples were

prepared from acidified 1 wt% (*ca.* 10 mM) peptide solutions wherein the same grids were mounted atop the gels for 5 minutes and then washed with DI water prior to staining. All samples were stained with a 2% uranyl acetate solution and the grids were allowed to dry prior to imaging. Images were acquired using a Philips EM 420 transmission electron microscope equipped with SIS Megaview III CCD digital camera, at an accelerating voltage of 100 kV. ImageJ 1.47 (National Institutes of Health, Bethesda, MD, USA) was used to approximate the widths of the nanostructures ($n=25$ per TEM image).

Scanning electron microscopy (SEM). SEM images were acquired using SEI Quanta 200 Environmental SEM. All hydrogel samples (1 wt%, acid-assembled) underwent gradual ethanol dehydration, after which they were critical point dried using a Tousimis Samdri-795 and sputtered using an Anatech USA Hummer 6.2.

3D Laser Scanning Microscopy. In order to characterize the surface roughness and height profile of the dried, acid-assembled peptide films on glass, all samples were observed under a Keyence Color 3R Laser Microscope VK-X100K/X200K.

Atomic force microscopy (AFM). Acidified peptide solutions (0.1 mg/ml, 0.1 mM) were dropcasted into SiO₂ substrates. Topography images were taken in tapping mode using a Dimensional 3100 AFM (Bruker Nano, Santa Barbara, CA). The images were visualized using the Nanoscope software (Bruker).

Rheological characterization. Oscillatory rheology measurements were performed using a G2 ARES (TA Instruments) rheometer system with a serrated, stainless steel parallel plate (8-mm diameter). Lyophilized π -conjugated peptides were prepared as 1 wt% aqueous solutions, and were sonicated then heated to 80 °C to ensure full solubilization. The solutions were kept undisturbed at room temperature for ~24 h prior to

use for rheology measurements. To form a gel, 40 μL of peptide solution was loaded in the rheometer lower plate, wherein 10 μL 1 M HCl was subsequently added and allowed to sit for 5 min prior to measurement. Gelation was immediately observed and no homogenization process was employed to conserve the architecture of the gel upon formation. To ensure that measurements are done within the linear viscoelastic regime, amplitude sweeps were done which showed that the limiting strain for all the hydrogel-forming peptides is not lower than 1%. To minimize evaporation and sample dehydration, a humid chamber with a water reservoir was used. All frequency sweeps (0.1 to 10 Hz) were done at 25°C with 0.3% strain. The measurements were done at least three times (loading a new gel each time). The error bars in the plots report the standard error mean. The reported strain sweeps were performed after a temperature sweep (4 °C to 40 °C).

Electrical characterization. Glass slides were used as substrates for resistivity measurements. All slides were cleaned in an ultrasonic acetone bath for 10 min. The slides were then dried with nitrogen gas flow. To the dried glass slides, 5 μL of 1 wt% peptide solutions were dropped and then exposed to acid vapors of concentrated (12 N) HCl for 5 minutes to initiate assembly. All acid-assembled samples were dried under ambient conditions for ~20 h prior to measurement. The resulting dropcast films were ~5mm in diameter and *ca.* 2-15 μm thick after drying. For each peptide, 3 separate dropcast films were measured. All sheet resistance (R_s) measurements were performed under ambient conditions on an Agilent 4155C semiconductor analyzer (van der Pauw method) using a four-point probe setup with InGa contacts to establish ohmic contacts. The R_s measurements were then multiplied to the mean thickness acquired from laser scanning microscopy analyses to get the resistivity (ρ) of the assembled peptide film. To assess the

photoconductive response of the dried films, a fiber optic illuminator was used (150 W halogen lamp).

Device fabrication and measurements. The OFET devices with π -conjugated peptide nanostructure films used as the semiconductor active layers were fabricated on silicon wafers (with 300 nm silicon dioxide; capacitance per area=11.5 nF/cm²). The wafers were cut into 1-inch by 1-inch square samples, which were cleaned by keeping them in piranha solution (3:1 ratio of concentrate concentrated sulfuric acid to hydrogen peroxide) for 3-4 hours followed by sonication in acetone and isopropanol for 30 minutes. The samples were blown dry using dry nitrogen flow. To each Si/SiO₂ substrate, 5 μ L of 1 wt% (*ca.* 10 mM) peptide solution was dropcast and then exposed to an acid chamber (closed chamber with concentrated HCl vapor) for 5 minutes prior to drying at ambient temperature and pressure. The Au electrodes (50 nm-thick) were deposited using a TEM grid as the shadow mask (W/L=10) by physical vapor deposition while keeping the chamber temperature below 60 °C.

For the OFET devices with the π -conjugated peptide nanostructures used as the gate, microscopic glass slides were cut into 1-inch by 1-inch squares and then subsequently cleaned by sonication in acetone followed by sonication in isopropanol. The glass substrate was blown dry by using dry nitrogen flow. Then, 2-cm by 3-mm rectangle Novec wells were painted on the glass substrates. The 1 wt% peptide solutions were dropcast on these wells and acidified as described earlier. The dielectric layer was then vapor-deposited on top of the assembled peptide films. Two different compounds were used to function as dielectric material: tetratetracontane (C₄₄H₉₀, C₄₄), and pentaerythritol. They were chosen to observe the effects of varying polarities of groups present (with tetratetracontane being a

wax and pentaerythritol having a large number of hydroxyl groups, approaching a solid form of “water”). The thickness of the dielectric was varied from 20 nm to 100 nm. For these devices with assembled peptides as the gates, 25 nm of pentacene was vapor-deposited as the active semiconductor layer as it has been widely studied and is a very reliable organic semiconductor. As the nanomaterial drop-cast films are hardly only ½ cm wide, TEM grid mask was used to deposit 50 nm-thick gold electrodes. All the OFET measurements were done using an Agilent 4155C semiconductor analyzer under ambient conditions.

Portions of this chapter were adapted in part from:

- Ardoña, H. A. M.; Besar, K.; Togninalli, M.; Katz, H. E. and Tovar, J.D. “Sequence-dependent mechanical, photophysical and electrical transport properties of pi-conjugated peptide hydrogelators.” *J. Mater. Chem. C* 2015, 3, 6505-6514.
- Besar, K.;* Ardoña, H. A. M.;* Tovar, J. D. and Katz, H. E. (*equal contribution), “Demonstration of hole transport and voltage equilibration in self-assembled pi-conjugated peptide nanostructures using field-effect transistor architectures.” *ACS Nano* 2015, 9, 12401–12409. Copyright 2015 American Chemical Society.
- Besar, K. “Organic Semiconductor Devices for Chemical Sensing and Bio Interfaces” (Ph.D. Dissertation), Johns Hopkins University, 2016.

Acknowledgements

The device fabrication and charge transport measurements were done by Dr. Kalpana Besar in the group of Professor Howard Katz (Johns Hopkins University). Matteo Tognanelli (research exchange undergraduate student, A.Y. 2013-2014) assisted in the peptide synthesis and steady state photophysical characterization.

References

- (1) Coropceanu, V., da Silva Filho, D. A., Olivier, Y., and Silbey, R. (2007) Charge transport in organic semiconductors. *Chem. Rev.* *107*, 926-952.
- (2) Kumar, R. J., MacDonald, J. M., Singh, T. B., Waddington, L. J., and Holmes, A. B. (2011) Hierarchical self-assembly of semiconductor functionalized peptide α -helices and optoelectronic properties. *J. Am. Chem. Soc.* *133*, 8564–8573.
- (3) Sun, Y., Jiang, L., Schuermann, K. C., Adriaens, W., Zhang, L., Boey, F. Y. C., De Cola, L., Brunsveld, L., and Chen, X. (2011) Semiconductive, one-dimensional, self-assembled nanostructures based on oligopeptides with π -conjugated segments. *Chem. Eur. J.* *17*, 4746-4749.
- (4) Guvendiren, M., Lu, H. D., and Burdick, J. A. (2012) Shear-thinning hydrogels for biomedical applications. *Soft Matter* *8*, 260-272.
- (5) Tovar, J. D. (2013) Supramolecular construction of optoelectronic biomaterials. *Acc. Chem. Res.* *46*, 1527-1537.
- (6) Li, Y., Liu, T., Liu, H., Tian, M.-Z., and Li, Y. (2014) Self-assembly of intramolecular charge-transfer compounds into functional molecular systems. *Acc. Chem. Res.* *47*, 1186-1198.
- (7) Boekhoven, J., and Stupp, S. I. (2014) Supramolecular materials for regenerative medicine. *Adv. Mater.* *26*, 1642-1659.
- (8) Gough, J. E., Saiani, A., and Miller, A. F. (2012) Peptide hydrogels: mimicking the extracellular matrix. *Bioinspired, Biomimetic Nanobiomater.* *1*, 4-12.
- (9) Silva, G. A., Czeisler C., Niece, K. L., Beniash, E., Harrington, D. A., Kessler, J. A., Stupp, S. I. (2004) Selective differentiation of neural progenitor cells by high-epitope density nanofibers. *Science* *303*, 1352-1355.
- (10) Kretsinger, J. K., Haines, L. A., Ozbas, B., Pochan, D. J., and Schneider, J. P. (2005) Cytocompatibility of self-assembled β -hairpin peptide hydrogel surfaces. *Biomaterials* *26*, 5177-5186.
- (11) Kopeček, J. (2007) Hydrogel biomaterials: A smart future? *Biomaterials* *28*, 5185-5192.
- (12) Slaughter, B. V., Khurshid, S. S., Fisher, O. Z., Khademhosseini, A., and Peppas, N. A. (2009) Hydrogels in regenerative medicine. *Adv. Mater.* *21*, 3307-3329.

- (13) Gazit, E. (2007) Self-assembled peptide nanostructures: the design of molecular building blocks and their technological utilization. *Chem. Soc. Rev.* 36, 1263-1269.
- (14) Dudukovic, N. A., and Zukoski, C. F. (2014) Mechanical properties of self-assembled Fmoc-diphenylalanine molecular gels. *Langmuir* 30, 4493–4500.
- (15) Adams, D. J., and Topham, P. D. (2010) Peptide conjugate hydrogelators. *Soft Matter* 6, 3707-3721.
- (16) Ahearne, M., Yang, Y., Haj, El, A. J., Then, K. Y., and Liu, K.-K. (2005) Characterizing the viscoelastic properties of thin hydrogel-based constructs for tissue engineering applications. *J. R. Soc. Interface* 2, 455-463.
- (17) Leon, E. J., Verma, N., Zhang, S., Lauffenburger, D. A., and Kamm, R. D. (1998) Mechanical properties of a self-assembling oligopeptide matrix. *J. Biomater. Sci. Polym. Ed.* 9, 297-312.
- (18) Kai, D., Prabhakaran, M. P., Stahl, B., Eblenkamp, M., Wintermantel, E., and Ramakrishna, S. (2012) Mechanical properties and in vitro behavior of nanofiber–hydrogel composites for tissue engineering applications. *Nanotechnology* 23, 095705.
- (19) Yan, C., and Pochan, D. J. (2010) Rheological properties of peptide-based hydrogels for biomedical and other applications. *Chem. Soc. Rev.* 39, 3528-3540.
- (20) Liu, Y., Terrell, J. L., Tsao, C.-Y., Wu, H.-C., Javvaji, V., Kim, E., Cheng, Y., Wang, Y., Ulijn, R. V., Raghavan, S. R., Rubloff, G. W., Bentley, W. E., and Payne, G. F. (2012) Biofabricating multifunctional soft matter with enzymes and stimuli-responsive materials. *Adv. Funct. Mater.* 22, 3004-3012.
- (21) Hughes, M., Frederix, P. W. J. M., Raeburn, J., Birchall, L. S., Sadownik, J., Coomer, F. C., Lin, I.-H., Cussen, E. J., Hunt, N. T., Tuttle, T., Webb, S. J., Adams, D. J., and Ulijn, R. V. (2012) Sequence/structure relationships in aromatic dipeptide hydrogels formed under thermodynamic control by enzyme-assisted self-assembly. *Soft Matter* 8, 5595-5602.
- (22) Haines-Butterick, L., Rajagopal, K., Branco, M., Salick, D., Rughani, R., Pilarz, M., Lamm, M. S., Pochan, D. J., and Schneider, J. P. (2007) Controlling hydrogelation kinetics by peptide design for three-dimensional encapsulation and injectable delivery of cells. *Proc. Natl. Acad. Sci. U. S. A.* 104, 7791-7796.
- (23) Javid, N., Roy, S., Zelzer, M., Yang, Z., Sefcik, J., and Ulijn, R. V. (2013) Cooperative self-assembly of peptide gelators and proteins. *Biomacromolecules* 14, 4368–4376.
- (24) Caplan, M. R., Schwartzfarb, E. M., Zhang, S., Kamm, R. D., and Lauffenburger, D. A. (2002) Control of self-assembling oligopeptide matrix formation through systematic variation of amino acid sequence. *Biomaterials* 23, 219-227.

- (25) Korevaar, P. A., Newcomb, C. J., Meijer, E. W., and Stupp, S. I. (2014) Pathway selection in peptide amphiphile assembly. *J. Amer. Chem. Soc.* *136*, 8540-8543.
- (26) Roy, S., Javid, N., Sefcik, J., Halling, P. J., and Ulijn, R. V. (2012) Salt-induced control of supramolecular order in biocatalytic hydrogelation. *Langmuir* *28*, 16664–16670.
- (27) Tang, C., Ulijn, R. V., and Saiani, A. (2011) Effect of glycine substitution on fmoc–diphenylalanine self-assembly and gelation properties. *Langmuir* *27*, 14438-14449.
- (28) Nagy, K. J., Giano, M. C., Jin, A., Pochan, D. J., and Schneider, J. P. (2011) Enhanced mechanical rigidity of hydrogels formed from enantiomeric peptide assemblies *J. Amer. Chem. Soc.* *133*, 14975-14977.
- (29) Hahn, M. E., and Gianneschi, N. C. (2011) Enzyme-directed assembly and manipulation of organic nanomaterials. *Chem. Commun.* *47*, 11814-11821.
- (30) Nguyen, M. M., Eckes, K. M., and Suggs, L. J. (2014) Charge and sequence effects on the self-assembly and subsequent hydrogelation of Fmoc-depsipeptides. *Soft Matter* *10*, 2693-2702.
- (31) Choi, I., Park, I.-S., Ryu, J.-H., and Lee, M. (2012) Control of peptide assembly through directional interactions. *Chem. Commun.* *48*, 8481–8483.
- (32) Greenfield, M. A., Hoffman, J. R., and la Cruz, de, M. O. (2009) Tunable mechanics of peptide nanofiber gels. *Langmuir* *26*, 3641-3547.
- (33) Pashuck, E. T., Cui, H., and Stupp, S. I. (2010) Tuning supramolecular rigidity of peptide fibers through molecular structure. *J. Amer. Chem. Soc.* *132*, 6041-6046.
- (34) Forciniti, L., Guimard, N. K., and Lee, S. (2010) Unique electrochemically synthesized polypyrrole: poly (lactic-co-glycolic acid) blends for biomedical applications. *J. Mater. Chem.* *20*, 8865-8874.
- (35) Sekine, J., Luo, S. C., Wang, S., and Zhu, B. (2011) Functionalized conducting polymer nanodots for enhanced cell capturing: the synergistic effect of capture agents and nanostructures. *Adv. Mater.* *23*, 4788-4792.
- (36) Schmidt, C. E., Shastri, V. R., and Vacanti, J. P. (1997) Stimulation of neurite outgrowth using an electrically conducting polymer. *Proc. Natl. Acad. Sci. U. S. A.* *94*, 8948–8953.
- (37) Hardy, J. G., Mouser, D. J., and Arroyo, N. (2014) Biodegradable electroactive polymers for electrochemically-triggered drug delivery. *J. Mater. Chem. B* *2*, 6809-6822.

- (38) Radisic, M., Park, H., Shing, H., Consi, T., Schoen, F. J., Langer, R., Freed, L. E., and Vunjak-Novakovic, G. (2004) Functional assembly of engineered myocardium by electrical stimulation of cardiac myocytes cultured on scaffolds. *Proc. Natl. Acad. Sci. U. S. A.* *101*, 18129-18134.
- (39) Au, H., Cheng, I., Chowdhury, M. F., and Radisic, M. (2007) Interactive effects of surface topography and pulsatile electrical field stimulation on orientation and elongation of fibroblasts and cardiomyocytes. *Biomaterials* *28*, 4277-4293.
- (40) Smits, E., Mathijssen, S., van Hal, P. A., and Setayesh, S. (2008) Bottom-up organic integrated circuits. *Nature* *455*, 956-959.
- (41) Feinberg, A. W., Feigel, A., and Shevkoplyas, S. S. (2007) Muscular thin films for building actuators and powering devices. *Science* *317*, 1366-1370.
- (42) Wilson, W. L., Tovar, J. D., and Schroeder, C. M. (2017) Non-equilibrium self-assembly of π -conjugated oligopeptides in solution. *ACS Appl. Mater. Interfaces* *9*, 3977-3984.
- (43) Thurston, B. A., Tovar, J. D., Ferguson, A. L. (2015) Thermodynamics, morphology, and kinetics of early-stage self-assembly of π -conjugated oligopeptides. *Mol. Simul.* *42*, 955-975.
- (44) Wall, B. D., Zhou, Y., Mei, S., Ardoña, H. A. M., Ferguson, A. L., and Tovar, J. D. (2014) Variation of formal hydrogen-bonding networks within electronically delocalized π -conjugated oligopeptide nanostructures. *Langmuir* *30*, 11375-11385.
- (45) Wall, B. D., Zacca, A. E., Sanders, A. M., Wilson, W. L., Ferguson, A. L., and Tovar, J. D. (2014) Supramolecular polymorphism: tunable electronic interactions within π -conjugated peptide nanostructures dictated by primary amino acid sequence. *Langmuir* *30*, 5946-5956.
- (46) Horowitz, G. (1998) Organic field-effect transistors. *Adv. Mater.* *10*, 365-377.
- (47) Levitt, M. (1978) Conformational preferences of amino acids in globular proteins. *Biochemistry* *17*, 4277.
- (48) Kim, C. A., and Berg, J. M. (1993) Thermodynamic β -sheet propensities measured using a zinc-finger host peptide. *Nature* *362*, 267-270.
- (49) Wall, B. D., Diegelmann, S. R., Zhang, S., Dawidczyk, T. J., Wilson, W. L., Katz, H. E., Mao, H.-Q., and Tovar, J. D. (2011) Aligned macroscopic domains of optoelectronic nanostructures prepared *via* shear-flow assembly of peptide hydrogels. *Adv. Mater.* *23*, 5009-5014.

- (50) Lehrman, J. A., Cui, H., Tsai, W.-W., Moyer, T. J., and Stupp, S. I. (2012) Supramolecular control of self-assembling terthiophene-peptide conjugates through the amino acid side chain. *Chem. Commun.* 48, 9711-9713.
- (51) Gao, Y., Zhang, Y., Gao, P., and Xu, B. (2010) Aromatic-aromatic interactions induce the self-assembly of pentapeptidic derivatives in water to form nanofibers and supramolecular hydrogels. *J. Amer. Chem. Soc.* 132, 2719-2728.
- (52) Baumann, M. K., Textor, M., and Reimhult, E. (2008) Understanding self-assembled amphiphilic peptide supramolecular structures from primary structure helix propensity. *Langmuir* 24, 7645-7647.
- (53) Gallaher, J. K., Aitken, E. J., Keyzers, R. A., and Hodgkiss, J. M. (2012) Controlled aggregation of peptide-substituted perylene-bisimides. *Chem. Commun.* 48, 7961-7963.
- (54) Croisier, E., Liang, S., Schweizer, T., Balog, S., Mionić, M., Snellings, R., Cugnoni, J., Michaud, V., and Frauenrath, H. (2014) A toolbox of oligopeptide-modified polymers for tailored elastomers. *Nat. Commun.* 5, 4728.
- (55) Houton, K. A., Morris, K. L., Chen, L., Schmidtman, M., Jones, J. T. A., Serpell, L. C., Lloyd, G. O., and Adams, D. J. (2012) On crystal versus fiber formation in dipeptide hydrogelator systems. *Langmuir* 28, 9797-9806.
- (56) Eckes, K. M., Mu, X., Ruehle, M. A., Ren, P., and Suggs, L. J. (2014) β -Sheets not required: combined experimental and computational studies of self-assembly and gelation of the ester-containing analogue of an Fmoc-dipeptide hydrogelator. *Langmuir* 30, 5287-5296.
- (57) Wall, B. D., Zhou, Y., Mei, S., Ardoña, H. A. M., Ferguson, A. L., and Tovar, J. D. (2014) Variation of formal hydrogen-bonding networks within electronically delocalized π -conjugated oligopeptide nanostructures. *Langmuir* 30, 11375-11385.
- (58) Davies, R. P. W., Aggeli, A., Beevers, A. J., Boden, N., Carrick, L. M., Fishwick, C. W. G., Mcleish, T. C. B., Nyrkova, I., and Semenov, A. N. (2006) Self-assembling β -Sheet tape forming peptides. *Supramol. Chem.* 18, 435-443.
- (59) Smith, A. M., Williams, R. J., Tang, C., Coppo, P., Collins, R. F., Turner, M. L., Saiani, A., and Ulijn, R. V. (2008) Fmoc-diphenylalanine self assembles to a hydrogel *via* a novel architecture based on π - π interlocked β -Sheets. *Adv. Mater.* 20, 37-41.
- (60) Lee, N. R., Bowerman, C. J., and Nilsson, B. L. (2013) Effects of varied sequence pattern on the self-assembly of amphipathic peptides. *Biomacromolecules* 14, 3267-3277.
- (61) Bakota, E. L., Sensoy, O., Ozgur, B., Sayar, M., and Hartgerink, J. D. (2013) Self-assembling multidomain peptide fibers with aromatic cores. *Biomacromolecules* 14, 1370-1378.

- (62) Anderson, J. M., Andukuri, A., Lim, D. J., and Jun, H.-W. (2009) Modulating the gelation properties of self-assembling peptide amphiphiles. *ACS Nano* 3, 3447-3454.
- (63) Salemme, F. R. (1983) Structural properties of protein β -sheets. *Prog. Biophys. Mol. Biol.* 42, 95-133.
- (64) Murphy, W. L., McDevitt, T. C., and Engler, A. J. (2014) Materials as stem cell regulators. *Nat. Mater.* 13, 547-557.
- (65) Hyun, K., Kim, S. H., Ahn, K. H., and Lee, S. J. (2002) Large amplitude oscillatory shear as a way to classify the complex fluids. *J. Non-Newtonian Fluid Mech.* 107, 51-65.
- (66) Alesi, S., Brancolini, G., Melucci, M., Capobianco, M. L., Venturini, A., Camaioni, N., and Barbarella, G. (2008) Water-soluble, electroactive, and photoluminescent quaterthiophene–dinucleotide conjugates. *Chem. Eur. J.* 14, 513-521.
- (67) Pratihari, P., Ghosh, S., Stepanenko, V., Patwardhan, S., Grozema, F. C., Siebbeles, L. D. A., and Würthner, F. (2010) Self-assembly and semiconductivity of an oligothiophene supergelator. *Beilstein J. Org. Chem.* 6, 1070-1078.
- (68) Meinardi, F., Cerminara, M., Blumstengel, S., Sassella, A., Borghesi, A., and Tubino, R. (2003) Broad and narrow bands in the photoluminescence spectrum of solid-state oligothiophenes: two marks of an intrinsic emission. *Phys. Rev. B* 67, 184205.
- (69) Tayi, A. S., Goldberger, J. E., Palmer, L. C., and Stupp, S. I. (2011) Self-assembly and conductivity of hydrogen-bonded oligothiophene nanofiber networks. *Chem. Commun.* 47, 5702–5704.
- (70) Guo, Z., Song, Y., Gong, R., Mu, Y., Jiang, Y., Li, M., and Wan, X. (2013) Assembly of peptide–thiophene conjugates: the influence of peptide content and location. *Supramol. Chem.* 26, 383-391.
- (71) Berova, N., Nakanishi, K. and Woody, R. W. (2002) Circular Dichroism: Principles and Applications. 2nd ed., Wiley-VCH, New York, Ch. 12, 337-376.
- (72) Manning, M. C., Illangasekare, M., and Woody, R. W. (1988) Circular dichroism studies of distorted alpha-helices, twisted beta-sheets, and beta-turns. *Biophys. Chem.* 31, 77-86.
- (73) Timoshevskii, V., Ke, Y., Guo, H., and Gall, D. (2008) The influence of surface roughness on electrical conductance of thin Cu films: an ab initio study. *J. Appl. Phys.* 103, 113705.
- (74) Braga, D., and Horowitz, G. (2009) High-performance organic field-effect transistors. *Adv. Mater.* 21, 1473-1486.

- (75) Martínez-Hardigree, J. F. and Katz, H. E. (2014) Through thick and thin: tuning the threshold voltage in organic field-effect transistors. *Acc. Chem. Res.* *47*, 1369-1377.
- (76) Fei, Z., Pattanasattayavong, P., Han, Y., Schroeder, B. C., Yan, F., Kline, R. J., Anthopoulos, T. D., and Heeney, M. (2014) Influence of side-chain regiochemistry on the transistor performance of high-mobility, all-donor polymers. *J. Amer. Chem. Soc.* *136*, 15154-15157.
- (77) Wong, L.-Y., Png, R.-Q., Silva, F. B. S., Chua, L.-L., Repaka, D. V. M., Gao, X.-Y., Ke, L., Chua, S.-J., Wee, A. T. S., and Ho, P. K. H. (2010) Interplay of processing, morphological order, and charge-carrier mobility in polythiophene thin films deposited by different methods: comparison of spin-cast, drop-cast, and inkjet-printed films. *Langmuir* *26*, 15494-15507.
- (78) Himmelberger, S., Vandewal, K., Fei, Z., Heeney, M., and Salleo, A. (2014) Role of molecular weight distribution on charge transport in semiconducting polymers. *Macromolecules* *47*, 7151-7157.
- (79) Kwiatkowski, J. J., Frost, J. M., and Nelson, J. (2009) The effect of morphology on electron field-effect mobility in disordered C₆₀ thin films. *Nano Lett.* *9*, 1085-1090.
- (80) Generali, G., Dinelli, F., Capelli, R., Toffanin, S., di Maria, F., Gazzano, M., Barbarella, G., and Muccini, M. (2011) Correlation among morphology, crystallinity, and charge mobility in OFETs made of quaterthiophene alkyl derivatives on a transparent substrate platform. *J. Phys. Chem. C* *115*, 23164-23169.
- (81) Kline, R. J., McGehee, M. D., Kadnikova, E. N., Liu, J., Fréchet, J. M. J., and Toney, M. F. (2005) Dependence of regioregular poly(3-hexylthiophene) film morphology and field-effect mobility on molecular weight. *Macromolecules* *38*, 3312-3319.
- (82) Noriega, R., Rivnay, J., Vandewal, K., Koch, F. P. V., Stingelin, N., Smith, P., Toney, M. F., and Salleo, A. (2013) A general relationship between disorder, aggregation and charge transport in conjugated polymers. *Nat. Mater.* *12*, 1038.
- (83) Tsai, W.-W., Tevis, I. D., Tayi, A. S., Cui, H., and Stupp, S. I. (2010) Semiconducting nanowires from hairpin-shaped self-assembling sexithiophenes. *J. Phys. Chem. B* *114*, 14778-14786.
- (84) Bonetti, S., Pistone, A., Brucale, M., Karges, S., Favaretto, L., Zambianchi, M., Posati, T., Sagnella, A., Caprini, M., Toffanin, S., Zamboni, R., Camaioni, N., Muccini, M., Melucci, M., and Benfenati, V. (2015) A lysinated thiophene-based semiconductor as a multifunctional neural bioorganic interface. *Adv. Healthc. Mater.* *4*, 1190-1202.
- (85) Lin, Y.-A., Ou, Y.-C., Cheetham, A. G., and Cui, H. (2013) Supramolecular polymers formed by ABC miktoarm star peptides. *ACS Macro Lett.* *2*, 1088-1094.

- (86) Hajlaoui, R., Horowitz, G., Garnier, F., Arce-Bouchet, A., Laigre, L., Kassmi, El, A., Demanze, F., and Kouki, F. (1997) Improved field-effect mobility in short oligothiophenes: quaterthiophene and quinquethiophene. *Adv. Mater.* *9*, 389-391.
- (87) Unni, K. N. N., Dabos-Seignon, S., and Nunzi, J.-M. (2006) Influence of the polymer dielectric characteristics on the performance of a quaterthiophene organic field-effect transistor *J. Mater. Sci.* *41*, 317-322.
- (88) Draper, E. R., Walsh, J. J., McDonald, T. O., Zwijnenburg, M. A., Cameron, P. J., Cowan, A. J., and Adams, D. J. (2014) Air-stable photoconductive films formed from perylene bisimide gelators. *J. Mater. Chem. C* *2*, 5570-5575.
- (89) Kraus, M., Richler, S., Opitz, A., Brütting, W., Haas, S., Hasegawa, T., Hinderhofer, A., and Schreiber, F. (2010) High-mobility copper-phthalocyanine field-effect transistors with tetratetracontane passivation layer and organic metal contacts. *J. Appl. Phys.* *107*, 094503.
- (90) Katsuyoshi-Nishinari, Shibuya, N., and Kainuma, K. (1985) Dielectric-relaxation in solid dextran and pullulan. *Makromol. Chem.* *186*, 433-438.
- (91) Amit, M., Appel, S., Cohen, R., Cheng, G., Hamley, I. W., and Ashkenasy, N. (2014) Hybrid proton and electron transport in peptide fibrils. *Adv. Funct. Mater.* *24*, 5873-5880.

CHAPTER THREE:

Non-Resonant Effects in Peptidic Nanostructures Bearing
 π -Conjugated Oligomers

Introduction

In π -conjugated peptide nanostructures, the peptides provide a matrix that confine functional π -electron units within the assemblies. Therefore, the material properties that are dependent on π -system organization are also influenced by the organization of the peptide moieties, as discussed in Chapter 2. Among other aspects, such effects on macroscopic properties that are dependent on the peptide matrix environment can be affected by the conformational constraint imposed on the individual π -electron units when assembled as 1-D nanostructures. This can then translate to influences in their optoelectronic properties due to steric constraints arising from close packing of peptide molecules in the self-assembled stacks and electronic delocalization through-space within the π -electron units mediated by the close π - π interactions. The incorporation of π -units within peptidic structures presents unusual quadrupolar influences not typically encountered in natural peptides, resulting in subtle but important perturbations of the internal structure of these assemblies relative to natural protein fibrils/plaques. Although there are several studies that investigate the influences of intermolecular coupling on the photophysics of aggregated organic π -conjugated systems,¹⁻³ the impacts of the coupling together with the geometric constraints arising due to assembly on photophysical outcomes and exciton transport within these π -systems, especially those under aqueous environments, are rarely discussed. From many functional perspectives, it is desirable that the π -electron units maintain their planarity to facilitate intermolecular communication, because planarity and effective conjugation correlate to organic semiconductors with higher conductivity, mobility⁴⁻⁶ and better optoelectronic response.⁷⁻⁹ Similarly, increased planarity can be associated with higher quantum yields in certain cases.¹⁰⁻¹² In one instance, rigidification

of the environment of the assembled π -system imposed a geometric constraint on the π -system assembly, leading to a more pronounced increase in the photoluminescence (PL) intensity of a *J*-aggregated, planar naphthalene diimide unit embedded in the peptide backbone owing to gelation of the peptides.¹³ The torsional dynamics of an oligo-aromatic chromophore can also be influenced by macroscopic variables such as temperature and local solvent viscosity.^{14,15} A preliminary assessment of the different torsional outcomes has shown that oligo-aromatic chromophores can maintain electronic communication in solid-state supramolecular assemblies.¹⁶

From a fundamental perspective, it is difficult to draw meaningful conclusions about the conformational state of individual π -electron segments (“non-resonant” effects) within an ensemble that is also demonstrating exciton coupling of the component chromophores (“resonant” effects). The difficulty in delineating these arises from the fact that while a chromophore unit with free rotation of conjugated sub-units exhibits a broad, featureless PL spectrum, spatial confinement arising from self-assembly causes rigidification of the unit which leads to lower energy, structured absorption and PL spectra. Electronic coupling among neighboring units within the assembly, for example in *H*-like aggregates, would cause a hypsochromic shift and quenching in the spectral intensity of the chromophore absorbance and a bathochromic shift and quenching in its emission. Excitonic couplings lead to occurrence of vibronic features in the spectra while excimeric interactions lead to broad, featureless spectra. Various combinations of these effects would therefore, lead to differences in resultant spectra which cannot be deconvoluted in a straightforward manner.

Considering the applications π -conjugated systems to biology, several chromophores have been used as fluorescent probes such as for membrane imaging,¹⁷ and the effect of membranous environments to the polarization and planarization of these conjugated probes are also rarely investigated.^{18,19} Among the known π -oligomers, the torsional flexibility of oligothiophenes have been one of the most extensively studied,^{20,21} and several of these reports have utilized methyl substitutions to perturb the π -system planarization.^{22,23} The rotation around the α,α' -dihedral angle between thiophene rings have a small energetic cost, making oligothiophenes sensitive towards torsional perturbation.¹⁷ It has been previously reported that oligothiophenes with zero, one, or two adjacent methyl groups in β -position are planar in their excited state while in the ground state, the central dihedral angle considerably varies.²³ Different alkyl-substituted oligothiophenes displaying varied torsional conformations on the Au (111) surface were also previously studied, showing that *cis-trans* torsional disorder may not be a significant source of electronic disorder for oligothiophenes.²⁴ In separate studies on the torsional motion about the central dihedral angles of oligothiophene, it was interestingly found that non-zero rates of charge transport were predicted even at 90° twists and that the twisting potentials are highly dependent on chain length.^{25,26} These studies provided insight on the torsional flexibility of oligothiophenes and its correlated impact on electronic properties. When the interchain interactions were considered for crystalline sexithiophene, planar configurations were predicted despite the flexibility of individual units due to a high energetic cost to torsional defects brought by the neighboring chains.²⁷

With the emerging use of π -oligomers towards bioelectronic applications, beyond their utility as imaging probes, several groups have utilized self-assembling biomolecules

to direct hierarchical ordering and act as a scaffold to establish better π - π interactions. Such strategies present diverse opportunities to functionalize the electronically-active systems with bioactive groups, as well as to impart more biologically relevant physical properties (*i.e.*, softer mechanical properties of hydrogels).²⁸⁻³¹ In this Chapter, we will discuss the implications of peptidic environments on the conformation of internal embedded π -systems within. Despite the extensive literature on π -segments appended to biomolecule assemblies and their applications, the effect of spatial constraints imposed by the assemblies on the conformation of individual π -units and dihedral angles between the aromatic units are not much investigated. This Chapter presents a series of photophysical investigations for two known π -systems, oligo(*p*-phenylenevinylene) (OPV3) and quaterthiophene (OT4), to elucidate the non-resonant effects of embedding the π -units within peptide 1D-nanostructures. OPV3 has well-studied photophysics and is known to facilitate exciton migration.^{32,33} The rotation of phenyl rings in OPV3 attached *via* two *trans*- double bonds is restricted due to the double bond geometry. Quaterthiophene (OT4) was used due to its widely understood properties and is known as nearly planar with *anti*-orientation of the thiophene rings,⁵ and its β -methylated derivative at the interior thiophene rings (OT4dM) which has a relatively less planar conformation than OT4.^{22,23} Moreover, the use of quaterthiophene-peptide assemblies as the active layer in a field-effect transistor have been successfully reported,³⁴⁻³⁶ and therefore merits further understanding of structure-property correlation. In order to understand the effect of assembly-induced constraints on the geometry and optoelectronic properties of the π -electron unit, it is imperative that the unit be held in a constrained local environment, but not interact with neighboring π -units. This was achieved by co-assembling peptides containing a flexible, central aliphatic chain with

peptides containing core π -electron units. This study helps to understand the influence of the local nanostructural environments of peptide- π -peptide molecules on their optoelectronic properties. This provides further insights into electronic delocalization within optoelectronically active peptidic nanomaterials and more generally, the photophysical effects upon exposing, or dispersing, these materials in lipid-like environments that would be useful for interfacing peptide electronics with hydrophobic biological membranes.³⁷⁻³⁹

Results and Discussion

Similar to the design considerations of the compounds in Chapter 2, the tripeptide sequences used to form peptide- π -peptide triblock molecules were designed such that the terminal aspartic acid (Asp, D) would impart pH sensitivity to the peptide. These aspartic acid residues ensure that the peptides are essentially dissolved under basic conditions due to Coulombic repulsion among negatively charged carboxylate units and are assembled under acidic conditions when these ionizable groups become protonated. The interior amino acids were either valine (Val, V), which has a high propensity toward β -sheet formation⁴⁰ and provides a hydrophobic environment, or aspartic acid (Asp, D), which provides an entirely hydrophilic backbone. The triblock peptide sequences prepared for these studies are shown in Figure 3.1. These two peptide sequences, DDD- and DVV-, allow us to infer the effects of local field “solvatochromism” on the photophysics of the embedded π -electron unit. Analogous to protein systems, the peptide matrix carries charged or polar groups that are expected to create a local field and influence the electronic states of the π -system core.^{41,42}

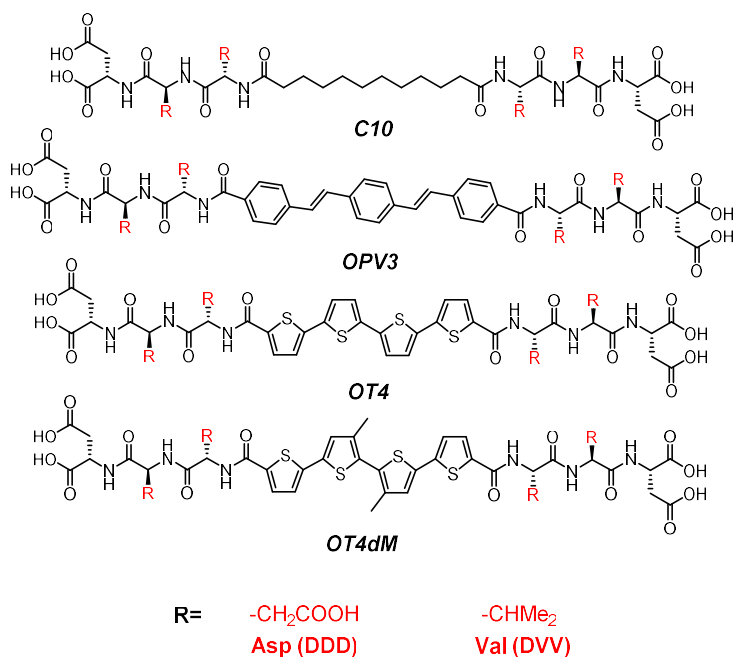


Figure 3.1. Molecular structures of peptides used in this study.

Here, the goal of this is to understand the relative contributions of torsional restriction and exciton coupling on the photophysics of peptide- π -peptide supramolecular assemblies, with OPV3 and OT4 as the π -electron units. The photophysical properties of the self-assembled peptide nanostructures were investigated using UV-vis absorption, PL, FT-IR and circular dichroism (CD) spectroscopies, while the nanostructure morphologies were determined using transmission electron microscopy (TEM). Previously, homo- and heterogeneous compositions of peptide- π -peptide triblock molecules were reported as assemblies with electronically delocalized nanostructures. This intermolecular electronic delocalization is facilitated by the exciton coupling among the internal π -electron groups. The steric interactions among neighboring π -electron groups may also restrict the torsional freedom among the aromatic groups that make up the core π -electron segments. In order to investigate the properties of isolated, individual π -electron units within nanostructural

confines, we diluted the optoelectronic nanostructure with an electronically “inert” peptide (*n*-decyl, C10) with the expectation that it will statistically minimize core π - π intermolecular interactions and provide a sufficiently viscous matrix to influence torsional dynamics. When a mixture of the OPV3 and C10 containing peptides is acidified, the two peptides can (i) form co-assemblies in which the minority component (OPV3) is dispersed to yield isolated units within the majority component (C10) matrix, (ii) form co-assemblies which contain stacks of OPV3 units and C10 units, resulting in sorted stacks within a nanostructure, or (iii) form separate stacks with no intermixing of the two peptides (Figure 3.2). Although the kinetic and thermodynamic control in favoring co-assembled or perfectly self-sorted structures in multicomponent mixtures of supramolecular systems is still a challenge in aqueous systems, it is well supported that pathways towards kinetic products that result in random component mixing are more often favored for larger π -systems under aqueous conditions due to hydrophobic effects.^{43,44}

As individual molecules in solution:

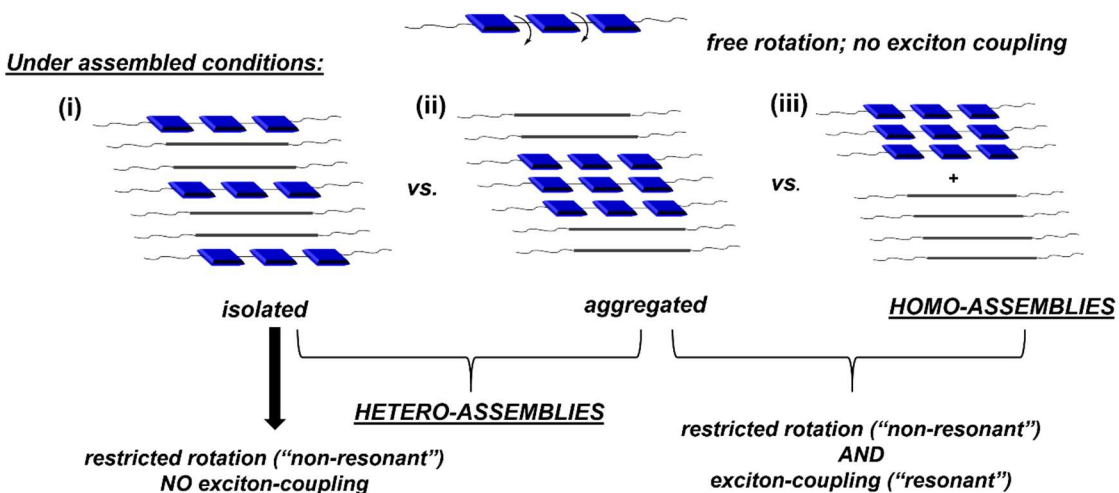


Figure 3.2. An illustration representing the possible structural outcomes of the co-assembled peptides that conform in a 1-D nanostructural geometry (■ = OPV3 π -electron unit; — = alkyl core; ~ = peptide matrix).

Because the self-assembly processes for the molecules presented herein involve abrupt acidification of the mixtures, we expect formation of kinetically-trapped structures wherein co-assembled C10 and OPV3 peptides randomly coexist in each 1-D nanostructure (Figure 3.2i, ii). Low OPV3 molar ratios in the co-assembled nanostructures should ideally promote their isolation in the C10 matrix (Figure 3.2, i) and minimize intermolecular electronic communication amongst the π -electron units. This would render the isolated OPV3 units as individual reporters of the self-assembled local environments. If aggregated π -stacks persisted or self-sorting were favored (Figure 3.2, ii and iii), the photophysical properties should be reminiscent of the homo-assemblies of each π -conjugated peptide due to intermolecular electronic coupling, from which we expect to see spectral signatures corresponding to exciton coupling between the π -components (*i.e.*, in H-like aggregates, which were consistently observed for these molecules, leading to a blue-shifted absorption peak and red-shifted, quenched PL peak as compared to the molecularly dissolved state). Broad, structureless absorption and PL spectra are expected when free rotation of phenyl rings is possible, while planar and rigid molecules (or molecules in rigid or viscous environments) should show distinct vibrational bands in their absorption and PL spectra. In previous studies involving OPV3-based peptide nanostructures, a broad, featureless peak at *ca.* 515 nm in the PL spectra was attributed to a purely excimeric interaction among adjacent units, while excitonic coupling led to a blue-shifted PL spectrum with well-defined vibronic peaks.³³

In order to visualize the assembled nanostructures, we recorded TEM images representing nanomaterials present in the solutions analyzed during the photophysical investigations (Figure 3.3 and 3.4). All peptides involved in this study formed one-

dimensional (1-D) nanostructures under acidic conditions as seen from the representative TEM images of nanostructures in aqueous suspensions. The self-assembled nanostructures generated from **DDD-C10**, **DDD-OPV3** and co-assemblies thereof consistently had 1-D morphologies likely consisting of fibrils or twisted tapes composed of stacked peptide molecules. Assemblies derived from **DVV-C10**, **DVV-OPV3** and co-assemblies thereof also resulted in 1-D nanostructures, with **DVV-C10** showing nanostructures with the most apparent helical character (*e.g.*, Figure 3.3, *top right*). The consistent 1-D nanostructure morphology present among the different samples used in this study allows for a more direct comparison of photophysical behavior.³³

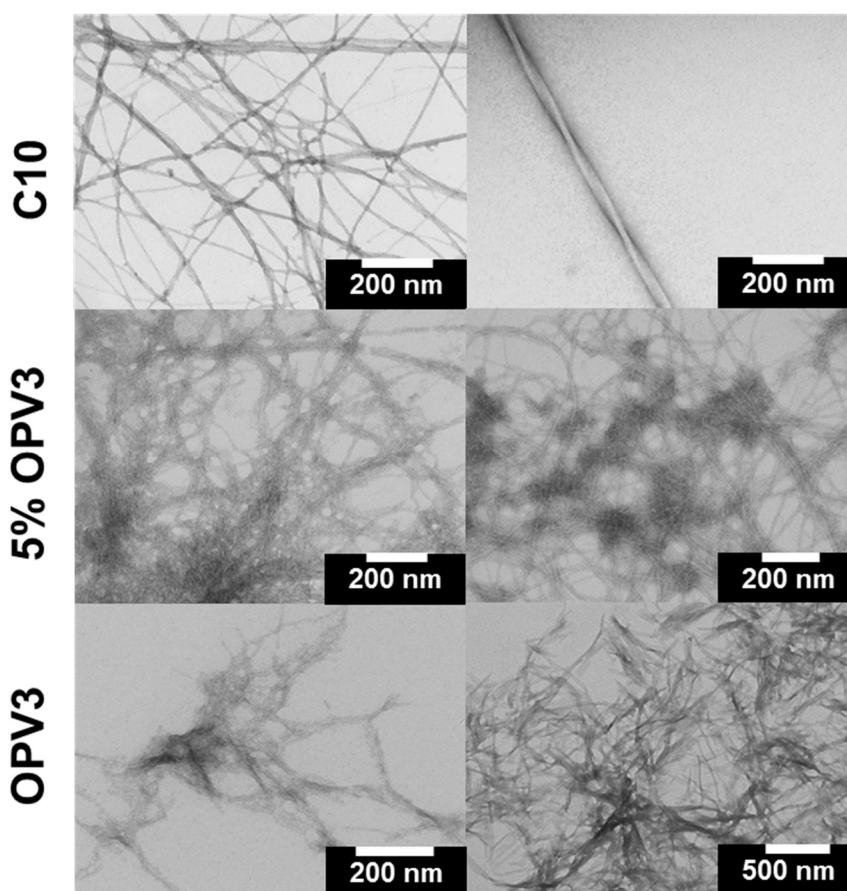


Figure 3.3. TEM images for **DDD-** (*left panel*) and **DVV-** (*right panel*) C10 assemblies and their respective co-assemblies (5 and 20 mol%) with **OPV3**.

For DDD peptide sequence with both OT4 and OT4dM π -electron units, nanostructures with uniform widths of *ca.* 30 nm were observed. These appear to resemble hollow nanotubes whereas both the pure DVV OT4 and OT4dM show nanostructures with smaller widths and are less rigid in nature as compared to the DVV C10 “twisted tape-like” structures. The nanostructure widths in the mixtures seem to be dominated by that of the C10. Figure 3.4 shows representative TEM images for OT4 and OT4dM peptide co-assemblies whereby 1-D nanostructure formation is maintained for both the DDD and DVV peptide series.

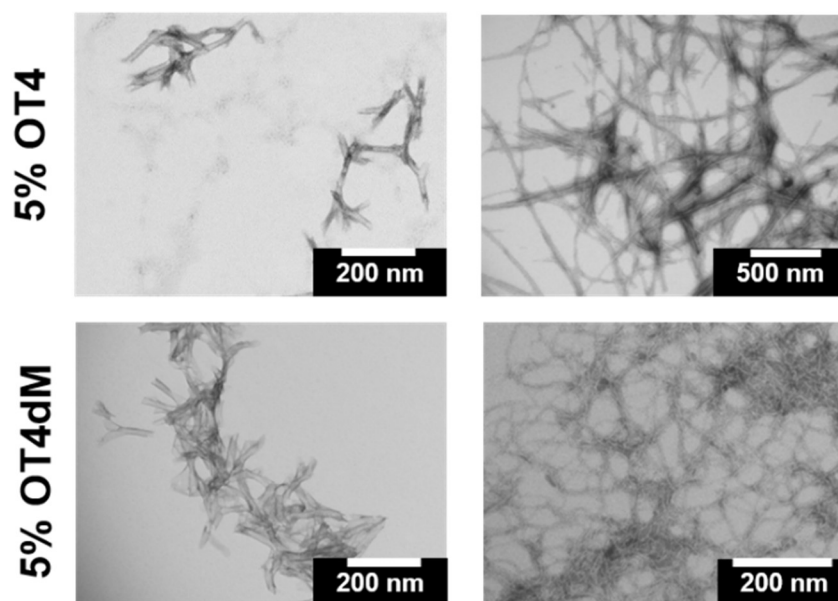


Figure 3.4. TEM images for 5 mol% DDD- (*left panel*) and DVV- (*right panel*) OT4 and OT4dM/ co-assemblies with C10 peptides.

The π - π^* transitions associated with the OPV3 unit contained in the peptides were measured in basic (*ca.* pH 10, molecularly dissolved state) and in acidic (*ca.* pH 1, assembled state) solutions of either the pure OPV3 peptides or their mixtures with the C10 peptides. The spectroscopic profiles recorded from these solutions should be treated as

ensemble averages of all possible local chromophore orientations. The changes observed in the photophysical properties after C10 dilution can be attributed to the torsional constraint created by the hydrophobic alkyl chains in the immediate environment of the π -electron unit within the co-assembled nanostructures. In order to identify which of the structural possibilities in Figure 3.2 dominates in our mixed systems, we prepared three sets of samples for each peptide system: (1) solutions of pure **DDD-** or **DVV-OPV3** (*homo-assemblies*); (2) solutions of **DDD-** or **DVV-OPV3** diluted with **DDD-** or **DVV-** C10 peptides under basic conditions, followed by acidification (*co-assemblies*); and (3) solutions of C10 and OPV3 peptides, separately acidified and then mixed into one solution (*separate assemblies*). To determine the dilution ratios to be used for the co-assembled and separately-assembled samples, the absorption and PL spectra of **DDD-** and **DVV-OPV3** peptide were recorded at different concentrations to approximate the critical aggregation concentration (CAC) of these peptides under acidic (*ca.* pH 1) conditions (Figure A3.30 and A3.31). We approximated the CAC so that any photophysical signal indicative of an isolated peptide behavior (Figure 3.2, i) at the determined lower dilution ratios is not due to the inability of the peptide to assemble by itself. The recorded CAC for **DDD-OPV3** (1.66 μM) was the minimum concentration needed to achieve an absorption or emission profile indicative of H-like aggregation. This concentration corresponds to 5 mol% **DDD-OPV3**, which is the minimum dilution ratio used in all experiments discussed here. We also performed dynamic light scattering experiments (DLS) on the **DDD-OPV3** solutions to relatively compare the aggregation states at different peptide concentrations (Figure A3.32), which supports the CAC estimated from absorption and PL measurements. In contrast, DLS experiments and the absorption and PL spectra for concentrations

corresponding to 1 mol% **DVV-OPV3** confirmed the existence of self-assembled nanostructures (Figure A3.31 and A3.33). For consistency, we used 5 mol% as the lower dilution limit to compare the photophysical behavior of **DDD-OPV3** and **DVV-OPV3** as homo-assemblies or when mixed with their corresponding C10 peptides.

The homo-assemblies of both **DDD-OPV3** and **DVV-OPV3** showed “*H*-like” aggregation of the OPV3 unit, as inferred from the blue-shifted and quenched absorption peak under acidic conditions (Figure 3.5a, d) with respect to the basic samples. The unassembled **DDD-OPV3** and **DVV-OPV3** peptides had absorption spectra centered at 369 nm and 366 nm, respectively, which blue-shifted to 342 nm and 343 nm, respectively, with low-energy shoulders at *ca.* 410 nm upon acidification and assembly. In the case of the **DDD-OPV3/ DDD-C10** co-assemblies (Figure 3.5b), the absorption spectra showed a very subtle blue-shift at 20 mol% **DDD-OPV3** and a more pronounced red-shift at 5 mol% OPV3 ($\lambda_{\text{max}} = 367$ nm) as compared to the **DDD-OPV3** homo-assemblies. At 5 mol% **DDD-OPV3**, the absorption λ_{max} of the spectra in both basic and acidic conditions remained almost identical, even as the intensity under acidic conditions was slightly lower. This close correspondence to the basic (molecular) **DDD-OPV3** spectrum suggests the effective isolation in the C10 matrix at this low concentration. In the case of the **DVV-OPV3/ DVV-C10** co-assemblies (Figure 3.5e), the λ_{max} of absorption spectra of the co-assembled nanostructures had very subtle blue-shifts with respect to the homo-assemblies with decreasing **DVV-OPV3** content in the co-assemblies, from 342 nm at 20 mol% OPV3 to 338 nm at 5 mol% OPV3. The DVV co-assemblies and the separately assembled mixtures (Figure 3.5e, f) showed similar absorption spectra, notably the shoulder at 410 nm that is also found in the **DVV-OPV3** homo-assemblies.

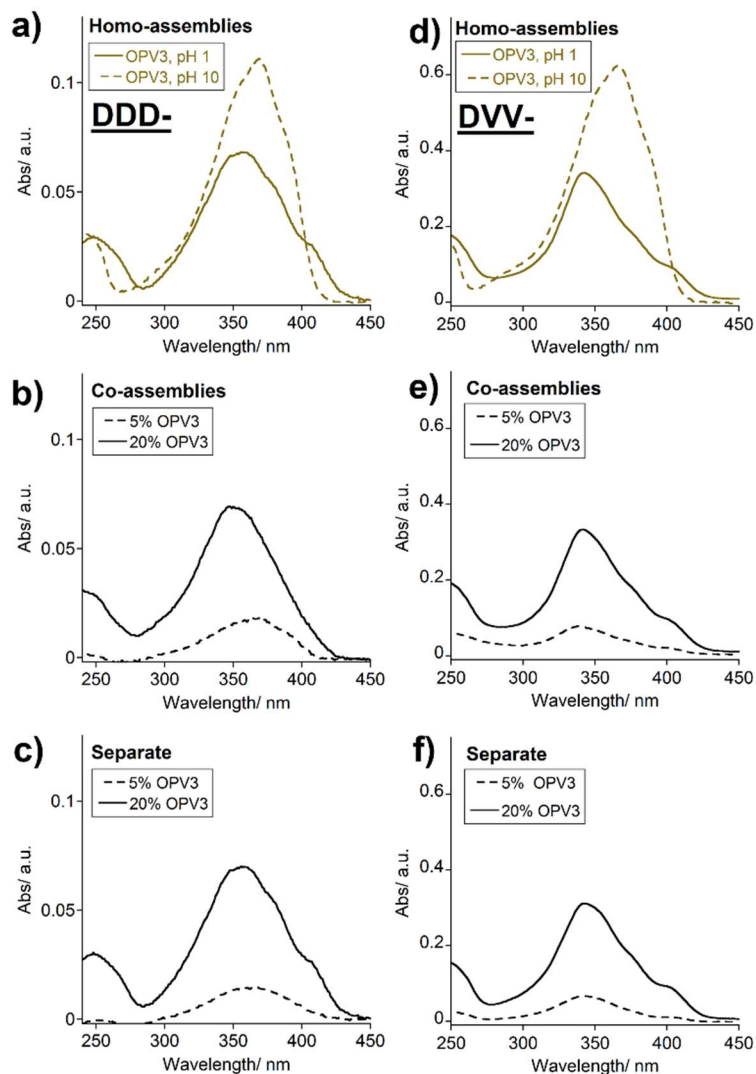


Figure 3.5. UV-vis absorption spectra of **DDD-OPV3** (a-c) and **DVV-OPV3** (d-f); homo-assemblies (a, d), co-assemblies (b, e) and separately assembled mixtures (c, f) with their respective C10 peptide equivalents; $[C10] = 33 \mu\text{M}$, kept constant for all the dilution ratios; concentration of OPV3 in homo-assemblies was the same as the 20 mol% OPV3 dilution, $[OPV3] = 8 \mu\text{M}$. Spectra recorded at room temperature (*ca.* 25 °C).

The PL spectra (Figure 3.6a, d) of **DDD-OPV3** and **DVV-OPV3** peptides show broad and featureless peaks under basic (molecular) conditions, with λ_{max} at 446 nm and 444 nm, respectively. Upon acidification, the PL spectral features varied significantly with the peptide sequence. The PL intensity was quenched in the **DDD-OPV3** homo-assemblies

and the λ_{max} red-shifted slightly with vibronic peaks at 426 nm and 449 nm and a shoulder at 510 nm, suggesting close electronic communication/excitonic coupling among neighboring OPV3 units. In contrast, **DVV-OPV3** homo-assemblies exhibit significantly red-shifted, broad, featureless PL spectra with λ_{max} at 478 nm and quenched intensity with respect to the molecular **DVV-OPV3**, which resembles more prominent excimeric coupling among neighboring OPV3 units. The subtle differences in the local environment of the OPV3 unit caused by varying the peptide sequence therefore affect the electronic communication within the peptide ensembles. This is in agreement with our previous work showing how the size and hydrophobicity of peptide residues impacted photophysical properties.⁵³ In both the **DDD-OPV3** and **DVV-OPV3** cases, the PL peaks are blue-shifted with respect to a purely excimeric OPV3 signature (*ca.* 515 nm),³³ which suggests that these spectra represent some combination of both excimeric and excitonic-like PL. As compared to this OPV3 π -electron unit, carbon- or silicon-bridged ladder-type oligo(phenylenevinylene)s containing three coplanar phenyl rings show much stronger vibronic features, with peaks at 376, 396 and 419 nm for a C-bridged system^{45,46} and at 424 and 447 nm for a Si-bridged system⁴⁷. The PL spectra of these materials also have prominent vibronic peaks at 433, 458 nm for the C-bridged molecules and 473 nm for the Si-bridged system,⁴⁷ owing to the planarity and extended conjugation. The considerable differences in spectral signatures of our systems to these planarized ladder-type oligo(phenylenevinylene)s, notably the less pronounced or absent vibronic profiles, suggest that dynamic conformations due to torsional freedom are likely predominant.

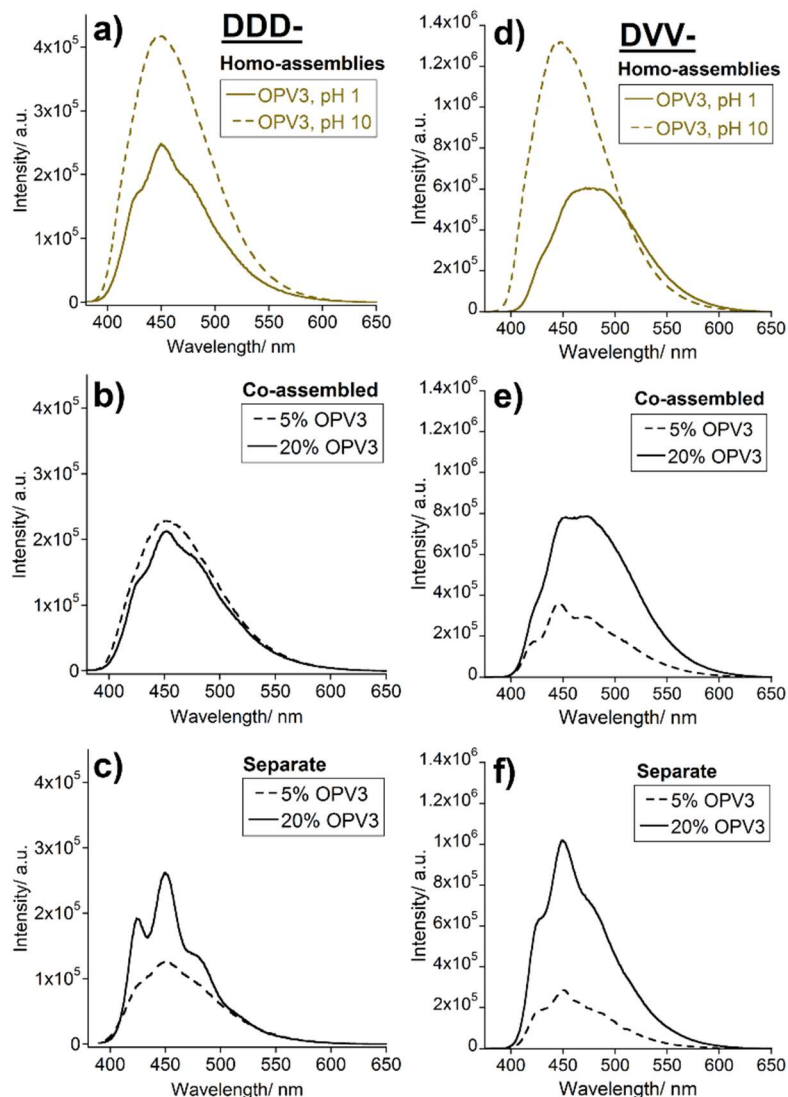


Figure 3.6. PL spectra of **DDD-OPV3** (a-c) and **DVV-OPV3** (d-f); homo-assemblies (a, d), co-assemblies (b, e) and separately assembled mixtures (c, f) with their respective C10 peptide equivalents; $[C10] = 33 \mu\text{M}$, kept constant for all the dilution ratios; concentration of OPV3 in homo-assemblies was the same as the 20 mol% OPV3 dilution, $[OPV3] = 8 \mu\text{M}$. Spectra recorded at room temperature (*ca.* 25 °C).

Co-assemblies of **DDD-** and **DVV-OPV3** with C10 peptides were prepared as described above. The PL spectrum of 20 mol% **DDD-OPV3** co-assemblies in **DDD-C10** showed structured vibronic peaks (similar to those observed in **DDD-OPV3** homo-assemblies), suggesting interchromophore communication (Figure 3.6b). At 5 mol% **DDD-**

OPV3, the spectrum appeared broad and featureless with λ_{max} at *ca.* 450 nm, much like that of the peptide in the molecularly dissolved state. The PL intensity at 5 mol% was also about five times higher than that at 20 mol%: the relative quantum yield of the 5 mol% co-assembly was 4.2-fold higher than that of the homo-assembly, while that of the 20 mol% co-assembly was only 0.8 times (Table A3.1). This further supports a decrease in aggregation of the OPV3 units within the more diluted nanostructures, which leads to a significant decrease in the extent of PL quenching in “H-like” aggregates. The ratio of PL intensities of acidic 5 mol% **DDD-OPV3** solution to its corresponding basic solution is 0.86 while that at 20 mol% **DDD-OPV3** is 0.19. These results suggest that the **DDD-OPV3** units are well distributed within the co-assembled peptide stacks and, at progressively lower molar concentrations, the communication among these units decreased due to dilution. Since the spectra at 5 mol% **DDD-OPV3** content under both basic and acidic conditions are quite similar, it is reasonable to assign that the observed photophysics correspond to those of isolated OPV3 units held in the self-assembled peptide nanostructures (Figure 3.2, i) and to expect that free-rotation between the aromatic units is still facilitated in an assembled *n*-decyl peptide environment. In contrast, even at 5mol%, the PL of the **DVV-OPV3/ DVV-C10** co-assemblies showed pronounced vibronic features with distinct maxima at 421, 446, 470 nm (Figure 3.6e). This is consistent with previous findings for related OPV3-peptide conjugates,³³ thus, we can infer that the DVV- sequence favors self-association within these co-assembled nanostructures wherein electronic communication among neighboring OPV3 units is maintained.

Besides concentration induced intensity differences, the steady-state spectral features observed by mixing separately-assembled nanostructures of **DDD-OPV3** and **DDD-C10** were similar to those observed in the case of the **DDD-OPV3** homo-assemblies (Figure 3.6c). The PL spectra had pronounced vibronic features at 20 mol%, which were less pronounced in the 5 mol% **DDD-OPV3** samples. Similar experiments on the 5 and 20 mol% separately-assembled **DVV-OPV3** showed a more pronounced vibrational progression in the high-energy region with an enhanced ~450 nm peak in the PL spectra as compared to the **DVV-OPV3** homo-assemblies (Figure 3.6f). This suggests a more excitonic-like emission when separately mixed with **DVV-C10**. The PL features of these separately assembled DVV-peptide mixtures are more similar to the co-assemblies than to the homo-assemblies. In this case, there are photophysical differences brought about by diluting pre-assembled **DVV-OPV3** nanostructures in a solution of pre-assembled **DVV-C10**, which can be attributed to the effect of minimizing the lateral bundling interactions between the stacks of peptides containing “electronically active” OPV3 units. Considering the similarities to the PL signals of DVV- co-assemblies, the photophysical measurements for the separately assembled mixtures of DVV-peptides further supports that **DVV-OPV3** prefers self-aggregation even under co-assembly conditions and that the contributions from excitonic-like emission are more prominent when diluted within (as co-assemblies) or with (as separate assemblies) **DVV-C10** than in the homo-assemblies.

The OT4 and OT4dM peptides follow the same general trend of photophysical properties as those observed for H-like aggregates (Figure 3.7 and 3.8). The methyl groups attached to the quaterthiophene units perturb the planarity of the π -system, thus inducing a blue-shift in the absorption spectrum as compared to OT4 (λ_{max} , pH 10, **DDD OT4**, 408

nm; **DVV OT4**, 419 nm; **DDD OT4dM**, 376 nm; **DVV OT4dM**, 367 nm). This can be attributed to the break in the conjugation as a consequence of deplanarization brought about by the methyl groups.²² Upon acidification, the absorption intensity was quenched and the λ_{max} red-shifted to 414 nm and 382 nm in the case of **DDD OT4** and **DDD OT4dM**, respectively. Such red-shifts in absorption spectra of quaterthiophene molecules have been previously observed, and attributed to planarization of the chromophore units upon confinement in space as well as exciton coupling between π -units within the assemblies.⁴⁸ In the case of **DVV OT4**, the absorption spectra blue-shifted to 397 nm upon acidification, while that of **DVV OT4dM** equivalent remained at 367 nm. Broad, featureless emission spectra were observed for **DDD OT4** and **DDD OT4dM** with maxima at 514 nm and 522 nm, respectively, and both **DVV OT4** and **DVV OT4dM** under the molecularly dissolved state had peaks centered at *ca.* 520 nm. Dimethylation of the core quaterthiophene unit is known to predominantly affect the absorption properties, whereas the chromophore should adopt a planar excited state conformation therefore resulting in an emission profile resembling that of the unfunctionalized α,ω -quaterthiophene (possibly accompanied with a lower quantum yield).^{23,49} Upon acidification, the spectrum red-shifted to 541 nm in the case of **DDD OT4** and slightly blue-shifted in the case of **DDD OT4dM** to 519 nm, while both maintained broad featureless peaks. In contrast, acidification of **DVV OT4** and **DVV OT4dM** resulted in more structured spectra with bands at \sim 520 and 550 nm that were more prominent in the case of OT4dM peptide.

Coassembly of these peptides with C10-containing peptides was carried out to understand the effects of varying chromophore geometries on the properties of the chromophores within peptide ensembles. Similar to the observation in the case of the planar

OPV3 chromophore in DDD peptide, both OT4 and OT4dM chromophore units appear to be isolated at low molar ratios in the **DDD C10** matrices (Figure 3.7). This can be seen from the gradual blue-shift in the absorption spectra with dilution from 413 nm at 20 mol% OT4 to 408 nm at 1 mol% OT4, as well as that in the emission spectra, from 531 nm at 20 mol% OT4 to 515 nm at 1 mol% OT4 content. The absorption spectra and the PL spectra of 1 mol% **DDD OT4/ DDD C10** peptides under alkaline conditions resemble that of the corresponding co-assembled nanostructures, although the absorption and emission intensities of the co-assembled nanostructures were slightly lower than those of the peptide mixture. This is similar to the observation in the case of **DDD OPV3** peptide, suggesting a similar behavior involving isolation of minority, **DDD OT4** peptide, within the predominantly **DDD C10** peptidic stacks. In the case of **DDD OT4dM/ DDD C10** coassembled nanostructures, no significant difference was observed in either the absorption or the emission spectra with dilution. However, the spectra of molecularly dissolved peptide mixture at 1 mol% **DDD OT4dM** did not overlap the spectral position of the co-assembled nanostructures, as was observed with the previous two chromophores. The absorption spectrum of the co-assembled nanostructures containing 1 mol% **DDD OT4dM** was red-shifted by 6 nm as compared to the molecularly dissolved peptide mixture.

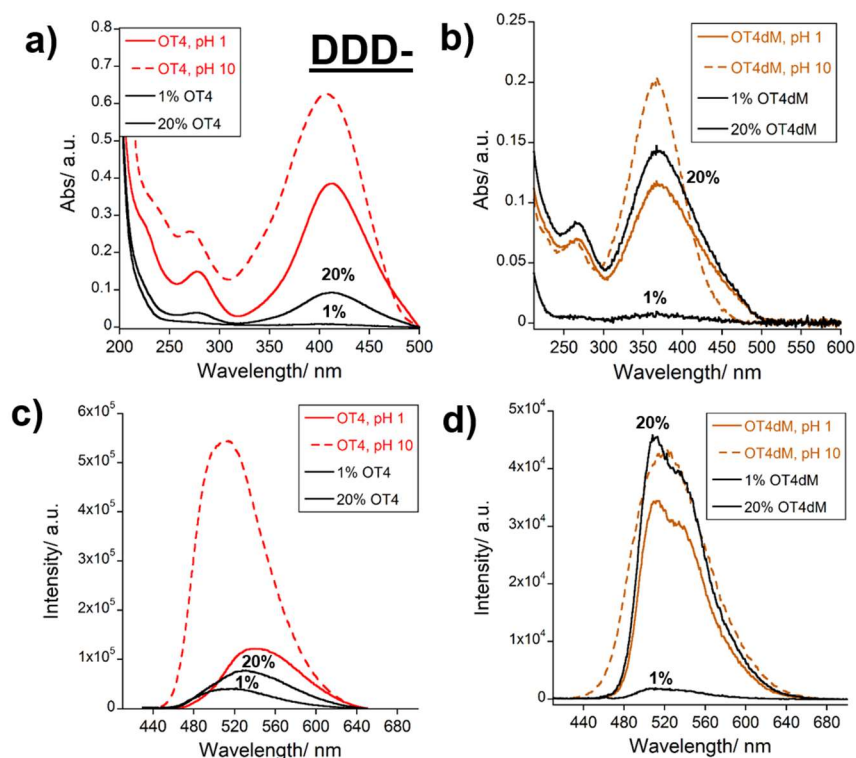


Figure 3.7. Absorption (a,b) and PL spectra of **DDD-OT4/OT4dM** homoassemblies and co-assemblies with their respective C10 peptide equivalents; pH 10 (---) and pH 2 (—); total peptide concentration for the co-assembled system is 33 μM . The OT4/OT4dM concentration in homo-assemblies are the same as the 20% dilution with C10. Spectra taken at room temperature (*ca.* 25 $^{\circ}\text{C}$).

In the case of DVV systems (Figure 3.8), the 1 mol% coassemblies for both chromophores show broad and less resolved spectra than the 20 mol%. Comparing the 20% chromophore dilution to the pure solutions investigated, the emission spectra show similar features but the quantum yield is higher with the coassembly. This relatively reduced quenching in the co-assembled case further supports the decrease in resonant effects upon dilution with C10 peptide matrices. Moreover, comparing the methylated system to OT4, the emission spectrum of basic **DVV OT4dM** is already quenched as compared to that of **DVV OT4**. In both cases, the dilution did not result a huge difference on the photophysical properties of the peptide. For the DVV series that prefers aggregation over isolation, the

blocks of OT4/OT4dM diluted within C10 or laterally interacting with other C10 stacks do not impose enough torsional strain to affect the planarity among the aromatic units of the chromophore.

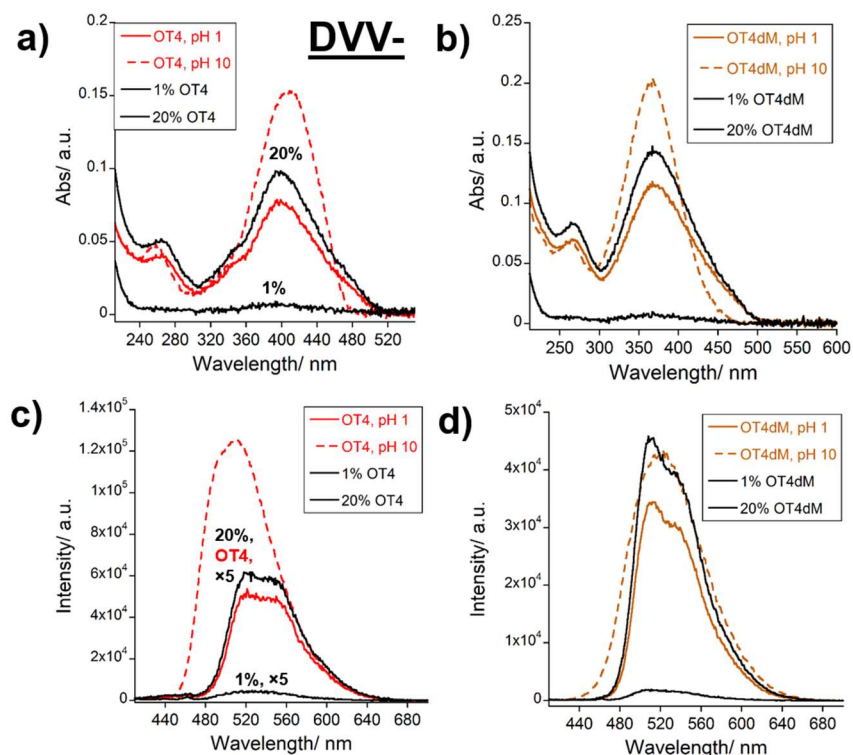


Figure 3.8. Absorption (a,b) and PL (c,d) spectra of **DVV-OT4/OT4dM** homo-assemblies, and co-assemblies with their respective C10 peptide equivalents; pH 10 (---); pH 2 (—); total peptide concentration for the co-assembled system is 33 μM . The OT4/OT4dM concentration in homo--assemblies are the same as the 25% dilution with C10. Spectra taken at room temperature (*ca.* 25 $^{\circ}\text{C}$).

In the case of mixtures of pre-assembled peptides (Figure 3.9), **DDD OT4** and **DDD C10** as well as **DDD OT4dM** and **DDD C10**, a decrease in intensity of absorbance as well as photoluminescence was observed as the concentration of the π -electron unit containing peptide was decreased. However, a change in spectral position was observed to accompany this change in the case of pre-assembled mixtures of **DDD OT4** and **DDD C10**, indicating some interactions amongst stacks in solution that would impart electronic communication

and hence spectral variation across the dilution series. For the **DVV OT4** peptide, the pre-assembled nanostructures show a broad peak with less resolved bands than the co-assemblies at 20 mol% while retaining the same features at 1 mol%. The **DVV OT4dM** pre-assembled nanostructures did not show any change in intensity or spectral features as compared to the corresponding coassembled nanostructures. This suggests that not all pre-assembled samples have exactly the same photophysical characteristics as their pure peptide counterparts because the presence of pre-assembled C10 fibers likely imposes different bundling interactions with stacks of π -electron unit containing peptide.

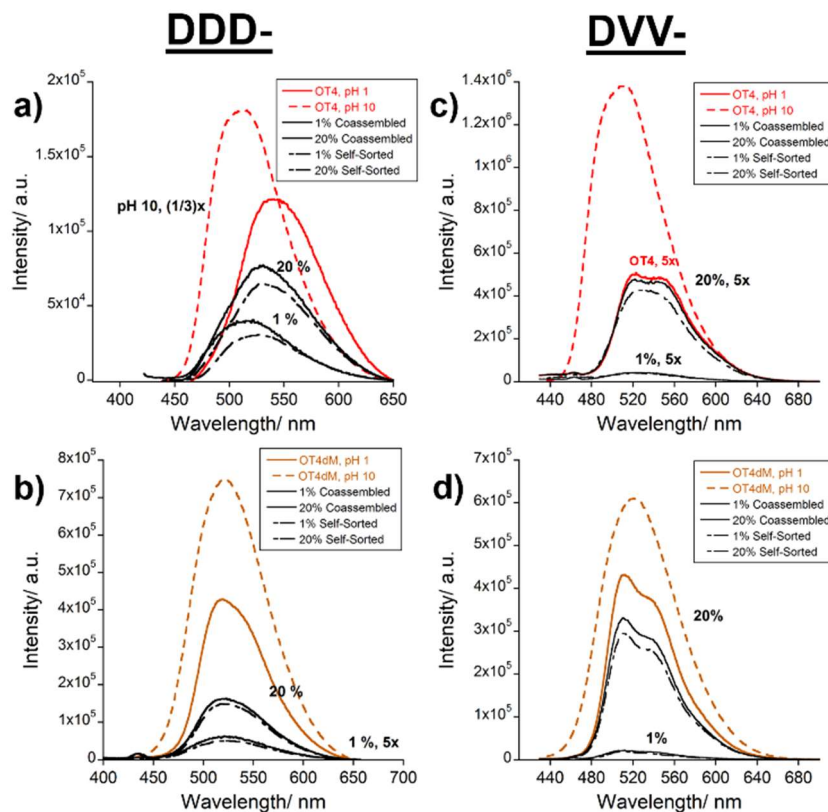


Figure 3.9. Comparison of emission spectra of pure assemblies, co-assembled and self-sorted **DDD-** (a, b) and **DVV-** (c, d) **OT4/OT4dM** peptides and their C10 coassemblies.

The CD spectra of coassembled nanostructures were recorded to understand the peptide structure as well as the local environments of the embedded π -electron units. All **DDD-OPV3** and **DVV-OPV3** homo-assemblies and co-assemblies, except 5 mol% **DDD-OPV3** co-assemblies (Figure 3.10), show bisignate Cotton bands corresponding to the coupled π - π^* (or other relevant) transition dipoles due to exciton-coupled π -electron units in local chiral environments. These features were observed in the low-energy spectral region of OPV3 absorption with the cross-over near the UV-vis absorption maximum, with consistent handedness throughout the dilution series. The signals within the 200-250 nm region show peak minima (at *ca.* 200-220 nm) corresponding to mixed contributions of random coil and twisted β -sheet motif for all peptides studied here. In this region of the CD spectra, **DDD-C10** shows a higher contribution from a random coil character, while **DVV-C10** shows more β -sheet characteristics (with minima that are red-shifted from the ideal values, indicating local twisting). The similarities of the signals in this low-wavelength spectral window for the C10 homo-assemblies and their co-assemblies with OPV3 peptides, viz. a sharp peak at 199 nm along with a shoulder at *ca.* 215 nm for **DDD-** and peak minima at \sim 200 and \sim 220 nm for **DVV-**, suggest that the incorporation of OPV3 peptides to generate these co-assemblies does not significantly affect the structural motif preference of the C10 matrix. The preference for β -sheet-like hydrogen-bonding interactions among the peptide segments is supported by the Amide I bands observed in the IR spectra of lyophilized acidic solutions at \sim 1630 cm^{-1} (Figure A3.23), which are more prominent for **DVV-** assemblies (1631 cm^{-1} for 5 mol% **DVV-OPV3** co-assemblies and **DVV-C10** homo-assemblies; 1630 cm^{-1} for **DVV-OPV3** homo-assemblies). It is important to recognize that signals attributed to amide bonds within non-natural, π -conjugated

peptide aggregates do not always provide definitive structural information^{33,50-52} Although the formation of a conventional β -sheet motif is not a strict requirement for the electronic delocalization between π -units,³³ the more prominent β -sheet character observed for the DVV-peptides is consistent with the higher preference of the DVV over the DDD sequence to maintain self-association and exhibit excitonic-like emission even under co-assembly conditions.

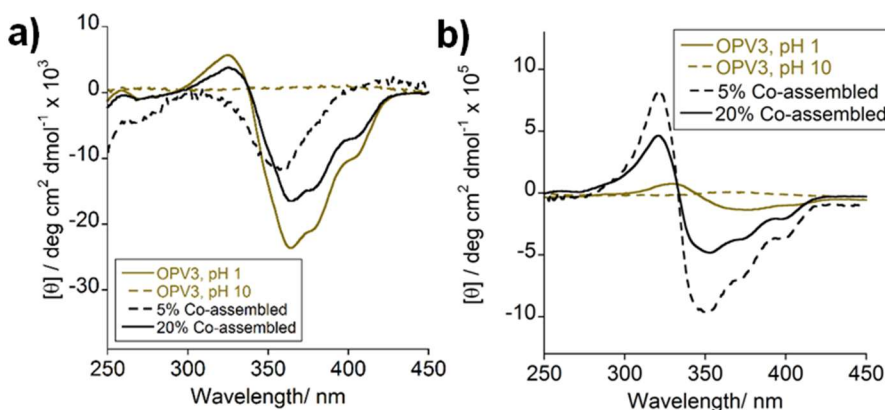


Figure 3.10. Circular dichroism spectra of **DDD-OPV3** (a) and **DVV-OPV3** (b) homo-assemblies, and co-assemblies with their respective C10 peptide equivalents; [C10] = 33 μ M, kept constant for all the co-assembly ratios; concentration of OPV3 in homo-assemblies was the same as the 20 mol% OPV3 dilution, [OPV3] = 8 μ M. Spectra recorded at room temperature (*ca.* 25 $^{\circ}$ C).

The local chirality of the OPV3 unit in the **DDD-OPV3/ DDD-C10** co-assemblies is maintained at 20 mol%. At 5 mol% **DDD-OPV3**, however, not only is the structure and intensity of this signal significantly diminished, but the bisignate nature of the signal is also lost. This indicates that, while local chirality of the OPV3 units is maintained, the exciton-coupling among neighboring units is interrupted. Considering that the homo-assemblies and the 20 mol% **DDD-OPV3** diluted case have the same final OPV3 concentration, the stronger signal in the homo-assemblies indicates that the exciton coupling decreases upon

dilution with **DDD-C10**. The co-assembled **DVV-OPV3/ DVV-C10** samples had a more pronounced blue-shift in the crossover point than **DVV-OPV3** homo-assemblies, consistent with the absorption spectra of these co-assemblies. The 20 mol% **DVV-OPV3** co-assembled nanostructures had five times more intense molar ellipticity than **DVV-OPV3** homo-assemblies with the same chromophore content, showing that exciton coupling is maintained after co-assembly and that the **DVV-C10** matrix fosters a more chiral local environment for the self-associated OPV3 units than the homo-assemblies of **DVV-OPV3**. This is further supported by the higher molar ellipticity for the 5 mol% **DVV-OPV3** co-assembly than the 20 mol%, indicating that the higher ratio of **DVV-C10** in the local environment of π -electron units induces a more chiral global assembly. These data confirm that the co-assembly of peptide- π -peptide assemblies with C10 peptides results in decreased exciton coupling for the DDD- peptides (suggesting isolation) while π - π interaction is maintained for DVV- peptides (suggesting self-association).

The exciton coupling between **OT4, OT4dM** π -electron units also results in a weak bisignate Cotton band within the region of chromophore absorption with the exception of the DDD co-assembled system (Figure 3.11). This suggests the lack of exciton coupling under co-assembly conditions as a consequence of the favorable chromophore isolation upon dilution with electronically inert C10 units. In addition, the signals in the higher energy region are primarily dominated by the ‘ β -sheet’ like C10 imprints. The peptides studied here have broad high energy minima which are red-shifted by ~ 20 nm from an ideal β -sheet signals, indicating some twisting within the motif and some random coil character. The less sharp higher energy peaks for OT4/ OT4dM peptides as compared to the C10 peptides could be due to the diverse chiral electronic environments created by the

polydisperse supramolecular peptide assemblies. Overall, similar to OPV3 assemblies, these chiral environments create a consistent direction of handedness for the chromophores even under diluted conditions for DVV peptides.

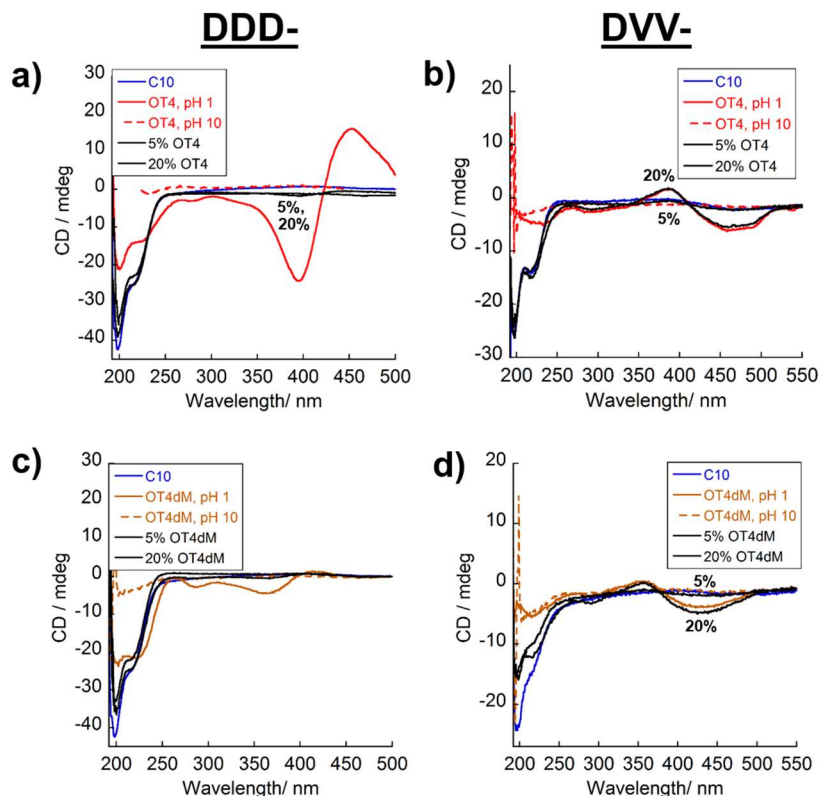


Figure 3.11. Circular dichroism spectra of **DDD-OT4/OT4dM** (a, c) and **DVV-OT4/OT4dM** (b, d) assemblies, and co-assemblies with their respective C10 peptide equivalents; pH 10 (---) and pH 2 (—); total peptide concentration for the co-assembled system is 33 μM . The OT4/OT4dM concentration in homo-assemblies are the same as the 25% dilution with C10. Spectra taken at room temperature (*ca.* 25 $^{\circ}\text{C}$).

To verify the excimeric/excitonic character of the PL spectra of OPV3, OT4, and OT4dM peptides and their co-assemblies, we performed PL lifetime experiments (Figure A3.34-35) and extracted individual lifetime components (Table 3.1). The lifetime decay profiles for both pure **DDD-OPV3** and **DVV-OPV3** peptides under basic conditions fit a single component decay ($\tau = 1.06$ ns and 1.00 ns, respectively) while those under acidic

conditions fit two-exponential decay with components at 0.76 ns and 5.46 ns ($\tau_{\text{avg}} = 0.96$ ns) for **DDD-OPV3** and 0.84 and 4.59 ns ($\tau_{\text{avg}} = 1.43$ ns) for **DVV-OPV3**. These lifetimes agree with previously reported values for OPV3 assemblies that display contributions from both excimeric and excitonic states.³³

Table 3.1. Photoluminescence lifetimes of **DDD-** and **DVV-OPV3** peptides, their co-assemblies with C10 peptides and mixtures of pre-assembled nanostructures ($\lambda_{\text{exc}} = 375$; $\lambda_{\text{em}} = 450$ nm).

mol% OPV3	τ / ns				
	Dissolved	Co-assembled		Separately assembled	
		τ (%)	τ_{avg}	τ (%)	τ_{avg}
5% DDD-	1.06	0.98 (100)	0.98	0.95 (100)	0.95
20% DDD-	1.07	0.66 (92); 3.73 (8)	0.92	0.61 (91); 3.07 (9)	0.84
100% DDD-	1.07	-	-	0.76 (95); 5.46 (5)	0.97
5% DVV-	0.98	1.03 (46.1); 4.67 (53.9)	2.99	1.38 (66.4); 5.70 (33.6)	2.83
20% DVV-	0.99	1.47 (55.4); 5.87 (44.6)	3.43	1.52 (52.7); 4.72 (48.3)	3.08
100% DVV-	1.00	-	-	0.84 (84.4); 4.59 (15.6)	1.43

The co-assembled samples showed differences in lifetime profiles based on the peptide sequence and OPV3 content. For instance, the lifetime of **DDD-OPV3/ DDD-C10** co-assembly with 20 mol% OPV3 content had components at 0.66 ns and 3.72 ns ($\tau_{\text{avg}} = 0.92$ ns), resembling the lifetime profile of **DDD-OPV3** homo-assemblies. Upon dilution to 5 mol% OPV3 content, the lifetime profile changed to a mono-exponential fit with a lifetime of 0.98 ns, resembling the pure **DDD-OPV3** peptide in the molecularly dissolved state. This further confirms the isolation of the OPV3 units in the C10 matrix at 5 mol% **DDD-OPV3**. A preliminary analysis of decay components (Equations 3.1 and 3.2) suggests that while the radiative lifetime remains fairly unchanged (2.35 ns (basic) and 2.26 ns (acidic)), the non-radiative lifetime changes from 1.93 ns (basic) to 1.73 ns (acidic) indicating the effect of difference in local environment of the π -electron unit on its PL

properties.⁵³ On the other hand, the lifetime of **DVV-OPV3/ DVV-C10** co-assembled nanostructures with 5 and 20 mol% OPV3 content both had longer lifetimes as compared to that observed in molecularly dissolved **DVV-OPV3**, and also maintains a two-component PL lifetime similar to that of the **DVV-OPV3** homo-assemblies.

The lifetime measurements for the solutions of separately assembled peptides were also recorded. These ideally self-sorted samples were strikingly similar to the analogous co-assembled variants. These similarities suggest potential dynamic interchange among the OPV3 and C10 stacks, leading to a co-mixed behavior in the separately assembled solutions over the duration of the lifetime measurements. For both the co-assemblies and separately assembled mixtures of DVV- peptides, there is a roughly comparable contribution from each of the ~1 ns and ~5 ns lifetime components. These results for DVV-peptides along with the structured vibronic bands in the steady-state spectra upon co-assembly, support the contributions from both an excitonic-like and excimeric-like emission due to the change in the local environment induced by the C10 environment to **DVV-OPV3**. Both these PL lifetime data and the steady-state PL spectra support that **DDD-OPV3** prefers isolation during co-assembly with **DDD-C10** and that the observed photophysics are indicative of the properties of the OPV3 unit held in a non-interacting self-assembled local environment at low mol% of OPV3, while **DVV-OPV3** prefers the formation of aggregated OPV3 units that maintains electronic communication even under dilute co-assembly conditions.

As summarized in Table 3.2, pure **DDD OT4** and **DVV OT4** peptides also fit a one-exponential decay model under basic conditions, with lifetimes of 0.43 ns and 0.53 ns, respectively. Under acidic conditions, the PL decay for **DDD OT4** peptide fit a bi-exponential decay profile with components at 0.69 ns and 0.18 ns ($\tau_{\text{avg}} = 0.40$ ns), while **DVV OT4** maintained a mono-exponential decay profile with a lifetime of 0.67 ns. Longer lifetimes under acidic conditions are indicative of electronic delocalization within the peptide nanostructure, in agreement with the steady state H-like aggregate behavior observed in both these peptides. Both co-assembled and self-sorted nanostructures of **DDD OT4** and **DDD C10** peptides at 20 mol% **DDD OT4** content showed lifetimes that fit a bi-exponential decay profiles. However, at lower molar ratios, both these kinds of assemblies reverted to mono-exponential decay profiles, with lifetimes around those observed in the case of molecularly dissolved samples. This suggests that the interaction among the π -electron units in the co-assembled nanostructures is disrupted leading to lifetimes similar to those observed in individual chromophore units. In the case of **DVV OT4** and **DVV C10** co-assembled nanostructures and mixtures of the pre-assembled nanostructures, the lifetime decay profiles remained bi-exponential in nature with considerably longer average lifetimes as compared to that in the molecularly dissolved state, indicating that electronic communication among π -electron units is maintained in all of these nanostructures despite the low molar ratios of OT4 containing peptide. This is similar to the observation with **DVV OPV3/ DVV C10** co-assemblies which promoted stacks of each of the constituent peptides within the co-assembled nanostructure rather than isolated units, further indicating that the DVV peptide sequence leads to such behavior.

Table 3.2. Fluorescence lifetimes of **DDD-** and **DVV-OT4** and solutions co-mixed with C10 peptides. (λ_{exc} = 375; λ_{em} = 520 nm for pH 10 and 540 nm for pH 1 samples).

mol% OT4	τ / ns				
	Dissolved	Co-assembled		Separately assembled	
		τ (%)	τ_{avg}	τ (%)	τ_{avg}
5% DDD-	0.44	0.41 (100)	0.41	0.45 (100)	0.45
9% DDD-	0.46	0.49 (100)	0.49	0.49 (100)	0.49
20% DDD-	0.43	1.88 (95); 0.38 (5)	0.45	0.69 (43); 0.18 (57)	0.40
100% DDD-	0.43	-	-	0.69 (43); 0.18 (57)	0.40
5% DVV-	0.51	6.48 (2.2); 0.58 (97.8)	0.71	3.93 (3.3); 0.58 (96.7)	0.69
9% DVV-	0.52	6.05 (2.3); 0.57 (97.7)	0.70	1.56 (10.4); 0.44 (89.6)	0.56
20% DVV-	0.52	4.24 (1.5); 0.63 (98.5)	0.68	5.77 (0.95); 0.59 (99.5)	0.62
100% DVV-	0.53	-	-	0.67 (100)	0.67

In the case of **DDD OT4dM** containing peptide and co-assemblies with **DDD C10** peptide (Table 3.3), no significant contribution from longer lifetime components were observed. The neat peptide solution had a mono-exponential photoluminescence decay with a lifetime of 0.40 ns in the molecularly dissolved state, which changed to a bi-exponential decay upon assembly with lifetime components of 6.83 ns (0.5%) and 0.35 ns (99.5%), and an average lifetime of 0.38 ns, similar to that observed in the molecularly dissolved state. This suggests that, long range electronic delocalization may not be possible in these nanostructures, in agreement with the steady state photophysical observations of no significant spectral position changes among the two pH conditions tested. Upon co-assembling the peptide with **DDD C10** peptide at different molar ratios, the lifetime at 20 mol% **DDD OT4dM** was similar to that of the pure peptide while further dilution led to a mono-exponential decay with lifetimes similar to those of the respective molecularly dissolved states. The inherent twist in the chromophore along with the impact of peptide sequence on the geometry of the assembly is likely to have a significant impact on this behavior. For **DVV OT4dM**, a mono-exponential decay with a lifetime of 0.38 ns was

observed in the molecularly dissolved state, which changed to a bi-exponential decay with an average lifetime of 0.49 ns in the acidic state. Upon co-assembling with **DVV C10** peptide, the decay maintained a bi-exponential profile throughout the dilution series, with significant contributions from longer lifetime components, except in the case of 9 mol% **DVV OT4dM**, where the longer lifetime component was only 0.85%. The impacts of peptide sequence on the local environment of the π -electron unit need to be investigated further to elucidate the governing principles behind these observations. Such studies are beyond the scope of our current experiments and will be undertaken in the future. Further computational analysis is required to understand this phenomenon.

Table 3.3. Fluorescence lifetimes of **DDD-** and **DVV-OT4dM** and solutions co-mixed with C10 peptides. ($\lambda_{\text{exc}} = 375$; $\lambda_{\text{em}} = 520$ nm for pH 10 and 540 nm for pH 1 samples).

mol% OT4dM	τ / ns				
	Dissolved	Co-assembled		Separately assembled	
		τ (%)	τ_{avg}	τ (%)	τ_{avg}
5% DDD-	0.38	0.41 (100)	0.41	0.42 (100)	0.42
9% DDD-	0.39	0.40 (100)	0.40	0.40 (100)	0.40
20% DDD-	0.40	6.67 (0.5); 0.41 (99.5)	0.44	4.11(0.5); 0.41 (99.5)	0.41
100% DDD-	0.40	-	-	6.83 (0.5); 0.35 (99.5)	0.38
5% DVV-	0.39	0.85 (26.4); 0.40 (73.6)	0.52	0.41 (81.1); 0.88 (18.9)	0.50
9% DVV-	0.39	3.20 (0.85); 0.53 (99.15)	0.55	0.24 (62.2); 0.69 (37.8)	0.41
20% DVV-	0.41	0.62 (52.4); 0.17 (47.6)	0.41	0.50 (91.6); 1.04 (8.4)	0.54
100% DVV-	0.38	-	-	0.44 (95.9); 1.7 (4.1)	0.49

In all these cases, the formation of peptide nanostructures was initiated by rapid acidification of alkaline solutions containing presumably well-solvated, molecularly dissolved peptides. The fast addition of acid to these solutions is expected to lead to formation of kinetically-trapped structures due to the rapid initiation of self-assembly and subsequent collapse into nanostructures. To further evaluate the effect of this process on the structure of the peptide ensembles and the local environment of the π -electron units

embedded within, we varied the temperature of the assembled solutions and monitored the spectroscopic effects of thermally annealing the assemblies. The OPV3 systems showed more distinct bands than the signals from OT4/OT4dM, and hence will be the focus of the temperature variation experiments in the subsequent discussions. At low temperatures (5 °C), lower thermal energy input is expected to impede rotational freedom of the molecules, which in turn should maintain the system in the initial conformation adopted upon acidification. Higher temperatures (60 °C), on the other hand, are expected to allow the system to access more co-planar conformations, due to the additional energy provided by the increase in temperature. Therefore, at low temperatures, a collection of randomly organized orientations is expected to lead to broader PL peaks, while at higher temperatures which can promote reorganization, well-resolved vibronic peaks arising from a higher degree of electronic communication in the π -electron units are expected. No significant changes were observed in the molecularly dissolved states of DDD- or DVV- peptides at these temperatures (Figure A3.36). TEM imaging verified that 1-D nanostructure formation was maintained through the tested temperature range (Figure A3.24-29).

The vibronic character of the co-assembled **DDD-OPV3/ DDD-C10** nanostructures at 5 °C disappeared along with a slight lowering of PL intensity compared to the **DDD-OPV3** homo-assembly (Figure 3.12a). No significant difference in intensity at 20 mol% and 5 mol% **DDD-OPV3** content was observed, suggesting lower extent of quenching and hence, weaker electronic communication among OPV3 units in the 5 mol% **DDD-OPV3** co-assembled nanostructures. The intensity of the bisignate CD feature decreased from 20 mol% to 5 mol% OPV3 content (Figure 3.12b), also indicating a decrease in electronic communication among the OPV3 units. At 60 °C, PL signals of the homo-assemblies were

much stronger and comparable to the 20 mol% co-assemblies, whereas a lower PL intensity was observed in the 5 mol% co-assembled nanostructures (Figure 3.12c). The bisignate nature of the peak in the CD spectra at 60 °C was not observed at 20 mol% OPV3 content and no signal was observed in the OPV3 absorption spectral window at 5 mol% OPV3 (Figure 3.12d), highlighting the significantly decreased excitonic coupling among OPV3 units. The lack of measurable CD signal from 5 mol% **DDD-OPV3** co-assemblies at 60°C is indicative of significantly lower local chirality as compared to that at room temperature or at 5°C, resulting from the greater availability of thermal energy at the elevated temperature that can promote disorder within the nanostructures.

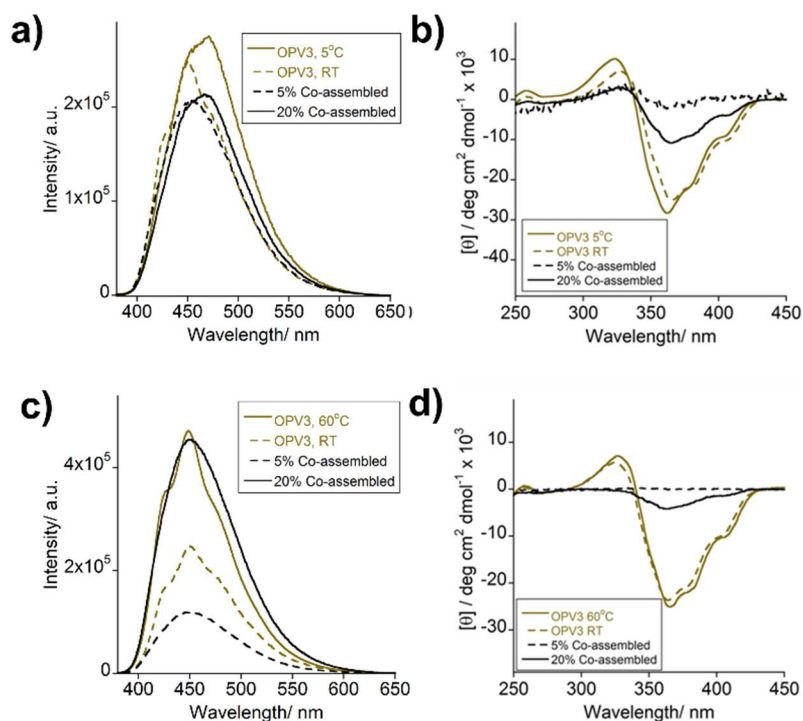


Figure 3.12. PL (a, c) and CD (b, d) spectra of acidic **DDD-OPV3** homo-assemblies and co-assemblies at 5 mol% and 20 mol% with **DDD-C10**; spectra taken at (a,b) 5 °C and (c, d) 60 °C in comparison to room temperature (RT); [C10] = 33 μM, kept constant for all the co-assembly ratios; concentration of OPV3 in homo-assemblies was the same as the 20 mol% **DDD-OPV3** dilution, [OPV3] = 8 μM.

The **DVV-OPV3** nanostructures (homo-assemblies and co-assemblies) displayed spectral features at 5 °C that mirrored the data recorded at room temperature, where the dilutions showed substantially more exciton coupling in the CD (Figure 3.13a, b). The similarities in molar ellipticities observed for the 5 mol% and 20 mol% co-assemblies at 5 °C, which are both higher than that of the homo-assemblies, suggests that C10 provides a more chiral environment to the OPV3 units within the assembly and that the ratio of π -electron unit to C10 peptides can affect the extent of observable non-resonant effects. In the PL spectra of solutions at 60 °C (Figure 3.13c), the bands of **DVV-OPV3** homo-assemblies had enhanced vibronic structure and red-shifted λ_{max} , suggesting a change in internal chromophore conformation or reorganization within the nanostructure. The heating encourages the formation of more metastable structures, but the PL profile of the 20 mol% **DVV-OPV3** co-assemblies still resembles that of the kinetically-trapped assemblies. These findings are similar to other OPV3 tetrapeptide nanostructures that remained assembled upon annealing at higher temperatures rather than dissolving and showed hysteresis in the photophysical behavior upon cooling back to room temperature.¹⁷ The existence of electronic communication among the π -electron units even in 5 mol% **DVV-OPV3** co-assemblies supports that the DVV- peptide sequence retains its tendency toward forming alternating blocks of peptide stacks rather than isolating them in the majority matrix at these higher temperatures. Unfortunately, the macroscopic aggregation due to heating at 60 °C created scattering artifacts in both the 200-250 nm region and region of chromophore absorption for the CD spectra (Figure 3.13d). A decrease in the molar ellipticity within the chromophore absorption window of co-assembled nanostructures containing 20 mol% **DVV-OPV3** peptide was also observed at 60 °C as compared to room

temperature. The signals in the higher energy region (200-250 nm) were also broader at 60 °C which could be due to the multiple assembly states and monomer conformations made accessible by the more dynamic environment created by the annealing process. The decrease in the intensity of the bisignate signal within the region of chromophore absorption at 60 °C as compared to room temperature also suggests the decrease in local chirality brought by a possible increase in assembly disorder upon heating **DVV-OPV3** homo-assemblies. Overall, the changes in conformation of individual OPV3 units, as well as in the stacking behavior, are already evident upon diluting with C10 but annealing allows access to other conformational states with different photophysical behavior.

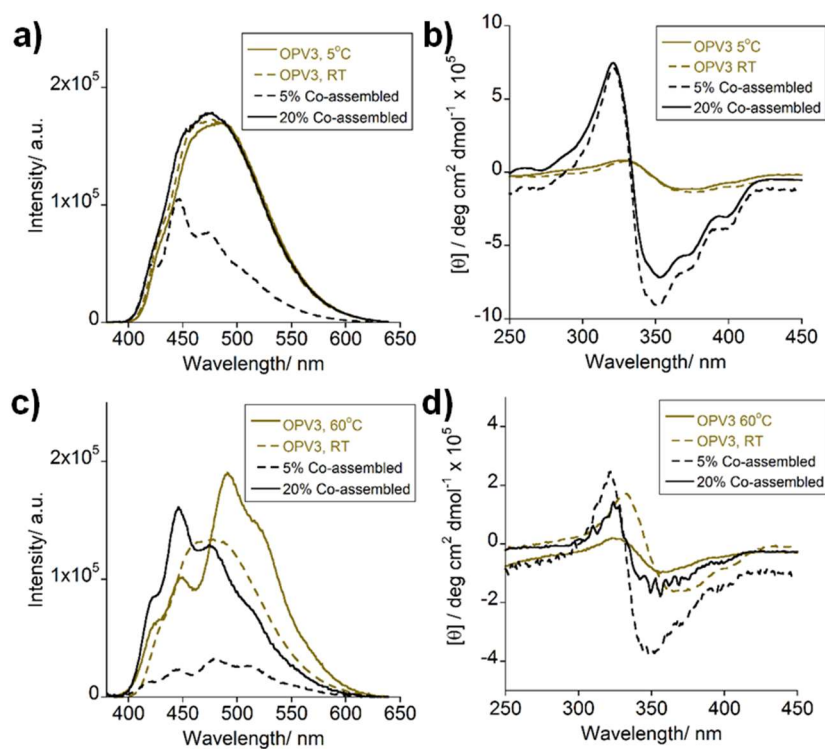


Figure 3.13. PL (a, c) and CD (b, d) spectra of acidic **DVV-OPV3** homo-assemblies and co-assemblies at 5 mol% and 20 mol% with **DVV-C10**; spectra taken at (a, b) 5 °C and (c, d) 60 °C in comparison to room temperature (RT); [C10] = 33 μ M, kept constant for all the co-assembly ratios; concentration of OPV3 in homo-assemblies was the same as the 20 mol% **DVV-OPV3** dilution, [OPV3] = 8 μ M.

Conclusions

This Chapter describes the systematic investigation of the effects of varying the local environment of peptide- π -peptide hybrid molecules on the overall photophysical properties of the assemblies with the aim of delineating the effects of self-assembly, the resultant close spatial packing of the π -electron units and electronic delocalization among these units on the photophysical properties of embedded individual π -electron units. This was achieved by co-assembling peptide- π -peptide molecules with peptides bearing an electronically inert decyl chain core (peptide-decyl-peptide) to introduce an electronically non-interacting hydrophobic environment in the peptide ensemble. Peptides containing π -electron units with double bond connectivities (OPV3) and single bond connectivities (OT4, OT4dM) between the aromatic units were used to investigate the non-resonant impacts of chromophore orientation on its photophysics. Two different peptide sequences were also investigated to study their impacts on coassembly of distinct peptides and the ensuing photophysical properties of the embedded π -electron unit. We found that the hydrophilic DDD tripeptide sequence has a tendency towards distributing peptides with unlike cores in the co-assembled nanostructure leading to isolation of π -electron units in the majority decyl chain local environment and allowing the observation of photophysical properties of individual π -electron units in peptide ensembles. In contrast, the relatively hydrophobic DVV peptide sequence promoted interactions within peptides with like cores leading to stacks enriched in π -electron units within the co-assembled nanostructures, not allowing for the individual π -electron unit photophysics to be observed. This was evident from the emission spectral profiles of the π -electron units at low molar ratios in the co-assembled nanostructures. Beyond the effects of the peptide sequence on the assembly behavior, it is

also important to consider the local field contributions from the peptide matrix that solvate the π -units.

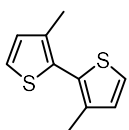
The variation in geometry of the π -electron unit also led to a differences in the observed photophysical properties of peptide ensembles with contributions from “resonant” and/or “non-resonant” effects. In the case of OPV3 chromophore unit, dilution with the peptide-decyl-peptide trimer led to a drastic change in the emission spectral profiles, with transition from a well-resolved emission profile of the pure peptide- π -peptide molecule to broad, featureless peaks observed at low molar ratios in co-assembled nanostructures resulting from isolation of the π -electron unit which ceases the electronic communication among adjacent π -electron units for the hydrophilic tripeptide DDD. In case of the hydrophobic DVV tripeptide sequence, a transition to well-resolved vibronic bands from the broad spectrum of the pure peptide- π -peptide molecule was observed, suggesting the coexistence of chromophore conformations that led to excitonic- and excimeric-like states. For the OT4/OT4dM systems, the C10 environment seemed to have less torsional impact than in the case of the OPV3 unit to deplanarize the quaterthiophene and has a higher impact on the lateral interactions between stacks (*i.e.*, creating a different solvation environment, varying solution viscosity, hydrophobicity, etc.).

From these results, it can be inferred that the peptide-decyl-peptide hybrid molecules promote a local environment that imposes spatial constraints on assembled π -electron units embedded in peptide- π -peptide molecules leading to conformational changes. By conducting temperature variation experiments on OPV3 systems, and thus varying the available thermal energy towards rotational freedom, it was confirmed that the initial kinetically-trapped states of peptide ensembles led to π -electron unit excited states that may

access different conformations if they are in spatially constrained environments with C10 peptides. Although these effects may be very specific to the design of a supramolecular synthon, this study contributes to a wider understanding of the coassembly process of self-assembling peptide-based systems containing two distinct interior units. Dispersing individual units or creating aggregated stacks of the π -electron units *via* coassembly in self-assembled systems can result in materials with multiple functions, however, the new local environment created during the mixing process and its effects on the overall function of the final material must be carefully considered when engineering functional materials for bioelectronics applications.

Experimental Details

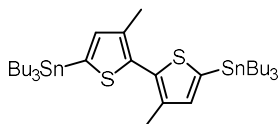
Peptide synthesis. All π -conjugated peptides were synthesized and purified according to our previous reports. Peptide segments were synthesized *via* standard solid phase peptide synthesis procedures and quaterthiophene was covalently attached to the peptides *via* Pd-catalyzed cross coupling between the resin bound peptides terminally *N*-acylated with a thienyl bromide and bis-stannylated bithiophene. The 1,4-distyrylbenzene was appended as the central peptide core *via* solid-phase amidation. Details can be found in the Appendix.



3,3'-dimethyl-2,2'-bithiophene.⁵⁴ 2-bromo-3-methyl thiophene (1.0 g, 5.7 mmol), 2-tributylstannyl-3-methylthiophene (2.2 g, 5.7 mmol) and tetrakis(triphenylphosphine)palladium (0.33 g, 0.28 mmol) were placed in a flame dried

100 mL Schlenk flask equipped with a magnetic stirrer. The flask was placed under vacuum for 15 min and then flushed with nitrogen gas. Freshly degassed, dry DMF (30 mL) was added *via* cannula and the reaction vessel was placed in a pre-heated oil bath at 80 °C. After 15 h, TLC (100% hexanes) indicated completion of reaction. The reaction mixture was cooled to room temperature and poured into 100 mL distilled water. The product was extracted into hexanes. The combined organic layer was dried using Na₂SO₄ and the solvent was removed *in vacuo* to obtain crude product which was purified using flash chromatography (100% hexanes) to obtain the product as a pale yellow oil (0.75 g, 3.9 mmol, 68% yield). The ¹H NMR was found to be in agreement with previous literature report.⁵⁴

(3,3'-dimethyl-[2,2'-bithiophene]-5,5'-diyl)bis(tributylstannane)⁵⁵ This product



was synthesized following a modification of the procedure reported previously in the literature. 3,3'-dimethyl-2,2'-bithiophene (0.6 g, 3.1 mmol) were placed in a flame dried 250 mL Schlenk flask equipped with a magnetic stirrer and the flask was placed under vacuum for 30 min. The flask was then back filled with nitrogen. Freshly distilled THF was degassed for 1 h and 70 mL were added to the flask *via* cannula. The solution was cooled to 0 °C and stirred for 30 min. To this solution, n-BuLi (2.48 M in hexanes, 2.7 mL, 6.8 mmol) was added drop-wise and the reaction was stirred at 0 °C for 1 h and then allowed to warm up to room temperature over 30 min. Tributyltin chloride (2.2 mL, 6.8 mmol) were added *via* syringe at room temperature. The reaction was continued for 3 h at room temperature after which it was quenched by addition of 10 mL water. The solvent was removed *in vacuo* and the crude product was dissolved in hexanes and washed thrice with 100 mL brine. The organic layer

was dried over Na₂SO₄ and the solvent was removed *in vacuo*. The crude product was filtered over neutral alumina using hexanes to obtain the pure product as a colorless oil (1.8 g, 75%). The ¹H NMR was found to be in agreement with literature.⁵⁵

DDD C10. Solid supported Wang-DDD-NH₂ (0.5 mmol) peptide was *N*-acylated using C10-diacid in 3 steps. First, 34.5 mg (0.15 mmol, 0.3 eq.) of C10-diacid was pre-activated with 156 mg (0.3 mmol, 0.6 eq.) of PyBOP in 20 mL of NMP. To this solution, 0.87 mL (5 mmol, 10 eq.) of DIPEA was added and the combined solution was poured into peptide chamber. The coupling was carried out at room temperature for 18 h with continuous gentle mixing. The peptide was then filtered and washed 2× with NMP. A second coupling was then carried out for 18 h using a mixture of 23 mg (0.1 mmol, 0.2 eq.) of C10-diacid pre-activated with 104 mg (0.2 mmol, 0.4 eq.) of PyBOP and 0.87 mL (5 mmol, 10 eq.) of DIPEA in 20 mL of NMP. After completion of coupling, the peptide was washed 2x with NMP. A blank coupling was then carried out using 156 mg (0.3 mmol, 0.6 eq.) of PyBOP and 0.87 mL (5 mmol, 10 eq.) of DIPEA in 20 mL of NMP for 1 h. The peptide was then filtered 3× with NMP, methanol and DCM. Following general cleavage and work-up, the peptide was obtained as a white powder (198 mg, 0.21 mmol). Following HPLC purification, the pure peptide was obtained in 9% yield (0.045 mmol, 0.041 g). MS (ESI) *m/z* 919.4 (M-H)⁻ (calc. 920.3), *m/z* 459.3 (M-2H)⁻² (calc. 459.2). ¹H NMR (400 MHz, D₂O) δ, ppm: 4.67-4.35 (m, 1H), 2.76-2.51 (m, 13H), 2.31 (m, 4H), 1.59 (m, 4H), 1.28 (s, 12H).

DDD OPV3. Solid supported Wang-DDD-NH₂ (0.5 mmol) peptide was *N*-acylated using OPV3-diacid in 3 steps. First, 56 mg (0.15 mmol, 0.3 eq.) of OPV3-diacid was pre-activated with 156 mg (0.3 mmol, 0.6 eq.) of PyBOP in 20 mL 2:1 v/v mixture of

NMP:DCM. To this solution, 0.87 mL (5 mmol, 10 eq.) of DIPEA was added and the combined solution was poured into peptide chamber. The coupling was carried out at room temperature for 18 h with continuous gentle mixing. The peptide was then filtered and washed 2× with NMP. A second coupling was then carried out for 18 h using a mixture of 37 mg (0.1 mmol, 0.2 eq.) of OPV3-diacid pre-activated with 104 mg (0.2 mmol, 0.4 eq.) of PyBOP and 0.87 mL (5 mmol, 10 eq.) of DIPEA in 20 mL 2:1 v/v mixture of NMP:DCM. After completion of coupling, the peptide was washed 2× with NMP. A blank coupling was then carried out using 156 mg (0.3 mmol, 0.6 eq.) of PyBOP and 0.87 mL (5 mmol, 10 eq.) of DIPEA in 20 mL 2:1 v/v mixture of NMP:DCM for 1 h. The peptide was then filtered 3× with NMP, methanol and DCM. Following general cleavage and work-up, the peptide was obtained as a yellow powder (103 mg, 0.097 mmol). Following HPLC purification, the pure peptide was obtained in 2% yield (0.008 mmol, 0.009 g). MS (ESI) m/z 1059.4 (M-H)⁻ (calc. 1059.3), m/z 529.3 (M-2H)⁻² (calc. 529.2). UV-Vis (H₂O) λ_{\max}/nm (log ϵ): 367 (4.17). QY (relative to quinine sulfate): 0.451. ¹H NMR (400 MHz, D₂O) δ , ppm: 7.85 (m, 4H, $J = 8.4$ Hz), 7.76 (m, 4H, $J = 8.4$ Hz), 7.72 (s, 4H), 7.41 (m, 4H, $J = 8.4$ Hz), 4.45 (m, 1H), 2.91 (m, 18H).

DDD OT4. Solid supported Wang-DDD-NH₂ (0.5 mmol) peptide was *N*-acylated with 2-bromo-5-thiophene carboxylic acid. The resin was subjected to the standard on-resin Stille coupling procedure using 5,5'-bis(tributylstannyl)-2,2'-bithiophene for 16 hours. Following general cleavage and work-up, the peptide was obtained as an orange powder (123 mg, 0.11 mmol). Following HPLC purification, the pure peptide was obtained in 3% yield (0.015 mmol, 0.017 g). MS (ESI) m/z 1107.2 (M-H)⁻ (calc. 1108.1), m/z 553.1 (M-

2H)⁻² (calc. 553.1). UV-Vis (H₂O) $\lambda_{\text{max}}/\text{nm}$ (log ϵ): 408 (4.28). ¹H NMR (400 MHz, D₂O) δ , ppm: 7.58 (m, 1H), 7.15 (m, 4H), 6.85 (m, 4H), 4.06 (m, 1H), 2.85 (m, 12H).

DDD OT4dM. Solid supported Wang-DDD-NH₂ (0.5 mmol) peptide was *N*-acylated with 2-bromo-5-thiophene carboxylic acid. The resin was subjected to the standard on-resin Stille coupling procedure using (3,3'-dimethyl-[2,2'-bithiophene]-5,5'-diyl)bis(tributylstannane) for 16 hours. Following general cleavage and work-up, the peptide was obtained as an orange powder (134 mg, 0.12 mmol). Following HPLC purification, the pure peptide was obtained in 4% yield (0.02 mmol, 0.023 g). MS (ESI) m/z 1135.2 (M-H)⁻ (calc. 1136.1), m/z 567.1 (M-2H)⁻² (calc. 567.1), m/z 377.9 (M-3H)⁻³ (calc. 377.7). UV-Vis (H₂O) $\lambda_{\text{max}}/\text{nm}$ (log ϵ): 376 (4.23). ¹H NMR (400 MHz, D₂O) δ , ppm: 8.44 (s, 1H), 7.67 (m, 2H), 7.34 (m, 2H), 7.28 (m, 2H), 4.39 (m, 1H), 2.59 (m, 18H), 2.22 (s, 6H).

DVV OPV3. 0.033 g (0.09 mmol) of OPV3-diacid and 0.094 g (0.18 mmol) of PyBOP was dissolved in 10 mL of 2:1 NMP:DCM solution, after which 0.52 mL of DIPEA was gradually added then mixed for 1 min. This solution was added to the solid-supported Wang-DVV-NH₂ (0.3 mmol) in a peptide chamber and mixed for 12 h. Resin was rinsed using the standard wash cycle. The resin was then subjected to a second round of coupling with 0.022 g (0.06 mmol) of OPV3-diacid and 0.062 g (0.12 mmol) of PyBOP dissolved in 10 mL of 2:1 NMP: DCM solution. The same amount of DIPEA as the first coupling was gradually added, then mixed for 1 min. This solution was added to the resin in a peptide chamber and mixed for 18 h. After rinsing the resin using the standard wash cycle, a final, blank coupling cycle was performed with only 0.094 g (0.18 mmol) of PyBOP and 0.52

mL of DIPEA in 10 mL of 2:1 NMP:DCM solution for 1 h. The resin was thoroughly washed again using the standard wash cycle. The general cleavage procedure was followed, only that the cleavage cocktail was diluted in a 1:1 ratio DCM and was mixed with the resin for 3 h. The peptide obtained was observed as a light yellow-green powder ($\lambda_{\max}=333$ nm, pH=8; 0.030 g, 20%). MS (ESI-) m/z 995.6 (M-H)⁻ (calc. 995.5), m/z 497.4 (M-2H)⁻² (calc. 497.2). ¹H NMR (400 MHz, D₂O) δ , ppm: 7.57 (d, 4H, $J=8.0$ Hz), 7.21-6.47 (m (b), 8H), 4.34-4.29 (m, 2H), 4.24 (d, 2H, $J=8.6$ Hz), 4.16 (d, 2H, $J=7.4$ Hz), 2.60-2.54 (m, 3H), 2.06-2.01 (m, 3H), 0.89-0.84 (m, 24H).

DVV OT4. Prepared according to literature procedure, *see Chapter 2*.

DVV OT4dM. Solid supported Wang-DVV-NH₂ (0.5 mmol) peptide was *N*-acylated with 2-bromo-5-thiophene carboxylic acid. The resin was subjected to the standard on-resin Stille coupling procedure using (3,3'-dimethyl-[2,2'-bithiophene]-5,5'-diyl)bis(tributylstannane) for 16 hours. Following general cleavage and work-up, the peptide was obtained as a yellow powder (218 mg, 0.20 mmol). Following HPLC purification, the pure peptide was obtained in 4% yield (0.01 mmol, 0.011 g). MS (ESI) m/z 1071.5 (M-H)⁻ (calc. 1071.3), m/z 535.6 (M-2H)⁻² (calc. 535.2). ¹H NMR (400 MHz, D₂O) δ , ppm: 8.37 (s, 2H), 7.40 (d, 2H, $J=3.3$ Hz), 6.64 (s, 2H), 4.30 (dd, 2H, $J=7.6$ Hz, 5.3 Hz), 4.20 (d, 2H, $J=8.9$ Hz), 4.15 (d, 2H, $J=7.2$ Hz), 2.58-2.44 (m, 4H), 2.05-1.95 (m, 2H), 1.73 (s, 6H), 0.86-0.84 (m, 12H), 0.78-0.74 (m, 12H).

UV-Vis absorption and photoluminescence spectroscopy. All samples for absorption and emission scans were prepared by dissolving lyophilized peptides in degassed Milli-Q water. The pH of the samples was adjusted accordingly (*ca.* pH 1 for

acidic samples and *ca.* pH 10 for basic samples) using 1 M HCl or 1 M KOH. Acidic and basic samples were separately prepared from a peptide stock solution (*ca.* pH 8; 100 μ M), keeping the final concentration for both samples the same (33 μ M). Temperature variation studies were done with a Peltier accessory (SPV-1X0). For each spectrum recorded at a specific temperature, a fresh sample is aliquoted from the stock solution at room temperature. Upon reaching the desired temperature, the equilibration time is 2 minutes before starting to record the spectrum. The absorption spectra in the UV-Vis region were obtained using a Varian Cary 50 Bio UV-Vis spectrophotometer. The photoluminescence spectra were obtained using a PTi Photon Technology International Fluorometer (QuantaMaster 40) with a 75-W Ushio Xenon short arc lamp and operated with Felix32 Version 1.2 software. All UV-Vis and PL spectra reported were recorded within an hour of sample preparation, unless otherwise stated. The excitation wavelengths used correspond to the λ_{max} observed in the absorption spectra of the peptides. The radiative lifetime (τ_R) and non-radiative (τ_{NR}) lifetime values were calculated using the equations shown below, as reported in the literature.²

$$\tau_R = \frac{\tau_{FL}}{QY} \dots \text{(Equation 3.1)}$$

$$\frac{1}{\tau_{NR}} = \frac{1}{\tau_{FL}} - \frac{1}{\tau_R} \dots \text{(Equation 3.2)}$$

For fluorescence lifetime measurements, a 375 nm LED lamp was used as an excitation source for peptide samples, and the total peptide concentration of the OT4 and OT4dM samples were doubled than that used for steady-state measurements.

Circular dichroism (CD). CD spectra were obtained using an AVIV Circular Dichroism Spectrometer Model 420. Spectroscopic samples were prepared by diluting the

peptide solution to the appropriate concentration in Millipore water. The pH was then adjusted by adding 10 μL of 1 M KOH (basic, pH 10) followed by 20 μL of 1 M HCl (acidic, pH 1).

Portions of this chapter were adapted in part from:

- Ardoña, H.A.M.;* Kale, T. S.;;* Ertel, A. and Tovar, J. D. (*equal contribution), “Non-resonant and local field effects on the photophysics of oligo(p-phenylenevinylene) segments within peptidic nanostructures,” *Langmuir* 2017, *in press*.
- Kale, T. S.;;* Ardoña, H.A.M.;* Ertel, A. and Tovar, J. D. (*equal contribution), “Torsional demands of quaterthiophene segments imposed within peptidic nanostructures,” *in preparation*.

Acknowledgements

Dr. Tejaswini Kale in the group of Professor John D. Tovar synthesized the (3,3'-dimethyl-[2,2'-bithiophene]-5,5'-diyl)bis(tributylstannane) as well as the DDD peptides. She also did the characterization experiments for the DDD peptides. Alyssa Ertel (Institute for NanoBioTechnology REU, 2015) assisted in the peptide synthesis and characterization.

References

- (1) Clark, J., Silva, C., Friend, R. H., and Spano, F. C. (2007) Role of intermolecular coupling in the photophysics of disordered organic semiconductors: aggregate emission in regioregular polythiophene. *Phys. Rev. Lett.* 98, 206406.
- (2) Hong, J.-H., Atta, A. K., Jung, K.-B., Kim, S.-B., Heo, J., and Cho, D.-G. (2015) Conformationally locked tolans, β -sheet structures, and photophysical properties. *Org. Lett.* 17, 6222-6225.
- (3) Siddiqui, S., and Spano, F. C. (1999) H- and J-aggregates of conjugated polymers and oligomers. *Chem. Phys. Lett.* 308, 99-105.

- (4) Noriega, R., Rivnay, J., Vandewal, K., Koch, F. P. V., Stingelin, N., Smith, P., Toney, M. F., and Salleo, A. (2013) A general relationship between disorder, aggregation and charge transport in conjugated polymers. *Nat. Mater.* *12*, 1038-1044.
- (5) Fichou, D. (2000) Structural order in conjugated oligothiophenes and its implications on opto-electronic devices. *J. Mater. Chem.* *10*, 571-588.
- (6) Coropceanu, V., da Silva Filho, D. A., Olivier, Y., and Silbey, R. (2007) Charge transport in organic semiconductors. *Chem. Rev.* *107*, 926-952.
- (7) Lin, Y., Li, Y., and Zhan, X. (2012) Small molecule semiconductors for high-efficiency organic photovoltaics. *Chem. Soc. Rev.* *41*, 4245-4272.
- (8) Kim, Y., Cook, S., Tuladhar, S. M., Choulis, S. A., Nelson, J., Durrant, J. R., Bradley, D. D. C., Giles, M., McCulloch, I., Ha, C.-S., and Ree, M. (2006) A strong regioregularity effect in self-organizing conjugated polymer films and high-efficiency polythiophene:fullerene solar cells. *Nat. Mater.* *5*, 197-203.
- (9) Yu, G., Gao, J., Hummelen, J. C., Wudl, F., and Heeger, A. J. (1995) Polymer photovoltaic cells: enhanced efficiencies via a network of internal donor-acceptor heterojunctions. *Science* *270*, 1789-1791.
- (10) Nijegorodov, N. I., and Downey, W. S. (1994) The influence of planarity and rigidity on the absorption and fluorescence parameters and intersystem crossing rate constant in aromatic molecules. *J. Phys. Chem.* *98*, 5639-5643.
- (11) Yang, Y., Su, X., Carroll, C. N., and Aprahamian, I. (2012) Aggregation-induced emission in BF₂-hydrazone (BODIHY) complexes. *Chem. Sci.* *3*, 610-613.
- (12) Berlman, I. B. (1970) Empirical correlation between nuclear conformation and certain fluorescence and absorption characteristics of aromatic compounds. *J. Phys. Chem.* *74*, 3085-3093.
- (13) Nandi, N., Basak, S., Kirkham, S., Hamley, I. W., and Banerjee, A. (2016) Two-component fluorescent semiconducting hydrogel from NDI-appended peptide with long chain amines: variation of thermal and mechanical strength of gels. *Langmuir*, *32*, 13226-13322.
- (14) Ortony, J. H., Newcomb, C. J., Matson, J. B., Palmer, L. C., Doan, P. E., Hoffman, B. M., and Stupp, S. I. (2014) Internal dynamics of a supramolecular nanofibre. *Nat. Mater.* *13*, 812-816.
- (15) Tovar, J. D., Claussen, R. C., and Stupp, S. I. (2005) Probing the interior of peptide amphiphile supramolecular aggregates. *J. Am. Chem. Soc.* *127*, 7337-7345.

- (16) Lewis, F. D., Yang, J.-S., and Stern, C. L. (1996) Ground and excited state aromatic–aromatic interactions with distance control by hydrogen bonding. *J. Am. Chem. Soc.* *118*, 2772-2773.
- (17) Verolet, Q., Soleimanpour, S., Fujisawa, K., Molin, M. D., Sakai, N., and Matile, S. (2015) Design and synthesis of mixed oligomers with thiophenes, dithienothiophene S, S-dioxides, thieno[3,4]pyrazines and 2,1,3-benzothiadiazoles: flipper screening for mechanosensitive systems. *ChemistryOpen* *4*, 264-267.
- (18) Chen, F., Zhang, J., and Wan, X. (2012) Design and synthesis of piezochromic materials based on push-pull chromophores: a mechanistic perspective. *Chem. Eur. J.* *18*, 4558-4567.
- (19) Chi, Z., Zhang, X., Xu, B., Zhou, X., Ma, C., Zhang, Y., Liu, S., and Xu, J. (2012) Recent advances in organic mechanofluorochromic materials. *Chem. Soc. Rev.* *41*, 3878-3896.
- (20) Mishra, A., Ma, C.-Q., and Bäuerle, P. (2009) Functional oligothiophenes: molecular design for multidimensional nanoarchitectures and their applications. *Chem. Rev.* *109*, 1141-1276.
- (21) Osaka, I., and McCullough, R. D. (2008) Advances in molecular design and synthesis of regioregular polythiophenes. *Acc. Chem. Res.* *41*, 1202-1214.
- (22) Doval, D. A., Molin, M. D., Ward, S., Fin, A., Sakai, N., and Matile, S. (2014) Planarizable push–pull oligothiophenes: in search of the perfect twist. *Chem. Sci.* *5*, 2819-2825.
- (23) Macchi, G., Medina, B. M., Zambianchi, M., Tubino, R., Barbarella, G., Gierschner, J., and Meinardi, F. (2009) Spectroscopic signatures for planar equilibrium geometries in methyl-substituted oligothiophenes. *Phys. Chem. Chem. Phys.* *11*, 984-990.
- (24) Kislitsyn, D. A., Taber, B. N., Gervasi, C. F., Zhang, L., Mannsfeld, S. C. B., Prell, J. S., Briseno, A. L., and Nazin, G. V. (2016) Oligothiophene wires: impact of torsional conformation on the electronic structure. *Phys. Chem. Chem. Phys.* *18*, 4842-4849.
- (25) Darling, S. B., and Sternberg, M. (2009) Importance of side chains and backbone length in defect modeling of poly (3-alkylthiophenes). *J. Phys. Chem. B*, *113*, 6215-6218.
- (26) Darling, S. B. (2008) Isolating the effect of torsional defects on mobility and band gap in conjugated polymers. *J. Phys. Chem. B*, *112*, 8891-8895.
- (27) Vujanovich, E. C., and Bloom, J. (2012) Impact of neighboring chains on torsional defects in oligothiophenes. *J. Phys. Chem. A* *116*, 2997-3003.
- (28) Aida, T., Meijer, E. W., and Stupp, S. I. (2012) Functional supramolecular polymers. *Science* *335*, 813–817.

- (29) Kim, S. H., and Parquette, J. R. (2012) A model for the controlled assembly of semiconductor peptides. *Nanoscale* 4, 6940–6947.
- (30) Tovar, J. D. (2013) Supramolecular construction of optoelectronic biomaterials. *Acc. Chem. Res.* 46, 1527-1537.
- (31) Jatsch, A., Schillinger, E. K., Schmid, S., and Bäuerle, P. (2010) Biomolecule assisted self-assembly of pi-conjugated oligomers. *J. Mater. Chem.* 20, 3563-3578.
- (32) Hoeben, F. J. M., Herz, L. M., Daniel, C., Jonkheijm, P., Silva, C., Meskers, S. C. J., Beljonne, D., Phillips, R. T., Friend, R. H., and Meijer, E. W. (2004) Efficient energy transfer in mixed columnar stacks of hydrogen-bonded oligo(*p*-phenylene vinylene)s in solution. *Angew. Chem. Int. Ed.* 116, 2010–2013.
- (33) Wall, B. D., Zacca, A. E., Sanders, A. M., Wilson, W. L., Ferguson, A. L., and Tovar, J. D. (2014) Supramolecular polymorphism: tunable electronic interactions within π -conjugated peptide nanostructures dictated by primary amino acid sequence. *Langmuir* 30, 5946–5956.
- (34) Sanders, A. M., Dawidczyk, T. J., Katz, H. E., and Tovar, J. D. (2012) Peptide-Based Supramolecular semiconductor nanomaterials via Pd- Catalyzed Solid-Phase “Dimerizations.” *ACS Macro Lett.* 1, 1326–1329.
- (35) Besar, K., Ardoña, H. A. M., Tovar, J. D., and Katz, H. E. (2015) Demonstration of hole transport and voltage equilibration in self-assembled π -conjugated peptide nanostructures using field-effect transistor architectures. *ACS Nano* 9, 12401-12409.
- (36) Wall, B. D., Diegelmann, S. R., Zhang, S., Dawidczyk, T. J., Wilson, W. L., Katz, H. E., Mao, H.-Q., and Tovar, J. D. (2011) Aligned macroscopic domains of optoelectronic nanostructures prepared via shear-flow assembly of peptide hydrogels. *Adv. Mater.* 23, 5009–5014.
- (37) Gwozdzińska, P., Pawłowska, R., Milczarek, J., Garner, L. E., Thomas, A. W., Bazan, G. C., and Chworos, A. (2014) Phenylenevinylene conjugated oligoelectrolytes as fluorescent dyes for mammalian cell imaging. *Chem. Commun.* 50, 14859-14861.
- (38) Garner, L. E., Park, J., Dyar, S. M., Chworos, A., Sumner, J. J., and Bazan, G. C. (2010) Modification of the optoelectronic properties of membranes via insertion of amphiphilic phenylenevinylene oligoelectrolytes. *J. Am. Chem. Soc.* 132, 10042-10052.
- (39) Hinks, J., Poh, W. H., Chu, J. J. H., Loo, J. S. C., Bazan, G. C., Hancock, L. E., and Wuertz, S. (2015) Oligo-polyphenylenevinylene-conjugated oligoelectrolyte membrane insertion molecules selectively disrupt cell envelopes of gram-positive bacteria. *Appl. Environ. Microbiol.* 81, 1949-1951.

- (40) Kim, C. A., and Berg, J. M. (1993) Thermodynamic beta-sheet propensities measured using a zinc-finger host peptide. *Nature* 362, 267-270.
- (41) Toptygin, D., Woolf, T. B., and Brand, L. (2010) Picosecond protein dynamics: The origin of the time-dependent spectral shift in the fluorescence of the single Trp in the protein GB1. *J. Phys. Chem. B* 114, 11323-11337.
- (42) Toptygin, D., Savtchenko, R. S., Meadow, N. D., and Brand, L. (2001) Homogeneous spectrally- and time-resolved fluorescence emission from single-tryptophan mutants of IIA Glc protein. *J. Phys. Chem. B* 105, 2043-2055.
- (43) Safont-Sempere, M. M., Fernández, G., and Würthner, F. (2011) Self-sorting phenomena in complex supramolecular systems. *Chem. Rev.* 111, 5784-5814.
- (44) Krieg, E., Bastings, M. M. C., Besenius, P., and Rybtchinski, B. (2016) Supramolecular polymers in aqueous media. *Chem. Rev.* 116, 2414-2477.
- (45) Zhu, X., Tsuji, H., Navarrete, J. T. L., Casado, J., and Nakamura, E. (2012) Carbon-bridged oligo(phenylenevinylene)s: stable π -systems with high responsiveness to doping and excitation. *J. Am. Chem. Soc.* 134, 19254-19259.
- (46) Morales-Vidal, M., Boj, P. G., Villalvilla, J. M., Quintana, J. A., Yan, Q., Lin, N.-T., Zhu, X., Ruangsupapichat, N., Casado, J., Tsuji, H., Nakamura, E., and Díaz-García, M. A. (2015) Carbon-bridged oligo(*p*-phenylenevinylene)s for photostable and broadly tunable, solution-processable thin film organic lasers. *Nat. Commun.* 6, 8458.
- (47) Yamaguchi, S., Xu, C., and Tamao, K. (2003) Bis-silicon-bridged stilbene homologues synthesized by new intramolecular reductive double cyclization. *J. Am. Chem. Soc.* 125, 13662-13663.
- (48) Lehrman, J. A., Cui, H., Tsai, W.-W., Moyer, T. J., and Stupp, S. I. (2012) Supramolecular control of self-assembling terthiophene-peptide conjugates through the amino acid side chain. *Chem. Commun.* 48, 9711-9713.
- (49) DiCésare, N., Belletête, M., Garcia, E. R., Leclerc, M., and Durocher, G. (1999) Intermolecular interactions in conjugated oligothiophenes. 3. optical and photophysical properties of quaterthiophene and substituted quaterthiophenes in various environments. *J. Phys. Chem. A* 103, 3864-3875.
- (50) Wall, B. D., Zhou, Y., Mei, S., Ardoña, H. A. M., Ferguson, A. L., and Tovar, J. D. (2014) Variation of formal hydrogen-bonding networks within electronically delocalized π -conjugated oligopeptide nanostructures. *Langmuir* 30, 11375-11385.
- (51) Dzwolak, W., Lokszejn, A., Galinska-Rakoczy, A., Adachi, R., Goto, Y., and Rupnicki, L. (2007) Conformational Indeterminism in Protein Misfolding: Chiral Amplification on Amyloidogenic Pathway of Insulin. *J. Am. Chem. Soc.* 129, 7517-7522.

- (52) Castelletto, V., Cheng, G., Greenland, B. W., Hamley, I. W., and Harris, P. J. F. (2011) Tuning the Self-Assembly of the Bioactive Dipeptide L-Carnosine by Incorporation of a Bulky Aromatic Substituent. *Langmuir* 27, 2980-2988.
- (53) Omogo, B., Aldana, J. F., and Heyes, C. D. (2013) Radiative and Nonradiative Lifetime Engineering of Quantum Dots in Multiple Solvents by Surface Atom Stoichiometry and Ligands. *J. Phys. Chem. C* 117, 2317-2327.
- (54) Maior, R. M. S., Hinkelmann, K., Eckert, H., and Wudl, F. (1990) Synthesis and characterization of two regiochemically defined poly(dialkylbithiophenes): a comparative study. *Macromolecules* 23, 1268-1279.
- (55) Sotgiu, G., Zambianchi, M., Barbarella, G., and Botta, C. (2002) Synthesis and optical properties of soluble sexithiophenes with one central head-to-head junction. *Tetrahedron* 58, 2245-2251.

CHAPTER FOUR:

Establishing Energy Gradients within Multicomponent
Assemblies of Optoelectronic Peptides

Introduction

Supramolecular assembly is a recurring theme in Nature that plays a significant role in the function of biological assemblies and is a widely used strategy to organize molecular components in organic electronic devices.¹⁻³ In both photosynthetic complexes and in most optoelectronic devices, the process of excitation energy transfer plays a central role.⁴⁻⁷ This generally occurs *via* diffusion of excitons, which are electronically excited states of molecules that are created by light absorption or other electron transfer processes. These transport processes are highly dependent on ordering effects at different scales,² whereby the direction and degree of intermolecular organization of π -conjugated assemblies are key factors that determine the efficiency of energy transport.⁸⁻¹⁰ The peptide-driven mesoscale organization of the chromophores in the photosynthetic membrane allows fast directional migration of excitation energy within the chromophore assemblies before being transferred to the reaction center (the final destination of the collected energy), which is crucial to the biological light-harvesting process.¹¹⁻¹⁴ In order to maximize the harvesting capacity of pigments, an exciton funneling system is involved in the overall photosynthetic process, wherein different antenna complexes with distinctive transition energies are used to expand the spectral light absorption.¹⁵

Multicomponent synthetic materials exhibiting supramolecular ordering and/or exciton migration have received considerable attention towards making good candidates for light-harvesting antenna mimics.¹⁶⁻¹⁸ There are several examples of multichromophoric assemblies aimed towards applications not only for photosynthetic mimicry, but also for excitonic solar cells,¹⁸ light-emitting assemblies,¹⁹⁻²² and as biophysical molecular rulers.²³ The synthetic details and characterization of energy transfer events are both equally

important for the development of multichromophoric arrays in such applications. For example, Friend, Rowan, Nolte and co-workers have developed Pt-porphyrin and perylene-bis(dicarboximide) units in polyisocyanopeptides (Figure 4.1a) and investigated the sequential energy and electron transfer between the donor and acceptor units.²⁴ Hodgkiss, Thordarson and co-workers reported a highly efficient multichromophore array based on perylene systems (Figure 4.1b), whereby efficient incoherent energy transfer was reported.²⁵ Basché, Müllen and co-workers reported terrylene and perylene diimide dyad systems (Figure 4.1c) and quantified singlet-singlet annihilation.^{26,27} Ajayaghosh and coworkers extensively investigated a library of oligo(*p*-phenylenevinylene) organogelators that are capable of excitation energy transfer between specific donor-acceptor systems.^{4,5,13,28-30} A system reported on C₃-symmetric self-sorted units of oligo(*p*-phenylenevinylene) and perylene bisimide was even utilized as a sensing platform for volatile aromatic compounds.³¹

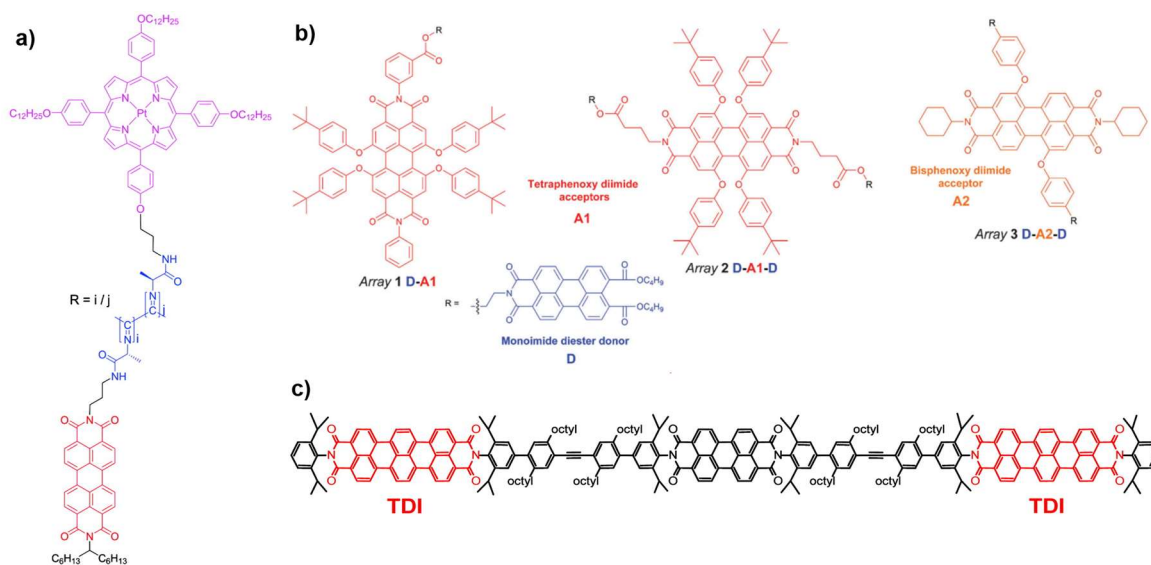


Figure 4.1. Molecular structures of some multichromophoric systems reported in the literature. Adapted from Ref. 24, 25, 26.

Moreover, multichromophoric dendrimers³² and ring-like harvesting units³³ are two of many molecular and other supramolecular forms that have been comprehensively studied in solution or in solid state (as hydrogels or organogels)¹¹ demonstrating the prospects for directional and near quantitative energy transfer in synthetic systems. Over the past decade, Meijer and co-workers reported exciton migration leading to energy transfer within supramolecular columnar stacks of oligo(*p*-phenylenevinylene) (OPV) in dodecane⁷ and hydrogen-bonded dimers between OPV-perylene bisimide in toluene.³⁴ Functionalized OPVs that act as hydrogelators were also extensively studied for exciton funneling by Ajayaghosh and co-workers, showing that confining the acceptor units within an organogel made of molecular wires results in a more efficient energy transfer.⁵ Currently, studies involving molecular wires composed of π -stacked monomers or supramolecular nanostructured assemblies are of particular interest due to their generally superior carrier transport along the stacking axis, which is beneficial for nanoscale optoelectronic devices.³⁵ Most studies of electronically responsive supramolecular analogs of biological structures are conducted in organic media; therefore, it is of great significance to explore aqueous supramolecular systems that could more efficiently mimic important bioenergetic processes under native conditions.³⁶⁻³⁸

Due to the intrinsic ability of peptides to self-assemble, several types of conjugated π -systems have been functionalized with peptides to further control specific intermolecular interactions that give rise to distinct assembly architectures and electronic delocalization.³⁹⁻⁴⁶ Previous studies on self-assembling peptides exhibiting energy transfer involve fluorescent dyes conjugated to peptide ends, showing efficient energy transfer in organic media or within hydrogels once a suitable acceptor dye has intercalated within the assembly

network.⁴⁷⁻⁵⁰ Furthermore, the dyes often used in contemporary studies are chosen for their molecular photophysical properties rather than for their abilities to promote semiconductive electronic behavior. Adams and co-workers reported self-sorted perylene bisimide and stilbene gelators, creating heterojunction arrays with self-sorted fiber networks that led to a photoconductive material.⁵¹ Side-chain functionalization of lysine units with tetraphenylporphyrin and naphthalene diimide and was shown to demonstrate a switch between H- or J-type of aggregation depending on the protonation state of the porphyrin.⁵² The formation of p-n heterojunction amongst self-sorted quaterthiophene- and perylene diimide organogelators with chiral cholesterol moieties was achieved *via* a heat-cool method, whereby the sequential dissociation and re-assembly was governed by the different dissociation constants of each component.⁵³

In Chapters 2 and 3, the implications of monomer structure to the material properties from molecular to macroscale were discussed, as well as the aggregation effects to the conformation of the π -units—both of which are efforts that help tune and understand the properties of this peptidic material in a rational way. This Chapter presents a strategy to engineer the energy transporting capabilities of these peptidic nanomaterials by creating coassembled structures of different peptide- π monomers bearing π -electron systems of varied intrinsic energy that demonstrates energy transfer within the nanostructures. The first part of this Chapter will discuss a two-component nanostructure composed of π -conjugated peptides containing donor and acceptor semiconducting π -units is presented, which exhibits energy transport in completely aqueous media when self-assembled. This pH-responsive self-assembling peptide system also exhibits temperature-dependent aggregation behavior. This nanomaterial design affords the inclusion of two

semiconducting units embedded within peptidic nanostructures and undergoes energy transport upon mixing and self-assembly under completely aqueous conditions, thereby providing a synthetic platform for energy harvesting and transporting aqueous nanomaterials. In the second part of this Chapter, this two-component coassembly strategy is further extended to create a spatiotemporally-controlled multichromophoric array of a self-assembling peptide system with a combination of energy donor-acceptor pairs and electron donor-acceptor pairs within one nanostructure. This potentially enables simultaneous and/or sequential energy- and electron-transfer events and allows for the creation of localized electric fields between the donor and acceptor units resulting from charge separation. The utility of different acidification triggers to control the kinetics of self-assembly will be presented, specifically the methods to control the spatial ordering of the chromophores within the peptidic nanostructure and systematically impact the unique energy transport processes fostered within these nanostructures.

Results and Discussion

I. *Oligo(p-phenylenevinylene)-Quaterthiophene Peptide System*

Similar to the peptidic nanomaterials described in the previous Chapters, the system herein involves two peptide- π -peptide triblock systems that have pH-dependent assembly, generally resulting in essentially dissolved structures under basic conditions (*ca.* pH 10) and 1D-nanostructures under acidic (*ca.* pH 2) conditions. Two π -conjugated molecules with known semiconducting properties were used as π -electron cores within the triblock system (Figure 4.2): 1,4-distyrylbenzene (OPV3) as the donor unit, an oligo(*p*-phenylenevinylene) which is known to facilitate efficient exciton migration and has well-

studied spectroscopic behavior, and quaterthiophene (OT4) as the acceptor unit, which is a known hole-transporting organic semiconductor and low-energy dye. OPV-based assemblies are discussed in this Chapter, which are well-established to have fast exciton diffusion processes and energy transfer processes possible within these types of ordered organic-based nanomaterials.^{14,54-56}

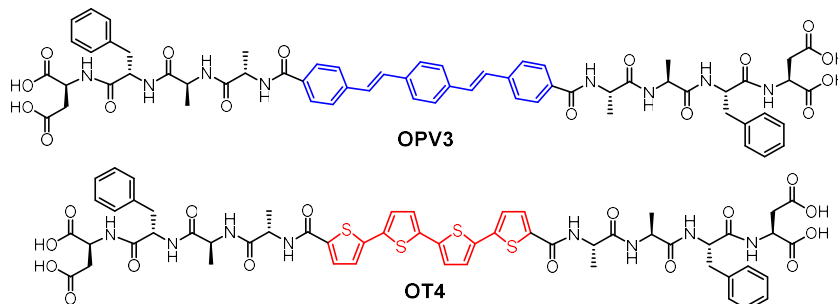


Figure 4.2. Molecular structures the **DFAA-OPV3** and **-OT4** peptides.

For OPV3 and OT4, both of these chromophores have separately been incorporated into peptide- π -peptide molecules that undergo self-assembly to form nanofibrillar structures with high aspect ratios in aqueous environments. The particular OPV3 and OT4 π -conjugated units were chosen because they have comparable molecular lengths and thus can be reasonably expected to encourage intermolecular hydrogen-bonding interactions within a coassembled nanostructure. The aspartic acid-phenylalanine-alanine-alanine (DFAA) tetrapeptide sequence was chosen because the OPV3-assemblies derived from the DFAA peptide sequence were shown previously to generate high-aspect ratio nanostructures with vibronic photoluminescence features associated with high-energy exciton-like emission, making it easier to differentiate the emission of the **DFAA-OPV3** donor from the **DFAA-OT4** acceptor peptide

Figure 4.3a shows an energy-minimized model generated from low-level equilibrium geometry calculations of a portion of 1D-assembly structure whereby the internal hydrogen-bonding networks deviate from ideal β -sheet architectures yet still allow for enthalpic stabilization. Our past molecular dynamics simulations on OPV3-embedded peptides found that the deviations of these assemblies from ideal β -sheet conformations can be attributed to the entropic mixing within the stacks and internal deformations that are brought by a combination of various stabilizing hydrogen-bonding interactions that do not solely rely on strict interpretations β -sheet interactions. As discussed in the previous Chapters, the quadrupole associated with the central π -conjugated structure presents a distinctly non-natural intermolecular interaction that further skews these oligopeptide assemblies from ideal protein secondary structures. This deviation is observed even in pure **DFAA-OPV3** or **DFAA-OT4** assemblies, but is more pronounced in the coassemblies.

Nevertheless, the generated structural models support the formation of 1D-stacks stabilized by intermolecular hydrogen-bonding interactions that place the donor and acceptor units into intimate intermolecular electronic contact. The IR spectra of assembled **DFAA-OPV3**, **DFAA-OT4** and mixtures (Figure A4.7 and A4.8), on the other hand, show the preference for β -sheet-like formation as supported by the presence of Amide I (~ 1630 cm^{-1}) and Amide II (~ 1530 cm^{-1}) bands in assembled **DFAA-OPV3** and even in the coassemblies (maintained up to 50 mol% **DFAA-OT4**). Transmission electron microscopy (TEM) was used to image the morphologies of the nanostructures formed in acidic **DFAA-OPV3/-OT4** mixtures. Unlike the previously reported high-aspect ratio morphology of **DFAA-OPV3**, the TEM images of pure **DFAA-OT4** show irregularly-shaped nanostructures under acidic conditions (Figure A4.9). However, TEM indicates that the

addition of acceptor **DFAA-OT4** did not significantly perturb the self-assembling ability of the donor **DFAA-OPV3** as shown by the 1D-nanostructure formation observed at different coassembly ratios up to 50 mol% OT4, which corroborates with the IR spectra. The only obvious difference was the change in the widths of each nanostructure as the **DFAA-OT4** component was increased, suggesting a change in the bundling behavior within each nanostructure upon coassembly (Figure 4.3b-c and Figure A4.10).

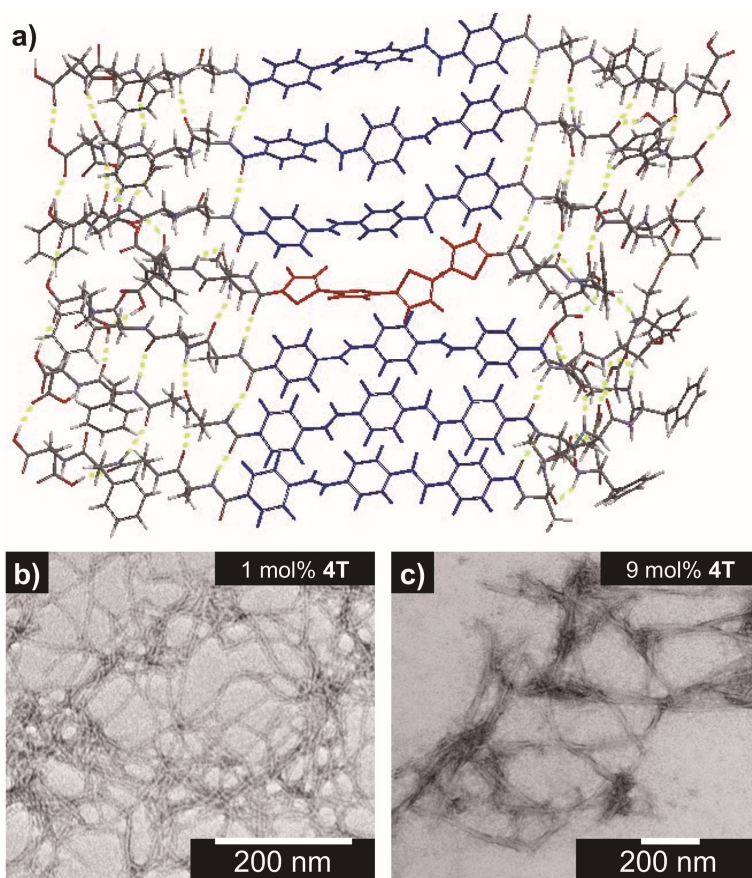


Figure 4.3. (a) Energy-minimized assembly model for a hypothetical portion of an **DFAA-OPV3/OT4** heterostructure with a single isolated **DFAA-OT4** unit within the **DFAA-OPV3** majority aggregate. TEM images (stained with 2% uranyl acetate) along with the observed widths of nanostructures formed from 0.1 wt% acidic, coassembled **DFAA-OPV3/OT4** solutions: (b) 1 mol% (5.6 ± 0.64 nm) and (c) 9 mol% **DFAA-OT4** (13.6 ± 2.3 nm).

The steady-state absorption and photoluminescence (PL) spectra of the donor and acceptor solutions (both dissolved and assembled) were recorded as baseline points (Figure 4.4a-c). Under basic (dissolved) conditions, **DFAA-OPV3** has an absorption λ_{max} at 367 nm and emission λ_{max} at 448 nm while **DFAA-OT4** absorbs at 416 nm and emits at 510 nm. Upon initiating assembly under acidic conditions, both **DFAA-OPV3** and **-OT4** show a blue-shift in absorbance with respect to their basic counterparts, having λ_{max} at 339 and 400 nm, respectively. A broad, featureless emission peak with a λ_{max} at 561 nm was observed for the assembled **DFAA-OT4** solution upon direct excitation at 450 nm. For the assembled **DFAA-OPV3** solution, vibronic features suggesting an excitonic emission were observed, with distinct peaks appearing at 431, 460 and 490 nm. These steady-state spectral properties are consistent with those found previously for **DFAA-OPV3**⁵⁷ and for a peptide sequence variant of **DFAA-OT4**,^{58,59} with the blue-shift in absorption and PL quenching and red-shift observed in acidic samples indicating the formation of “H-like” aggregates. The differences in PL inherent to these two chromophores allow us to distinguish spectral signatures originating from the **DFAA-OPV3** donor and the **DFAA-OT4** acceptor peptide.

As for the coassembled heterostructures, UV-vis absorption and PL spectra of the **DFAA-OPV3/-OT4** mixtures were recorded during titration experiments where **DFAA-OPV3** concentration was held constant ([OPV3]= 3.2 μM) in order to monitor the photophysical events during the coassembly process. The emission spectra of the mixtures shown in Figure 4.4c correspond to solutions that were excited at 320 nm (basic) and 330 nm (acidic), the wavelengths at which **DFAA-OPV3** has reasonable absorption but **DFAA-OT4** has minimum absorption. The absorption profile consistently shows a blue-shifted absorption of acidic against the basic solutions in all mol% **DFAA-OT4**, indicating the

fidelity of the “H-like” aggregation (Figure 4.4b). In the dissolved state (*ca.* pH 10), discrete spectral peaks for **DFAA-OPV3** and **DFAA-OT4** in the absorption spectra (Figure 4.4a) and peaks characteristic of dissolved **DFAA-OPV3** in the emission spectra were observed for mixtures of **DFAA-OPV3** and **-OT4** wherein [**DFAA-OPV3**] was kept constant.

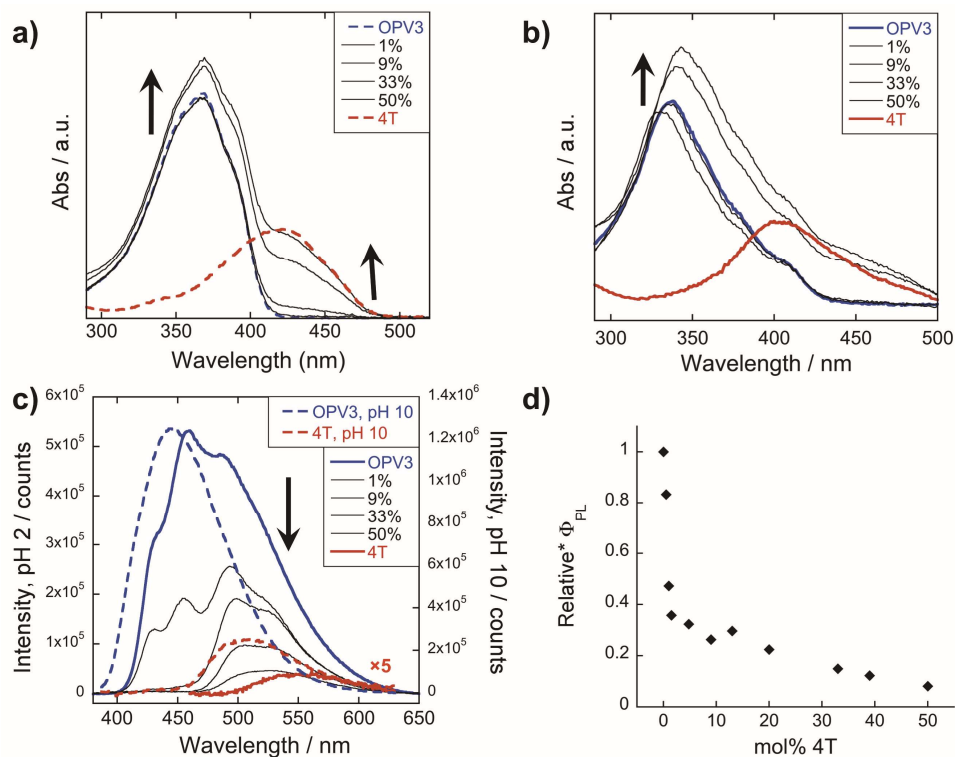


Figure 4.4. Absorption spectra of **DFAA-OPV3**, **DFAA-OT4**, and their co-mixtures under basic (a) and acidic (b) conditions. Emission spectra (c) recorded at pH=10 (---, λ_{exc} = 320 nm) and pH=2 (—, λ_{exc} = 330 nm). For comparison, a direct excitation of **OT4** molecules and assemblies at 450 nm is shown in (c). [**DFAA-OPV3**]= 3.2 μ M, [**DFAA-OT4**]= 0.03-3.2 μ M; arrows show trends as mol% **DFAA-OT4** is increased. Relative* quantum yields (d) of the **DFAA-OPV3**/**-OT4** mixtures at pH=2 (λ_{exc} = 330 nm), reported as the ratio of sample absorption \times PL peak area of **DFAA-OPV3**/**-OT4** mixtures with respect to **DFAA-OPV3**.

When the overall chromophore concentration is kept constant, discrete spectral peaks for **DFAA-OPV3** and **DFAA-OT4** emission were observed for the basic solutions,

further illustrating the absence of interactions (*e.g.*, collisional quenching) and energy transfer between the donor-acceptor pair in their dissolved state. For the acidic mixtures, where nanostructure formation is expected to occur, the emission peaks characteristic of the donor **DFAA-OPV3** became quenched along with the decrease in relative quantum yield (Figure 4.4d) upon the addition of the acceptor **DFAA-OT4**, giving rise to a new spectral feature ($\lambda_{em} \sim 540$ nm) reminiscent of **DFAA-OT4** emission. The progressively red-shifted PL spectral features of the coassembled solutions as the acceptor concentration increases are also indicative of energy transfer. The donor peak quenching was observed even by adding 1 mol% of the acceptor **DFAA-OT4**, leading to the decrease in the PL peak area down to 47%. This suggests that during the lifetime of the **DFAA-OPV3** excited state, a significant fraction of the photogenerated excitons can migrate to the **DFAA-OT4** acceptor dopant. In an analogous study by Adams and co-workers, where donor and acceptor π -systems were conjugated to dipeptides within a hydrogel, only a 15% decrease in the emission intensity of the donor at 0.8 mol% acceptor was observed.⁴⁷ Nalluri and Ulijn were able to increase the efficiency by using a related dipeptide that formed a gelator system using an enzymatic assembly trigger and observed complete quenching of donor PL at an acceptor concentration of about 3 mol%.⁵⁰ Both of these examples demonstrated energy transfer using end-functionalized peptide hydrogelators with alkoxy naphthalene donor combined with a dansyl derivative acceptor whereas here, a peptide-based donor-acceptor pair is presented with a comparable energy transfer efficiency occurring between the semiconductor units that are buried within peptide- π -peptide nanostructures. At 9 mol% **DFAA-OT4**, complete quenching of the higher energy vibronic features characteristic to aggregated **DFAA-OPV3** emission peak was observed. In parallel studies involving more

hydrophobic peptide sequences attached to the quaterthiophene core, similar PL profiles were found under acidic, self-assembling conditions as observed with the 9 mol% **DFAA-OT4** acidic solution. The broad, featureless peak observed from 33 to 50 mol% **DFAA-OT4** exhibits a red shift as the mol% **DFAA-OT4** increases within this range, and can be attributed to the contribution of **DFAA-OT4** emission due to the absence of spectral features characteristic of assembled **DFAA-OPV3**. This broad peak is an apparent superposition of the emission λ_{max} peaks associated with dissolved (510 nm) and aggregated (561 nm) OT4, and suggests the coexistence of “isolated” and “aggregated” **DFAA-OT4** exciton traps diluted within the aggregated **DFAA-OPV3** π -stacked nanostructures.

The emission spectra were then recorded after excitation at other wavelengths (Figure 4.5): one at a higher energy wherein both **DFAA-OPV3** and **DFAA-OT4** strongly absorbs (380 nm for basic and 370 nm for acidic) and one at a lower energy wherein **DFAA-OT4** absorbs but **DFAA-OPV3** does not (450 nm). With the higher energy excitation, the resulting emission spectral features of both the basic and acidic solutions are similar to that excited at 320 or 330 nm, only varying in intensities due to the higher extinction coefficient of the system at the latter longer wavelengths. The extent of quenching at 1 mol% **DFAA-OT4** was also similar (peak area decreased down to 47%) when the solutions are excited at 320 and 330 nm.

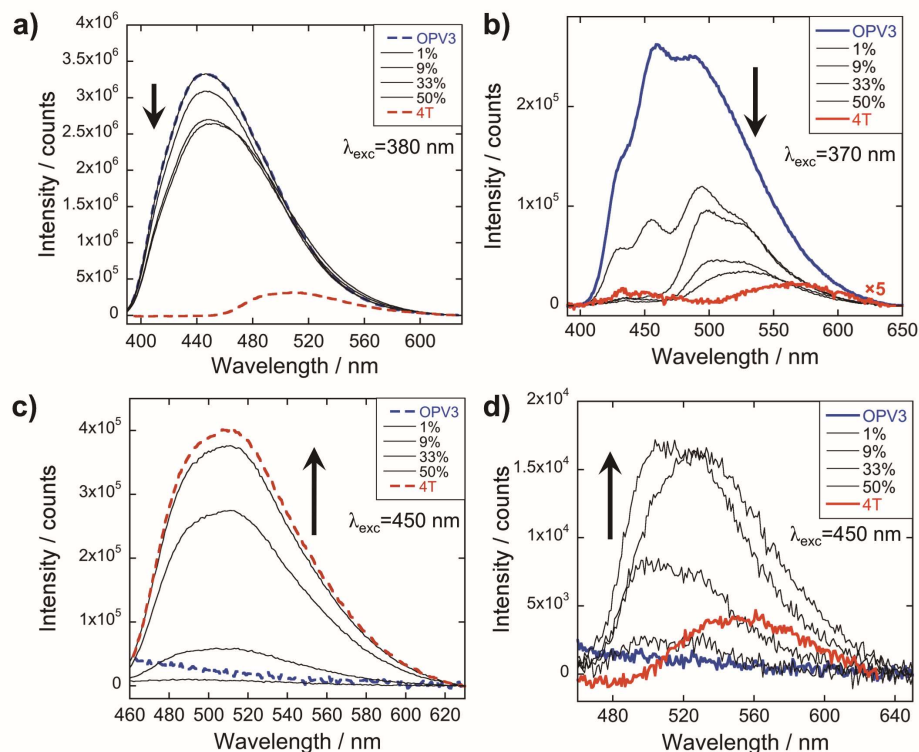


Figure 4.5. PL spectra for **DFAA-OPV3** and **DFAA-OT4** coassemblies (arrows indicate increasing mol% **DFAA-OT4**) at different excitation wavelengths; solutions in (a) and (c) are at pH=10 (---), (b) and (d) at pH=2 (—).

On the other hand, having the excitation at 450 nm, wherein only **DFAA-OT4** strongly absorbs, the resulting emission profiles for the basic solutions only correspond to **DFAA-OT4**. The PL peaks for the coassemblies are blue-shifted with respect to pure **DFAA-OT4** emission that is possibly due to the less planar **DFAA-OT4** conformation when locked within the stacks of **DFAA-OPV3** than within **DFAA-OT4** units as observed in the energy-minimized models. At 9 mol % **DFAA-OT4**, the PL intensity when the acidic solution is excited at 330 nm is about 25-fold higher than when the **DFAA-OT4** is directly excited at 450 nm—confirming the contributions of energy transfer from **DFAA-OPV3** to **DFAA-OT4** in the coassembled nanostructures.

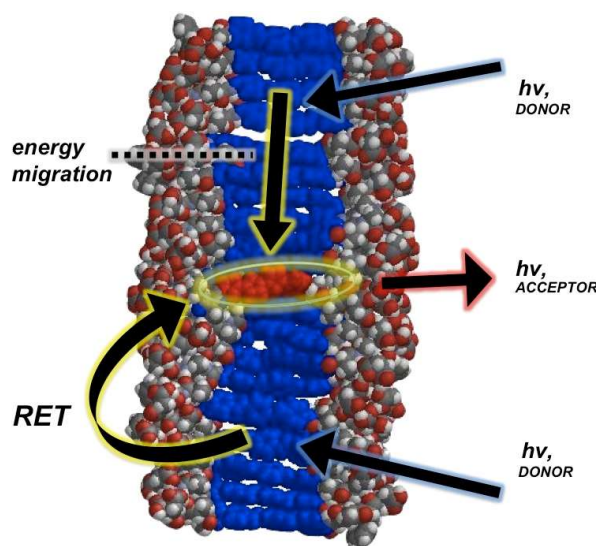


Figure 4.6. Space-filling, energy-minimized model of **DFAA-OT4** coassembled within 1D-stacks of **DFAA-OPV3**, illustrating the possible energy transfer processes (resonance energy transfer (RET) and carrier migration).

In general, a Förster-like energy transfer that is governed by dipole-dipole interactions requires the donor-acceptor system to have strong spectral overlap between the donor emission and acceptor absorbance. Such requirement is achieved in both the dissolved and aggregated states of **DFAA-OPV3** and **DFAA-OT4** donor-acceptor pair (Figure A4.12). These nanomaterials can be envisioned as ensembles of different local intermolecular chromophore distances and dipole orientations, so extracting specific geometric information or otherwise modelling Förster-type processes would be unreliable. The chosen donor-acceptor pair can foster a direct resonance energy transfer, given the spectral overlap, but the significant changes in the emission spectral features observed even at very low loadings of the **DFAA-OT4** acceptor within the coassemblies and the fact that OPV-based stacks are known to facilitate fast exciton migration implies that other mechanisms are potentially involved for the overall transport process (Figure 4.6). In addition, increasing the proximity between donor-acceptor units by trapping them within

the 1D-nanostructures potentially allows shorter-range energy transfer processes that result from direct wavefunction overlap between the interacting chromophores to occur, which are generally known to increase transport within a chain of conjugated polymers as compared to those solely dictated by dipole-dipole interactions.⁶⁰

To further support that the spectral changes observed above are consequences of the funneling of energy from **DFAA-OPV3** to **DFAA-OT4** *via* exciton migration, fluorescence lifetime measurements were recorded at different **DFAA-OPV3** and **DFAA-OT4** mixture ratios (Table 1; Figure A4.13-A4.14). The PL decay profiles for pure **DFAA-OPV3** and **DFAA-OT4** assemblies as well as their coassemblies can be fit to a two-component exponential while a single component fit was suitable for the decay profiles of basic solutions. The drastic decrease in the average lifetime starting at 1 mol% **DFAA-OT4** at the excitation wavelengths where **DFAA-OPV3** only significantly absorbs and where **DFAA-OT4** has minor absorbance contributions (340 and 375 nm, respectively), similar to the observation in energy-transporting oligo(*p*-phenylenevinylene) gels studied by Ajayaghosh and co-workers,¹³ and the progressively decreasing fraction of the long-lived component upon increasing the mol% of the acceptor under acidic conditions supports the energy transfer within the coassemblies.

This also supports the minimal contributions from **DFAA-OPV3** excimer formation, which would result in a low-energy charge transfer band that would overlap with the OT4 emission profile but has a longer-lived lifetime.^{57,61} In addition, the absence of energy transfer in the dissolved solutions and the need for nanostructure formation to initiate the energy transfer within an ordered matrix, which is also found important in the systems studied by Meijer and co-workers, is further verified by the unchanging lifetime

decay values of the **DFAA-OPV3/-OT4** basic mixtures with respect to pure, basic **DFAA-OPV3** solution.^{14,56} It will be interesting to further study the exciton dynamics within these assemblies, however, OPV nanostructures are known to exhibit ultrafast exciton migration dynamics faster than what can be captured by the time-resolved measurements performed herein.

Table 4.1. Fluorescence lifetimes of **DFAA-OPV3**, **DFAA-OT4**, and their coassemblies^a (pH 2; λ_{exc} = 340, 375 nm; λ_{em} = 490, 510 nm) (pH 10; λ_{exc} =375 nm; λ_{em} = 510 nm).

OT4 mol%	τ / ns				
	pH 10	pH 2, λ_{exc} = 375 nm		pH 2, λ_{exc} = 340 nm	
		τ (%)	τ_{avg}	τ (%)	τ_{avg}
0%	1.06	1.10 (69.8); 5.28 (30.2)	2.03	1.08 (64.1); 5.06 (35.9)	2.51
1%	1.06	0.968 (78.6); 4.84 (21.4)	1.79	0.752 (80.5); 4.48 (19.5)	1.48
5%	1.06	0.767 (94.6); 3.39 (5.44)	0.91	0.748 (91.7); 5.72 (8.33)	1.16
13%	1.05	0.720 (98.0); 6.71 (2.00)	0.84	0.663 (97.9); 5.89 (2.05)	0.77
26%	1.06	0.664 (99.2); 4.13 (0.78)	0.69	0.610 (97.5); 4.85 (2.48)	0.72 ^b
33%	1.06	0.631 (99.6); 4.02 (0.36)	0.64	0.614 (98.6); 4.81 (1.39)	0.67 ^b
100%	0.55	0.528 (82.0); 1.67 (18.0)	0.73	N/A ^c	N/A ^c

^aFull decay traces can be found in Figure A4.13-14; ^bEmission recorded at 510 nm where PL intensities are higher for these data points; ^cInsufficient intensities observed for meaningful measurements.

Transient absorption spectra were also collected for the coassembled **DFAA-OPV3** and **DFAA-OT4** peptides to further understand the dynamic nature of the excited states. Figure 4.7 shows the pure **DFAA-OT4** spectra (excitation of the OT4 unit by high fluence 400 nm source). Under basic conditions, shorter-lived features were observed within the 700-800 nm region and longer-lived features with peaks at ~630 and ~740 nm. Under acidic conditions, the peak shapes drastically changed with more spectral features at ~470, ~525 and ~670-720 nm. The peaks between 700-850 nm region correspond to the absorption of the short-lived singlet **DFAA-OT4** excited states, and were observed for both

assembled and essentially dissolved samples but are longer lived under the assembled conditions.

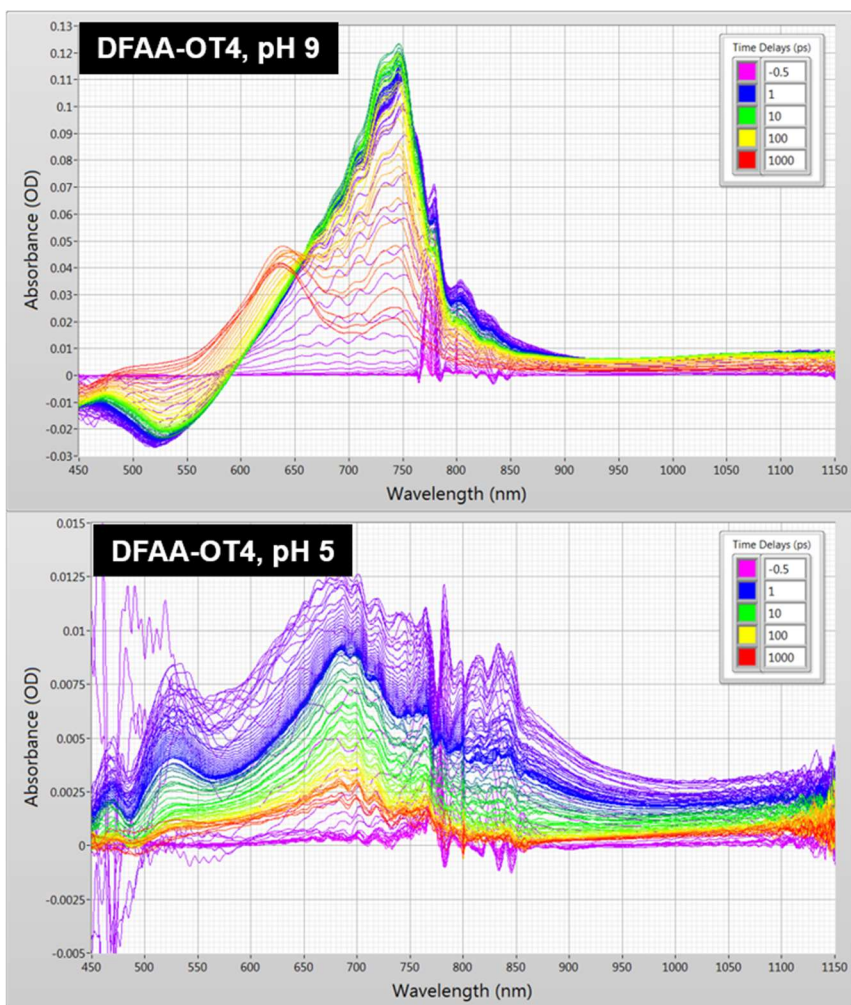


Figure 4.7. Transient absorption spectra ($\lambda_{\text{ex}} = 400$ nm) of **DFAA-OT4** under basic and acidic conditions.

At 10 mol% **DFAA-OT4** coassembly with **DFAA-OPV3**, the steady-state PL spectra in Figure 4.4 shows that the contributions from OPV3 emission signal becomes essentially quenched. This coassembly ratio was then chosen for further analysis with transient absorption. At 400 nm excitation, the basic samples show a sharp band centered at 720 nm was observed which decays and blue shifts at longer timescales (100 ps) but

shifts back to the red (1000 ps) which was attributed to possible photooxidation events (Figure 4.8). Under acidic conditions, a broad absorption with multiple features centered at 790 nm that also blue shifts while decaying. Due to the issues related to the photodegradation of OPV3, all the samples with OPV3 components were sparged with N₂ for 15 minutes prior to measurement.

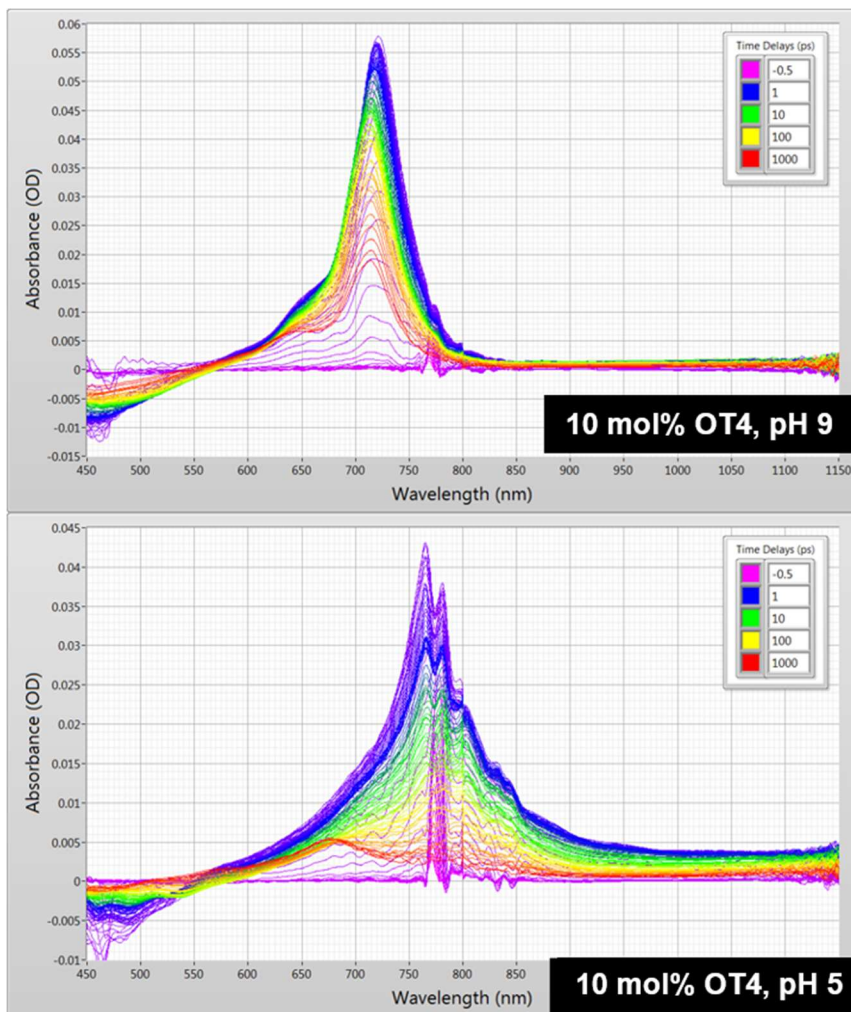


Figure 4.8. Transient absorption spectra ($\lambda_{\text{ex}}=400$ nm) of DFAA-OPV3/-OT4 (10 mol% OT4) under basic and acidic conditions, with the samples sparged with N₂.

At 330 nm where only the OPV3 units were excited, a new prominent spectral feature was observed, centered at 570 nm (Figure 4.9). Further studies revealed that this

band is correlated to the photooxidation of OPV3. Broadband polarization anisotropy scans were also conducted for the 10 mol% **DFAA-OT4** acidic solutions showing highly localized and trapped excitation for the photooxidized region which does not decay at 570 nm. There is a notable decay observed around the region of **DFAA-OT4** excited state (~750 nm) supporting the occurrence of energy transfer, which might be helpful in future studies involving the details of exciton migration.

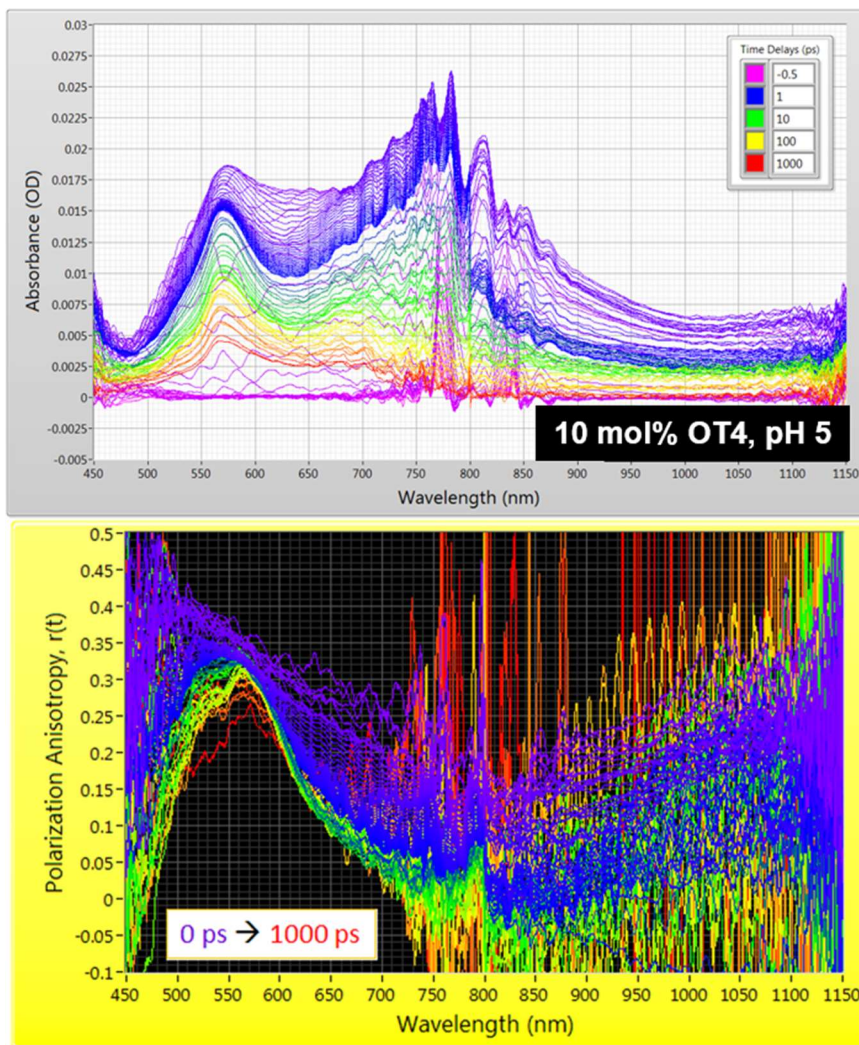


Figure 4.9. Transient absorption spectra (*top*) ($\lambda_{\text{ex}} = 330$ nm) of **DFAA-OPV3/-OT4** (10 mol% OT4) under basic and acidic conditions and broadband polarization anisotropy spectra (*bottom*).

The potential mechanisms of energy transfer proposed for this system involve exciton migration along intimately stacked donor chromophores within a 1D-assembly that is trapped by the acceptor. In order to further investigate how this nanoscale ordering improves energy transfer, the emission spectra of donor-acceptor mixtures were monitored with a pre-assembled **DFAA-OPV3** that was separately prepared as an acidic solution and then titrated against neutral **DFAA-OT4** (Figure 4.10). The TEM images for a 1:1 coassembled **DFAA-OPV3/-OT4** mixture under this condition (Figure A4.1 1b) shows that this forms different aggregate morphologies (nanofibers and random aggregates) that are indicative of the favored separate aggregation of **DFAA-OPV3** and **DFAA-OT4**, potentially generating nanomaterial interfaces similar to p-n heterojunctions^{53,62} for the semiconductor chromophores.

Unlike the coassemblies reported upon in Figure 4.4 and 4.5 prepared by acidification of dissolved solutions of **DFAA-OPV3** and **DFAA-OT4**, wherein **DFAA-OT4** can serve as a local trap for diffusing excitons along the 1D-nanostructures, assemblies formed from the solution wherein **DFAA-OT4** was titrated with a pre-assembled **DFAA-OPV3** is expected to foster an energy transfer process that would mostly rely on non-specific dipole interactions or diffusive encounters. Supramolecular assemblies are presumed to be dynamic in nature, so it is possible to envision free **DFAA-OT4** molecules being able to intercalate within a pre-assembled **DFAA-OPV3** nanostructure. However, it is expected that the **DFAA-OT4** molecules should be driven to assemble under these solution conditions into segregated nanostructures, as supported by the TEM observations. At 1 mol% **DFAA-OT4**, the peak area of the emission profile of assemblies (Figure 4.10a) generated from this condition only decreased down to 82% with respect to

pure **DFAA-OPV3**, showing a much less efficient energy transfer than when the **DFAA-OPV3** and **DFAA-OT4** are intimately coassembled. Moreover, the complete quenching of the donor vibration features at ~ 430 and 460 nm, which was observed at 9 mol% for the coassembled mixtures, was only observed starting at 33 mol% **DFAA-OT4** when **DFAA-OT4** is titrated against pre-assembled **DFAA-OPV3** nanostructures.

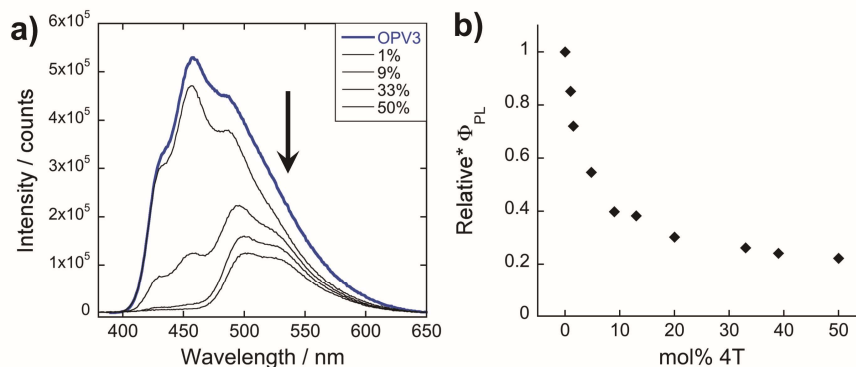


Figure 4.10. (a) PL spectra ($\lambda_{exc}=330$ nm) of resulting solutions from titrating **DFAA-OT4** to a pre-assembled **DFAA-OPV3** acidic solution (arrows indicate increasing mol% **DFAA-OT4**) and (b) their corresponding relative* quantum yields, reported as the ratio of sample absorption \times PL peak area of **DFAA-OPV3/OT4** mixtures with respect to **DFAA-OPV3**.

The dynamic nature of these coassembled nanostructures were also explored when exposed to different environmental stimuli such as pH and temperature. These conditions would allow us to investigate different kinetic regimes for nanostructure formation beyond the kinetically-trapped state obtained upon initial solution acidification. The pH-dependence of nanostructure formation for these π -conjugated peptides is already well-established, but its reversibility and the underlying consequences of pH switching to the energy transfer within our peptide heterostructure system are not yet explored. Similarly, an effort was also made to explore the thermal response of both nanostructure formation and efficiency of energy transfer due to the temperature-dependent assembly mechanisms

existing in the related energy-transporting oligo(p-phenylenevinylene)-based systems studied by Meijer and co-workers.^{14,56}

Interestingly, energy transfer was observed to be reversible within a pH-controlled assembly-dissolution cycle. From the acidic coassembled samples, it was tested whether pH could be used as a “switch” that could turn on or off the occurrence of energy transfer within the assemblies. Upon adding base, the solution goes back to the dissolved state that does not demonstrate energy transfer as confirmed by the absorption and emission spectra (Figure 4.11a and 4.11c).

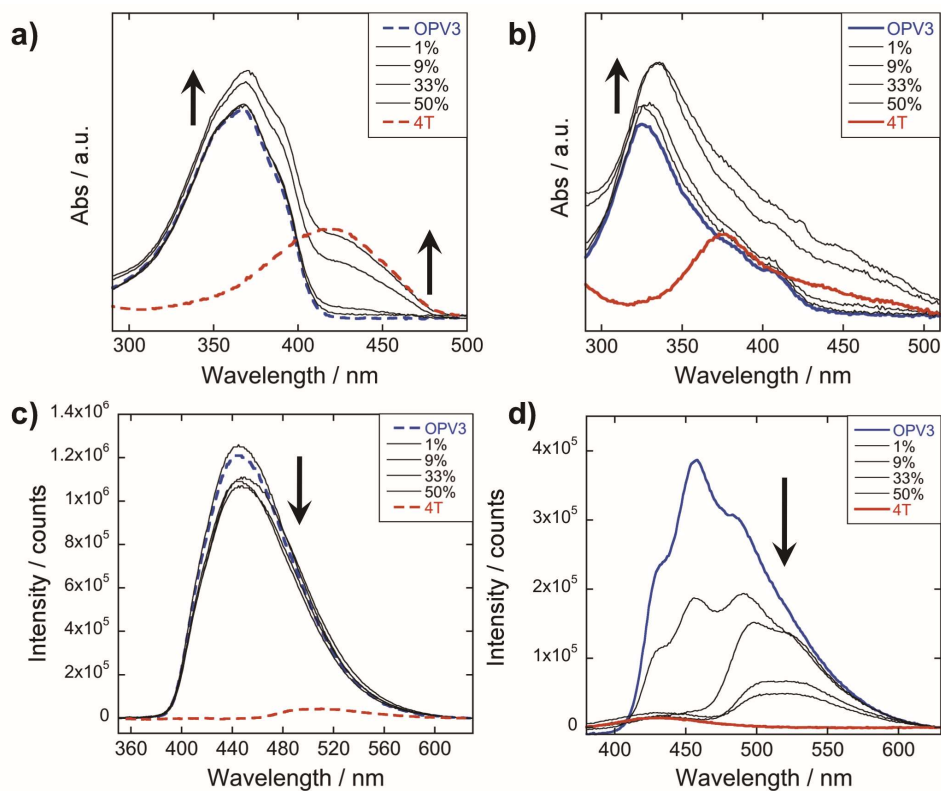


Figure 4.11. UV-Vis (a,b) and PL (c,d) spectra of (a,c) re-basified ($\lambda_{exc}=320$ nm) and (b,d) re-acidified solutions used in Figure 4.4a and 4.4c ($\lambda_{exc}=330$ nm); pH 10 (---); pH 2 (—); arrows indicate increasing mol% DFAA-OT4.

After reacidifying these samples, quenching of the **DFAA-OPV3** donor emission peaks, along with the development of the new spectral peaks reminiscent of **DFAA-OT4** emission, suggests that the re-assembled structure still fosters the energy transfer process (Figure 4.11b and 4.11d). Comparing these to the emission spectra shown in Figure 4.4c, an enhancement in the intensity in the central vibronic feature at 455 nm relative to 430 and 490 nm shoulder intensities was observed. However, the intensity of this 455 nm decreased by ~25% as compared to the 460 nm peak of the initial acidic **DFAA-OPV3**, which can be attributed to environmental degradation. The nearly complete quenching of the 430 and 455 nm peaks still occurred at 9 mol% **DFAA-T4**. These observed trends in the changes of the emission signals were also the same as that of the initial acidic solution when excited at 380 and 450 nm. These observations show an important characteristic of these 1D-nanostructures that even though kinetically-trapped states are formed from rapid re(acidification), the ensemble photophysics remain reproducible.

In general, an efficient energy transfer occurs in a state wherein the assembled structure of the donor-acceptor pair represents a local thermodynamic minimum within the free energy landscape.^{50,63} By subjecting the acidic samples to a heating-cooling cycle (25°C to 80°C to 25°C) as a form of annealing, we could access thermodynamic minima that are potentially different from the initial trapped state formed after rapid sample acidification. The emission spectra of the thermally annealed, acidic samples were observed to have vibronic features similar to the reacidified sample in Figure 4.11d. The existence of quenched vibronic features at 430 and 460 nm observed for the annealed 9 mol% **DFAA-OT4** solution, which deviates from the observed complete quenching of these signals for the initial 9 mol% **DFAA-OT4** acidic samples at 25°C in Figure 4.4c,

suggests that the annealed aggregate has an assembly structure that results in excitons being more easily trapped within the donor matrix rather than reaching the acceptor site—leading to the appearance of donor emission features even up to 25 mol% **DFAA-OT4**. It is possible that exposure at high temperatures and subsequent cooling leads to more local disorder at the donor-acceptor interface, thus allowing for more excitons to be trapped within the donor matrix. The PL spectra taken for “aged” acidic samples after *ca.* 16 hours of initial preparation resembled the spectral features observed for annealed samples, supporting that there are other temporally accessible thermodynamic minima beyond the initial trapped state formed by rapid acidification, as would be anticipated for any type of oligopeptide self-assembly platform. These different assembly minima have different energy transfer dynamics which we plan to explore in our future work.

To obtain more information about the assembly dynamics and energy transfer as the temperature increases, emission spectra of high temperature samples were taken (*ca.* 60-70°C) for **DFAA-OPV3**, **DFAA-OT4**, and 9 mol% **DFAA-OT4** coassembly and monitored the signals as the solutions cool down (Figure 4.12). At a high temperature, the emission signature is still reminiscent of an exciton-coupled structure instead of the dissolved state reported in previous studies of oligo(*p*-phenylenevinylene)-based systems at higher temperatures in organic solvents.^{7,14} At 9 mol% **DFAA-OT4**, wherein we started to observe the complete quenching of donor emission for the acidic samples, quenched signals were also observed for the heated samples but the ~430 and 460 nm peaks associated with the **DFAA-OPV3** vibronic couplings were still present. This indicates that energy transfer is still facilitated in the potentially new aggregate structure formed by heating, however, the efficiency of energy transfer decreased. Moreover, the PL spectra of

both OPV3 and 9 mol% **DFAA-OT4** annealed solutions both showed blue-shifted signals (~ 10 nm) as compared to the acidic samples at 25°C , which is maintained throughout the cooling period. These observations reflect the resistance of these peptide-bound π -systems towards nanostructure disassembly in aqueous environments, even at biologically “extreme” temperatures. The unchanging emission profile upon cooling is also consistent with the recent report by Stupp and co-workers about the hysteresis effect upon heating and cooling back their peptide amphiphiles under different solvent conditions.⁶⁴ It is also interesting to note that following the addition of base to the annealed samples and subsequently reacidifying, the signal recovers back to the initial acidic emission profile. The persistence of self-assembled structures under extreme conditions, as shown by the system studied herein, is important because it is generally addressed that the development of supramolecular polymers that do not break apart at high temperatures remains as a challenge in the field.⁶⁵

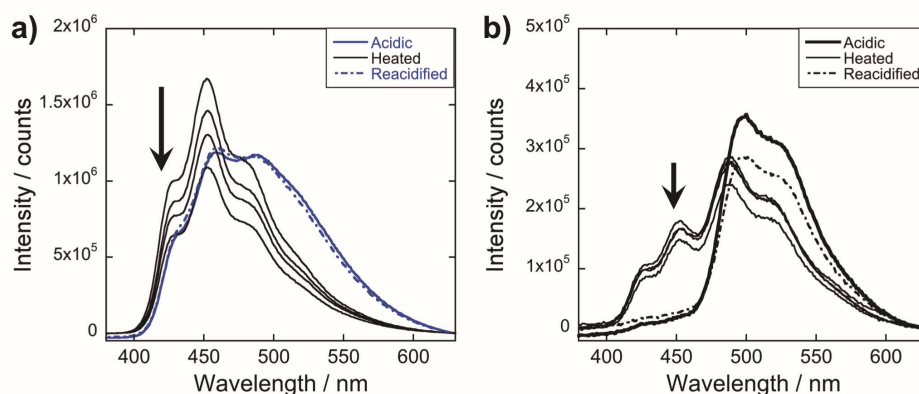


Figure 4.12. Monitoring the emission $\lambda_{\text{exc}}=330$ nm during the thermal cycling process for acidic samples of (a) **DFAA-OPV3** and (b) 9 mol% **DFAA-OT4** solutions; acidic samples (bold line) were heated to 80°C for 30 minutes, readings taken at ca. $60\text{--}70^\circ\text{C}$ and then cooled back to room temperature (thin line); arrows indicate increasing time of cooling within 4 hours; base was then added to these annealed samples and were then reacidified (broken line); $[\text{OPV3}]=3.2\ \mu\text{M}$.

In our peptide- π -peptide triblock system, we can attribute this structure stability to the contributions of the hydrogen-bonding networks among the peptide segments. The CD spectrum (Figure 4.13a) of pure **DFAA-OPV3** under acidic conditions shows a large negative Cotton effect and a high-energy minimum at ~ 220 nm, indicative of β -sheet formation of the peptide moiety that corroborates with the ATR-IR data. On the other hand, the CD spectrum of pure **DFAA-OT4** under acidic conditions shows weak Cotton effect with no signals in the high-energy region. The CD spectra of the dissolved basic samples showed no low energy features, but a bisignate Cotton effect within the chromophore absorption region for the coassembled acidic samples was observed at all mol% **DFAA-OT4**, indicating the existence of exciton-coupled chromophores held within a chiral environment. This supports that the occurrence of 1-D stacking of π -units in a chiral environment is maintained during the coassembly process. Upon annealing the acidic solutions, the high-energy signature indicative of β -sheet formation in the CD spectra for acidic **DFAA-OPV3** and the coassemblies (Figure 4.13b) became more pronounced. Since the energy-minimized structures previously discussed do not show an ideal β -sheet assembly, the enhanced high-energy spectral signature in CD supports the possibility that heating of the 1D-nanostructures leads to a more thermodynamically favored “ β -sheet-like” motif that subsequently alters the spatial orientation of the transition dipoles of the chromophores within the aggregate, and thus, their corresponding photophysics as observed in Figure 4.12.

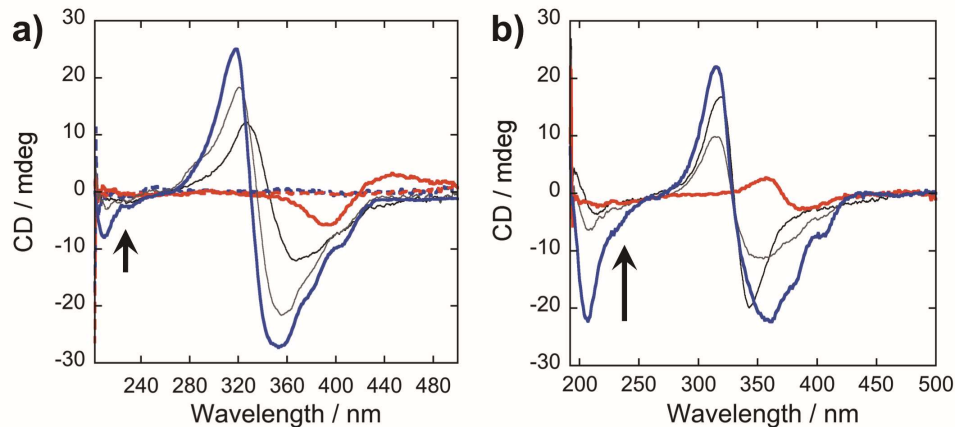


Figure 4.13. CD spectra of (a) acidic (—; pH 2), basic (---; pH 10), and (b) annealed DFAA-OPV3/-OT4 coassembled solutions [OPV3]= 3.2 μ M; arrows indicate increasing mol % DFAA-OT4 (4.8%, 50% to 100%).

II. *Oligo(p-phenylenevinylene)-Quaterthiophene-Naphthalenediimide Peptide System*

This second part of Chapter 4 reports the comparison of the photophysical responses of self-sorted and randomly coassembled binary mixtures of peptides bearing different π -electron systems (Figure 4.14). To achieve such control over the spatial ordering of the binary peptide mixtures, we modulate the rate of acidification. Although there are several studies conducted on controlling the supramolecular polymerization of multicomponent systems,⁶⁶ the accurate control over the assembly dynamics and spatial ordering are rarely discussed in the context of engineering the optoelectronic function of a material. A previous report from Tovar group on the non-equilibrium hydrogelation of a quaterthiophene⁶⁷ demonstrated that the nanoscale morphologies vary depending on the rate of acid diffusion into the peptide solution: the rapid assembly leads to random but dense, matted fiber networks while the relatively slower assembly results in a more homogenous and anisotropic fiber network.

Here, we use different assembly triggers that lower the pH of the peptide solutions at different rates in order to have control over the kinetics of assembly and the molecular ordering of binary peptide mixtures. Self-sorting was induced *via* chemical programming, utilizing the difference in the pK_a of the two components as the pH is gradually decreased upon the slow hydrolysis of glucono- δ -lactone (GdL).^{62,68} Thus, as the pH slowly decreases, we expect a greater extent of protonation/ charge screening for the higher pK_a peptide that triggers it to preferentially assemble first. This should favor the formation of essentially self-sorted structures (Figure 4.14b). To form the randomly coassembled structures, acid was rapidly added to solutions of essentially dissolved peptide units whereby global protonation/ charge screening of all peptides occurs regardless of the pK_a (Figure 4.14c). The Asp-Val-Val and Lys-Ala-Ala peptide sequences were chosen for the oligo(*p*-phenylenevinylene)- and quaterthiophene-appended peptide (**OPV3** and **OT4-NDI**), respectively, to establish a difference in the pK_a of each component (see below). The 1,4-distyrylbenzene, an oligo(*p*-phenylenevinylene), serves as an energy donor upon photoexcitation that can funnel the energy to a quaterthiophene unit acceptor. Similarly, the quaterthiophene serves as an excited state electron donor to the naphthalenediimide in **OT4-NDI**, as described from a previous work by Allix Sanders in the Tovar group.⁷² A control molecule was also synthesized where the side chain amine was acylated instead of bearing naphthalenediimide groups (**OT4-Ac**). This control molecule allows us to observe photonic energy transfer events without associated electron transfer. We investigate the occurrence of energy transport processes under aqueous environments in solution phase, whether the components are self-sorted due to the slow GdL hydrolysis or kinetically coassembled due to rapid acidification.

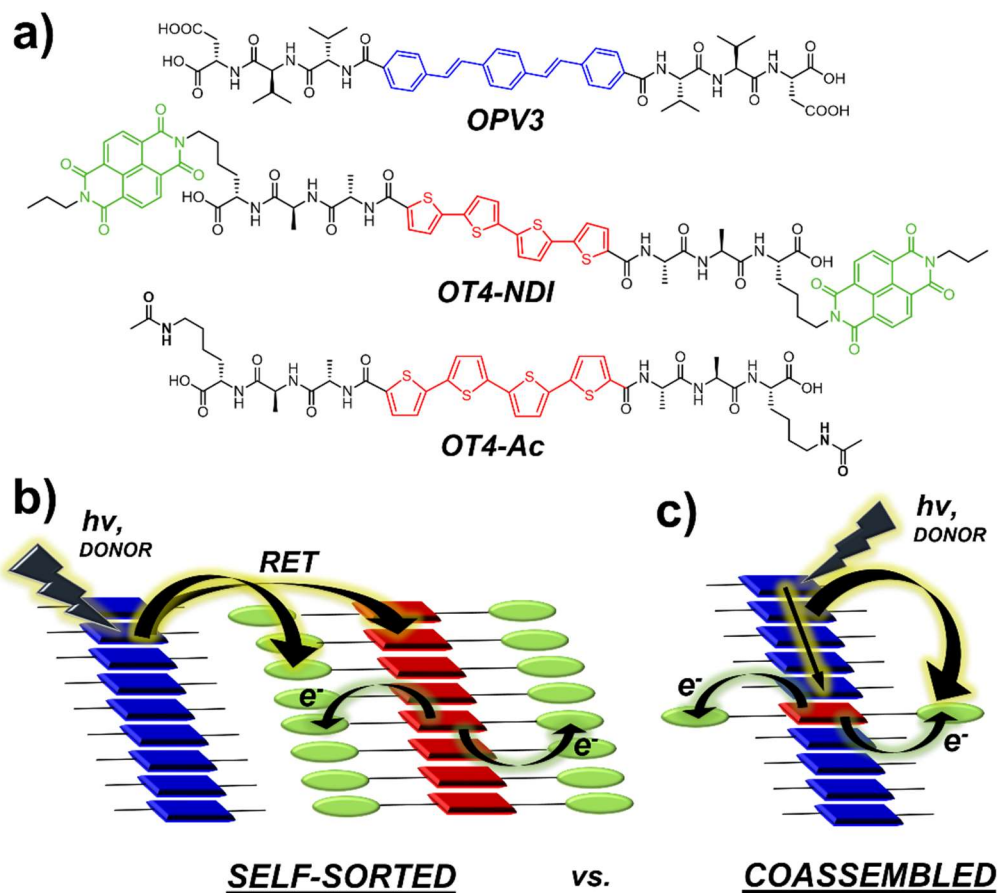


Figure 4.14. (a) Molecular structures of the peptides studied herein and (b,c) diagrams of the potential energy (e.g., resonance energy transfer, RET) and electron transfer events occurring within a two-component peptidic nanostructure with three π -electron units for b) self-sorted and c) randomly coassembled systems.

The apparent pK_a s of **OPV3** donor, **OT4-NDI** acceptor and **OT4-Ac** control acceptor were observed as pH 6.2, 6.5, and 5.4, respectively (Figure A4.21). The **OT4-NDI** containing samples showed buffering regions at around pH 12. The gradual titration with aqueous HCl for 1:1 binary mixtures of **OPV3/ OT4-NDI** and **OPV3/ OT4-Ac** only showed one apparent pK_a rather than a distinct pK_a for each component. To initiate the self-sorting behavior within the two-component peptide hydrogels, 30 mg/mL of GdL was added to the peptide solutions containing 5 mg/mL of each component. In previous studies

with related peptides appended with π -systems, only 5 to 10 mg/mL of GdL was necessary to form hydrogels from 5 mg/mL one-component or binary peptide gelator solutions.^{62,68} The higher GdL concentration necessary for the hydrogelation of the systems reported herein can be possibly attributed to the multiple carboxylates (total of four, two from the backbone termini and two from the aspartic acid side chains, for the **OPV3** donor units) that needs to be protonated to favor the self-assembly process. To further monitor the self-assembly process with GdL, we followed the disappearance of ¹H NMR peaks corresponding to the assembly of each gelator component together with the *in situ* measurement of pH.⁶⁹ The assembly is correlated to the disappearance of unique NMR peaks of each component over time and the results showed a sequential assembly for the 1:1 **OPV3** and **OT4-Ac** mixture (Figure 4.15a) whereby **OPV3** assembles first. On the other hand, the 1:1 **OPV3** and **OT4-NDI** mixture (Figure A4.22) did not show any peaks for **OT4-NDI** even at the beginning of the measurement (before the addition of GdL), suggesting that the assembly might have already started for this component even at higher pH conditions (*ca.* pH 8). This observation of assembly formation even at higher pH was analogous to a previously reported hydrophobic oligo(*p*-phenylenevinylene) dipeptide, which favors the formation of worm-like micelles.⁷⁰ All homoassemblies (one-component samples) and 1:1 mixed assemblies successfully formed self-supporting gels, as confirmed by the rheology measurements (Figure 4.15b and A4.23; storage moduli, G', an order of magnitude larger than the loss moduli, G'', at the end of the time sweep measurements). The storage moduli values for these hydrogels spanned from 0.02 to 2.5 kPa, with the 1:1 **OPV3** and **OT4-NDI** mixed assemblies having the lowest G' values and the 1:1 **OPV3** and **OT4** mixed assemblies with the highest G' values. For the 1:1 **OPV3** and **OT4-NDI** mixed

assembled hydrogel with a total of 10 mg/mL peptide content, the G' is even lower than its individual components at 5 mg/mL, which demonstrates the complex and non-linear nature of the mechanical properties of two-component supramolecular systems that were also observed in another related binary system comprised of dipeptide components appended with naphthalene units.⁷¹

Considering the apparent pK_a values from the titration experiments and the spectral information from time-resolved NMR measurements, **OT4-NDI** assembles first, followed by **OPV3**, and then **OT4-Ac**. The rheology plots show that the **OT4-Ac** forms the hydrogel the fastest, followed by **OPV3**, and then **OT4-NDI** (Figure A4.23). Correlating the ^1H NMR results, which probe molecular aggregation events, to the time frame of gelation observed from rheological measurements, the aggregation time does not coincide with the amount of time required to observe the inflection points for G' and G'' plots for this peptidic system. These suggest that for this material and the conditions imposed upon assembly, the kinetics of aggregation of the individual components do not directly correlate to the rate at which the fibrillar network reaches the critical fiber network density to form a hydrogel. Furthermore, because the fiber network density is linked to the bulk mechanical property of hydrogels, there is also no direct correlation that can be made between the kinetics of assembly formation and hydrogel stiffness for these systems.

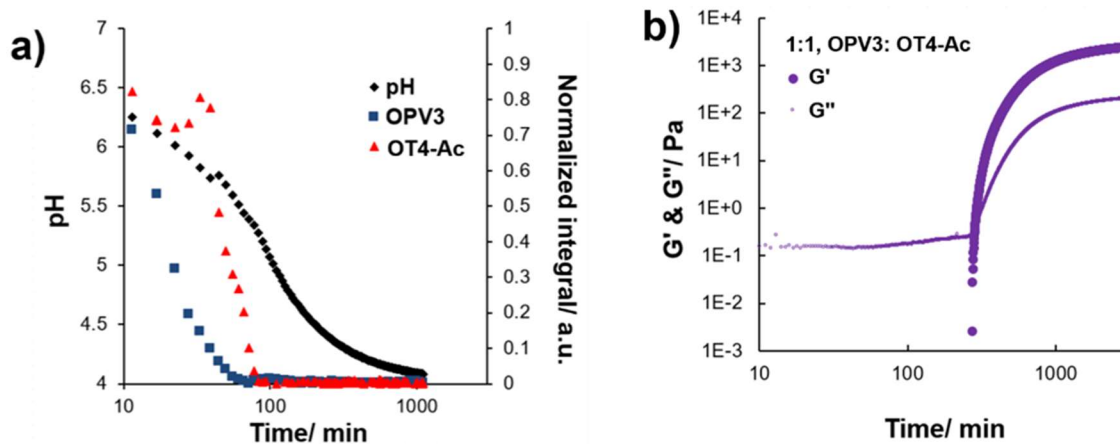


Figure 4.15. Monitoring of peptide assembly and hydrogel formation for 1:1 **OPV3** and **OT4-Ac** solutions prepared with 30 mg/mL GdL *via* a) ^1H NMR and b) rheology (G' =solid circles; G'' =smaller circles). Each peptide component is at 5 mg/mL (total of 10 mg/mL peptides for the 1:1 mixed sample).

Further monitoring of the GdL hydrolysis-triggered gelation process *via* fiber X-ray diffraction supports the occurrence of self-sorting based on the presence of distinct signals from the individual components (Figure 4.16). No diffraction pattern was observed for **OT4-NDI** due to the difficulty in aligning the weaker gels ($G' < 100$ Pa) between the capillaries used for the measurements. The persistence of diffraction signals from pure **OPV3** (9.3 Å and 4.61/4.69 Å, Figure 4.16a) and pure **OT4-Ac** (5.6 Å and 4.61 Å, Figure 4.16b) in the mixed peptide assemblies prepared with GdL indicate the self-sorted nature of the nanostructures (Figure 4.16c, d).⁶² From these characterization techniques, we determined the chronology of aggregation, onset of peptide gelation, and established that self-sorting occurs when hydrogels are prepared with GdL for both **OPV3:OT4-Ac** and **OPV3:OT4-NDI** systems.

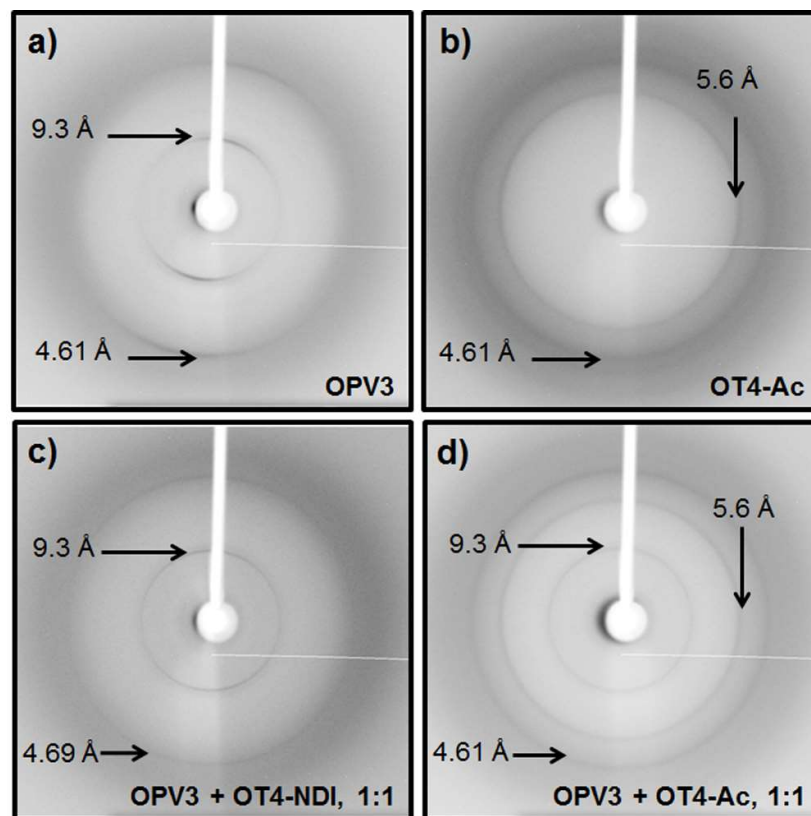


Figure 4.16. Fiber X-ray diffraction data for hydrogels prepared with 30 mg/mL GdL, comprised of one peptide component (a, **OPV3** only; b, **OT4-Ac** only) and two peptide components (c, **OPV3:OT4-NDI**; d, **OPV3:OT4-Ac**; both 1:1). Each peptide component is at 5 mg/mL (total of 10 mg/mL peptides for the 1:1 mixed samples).

TEM was used to visualize the nanostructures resulting from GdL or HCl addition (*ca.* 3 μ M peptide concentration for each component). Under such dilute conditions, 10 mg/mL GdL was enough to observe nanostructure formation. For the **OPV3** and **OT4-Ac** homoassemblies (Figure A4.24), both methods of triggering assembly resulted in the same type of 1-D morphologies. For the **OT4-NDI** peptides, rapid acidification with HCl shows some evidence of micellar-shaped random aggregates while the addition of GdL results in structures with 1-D morphology coexisting with these micellar structures. The predominantly micellar nature of nanostructures formed by **OT4-NDI** with GdL and HCl

further supports the formation of a relatively weaker gels than the other peptides because such low aspect ratio structures generally have a lower propensity to form crosslinks among the nanostructures. For the **OPV3** and **OT4-NDI** mixed assemblies, both the rapid acidification with HCl and addition of GdL results in the formation of micellar structures along with 1-D nanostructures (Figure 4.17a,b). In contrast, the mixed assemblies of **OPV3** and **OT4-Ac** (Figure 4.17c,d), both show 1-D nanostructures with high aspect ratios.

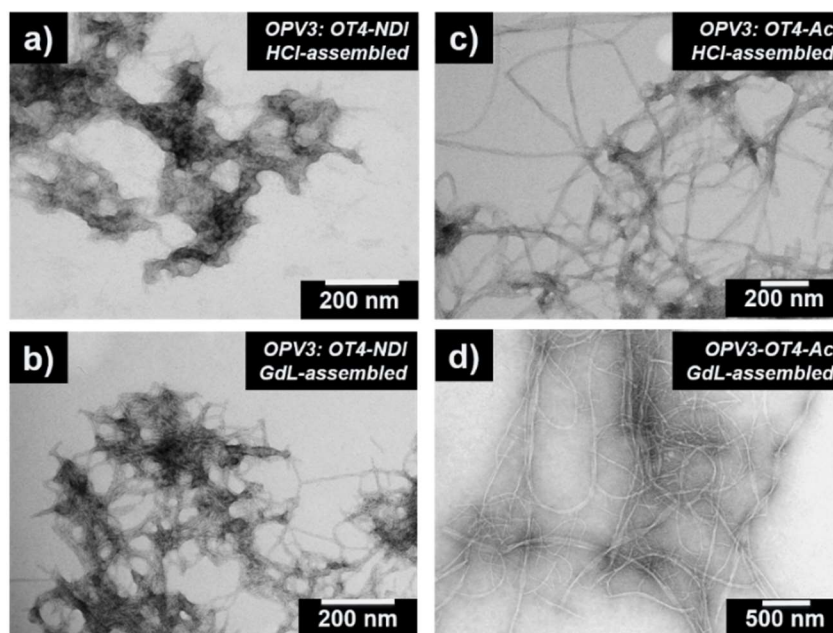


Figure 4.17. TEM images of 1:1 mixed assemblies (3 μM peptide concentration for each component) of **OPV3** with (a,b) **OT4-NDI** or (c,d) **OT4-Ac** (1:1) assembled *via* (a,c) HCl addition and (b,d) GdL (10 mg/mL) hydrolysis.

We utilized the π -electron units embedded in the peptidic moieties, each with unique spectroscopic signatures, as reporters to obtain more information about the spatial organization occurring within the nanostructures under HCl or GdL assembly conditions. The steady-state photophysical spectra of the homo- and mixed assemblies triggered to assemble *via* HCl and GdL in aqueous solution phase (Figure 4.18, 4.19 and A4.25)

consistently showed trends for H-like aggregation, namely, blue-shifted, quenched absorption and red-shifted, quenched photoluminescence (PL) of the assembled samples as compared to their molecularly dissolved states. The recorded spectra from these aqueous solutions should be treated as ensemble averages of the response from polydisperse solutions of peptide assemblies. The spectra for HCl-triggered solutions were measured immediately after acidification (*i.e.*, within 1 h) while the GdL-triggered samples were measured at 20 h to allow enough time for the lactone to hydrolyze and produce enough acid to achieve the same pH as the HCl-triggered solutions. The HCl-assembled samples were then aged for the same amount of time that the GdL was allowed to hydrolyze, after which the absorption and PL spectra were then re-measured. For this multichromophoric system, the spectral overlap between the emission of oligo(*p*-phenylenevinylene) donor with the absorption of quaterthiophene or naphthalenediimide acceptors encourages energy transfer *via* exciton migration or resonance energy transfer (RET) from the donor to these acceptors, with a better spectral overlap with quaterthiophene. On the other hand, the relative HOMO and LUMO levels of quaterthiophene and naphthalenediimide encourage excited-state electron transfer and inhibit energy transfer upon photoexcitation as previously reported.⁷² As a point of reference, the spectral properties of the homoassemblies prepared *via* GdL- and HCl-mediated assembly showed no apparent differences in the maximum absorption peaks except for some slight intensity variations (Figure 4.18a-c). The aged HCl-assembled samples more closely resemble the absorption spectra of the GdL-assembled samples, suggesting the presence of metastable structures formed by rapid acidification and the dynamic nature of these assemblies that allow some extent of reorganization over time.

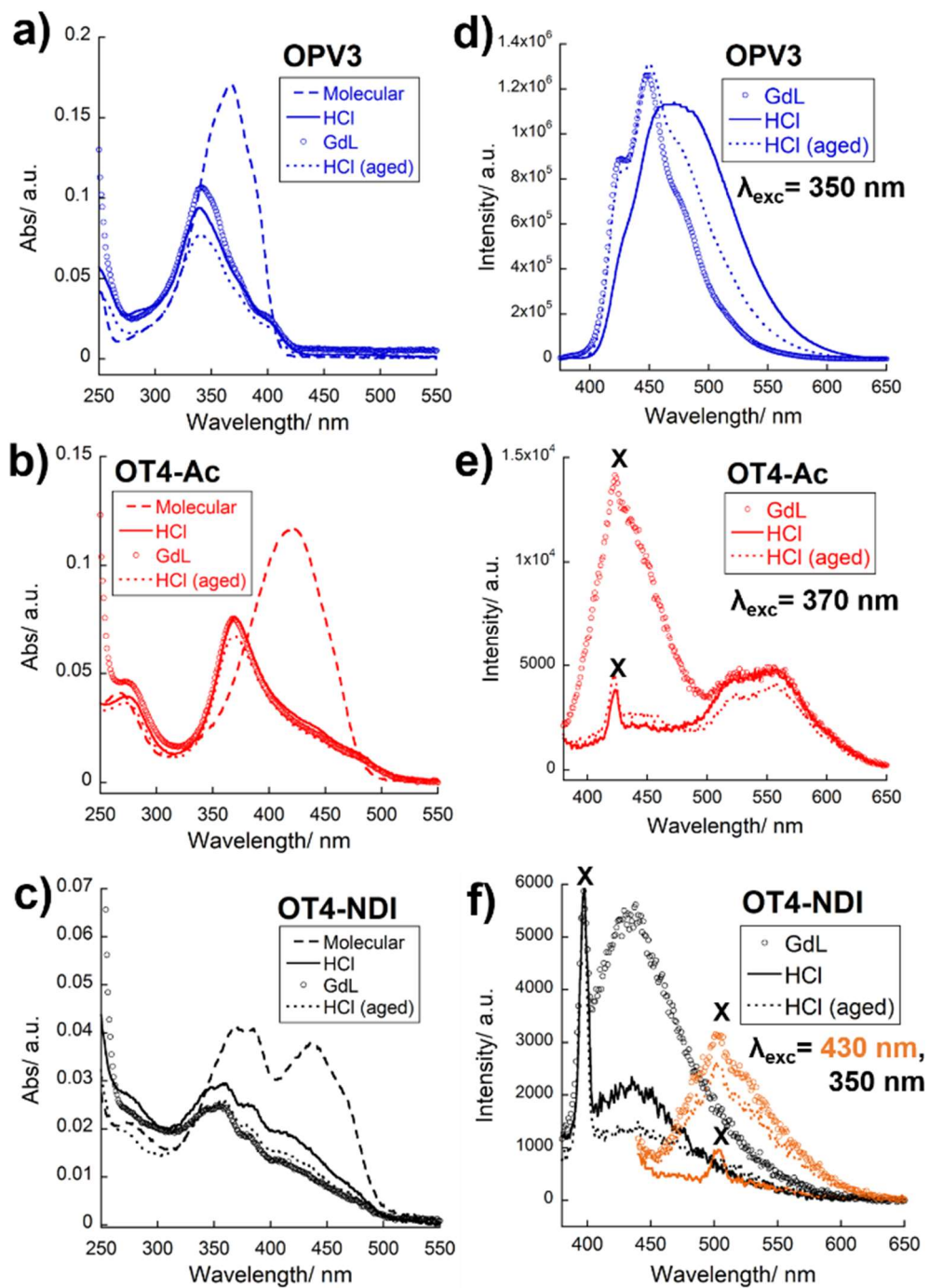


Figure 4.18. Solution phase UV-vis absorption (a-c) and steady-state emission (d-f) spectra for GdL- (10 mg/mL) or HCl-assembled peptide homoassemblies of (a) **OPV3** (blue), (b) **OT4-Ac** (red), and (c) **OT4-NDI** (black); solutions measured under different conditions: molecularly dissolved samples (---), (a, d) with GdL (empty circles), (b, e) with HCl (—), and (c, f) with HCl, aged (...); [peptide] = 3 μ M; **X**= Raman scatter of water.

The PL spectra for the homoassemblies of **OPV3**, **OT4-Ac**, and **OT4-NDI** all showed different features when assembled *via* GdL hydrolysis or *via* rapid HCl addition (Figure 4.18d-f). The HCl-assembled **OPV3** shows a broad emission with $\lambda_{\text{max}}=470$ nm which is consistent with our previous report⁷³ while the aged HCl and GdL-triggered assemblies show blue-shifted peaks with more resolved vibronic bands at 420, 440 and 470 nm suggesting a different packing pattern than the initially trapped HCl-assemblies. These bands can be assigned to strong exciton coupling and are consistent with those we have observed for the thermally annealed structures of other **OPV3** tetrapeptides.⁷⁴ These results support that the slower hydrolysis of GdL could be achieving a more thermodynamically favored structure that is accessed after a dynamic rearrangement due to heating or aging of the metastable structures formed after rapid acidification.^{64,75,76} For **OT4-Ac** and **OT4-NDI** excited at 370 and 350 nm (maximum absorption for assembled **OT4-Ac** and **OPV3**, respectively; naphthalenediimide has minimal absorption at 350 nm), the PL peak of the aged HCl-assembled solutions does not vary from the early time point measurements. The **OT4-NDI** peptide excited at 350 nm shows an emission profile that corresponds to minimal PL contributions from naphthalenediimide. However, excitation at 430 nm, which corresponds to the quaterthiophene component of **OT4-NDI**, the GdL-assembled and aged-HCl samples both show a very weak 510 nm peak similar to the maximum PL peak for a monomeric quaterthiophene peptide. The aged HCl-assembled sample shows a completely quenched spectrum (430 nm excitation), with the Raman peak from water at 500 nm as the only apparent feature. Figures 4.17e and 4.17f show signals with very weak intensities and apparent Raman scattering peaks for water. The weak signals are expected

from the weakly fluorescent quaterthiophene assemblies but can also be a consequence of the electron transfer from quaterthiophene to naphthalenediimide units.

For the mixed assemblies, analogous to the observations in our previous study for an oligo(*p*-phenylenevinylene)-based donor-acceptor system,⁷⁷ it is expected that the photophysical behavior will reflect the spatial organization of the π -electron units, whether it is self-sorted *via* GdL-triggered assembly or randomly coassembled *via* HCl-triggered assembly. The absorption profiles are dominated by the **OPV3** signals, which have the highest extinction coefficient amongst the three chromophores studied, even at 50 mol% of the acceptor units (Figure A4.25). At 10 and 50 mol%, higher intensity shoulders at 450 nm are more evident for the HCl-assembled than the GdL-assembled co-mixtures. For the PL spectra of mixed assemblies, the samples were excited at 350 nm (where oligo(*p*-phenylenevinylene) has the strongest absorption among the three chromophores) and at 430 nm (where only the quaterthiophene component absorbs). The 10 and 50 mol% **OT4-Ac** in **OPV3** and **OT4-NDI** in **OPV3** are compared under different assembly conditions. In all cases, the PL peak intensities of these mixed peptide solutions under acidic conditions are lower than that of the **OPV3** homoassemblies as shown in Figure 4.18d. The 10 and 50 mol% **OT4-Ac** in **OPV3** GdL self-sorted assemblies excited at 350 nm (Figure 4.19a) both show quenched emission peaks in the **OPV3** region with bimodal peaks around 490 and 520 nm that resemble assembled oligothiophene emission in more hydrophobic environments,^{46,78-80} demonstrating some extent of energy transfer. The self-sorted **OT4-NDI** and **OPV3** GdL-assembled samples showed less extent of **OPV3** peak quenching than the **OT4-Ac** and **OPV3** self-sorted assemblies but maintained the **OPV3** vibronic progression. The HCl-assembled samples (Figure 4.19b) showed similar trend for

quaterthiophene PL signatures but with less-resolved spectral features. Compared to the GdL-assembled samples, the **OPV3** emission region was completely quenched and the peak was further red-shifted to 540 nm at 50 mol%, showing a higher efficiency of energy transfer as expected from a more intimate co-mixing for HCl-assembled samples. Upon aging (Figure 4.19c), the HCl-assembled samples show more vibronic features in the **OPV3** region but is still more quenched than the self-sorted assemblies prepared with GdL. Furthermore, comparing **OT4-Ac** and **OT4-NDI** coassemblies with **OPV3** prepared with HCl, the intensities (*i.e.*, relative quantum yields) of the **OT4-NDI** coassemblies are much lower than the **OT4-Ac** coassemblies with **OPV3**, verifying the complete energy funneling from oligo(*p*-phenylenevinylene) to quaterthiophene, to relatively spectrally-dark naphthalenediimide in the **OT4-NDI/ OPV3** coassemblies. This is indicative that energy transfer is still more efficient in the aged HCl-assembled samples than the GdL-assembled, showing that the reorganization that occurs in the metastable structures formed upon rapid acidification does not achieve the complete self-sorting that is induced with GdL hydrolysis.

For the mixed assemblies excited at 430 nm (Figure 4.19d-f), the emission spectra provide information on any energy transfer events that occur from quaterthiophene. The PL signals for self-sorted **OT4-Ac** and **OPV3** mixed assemblies prepared with GdL coincide with the emission of assembled **OT4-Ac** homoassemblies, which is consistent with self-sorting. For the HCl-assemblies at 50 mol% **OT4-Ac**, the PL spectrum has a maximum emission peak at *ca.* 540 nm, which coincides with what was previously reported for quaterthiophene peptides,^{59,78} while the maximum emission peak at 10 mol% **OT4-Ac** at 510 nm is reminiscent of molecularly dissolved samples prepared under basic conditions.

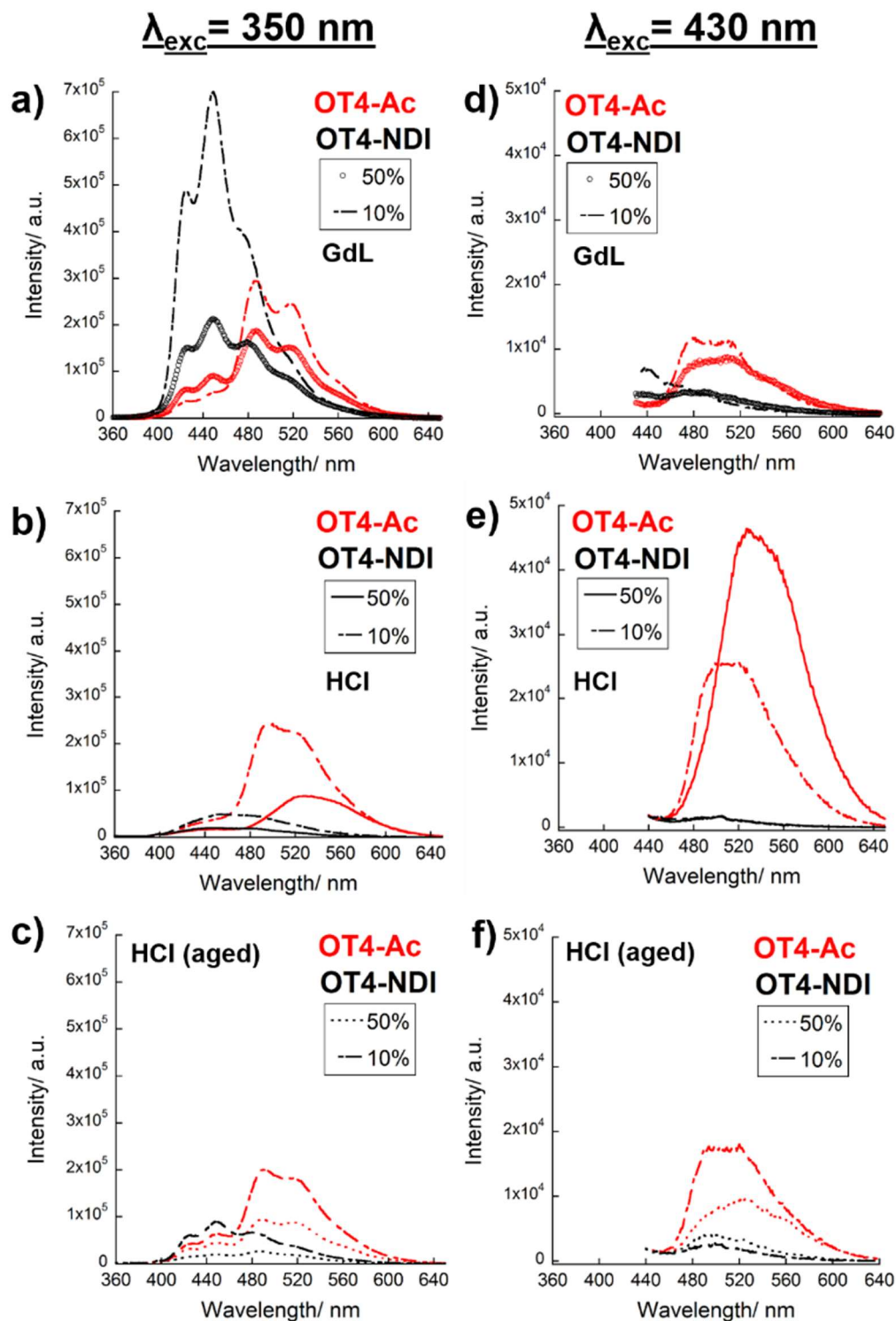


Figure 4.19. Solution phase steady-state PL spectra for mixed peptide structures of OPV3 with **OT4-Ac** (red) and with **OT4-NDI** (black) prepared with GdL- (10 mg/mL) or HCl; measured under different conditions: (a, b, c) $\lambda_{exc} = 350 \text{ nm}$; (d, e, f) $\lambda_{exc} = 430 \text{ nm}$; a) with GdL (empty circles), b) with HCl (—), and c) with HCl, aged (...); [OPV3] = 3 μM .

At 10 mol%, where **OT4-Ac** is a minority component in the co-mixture, the similarity of the PL profile to molecularly dissolved samples suggests that most of the **OT4-Ac** units are isolated within 90 mol% **OPV3** 1D-nanostructures. Upon aging of the HCl-assembled samples, the 50 mol% **OT4-Ac** sample showed a similar bimodal peak observed in GdL-assembled samples while the 10 mol% sample showed a broader, quenched peak. For the **OT4-NDI/ OPV3** HCl-triggered mixed assemblies, the quaterthiophene PL region showed a significant quenching as compared to **OT4-Ac** and **OPV3** samples which are prepared with the same concentration of quaterthiophene units.

These results support that the selective electron transfer from quaterthiophene to naphthalenediimide upon excitation at 430 nm efficiently occurs without preference in the assembly method used. For the mixed assemblies excited at 350 nm, the steady-state emission behavior supports that the sequential and/or concerted energy/electron transfer events from **OPV3** to **OT4-Ac/OT4-NDI** occur more efficiently when the components are randomly mixed (prepared with HCl) than self-sorted (prepared with GdL). These data demonstrate the dependence of the photophysical behavior on the choice of assembly trigger (GdL vs. HCl) for solution phase assembly, hence the spatial organization of the chromophores within the peptide nanostructures, coincide with the structural information obtained for these samples in gel phase *via* ¹H NMR and fiber XRD (Figure 4.15a and 4.16).

Circular dichroism (CD) measurements confirm that both the HCl and GdL-assembled peptide nanostructures maintain similar chirality in both pure and mixed assemblies, except for **OT4-NDI** (Figure A4.26). Low intensity CD signals were recorded for **OT4-NDI** homoassemblies corresponding to naphthalenediimide region of absorption

but not for quaterthiophene. Bisignate signals within the region of chromophore absorption corresponding to an exciton-coupled Cotton band were observed for all other peptide nanostructures prepared under both assembly conditions, which is indicative of the local chiral environment of the π -systems undergoing exciton coupling. The CD signals within the high-energy region that distinguish the structural motifs for conventional peptides were not observed for GdL-assembled samples due to high intensity signal from chiral GdL and gluconic acid, as well as interference from sample scattering (Figure A4.27). For the HCl-assembled samples, the broad peak with minima at ~ 250 nm corresponds to a red-shifted β -sheet signal which is correlated to local twisting within individual assembly units.^{81,82}

Conclusions

In this Chapter, the ability of two-component peptidic nanostructures with embedded chromophores to demonstrate energy transport within peptide nanostructures in completely aqueous environments is presented. The first part of this Chapter shows the utility of a system that shows an energy transfer process that involves multiple mechanisms such as exciton migration and resonance energy transfer. This study also supports the importance of nanoscale order to obtain an efficient energy transport as mediated by the funneling of excitons to the acceptor sites and how these processes are impacted by thermal annealing and repetitive changes in pH. The acquired photophysical data reveal that the nanostructures do not result in complete dissolution upon increasing the temperature to $\sim 70^\circ\text{C}$ but instead reflects the formation of another rearranged structure that exhibits hysteresis—indicating nanostructure stability. These interesting assembly features were attributed to the dynamic and stable nature of hydrogen bonds and side chain interactions

of the peptide segments that stabilizes the anisotropic π - π interactions between the monomers. Although the heterostructure reversibility provides insights to the dependence of energy transfer efficiency into appropriately assembled donor-acceptor pair and the stability of this system, a more accurate elucidation of energy transfer mechanism within the annealed 1D-heterostructures requires further investigation of the temperature-dependent nanostructure morphology changes.

For the two-component peptide hydrogelator system with multichromophoric units, the results show that the π -electron units can be spatially-engineered based on the choice of the assembly trigger. The slow hydrolysis of GdL provides access to self-sorted structures if each of the components has a different pK_a whereas rapid addition of HCl to the peptide solutions favors the random co-mixing of two components within the same nanostructure, which can reorganize upon aging. Both methods of assembly led to the formation of self-supporting hydrogels. ^1H NMR spectroscopy and fiber XRD support that self-sorting behavior is induced when GdL is added to the binary peptide mixtures. Correlating the ^1H NMR spectra and rheology profiles, aggregation occurs the fastest for **OT4-NDI**, but the fastest gelation was achieved with **OT4-Ac**. Thus, aggregation can start earlier among one component but the propagation of the supramolecular polymerization leading to entangled networks that can support a hydrogel structure can occur at a different rate. Whether the two components were randomly coassembled or self-sorted, the chirality within the nanostructures was maintained as evidenced by the exciton-coupled CD bands within the region of the peptide-embedded chromophore absorptions. Both randomly coassembled and self-sorted peptide nanostructures showed evidence for energy and electron transfer. Selectively exciting **OPV3** initiates exciton migration and resonance

energy transfer, which both occur more efficiently if the chromophores are randomly coassembled within one nanostructure. On the other hand, the excited-state electron transfer from quaterthiophene to naphthalenediimide does not require any specific co-mixing. These findings reported herein provide new insights on the photophysical behavior of multichromophoric peptide assemblies whether the components are self-sorted, which is useful for establishing p-n heterojunctions, or randomly co-mixed, which is useful for creating photosynthetic mimics that require high energy transfer efficiency. The observation of multiple energy transport processes under completely aqueous environments, along with the ability to spatially control the distribution of π -electron units within peptidic nanostructures, is an important step to continued engineering of functional bioelectronic materials.

Overall, this Chapter presents a strategy to design bioelectronic materials that utilizes multicomponent peptide systems. The peptidic interactions that can lead to coassembled or self-sorted structures allow for spatial control over chromophore interactions, and thus energy transfer efficiency within the nanostructures. The observation of energy transport processes under completely aqueous environments along with the utility of methods that can spatially control the location of π -electron units within nanostructures, which were successfully achieved for these peptide- π hybrid systems, are highly important in engineering functional electronic materials for biointerfacing. This nanomaterial design is applicable to a range of emerging biologically-relevant optoelectronic devices such as artificial photonic antenna systems and other photosynthetic unit mimics, as well as for establishing nanoscale energy gradients within peptide hydrogels.

Experimental Details

Peptide synthesis. All π -conjugated peptides were synthesized and purified according to our previous reports. Peptide segments were synthesized *via* standard solid phase peptide synthesis procedures and quaterthiophene was covalently attached to the peptides *via* Pd-catalyzed cross coupling between the resin bound peptides terminally *N*-acylated with a thienyl bromide and bis-stannylated bithiophene. The 1,4-distyrylbenzene was appended as the central peptide core *via* solid-phase amidation. Details can be found in the Appendix. The *N*-propyl-1,4,5,8-naphthalenetetracarboxylic acid monoanhydride was prepared according to literature procedure,^{40,72} and the characterization matches that of the literature.

DFAA-OPV3. Prepared according to literature procedure;⁵⁷ characterization data matches that of the literature. Crude peptide obtained was observed as a yellow powder ($\lambda_{\text{max}}=367$ nm at pH=8; HPLC purified, 52.6 mg, 18%). MS (ESI⁻) 1177.7 (M-1H)⁻ (calc. 1177.46), m/z 588.3 (M-2H)²⁻ (calc. 588.2). ¹H NMR (400 MHz, d₆-DMSO) δ , ppm: 8.51 (d, 1H, $J=7.3$ Hz), 8.03 (d, 1H, $J=6.4$ Hz), 8.02 (d, 1H, $J=7.1$ Hz), 7.92 (d, 2H, $J=8.4$ Hz), 7.71 (t, 3H, $J=8.4$ Hz), 7.41 (m, 2H), 7.23 (d, 4H, $J=4.4$ Hz), 7.21-7.13 (m, 1H), 4.50-4.42 (m, 2H), 4.28-4.20 (m, 1H), 3.07 (dd, 1H, $J=15.2, 4.3$ Hz), 2.82 (dd, 1H, $J=16.8, 11.0$ Hz), 2.44-2.36 (m, 1H), 1.31 (d, 3H, $J=7.2$ Hz), 1.21 (d, 3H, $J=7.0$ Hz).

DFAA-OT4. Solid-supported Wang-DFAA-NH₂ peptide *N*-acylated with 5-bromothiophene-2-carboxylic acid was prepared (0.5 mmol). The peptide was coupled with 5,5'-bis-tributylstannyl-[2,2']-bithiophene (0.25 mmol, 0.186 g) in the presence of Pd(PPh₃)₄ (0.02 mmol, 0.023 g) using the general on-resin Stille coupling procedure. The resin was then subjected to the general cleavage procedure. Crude peptide obtained was

observed as an orange powder ($\lambda_{\text{max}}=416$ nm at pH=8; HPLC purified, 43.5 mg, 14%). MS (ESI⁻) m/z 1225.5 (M-1H)⁻ (calc. 1225.3), m/z 1247.5 (M-2H⁺Na)⁻ (calc. 1247.3), m/z 1291.5 (M-4H⁺3Na)⁻ (calc. 1291.3), m/z 612.4 (M-2H)²⁻ (calc. 612.2), m/z 311.2 (M-5H⁺Na)⁴⁻ (calc. 311.1) m/z 325.2 (M-6H⁺2K)⁴⁻ (calc. 324.6). ¹H NMR (400 MHz, d₆-DMSO) δ , ppm: 8.62 (d, 1H, $J=7.8$ Hz), 8.34 (br s, 1H), 8.05 (dd, 2H, $J=16.0, 7.9$ Hz), 7.86 (d, 1H, $J=4.0$ Hz), 7.76 (d, 1H, $J=6.2$ Hz), 7.43 (d, 1H, $J=3.8$ Hz), 7.38 (d, 2H, $J=3.8$ Hz), 7.22 (d, 4H, $J=4.3$ Hz), 7.18-7.14 (m, 1H), 4.45-4.41 (m, 2H), 4.27-4.19 (m, 1H), 4.11-4.03 (m, 1H), 3.06 (dd, 2H, $J=14.6, 4.2$ Hz), 2.86-2.78 (dd, 2H, $J=16.0, 8.7$ Hz), 2.44 (m, 1H), 2.36 (dd, 1H, $J=15.8, 2.4$ Hz), 1.28 (d, 3H, $J=7.2$ Hz), 1.21 (d, 3H, $J=7.1$ Hz).

OPV3 peptide. Prepared according to literature procedure, *see Chapter 3*.

OT4-Ac peptide. Fmoc-Lys(NH₂)-Wang resin was acetylated by adding a 1:2:7 (by volume) mixture of acetic anhydride: diisopropylethylamine: DMF to a peptide chamber containing the resin for 30 minutes (repeated until the resin shows a negative Kaiser test). Solid supported K(Ac)AA-NH₂ (0.5 mmol) peptide was *N*-acylated with 2-bromo-5-thiophene carboxylic acid. The resin was subjected to the standard on-resin Stille coupling procedure using (3,3'-dimethyl-[2,2'-bithiophene]-5,5'-diyl)bis(tributylstannane) for 16 hours. Following HPLC purification, the pure peptide was obtained in 4% yield (11 mg). MS (ESI⁻) m/z 1041.5 (M-H)⁻ (calc. 1041.3), m/z 520.4 (M-2H)²⁻ (calc. 520.2). ¹H NMR (400 MHz, d₆-DMSO) δ , ppm: 7.37 (s, 1H), 6.54 (br s, 2H), 6.31 (br s, 1H), 4.38-4.30 (m, 1H), 3.98 (t, 1H, $J=6.4$ Hz), 2.93 (t, 2H, $J=6.0$ Hz), 1.76-1.50 (m, 6H), 1.43 (d, 3H, $J=7.4$ Hz), 1.31 (d, 5H, $J=7.0$ Hz), 1.19 (m, 3H).

OT4-NDI peptide. Solid-supported Wang-K(Mtt)AA-NH₂ peptide *N*-acylated with 5-bromothiophene-2-carboxylic acid was prepared (0.5 mmol). The peptide was

coupled with 5,5'-bistributylstannyl-[2,2']-bithiophene (0.25 mmol, 0.186 g) in the presence of Pd(PPh₃)₄ (0.02 mmol, 0.023 g) using the general on-resin Stille coupling procedure for 15 h. The Mtt-protected lysine residues of the resulting solid-supported peptide were then subjected to the deprotection with 5% TFA solution (2×). After washing the deprotection solution, the resin was dried and placed with and *N*-propyl-1,4,5,8-naphthalenetetracarboxylic acid monoanhydride (3 eq.) in a Schlenk tube equipped with a reflux condenser. DMF (10 mL) was added and the mixture was heated to 50°C for 1 hour, with continuous N₂ bubbling through the solution. The suspension was then heated to 110°C for 22 hours. The mixture was allowed to cool, then the resin was transfer to a peptide chamber and subjected to a wash cycle (3× NMP, 3× DMF, 2× iPrOH, 2× H₂O, 2× (2× THF, 2× iPrOH), 2× acetonitrile, 2× diethylether, 2× hexanes). Following general cleavage procedure, crude peptide was obtained as an orange-brown powder in 1% yield (4.3 mg). MS (ESI) *m/z* 769.7 ((M-2H⁺)) (calc. 769.7), *m/z* 519.1 ((M-4H⁺+Na⁺)/3) (calc. 519.8).

Apparent p*K*_a and pH measurements. The apparent p*K*_a of the peptide gelator solutions and the 1:1 coassembly mixtures were obtained by a titration experiment, whereby the pH values were recorded after the addition of 10 μL increments of 0.1 M aqueous HCl. For these pH titration experiments, the peptide samples used were prepared with a final peptide concentration of 5 mg/mL for each component, from the 10 mg/mL aqueous stock solutions of the peptides containing equimolar amounts of NaOH (from a 0.1 M NaOH aqueous stock solution). We used a FC200 pH probe with a 6 mm x 10 mm conical tip and a ±0.1 accuracy (HANNA instruments). The temperature of the sample was maintained at 25 °C during the measurements by using a circulating water bath. To ensure

the homogeneity of the solutions and the accuracy of the readings, the solutions were gently stirred using a magnetic stir bar throughout the titration process and the pH value was recorded only when a stable value was reached.

NMR measurements for probing the aggregation time. The 10 mg/mL stock solutions of the peptide gelators for these experiments were prepared in deionized H₂O, with equimolar amounts of NaOH added (from a 0.1 M NaOH aqueous stock solution). To prepare the gels, 50 μ L of each 10 mg/mL solutions of the peptide component were mixed (50 μ L peptide solution + 50 μ L H₂O for one-component samples), followed by the addition of 1 μ L a solution containing indicator compounds for the *in situ* measurement of pH by NMR spectroscopy.⁴ The final concentration of each peptide component is therefore 5 mg/mL. The following compounds comprise the indicator solution used for the *in situ* measurement of pH: sodium glycinate (0.2 M), disodium methylphosphonate (0.2 M), sodium acetate (0.2 M), sodium formate (0.4 M) and sodium methanesulfonate (0.1 M). The solution was then mixed with glucono- δ -lactone (30 mg/mL) and injected into a 75 μ L glass capillary (New Era Enterprises). The capillary was then sealed with PTFE tape, gently centrifuged on a hand-wound centrifuge to drive the solution to the bottom, capped, and then transferred to a 5 mm NMR tube (New Era Enterprises) containing 30 mM 3-(trimethylsilyl)propionic-2,2,3,3-d₄ acid sodium salt (TSP) in D₂O. NMR spectra were recorded on a Bruker Avance II 400 MHz (¹H) wide-bore spectrometer. The spectra were acquired with presaturation applied to the H₂O resonance. Presaturation was accomplished using a train of 98 Gaussian pulses, each of 50 ms duration with a peak power of 76 Hz, separated by 1 ms. After presaturation, a spoil gradient was applied (1 ms, 27 G/cm) followed by a $\pi/2$ pulse and signal acquisition (15 ppm sweep width, 65536 datapoints, 5.5

s). Two dummy scans and eight scans were acquired, giving a total acquisition time of 105 s for each spectrum. The presaturation did not significantly attenuate the gelator integrals; identical integrals were obtained using a hard-pulse WATERGATE sequence (data not shown). In all cases, TSP was used as a reference for integration. The time plotted corresponds to the total time elapsed since the addition of GdL. All the plotted integrals are normalized to their value measured at high pH prior to the addition of GdL (time zero).

Rheological measurements. The 10 mg/mL peptide stock solutions used for rheology experiments were prepared in deionized H₂O, with equimolar amounts of NaOH added (from a 0.1 M NaOH aqueous stock solution). A total of 400 μ L of peptide gelator solutions with a final concentration of 5 mg/mL for each peptide component (200 μ L of each 10 mg/mL peptide component were mixed for a 1:1 coassembly; 200 μ L 10 mg/mL peptide solution + 200 μ L H₂O for one-component samples) were prepared with GdL (30 mg/mL). Immediately after the addition of GdL, samples were transferred onto the bottom plate on the rheometer followed by the lowering of the top plate onto it, ensuring that the top plate was completely covered with the gelator solution. The storage moduli (G') and loss moduli (G'') were recorded over time until the values plateaued with G' and an order of magnitude larger than G'' , indicating gelation had occurred. These experiments were conducted with a 25-mm parallel plate in an Anton Paar Physica MCR101 and MCR301 rheometer, where the plate gap was maintained at 0.7 mm. All experiments were performed at 25 °C, at 1 Hz and 1% strain, which is within the viscoelastic regime of this series of peptidic materials.⁵ The bottom plate was flooded with oil to ensure that no evaporation occurred during the experiments.

Transmission electron microscopy (TEM). Imaging was performed on a Philips EM 420 transmission electron microscope equipped with an SIS Megaview III CCD digital camera at an accelerating voltage of 100 kV. The samples were prepared by pipetting a drop of assembled peptide solutions in water onto 200 mesh copper grids coated with Formvar film (Electron Microscopy Sciences) and adsorbed for 5 min at room temperature. Each solution contains *ca.* 3 μ M of each peptide component (for both the homoassemblies and coassemblies; [OPV3]= 3.0 μ g/mL; [OT4-Ac] = 3.1 μ g/mL ; [OT4-NDI]= 4.6 μ g/mL). The samples prepared with either 10 mg/mL of GdL or by addition of 1 M HCl in 10 μ L increments (until the pH drops to \sim 2-3). The grid was washed with deionized water and the excess solution was wicked off by touching the side of the grid to filter paper. The sample was then stained with a 2% uranyl acetate solution, washed with deionized water and excess moisture was wicked off. The grid was allowed to dry in air before imaging.

Fiber X-ray diffraction (fXRD). Similar to the hydrogel preparation for time-resolved NMR measurements and rheology experiments, the peptide samples were prepared by mixing 10 mg/mL of each peptide component, with a final concentration of 5 mg/mL for each component. The hydrogels were prepared by adding 30 mg/mL of GdL. Alignment was achieved by suspending a droplet of the solution mixtures (including GdL) between two wax-tipped capillary tubes and then allowed to align in the dark, in sealed dishes overnight, at room temperature.⁶⁻⁸ Fiber samples formed on the end of the capillary tubes and these were mounted on a goniometer head. The X-ray fiber diffraction patterns were collected using a Rigaku 007HF Cu K-alpha (1.5419 Å) rotating anode generator with VariMax-HF mirrors and Saturn 944 μ CCD (charge-coupled device) detector. Exposure

times were 20 s at specimen to detector distances of 50 mm. Diffraction patterns were converted to .tiff files using mosflm and processed using CLEARER.⁹

UV-Vis absorption and photoluminescence (PL) spectroscopy. UV-Vis absorption spectra were obtained using a Varian Cary 50 Bio UV-Vis spectrophotometer. Photoluminescence spectra were obtained using a PTi Photon Technology International Fluorometer (QuantaMaster 40) with a 75-W Ushio Xenon short arc lamp and operated with Felix32 Version 1.2 software. Spectroscopic samples were prepared by first, preparing a 0.1 mM stock solution of the pure peptides in Milli-Q filtered H₂O, and then diluting this peptide stock solution to the appropriate concentration to achieve an optical density near 0.1 under assembled conditions. In this case, for the homoassemblies, 100 μ L of 0.1 mM stock peptide solution was taken and then added to a 3.1 mL H₂O solution. For the coassemblies, 100 μ L of 0.1 mM **OPV3** solution was taken and then added to a 3 mL H₂O solution ([**OPV3**]= *ca.* 3 μ M or 3 μ g/mL), followed by the addition of the appropriate amounts of **OT4-Ac** or **OT4-NDI** (10 μ L peptide + 90 μ L H₂O for 10 mol% or 100 μ L peptide for 50 mol%). The pH was then adjusted by adding 10 μ L of 1 M KOH (basic, *ca.* pH 11.5) followed by 20 μ L of 1 M HCl (acidic, *ca.* pH 2.5). For the HCl-assembled solutions, the spectra were measured immediately upon the addition of acid (*i.e.*, no more than 1 h after sample acidification) while the GdL-triggered samples were measured \sim 20 h after the addition of GdL (10 mg/mL). Upon mixing with the GdL, the pH of the solution was *ca.* pH 6, which decreased down to pH 2.82 ± 0.05 (if 30 mg/mL GdL was used, pH 2.46 ± 0.02) after \sim 20 h. For the aged HCl-assembled samples, the solutions were stored in the dark (at room temperature) for the same amount of time that the GdL was allowed to hydrolyze before the measurements were taken. The pH values of the aged samples did

not significantly change from the freshly prepared samples with HCl (pH is within ± 0.03). The pH measurements for these samples were obtained using a SevenCompact pH/ion meter (Mettler Toledo). The excitation wavelengths used correspond to the λ_{\max} observed in the absorption spectra of the peptides, unless otherwise specified. Thermally annealed samples were prepared from acidic solutions that were heated to 80°C for 30 mins and then cooled down to room temperature.

Ultrafast transient absorption spectroscopy. The samples were prepared similar to those used for steady-state UV-Vis absorption and photoluminescence measurements. Every sample was stirred throughout the time of data collection (30 min- 1 h). The characterization was accomplished using an amplified Ti:Sapphire system as described in previous reports.^{83,84} Similar to the protocol used for a previous work related to the systems reported herein,⁷² the ultrafast laser pulses (~ 35 -fs duration, 800-nm center wavelength) were generated with an amplified Ti:sapphire laser system (Coherent Legend Elite), producing approximately 4.0 W at a repetition rate of 990Hz. A small fraction of the beam (< 1 mW) was focused into a sapphire crystal to generate a broadband white-light continuum covering a range of 450-1150 nm. Another fraction of the amplifier output was passed through a Type I BBO, SHG crystal or used to pump a femtosecond optical parametric amplifier (Coherent, OPerA Solo) to generate the photoexcitation pulses. Optical delay of the photoexcitation pulse relative to the probe continuum was controlled with a translation stage (Newport). Excitation pulses were focused to diameters of 0.5-1.0 mm that ensured complete coverage of the white light spot (~ 100 micron) and prevented effects due to spatial chirp. The dispersed spectrum of the probe beam was collected after the sample using an Acton SP 2360 spectrograph outfitted with a Pixis 100BR CCD-array

detector. All images were produced by chirp correcting and combining signals from regions of stable white light. The **DFAA OPV3** samples suffered degradation due to laser exposure or storage over the timeframe of the conducted measurements, and required dry N₂ sparging for 10-15 min.

Circular dichroism (CD). Samples for CD analyses were dissolved in Milli-Q water with pH values adjusted accordingly (~pH 2 for acidic samples and ~pH 10 for basic samples) using 1 M HCl or 1 M KOH. The spectra were collected using a Jasco J-810 spectropolarimeter (Part I) or AVIV Circular Dichroism Spectrometer, Model 420 (Part II) at ~20 °C (unless otherwise stated), taking the final spectrum from the average of three scans.

Portions of this chapter were adapted in part from:

- Ardoña, H.A.M. and Tovar, J.D. “Energy transfer within pi-conjugated peptide heterostructures in aqueous environments” *Chem. Sci.*, 2015, 6, 1474-1484
- Ardoña, H.A.M., Draper, E. R., Citossi, F., Wallace, M., Citossi, F., Serpell, L., Adams, D.J and Tovar, J.D. “Multichromophoric peptide nanostructures with local energy gradients,” *J. Am. Chem. Soc.* 2017, *in press*.

Acknowledgements

The transient absorption spectra for **DFAA-OPV3** and **-OT4** peptides were obtained by Timothy Magnanelli in Professor Arthur Bragg’s group (Johns Hopkins University). Matthew Wallace, in the group of Professor Dave Adams (University of Liverpool) conducted the NMR experiments for peptide self-assembly monitoring. Dr.

Francesca Citossi in the group of Professor Louise Serpell (University of Sussex) performed the fiber X-ray diffraction experiments.

References

- (1) Aida, T., Meijer, E. W., and Stupp, S. I. (2012) Functional supramolecular polymers. *Science* 335, 813–817.
- (2) Sirringhaus, H., Brown, P. J., Friend, R. H., and Nielsen, M. M. (1999) Two-dimensional charge transport in self-organized, high-mobility conjugated polymers. *Nature* 401, 685-688.
- (3) Boekhoven, J., and Stupp, S. I. (2014) Supramolecular materials for regenerative medicine. *Adv. Mater.* 26, 1642-1659.
- (4) Praveen, V. K., Ranjith, C., and Bandini, E. (2014) Oligo(phenylenevinylene) hybrids and self-assemblies: versatile materials for excitation energy transfer. *Chem. Soc. Rev.* 43, 4222-4242.
- (5) Ajayaghosh, A., Praveen, V. K., Vijayakumar, C., and George, S. J. (2007) Molecular wire encapsulated into π organogels: efficient supramolecular light-harvesting antennae with color-tunable emission. *Angew. Chem. Int. Ed.* 46, 6260-6265.
- (6) Sakakibara, K., Chithra, P., Das, B., Mori, T., Akada, M., Labuta, J., Tsuruoka, T., Maji, S., Furumi, S., Shrestha, L. K., Hill, J. P., Acharya, S., Ariga, K., and Ajayaghosh, A. (2014) Aligned 1-D nanorods of a π -gelator exhibit molecular orientation and excitation energy transport different from entangled fiber networks. *J. Am. Chem. Soc.* 136, 8548-8551.
- (7) Hoeben, F. J. M., Herz, L. M., Daniel, C., Jonkheijm, P., Silva, C., Meskers, S. C. J., Beljonne, D., Phillips, R. T., Friend, R. H., and Meijer, E. W. (2004) Efficient energy transfer in mixed columnar stacks of hydrogen-bonded oligo(*p*-phenylenevinylene)s in solution. *Angew. Chem.* 116, 2010–2013.
- (8) Roncali, J. (2007) Molecular Engineering of the band gap of π -conjugated systems: facing technological applications. *Macromol. Rapid Commun.* 28, 1761-1775.
- (9) Cornil, J., Beljonne, D., Calbert, J. P., and Brédas, J. L. (2001) Interchain interactions in organic π -conjugated materials: impact on electronic structure, optical response, and charge transport. *Adv. Mater.* 13, 1053-1067.

- (10) Botelho, A. L., Shin, Y., Liu, J., and Lin, X. (2014) Structure and optical bandgap relationship of π -conjugated systems. *PLoS One* 9, e86370.
- (11) Nakashima, T., and Kimizuka, N. (2002) Light-harvesting supramolecular hydrogels assembled from short-legged cationic *L*-glutamate derivatives and anionic fluorophores. *Adv. Mater.* 14, 1113-1116.
- (12) Schulze, J., Torbjörnsson, M., Kühn, O., and Pullerits, T. (2014) Exciton coupling induces vibronic hyperchromism in light-harvesting complexes. *New J. Phys.* 16, 045010.
- (13) Vijayakumar, C., Praveen, V. K., Kartha, K. K., and Ajayaghosh, A. (2011) Excitation energy migration in oligo(*p*-phenylenevinylene) based organogels: structure-property relationship and FRET efficiency. *Phys. Chem. Chem. Phys.* 13, 4942-4949.
- (14) Hoeben, F. J. M., and Meijer, E. W. (2005) Energy-transfer efficiency in stacked oligo(*p*-phenylenevinylene)s: pronounced effects of order. *ChemPhysChem* 6, 2337-2342.
- (15) Fassioli, F., Dinshaw, R., Arpin, P. C., and Scholes, G. D. (2013) Photosynthetic light harvesting: excitons and coherence. *J. R. Soc. Interface* 11, 20130901.
- (16) Wasielewski, M. R. (1992) Photoinduced electron transfer in supramolecular systems for artificial photosynthesis. *Chem. Rev.* 92, 435-461.
- (17) Choi, M.-S., Aida, T., Yamazaki, T., and Yamazaki, I. (2001) A large dendritic multiporphyrin array as a mimic of the bacterial light-harvesting antenna complex: molecular design of an efficient energy funnel for visible photons. *Angew. Chem. Int. Ed.* 40, 3194-3198.
- (18) Gust, D., Moore, T. A., and Moore, A. L. (2009) Solar fuels via artificial photosynthesis. *Acc. Chem. Res.* 42, 1890-1898.
- (19) Praveen, V. K., Ranjith, C., Bandini, E., Ajayaghosh, A. and Armaroli, N. (2014) White-light-emitting supramolecular gels. *Chem. Soc. Rev.* 43, 4222-4242.
- (20) Vijayakumar, C., Praveen, V. K. and Ajayaghosh, A. (2009) RGB emission through controlled donor self-assembly and modulation of excitation energy transfer: a novel strategy to white-light-emitting organogels *Adv. Mater.* 21, 2059-2063.
- (21) Abbel, R., van der Weegen, R., Pisula, W., Surin, M., Leclère, P., Lazzaroni, R., Meijer, E. W. and Schenning, A. P. H. J. (2009) Multicolour self-assembled fluorene co-oligomers: from molecules to the solid state via white-light-emitting organogels *Chem. Eur. J.* 15 (38), 9737-9746.
- (22) Giansante, C., Schafer, C., Raffy, G. and Del Guerzo, A. (2012) Exploiting direct and cascade energy transfer for color-tunable and white-light emission in three-component self-assembled nanofibers. *J. Phys. Chem. C.* 116, 21706-21716.

- (23) Sapsford, K. E., Berti, L., and Medintz, I. L. (2006) Materials for fluorescence resonance energy transfer analysis: beyond traditional donor–acceptor combinations. *Angew. Chem. Int. Ed.* 45, 4562-4589.
- (24) Huang, Y.-S., Yang, X., Schwartz, E., Lu, L. P., Albert-Seifried, S., Finlayson, C. E., Koepf, M., Kitto, H. J., Ulgut, B., Otten, M. B. J., Cornelissen, J. J. L. M., Nolte, R. J. M., Rowan, A. E., and Friend, R. H. (2011) Sequential energy and electron transfer in polyisocyanopeptide-based multichromophoric arrays. *J. Phys. Chem. B* 115, 1590-1600.
- (25) Webb, J. E. A., Chen, K., Prasad, S. K. K., Wojciechowski, J. P., Falber, A., Thordarson, P., and Hodgkiss, J. M. (2016) Quantifying highly efficient incoherent energy transfer in perylene-based multichromophore arrays. *Phys. Chem. Chem. Phys.* 18, 1712-1719.
- (26) Fockel, B., Hinze, G., Nolde, F., and Müllen, K. (2010) Quantification of the singlet–singlet annihilation times of individual bichromophoric molecules by photon coincidence measurements. *J. Phys. Chem. A* 114, 7671-7676.
- (27) Stappert, S., Li, C., Müllen, K., and Basche, T. (2016) Synthesis of an acceptor–donor–acceptor multichromophore consisting of terrylene and perylene diimides for multistep energy transfer studies. *Chem. Mater.* 28, 906-914.
- (28) Ghosh, S., Praveen, V. K. and Ajayaghosh, A. (2015) The chemistry and applications of π -gels. *Annu. Rev. Mater. Res.* 46, 235–262.
- (29) Babu, S. S., Praveen, V. K. and Ajayaghosh, A. (2014) Functional π -gelators and their applications *Chem. Rev.* 114, 1973–2129.
- (30) Ajayaghosh, A., Praveen, V. K. and Vijayakumar, C. (2008) Organogels as scaffolds for excitation energy transfer and light harvesting. *Chem. Soc. Rev.* 37, 109–122.
- (31) Sandeep, A., Praveen, V. K., Kartha, K. K., Karunakaran, V. and Ajayaghosh, A. (2016) Supercoiled fibres of self-sorted donor–acceptor stacks: a turn-off/turn-on platform for sensing volatile aromatic compounds. *Chem. Sci.* 7, 4460–4467.
- (32) Serin, J. M., Brousmiche, D. W., and Fréchet, J. M. J. (2002) Cascade energy transfer in a conformationally mobile multichromophoric dendrimer. *Chem. Commun.* 2605-2607.
- (33) Haycock, R. A., Yartsev, A., Michelsen, U., Sundström, V., and Hunter, C. A. (2000) Self-assembly of pentameric porphyrin light-harvesting antennae complexes. *Angew. Chem. Int. Ed.* 39, 3616-3619.
- (34) Neuteboom, E. E., Beckers, E. H. A., Meskers, S. C. J., Meijer, E. W., and Janssen, R. A. J. (2002) Singlet-energy transfer in quadruple hydrogen-bonded oligo(*p*-phenylenevinylene)perylene-diimide dyads. *Org. Biomol. Chem.* 1, 198-203.

- (35) Gierschner, J. (2012) Directional exciton transport in supramolecular nanostructured assemblies. *Phys. Chem. Chem. Phys.* 14, 13146-13153.
- (36) Bradford, V. J., and Iverson, B. L. (2008) Amyloid-like behavior in abiotic, amphiphilic foldamers. *J. Am. Chem. Soc.* 130, 1517-1524.
- (37) Ponnuswamy, N., Cougnon, F. B. L., Clough, J. M., Pantos, G. D., and Sanders, J. K. M. (2012) Discovery of an organic trefoil knot. *Science* 338, 783-785.
- (38) Oshovsky, G. V., Reinhoudt, D. N., and Verboom, W. (2007) Supramolecular chemistry in water. *Angew. Chem. Int. Ed.* 46, 2366-2393.
- (39) Jahnke, E., Lieberwirth, I., Severin, N., Rabe, J. P., and Frauenrath, H. (2006) Topochemical polymerization in supramolecular polymers of oligopeptide-functionalized diacetylenes. *Angew. Chem. Int. Ed.* 45, 5383-5386.
- (40) Shao, H., and Nguyen, T. (2009) Self-assembly of 1-D n-type nanostructures based on naphthalene diimide-appended dipeptides. *J. Am. Chem. Soc.* 131, 16374-16376.
- (41) Matmour, R., De Cat, I., George, S. J., Adriaens, W., Leclère, P., Bomans, P. H. H., Sommerdijk, N. A. J. M., Gielen, J. C., Christianen, P. C. M., Heldens, J. T., van Hest, J. C. M., Löwik, D. W. P. M., De Feyter, S., and Meijer, E. W. (2008) Oligo(*p*-phenylenevinylene)-peptide conjugates: synthesis and self-Assembly in solution and at the solid-liquid interface. *J. Am. Chem. Soc.* 130, 14576-14583.
- (42) Diegelmann, S. R., Gorham, J. M., and Tovar, J. D. (2008) One-dimensional optoelectronic nanostructures derived from the aqueous self-assembly of π -conjugated oligopeptides. *J. Am. Chem. Soc.* 130, 13840-13841.
- (43) Schillinger, E.-K., Mena-Osteritz, E., Hentschel, J., Börner, H. G., and Bäuerle, P. (2009) Oligothiophene versus beta-sheet peptide: synthesis and self-assembly of an organic semiconductor-peptide hybrid. *Adv. Mater.* 21, 1562-1567.
- (44) Li, D., Borkent, E.-J., Nortrup, R., Moon, H., Katz, H., and Bao, Z. (2005) Humidity effect on electrical performance of organic thin-film transistors. *Appl. Phys. Lett.* 86, 042105.
- (45) Zelzer, M., and Ulijn, R. V. (2010) Next-generation peptide nanomaterials: molecular networks, interfaces and supramolecular functionality. *Chem. Soc. Rev.* 39, 3351-3357.
- (46) Stone, D. A., Hsu, L., and Stupp, S. I. (2009) Self-assembling quinquethiophene-oligopeptide hydrogelators. *Soft Matter* 5, 1990-1993.
- (47) Chen, L., Revel, S., Morris, K., and Adams, D. J. (2010) Energy transfer in self-assembled dipeptide hydrogels. *Chem. Commun.* 46, 4267-4269.

- (48) Channon, K. J., Devlin, G. L., Magennis, S. W., Finlayson, C. E., Tickler, A. K., Silva, C., and MacPhee, C. E. (2008) Modification of fluorophore photophysics through peptide-driven self-assembly. *J. Am. Chem. Soc.* *130*, 5487-5491.
- (49) Channon, K. J., Devlin, G. L., and MacPhee, C. E. (2009) Efficient energy transfer within self-assembling peptide fibers: a route to light-harvesting nanomaterials *J. Am. Chem. Soc.* *131*, 12520-12521.
- (50) Nalluri, S. K. M., and Ulijn, R. V. (2013) Discovery of energy transfer nanostructures using gelation-driven dynamic combinatorial libraries. *Chem. Sci.* *4*, 3699–3705.
- (51) Draper, E. R., Lee, J. R., Wallace, M., Jäckel, F., Cowan, A. J., and Adams, D. J. (2016) Self-sorted photoconductive xerogels. *Chem. Sci.* *7*, 6499-6505.
- (52) Nakayama, T., Tashiro, K., Takei, T., and Yamamoto, Y. (2017) Controlled self-assembly of oligopeptides bearing electron donor and acceptor units on the side chains to form β -sheets with selective π -stacking configuration. *Chem. Lett.*, *in press*.
- (53) Sugiyasu, K., Kawano, S., Fujita, N., and Shinkai, S. (2008) Self-sorting organogels with p - n heterojunction points. *Chem. Mater.* *20*, 2863-2865.
- (54) Herz, L. M., Daniel, C., Silva, C., Hoeben, F. J. M., Schenning, A. P. H. J., Meijer, E. W., Friend, R. H., and Phillips, R. T. (2003) Fast exciton diffusion in chiral stacks of conjugated p -phenylene vinylene oligomers. *Phys. Rev. B: Condens. Matter Mater. Phys.* *68*, 045203.
- (55) Schmid, S. A., Abbel, R., Schenning, A. P. H. J., Meijer, E. W., and Herz, L. M. (2012) Energy transfer processes along a supramolecular chain of π -conjugated molecules. *Philos. Trans. R. Soc. A* *370*, 3787-3801.
- (56) Hoeben, F. J. M., Herz, L. M., Daniel, C., Jonkheijm, P., Silva, C., Meskers, S. C. J., Beljonne, D., Phillips, R. T., Friend, R. H., and Meijer, E. W. (2004) Efficient energy transfer in mixed columnar stacks of hydrogen-bonded oligo(p -phenylenevinylene)s in solution. *Angew. Chem. Intl. Ed.* *43*, 1976-1979.
- (57) Wall, B. D., Zacca, A. E., Sanders, A. M., Wilson, W. L., Ferguson, A. L., and Tovar, J. D. (2014) Supramolecular polymorphism: tunable electronic interactions within π -conjugated peptide nanostructures dictated by primary amino acid sequence. *Langmuir* *30*, 5946-5956.
- (58) Sanders, A. M., Dawidczyk, T. J., Katz, H. E., and Tovar, J. D. (2012) Peptide-Based Supramolecular semiconductor nanomaterials via Pd-Catalyzed Solid-Phase “Dimerizations.” *ACS Macro Lett.* *1*, 1326–1329.

- (59) Wall, B. D., Diegelmann, S. R., Zhang, S., Dawidczyk, T. J., Wilson, W. L., Katz, H. E., Mao, H.-Q., and Tovar, J. D. (2011) Aligned macroscopic domains of optoelectronic nanostructures prepared via shear-flow assembly of peptide hydrogels. *Adv. Mater.* *23*, 5009-5014.
- (60) Rose, A., Tovar, J. D., Yamaguchi, S., Nesterov, E. E., Zhu, Z., and Swager, T. M. (2007) Energy migration in conjugated polymers: the role of molecular structure. *Philos. Trans. R. Soc. A* *365*, 1589-1606.
- (61) Sherwood, G. A., Cheng, R., Smith, T. M., Werner, J. H., Shreve, A. P., Peteanu, L. A., and Wildeman, J. (2009) Aggregation effects on the emission spectra and dynamics of model oligomers of MEH-PPV. *J. Phys. Chem. C* *113*, 18851-18862.
- (62) Morris, K. L., Chen, L., Raeburn, J., Sellick, O. R., Cotanda, P., Paul, A., Griffiths, P. C., King, S. M., O'Reilly, R. K., Serpell, L. C., and Adams, D. J. (2013) Chemically programmed self-sorting of gelator networks. *Nat. Commun.* *4*, 1480.
- (63) Hirst, A. R., Roy, S., Arora, M., Das, A. K., Hodson, N., Murray, P., Marshall, S., Javid, N., Sefcik, J., Boekhoven, J., van Esch, J. H., Santabarbara, S., Hunt, N. T., and Ulijn, R. V. (2010) Biocatalytic induction of supramolecular order. *Nat. Chem.* *2*, 1089-1094.
- (64) Korevaar, P. A., Newcomb, C. J., Meijer, E. W., and Stupp, S. I. (2014) Pathway selection in peptide amphiphile assembly. *J. Amer. Chem. Soc.* *136*, 8540-8543.
- (65) Krieg, E., Weissman, H., Shimoni, E., Ustinov, A. B. O., and Rybtchinski, B. (2014) Understanding the effect of fluorocarbons in aqueous supramolecular polymerization: ultrastrong noncovalent binding and cooperativity. *J. Amer. Chem. Soc.* *136*, 9443-9452.
- (66) Besenius, P. (2017) Controlling supramolecular polymerization through multicomponent self-assembly. *J. Polym. Sci. A Polym. Chem.* *55*, 34-78.
- (67) Li, B., Li, S., Zhou, Y., Ardoña, H. A. M., Valverde, L. R., Wilson, W. L., Tovar, J. D. and Schroeder, C. M. (2017) Non-equilibrium self-assembly of π -conjugated oligopeptides in solution. *ACS Appl. Mater. Interfaces* *9*, 3977-3984.
- (68) Draper, E. R., Eden, E. G. B., McDonald, T. O., and Adams, D. J. (2015) Spatially resolved multicomponent gels. *Nat. Chem.* *7*, 848-852.
- (69) Wallace, M., Iggo, J. A., and Adams, D. J. (2015) Using solution state NMR spectroscopy to probe NMR invisible gelators. *Soft Matter* *11*, 7739-7747.
- (70) Castilla, A. M., Wallace, M., Mears, L. L. E., Draper, E. R., Douth, J., Rogers, S., Adams, D. J. (2016) On the syneresis of an OPV functionalised dipeptide hydrogel. *Soft Matter* *12*, 7848-7854.

- (71) Draper, E. R., Wallace, M., Schweins, R., Poole, R. J., Adams, D. J. (2017) Nonlinear effects in multicomponent supramolecular hydrogels. *Langmuir*, 33, 2387-2395.
- (72) Sanders, A. M., Magnanelli, T. J., and Bragg, A. E. (2016) Photoinduced electron transfer within supramolecular donor–acceptor peptide nanostructures under aqueous conditions. *J. Am. Chem. Soc.* 138, 3362-3370.
- (73) Ardoña, H. A. M., Kale, T. S., Ertel, A., and Tovar, J. D. (2017) Non-resonant and local field effects in peptidic nanostructures bearing oligo(*p*-phenylenevinylene) units. *Langmuir*, in press.
- (74) Ardoña, H. A. M., and Tovar, J. D. (2015) Energy transfer within responsive pi-conjugated coassembled peptide-based nanostructures in aqueous environments. *Chem. Sci.*, 6, 1474-1484.
- (75) Tantakitti, F., Boekhoven, J., Wang, X., Kazantsev, R. V., Yu, T., Li, J., Zhuang, E., Zandi, R., Ortony, J. H., Newcomb, C. J., Palmer, L. C., Shekhawat, G. S., Olvera de la Cruz, M., Schatz, G. C., and Stupp, S. I. (2016) Energy landscapes and functions of supramolecular systems. *Nat. Mater.* 16, 469-476.
- (76) Raeburn, J., Cardoso, A. Z., and Adams, D. J. (2013) The importance of the self-assembly process to control mechanical properties of low molecular weight hydrogels. *Chem. Soc. Rev.* 42, 5143-5156.
- (77) Ajayaghosh, A., Vijayakumar, C., Praveen, V. K., Babu, S. S., and Varghese, R. (2006) Self-location of acceptors as “isolated” or “stacked” energy traps in a supramolecular donor self-assembly: a strategy to wavelength tunable FRET emission. *J. Am. Chem. Soc.* 128, 7174-7175.
- (78) Ardoña, H. A. M., Besar, K., Tovar, J. D., Togninalli, M., Katz, H. E., and Tovar, J. D. (2015) Sequence-dependent mechanical, photophysical and electrical properties of pi-conjugated peptide hydrogelators. *J. Mater. Chem. C* 3, 6505-6514.
- (79) Pratihari, P., Ghosh, S., Stepanenko, V., Patwardhan, S., Grozema, F. C., Siebbeles, L. D. A., and Würthner, F. (2010) Self-assembly and semiconductivity of an oligothiophene supregelator. *Beilstein J. Org. Chem.* 6, 1070-1078.
- (80) Guo, Z., Song, Y., Gong, R., Mu, Y., Jiang, Y., Li, M., and Wan, X. (2013) Assembly of peptide–thiophene conjugates: the influence of peptide content and location. *Supramol. Chem.* 26, 383-391.
- (81) Aggeli, A., Nyrkova, I. A., Bell, M., Harding, R., Carrick, L., McLeish, T. C. B., Semenov, A. N., and Boden, N. (2001) Hierarchical self-assembly of chiral rod-like molecules as a model for peptide β -sheet tapes, ribbons, fibrils, and fibers. *Proc. Natl. Acad. Sci. U. S. A.* 98, 11857-11862.

- (82) Manning, M. C., Illangasekare, M., and Woody, R. W. (1988) Circular dichroism studies of distorted alpha-helices, twisted beta-sheets, and beta-turns. *Biophys Chem*, *31*, 77-86.
- (83) Magnanelli, T. J. and Bragg, A. E. (2015) Time-resolved Raman spectroscopy of polaron pair formation in poly(3-hexylthiophene) aggregates. *J. Phys. Chem. Lett.* **2015**, *6*, 438-445.
- (84) Zhou, J., Guo, X., Katz, H. E. and Bragg, A. E. (2015) Molecular switching via multiplicity-exclusive *E/Z* photoisomerization pathways. *J. Am. Chem. Soc.* *137*, 10841-10850.

CHAPTER FIVE:

Probing the Local Nanostructure of π -Conjugated
Peptide Coassemblies

Introduction

Multicomponent nanostructures have recently caught a lot of attention for creating functional materials applicable to various fields such as energy harvesting or drug delivery. For example, in Chapter 4, binary peptide systems with multiple chromophores within the structure that can facilitate energy transport were presented. In such systems, spatial control that favors either *social coassembly* or *self-sorting*, is important in modulating material function. As discussed in detail by Würthner and co-workers regarding multicomponent systems, *narcissistic self-sorting* can be defined as the assembly process with strict recognition for the affinity among similar molecules while *social coassembly* involves the affinity to other molecules (Figure 5.1).¹ Either system could be thermodynamic or kinetic assemblies—whether they have reached a thermodynamic equilibrium (which is majority of the reported supramolecular systems) or if trapped species have formed under kinetic control.

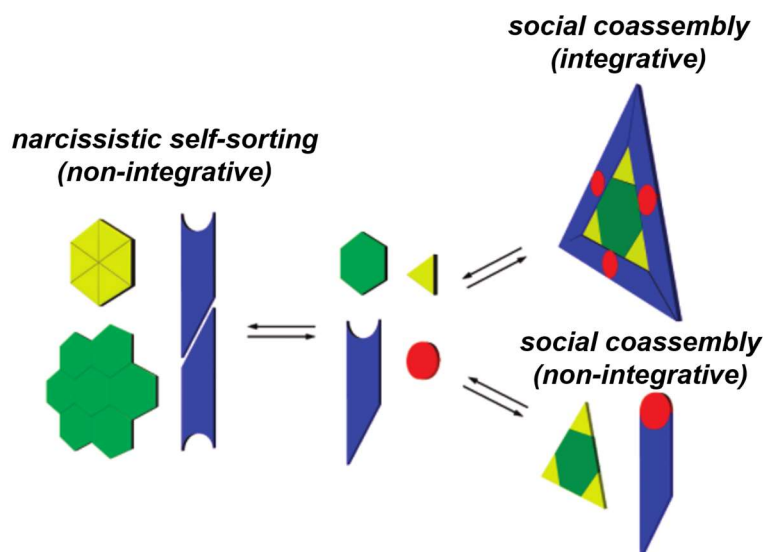


Figure 5.1. Schematic representation of narcissistic self-sorting and social coassembly under thermodynamic equilibrium. Adapted from Ref. 1.

Due to the dynamic nature of structures of supramolecular assemblies held by non-covalent interactions, it is a challenge to spatially engineer multicomponent systems with utmost control (*i.e.*, whether a self-sorted or coassembled system will form) and accurately characterize them. The non-crystalline nature of supramolecular assemblies further makes it challenging to characterize these materials using traditional methods. Several groups have reported excellent ways of elucidating steady state or dynamic structural information from peptide fibrillar structures such as *via* nuclear magnetic resonance (NMR), UV-vis absorption, circular dichroism (CD) and fluorescence spectroscopies, X-ray diffraction (XRD), transmission electron microscopy (TEM), scanning electron microscopy (SEM) and atomic force microscopy (AFM).²⁻⁵

More recently, contemporary microscopic techniques have been utilized to provide dynamic information on the structural diversity within individual fibrillar structures. Stupp and co-workers recently utilized super-resolution microscopy to study the molecular exchange between peptide amphiphile nanofibers.⁶ Nanofiber solutions were labelled with either Cy3 or Cy5 dyes were mixed and the distribution of dyes were quantified to show that some clusters of peptide units insert within a fiber, hence proving a dynamic exchange mechanism. Hamachi and co-workers also used super-resolution microscopy to conduct *in situ* real time imaging of self-sorted fiber formation.⁷ From these experiments, they elucidated a stochastic non-synchronous fiber formation that follows a cooperative mechanism of supramolecular polymerization. Although these structural elucidation techniques provide detailed information regarding a two-component assembly, these are only applicable for monomers bearing fluorescent labels, some of which provide steric bulk that could alter the mixing behavior from the unlabeled monomers.

The characterization of minor components incorporated or co-existing with the larger domains of the major component could also be highly challenging because of the smaller domain size that the minority aggregates can form. Moreover, it has been a challenge to probe local structural information close to atomic resolution and describing different levels of structural organization for functional nanostructures. Electron microscopy techniques show micro- to nano-scale features but only show representative assemblies and do not provide statistical information on the distribution of minor components along the structure of the major component. Considering the broad range of length scales that could be characterized, small-angle neutron scattering (SANS) offers an advantage over microscopic techniques as it covers a wider range of mesoscopic length scales (1-100 nm)⁸⁻¹² and can provide structural information that represents a statistical average and not just within a limited region of interest of a microscopic sample. On the other hand, solid state NMR (ssNMR) spectroscopy also presents the advantage of providing structural information that can be extracted near atomic resolution *via* cross polarization experiments.

This Chapter will discuss the first attempts to conduct a detailed structural investigation of two-component π -conjugated peptide nanomaterials using SANS and ssNMR experiments, particularly for energy transporting binary peptide systems mixed within hydrogels— quaterthiophene (OT4)-appended HO-Glu-Ala-Ala- (EAA) and HO-Val-Ala-Val-Lys-Ile-Glu-Ala-Ala (VAVKIEAA) OT4, and oligo(*p*-phenylenevinylene)- (OPV3) or OT4-appended Asp-Phe-Ala-Ala (DFAA). The first system, **EAA-** and **VAVKIEAA-OT4**, ideally forms a coassembled system that can present a laminin-derived epitope (IKVAV, relevant for neurite outgrowth^{13,14}) on the surface of **EAA-OT4**

assemblies (Figure 5.2). Such is the case if mixing the components of this system with the same OT4 core but different peptide lengths allow the social coassembly between both peptides in an H-aggregated manner. Surface-functionalization of these optoelectronic nanostructures with bioactive epitopes that can elicit chemical cues for cell adhesion or influence cell behavior are important for the development of biological scaffolds. The other system, **DFAA-OPV3** and **-OT4**, are energy donor-acceptor pairs discussed in the first part of Chapter 4. For this system with similar peptide lengths, the nature of assemblies formed will either allow both resonant energy transfer and exciton migration if coassembled, or only distance-dependent energy transfer dictated by dipole-dipole interactions (Förster-like) if self-sorted.¹⁵

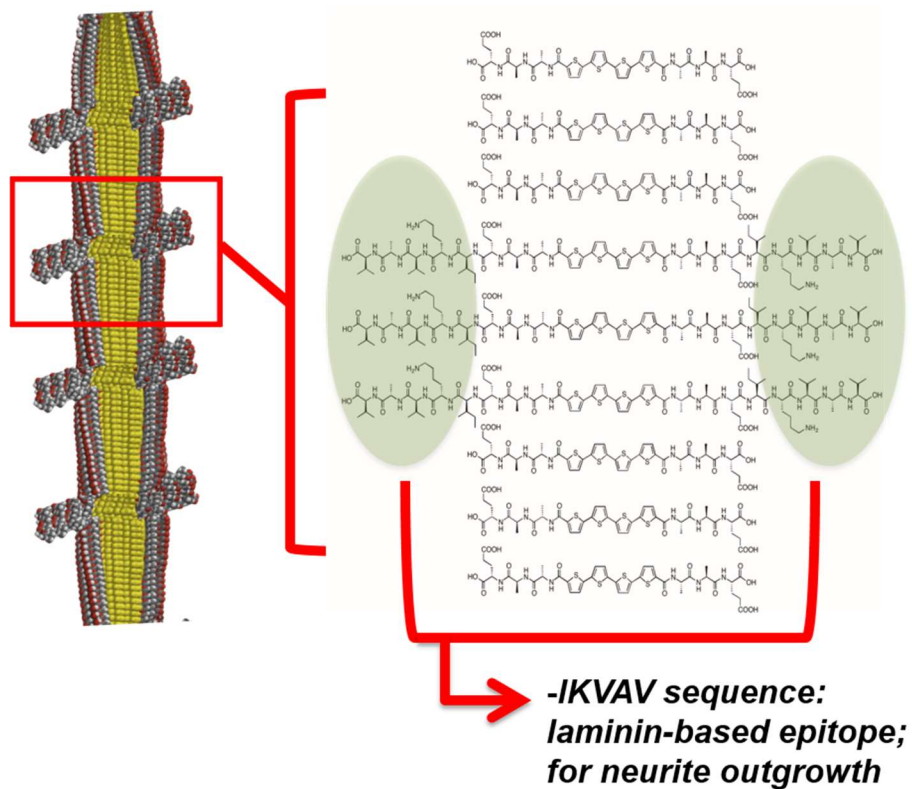


Figure 5.2. Schematic representation of an ideally coassembled 1D-structure that can be formed by **EAA-** and **VAVKIEAA OT4** binary peptide system.

Results and Discussion

For the systems studied herein, the peptide components were isotopically labelled at specific locations (^2H (D), ^{13}C , ^{15}N), according to the requirements of each experiment for the investigation of coassembly structure formation. Figure 5.3 shows the molecular structures of the peptides studied herein.

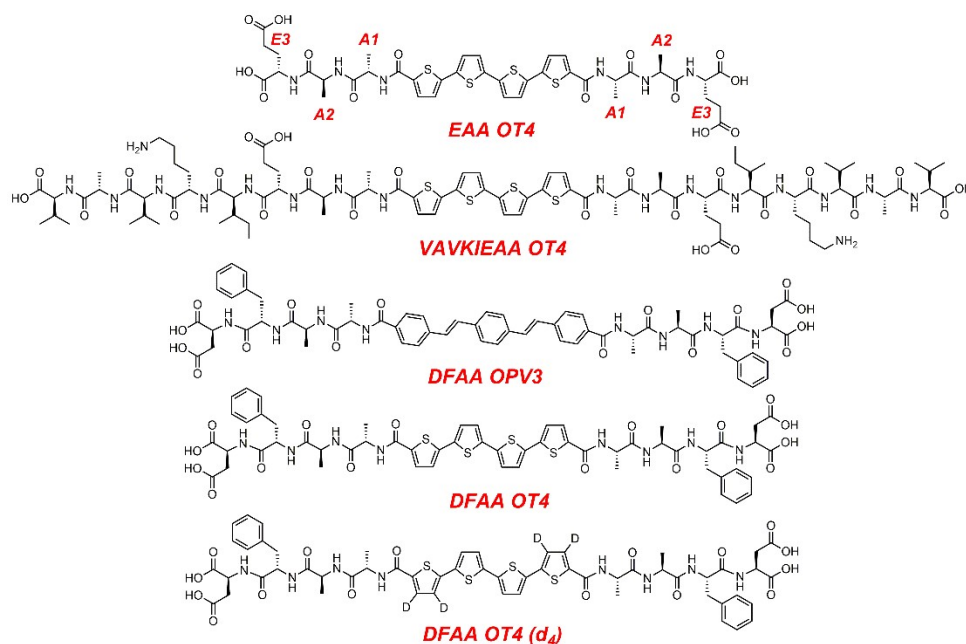


Figure 5.3. Molecular structures of the symmetrical π -conjugated compounds used in these studies. A sample labeling scheme for each amino acid residue is shown for **EAA-OT4**. The amino acid residues were numbered according to their distance from the central π -electron system (*i.e.*, the nearest residue to the π -unit being 1; *e.g.* A1 for the alanine nearest the OT4 core).

In the first section, the results of different solid state NMR experiments for both one-component and two-component self-assembled hydrogels will be discussed. A heteronuclear correlation experiment (particularly *NCO*, transfer of magnetization from amide nitrogens to carbonyl carbons) was initially conducted to observe polymorphism or variation in the local packing environment within a nanostructure. Beyond computational

work,^{16,17} polymorphism was not experimentally observed for these systems due to the limited techniques accessible. In addition, dipolar coupling together with recoupling schemes, such as *Dipolar Recoupling With A Windowless Sequence* (DRAWS) for homonuclear recoupling and *Transferred-Echo DDouble Resonance* (TEDOR) for heteronuclear coupling, were utilized to obtain accurate distance measurements between the monomer units stacked within the nanostructure. Listed in Table 1 are the isotope-labelled samples/sample mixtures that comprise the hydrogels studied herein using ssNMR. For these samples, ¹³C- and ¹⁵N-labelling was positioned at the carbonyl carbon of A1 and the amide nitrogen of A2, respectively.

Table 5.1. List of EAA- and VAVKIEAA-OT4 coassembled hydrogel components.*

Sample #	Major Component	Minor Component
1	N. A. ** EAA-OT4	-
2	A1- ¹³ C-A2- ¹⁵ N-EAA-OT4	-
3	85% N. A. ** EAA-OT4	15% A1- ¹³ C-A2- ¹⁵ N-EAA-OT4
4	A1- ¹³ C-EAA-OT4	-
5	A2- ¹⁵ N-EAA-OT4	-
6	75% A2- ¹⁵ N-EAA-OT4	25% A1- ¹³ C-VAVKIEAA-OT4
7	85% A2- ¹⁵ N-EAA-OT4	15% A1- ¹³ C-VAVKIEAA-OT4
8	90% A2- ¹⁵ N-EAA-OT4	10% A1- ¹³ C-VAVKIEAA-OT4
9	N. A. ** DFAA OPV3	-
10	A1- ¹³ C-A2- ¹⁵ N-DFAA-OPV3	-
11	A1- ¹³ C-DFAA-OT4	-
12	A2- ¹⁵ N-DFAA-OPV3	-
13	75% A2- ¹⁵ N-DFAA-OPV3	25% A1- ¹³ C-DFAA-OT4
14	90% A2- ¹⁵ N-DFAA-OPV3	10% A1- ¹³ C-DFAA-OT4

*All the component percentages are nominal ratios.

**N.A. = natural abundance

Polymorphism phenomena were observed in both **EAA-OT4** and **DFAA-OPV3** nanofibrils, using Samples **2** (A1-¹³C-A2-¹⁵N-EAA-OT4) and **10** (A1-¹³C-A2-¹⁵N-DFAA-OPV3) with NCO experiments. If there is a homogenous packing environment, only one

NCO peak is expected from the adjacent pairs of C^{13} and N^{15} . However, Figure 5.4 shows that **EAA-OT4** has 5 peaks (listed in Table A5.1), with the most prominent peak at 40.8%. On the other hand, **DFAA-OPV3** has 6 peaks (listed in Table A5.2), with the major contributor at 22.8%. All the secondary chemical shifts of $A1-^{13}C$ with respect to a random coil have negative values, indicating β -sheet environments for both **EAA-OT4** and **DFAA-OPV3**. The assumption is that these peaks arise from the polymorphs of different secondary or higher order structures. It was observed that the intensity of each peak varies on the hydrogel preparation (*e.g.*, with or without thermal annealing after gelation, final pH values, and temperature). We have then ensured that the sample preparation is kept consistent among Samples **1** to **14**. However, no further experiments were conducted to determine the structural differences among the different polymorphs and which polymorph dominates for a specific sample preparation route. All the distance measurements between the monomers were then calculated from the average of all the polymorphs.

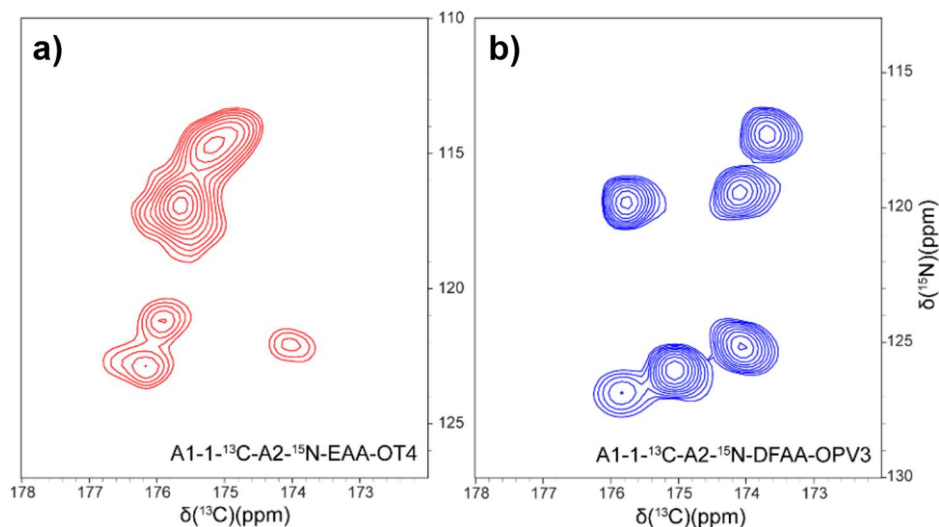


Figure 5.4. 2-D NCO spectra of 1 wt% hydrogels from (a) Sample **2**, A1-1- ^{13}C -A2- ^{15}N -EAA-OT4, and (b) Sample **10**, A1-1- ^{13}C -A2- ^{15}N -DFAA-OPV3.

As control experiments for the runs with the mixed nanostructures, DRAWS and TEDOR experiments were conducted with Samples **3** (85% N. A. ** EAA-OT4 and 15% 15% A1- ^{13}C -A2- ^{15}N -EAA-OT4) and a 1:1 mixture of **4** and **5** (A1- ^{13}C -EAA-OT4 and A2- ^{15}N -EAA-OT4). The actual ratios determined from 1-D $^{13}\text{C}/^{15}\text{N}$ solid state NMR integrals are listed in Table A5.3. Figure 5.5 shows a schematic representation of the dipolar coupling interaction between A1- ^{13}C and A2- ^{15}N that leads to the signals observed for the TEDOR experiments ran on these systems. The signals from natural abundance ^{13}C , as determined from a control experiment with Sample **5**, was subtracted from the spectra.

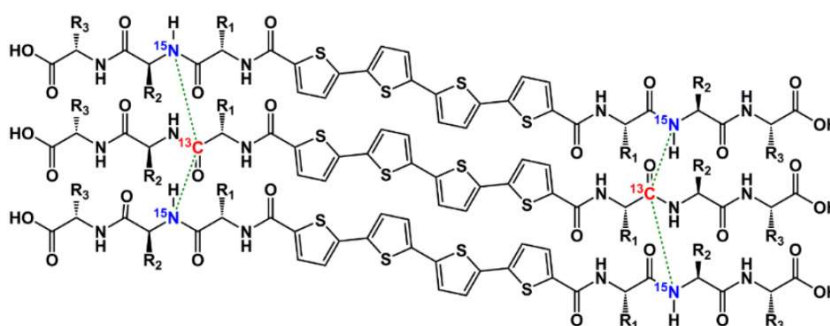


Figure 5.5. A generalized stacking scheme between peptide-OT4 monomer units with labeled ^{13}C and ^{15}N pairs interacting for the TEDOR experiment.

The initial DRAWS experiments with Sample **2** hydrogels resulted in a 4.58 Å distance between the ^{13}C - $^{13}\text{C}'$ neighboring pairs (Figure 5.6a), which is a value that falls within the range of typical interstrand distances for parallel, in-register β -sheet strands. The DRAWS experiments on Sample **3** hydrogels were used to further verify these methods to characterize mixed samples. With the labelling scheme for these peptides, the dilution of ^{13}C labels amongst neighboring ^{12}C nuclei can attenuate the double-quantum efficiency (DQE). This parameter, if the experimental matches with calculated, validates the method. The calculated DQE values consider the probabilities of ^{13}C dilution (an illustration shown

in Figure A5.22). Experimentally, DQE is measured as the DRAWS integral divided by the cross polarization integral. For Sample 3 and 1:1 mixture of 4 and 5 (Table A5.3), the calculated DQEs are 68% and 26%, successfully approaches the experimental DQE values at 62% and 26%. For the TEDOR experiments on the 1:1 mixture Samples of 4 and 5 (Figure 5.6b), considering the results from DRAWS of Sample 2, the simulation curves were fit using the model for a parallel, in-register β -sheet strands. The distance between ^{13}C - ^{15}N neighboring pairs was determined to be 4.74 Å, which approaches the value obtained from the DRAWS experiments. These distance measurements were not conducted for VAVKIEAA-OT4 due to the inability of this peptide to form a hydrogel at 1wt%.

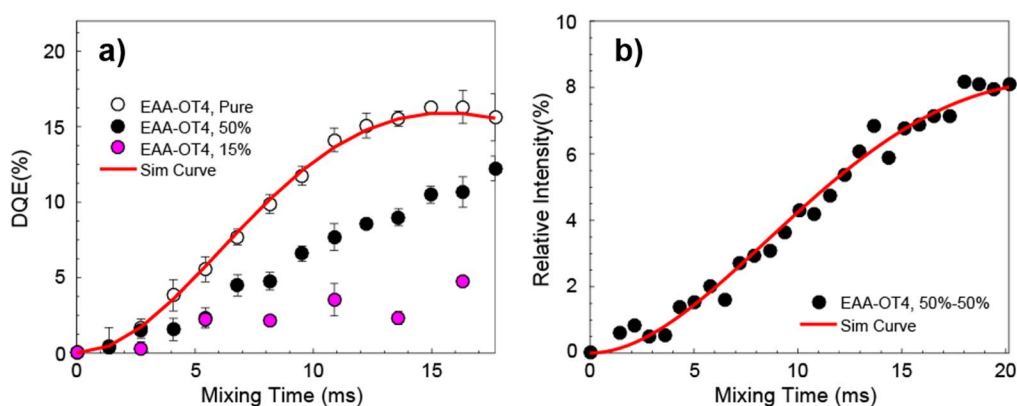


Figure 5.6. DRAWS and TEDOR curves for EAA-OT4. (a) DRAWS of pure A1- ^{13}C -A2- ^{15}N -EAA-OT4 (white circle with error bar), 50% A1- ^{13}C -EAA-OT4 and 50% A2- ^{15}N -EAA-OT4 (black circle with error bar), and 15% A1- ^{13}C -A2- ^{15}N -EAA-OT4 in 85% N. A. EAA-OT4 (magenta circle with error bar). Solid red line: simulation curve, $r = 4.58 \pm 0.03$ Å, and $t_{2, \text{SQ}} = 19.3 \pm 0.7$ ms. (b) TEDOR of 50% A1- ^{13}C -EAA-OT4 and 50% A2- ^{15}N -EAA-OT4. Filled circles: experimental data points (signal from intramolecular natural abundance ^{13}C already deducted); solid red line: simulation curve, $r = 4.74$ Å.

The DRAWS experiments for the energy donor/acceptor pair, DFAA-OPV3 and OT4, were ran with Samples 10 (A1- ^{13}C -A2- ^{15}N -DFAA-OPV3) and 11 (A1- ^{13}C -DFAA-OT4). The average distance of neighboring ^{13}C - $^{13}\text{C}'$ pairs for Samples 10 and 11 were determined to be 4.55 Å and 4.65 Å, respectively (Figure 5.7). Both distances also agree

well with a parallel, in-register β -sheet environment. It is interesting that even though no structures with high aspect ratio were observed under TEM (0.1 wt%) for **DFAA-OT4** peptides in Chapter 4,¹⁵ the DRAWS signals obtained still support a predominantly β -sheet environment at 1 wt% hydrogels.

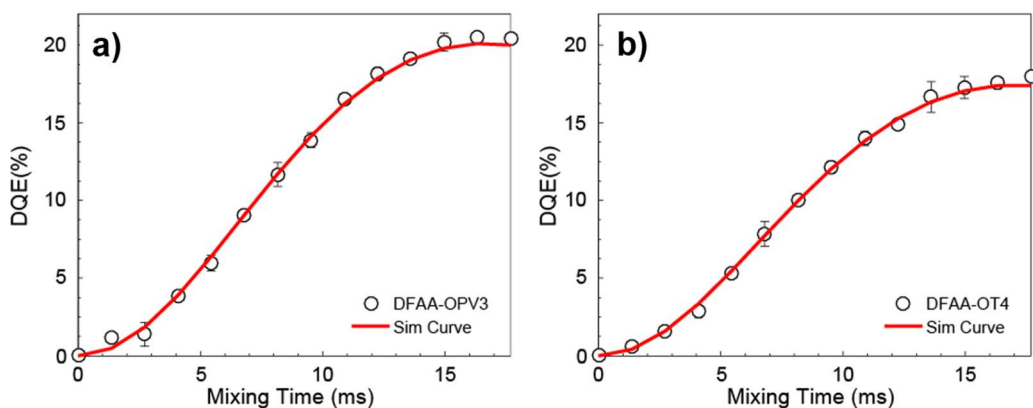


Figure 5.7. DRAWS curves for **DFAA-OPV3** and **-OT4**. (a) DRAWS of A1-¹³C-A2-¹⁵N-DFAA-OPV3; Open circles with error bar: experimental data points, solid red lines: simulation curve, $r = 4.55 \pm 0.03 \text{ \AA}$, and $t_{2, \text{SQ}} = 41.59 \pm 4.84 \text{ ms}$. (b) DRAWS of A1-¹³C-DFAA-OT4. Open circles with error bar: experimental data points, solid red lines: simulation curve, $r = 4.65 \pm 0.02 \text{ \AA}$ and $t_{2, \text{SQ}} = 26.85 \pm 1.65 \text{ ms}$.

For the mixed peptides, the major peptide components (**EAA-OT4**, **DFAA-OPV3**) were labelled with ¹⁵N at A1 while the minor peptide components (**VAVKIEAA-OT4**, **DFAA-OT4**) were labelled with ¹³C at A2. This allows the differentiation of signals from homonuclear ¹³C-¹³C' against heteronuclear ¹³C-¹⁵N dipolar coupling. For these experiments, it is important that the nominal ratios of the peptide components are maintained even after packing of the hydrogel samples within the solid-state rotor. The actual packed ratios were determined using 1-D ¹³C/¹⁵N analysis, similar to that done for one-components samples discussed above. The tabulated nominal and actual ratios for all the mixed samples are listed in Table A5.4. DRAWS experiments were ran with Samples **6**, **7**, and **8** (mixed A2-¹⁵N-EAA-OT4 and A1-¹³C-VAVKIEAA-OT4 at different

component ratios), which showed similar DRAWS build-up curves and experimental DQE values amongst all hydrogel mixtures. The simulation based on the average of curves for these three hydrogel mixtures shows a ^{13}C - $^{13}\text{C}'$ distance of 4.76 Å (Figure 5.8a). The TEDOR curves for Sample 6, with the highest A1- ^{13}C -VAVKIEAA-OT4 content, have a very low signal intensity that does even not build-up over time (Figure 5.8b). The DRAWS and TEDOR results that show very minimal interaction between ^{13}C and ^{15}N units suggest that mixing VAVKIEAA-OT4 and EAA-OT4 prefer self-sorted structures or aggregated blocks of each component within each 1-D assembled stack over isolation of the monomer units. In addition, this shows that the co-mixing behavior between these peptides of different lengths does not strongly support the isolation of minority units diluted within.

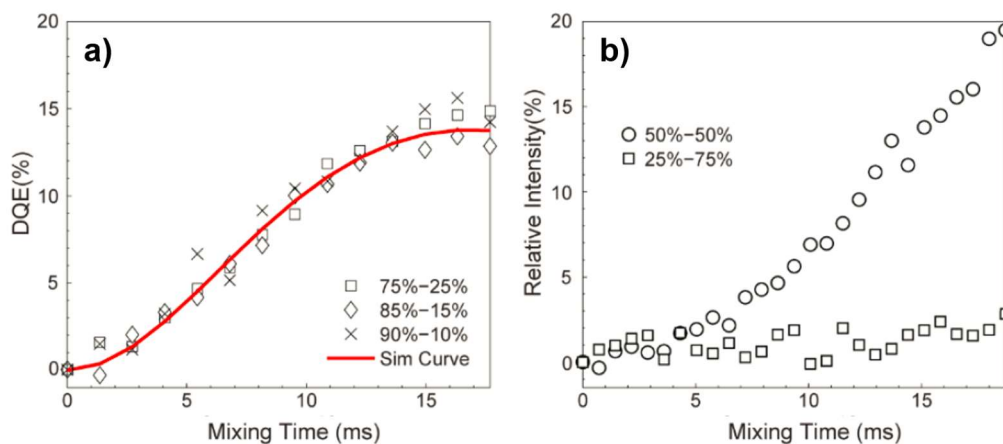


Figure 5.8. DRAWS and TEDOR curves of mixed **EAA-** and **VAVKIEAA-OT4**. (a) DRAWS curves: square, diamond and cross for samples containing 25%, 15% and 10% A1- ^{13}C -VAVKIEAA-OT4. Solid red line: simulation curve of the average DQE of the three samples, assuming all the DRAWS signals were from either self-sorted structures or aggregated blocks of **VAVKIEAA-OT4** supramolecular structure; $r = 4.765 \pm 0.048$ Å and $t_{2, \text{SQ}} = 16.78 \pm 1.57$ ms. (b) TEDOR of 75% A2- ^{15}N -EAA-OT4 mixed with 25% A1- ^{13}C -VAVKIEAA-OT4 (square) and 50% A1- ^{13}C -EAA-OT4 mixed with 50% A2- ^{15}N -EAA-OT4 (circle).

DRAWS experiments were also conducted for Samples 13 and 14 (mixed samples of A2- ^{15}N -DFAA-OPV3 and A1- ^{13}C -DFAA-OT4, Figure 5.9a) under similar conditions

as the experiments performed with Samples **6** to **8**. For both **13** and **14**, the experimental DQE values (77% for **13** and 79% for **14**) were higher than the calculated DQE values (Table A5.3). These DQE values suggest a homogenous incorporation of the dopant acceptor units that are in close proximity with the donor units of supramolecular stacks that forms upon acidification. From these data, 27% and 22% of A1-¹³C-DFAA-OT4 units in Samples **13** and **14**, respectively, are completely incorporated or coassembled with A2-¹⁵N-DFAA-OPV3 (with ~8% and ~2% OT4 units in the final mixed nanostructures). Using the data from TEDOR experiments (Figure 5.9b), 18% and 16% of A1-¹³C-DFAA-OT4 units are incorporated within the supramolecular stacks of Samples **13** and **14**, respectively, with ~5% and ~2% OT4 units in the final mixed nanostructures. The detected extent of OT4-peptide incorporation is lower in the TEDOR experiments that with DRAWS, possibly due the distortion of signal attenuation influenced by the differences in the aromatic cores of donor and acceptor peptides when ran with TEDOR sequence.

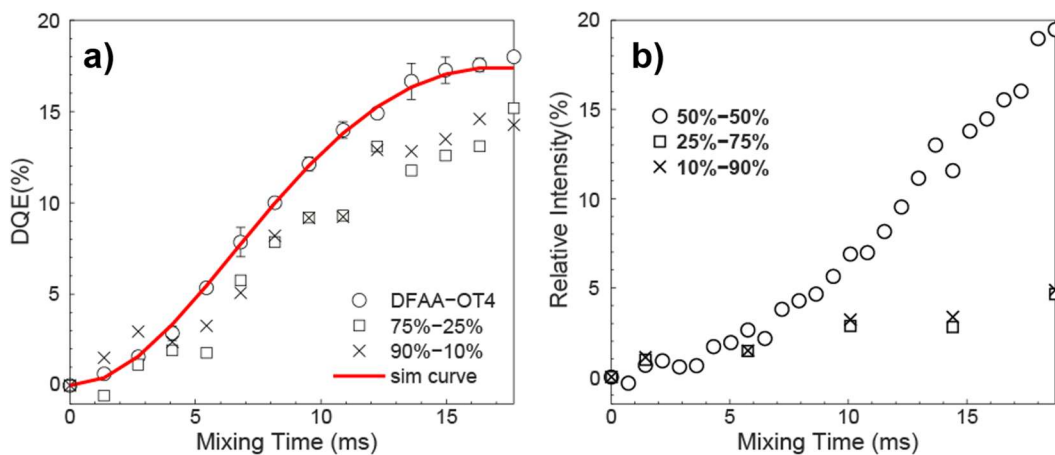


Figure 5.9. DRAWS and TEDOR curves of mixed **DFAA-OPV3** and **-OT4**. (a) DRAWS build-up curves, white circle with error bar: pure A1-¹³C-DFAA-OT4; square for 75:25; cross for 90:10; solid red line: simulation curve; $r = 4.654 \pm 0.025 \text{ \AA}$, and $t_2, \text{SQ} = 26.854 \pm 1.652 \text{ ms}$. (b) TEDOR build-up curves in comparison with mixed 50:50 A1-¹³C-EAA-OT4 and A2-¹⁵N-EAA-OT4 (circle).

Comparing the data for the binary peptide pairs coassembled herein, the ssNMR studies show that under the hydrogelation conditions used for both systems, the donor-acceptor pair shows a higher extent of “dopant” peptide incorporation within the supramolecular stacks of the majority donor peptide component. This suggests that peptide length matters for the extent of co-incorporation of two peptides within a nanostructure, which particularly shows that the peptide pairs with dissimilar lengths (*i.e.*, **EAA-** and **VAVKIEAA-OT4**, in this case) prefers to exist as self-sorted structures or aggregated structures (Figure 5.10a). On the other hand, the donor-acceptor **DFAA-OPV3** and **-OT4** peptide pair, with more comparable monomer unit lengths, has a higher extent of OT4-peptide incorporation in an isolated manner, but does not eliminate the probability of coexisting self-sorted or aggregated structure due to the complex nature of multicomponent supramolecular assemblies that are complex¹⁸ and polymorphic in nature (Figure 5.10b). From the steady-state and time-resolved photoluminescence studies in Chapter 4,¹⁵ we can conclude that the coassembled (either aggregated or isolated dopants within) structures are more predominant than the self-sorted structures for the DFAA peptide mixtures.

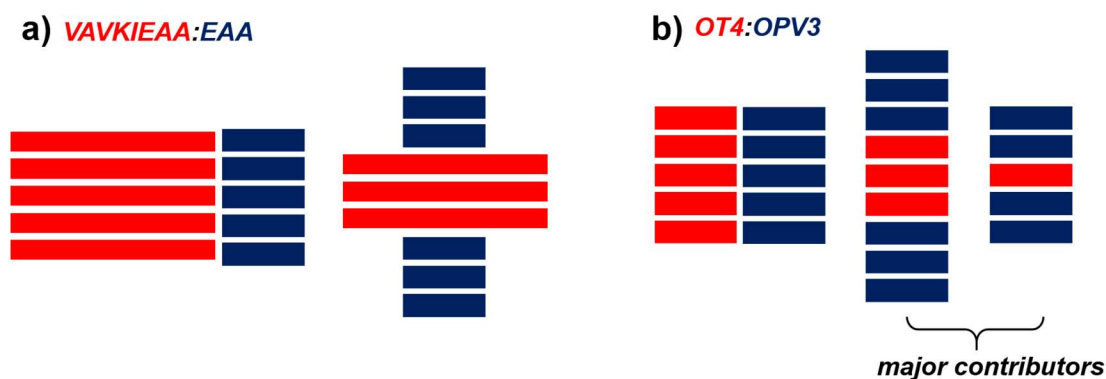


Figure 5.10. Schematic representation of structural contributors for mixed two-component π -conjugated peptides with different (a) and similar (b) monomer lengths, as assessed from the ssNMR experiments.

To the donor-acceptor peptide pair (**DFAA-OPV3** and **-OT4**) that exhibits a better extent of coassembly than the peptide coassembly pair with different lengths, both the solution phase (0.2 wt%) and hydrogel phase (1 wt%) samples were further studied with SANS. At 0.2 wt%, the samples exist as homogenous solutions with peptidic nanostructures that form upon acidification. On the other hand, at 1 wt%, the solutions can afford the formation of self-supporting hydrogels upon acidification (Figure A5.23). In order to distinguish between the donor and acceptor units studied here, the outer thiophene units of the **DFAA-OT4** peptide were deuterated (Figure 1, **DFAA-OT4 (d₄)**). Deuterium has a higher scattering length density than hydrogen and thus, deuteration of one component creates a contrast between the scattering due to the deuterated and non-deuterated components. To achieve contrast variation between the components, three different solvent systems were used: H₂O, D₂O and 40% D₂O in H₂O. By individually calculating the neutron scattering length of the deuterated core and peptide flanking regions of **DFAA OT4 (d₄)**, the maximum contrast matching of the flanking regions was determined to occur if the solvent system is 40% D₂O. The accessible scattering vector (*Q*) range of the EQ-SANS instrument used was $0.002 \text{ \AA}^{-1} < Q < 1.4 \text{ \AA}^{-1}$ (~0.2 to 150 nm to scales), which should be sensitive to both the cross-sectional nature of the fibrillar-like nanostructures as well as higher-order aggregation lengths. By imposing model fits onto these curves, we expect to obtain data on the nature of structural shapes, dimensions, effect of temperature variation and the aggregation length of the acceptor clusters as we vary its percent composition with respect to the donor. The scattering curves collected from both solution (0.2 wt%) and gel phase (1 wt%) of one-component samples are presented in Figure 5.11. Both of the generated experimental curves fit a a shape-independent Guinier-

Porod model and a shape-dependent model based on a parallelepiped structure, unless otherwise specified below. In these models, it should be considered that the calculated dimensions do not only correspond to a single stack of self-assembled peptides. The aggregate structures comprised of laterally bundled stacks due to “interfibril association” (as discussed in Chapter 2, Figure 2.2) should also be considered.

For the pure peptide samples, the non-deuterated **DFAA-OPV3** and **DFAA-OT4** (**H**) ideally achieves the highest scattering intensity if the solvent is D₂O. Both samples showed curves under basic conditions at D₂O with only predominant features at higher Q region, suggesting that at the concentrations used for these runs, the system still affords some aggregation even at high pH. The samples showed peak features at the lower Q values (~μm scales) that can be attributed to larger aggregates or bundles of fibrillar-like nanostructures. Applying the Guinier-Porod model, the calculated radius of gyration (R_g) are still lower for the basic solutions than in the acidic (Figure A5.24). To correlate to the size dimension of the scattering aggregates, we can assume a thin rod shape model where $R_g = \text{length}/\sqrt{12}$.¹² Using a shape-dependent model (parallelepiped), the dimensions of the aggregates can also be approximated (Table A5.5). Figure 5.11 shows the scattering curves overlaid with the fits using the parallelepiped model, and the values for the calculated dimensions when the longest axis is fixed to 4000 Å (chosen to be much longer than the maximum accessible size for the SANS configuration used) are tabulated in Table 5.5. These values suggest that interfibril bundling occurs because the *a* parameter (~3-5 nm) is consistent with the molecular lengths of a single peptide monomer while the *b* parameter can be correlated to the bundling length. Figure 5.12 shows an idealized assembly model based on the parallelepiped fit for these peptides.

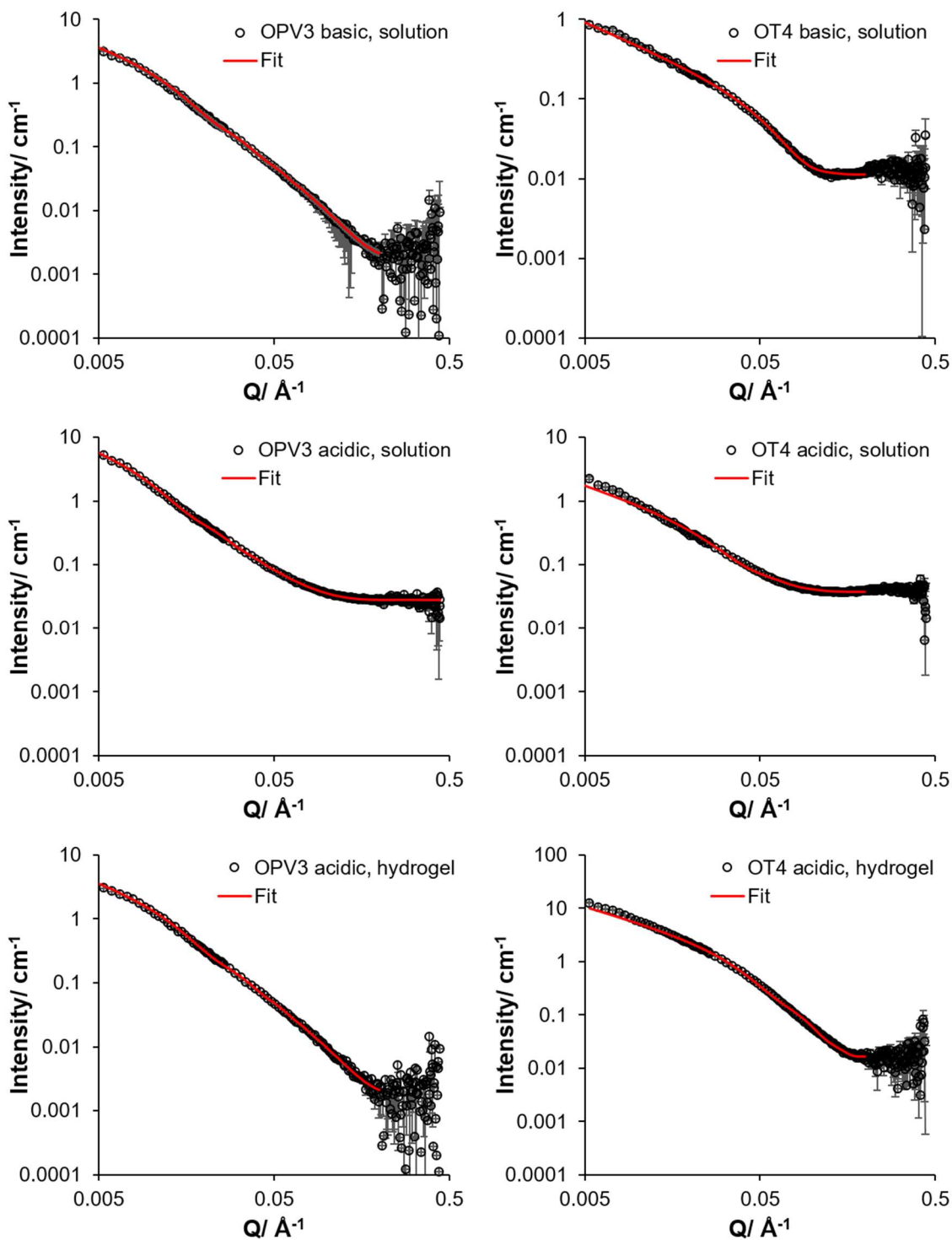


Figure 5.11. SANS curves for DFAA-OPV3 and DFAA-OT4 (*H*) at 0.2 wt% and 1 wt% solutions in D₂O. Data fitting was done with a parallelepiped model.

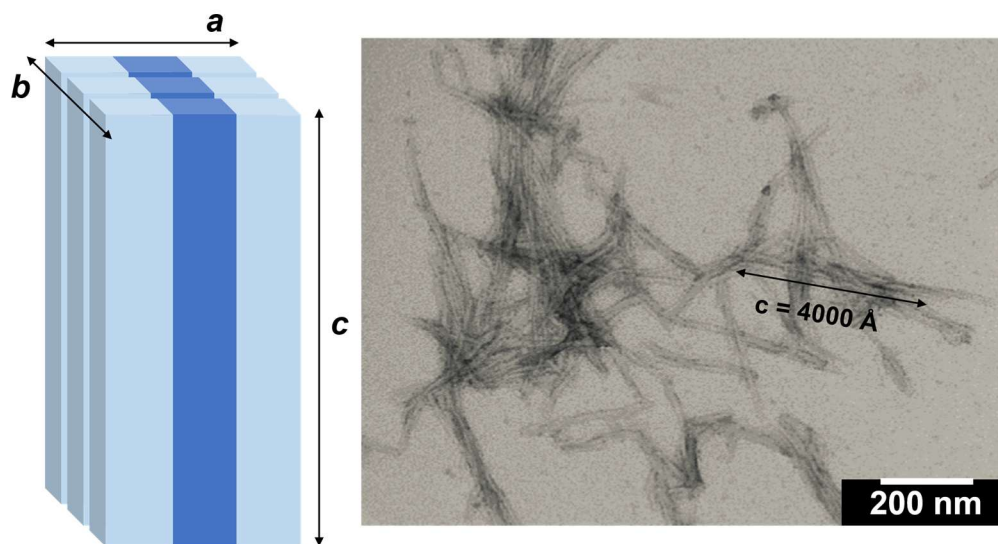


Figure 5.12. An idealized parallelepiped model for the assembly of DFAA- π peptides; correlated with a representative TEM image for **DFAA-OPV3** whereby the longest axis for the fitting curves was fixed to 4000 Å.

Pair-distribution analysis was performed (Figure 5.9) for the samples ran in 40% D₂O to obtain a histogram of atomic correlations and investigate the correlation distances between the deuterated **DFAA-OT4 (d₄)** units. Although the 40% D₂O solvent system creates the highest contrast between the deuterated and non-deuterated regions, it should be considered that it has the lowest signal-to-noise ratio amongst the solvents used for the neutron scattering runs. From these data, the highest distribution of correlation distances occurs at ~ 10 Å can be associated to interfibril distances, with the maximum distances at ~ 160 Å. The calculated overall R_g for these samples range from ~ 60 -70 Å except for the 25 mol% **DFAA-OT4 (d₄)**. Using the ~ 4.5 Å inter-monomer distances calculated from the ssNMR experiments, and the estimated 160 Å maximum linear dimension, a maximum scenario of up to 35 peptide units within a given OT4 aggregate cluster are approximated. Considering that the SANS experiments provide data that represent a statistical average of

the sample, these results show that the some small aggregates or clustered regions of the deuterated units exist within **DFAA-OPV3** nanostructures which appear to predominate over the isolation of **DFAA-OT4 (d4)**. As discussed in Chapters 3 and 4, the complex behavior of multicomponent assemblies does not eliminate the existence of isolated OT4 peptide units and is further supported by the existence of a small distribution for large correlation distances at ~ 160 Å. The parallelepiped fits for these samples can be found in Figure A5.25.

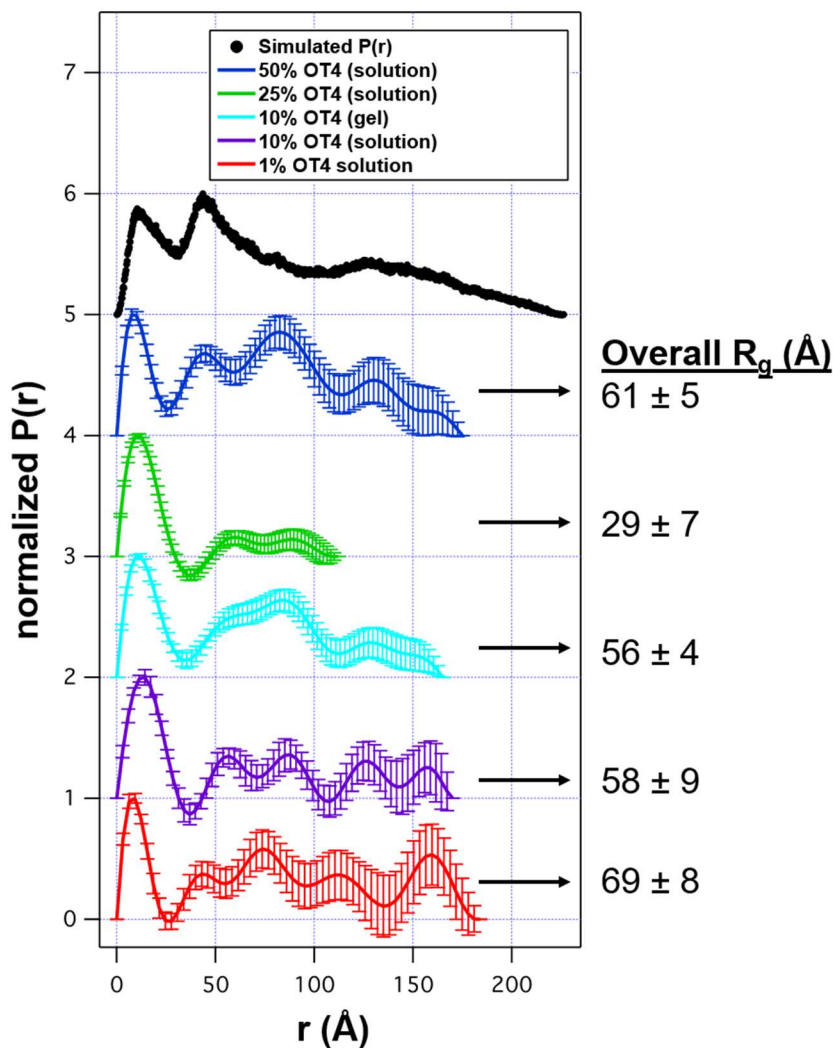


Figure 5.13. Histogram of atomic correlations from pair-distribution analysis for peptide samples in 40% D_2O . The y-axis is shifted for each sample for clarity.

Lastly, at 10 mol% **DFAA-OT4** where we previously observed the complete quenching of higher energy emission bands from **DFAA-OPV3** based on steady-state and lifetime photoluminescence studies,¹⁵ temperature variation experiments were conducted in both gel and solution phase (Figure A5.26). These experiments interestingly show an increasing trend in R_g for the 1 wt% hydrogel samples. These are consistent with the photoluminescence investigations whereby thermal annealing does not result to nanomaterial dissolution but only decreases the energy transfer efficiency. Further simulations are ongoing to possibly quantify the energy transfer distances in relation to the aggregated OT4 units within OPV3 nanostructures.

Table 5.2. Different R_g values calculated from Guinier-Porod model fits at different temperatures; all under acidic conditions.

	10% OT4 (<i>d_t</i>), 0.2 wt%	10% OT4 (<i>H</i>), 0.2 wt%	10% OT4 (<i>d_t</i>), 1 wt%	10% OT4 (<i>H</i>), 1 wt%
5 °C	114.8	107.0	90.5	95.3
37 °C	110.0	117.9	90.4	95.9
60 °C	106.0	120.1	94.8	98.4
80 °C	137.1	126.4	99.4	104.0

Conclusions

In this Chapter, solid state nuclear magnetic resonance spectroscopy and small-angle neutron scattering techniques were employed to further understand the assembly behavior and structural outcomes of a two-component peptide mixture when coassembled within nanostructures. The ssNMR experiments shed light as to how matching the lengths of the peptide coassembly pair matters towards the preference of the components to self-sort or co-mix. These experiments also provided structural information on a molecular

scale, verifying the polymorphic β -sheet nature of the assemblies and the inter-monomer distances within the supramolecular polymers that form upon rapid acidification. Correlating these distances and the pair-distribution correlation analyses using SANS, aggregate or cluster formation of OT4 units within OPV3 are determined as the more statistically predominant assembly preference for these donor-acceptor. Experiments as such will help inform future coassembled optoelectronic peptide designs, specifically for controlling the surface presentation of bioactive epitopes in 1-D multicomponent nanomaterials or understanding distance-dependent energy transport mechanisms.

Experimental Details

Peptide synthesis. All peptides reported here were synthesized using solid-phase peptide synthesis, followed by on-resin coupling of the π -electron unit to the peptide *via* Pd-catalyzed cross coupling reactions or *via* amidation with the appropriate diacid, according to our previous reports. Details of the synthesis and purification methods can be found in the Appendix. The isotope-labeled derivatives of **EAA-OT4**, **DFAA-OPV3** and **DFAA-OT4** were synthesized by coupling with ^{13}C - and ^{15}N -labeled Fmoc-Ala (Cambridge Isotope Laboratories).

Sample preparation. Aqueous stock solutions (0.1 wt% or 1 wt% total peptide content) were prepared from lyophilized and HPLC purified peptides. The pH of the stock solutions were adjusted to ~ 8 by incremental addition of 1 M KOH solution. From these stock solutions, the co-assemblies were prepared by mixing each peptide component at the appropriate molar ratio, followed by the incremental addition of 1 M HCl (until *ca.* pH 2-3). The solution phase assemblies were prepared from 0.1 wt% stock solutions while the

hydrogels were prepared from 1 wt% samples. Formation of self-supporting hydrogels are shown in Figure A5.23. For the ssNMR experiments, the hydrogels were centrifuged at 100,000 rpm (541,000 g) in a TLA 100.3 rotor using Optima MAX-XP ultracentrifuge (Beckman Coulter, Inc. Brea, CA) for 2 h to a pellet. The pellet was then transferred directly into a 3.2 mm, 36 μ L solid-state NMR rotor by a scoop and then pressed by a metallic rod. For each run, the rotor contains ~5-10 mg of sample. For the SANS experiments, solution phase samples were loaded in a 1 mm pathlength circular-shaped quartz cuvettes (Hellma USA, Plainville, NY) while the hydrogels were loaded onto demountable titanium cells with circular quartz windows and also 1 mm pathlength. The total sample volume for each condition was 400 μ L.

2,5-dibromothiophene-d₂. Thiophene-d₄ (CDN Isotope Labs; 0.50 g, 5.7 mmol) was stirred with *N*-bromosuccinimide (2.12 g, 11.9 mmol) in glacial acetic acid (2.90 mL) for 80 minutes at room temperature followed by sonication for 5 minutes. The mixture was diluted with diethyl ether and washed with 1 M sodium hydroxide and water, then dried over magnesium sulfate. The solvent was removed *in vacuo* to provide 0.96 g of the oil product (3.9 mmol, 70%). ¹³C NMR (400 MHz, CDCl₃) δ , ppm: 130.2 (t, *J*= 106 Hz), 111.6 (t, *J*= 10 Hz).

5-bromothiophene-2-carboxylic acid-d₂. 2,5-dibromothiophene-d₂ (0.86 g, 3.5 mmol) was dissolved with THF (18 mL) in a flame-dried Schlenk flask under N₂. The solution was purged with N₂ for 15 minutes while the reaction vessel was cooled to -78 °C. Then, *n*-butyllithium (1.63 M solution in hexanes, 3.9 mmol, 2.4 mL) was added dropwise. The solution was allowed to stir at -78 °C for 1 h. Dry ice (approx. 10 g) was added to the reaction mixture, and was allowed to stir and return to room temperature for 19 h under N₂.

The light brown suspension was filtered and the solids were stirred in 2 M HCl for 1 h. The suspension was filtered to yield a light brown solid (0.27 g, 37%). The sample was not purified prior to peptide coupling. ^{13}C NMR (400 MHz, DMSO) δ : 162.0 (s), 136.3 (s), 133.7 (t, $J= 106.4$ Hz), 131.6 (t, $J= 102.8$ Hz), 118.9 (s). MS (ESI⁺) m/z 208.9 (M+H⁺) (calc. 208.92).

EAA-OT4. Prepared according to literature procedure; *see Chapter 2.*

A1- ^{13}C -VAVKIEAA-OT4. Solid-supported Wang-VAVKIEAA-NH₂ peptide *N*-acylated with 5-bromothiophene-2-carboxylic acid was prepared (0.50 mmol). The peptide was coupled with 5,5'-bistributylstannyl-[2,2']-bithiophene (0.25 mmol, 0.19 g) in the presence of Pd(PPh₃)₄ (0.020 mmol, 0.023 g) using the general on-resin Stille coupling procedure for 15 h. Resin was then subjected to the general cleavage procedure. The isotope-labeled derivative was coupled with ^{13}C -Fmoc-Ala (Cambridge Isotope Laboratories). Crude peptide was obtained as an orange powder ($\lambda_{\text{max}}=418$ nm, pH=8, 0.054 g, 11%) MS (ESI⁻) m/z 990.9 ((M+2H⁺)/2) (calc. 990.5).

DFAA-OPV3. Prepared according to literature procedure; *see Chapter 4.*

DFAA-OPV3. Prepared according to literature procedure; *see Chapter 4.*

DFAA-OT4(d₄). Solid-supported Wang-DFAA-NH₂ peptide *N*-acylated with 5-bromothiophene-2-carboxylic acid (d₂) was prepared (0.5 mmol). The peptide was coupled with 5,5'-bis-tributylstannyl-[2,2']-bithiophene (0.25 mmol, 0.186 g) in the presence of Pd(PPh₃)₄ (0.02 mmol, 0.023 g) using the general on-resin Stille coupling procedure. The resin was then subjected to the general cleavage procedure. Crude peptide was obtained as an orange powder ($\lambda_{\text{max}}=416$ nm at pH=8; HPLC purified, 17.4 mg, 6%). MS (ESI⁻) m/z 1229.6 (M-H⁺) (calc. 1229.3), m/z 614.5 ((M-2H⁺)/2) (calc. 614.2).

Solid-state NMR (ssNMR) experiments. All ssNMR experiments except were carried out with a Varian wide bore 500MHz spectrometer, equipped with a three channel BioMAS probe, operating at the frequencies of 499.8 MHz for ^1H , for 125.7 MHz ^{13}C and for 50.6 MHz for ^{15}N . All measurements were taken at 4 °C. The magic angle spinning (MAS) rate was at 5, 882 Hz for DRAWS and 11, 111 Hz for all the other experiments. The contact time for all 1-D cross polarization (CP) experiments was 1.2 ms. The ^1H - ^{13}C CP experiments used 61 kHz on ^1H and 50 kHz on ^{13}C , at 11, 111 Hz MAS rate; 56 kHz on ^1H and 50 kHz on ^{13}C at 5, 882 Hz MAS rate. The ^1H - ^{15}N CP used 50.0 kHz on ^1H and 38.9 kHz on ^{15}N . The 2nd CP on 2D NCO used continuous wave (CW) pulses of 38.9 kHz on ^{15}N and 50.0 kHz on ^{13}C for 4 ms. ^1H CW decoupling frequency was at 100 kHz for DRAWS and TEDOR mixing time, and two-pulse phase-modulated (TPPM) decoupling frequency was at 71 kHz during acquisition. Recycle delay was 2.5s. Simulation of DRAWS and TEDOR curves were run on SPINEVOLUTION program,¹⁹ with explicit chemical shift anisotropy (CSA) values. For DRAWS, a 5-spin model was used, wherein five ^{13}C nuclei arrange in a straight line with equal distance between any two neighboring nuclei. The experimental data was fit for both the separation and single transverse relaxation time constant. For TEDOR, a 3-spin model was used, wherein the middle spin is ^{13}C , and it can have one or two neighboring ^{15}N spin(s) in one of or both its upper and lower neighboring monomer. The inter-monomer distance was increased step-by-step, with the distance between ^{13}C to ^{15}N changing according to the aforementioned model and the generated simulation curves. Transverse relaxation time constant was measured by spin echo experiment. The “relaxation-free” experimental data was least-square-fit to the simulation curves.

Small-angle neutron scattering (SANS) measurements. The SANS experiments were performed with the Extended Q-Range Small Angle Neutron Scattering Diffractometer (EQ-SANS, BL-6) at the Spallation Neutron Source in Oak Ridge National Laboratory (Oak Ridge, TN). The instrument was operated with a sample-to-detector distance of 4 m and in 30 Hz mode to achieve two wavelength bands (2.5-6.1 and 9.4-13.4 Å) to cover a broad Q range from about 0.004 to 0.4 Å⁻¹.²⁰ Scattered neutrons were detected with a 1 × 1 m two-dimensional position-sensitive detector with 192 × 256 pixels. All measurements were performed at 25 °C, unless otherwise stated. For solution phase samples that are heated, a rotating tumbler was used to maintain a homogenous sample distribution within the cuvettes because of sample aggregation that occurs due to thermal annealing. Data reduction followed standard procedures using MantidPlot.²¹ The measured scattering intensity was corrected for the detector sensitivity and scattering contribution from the solvent and empty cells, and then placed on absolute scale using a calibrated standard.²² Data fitting for all SANS curves was performed with SasView 3.0.0.²³ The scattering length densities (ρ) of the peptides were calculated using the MULCH program.²⁴ The pair distance distribution function, $P(r)$, was calculated from the scattering intensity, $I(Q)$, using the indirect Fourier transform method implemented in the GNOM program.²⁵ The $P(r)$ function was set to zero for $r = 0$ and $r = D_{max}$, the maximum linear dimension of the scattering object. D_{max} was explored to optimize the $P(r)$ solution and excellent quality solutions were found in each case. The $P(r)$ solution to the scattering data yielded the real-space radius of gyration, R_g , and scattering intensity at zero angle, $I(0)$.

Portions of this chapter were adapted in part from:

- Qi, Z. “Peptide and Protein Supramolecular Assemblies Studied by Solid-State NMR Spectroscopy” (Ph.D. Dissertation), Ohio State University, 2017.

Acknowledgements

All the solid state NMR experiments were performed by Zhe Qi in the group of Professor Christopher Jaroniec (Ohio State University). A portion of this research at the Spallation Neutron Source of Oak Ridge National Laboratory (ORNL) was sponsored by the Scientific User Facilities Division, Office of Basic Energy Sciences, U.S. Department of Energy. These small-angle neutron scattering experiments, along with the data analyses, were performed with the help of Dr. Christopher B. Stanley. Training and access for the ORNL facilities were obtained through the National School on Neutron and X-ray Scattering (2015).

References

- (1) Safont-Sempere, M. M., Fernández, G., and Würthner, F. (2011) Self-sorting phenomena in complex supramolecular systems. *Chem. Rev.* *111*, 5784-5814.
- (2) Görl, D., Zhang, X., Stepanenko, V., and Würthner, F. (2015) Supramolecular block copolymers by kinetically controlled co-self-assembly of planar and core-twisted perylene bisimides. *Nat. Commun.* *6*, 7009.
- (3) Morris, K. L., Chen, L., Raeburn, J., Sellick, O. R., Cotanda, P., Paul, A., Griffiths, P. C., King, S. M., O'Reilly, R. K., Serpell, L. C., and Adams, D. J. (2013) Chemically programmed self-sorting of gelator networks. *Nat. Commun.* *4*, 1480.
- (4) Draper, E. R., Eden, E. G. B., McDonald, T. O., and Adams, D. J. (2015) Spatially resolved multicomponent gels. *Nat. Chem.*, *7*, 848-852.
- (5) Yu, G., Yan, X., Han, C., and Huang, F. (2013) Characterization of supramolecular gels. *Chem. Soc. Rev.* *42*, 6697-6722.

- (6) da Silva, R. M. P., van der Zwaag, D., Albertazzi, L., Lee, S. S., Meijer, E. W., and Stupp, S. I. (2016) Super-resolution microscopy reveals structural diversity in molecular exchange among peptide amphiphile nanofibres. *Nat. Commun.* 7, 11561.
- (7) Onogi, S., Shigemitsu, H., Yoshii, T., Tanida, T., Ikeda, M., Kubota, R., and Hamachi, I. (2016) In situ real-time imaging of self-sorted supramolecular nanofibres. *Nat. Chem.* 8, 743-752.
- (8) Pochan, D. J., Pakstis, L., Ozbas, B., Nowak, A. P., and Deming, T. J. (2002) SANS and cryo-TEM study of self-assembled diblock copolypeptide hydrogels with rich nano-through microscale morphology. *Macromolecules* 35, 5358-5360.
- (9) Cardoso, A. Z., Mears, L. L. E., Cattoz, B. N., Griffiths, P. C., Schweins, R., and Adams, D. J. (2016) Linking micellar structures to hydrogelation for salt-triggered dipeptide gelators. *Soft Matter* 12, 3612-3621.
- (10) Hule, R. A., Nagarkar, R. P., Hammouda, B., Schneider, J. P., and Pochan, D. J. (2009) Dependence of self-assembled peptide hydrogel network structure on local fibril nanostructure. *Macromolecules* 42, 7137-7145.
- (11) Hule, R. A., Nagarkar, R. P., Altunbas, A., Ramay, H. R., Branco, M. C., Schneider, J. P., and Pochan, D. J. (2008) Correlations between structure, material properties and bioproperties in self-assembled β -hairpin peptide hydrogels. *Faraday Discuss.* 139, 251-264.
- (12) Guilbaud, J.-B., and Saiani, A. (2011) Using small angle scattering (SAS) to structurally characterise peptide and protein self-assembled materials. *Chem. Soc. Rev.* 40, 1200-1210.
- (13) Rao, S. S. and Winter, J. O. (2009) Adhesion molecule-modified biomaterials for neural tissue engineering. *Front. Neuroengineering* 6, 1-14.
- (14) Tashiro, K., Nagata, I., Yamashita, N., Okazaki, K., Ogomori, K., Tashiro, N., and Anai, M. (1994) A synthetic peptide deduced from the sequence in the cross-region of laminin A chain mediates neurite outgrowth, cell attachment and heparin binding. *Biochem. J.* 302, 73-79.
- (15) Ardoña, H. A. M. and Tovar, J. D. (2015) Energy transfer within responsive π -conjugated coassembled peptide-based nanostructures in aqueous environments. *Chem. Sci.* 6, 1474-1484.
- (16) Thurston, B. A., Tovar, J. D., Ferguson, A. L. (2015) Thermodynamics, morphology, and kinetics of early-stage self-assembly of π -conjugated oligopeptides. *Mol. Simul.* 42, 955-975.

- (17) Wall, B. D., Zhou, Y., Mei, S., Ardoña, H. A. M., Ferguson, A. L., and Tovar, J. D. (2014) Variation of formal hydrogen-bonding networks within electronically delocalized π -conjugated oligopeptide nanostructures. *Langmuir* 30, 11375-11385.
- (18) Draper, E. R., Wallace, M., Schweins, R., Poole, R. J., Adams, D. J. (2017) Nonlinear effects in multicomponent supramolecular hydrogels. *Langmuir*, 33, 2387-2395.
- (19) Veshtort, M., and Griffin, R. G. (2006) SPINEVOLUTION: A powerful tool for the simulation of solid and liquid state NMR experiments. *J. Magn. Reson.* 178, 248-282.
- (20) Zhao, J. K., Gao, C. Y., and Liu, D. (2010) The extended Q -range small-angle neutron scattering diffractometer at the SNS. *J. Appl. Crystallogr.* 43, 1068–1077.
- (21) O. Arnold et al., Mantid - Data analysis and visualization package for neutron scattering and μ SR experiments. Nucl. Instruments Methods Phys. Res. Sect. A Accel. Spectrometers, Detect. Assoc. Equip. 764, 156–166 (2014).
- (22) G. D. Wignall, F. S. Bates, Absolute calibration of small-angle neutron scattering data. *J. Appl. Crystallogr.* 20, 28–40 (1987).
- (23) <http://www.sasview.org/>
- (24) A. E. Whitten, S. Cai, J. Trehella, MULCh: Modules for the analysis of small-angle neutron contrast variation data from biomolecular assemblies. *J. Appl. Crystallogr.* 41, 222–226 (2008).
- (25) D. I. Svergun, Determination of the regularization parameter in indirect-transform methods using perceptual criteria. *J. Appl. Crystallogr.* 25, 495–503 (1992).

CHAPTER SIX:

Aligned Bioscaffolds with π -Conjugated Systems for
Electrosensitive Cells

Introduction

In the previous Chapters, different aspects of the development of synthetic optoelectronic peptidic nanomaterials are discussed—from the material properties at different length scales, design strategies that yield energy transport, up to the photophysical and structural studies of coassembly behavior. Inspired by the growing interest to develop innovative soft materials for tissue engineering, this Chapter will present the efforts made towards the translation of these peptidic materials and related π -conjugated polymers as aligned biological scaffolds that are robust under cell culture or physiological conditions and can potentially impart physicochemical and optoelectronic stimuli to the cells interfaced with them.

Tissue repair, replacement or regeneration caused by associated diseases, injury or trauma poses a longstanding clinical challenge that requires intense research efforts from multiple fields of discipline. Failure at the tissue or organ-level is in fact a major health problem in the United States that accounts for half of the country's healthcare expenditures since early 1990's.¹ Current treatments involve transplanting a tissue from one site to another in the same patient (*autograft*) or from one individual to another (*allograft* or *transplant*). For years, such treatments have been the standard; however, the procedure is typically expensive, painful, causes donor-site morbidity (for autografts) or presents the risk of host rejection (for allografts).² The field of tissue engineering, despite the several advancements and developments over the past decade, continuously aims to address such and other related biomedical challenges by combining cells from the body with accurately engineered porous scaffold that can mimic the natural niche of cells and provide a template

for tissue regeneration (Figure 6.1).³ The use of scaffolds in tissue engineering, or biological scaffolding, has been proven to be important in manipulating cell function, guiding the formation of new tissue structures, and promoting cell differentiation.^{2,4} The morphology, porosity and topography of the scaffold plays a critical role in the physiological response of the cells or tissues regrowing within.⁵⁻⁸ By merging engineering approaches to biological principles, tissue engineering remains essential nowadays for providing revolutionary materials that addresses the rapidly growing needs of patients that suffer from the debilitating damages of tissue or organ impairment.

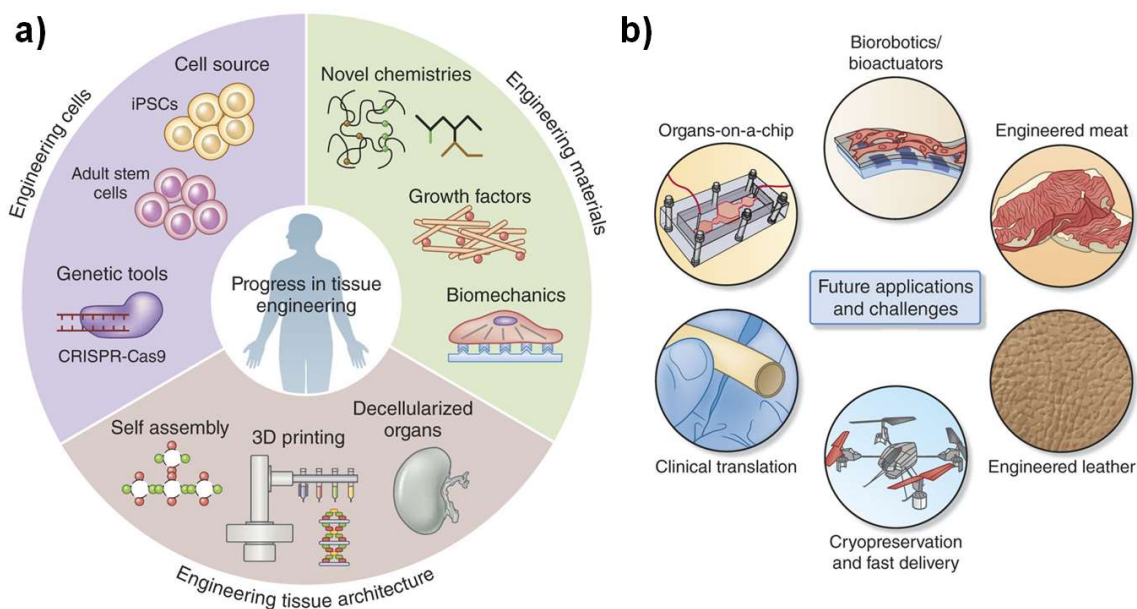


Figure 6.1. Schematic diagrams summarizing a) the progress in the field of tissue engineering for the past decade, b) its future, and the different ongoing challenges. Adapted from Ref 3.

This Chapter will present materials that can be used as a biological scaffold and consequently have the potential to facilitate electrical conduction or energy propagation when interfaced with cells—whether by application of voltage bias or light stimulation. Beyond mimicking the natural environment of cells, engineered scaffolds along with the

stimuli that they impart aims to accelerate tissue regrowth and improve cellular behavior. Electrically conducting bioscaffolds are particularly helpful for the regrowth and maturation of electrosensitive cells such as neurons or regenerating damaged nerves, because electrical stimulation treatments⁹⁻¹² have been shown to modulate nerve activity, induce cell adhesion and differentiation, and upregulate neurotrophic factors to accelerate axonal outgrowth.¹³⁻¹⁵ Treatments as such are important because axons in the central nervous system (CNS) do not regrow spontaneously while those in the peripheral nervous system (PNS) regenerate very slowly.¹⁶ Furthermore, this spontaneous regeneration in the PNS is limited to small gaps, and is not the case for large nerve defects that are more debilitating.^{17,18} The rate of axonal outgrowth under *in vitro* and *in vivo* conditions is a critical parameter for the improvement of functional recovery from a nerve injury. Therefore, there is a need to continuously develop methods for accelerating axonal regeneration that can provide the aforementioned benefits from electrical stimulation while minimizing the perturbation of the natural cell environment.

Since the pioneering report of Langer and co-workers on the stimulation of neuron-like PC-12 cells seeded on polypyrrole (PPy)-coated substrates,¹² numerous reports were then published showing the positive response in the growth and function of neurons when grown and stimulated on other conducting organic substrates such as polyaniline (PAni), polythiophene (PT), poly(3,4-ethylenedioxythiophene) (PEDOT) and piezoelectric polymer films [made of poly(vinylidene fluoride) or poly(vinylidene fluoride-co-trifluoroethylene)].¹⁹⁻²² Among these, polypyrrole is the most extensively used conducting polymer for biological interfacing due to its excellent environmental stability, mechanical properties, high conductivity, biocompatibility and ease of preparation in aqueous

solutions.^{23,24} The use of conducting scaffolds are also relevant for muscle or cardiac tissue regeneration, and in restoring the function of tissues in limb, bladder and bowel.²⁵ Table 6.1 presents the conductivities of some electrically conducting polymers currently used as a processed hydrogel for bioscaffolds.

Table 6.1. Common electrically conducting polymers used in tissue engineering.²⁶

Polymer*	Conductivity (S/cm)
PAni-PAMPS	1.3×10^{-3}
PAni-polyacrylate	2.3×10^{-3}
PAni-PAAm	0.62
Aniline tetramer-PLA-PEG-PLA	4.7×10^{-7} - 1.1×10^{-4}
PAni-PVA	9.7×10^{-5} - 1.3×10^{-4}
pPy-pHEMA composite	7.6×10^{-4}
PEDOT-PSS	4.1×10^{-3}
PEDOT-S	10^{-2} - 10^{-1}
PTAA-HClO ₄	10^{-2}

***PAni:** poly(aniline); **PAMPS:** poly(2-acrylamido-2-methyl propane sulfonic acid); **PAAm:** poly(acrylamide); **PLA:** poly(lactic acid); **PEG:** poly(ethylene glycol); **PVA:** poly(vinyl alcohol); **pPy:** poly(pyrrole); **pHEMA:** poly(hydroxyethyl methacrylate); **PEDOT-PSS:** poly(3,4-ethylenedioxythiophene)-poly(styrene sulfonate); **PTAA:** poly(3-thiopheneacetic acid)

Although it is well established that electrical stimulation positively affects neuronal behavior, the use of a physical electrode during stimulation still poses some complications when the electrodes integrate with tissues such as toxicity upon contact. One strategy is to use photocurrent-generating materials, whereby the current can be produced without the need for electrode-tissue interaction. Photocurrent therapy with using light and electrical stimulations could be an innovative and promising approach in regenerative medicine, especially for skin and nerve regeneration.²⁷ One of the photosensitive scaffolds reported in the literature is electrospun poly(3-hexylthiophene)/polycaprolactone (P3HT/PCL) composite for skin regeneration.²⁸ Figure 6.2 illustrates how the photocurrents generated by P3HT networks can influence the protein signaling cascade related to neuronal re/growth and behavior.

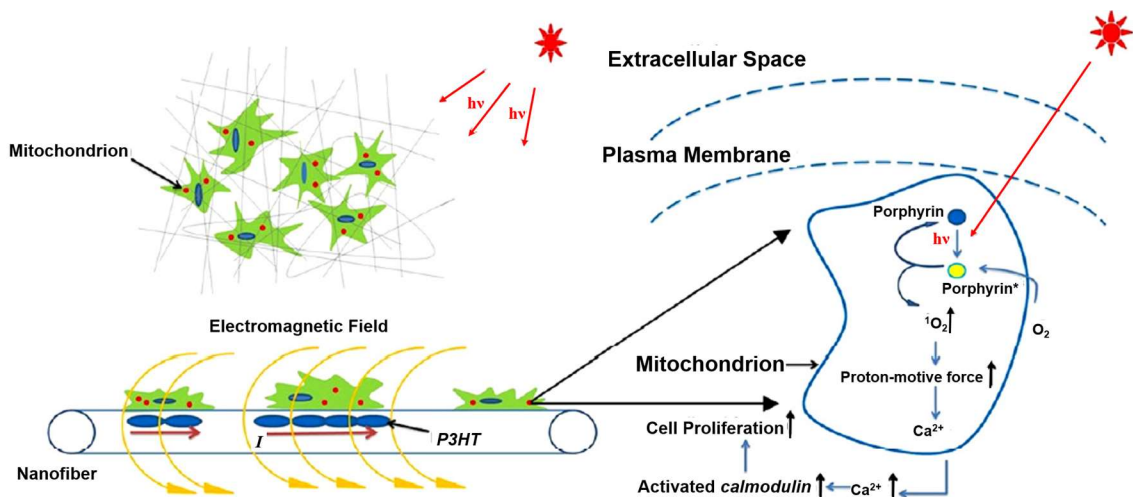


Figure 6.2. Schematic illustration of photocurrent stimulation of cells and how it affects intracellular signaling (Adapted from Ref. 27).

Similar to 2-D materials that are capable of charge transport such as graphene, photoconductive materials can afford coupling of the conductive interface to transmembrane ionic currents that leads to a local change in dipole voltage or chemical potential of the cell wall.²⁹ As Ca²⁺ ion translocates through the cell-membrane voltage-gated calcium channels, cytosolic Ca²⁺ increases which activates calmodulin. Activated calmodulin is known to promote nucleotide synthesis and cellular proliferation. Light stimulation can also excite porphyrins, which can increase the proton-motive force (PMF) by exciting triplet ground state O₂ to singlet excited O₂. This oxidant can cause the release of more Ca²⁺ to the cytoplasm from the mitochondria, leading to PMF changes.

In addition to using these organic polymers as a biological scaffolding platform for the electrical stimulation of primary neurons, neural stem cells and myocytes, flexible organic materials are also ideal as electrodes for cellular signal recording. The only difference between the electrical mode of operation for stimulation and recording is the sequence of charge movements and the smaller current magnitudes for recording.³⁰ The

charges are delivered to the electrode with a subsequent shift in the cellular membrane potential for stimulation, while it is the fluctuations in the membrane potential that causes current flux in the electrode for recording modality. In both cases, mechanical matching between the tissue-contact sites is highly important because any micromotion caused by the mismatch can lead to inflammation inside the tissue. However, some of the pure electrically conducting polymers are inherently brittle or soluble, which requires them to be processed as a composite material with other more mechanically robust polymers or with a 3-D architecture.³¹

Considering the mechanical requirements for cellular interfacing applications, hydrogels provide an attractive platform that can be interfaced with biological systems since they (1) have the ability to mimic the physical properties of tissue environments; (2) are potentially biocompatible; (3) are potentially responsive to environmental cues (*i.e.*, pH, ion concentration); (4) have the ability to store functional molecules; and (5) have controllable porosity and low mechanical modulus—making them attractive as soft tissue engineering constructs.³²⁻³⁶ For nerve regeneration purposes, the use of hydrogels as a soft material scaffold is also desirable, since the stiffness of the hydrogels must match the soft nerves that being regenerated.^{37,38} To date, peptide-based hydrogels are among the emerging scaffolds that are used for cell and tissue growth.³⁹⁻⁴² Provided that a negative immune response does not occur, the use of natural amino acids in such materials increases their potential biocompatibility as compared to those built with non-natural building blocks.⁴² Natural enzymatic degradation of peptides when implanted *in vivo* also provides a degradability aspect, the kinetics of which can be modified and tuned by non-natural modifications in the peptide backbone. Peptide hydrogels further present a biological

advantage for use as scaffolds for “soft” tissues over other standard biomaterials in terms of mechanical properties.⁴³⁻⁴⁵ This advantage corroborates with the fact that the peptide sequence is easy to synthesize (*i.e.*, given the number of standard techniques used to prepare peptides such as solid-phase synthesis), to functionalize and that the self-assembly of peptides is extensively studied to support the design of materials with specific architectures. It is worth noting that a number of peptide-based materials are also known to self-assemble or form hydrogels under aqueous conditions—further supporting the physiological relevance of this material.⁴³ The direct conjugation of peptides or having peptides as the component in a cell or tissue scaffold allows certain epitopes to be synthetically interfaced with biotic systems, thus, making the scaffolds simulate the features of extracellular matrix (ECM) which provides an *in vivo*-like environment in terms of three-dimensionality, water content, and environmental cues.

Along with mechanical matching, electrical stimulation and biochemical mimicking of ECM features, imparting topographical guidance to the cells *via* substrate alignment is another critical bioscaffold feature that can aid in cellular organization. For neurons, the recovery from the proximal to the correct distal stump of the damaged nerve is critical to achieving the correct functional recovery.^{46,47} For cardiac cells, it is vital for an artificial scaffold to recapitulate the anisotropic electromechanical environment of a healthy myocardial tissue to ensure proper electrical propagation and synchronous contraction.⁴⁸ Several examples of fibrous scaffolds as nerve guides have been reported, offering the advantage of efficient permeability of biochemical cues as well as the high surface area for cell attachment and growth.^{5,7,49,50} Stupp and co-workers showed that when neurons are encapsulated within aligned peptide hydrogels containing bioactive epitopes

such as IKVAV or RGDS, contact guidance is provided by the alignment and the neuronal outgrowth is enhanced due to the epitopes.⁵¹ As an improvement to conventional electrospinning methods to fabricate fibrous scaffolds, Mao and co-workers have developed a method to process fibrous protein hydrogels with internal alignment⁵¹ that could be more reproducible than the manual shear-flow assembly techniques such as those presented by Stupp and co-workers⁵² employed for peptide hydrogels. Among the efforts to improve electrospinning-based methods of aligned fiber scaffold formation for tissue engineering applications, Parker and co-workers have also developed several nanofiber fabrication techniques that do not require high-voltage electric fields and have high rates of production that are relevant for industrial scale-ups.⁵³⁻⁵⁵ Taken altogether, there are numerous preliminary works that show how electrosensitive cells such as neurons and cardiomyocytes benefit from electrical stimulation and topographical guidance imparted by aligned scaffolds that can also deliver specific biochemical cues in a spatiotemporal manner.

The first part of this Chapter will discuss the utility of synthetic π -conjugated peptides as a biological scaffold that can be used to influence the behavior of primary neurons, human neural stem cells and related cell types. Ideally, with our π -conjugated peptide hydrogelators, we can create macroscopically aligned hydrogels⁵⁶ with monomers that are appended with bioactive peptide sequences in the termini such as with a laminin derived IKVAV sequence (relevant for neurite outgrowth). However, the ability of π -conjugated peptide monomers to form a hydrogel is highly sequence-dependent and our model peptide, HO-VAVKIEAA-OT4 as studied in Chapter 5 (or other iterations of

IKVAV bearing OT4 monomers, do not form a hydrogel unless they are doped within the network of a known hydrogelating sequence such as **EAA-OT4** (Figure 6.3).

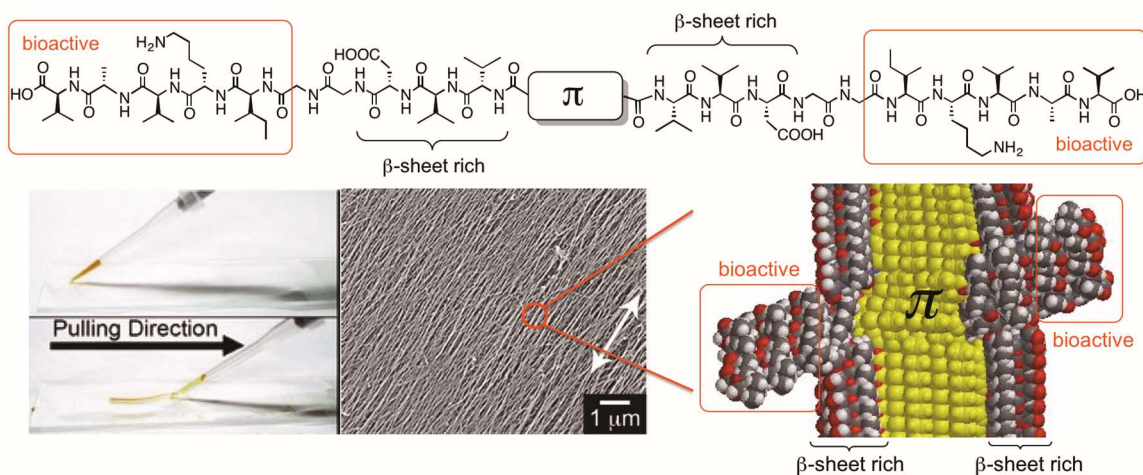


Figure 6.3. General structure of a peptide- π -peptide monomer with bioactive segment (*top*); making an aligned hydrogel by shear-flow assembly, with a representative SEM image¹⁸ showing the aligned nanostructures and an idealized molecular model of a coassembled π -conjugated peptide (*bottom*).

As these were the first efforts to bridge the synthetic aspects of the material development with *in vitro* experiments to prove the potential of these materials to perform as biological scaffolds, much of the initial efforts that will be discussed below will be geared towards creating a stable platform that does not degrade quickly under cell culture conditions. Although degradable materials are ideal for tissue regeneration, the degradation kinetics must be long enough to allow the cell or tissue to regrow before the scaffold degrades. Two approaches were taken to circumvent this issue with peptide hydrogels: (1) creating a composite material between π -conjugated peptides and a more stable aligned hydrogel platform, and (2) developing π -conjugated peptide monomers that can undergo covalent crosslinking as a post-modification after hydrogel formation *via* self-assembly.

A previous report by Wathsala Liyanage in the Tovar group⁵⁷ presented a library of quaterthiophene-bearing peptides that utilized guest molecules that can covalently crosslink the peptide monomers to ensure the formation of mechanically-robust hydrogels that are stable against degradation at 37 °C and upon exposure to the cell culture medium within the duration of cell culture (Figure 6.4). In this study, human neural stem cells (NSCs) seeded on IKVAV-bearing hydrogels exhibited significant neurite extension and expressed an early neuronal marker (Tuj 1) even only after five days in culture. In addition to creating covalent crosslinks within the peptide moiety to ensure material stability, the subsequent sections will present the utility of topochemically-polymerizable diacetylene-bearing peptides whereby the crosslinks are established along the axis for π - π stacking direction and can easily be polymerized by irradiating pre-assembled peptide hydrogels with UV light.

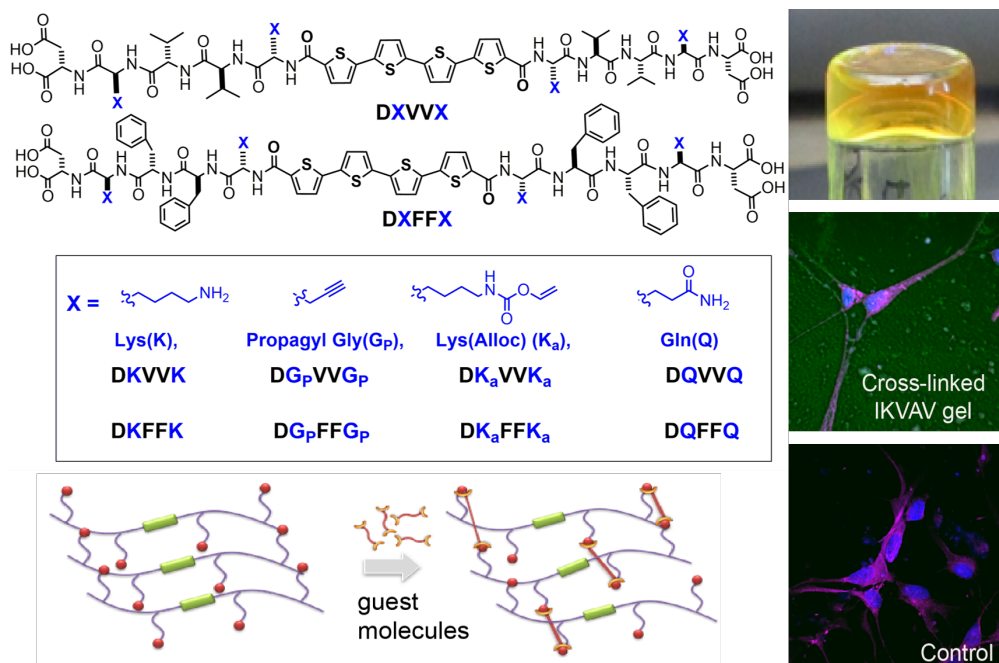


Figure 6.4. Molecular structures of previously studied π -conjugated peptide monomers that are crosslinkable by guest molecules upon hydrogelation (*left*); The *right panel* shows an image of a self-supporting, crosslinked gel and the confocal microscopy images of human neural stem cells on a crosslinked gel and on tissue culture polystyrene.

The second part of this Chapter will discuss aligned fibrous materials based on π -conjugated polymer composites that can be used as bioscaffolds for both neurons and cardiomyocytes. (Figure 6.5). An efficient donor-acceptor π -system pair that is ubiquitously reported in the literature, poly(3-hexylthiophene) P3HT and phenyl-C₆₁-butyric acid methyl ester (PCBM) will be used to test photocurrent stimulations with human NSCs. On the other hand, a composite material based on fibrin and PPy that creates a conductive and elastic material will be presented as a scaffold that can potentially facilitate a synchronous contraction and anisotropic signal propagation between cardiomyocytes. For these conducting materials, the effect of topographical guidance due to these aligned fibrous substrates will be highlighted in the discussions below.

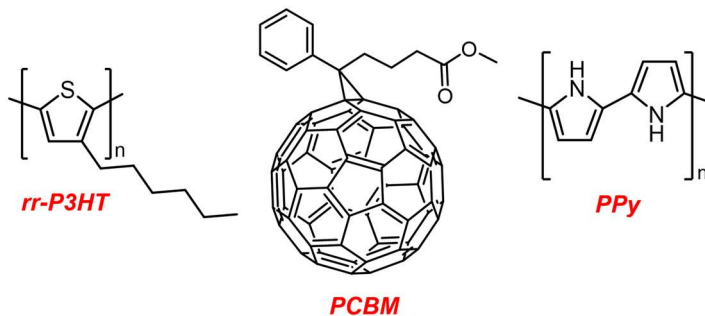


Figure 6.5. Molecular structures of the π -conjugated systems used for electrospun fiber scaffolds.

Results and Discussion

Bioscaffolds based on π -conjugated peptides. Previous reports on the formation macroscopically aligned hydrogels from these synthetic optoelectronic peptides have shown how simple manual shearing can be utilized to induce fiber nanostructure alignment within hydrogels, as well as to observe anisotropy in carrier mobility.^{56,58} Figure 6.6 shows some aligned hydrogels processed by following this reported method. These successful

examples are appended with DVV peptide moieties, which is interestingly the sequence with the highest shear moduli values as discussed Chapter 2.

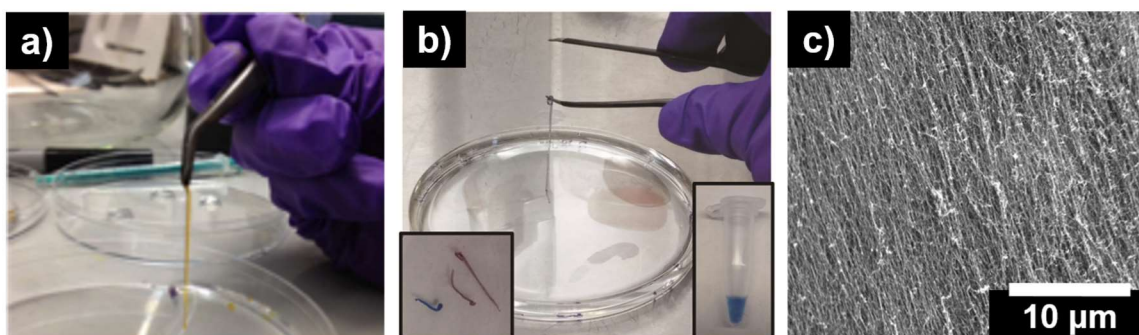


Figure 6.6. Representative images of mechanically-robust HO-DVV-peptide hydrogels with a) OT4 and b) polydiacetylene core; c) representative SEM image of the peptide system in (a).

Although tripeptide sequences that can afford hydrogelation were screened and optimized in Chapter 2, it is also important to consider approaches that can incorporate bioactive peptide epitopes such as IKVAV-OH, YIGSR-OH (also laminin-derived, and for neurite outgrowth), and RGD-OH (fibronectin-derived; for cell adhesion) within the nanostructure. Upon synthesizing peptide monomers with these three epitopes at the termini appended to E-, D- EAA-, or DVV-, attempts were made to produce hydrogels under different conditions but none were successful. Chapter 5 presented a model system, **EAA-** and **VAVKIEAA-OT4**, which utilizes a short peptide hydrogelator (**EAA-OT4**) doped with the longer bioactive containing peptide as an approach to afford epitope incorporation in a hydrogel. Because only the **EAA-OT4** peptide affords the formation the formation of macroscopically aligned peptide hydrogels when shear-flow assembled onto a 200 mM CaCl_2 bath, the increasing the mol% **VAVKIEAA-OT4** coassembled with **EAA-OT4** can affect the fidelity of alignment despite increasing the loading of the peptides

with bioactive epitopes. Figure 6.7 shows representative SEM images that qualitatively show the effect of doping with **VAVKIEAA-OT4** on the alignment within **EAA-OT4** hydrogels. Aligned and unaligned regions were both observed at 25 mol% **VAVKIEAA-OT4** loading and unaligned structures were mainly observed at 50 mol%.

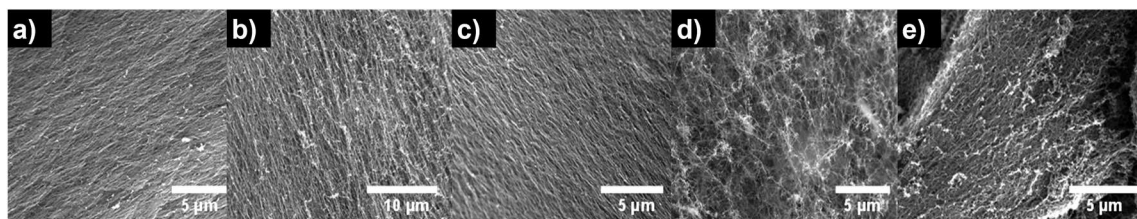


Figure 6.7. SEM images showing the alignment within shear-assembled hydrogels comprised of different ratios (v/v) of 1 wt% aqueous solutions of **EAA-OT4**: **VAVKIEAA-OT4**; a) 100:0; b) 90:10; c, d) 75:25; e) 50:50.

Preliminary work showed successful Schwann cell attachment onto 100:0 and 90:10 hydrogels, however, material degradation even after 3 days of culture with surface erosion and material precipitation after 7 days were both observed. Such was also the case when a one-component DVV-OT4 was tested for stability under cell culture conditions. Rather than merely using a binary peptide mixture, forming composite materials between **VAVKIEAA-OT4** and known larger biopolymers that can form fibrous materials when electrospun was another strategy that was used to circumvent these issues. Utilizing the modified electrospinning methods to create fibrous hydrogels with internal alignment developed by Dr. Shuming Zhang and Brian Ginn in the Mao group,⁵¹ alginate with **VAVKIEAA-OT4** was successful in forming aligned hydrogels (Figure 6.8) with a storage modulus (G') of ~ 8 kPa and loss modulus (G'') of ~ 2 kPa (Figure A6.12).

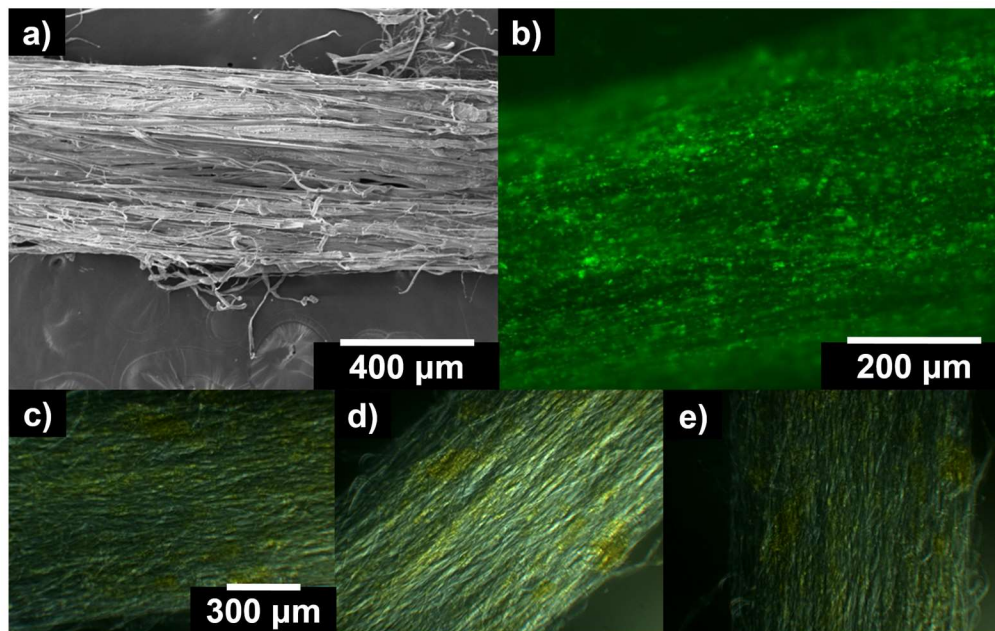


Figure 6.8. (a) SEM image showing the macroscopic alignment between the bundled hydrogel fibers formed by electrospinning 1.5 wt% alginate with 1.5 wt% VAVKIEAA-OT4; (b) epifluorescence image showing the distribution of OT4 units within the spun fibers; (c-e) birefringence due to alignment as observed under a polarized optical microscope.

In order successfully form electrospun materials (setup description in Figure A6.10), the solution being extruded out between the electrically biased syringe and grounded collector plate must be viscous. One technique to increase the viscosity of the solution to be electrospun is by adding small amounts of poly(ethylene oxide) (PEO).⁶² However, the addition of more insulating and bulky components may perturb a continuous π - π interaction along the axis of self-assembled nanostructures. Moreover, adding viscous components can alter the photophysical behavior of the incorporated π -conjugated peptides and is different that what will be observed in a one-component hydrogel. Although PEO loading was minimized as a compromise between achieving the appropriate viscosity and allowing self-assembly to occur, the epifluorescence image in Figure 6.8b shows a homogenous distribution but non-continuous fluorescent regions which should correspond to the spatial

distribution of OT4 units within this composite material. Nonetheless, this strategy provided a reliable platform to test the cytocompatibility of these π -conjugate peptides (Figure A6.11). Using Schwann cells for this assay, results show that the cells are viable for 5 days, but at 11.8% relative proliferation rate as compared to the TCPS control (100%). The cell-fiber interaction was observed using SEM (Figure 6.9), and the more rounded morphology of the cell suggests that the adhesion between those interface needs to improve and can be further optimized.

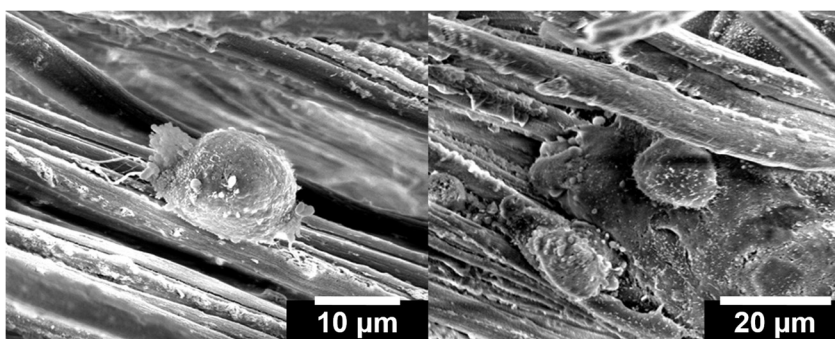


Figure 6.9. SEM images of Schwann cells adhered on the alginate: VAVKIEAA-OT4 (1:1) composite hydrogel.

Aside from forming a composite material to stabilize these peptidic assemblies, the other strategy employed is to establish covalent crosslinks between the monomers after self-assembly. As discussed above, crosslinks within the peptide region by using guest molecules afforded the formation bioscaffolds for neural stem cells. With photopolymerizable diacetylene units conjugated to peptides, stable hydrogel bioscaffolds that are covalently polymerized along the axis of π -conjugation can be developed. Polydiacetylene (PDA), which was also described in Chapter 1, has been one of the most explored conjugated polymers, with interesting linear and non-linear optical properties due to the one-dimensional nature of the conjugated polymer.⁵⁹⁻⁶¹ Moreover, it has served as

the model for studying the physics of one-dimensional optical and electrical phenomena in organic-based polymers.⁶² Diacetylenes undergo topochemical polymerization when exposed to appropriate stimuli, such as heat or light (UV or γ -irradiation).⁵⁹ Upon initial thermal or UV irradiation, diacetylene monomers produce biradical intermediates and subsequently rearrange to carbenes.⁶³ This leads to a 1,4-addition polymerization that produces a network of fully extended conjugated polydiacetylene backbone.⁶⁴ It is necessary to achieve the alignment or packing of diacetylene monomers during exposure to stimuli (Figure 6.10), otherwise, it will proceed *via* alternative reaction pathways (*e.g.*, 1,2-addition, 1,6-additions, hydrolysis) that do not produce PDA.⁶⁵

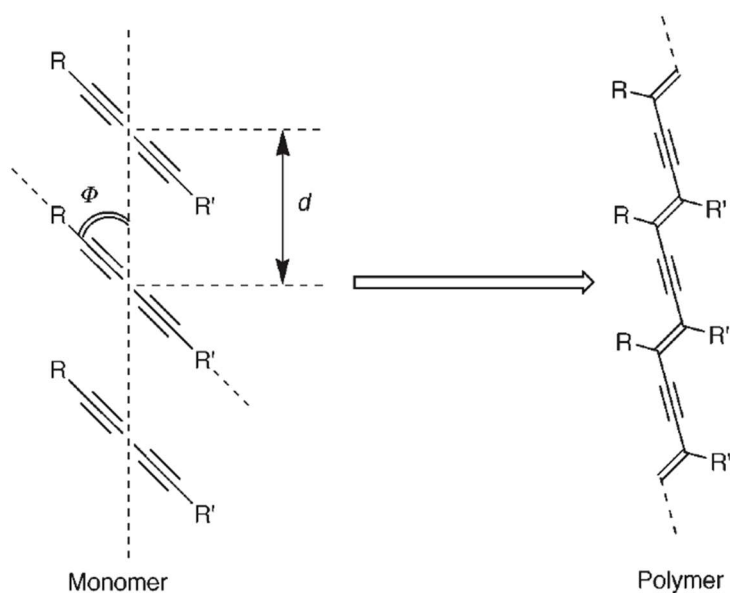


Figure 6.10. Dependence of the 1,4-polymerization of diacetylene on the molecular packing of monomers. Adapted from Ref. 65.

One approach to access the required packing parameters to polymerize diacetylenes is to utilize sidechains, such as peptides, that have inherent non-covalent intermolecular interactions.⁶⁰ Even though the electronic, optical and electrical properties of PDAs are

primarily dominated by the backbone, theoretical and experimental investigations clearly suggest the marked influence of side groups on these and other properties.⁶⁶ Adapting the design rules for peptide monomers that afforded diacetylene polymerization from a previous work by Stephen Diegelmann in the Tovar group⁵⁸ and the hydrogelation parameters learned from Chapter 2, the two peptide monomers shown in Figure 6.11 were mainly used as the hydrogels for the bioscaffolding experiments discussed below.

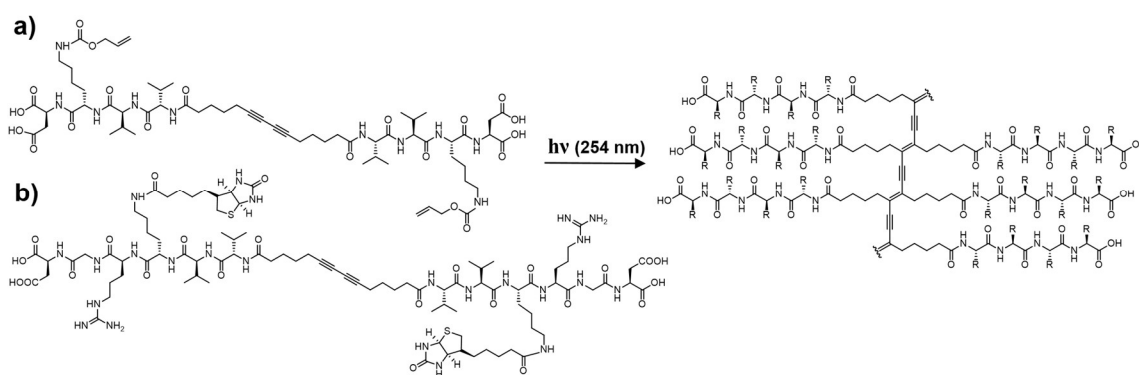


Figure 6.11. Molecular structures of the peptide-diacetylene monomers used for the hydrogel bioscaffolds used; (a) **DK(Alloc)VV-diacetylene**; (b) **DK(biotin)VV-diacetylene**. After assembling the peptides in a solution with high ionic strength (~ 200 mM CaCl_2) or adding GdL, the hydrogels that formed were exposed to a 254 nm 4-W light source to yield the polydiacetylenes.

Using the base sequence HO-Asp-Lys-Val-Val, hydrogels were successfully created that are either anisotropic or randomly aligned which can be further functionalized at the free amine sites of the Lys residue. Finally, these hydrogels are found to be robust and is stable even for cell culture that lasts up to 40 days. While the Asp residues at the termini help facilitate the ionic strength- or pH-triggerable assembly behavior of these peptides, Val residues adjacent to the diacetylene core allows increased propensity for β -sheet formation that might be necessary to access the monomer packing necessary for the polymerization to occur. The Lys residues between Asp and Val were amidated with Alloc

groups or biotin. The Alloc units (Figure 6.11a) presents free allyl groups that can be used for post-functionalization with thiol-containing peptide epitopes *via* thiol-ene click chemistry while biotin units (Figure 6.11b) can be useful for functionalizing hydrogels with Streptavidin (SAv)-tagged growth factors. The interaction between streptavidin (a tetramer protein found in *Streptomyces avidinii*, and is homologous to avidin) and biotin (a vital enzymatic cofactor, also known as Vitamin H) is one of the strongest known protein-ligand interaction reported in the literature, $K_f = 10^{15} \text{ M}^{-1}$ and 10^7 M^{-1}).⁶⁷ For the biotin-containing hydrogels, 5 minutes is enough to observe a polymerized hydrogel (as characterized by a change from colorless to purple gels, and $G' > G''$) but the G' surprisingly decreases with longer irradiation times. While such longer irradiation times can translate to longer polydiacetylene chains, prolonged exposure to UV could be inducing material degradation which causes the lowering of G' (Figure A6.13).

Peptide-polydiacetylene hydrogels as a platform for aligned hNSC and DRG explant outgrowth. Using the shear-flow assembled peptide-polydiacetylene hydrogels following previously reported techniques,^{56,58} we created aligned scaffolds for human NSCs and dorsal root ganglion (DRG) explants. To immobilize these aligned hydrogel “strings” at the bottom of cell culture wells, agarose channels were made to hold the substrate hydrogels that are applied with a very thin layer of silicone adhesive at the bottom (cells are seeded on top) to avoid floating of the hydrogels out of the cell culture medium (Figure 6.12b-c). Cellular alignment due to the influence of substrate topography is observable even as early as four days in culture (Figure 6.12a).

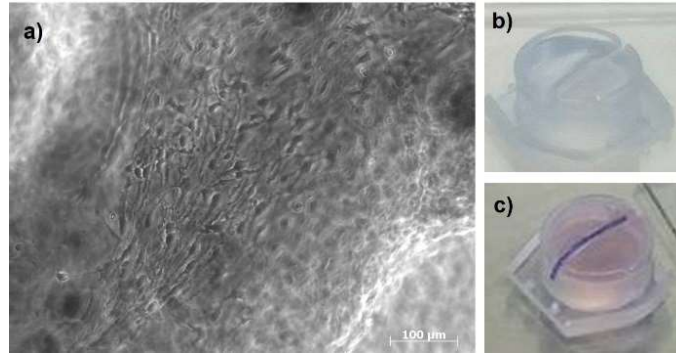


Figure 6.12. a) Human neural stem cells at Day 4 under a brightfield microscope, seeded on top on 2 wt% **DK(biotin)VV-polydiacetylene**; agarose channels with the peptide hydrogel b) before and c) after exposure to cell culture medium and depositing the aligned peptide hydrogel.

For both human NSCs and primary DRG explants, guided outgrowth with the extensions following the alignment of the long axis of fiber formation were successfully observed (Figure 6.13). The stem cells also stained positive for Tuj1 (early neuronal marker) which also confirms a successful differentiation towards neuronal lineage.

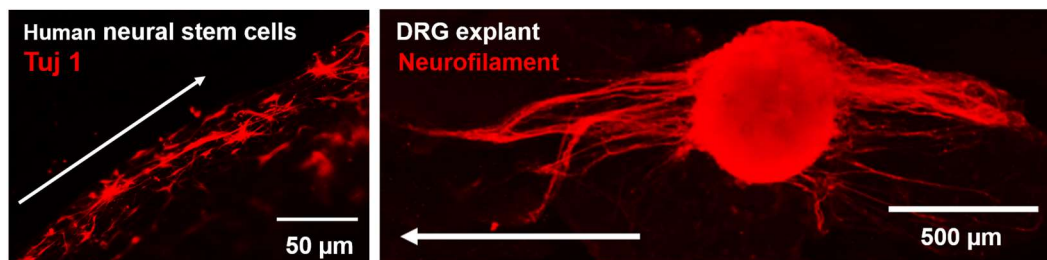


Figure 6.23. Topographical guidance provided by peptide-polydiacetylene hydrogels to human NSCs (7 days in culture on **DK(biotin)VV-diacetylene** gels) and DRG explant (8 days in culture on **DK(Alloc)VV-diacetylene** gels).

As a comparison, the directionality of outgrowth extensions for human NSCs seeded on a peptide hydrogel without alignment (“random gel”) and stiff tissue-culture polystyrene (TCPS) substrate are shown in Figure 6.14. Clearly, without an aligned substrate, the growth is highly isotropic without any cellular organization. Although the

cell density is still much higher in the flat and coated with Matrigel for adhesion, the difference between the outgrowth anisotropy is still achieved only with the aligned peptide hydrogels. For the DRG explants, the representative image of an early-stage explant and those seeded in TCPS is shown in Figure A6.14. The TCPS-seeded explants interestingly show longer extensions (> 1 mm lengths) than those seeded on aligned peptide hydrogels (>500 μm lengths), as well as apparent synaptic connections, but are also clearly isotropic in nature.

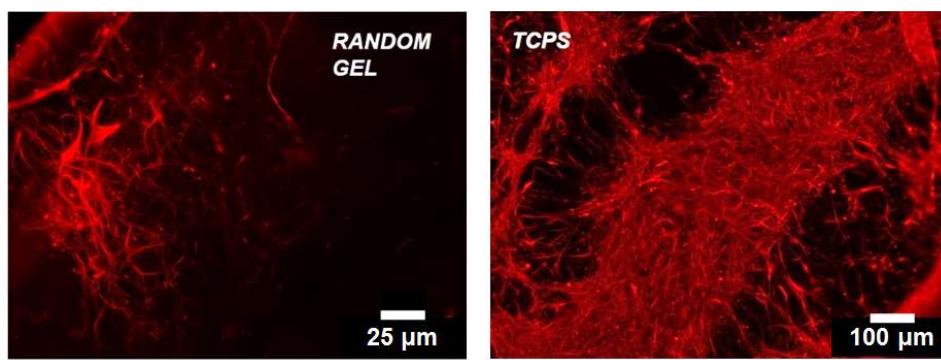


Figure 6.14. Control setups for the human neural stem cells (Tuj1+; 7 days in culture) on **DK(biotin)VV-diacetylene** “random gels” (*left*) and in Matrigel-coated TCPS (*right*).

With these results, the Alloc- and biotin-functionalized peptide diacetylenes that can form aligned hydrogels can therefore be used as a platform to conduct mechanistic investigations as to how such topographical guidance along with presentation of biochemical cues and electrical stimulation can affect the growth and behavior of these cellular models (Figure 6.15). A two-electrode setup with Ag contacts at the ends of the hydrogels was used to apply a constant voltage of 150 mV/mm for 10 minutes ($\times 3$) every 5 minutes for 3 consecutive days. For functionalizing with biochemical cues, initial work was done with biotin-appended hydrogels with SA_v-brain derived neurotrophic factor (BDNF). BDNF was chosen as the test growth factor because literature precedents show

that this growth factor gets upregulated upon applying external electrical stimuli under physiological conditions.^{68,69} However, application of a constant voltage under such conditions only resulted in a decrease in outgrowth. As for the BDNF treatment, although there are no significant differences between the randomly aligned gels with and without BDNF, growth factor loading concentrations can be optimized. BDNF is also more known in encouraging differentiation towards neurons, and, thus might have a better effect when used in hNSC culture rather than in DRG explants. Nonetheless, among these groups, the alignment within the material (without stimulation) still interestingly correlates to longer neurite extensions.

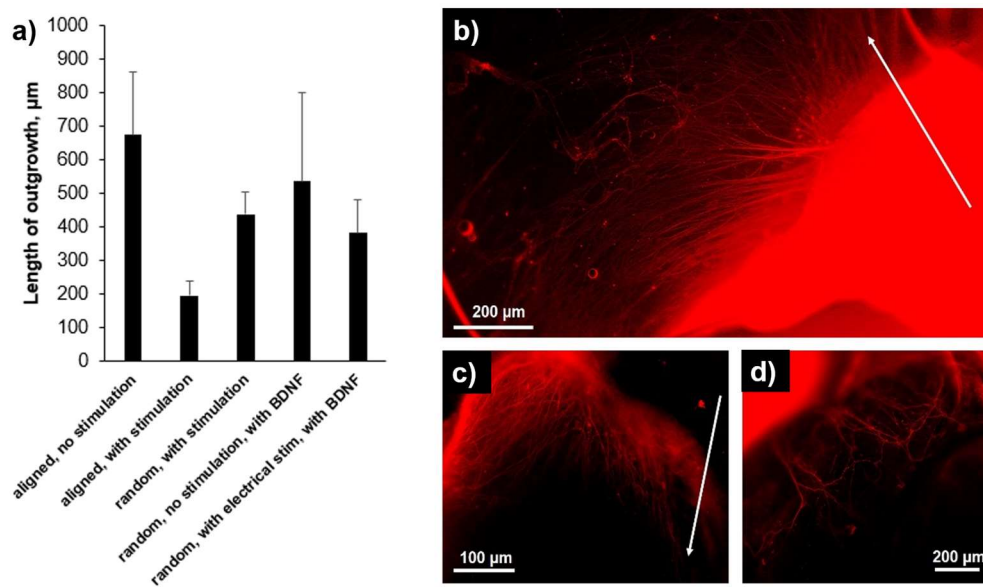


Figure 6.15. (a) Comparison of neurite outgrowth lengths under different imposed conditions (*with electrical stimulation*: 150 mV/mm; *with BDNF*: hydrogels were soaked in 5 ng/mL BDNF in room temperature for 1 h); (b-d) representative DRG explants on polydiacetylene peptide gels after 10 days (immunostained against **neurofilament**).

In addition to primary neurons, the presentation of physicochemical cues to control the differentiation of neural stem cells (NSCs) is another interesting direction. NSCs have been shown to differentiate and mature to functioning neurons as well as glial cells such as

astrocytes and oligodendrocytes.⁷⁰ Despite the numerous doors that these stem cells can open for therapies for in the CNS, with CNS having a much slower regeneration than PNS, controlling the differentiation of NSCs towards a specific lineage and making them functional cells is a challenging endeavor. Preliminary work was conducted with human NSCs on DK(Alloc)VV-diacetylene hydrogels with constant voltage application during its first 7 days in culture. Qualitatively comparing the protein markers expression for neuronal (Tuj 1) and astrocytic (GFAP, glial fibrillary acidic protein) lineage differentiation over several representative images, astrocytic differentiation is more predominant for the untreated samples (Figure 6.16). This shows decreased yield in glial differentiation when electrically-stimulated, but this requires further confirmatory experiments to obtain the quantitative yields. Beyond the demonstration of the effect of electrical field stimulation on encouraging an increased rate of axonal outgrowth related to peripheral nerve regeneration, investigating the effects of this unique stimulation platform on human neural stem cells will be beneficial for extending this technology for central nervous system repair, which is more physiologically challenging than in the case of peripheral nervous system as discussed earlier.

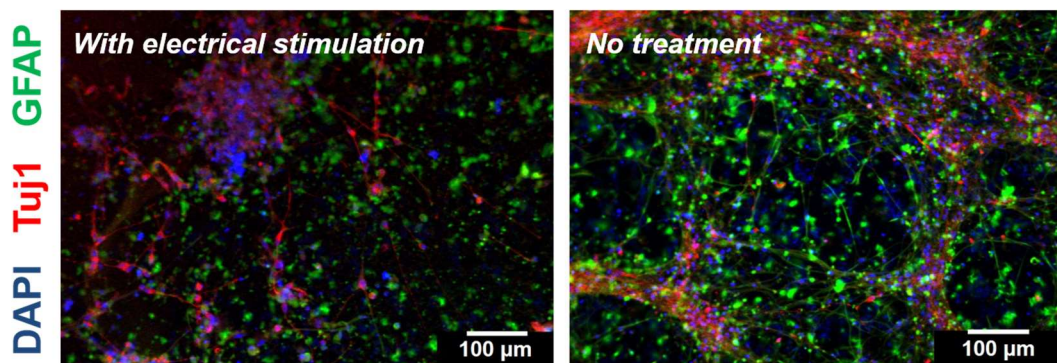


Figure 6.16. Comparing the TuJ+ vs. GFAP+ cells (12 days in culture) seeded on 2 wt% DK(Alloc)VV-diacetylene “random” hydrogels, with (100 mV/mm) or without stimulation.

Experiments are underway to continuously explore the synergistic effects of environmental cues that these peptidic bioscaffolds can provide, not only on the cell maturation, but also on signal propagation that can be deduced from the imaging of calcium transients. Because of the apparent negative outcome obtained by the application of constant voltage to human NSCs, pulsed electrical stimulation under different frequencies while optimizing the nature of the contact electrodes on these cellular models seeded on peptide scaffolds are currently investigated.

Towards photoconductive peptide hydrogel scaffolds. Ultimately, with the materials presented in Chapter 4, our aim is to construct photoconductive biological scaffolds based on the coassembly strategy. This can open doors for the development of platforms that can induce light-generated local electric fields between donor-acceptor moieties within the scaffolds, to eliminate the need for interfacing the cells with an external electrode. One important control experiment is to see the effect of light irradiation on the differentiation of human neural stem cells seeded on bare culture plates (*i.e.*, phenotype levels) and the phototoxicity dose limits of irradiation. Unfortunately, the systems investigated in Chapter 4 requires excitation wavelengths < 400 nm for the donor π -system, which appears to be cytotoxic to cells. Although they successfully form hydrogels, these systems are also not covalently-crosslinked and optimized for stability during cell culture. Figure 6.17 shows some representative images of human NSCs seeded on Matrigel-coated TCPS showing untreated cells and those irradiated at 365 nm (within the region of OPV3 absorption) and 470 nm (within the region of polydiacetylene absorption). The LED sources used for both wavelengths have both 10-W power, but do not necessarily imply the same irradiation intensity. For this assessment experiment, 10-minute continuous

irradiation of the samples ($\times 3$, every 10 minute intervals; for a total of 50 minutes treatment duration). The untreated and 470 nm-irradiated samples do not show any significant morphological differences. However, those irradiated at 365 nm showed rounded morphologies without any extensions, and did not show any positive expression towards Tuj1. Also, optical stimulation on polydiacetylene-peptide gel platform was also attempted but the resulting photocurrents are very minimal ($\sim nA-\mu A$) as compared to what is required for electrical stimulation (mA). Moving forward with this endeavor, it is necessary to append central π -cores with donor-acceptor pairs with a donor core that have a more shifted absorption maxima.

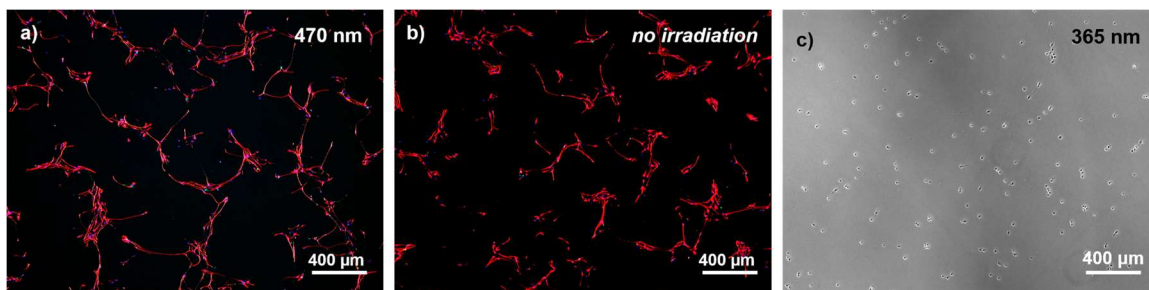


Figure 6.17. (a-c) Representative images of tissue-culture plate grown samples (7 days in culture), with and without irradiation.

To assess whether photocurrent-generating materials indeed can influence the differentiation pathway of humans NSCs, an established donor-acceptor polymer blend (P3HT-PCBM) was used. Lanzani and co-workers previously reported neural photoactivation using a P3HT-PCBM spun-coated substrate with primary hippocampal neurons.^{71,72} They presented a strategy to optically stimulate neuronal cells in a network by shaping visible light pulses at the polymer/electrolyte interface. This type of approach provides an alternative to widely used neuron optogenetic photostimulation techniques, which requires gene modification that can be potentially hazardous. Although spatial

selectivity of photostimulation is highly dependent on the shape of the light source, cell selectivity is also an issue for genetic encoding. This presents a new strategy that allows to stimulate neuronal stem cells by utilizing photoconductive platforms that are biocompatible. Since the literature reports on P3HT-PCBM photoactivation focuses on neurons only, the use of P3HT-PCBM as a platform to photoactivate and influence the differentiation pathway of human neural stem cells is an interesting exploratory direction. The spectral current response has a maximum at ~ 530 nm, thus, a 10-W 528 nm LED was used for the experiments discussed below (Figure 6.18a). No beam shaping and pulsing was introduced in the studies reported below. For comparison, studies were done for both spun-coated films and electrospun fibers with alignment (Figure 6.18b).

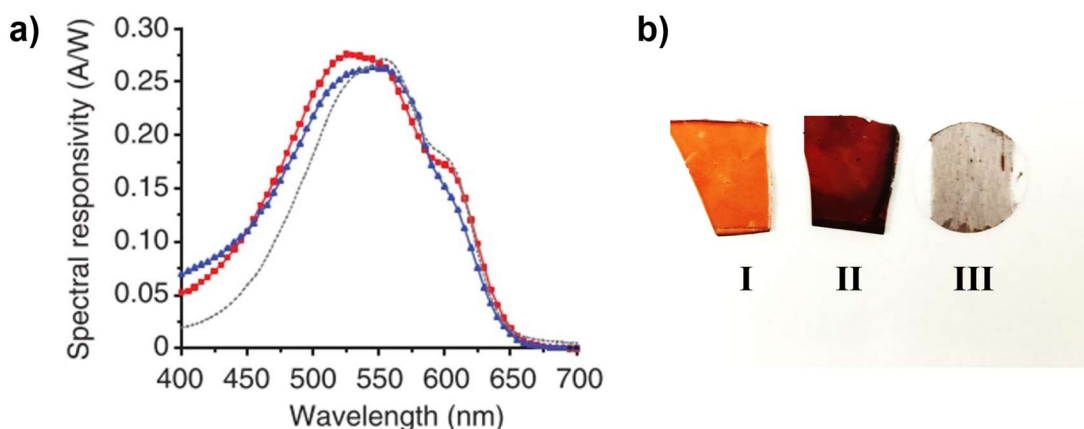


Figure 6.18. (a) Spectral responsivity curve of a 1:1 P3HT/PCBM film blend (from Ref. 72); (b) representative optical images of P3HT/PCBM films (I, II) and spun fibers (III); films before (I) and after (II) annealing are shown.

The effect of light irradiation on seeded human NSCs was first examined when they are seeded onto an ITO/glass substrate spun-coated with P3HT-PCBM. The stem cell culture was kept for 10 days before fixing wherein the stimulation was started on the third day. In this case, the light stimulation was employed every 24 h, a total of 10 minute-

stimulation per slide was performed (1 min continuous irradiation, and 1 min gap before the next irradiation). Interestingly, human NSCs are Tuj1+ in all P3HT/PCBM-seeded cells but with higher proliferation density under irradiated and non-irradiated conditions (Figure 6.19). However, when the relative mRNA expression was compared for irradiated and non-irradiated samples, having those conditions imposed on P3HT/PCBM films and TCPS substrates as controls (Figure A6.15), the Tuj1 expression is still the highest for the non-irradiated TCPS control while the other 3 conditions have relatively the same expression levels. It was noticeable that P3HT/PCBM without irradiation maintains a high expression of Nestin (~2-fold higher than non-irradiated TCPS, which indicates a high-number of undifferentiated cells remain under such condition. The GFAP (astrocytic marker) expression of non-irradiated cells in P3HT/PCBM is also ~1.5-fold higher than the non-irradiated TCPS showing an increased astrocytic differentiation. For MAP2 (microtubule associated protein 2) expression, a dendritic marker, both the irradiated samples in TCPS and P3HT/PCBM show higher levels than the control. It is therefore necessary to investigate if the light excitation conditions, without the photogenerated currents, cause this increase in MAP2 expression.

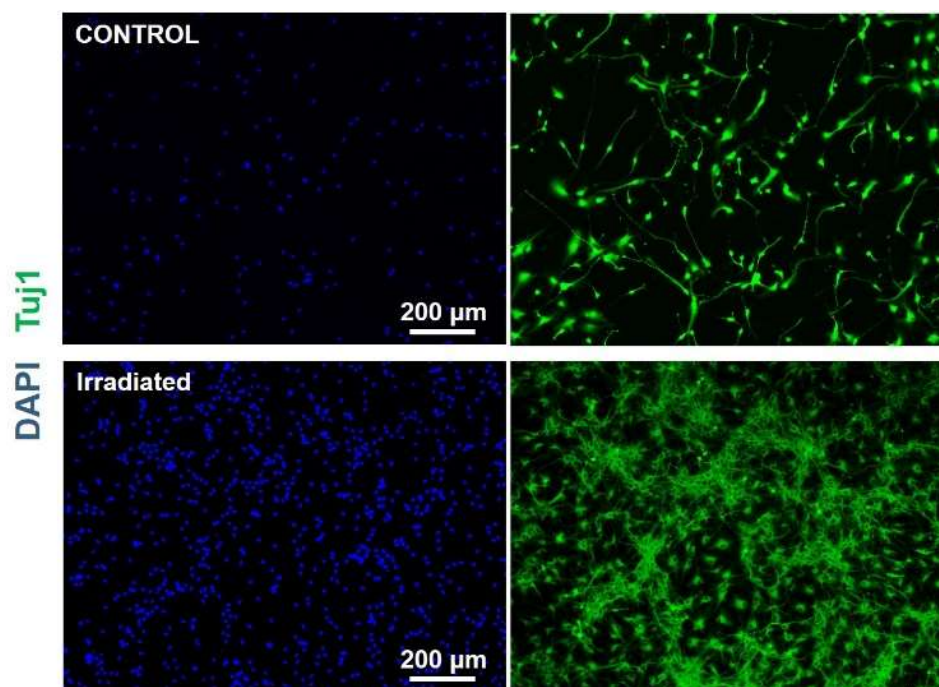


Figure 6.19. Human neural stem cells (10 days in culture) on top of spin-coated P3HT:PCBM films.

When hNSCs were seeded as spheroids on top of aligned, electrospun P3HT:PCBM fibers, the GFAP expression is still predominant over TuJ1. It is however noticeable that the migration from the spheroid core is apparently faster under irradiated conditions (as the spheroid core size decreased faster for the irradiated samples). These substrates were also successful in maintaining an aligned direction of axonal outgrowth which follows the general direction of fiber alignment, under irradiated and non-irradiated conditions (Figure 6.20). Further optimization of electrospinning parameters is however needed, due to the “beading” of fibers that was observed under SEM for the coaxial electrospinning conditions imposed for these samples.

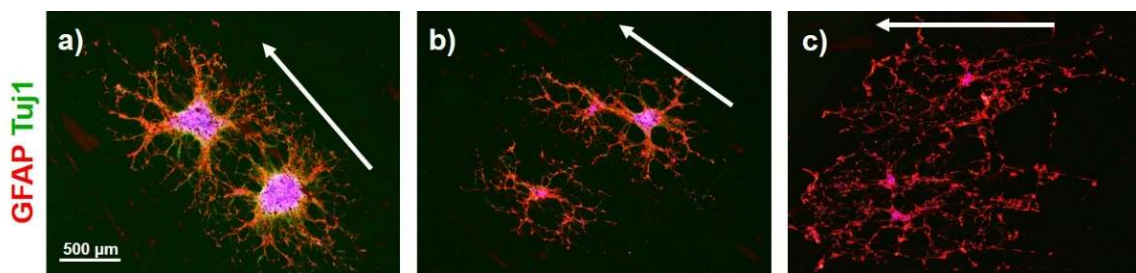


Figure 6.203. Human neural stem cell spheroids (10 days in culture) on top of P3HT:PCBM aligned, electrospun fibers under (a,c) irradiated (10-W 528 nm LED source) and (b) non-irradiated conditions; (a) fibers with an insulating poly(vinylpyrrolidone) coating.

Although this strategy presents a known donor-acceptor organic material and has been reported to positively influence the rate of axonal outgrowth of hippocampal neurons, the irradiation conditions imposed in these studies for both film and fibrous P3HT/PCBM does not dramatically increase the yield of functional neurons from the stem cell differentiation. Further investigations will require a more intricate excitation setup, with potentially better attenuation and higher light source power. While it is possible that the $\sim\mu\text{A}$ photocurrents produced by P3HT/PCBM are not enough to influence NSC differentiation and maturation, this standard donor-acceptor pair is a good system to do optimization studies for the influencing stem cell behavior *via* photocurrents because π -conjugated peptide hydrogels will most likely produce lower photocurrents than this system.

Potential aligned scaffolds as cardiac patches: synergistic application of mechanical and electrical stimulation. In this last section, a material that has a potential cardiac patching applications will be presented. In considering scaffolds for cardiomyocyte growth, the architecture of the scaffold that allows cellular organization as well as the ability of the scaffold to facilitate the electrical signal propagation between cells important

factors that determine the success for cardiac patching.⁷³ Kohane, Langer, Parker and co-workers have shown the first example of a composite material of inorganic nanocomposite and polymeric matrices (alginate scaffolds doped with gold nanowires) used as cardiac patches.⁷⁴ This material allowed homogeneous electrical propagation and have robust mechanical properties that facilitates the strong contractile motions of cardiomyocytes seeded onto these patches. Another relevant composite material was developed by Tang, Khademhosseini, and co-workers which has carbon nanotubes embedded within gelatin-methacrylate hydrogels.⁷⁵ A more recent report from Murphy and co-workers has shown a composite material from a porous silk scaffold and PPy geared towards both 2-D and 3-D bioscaffolding.²³ These materials combine the mechanical integrity of a known biopolymer together with electrically-conducting components to form scaffolds. Here, a composite material between aligned fibrin hydrogels and PPy is presented. Fibrin is a natural protein matrix that can be enzymatically crosslinked by thrombin under physiological conditions.⁷⁶ The preparation of this material involves the formation of aligned fibrin bundles according to the electrospinning procedure developed by Mao and co-workers,⁵¹ followed by exposing the bundles to $(\text{NH}_4)_2\text{S}_2\text{O}_8$ (an oxidant), and then to a pyrrole solution to induce the oxidative polymerization to PPy. Comparing the SEM images of the fibrin and fibrin-PPy, the post-modification of electrospun fibrin bundles with *in situ* polymerization of pyrrole does not disturb the initial alignment of the material (Figure 6.21).

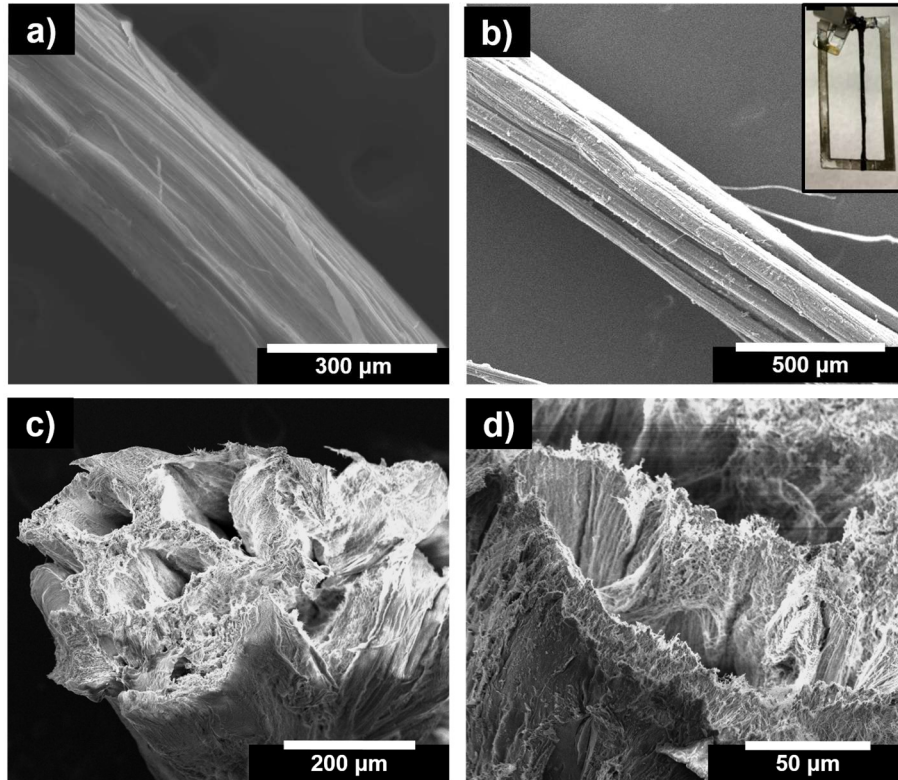


Figure 6.21. Representative SEM images for electrospun fiber bundles of fibrin (a,c) and fibrin-PPy composite (b,d); inset: optical image of the actual fibrin-PPy composite.

The mechanical properties of the fibrin and fibrin-polypyrrole microbundles were also measured by dynamic mechanical analysis. It is interesting that the elastic moduli of the fibrin bundles were improved with polypyrrole but the % strain to failure values remain the same. This shows that the polypyrrole infusion to this material even improves the mechanical integrity of the scaffold. To further investigate the polymer network formed by PPy within the material, the bundles were treated with plasmin from human plasma. With 15 CU/mL plasmin in a serum-free media, fibrin-only bundles are completely degraded and is consistent with the observations from a literature precedent.⁷⁷ However, the fibrin-PPy bundles, as shown in Figure 6.22, only decreases the width of the material. This

suggests that the PPy does not merely coat around the pre-formed fibrin bundles, but instead forms a network that is mingled with the fibrin network.

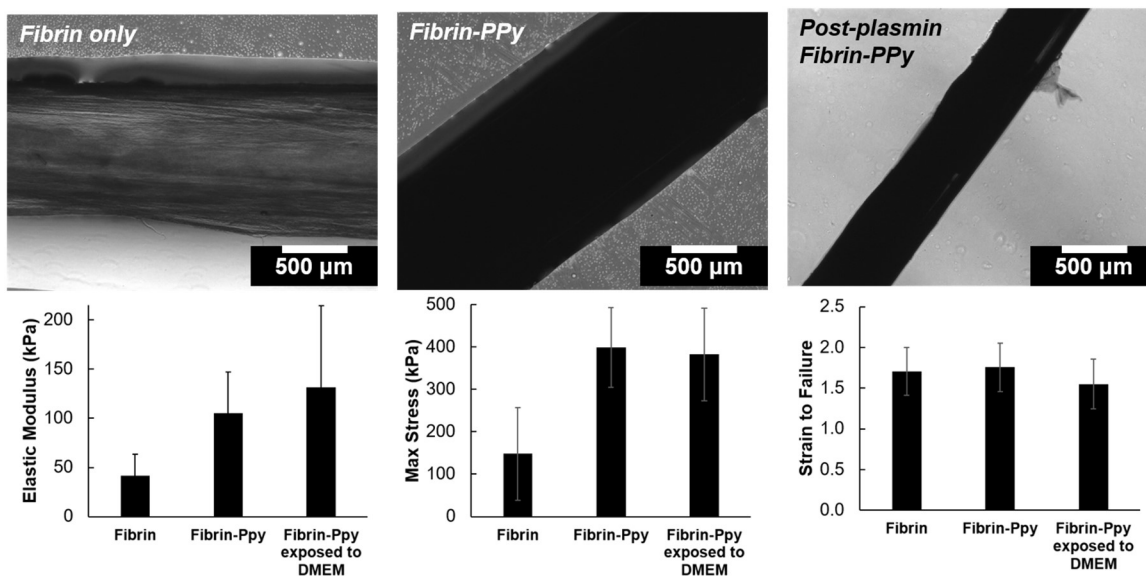


Figure 6.224. Representative optical microscopy images of fibrin and fibrin-PPy bundles (before and after plasmin treatment) and the results of the dynamic mechanical analysis for these aligned bundles.

Considering the properties of this material, the goal is to use this as a scaffold for cardiomyocytes and be able to synergistically induce mechanical and electrical stimulation, potentially to improve the homogeneity of electrical propagation, cellular organization, and maturation. The fibrin-PPy bundles interestingly show a current response change when cyclically strained over time while in a highly electrolytic medium, but not in deionized water (Figure 6.23a and A6.17). This strain-induced behavior opens another aspect of investigation, where a local ionic flux within the material is induced by the cyclic strain. Using the van der Pauw method discussed in Chapter 2, the sheet resistance of the dried fibrin-PPy were measured to be $266.98 \pm 4.02 \Omega/\text{sq}$ (Figure 6.23b). Other related polypyrrole composites that were also chemically polymerized have sheet resistance values ranging from 10^2 – $10^3 \Omega/\text{sq}$.^{23,31}

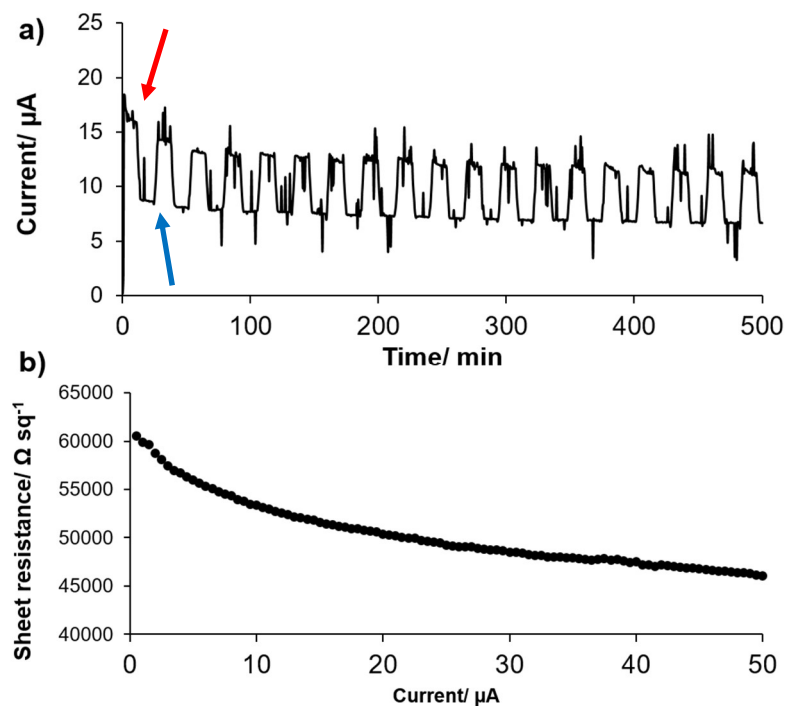


Figure 6.23. (a) Current response over time of fibrin-PPy bundles exposed in an electrolytic cell culture medium, with 10% strain applied every 10 s using a bioreactor setup⁷⁸; (b) representative sheet resistance curve obtained using van der Pauw method. Arrows indicates the first onset (red) and release (blue) of strain.

Experiments regarding the synergistic effect of alignment and mechanical stimulation, as well as potential strain-induced increase in ionic conductivity, are ongoing for these fibrin-PPy composite materials seeded with neonatal rat ventricular myocytes (NRVMs). When Matrigel-coated, both fibrin and fibrin-PPy bundles show considerable cell adhesion as shown in Figure 6.24. We expect that the calcium mapping experiments will provide insights on the unidirectional signal propagation along the aligned constructs (induced *via* point stimulation) and homogenous beating brought by using a conductive, aligned, and mechanically compliant scaffold.

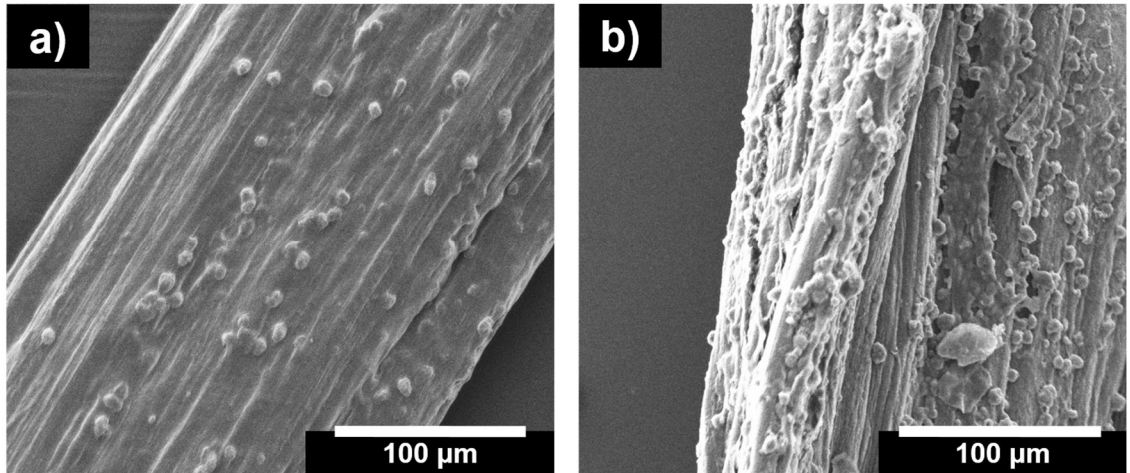


Figure 6.24. Representative images of neonatal rat ventricular myocytes seeded on top of aligned, electrospun (a) fibrin and (b) fibrin-PPy bundles.

Conclusions

This Chapter presents different approaches that could be utilized to develop stable bioscaffolds that exhibit the properties required for a successful regrowth and maturation of electrosensitive cells. The material design, along with engineering and biological considerations discussed herein, provide insight for the ongoing and future experiments involving a more mechanistic approach on the effect of these biological scaffolds and the cues that they impart to different electrosensitive cells. The results shown here highlight the materials that are successful in inducing contact guidance towards the alignment of cells interfaced with the material. This is also the first demonstration of the utility of π -conjugated peptide hydrogels as a biomaterial, which specifically resulted in the aligned outgrowth for both human neural stem cells and whole dorsal root ganglion neuron explants—both of which are relevant cellular models for therapies involving central nervous system damage.

Experimental Details

Peptide synthesis. All peptides reported here were synthesized using solid-phase peptide synthesis, followed by on-resin coupling of the π -electron unit to the peptide *via* Pd-catalyzed cross coupling reactions or *via* amidation with the appropriate diacid, according to our previous reports (*see* Appendix).

DVV- and **EAA-OT4.** Prepared according to literature procedure; *see* Chapter 2.

VAVKIEAA-OT4. Procedure reported in Chapter 5.

DK(Alloc)VV-diacetylene. A 0.037 g (0.15 mmol) of tetradeca-6,8-diyndioic acid and 0.16 g (0.30 mmol) of PyBOP was dissolved in 15-mL of 2:1 NMP:DCM solution, after which 0.87 mL of DIPEA was gradually added then mixed for 1 min. This solution was added to the solid-supported Wang-DK(Alloc)VV-NH₂ (0.5 mmol) in a peptide chamber and mixed for 20 h. Resin was rinsed using the standard wash cycle. The resin was then subjected to a second round of coupling with 0.025 g (0.1 mmol) of tetradeca-6,8-diyndioic acid and 0.10 g (0.20 mmol) of PyBOP dissolved in 15-mL of 2:1 NMP:DCM solution. The same amount of DIPEA as the first coupling was gradually added, then mixed for 1 min. This solution was added to the resin in a peptide chamber and mixed for 15 h. After rinsing the resin using the standard wash cycle, a final, blank coupling cycle was performed with only 0.16 g (0.30 mmol) of PyBOP and 0.5 mL of DIPEA in 10-mL of 2:1 NMP:DCM solution for 1 h. The resin was thoroughly washed again using the standard wash cycle. Resin was subjected to the general cleavage procedure. Crude peptide obtained was observed as white solid. MS (ESI⁻) m/z 1337.9 (M-2H⁺+K⁺) (calc. 1337.7), m/z 1299.9 (M-H⁺) (calc. 1299.7), m/z 649.6 ((M-2H⁺)/2) (calc. 649.4). ¹H NMR (400 MHz, D₂O) δ , ppm: 5.21 (d, 1H, J = 17.8 Hz), 5.14 (d, 1H, J = 9.0 Hz), 4.45 (d, 4H, J = 4.5 Hz),

4.30-4.24 (m, 4H), 4.01 (dd, 4H, $J=14.4$ Hz, 8.6 Hz), 3.01 (t, 6H, $J=6.2$ Hz), 2.56 (d, 1H, $J=4.5$ Hz), 2.52 (d, 2H, $J=4.6$ Hz), 2.46 (d, 2H, $J=8.4$ Hz), 2.42 (d, 1H, $J=8.4$ Hz), 2.29-2.19 (m, 12H), 1.99-1.88 (m, 6H), 1.8-1.7 (br, 3H), 1.65-1.55 (m, 9H), 1.44-1.38 (m, 12H), 1.33-1.20 (br, 6H), 0.86-0.83 (m, 30H), 0.81 (d, 12H, $J=6.8$ Hz).

DK(biotin)VV-diacetylene. A 0.023 g (0.090 mmol) of tetradeca-6,8-diyndioic acid and 0.094 g (0.18 mmol) of PyBOP was dissolved in 10-mL of 2:1 NMP:DCM solution, after which 0.52 mL of DIPEA was gradually added then mixed for 1 min. This solution was added to the solid-supported Wang-DK(Mtt)VV-NH₂ (0.3 mmol) in a peptide chamber and mixed for 20 h. Resin was rinsed using the standard wash cycle. The resin was then subjected to a second round of coupling with 0.015 g (0.060 mmol) of tetradeca-6,8-diyndioic acid and 0.062 g (0.12 mmol) of PyBOP dissolved in 10-mL of 2:1 NMP:DCM solution. The same amount of DIPEA as the first coupling was gradually added, then mixed for 1 min. This solution was added to the resin in a peptide chamber and mixed for 15 h. After rinsing the resin using the standard wash cycle, a final, blank coupling cycle was performed with only 0.094 g (0.18 mmol) of PyBOP and 0.52 mL of DIPEA in 10-mL of 2:1 NMP:DCM solution for 1 h. The resin was rinsed with the standard wash cycle, then treated with 1% TFA for 30 min⁷⁹ for Mtt deprotection. After rinsing the resin again with the standard wash cycle, a 10 mL NMP solution containing 0.22 g (0.90 mmol) *D*-biotin and 0.33 g (0.87 mmol) of HBTU was added to the resin and stirred for 3 h. This coupling was repeated for another 1 h, followed by a final rinsing the resin with the standard wash cycle. Peptide was cleaved from the resin using the general cleavage procedure. Crude peptide was obtained white solid (40.4 mg, 17%). MS (ESI-) m/z 1584.3 (M-H⁺) (calc. 1583.8), m/z 791.9 (M-H⁺) (calc. 791.4). ¹H NMR (400 MHz, D₂O) δ , ppm:

4.47 (dd, 2H, $J = 8.0$ Hz, 4.0 Hz), 4.29 (dd, 2H, $J = 8.4$ Hz, 4.4 Hz), 4.24-4.12 (m, 10H), 3.22-3.17 (m, 2H), 3.12-2.99 (m, 6H), 2.88 (d, 1H, $J = 5.0$ Hz), 2.84 (d, 2H, $J = 4.8$ Hz), 2.65 (d, 2H, $J = 13.0$ Hz), 2.54 (d, 1H, $J = 4.6$ Hz), 2.50 (d, 2H, $J = 4.3$ Hz), 2.44 (d, 2H, $J = 8.6$ Hz), 2.40 (d, 1H, $J = 8.6$ Hz), 2.21-2.15 (m, 10H), 2.12 (t, 6H, $J = 7.3$ Hz), 1.81-1.71 (br, 2H), 1.63-1.46 (m, 18H), 1.42-1.35 (m, 12H), 1.25 (dd, 24H, $J = 13.2$ Hz, 6.8 Hz).

Aligned peptide hydrogel preparation by shear-flow assembly.^{52,56,58}

Lyophilized peptide solids were dissolved in Milli-Q water and prepared as 1.0 to 1.5 wt% solution. A few drops of 1 M KOH were added to fully dissolve the peptide (pH~ 7-8). The OT4 peptide solutions were sonicated for 5 min and heated at 80°C for 30 min. The PDA peptide solutions were sonicated, followed by irradiation of the 2 wt% neutral solution prior to shear flow assembly. Upon cooling and allowing to sit undisturbed for at least 30 min, the solution was transferred to a syringe with 30-gauge needle tip and then dispensed with shear stress into a Petri dish containing the appropriate crosslinker solution (*e.g.* 200 mM CaCl₂) at a rate of ~20 cm/s.

Electrospun hydrogel composite preparation.⁵¹ The general setup for hydrogel electrospinning consists of a voltage power supply (Gamma High Voltage Research, Ormond Beach, FL, aluminum rotating collection plate containing the crosslinker solution, DC motor controller (Dart Controllers Inc) and syringe pump (Fisher). A voltage of 3 to 5 kV was applied between the syringe tip and grounded rotating collection plate (~30-45 rpm). All electrospun solutions were delivered using a 1 mL plastic syringe with a 27-gauge blunt needle. The tip to collector distance ranged from 1-3 cm depending on the charge of the peptide solution used and applied voltage. All experiments were run at room temperature. The alginic acid sodium salt (1.5 wt%), ~250 cps, was mixed with

VAVKIEAA-OT4 (1 wt%) in a 1:1 v/v ratio and with a total of 0.2 wt% polyethylene oxide (PEO, 4M M_z) (Sigma) in the final solution in the syringe.

Fibrin and fibrin-PPy hydrogel microfiber bundles were formed by a modified electrospinning process where fibers were collected on a rotating bath containing a crosslinker bath. Briefly, a 2 wt% fibrinogen (Sigma, St. Louis, MO, USA) was dissolved in 0.2 wt% PEO and loaded into a blunted 27-gauge tip syringe. The loaded syringe was then placed into a syringe pump and extruded at a flowrate of 3.25 ml/h. A positive voltage of 4.5 kV was applied to the syringe tip to propel the fibrinogen-PEO solution jet onto a grounded and rotating collection bath (45 rpm) containing 50 mM CaCl_2 (Fisher Scientific, Waltham, MA, USA) and 20 units/mL thrombin (BioPharm Laboratories LLC, Bluffdale, UT, USA) in deionized water to form fibrin hydrogel fibers. Sheets were formed by rastering the landing position back and forth for 10 min after placing the syringe pump on a linear stage. Upon completion of the spin, 1 cm^2 sheets were collected by wrapping six layers of sheet from the collection bath onto PET frames. Samples were then soaked in DI water overnight to remove residual thrombin and calcium. Following this, the fibrin sheets were exposed to an aqueous bath of 0.25 M $(\text{NH}_4)_2\text{S}_2\text{O}_8$ for at least 24 h at 4 °C. After washing this with 1:1 EtOH/ H_2O solution ($\times 3$), the sheets were transferred to a bath of 10% pyrrole in 1:1 EtOH/ H_2O solution for an hour at room temperature. The sheets were then soaked in water at least thrice (15 min each) to let EtOH passively diffuse out of the fibers, followed by storing them in water at 4 °C for another 24 h. The sheets were kept sterile throughout the process. To improve cell attachment during seeding, the fiber bundle sheets were partially dried by using sterile Kimwipes to briefly wick away excess water by placing the wipe against the edge of the PET frame. Once partially dried fibrin sheets are stored at

4 °C until seeding to retain moisture and may be stored in such a manner for at least two months. Fibrinogen and crosslinker bath solutions were filtered with 0.22 µm filter before use and sheets were spun under sterile conditions in a biosafety cabinet.

P3HT/PCBM film preparation.⁷² Following literature procedure, 1,2-chlorobenzene solutions of P3HT and PCBM were prepared separately, with a concentration of 7.5 mg/mL, and then mixed (1:1 v/v) using a magnetic stirrer. The solution was then heated at 50 °C, stirred and finally deposited on the ITO-covered glass substrate by spin coating. The spinning parameters are as follows: first step—800 r.p.m., angular acceleration 1,500 rad s⁻², rotation duration 2 s; second step—1,500 r.p.m., angular acceleration 4,000 rad s⁻², rotation duration 30 s) After deposition, organic layers were annealed by heating at 120 °C for at least 2 h. Control substrates (ITO-covered glass substrates) were UV sterilized.

P3HT/PCBM electrospinning. 3.5/1 wt% P3HT/PCBM in chloroform/toluene (1:1 v/v) and 10 wt% PVP in chloroform/ethanol (1:1 v/v) were prepared separately, mixed, stirred well and subjected to electrospinning. The positive terminal of a high voltage DC power supply was connected to the metallic needle of the syringe. A grounded, rotating collector plate with 15mm glass cover slips was placed 13 cm from the tip of the needle. P3HT/PCBM and PVP were used as the core and shell materials, with flow rates of the inner and outer capillaries were set at a rate of 1.3 mL/h, 0.8 mL/h, respectively. All the experiments were conducted at room temperature with a relative humidity of 50–60 %. The collected fibers on glass cover slips were soaked in ethanol for ~20 minutes to remove the PVP shell. This protocol was modified from Ref. 80.

Schwann cell culture. Human immortalized Schwann cells (hiSCs) were obtained from Dr. Ahmet Hoke (JHU School of Medicine) and used for all the *in vitro* studies. This immortalized cell line was cultured in Dulbecco's Modified Eagle Medium (DMEM), supplemented with 0.2% glucose, 2 mM *L*-glutamine, 10% fetal bovine serum (FBS) and 1% penicillin/streptomycin. The FBS was acquired from Sigma and all the other components were from Gibco. Cells were cultured in a tissue culture flask, which was then kept in a humid, 5% CO₂ environment in an incubator at 37°C. For passaging, hiSCs were treated with trypsin (TrypLE Express, Gibco) and centrifuged to form a pellet. Cell counting was performed with a hemocytometer with Trypan blue (Gibco) staining (1:1, stain/media with cells). All cell studies were performed with a seeding density of 10,000 cells/μL loading a total of 50,000 per scaffold sample.

Human neural stem cell culture. Human neural stem/progenitor cells (hNSCs) were obtained from Millipore (Billerica, MA). The cells were derived from the ventral mesencephalon region of human fetal brain and immortalized by retroviral transduction with the v-Myc oncogene. Matrigel (Corning, from Engelbreth-Holm-Swarm Mouse Tumor, 50 μg/mL final coating concentration) or laminin (Sigma-Aldrich, 20 μg/mL final coating concentration) was used to coat substrates at least 2 h before cell seeding. Human NSCs were incubated at a 37°C under 5% CO₂ and used before the 15th passage. For differentiation studies, hNSCs were cultured with the medium without FGF-2 and EGF. Cells were allowed to adhere overnight at 37°C and 5% CO₂ before lifting the growth factors from the culture medium.

Dorsal root ganglion explant isolation and culture. All animal procedures were conducted in accordance with protocols approved by the Institutional Animal Care and Use

Committee at the Johns Hopkins University. Following a literature protocol,⁸¹ DRG explants were isolated from P5 Sprague-Dawley rat pups (Charles River, Wilmington, MA) and seeded immediately onto Matrigel-coated (Corning, from Engelbreth-Holm-Swarm Mouse Tumor, 50 µg/mL final coating concentration) peptide hydrogel samples or tissue culture polystyrene in neurobasal medium (Invitrogen, Eugene, OR) with B-27 supplement, *L*-glutamine, and penicillin–streptomycin. Each sample substrate was seeded with one whole DRG explant and kept in a humid, 5% CO₂ environment at 37°C.

Neonatal rat ventricular myocyte isolation and culture. The ventricles of a 2-days old Sprague-Dawley neonatal rat pups were excised and enzymatically dissociated with 0.25 mg/mL trypsin in Hanks' balanced salt solution (HBSS) at 4 °C, followed by treatment with 1 mg/mL collagenase in HBSS. The isolated neonatal rat ventricular myocytes (NRVMs) were cultured in Medium 199 (M199), supplemented with 10% HEPES buffer solution, 10% MEM non-essential amino acids, 0.35 wt% glucose (from a pre-dissolve 44 wt% stock), 2 mM *L*-glutamine, 0.2% Vitamin B12/Penicillin solution and 6% heat-inactivated fetal bovine serum (FBS). Upon seeding the isolated NRVMs in the desired substrate, the medium was replaced immediately after 24 h and then every 48 h for the succeeding days. NRVMs were allowed to mature in culture for at least 14 days before applying any strain to the scaffold. The culture was kept in a humid, 5% CO₂ environment at 37°C.

Scanning electron microscopy (SEM). SEM images were acquired using an SEI Quanta 200 Environmental SEM. Samples underwent gradual ethanol dehydration (25%, 50%, 75% 100%), after which they were critical point dried using a Tousimis Samdri-795 and sputtered with 4 nm of Pd layer using an Anatech USA Hummer 6.2. Samples with

cells were first fixed prior to dehydration. From the culture media, hydrogel fibers were washed with Dulbecco's Phosphate Buffer Saline (DPBS, 1X, Cellgro) three times and fixed with 4% paraformaldehyde at 4°C overnight. Fibers were washed again with DPBS three times prior to ethanol dehydration (25%, 50%, 60% 70%, 80%, 90%, 100%). Analysis of fiber widths was conducted using ImageJ.

Epifluorescence microscopy. Aligned hydrogels, drop cast and electrostretched fibers containing the π -conjugated peptides were prepared under a sterile environment prior to seeding cells on top of each material. All of these materials were directly placed within the tissue culture plate, with the electrostretched fibers specifically wrapped around a PET frame. All fluorescence images were taken under a Zeiss AXIO Observer.A1 epifluorescence microscope equipped with an AxioCam MRm or an LSM_510 Zeiss confocal microscope.

Polarized optical microscopy (POM). Imaging was performed on an Zeiss Axioplan II optical microscope equipped with crossed polarizers and a QICLICK-F-CLR-Q (QImaging) 12-bit CCD camera.

Rheology measurements. Time sweep oscillatory rheology measurements were performed on G2 ARES (TA Instruments) rheometer system with an 8-mm diameter parallel plate geometry and 200 μm gap size. All rheological tests were performed at 37°C. Electro-stretched fibers were wrapped around a polyethylene (PET) frame support, and the frame was placed on top of the sample holder, making sure that only the sample touches the parallel plate. Single frequency (1 Hz) and steady shear strain (5%) were used for all the tests.

Dynamic mechanical analysis. Tests were done using a Q800 DMA in force ramp mode where force application was increased by 0.15 N/min until fiber failure.

Proliferation and viability assay. To the electrostretched alginate-peptide hybrid hydrogel, a WST-1 viability assay was conducted in order to assess the cytocompatibility of the scaffold. Fibers were wrapped around a (PET) frame wherein each frame was separately placed in a 6-well tissue culture plate (BD Falcon). To each well, 100 μ L of WST-1 (Roche Applied Science) was added on the day that the absorption was read. The WST-1 was incubated in each of the wells for 2 hours and was gently mixed. From each well, a 100 μ L aliquot (n=3 per well) was taken out and transferred to a 96-well tissue culture plate to eliminate any background absorption from the peptides. Same treatment was followed for the controls: electrospun alginate fibers, drop cast peptide, and tissue culture polystyrene surface (TCPS). Readings were made at four time periods, 120 minutes, 1, 2 and 5 day(s), taking measurements from five and three samples per day for the hybrid scaffold and controls, respectively. Measurements were performed at 450 nm using a BioTek Synergy 2 plate reader. A calibration curve was prepared with human immortalized Schwann cells in order to convert absorbance to cell numbers. Morphology changes after the first and the fifth day were viewed under SEM, following the procedure described above.

Electrical and light stimulation protocol. For the electrical stimulation, a two-electrode setup with Ag contacts (~1 cm apart) to the ends of the hydrogels were used. Chronoamperometry experiments were performed with a PARSTAT 2273 (Princeton Applied Research) potentiostat. For the light stimulation, 10-W LED sources (LED-Engin) at different wavelengths powered by an Instek GPS-1850D source or an Instek GFG-

8216A function generator was used. The distance between the LED and the hydrogel was kept between 1.5 to 2 cm. The amount of time for stimulation for each specific experiment is described in the *Results and Discussion*.

Real-time PCR analysis. The levels of mRNA for human neural stem cell markers (Nestin, GFAP, Tuj1, MAP2) were assessed using real-time PCR. Total cellular RNA was isolated by RNeasy Mini Kits (QIAGEN). First strand cDNA synthesis reactions were performed with a light cycler apparatus (Biometra TPERSONAL, German), using High Capacity cDNA Reverse Transcription Kit (Invitrogen). Real-time PCR was performed using TaqMan Gene Expression Master Mix (Invitrogen) with a light cycler apparatus (StepOnePlus™ Real-Time PCR System, Applied Biosystems™). PCR cycling consisted of 40 cycles of amplification of the template DNA with primer annealing at 60 °C. The relative level of expression of each target gene was then calculated using the $2^{-\Delta\Delta C_t}$ method. The amplification efficiencies of primer pairs were validated to enable quantitative comparison of gene expression. All primers were Taqman primers (Invitrogen). Each quantitative PCR was performed 3 times on 3 different experimental replicates, and results were normalized to those obtained with the reference gene (GAPDH).

Plasmin treatment for aligned bundles. The aligned fiber bundles were treated with 15 CU/mL of plasmin from human plasma (Athens Research and Technology, Athens, GA, USA) in DMEM (Life Technologies) for at least 24 h in a humidified incubator (37 °C and 5% CO₂). The samples were washed with deionized water thrice, and then immediately imaged while the fibers are in their hydrated state.

Acknowledgements

Brian Ginn in the group of Professor Hai-Quan Mao (Johns Hopkins University) performed the dynamic mechanical analysis for the fibrin and fibrin-polypyrrole composite hydrogels. The isolation of neonatal rat ventricular myocytes and optical mapping were done by Justin Morrissette-McAlmon in the group of Professor Warren Grayson (Johns Hopkins University). Experiments involving the bioreactor setup⁷⁸ were conducted with the help from Sarah Somers (also from Grayson Group). The sheet resistance measurements for fibrin-PPy was done by Dr. Tejaswini Kale. All the ongoing calcium imaging experiments are currently done with the help of Professor Ivy Dick (University of Maryland-Baltimore).

References

- (1) Langer, R., and Vacanti, J. (1993) Tissue engineering. *Science* 260, 920-926.
- (2) Chen, G., Ushida, T., and Tateishi, T. (2002) Scaffold design for tissue engineering. *Macromol. Biosci.* 2, 67-77.
- (3) Khademhosseini, A., and Langer, R. (2016) A decade of progress in tissue engineering. *Nat. Protoc.* 11, 1775-1781.
- (4) Ortinou, S., Schmich, J., Block, S., Liedmann, A., Jonas, L., Weiss D. G., Helm, C. A., Rolfs, A. and Frech M. J. (2010) Effect of 3D-scaffold formation on differentiation and survival in human neural progenitor cells. *Biomed. Eng. Online* 9, 70.
- (5) Jiang, X., Lim, S. H., Mao, H.-Q., and Chew, S. Y. (2010) Current applications and future perspectives of artificial nerve conduits. *Exp. Neurol.* 223, 86-101.
- (6) Wang, H., and Heilshorn, S. C. (2015) Adaptable hydrogel networks with reversible linkages for tissue engineering. *Adv. Mater.* 27, 3717-3736.
- (7) Chew, S. Y., Mi, R., Hoke, A. and Leong, K. (2007) Aligned protein-polymer composite fibers enhance nerve regeneration: a potential tissue-engineering platform. *Adv. Funct. Mater.* 17, 1288-1296.

- (8) Lampe, K. J., and Heilshorn, S. C. (2012) Building stem cell niches from the molecule up through engineered peptide materials. *Neurosci. Lett.* 519, 138-146.
- (9) Ghasemi-Mobarakeh, L., Prabhakaran, M. P., Morshed, M., Nasr-Esfahani, M. H., and Ramakrishna, S. (2009) Electrical stimulation of nerve cells using conductive nanofibrous scaffolds for nerve tissue engineering. *Tissue Eng. Part A* 15, 3605-3619.
- (10) Gordon, T. (2016) Electrical stimulation to enhance axon regeneration after peripheral nerve injuries in animal models and humans. *Neurotherapeutics* 2, 295-310.
- (11) Leppik, L. P., Froemel, D., Slavici, A., Ovadia, Z. N., Hudak, L., Henrich, D., Marzi, I., and Barker, J. H. (2015) Effects of electrical stimulation on rat limb regeneration, a new look at an old model. *Sci. Rep.* 5, 18353.
- (12) Schmidt, C. E., Shastri, V. R., Vacanti, J. P. and Langer, R. (1997) Stimulation of neurite outgrowth using an electrically conducting polymer. *Proc. Natl. Acad. Sci. U. S. A.* 94, 8948–8953.
- (13) Koppes, A. N., Seggio, A. M., and Thompson, D. M. (2011) Neurite outgrowth is significantly increased by the simultaneous presentation of Schwann cells and moderate exogenous electric fields. *J. Neural Eng.* 8, 046023.
- (14) Bellamkonda, R. V. (2006) Peripheral nerve regeneration: an opinion on channels, scaffolds and anisotropy. *Biomaterials* 27, 3515-3518.
- (15) Saracino, G. A. A., Cigognini, D., Silva, D., Caprini, A., and Gelain, F. (2013) Nanomaterials design and tests for neural tissue engineering. *Chem. Soc. Rev.* 42, 225-262.
- (16) Ertürk, A., Hellal, F., Enes, J., and Bradke, F. (2007) Disorganized microtubules underlie the formation of retraction bulbs and the failure of axonal regeneration. *J. Neurosci.* 27, 9169-9180.
- (17) Goldberg, J. L. (2003) How does an axon grow? *Genes & Dev.* 17, 941-958.
- (18) He, Z., and Jin, Y. (2016) Intrinsic control of axon regeneration. *Neuron* 90, 437-451.
- (19) Subramanian, A., Krishnan, U. M., and Sethuraman, S. (2009) Development of biomaterial scaffold for nerve tissue engineering: biomaterial mediated neural regeneration. *J. Biomed. Sci.* 16, 108.
- (20) Lee, J. Y., Lee, J. W., and Schmidt, C. E. (2009) Neuroactive conducting scaffolds: nerve growth factor conjugation on active ester-functionalized polypyrrole. *J. R. Soc. Interface* 6, 801-810.
- (21) Guarino, V., Alvarez-Perez, M. A., Borriello, A., Napolitano, T., and Ambrosio L. (2013) Conductive PANi/PEGDA macroporous hydrogels for nerve regeneration. *Adv. Healthc. Mater.* 2, 218-227.

- (22) Chikar, J. A., Hendricks, J. L., Richardson, S. M., Raphael, Y., Pflingst, B.E., Martin, D.C. (2012) The use of a dual PEDOT and RGD-functionalized alginate hydrogel coating to provide sustained drug delivery and improved cochlear implant function. *Biomaterials* 33, 1982-1990.
- (23) Severt, S. Y., Ostrovsky-Snider, N. A., Leger, J. M., and Murphy, A. R. (2015) Versatile method for producing 2D and 3D conductive biomaterial composites using sequential chemical and electrochemical polymerization. *ACS Appl. Mater. Interfaces* 7, 25281-25288.
- (24) O'Grad, M. L., and Parker, K. K. (2008) Dynamic control of protein-protein interactions. *Langmuir* 24, 316-322.
- (25) Liu, X., Gilmore, K. J., and Moulton, S. E., Wallace, G. G. (2009) Electrical stimulation promotes nerve cell differentiation on polypyrrole/poly (2-methoxy-5 aniline sulfonic acid) composites. *J. Neural Eng.* 6, 065002.
- (26) Mawad, D., Stewart, E., Officer, D. L., Romeo, T., Wagner, P., Wagner, K., and Wallace, G. G. (2012) A single component conducting polymer hydrogel as a scaffold for tissue engineering. *Adv. Funct. Mater.* 22, 2692-2699.
- (27) Jin, G., Prabhakaran, M. P., Liao, S., and Ramakrishna, S. (2011) Photosensitive materials and potential of photocurrent mediated tissue regeneration. *J. Photochem. Photobiol. B* 102, 93-101.
- (28) Jin, G., Prabhakaran, M. P., Kai, D., Kotaki, M., and Ramakrishna, S. (2013) Electrospun photosensitive nanofibers: potential for photocurrent therapy in skin regeneration. *Photochem. Photobiol. Sci.* 12, 124-134.
- (29) Nguyen, P., and Berry, V. (2012) Graphene interfaced with biological cells: opportunities and challenges. *J. Phys. Chem. Lett.* 3, 1024-1029.
- (30) Kotov, N. A., Winter, J. O., Clements, I. P., Jan, E., Timko, B. P., Campidelli, S., Pathak, S., Mazzatenta, A., Lieber, C. M., Prato, M., Bellamkonda, R. V., Silva, G. A., Kam, N. W. S., Patolsky, F., and Ballerini, L. (2009) Nanomaterials for neural interfaces. *Adv. Mater.* 21, 3970-4004.
- (31) Romero, I. S., Schurr, M. L., Lally, J. V., Kotlik, M. Z., and Murphy, A. R. (2013) Enhancing the interface in silk-polypyrrole composites through chemical modification of silk fibroin. *ACS Applied Materials & Interfaces* 5, 553-564.
- (32) Murphy, N. P., and Lampe, K. J. (2015) Mimicking biological phenomena in hydrogel-based biomaterials to promote dynamic cellular responses. *J. Mater. Chem. B* 3, 7867-7880.
- (33) Guvendiren, M., Lu, H. D., and Burdick, J. A. (2012) Shear-thinning hydrogels for biomedical applications. *Soft Matter* 8, 260-272.

- (34) Kopeček, J. (2007) Hydrogel biomaterials: a smart future? *Biomaterials* 28, 5185-5192.
- (35) Geisler, I. M., and Schneider, J. P. (2012) Evolution-based design of an injectable hydrogel. *Adv. Funct. Mater.* 22, 529-537.
- (36) Slaughter, B. V., Khurshid, S. S., Fisher, O. Z., Khademhosseini, A., and Peppas, N. A. (2009) Hydrogels in regenerative medicine. *Adv. Mater.* 21, 3307-3329.
- (37) Murphy, W. L., McDevitt, T. C., and Engler, A. J. (2014) Materials as stem cell regulators. *Nat. Mater.* 13, 547-557.
- (38) Wen, J. H., Vincent, L. G., Fuhrmann, A., Choi, Y. S., Hribar, K. C., Taylor-Weiner, H., Chen, S., and Engler, A. J. (2014) Interplay of matrix stiffness and protein tethering in stem cell differentiation. *Nat. Mater.* 13, 979-987.
- (39) Francis, N. L., Bennett, N. K., Halikere, A., Pang, Z. P., and Moghe, P. V. (2016) Self-assembling peptide nanofiber scaffolds for 3-D reprogramming and transplantation of human pluripotent stem cell-derived neurons. *ACS Biomater. Sci. Eng.* 2, 1030-1038.
- (40) Gough, J. E., Saiani, A., and Miller, A. F. (2012) Peptide hydrogels: mimicking the extracellular matrix. *Bioinspir. Biomim. Nan.* 1, 4-12.
- (41) Mart, R. J., Osborne, R. D., Stevens, M. M., and Ulijn, R. V. (2006) Peptide-based stimuli-responsive biomaterials. *Soft Matter* 2, 822-835.
- (42) Boekhoven, J., and Stupp, S. I. (2014) 25th Anniversary article: supramolecular materials for regenerative medicine. *Adv. Mater.* 26, 1642-1659.
- (43) Adams, D. J., and Topham, P. D. (2010) Peptide conjugate hydrogelators. *Soft Matter* 6, 3707-3721.
- (44) Yan, C., and Pochan, D. J. (2010) Rheological properties of peptide-based hydrogels for biomedical and other applications. *Chem. Soc. Rev.* 39, 3528-3540.
- (45) Altunbas, A., and Pochan, D. J. (2011) Peptide-based and polypeptide-based hydrogels for drug delivery and tissue engineering. *Top. Curr. Chem.* 310, 135-167.
- (46) Bettinger, C. J., Langer, R., Borenstein, J. T. (2009) Engineering substrate topography at the micro- and nanoscale to control cell function. *Angew. Chem. Int. Ed.* 48, 5406-5415.
- (47) Rajnicek, A., Britland, S., and McCaig, C. (1997) Contact guidance of CNS neurites on grooved quartz: influence of groove dimensions, neuronal age and cell type. *J. Cell Sci.* 110, 2905-2913.
- (48) Capulli, A. K., MacQueen, L. A., Sheehy, S. P. and Parker, K. K. (2016) Fibrous scaffolds for building hearts and heart parts. *Adv. Drug Deliv. Rev.* 96, 83-102.
- (49) Besenius, P. (2016) Controlling supramolecular polymerization through multicomponent self-assembly. *J. Polym. Sci. A Polym. Chem.* 55, 34-78.

- (50) Lim, S. H., Liu, X. Y., Song, H., Yarema, K. J., and Mao, H.-Q. (2010) The effect of nanofiber-guided cell alignment on the preferential differentiation of neural stem cells. *Biomaterials* 31, 9031-9039.
- (51) Zhang, S., Liu, X., Barreto-Ortiz, S. F., Yu, Y., Ginn, B. P., DeSantis, N. A., Hutton, D. L., Grayson, W. L., Cui, F.-Z., Korgel, B. A., Gerecht, S., and Mao, H.-Q. (2014) Creating polymer hydrogel microfibrils with internal alignment via electrical and mechanical stretching. *Biomaterials* 35, 3243-3251.
- (52) Zhang, S., Greenfield, M. A., Mata, A., Palmer, L. C., Bitton, R., Mantei, J. R., Aparicio, C., la Cruz, de, M. O., and Stupp, S. I. (2010) A self-assembly pathway to aligned monodomain gels. *Nat. Mater.* 9, 594-601.
- (53) Capulli, A. K., Emmert, M. Y., Pasqualini, F. S., Kehl, D., Caliskan, E., Lind, J. U., Sheehy, S., Park, S. J., Ahn, S., Weber, B., Goss, J. A., Hoerstrup, S. P., and Parker, K. K. (2017) JetValve: rapid manufacturing of biohybrid scaffolds for biomimetic heart valve replacement. *Biomaterials* 133, 229-241.
- (54) Deravi, L. F., Sinatra, N. R., Chantre, C. O., Nesmith, A. P., Yuan, H., Deravi, S. K., Goss, J. A., MacQueen, L. A., Badrossamy, M. R., Gonzalez, G. M., Philips, M. D., and Parker, K. K. (2017) Design and fabrication of fibrous nanomaterials using pull spinning. *Macromol. Mater. Eng.* 302, 1600404.
- (55) Gonzalez, G. M., MacQueen, L. A., Lind, J. U., Fitzgibbons, S. A., Chantre, C. O., Huggler, I., Golecki, H. M., Goss, J. A. and Parker, K. K. (2017) Production of synthetic, para-aramid and biopolymer nanofibers by immersion rotary jet-spinning. *Macromol. Mater. Eng.* 302, 1600365.
- (56) Wall, B. D., Diegelmann, S. R., Zhang, S., Dawidczyk, T. J., Wilson, W. L., Katz, H. E., Mao, H.-Q., and Tovar, J. D. (2011) Aligned macroscopic domains of optoelectronic nanostructures prepared via shear-flow assembly of peptide hydrogels. *Adv. Mater.* 23, 5009–5014.
- (57) Liyanage, W., Ardoña, H. A. M., Mao, H. -Q. and Tovar, J. D. (2016) Cross-linking approaches to tuning the mechanical properties of peptide π -electron hydrogels. *Bioconjugate Chem.* 28, 751-759.
- (58) Diegelmann, S. R., Hartman, N., Markovic, N., and Tovar, J. D. (2012) Synthesis and alignment of discrete polydiacetylene-peptide nanostructures. *J. Am. Chem. Soc.* 134, 2028–2031.
- (59) Sun, X., Chen, T., Huang, S., Li, L., and Peng, H. (2010) Chromatic polydiacetylene with novel sensitivity. *Chem. Soc. Rev.* 39, 4244–4257.
- (60) Sarkar, A., Okada, S., Matsuzawa, H., and Matsuda, H. (2000) Novel polydiacetylenes for optical materials: beyond the conventional polydiacetylenes. *J. Mater. Chem.* 10, 819-828.

- (61) Patel, G. N., Chance, R. R., and Witt, J. D. (1978) A visual conformational transition in a polymer solution. *J. Polym. Sci. A Polym. Lett.* *16*, 607-614.
- (62) Britt, D. W., Hofmann, U. G., Möbius, D., and Hell, S. W. (2001) Influence of substrate properties on the topochemical polymerization of diacetylene monolayers. *Langmuir* *17*, 3757-3765.
- (63) Patel, G. N., Chance, R. R., and Witt, J. D. (1979) A planar–nonplanar conformational transition in conjugated polymer solutions. *J. Chem. Phys.* *70*, 4387-4392.
- (64) Rubner, M. F. (1986) Novel optical properties of polyurethane-diacetylene segmented copolymers. *Macromolecules* *19*, 2129-2138.
- (65) Diegelmann, S. R., and Tovar, J. D. (2013) Polydiacetylene-peptide 1D nanomaterials. *Macromol. Rapid Commun.* *34*, 1343–1350.
- (66) Carpick, R. W., Sasaki, D. Y., Marcus, M. S., Eriksson, M. A., and Burns, A. R. (2004) Polydiacetylene films: a review of recent investigations into chromogenic transitions and nanomechanical properties. *J. Phys.: Condens. Matter* *16*, R679–R697.
- (67) Wilchek, M., Bayer, E. A., and Livnah, O. (2006) Essentials of biorecognition: the (strept) avidin–biotin system as a model for protein–protein and protein–ligand interaction. *Immunol. Lett.* *103*, 27-32.
- (68) Xu, H., and Heilshorn, S. C. (2012) Microfluidic investigation of BDNF-enhanced neural stem cell chemotaxis in CXCL12 gradients. *Small* *9*, 585-595.
- (69) Willand, M. P., Rosa, E., Michalski, B., Zhang, J. J., Gordon, T., Fahnstock, M., and Borschel, G. H. (2016) Electrical muscle stimulation elevates intramuscular BDNF and GDNF mRNA following peripheral nerve injury and repair in rats. *Neuroscience* *334*, 93-104.
- (70) Kornblum, H. I. (2007) Introduction to neural stem cells. *Stroke* *38*, 810-816.
- (71) Ghezzi, D., Antognazza, M. R., Maccarone, R., Bellani, S., Lanzarini, E., Martino, N., Mete, M., Pertile, G., Bisti, S., Lanzani, G., and Benfenati, F. (2013) A polymer optoelectronic interface restores light sensitivity in blind rat retinas. *Nat. Photonics* *7*, 400-406.
- (72) Ghezzi, D., Antognazza, M. R., Maschio, M. D., Lanzarini, E., Benfenati, F., and Lanzani, G. (2011) A hybrid bioorganic interface for neuronal photoactivation. *Nat. Commun.* *2*, 166.
- (73) Capulli, A. K., MacQueen, L. A., Sheehy, S. P., and Parker, K. K. (2016) Fibrous scaffolds for building hearts and heart parts. *Adv. Drug Deliv. Rev.* *96*, 83-102.
- (74) Dvir, T., Timko, B. P., Brigham, M. D., Naik, S. R., Karajanagi, S. S., Levy, O., Jin, H., Parker, K. K., Langer, R., and Kohane, D. S. (2011) Nanowired three-dimensional cardiac patches. *Nat. Nanotechnol.* *6*, 720-725.

- (75) Shin, S. R., Jung, S. M., Zalabany, M., Kim, K., Zorlutuna, P., Kim, S. B., Nikkhah, M., Khabiry, M., Azize, M., Kong, J., Wan, K.-T., Palacios, T., Dokmeci, M. R., Bae, H., Tang, X. S., and Khademhosseini, A. (2013) Carbon-nanotube-embedded hydrogel sheets for engineering cardiac constructs and bioactuators. *ACS Nano* 7, 2369-2380.
- (76) Sakiyama, S. E. and Hubbell, J. A. (2000) Development of fibrin derivatives for controlled release of heparin-binding growth factors. *J. Control. Release* 65, 389-402.
- (77) Barreto-Ortiz, S. F., Fradkin, J., Eoh, J., Trivero, J., Davenport, M., Ginn, B., Mao, H. Q., and Gerecht, S. (2015) Fabrication of 3-dimensional multicellular microvascular structures. *FASEB J.* 29, 3302-3314.
- (78) Cook, C. A., Huri, P. Y., Ginn, B. P., Gilbert-Honick, J., Somers, S. M., Temple, J. P., Mao, H.-Q., and Grayson, W. L. (2016) Characterization of a novel bioreactor system for 3D cellular mechanobiology studies. *Biotechnol. Bioeng.* 113, 1825-1837.
- (79) Isidro-Llobet, A., Álvarez, M., and Albericio, F. (2009) Amino acid-protecting groups. *Chem. Rev.* 109, 2455-2504.
- (80) Sundarrajan, S., Murugan, R., Nair, A. S., and Ramakrishna, S. (2010) Fabrication of P3HT/PCBM solar cloth by electrospinning technique. *Mater. Lett.* 64, 2369-2372.
- (81) Roman, J. A., Reucroft, I., Martin, R. A., Hurtado, A., and Mao, H.-Q. (2016) Local release of paclitaxel from aligned, electrospun microfibers promotes axonal extension. *Adv. Healthc. Mater.* 5, 2628-2635.

CHAPTER SEVEN:

Future Directions and Concluding Remarks

Future Directions

This dissertation presented different aspects of the development of π -conjugated peptide hydrogelators as biological scaffolds that can impart topographical and potentially, electrical and biochemical stimuli. The implications of these results have opened a couple of research questions and directions which will be presented in the subsequent sections. Alternative material characterization techniques, new design derivatives, and applications to other cellular models will be discussed.

In Chapter 2, the mechanical properties were investigated using rheological measurements, which reflect the bulk property of the material. When used as a bioscaffold, the cellular adhesion and mechanotransduction at the cell-to-scaffold interface occurs within the size scale of the fibers that comprise the hydrogels or fiber bundles presented in earlier Chapters—which are within the nano- to microscale. To better characterize the mechanical properties in a more localized region, atomic force microscopy (AFM) nanoindentation can be used. This measurement involves a glass microsphere with an accurately measured radius, R , which is attached at the end of the AFM cantilever and interacts with the substrate. The deflection of the cantilever, indentation distance and elastic moduli of the surface where the microsphere is being pressed, can be correlated by the Hertz model as shown in Figure 7.1. Preliminary attempts to characterize the peptides in Chapter 2 using this technique with Prof. Patricia McGuiggan, which are one-component and uncrosslinked, resulted in hydrogel destruction and sticking of the gel components to the microsphere. It would be interesting to use this technique for the peptide hydrogels in Chapter 6 that are crosslinked, which could be more stable towards this characterization.

Hertz model of an incompressible sphere:

$$F = \frac{4E\sqrt{R}}{3(1-\nu^2)} (\delta)^{3/2}$$

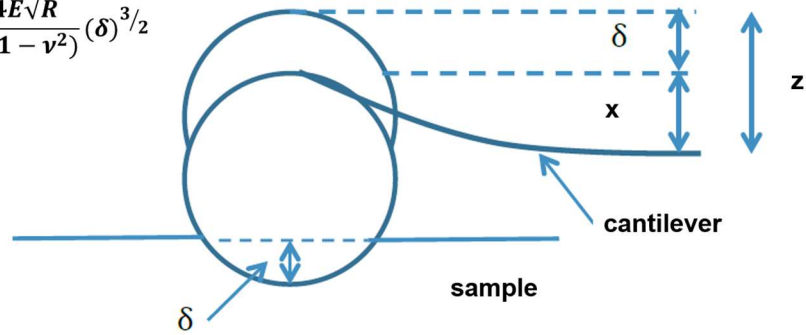


Figure 7.1. Schematic diagram of an AFM nanoindentation setup. The Hertz model relates the force (F) of indentation to the indentation distance (δ), and to the elastic modulus (E) of a material with a specific Poisson ratio (ν). Figure courtesy of Prof. Patricia McGuiggan.

As a potential bioscaffold, it is also important to understand how the cell-hydrogel adhesion forces affect the microstructure of the hydrogels. The spatial order of the network of hydrogen-bonded and π -stacked peptide- π -peptide monomers within the hydrogel is highly correlated to its mechanical properties and electrical conductivity (*i.e.*, considering the “connectivity” of the peptide nanowires). In the case of the materials presented in Chapter 4, any change in spatial ordering results in a change in the energy transfer efficiency. There are a lot of rheological studies that address the stiffness compatibility between the substrate and the tissue/cell but the effect of cell adhesion on the stiffness and structure of the material is rarely addressed. For example, fibrin was found to have a localized effect on the fibers and increase the bulk gel stiffness when seeded with fibroblasts whereas polyacrylamide does not.¹ Learning about these microstructural changes in the presence of cells would also inform us how these affect the optoelectronic function of the material under culture conditions, thus, allowing us to better engineer the properties of this biomaterial. Without needing to seed cells, the RheoSANS technique can also be employed for these peptide hydrogels to simulate the shear forces exerted by cells

through applying different strain values during rheology experiments for one- or two-component hydrogels and study the structural impacts.

With the successful demonstration of field-effect in the devices also presented in Chapter 2, along with other previous reports where π -conjugated peptides were used as active semiconducting and gate layers, it would be interesting to create a field-effect transistor comprised of *all peptide-based layers*. Guha and co-workers demonstrated the ability of *L,L*-diphenylalanine processed as a film of micro/nanostructures to perform as dielectric.² Using a diphenylalanine-Fmoc hydrogel as the dielectric, **EAA-OT4** can be used as both the gate contact and semiconducting layer. The challenge is to be able to deposit each of the layers and create a clear interface by preventing any possible intermixing within the layers. Deposition of each layer as a hydrogel, followed by air-drying before adding the next layer, resulted in film layers with a clear interface (Figure 7.2) as observed under SEM. This is an interesting direction as a proof of principle for the functional abilities of these peptides. It will be interesting if this approach is also applicable for crosslinked peptides, and if field-effect is still observable even when the devices are in aqueous conditions which is more relevant for the biological applications.

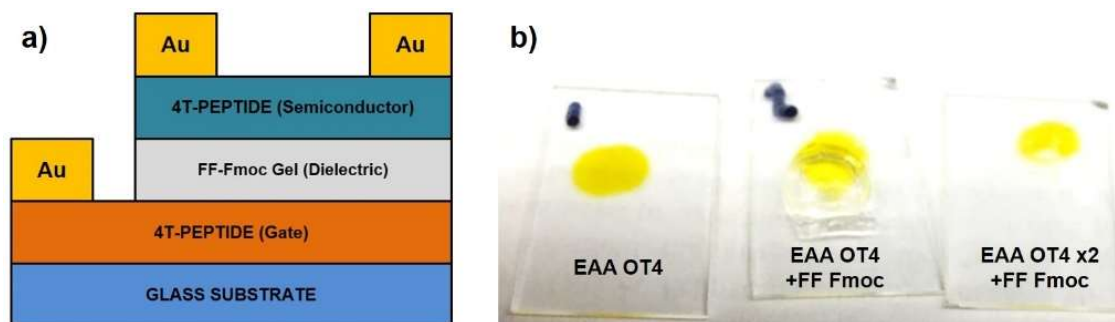


Figure 7.2. a) Proposed components for the active layers of an *all-peptide* transistor; b) image of the layers showing a clear interface between EAA-OT4 and FF-Fmoc without dissolution.

In Chapter 5, the inter-monomer distances and the structure of two-component hydrogels that are kinetically assembled by rapid acidification were studied with solid-state NMR. Structural information was successfully obtained for two-component hydrogels. However, the experiments were limited to 10 mol% acceptor loading because of the limitations imposed by the instrument. To circumvent this issue, dynamic nuclear polarization (DNP) can be used for signal enhancement and decreasing the acquisition time. This technique, however, required the addition radical agent to facilitate the polarization. Using AMUPol as a radical agent for a preliminary test, color changes were observed (orange to greenish-brown) which might suggest OT4 oxidation induced by AMUPol. Although the simulation curves obtained with DNP resulted in calculated distances similar to those reported in Chapter 5 ($r = 4.376 \pm 0.045$), the reactivity of OT4 to radical agents usable for DNP experiments and their possible effects in the peptide nanostructure (Figure 7.3b-c) should be further investigated. Characterization of the nanostructures with lower acceptor loading limits (*i.e.*, 1 mol%) to the majority donor components is also important for studying donor-acceptor assemblies such as these.

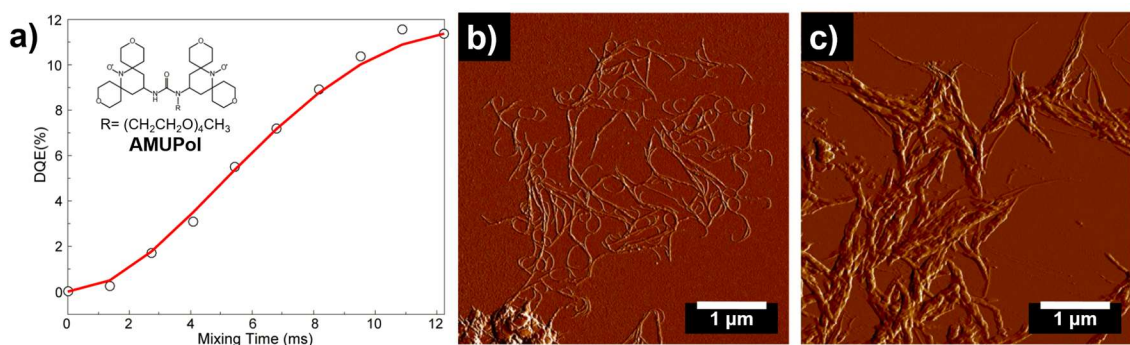


Figure 7.3. (a) DRAWS curve of A1-¹³C-EAA-OT4 under dynamic nuclear polarization conditions (inset: structure of AMUPol, the biradical agent used for these DNP runs); (b,c) AFM images (in peak force error mode) of EAA-OT4 nanostructures in (b) 70 mM HCl solution and in (c) 3:2 glycerol:70 mM HCl solution.

With the polydiacetylene-peptide materials introduced in Chapter 6, the ease of installing functional group handles in the peptide backbone that can be used for molecular recognition also allows for the potential biosensing applications of this material. Polydiacetylene (PDA) is known to exhibit biochromism or affinochromism, changing its photophysical properties upon binding of specific targets due to the conformational changes that affects the planarity of conjugated units.^{3,4} By covalently attaching biotin to a diacetylene-conjugated peptide, we can utilize the high affinity interaction between biotin and Streptavidin as a ligand-protein pair to probe any induced conformational changes in the PDA backbone. Figure 7.4 shows a representative TEM image of peptide-diacetylene nanostructures stained with Streptavidin-tagged gold nanoparticles, along with the notable pH-triggered chromic transitions in both the solution and gel states. These simple chromic transitions can also be potentially driven by the protein-ligand binding event that can cause twisting within these 1-D peptide nanostructures. This presents an interesting biosensing technique, wherein the recognition occurs due to molecular conformational changes in a completely aqueous solution and leads to easily perceivable color changes.

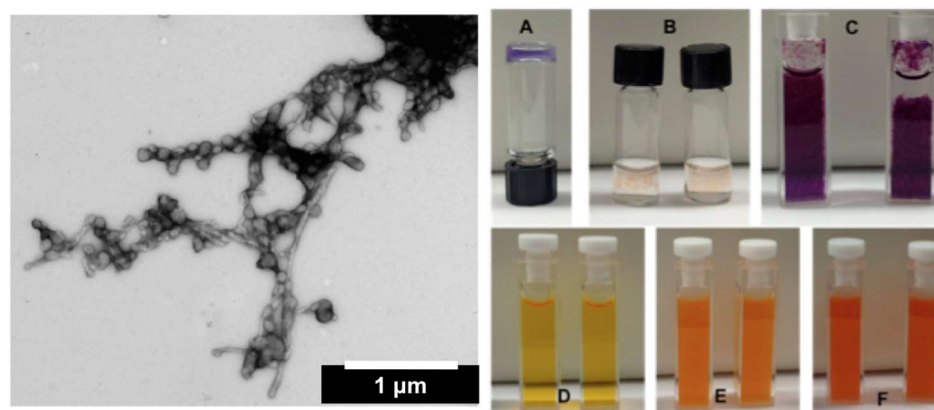


Figure 7.4. (left) SAu units bound to PDA-peptide 1-D nanostructures; (right) PDA-peptide solutions at 10^{-3} M. (A) acidified/polymerized gel; (B) heated/acidified/polymerized, without and with SAu; (C) acidified/ polymerized solution, without and with SAu; (D) after addition of base to C; (E) after addition of acid to D; (F) 20 minutes after E.

Several derivatives of the polydiacetylene-peptides presented in Chapter 6 can be further developed, along with the library of epitopes and growth factors that can be appended to the peptide backbone (*i.e.*, *via* thio-ene click reaction, ligand-protein interaction, etc.). Ultimately, the future direction for these functional bioscaffolds is geared not only to be a 2-D substrate for cells and tissues, but as an integrated 3-D material that can deliver environmental cues (topographical, optoelectronic, biochemical) in a spatiotemporal manner and with controlled degradation kinetics under physiological conditions. Moreover, the promise for photocurrent-generating bioscaffolds with multichromophoric components is an extremely exciting direction. The investigations on interfacing these materials with neural stem cells and dorsal root ganglion neurons are currently being extended to primary hippocampal neurons and cardiomyocytes as a part of the continuous efforts to show the versatility of the peptide hydrogels developed herein as a scaffolding platform to various electrosensitive cells.

Concluding Remarks

In this dissertation, several efforts were made not only to demonstrate the function of these materials, but also to engineer their function in a tunable manner based on the molecular design. Chapter 2 showed the first attempts to characterize the bulk mechanical properties of these peptide hydrogelators. These rheological measurements, along with bulk electrical properties and photophysical investigations, showed how to modulate these properties based on simple amino acid substitutions. It was found that the amino acid bulk and hydrophobicity are not the only restrictive parameters that dictate the final mechanical strength of the hydrogels, but it is the inherent propensity of each amino acid component

to form β -sheet structures that plays a more important role. It was also shown that such simple variations can result in differences in the hole mobility when the material is used as a semiconductor in a field-effect transistor geometry. These resulted in calculated mobility values for the nanomaterial active layers that span over three orders of magnitude ($\sim 5 \times 10^{-5}$ to $0.02 \text{ cm}^2 \text{ V}^{-1} \text{ s}^{-1}$) when the nanostructures had quaterthiophene cores and the assembled peptide materials spanned source and drain electrodes. It was also shown that the nanomaterials could act as gate electrodes. By varying the gate dielectric layer thickness in devices where the conventional organic semiconductor pentacene spanned the source and drain electrodes in a top-contact organic field-effect transistor, the optimum performance was observed when the dielectric thickness was 35-40 nm. These studies contribute to establishing structure-function correlation in this material and show that these peptides that self-assemble in aqueous environments can be used successfully to transmit electronic signals over biologically relevant distances.

In addition to exploring ways for the rational tuning of material properties, Chapter 3 presented how the photophysical properties of π -segments can be affected by the geometric constraints imposed by the assembled peptide matrix. Systematic studies on the effects of varying the local environment of peptide π peptide hybrid molecules on the overall photophysical properties of the assemblies were conducted with the aim of delineating the effects of self-assembly, the resultant close spatial packing of the π -electron units and electronic delocalization among these units on the photophysical properties of embedded individual π -electron units. The dilutions of π -conjugated peptides within an electronically-inert peptide matrix allowed for the observation of torsional restriction (due to reduced rotational freedom along the π -electron conjugated backbone) while minimizing

the influence of inter-chromophore exciton coupling commonly found in homo-assemblies of peptide- π -peptide triblocks. The emission spectra also showed that the peptide matrix provides a local field solvatochromism, hence the polarity of the peptide groups can affect the photophysical properties in addition to potential deplanarization due to the assembly. Using temperature variation experiments, and thus varying the available thermal energy towards rotational freedom, we confirmed that the initial kinetically trapped states of peptide ensembles led to π -electron unit excited states that may access different conformations if they are in spatially constrained environments within the peptide nanostructures.

In Chapter 4, coassembled peptide hydrogels with optoelectronic function were introduced as a platform energy-transporting hydrogelators. Using steady-state and time-resolved spectroscopy, energy transfer within coassemblies of oligo(*p*-phenylenevinylene) donor and quaterthiophene acceptor units attached to peptides was successfully shown. The energy-transfer processes were found to be sensitive to pH and temperature changes. This design was further extended to peptidic nanostructures bearing three π -systems that can facilitate both exciton migration and charge transfer among oligo(*p*-phenylenevinylene), quaterthiophene and naphthalenediimide. These important findings show that nanostructural energy transport in these materials is possible under completely aqueous and potentially, physiological conditions. Considering the high utility that multicomponent hydrogels present for future applications, efforts were made to characterize the structure of two sets of coassembled peptide hydrogels, as presented in Chapter 5. The solid state NMR results suggest that matching the lengths of the peptide monomers result in a more favored social coassembly rather than self-sorting. Further characterization of the DFAA donor-

acceptor peptide system in Chapter 4 with small-angle neutron scattering suggests that aggregated blocks of quaterthiophene are more predominant than the existence of isolated units co-mixed within the stacks of donor. This Chapter also introduced methods to characterize the assembly parameters for two-component peptides in hydrogel state that are rarely discussed.

Lastly, Chapter 6 presented how the hydrogels created from these π -conjugated peptides can offer a unique platform for biological scaffolding. In addition to the processability of these solutions as aligned hydrogels with biofunctionalizable peptide surfaces, we envision that these aspects can act synergistically to influence the behavior of cells on this synthetic bioscaffold. Several strategies, such as using covalent crosslinking between monomers within the peptide region or along photopolymerizable diacetylene cores, were employed in order to achieve hydrogel stability under cell culture conditions. These peptidic materials do not show any significant cytotoxicity and more importantly, the topographical cue provided by aligned polydiacetylene-peptide hydrogels guided the direction of neurite outgrowth of human neural stem cells and dorsal root ganglion neuron explants. Studies are underway for showing how conventional electrical field or photocurrent stimulation, together with alignment, affects neurite outgrowth and cell maturation. The use of related organic polymer donor-acceptor blend (P3HT and PCBM) did not significantly affect the differentiation pathway of the human neural cells seeded on them, but a clear effect on the directionality of outgrowth was observed for their aligned electrospun equivalents. A composite material based on fibrin and polypyrrole blends was also presented as a potential material that can be used as a scaffold for cardiac cells, due to the mechanical robustness of the material and the interesting strain-induced current

propagation behavior that can synergistically influence the growth and maturation of cardiomyocytes.

Overall, the aforementioned research efforts contributes to three important aspects of the development of π -conjugated peptides as bioelectronic materials: (1) engineering new derivatives of π -conjugated peptide hydrogels to achieve the desired function (peptide donor-acceptor coassemblies to facilitate energy transfer; epitope- or growth factor-containing hydrogels for a more efficient bioscaffolding; covalently crosslinked π -conjugated peptide hydrogels to improve stability under physiological conditions); (2) understanding structure-function correlation aspect of the material and details of the coassembly structure; and (3) using π -conjugated peptide hydrogels and related conjugated organic polymers as substrates for human neural stem cell and dorsal root ganglion neuronal culture, which are relevant cell lines for studying central nervous system repair. In addition to the interesting aspects of material development that have flourished from the research efforts for this dissertation, it is hoped that the future investigations will benefit from the results presented herein and can bring these synthetic optoelectronic peptides closer to their translation as a biological scaffold for in vivo models.

References

(1) Winer, J. P., Oake, S., and Janmey, P. A. (2009) Non-linear elasticity of extracellular matrices enables contractile cells to communicate local position and orientation. *PLoS ONE* 4, e6382.

- (2) Cipriano, T., Knotts, G., Laudari, A., Bianchi, R. C., Alves, W. A., and Guha, S. (2014) Bioinspired peptide nanostructures for organic field-effect transistors. *ACS Appl. Mater. Interfaces* 6, 21408-21415.
- (3) Carpick, R. W., Sasaki, D. Y., Marcus, M. S., Eriksson, M. A., and Burns, A. R. (2004) Polydiacetylene films: a review of recent investigations into chromogenic transitions and nanomechanical properties. *J. Phys. Condens. Matter* 16, R679–R697.
- (4) Jelinek, R., and Ritenberg, M. (2013) Polydiacetylenes—recent molecular advances and applications. *RSC Adv.* 3, 21192–21201.

APPENDIX:

Characterization Data and Supporting Information

General Materials and Methods

Synthetic considerations. The chemicals used for 9-fluorenylmethoxycarbonyl (Fmoc)-based solid phase peptide synthesis (*N*-methylpyrrolidone (NMP), *O*-(benzotriazol-1-yl)-*N,N,N',N'*-tetramethyluronium hexafluorophosphate (HBTU), *N,N*-diisopropylethylamine (DIPEA), diisopropylamine (DIPA), benzotriazol-1-yl-oxytripyrrolidinophosphonium hexafluorophosphate (PyBOP), Wang resin, Fmoc- and Mtt-protected amino acid, *D*-biotin, and (trimethylsilyl)acetylene) were obtained from Oakwood Products, Inc. or Advanced ChemTech. Fmoc-Lys(Mtt)-Wang resin was acquired from Chem-Impex International (IL, USA). All amino acids used for peptide synthesis are *L*-amino acids. Tetrahydrofuran (THF) was obtained from an Innovative Technologies PureSolv solvent purification system and dried over 4 Å molecular sieves (Sigma-Aldrich). *N,N*-dimethylformamide (DMF) was obtained from either Sigma-Aldrich or EMD Millipore Chemicals. *N,N,N',N'*-tetramethylethylenediamine (TMEDA) was obtained from Acros Organics. DIPEA, THF, DMF and pyridine were degassed by sparging with N₂ for 1 h. Tetrakis(triphenylphosphine)palladium (Pd(PPh₃)₄) was obtained from Strem Chemicals. The Biotech- grade cellulose ester dialysis tubings (MWCO 500-1000), with flat width of either 16-mm or 31-mm were obtained from Spectrum Labs. Streptavidin was purchased from New England Biolabs, Inc. Fmoc-protected *L,L*-diphenylalanine was purchased from BAChem. Poly(3-hexylthiophene) and phenyl-C₆₁-butyric acid-methyl ester (both electronic grade) were from Rieke Metals and Nano-C, respectively. Thiophene (d₄) was from CDN Isotope Labs. All other reagents and starting materials were obtained from Sigma-Aldrich and were used as received. The π -unit

precursors: 5-bromothiophene-2-carboxylic acid, 5,5'-bis-tributylstannyl-[2,2']-bithiophene,^{1,2} 4,4'-((1*E*,1'*E*)-1,4-phenylenebis(ethene-2,1-diyl))dibenzoic acid (OPV3 diacid)³ and tetradeca-6,8-diyne-dioic acid (C4DA)⁴ were prepared using literature procedures. ¹H-NMR spectra were obtained using a Bruker Avance 400 or 600 MHz FT-NMR spectrometer and the data was processed using Bruker Topspin 1.3. For the compounds containing peptide sequences, all ¹H-NMR spectra were acquired using a pre-saturation pulse to suppress the H₂O signal. Chemical shifts are reported in parts per million relative to residual protio solvent [CHCl₃ δ: 7.26 (¹H), *d*₅-DMSO δ: 2.50 (¹H), HOD δ: 4.79 (¹H)].

Solid phase peptide synthesis (SPPS). All peptides were synthesized using the standard Fmoc solid-phase technique with Wang resin pre-loaded with the terminal amino acid (Wang-Glu= 0.5 mmol/g, Wang-Asp= 0.6 mmol/g, Wang-Val=0.7 mmol/g). To the resin in a peptide chamber, Fmoc-deprotection was accomplished by adding a (1:4) piperidine/DMF solution twice (successive 5- and 10-min treatment, 10 mL for 0.3 mmol scale) and then washing with NMP, methanol and dichloromethane (DCM). For the amino acid couplings, 3.0 eq. of the Fmoc-protected amino acid (1.0 eq of the Fmoc-deprotected peptide bound to the resin) underwent external activation with 2.9 eq. of HBTU and 10 eq. DIPEA in NMP. The activated amino acid mixture was mixed for 1 min prior to addition in the peptide chamber. The reaction mixture was allowed to mix for 60-120 min, after which was rinsed with NMP, methanol and DCM. The completion of all couplings was monitored using a Kaiser test on a few dry resin beads, repeating same amino acid coupling as needed. The general procedure for amino acid coupling was repeated until the desired peptide sequence was obtained.

***N*-acylation procedure for peptides.** Following a procedure reported in the literature,¹ a solution containing 2.1 eq. of 5-bromothiophene-2-carboxylic acid that was activated by HBTU (2.0 eq.) with DIPEA (10 eq.) was mixed in NMP for 180 min with the resin containing the completed peptide sequence. The resin was rinsed with NMP, methanol and DCM. The resin was treated again with 1.1 eq. of 5-bromothiophene-2-carboxylic acid that was activated by HBTU (1.0 eq.) with DIPEA (10 eq.) for 60 min. After rinsing the resin with the standard wash cycle (NMP-methanol-DCM), completion was assessed using a Kaiser test on a few dry resin beads. Treatment with 1.1 eq. of the activated 5-bromothiophene-2-carboxylic acid was repeated as needed.

On-resin Stille coupling procedure. Following a procedure reported in the literature,¹ the *N*-acylated peptide resin made by following the general procedures described above was transferred to a Schlenk flask topped with a reflux condenser. The dried resin with Pd(PPh₃)₄ (4.0 mol % relative to the amino acid loading in the resin) was kept in the Schlenk flask under a nitrogen (N₂) atmosphere. In a separate vessel, a ~15 mM solution of 5,5'-bis-tributylstannyl-[2,2']-bithiophene was prepared in DMF. This was then added to the reaction flask *via* syringe. The reaction mixture was heated up to 80°C while agitating by constantly bubbling nitrogen (N₂) gas in the solution. The said conditions were maintained for 16 h, and then the reaction mixture was allowed to cool to room temperature. The resin was washed with DMF (3×) in a peptide chamber, followed by the standard wash cycle. The synthesized π -conjugated peptides were then subjected to cleavage procedure.

General cleavage procedure for peptides. The cleavage cocktail was prepared with 9.5 mL of trifluoroacetic acid, 250 μ L Milli-Q water, and 250 μ L of triisopropylsilane. The resin was treated with 10 mL of cleavage cocktail in a peptide chamber for 3 h. The

filtrate was drained and the resin was washed with DCM (3×). The filtrate was concentrated under reduced pressure. The crude peptide was precipitated out of the filtrate by adding 90 mL of cold Et₂O, allowing the suspension to sit for 5 min at 4°C. The pellet formed was isolated by centrifugation, followed by decanting the solvent and drying the solid formed. The pellet was redissolved in Milli-Q water with a few drops of ammonium hydroxide (to completely dissolve the solid) and was subjected to lyophilization. All peptides (both crude and purified) were stored as lyophilized solids at 4 °C in dark conditions.

Reverse phase high-performance liquid chromatography (RP-HPLC).

Peptides that underwent Stille coupling were dialyzed prior to HPLC purification in order to completely remove any excess Pd. The HPLC samples were prepared from lyophilized peptide solids after the dialysis procedure and were dissolved in Milli-Q water as basic samples by adding μL amounts of 1 M KOH until the solution reaches pH 8 to 9. Purification and analysis were performed using an Agilent SD1 PrepStar System with a Phenomenex C8 column (Luna 5 μm, 250×21.20 mm and 250×4.60 mm). The mobile phase used consists of an ammonium formate aqueous buffer (1% v/v; ~pH 8) and acetonitrile.

Electrospray Ionization Mass Spectrometry (ESI-MS).

Samples for ESI-MS analyses were prepared in a 1:1 methanol and water solution with 1.0% (v/v) ammonium hydroxide. Mass spectra were collected using a Thermo Finnigan LCQ Deca Ion Trap Mass Spectrometer in negative mode.

Nuclear magnetic resonance (NMR) spectroscopy.

¹H-NMR spectra were obtained using a Bruker Avance 400 MHz FT NMR spectrometer, and processed with

Bruker Topspin 1.3. Peptide ^1H NMR spectra were acquired using a pre-saturation pulse to suppress water when D_2O was used as the solvent.

Fourier transform infrared (FT-IR) spectroscopy. All data were obtained on dried peptides using a Thermo Scientific Nicolet Nexus 670 FT-IR spectrometer. The samples were prepared by lyophilizing acidic peptide solutions.

Dynamic light scattering (DLS). All samples were prepared from lyophilized peptide solids and dissolved in Milli-Q water. The pH of the samples was adjusted using 1 M HCl or 1 M KOH (pH 1 for acidic samples and pH 10 for basic samples). All measurements were recorded using a Malvern Instruments Zetasizer Nano-ZS90.

Transmission electron microscopy (TEM). Imaging was performed on a Philips EM 420 transmission electron microscope equipped with an SIS Megaview III CCD digital camera at an accelerating voltage of 100 kV. The solution phase samples were prepared by pipetting a drop of 1 mg/mL solution of assembled peptide in water onto 200 mesh copper grids coated with Formvar film (Electron Microscopy Sciences) and adsorbed for 5 minutes at room temperature. For hydrogel samples, the grids were placed on top of 1 wt% gels for at least 5 minutes. The grid was then washed with DI water and the excess solution was wicked off by touching the side of the grid to filter paper. The sample was then stained with a 2% uranyl acetate solution, washed with DI water and excess moisture was wicked off. The grid was dried in air before imaging.

Chapter 2

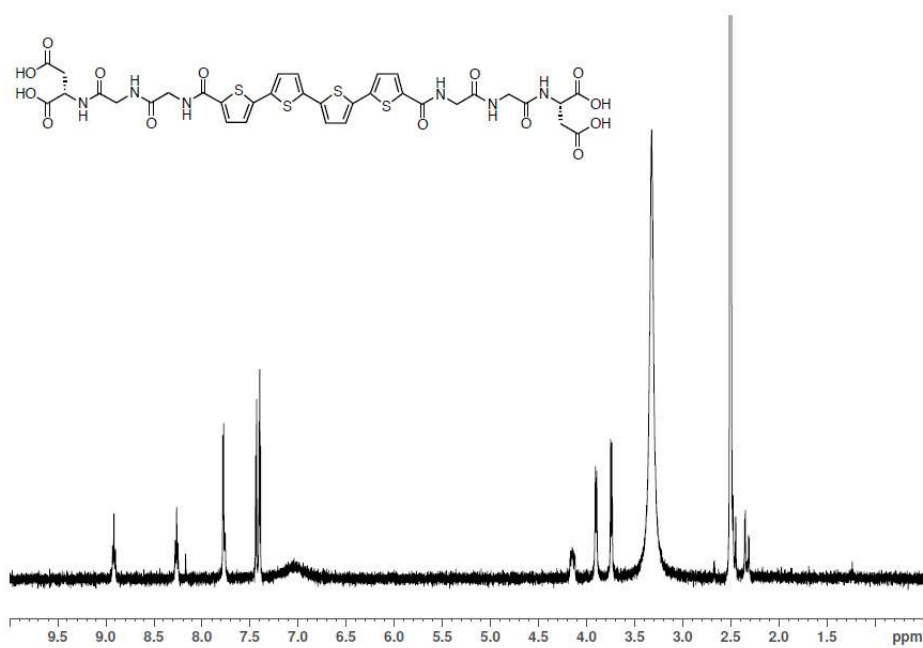


Figure A2.1. ¹H (400 MHz, d₆-DMSO) NMR spectrum of **DGG OT4** peptide.

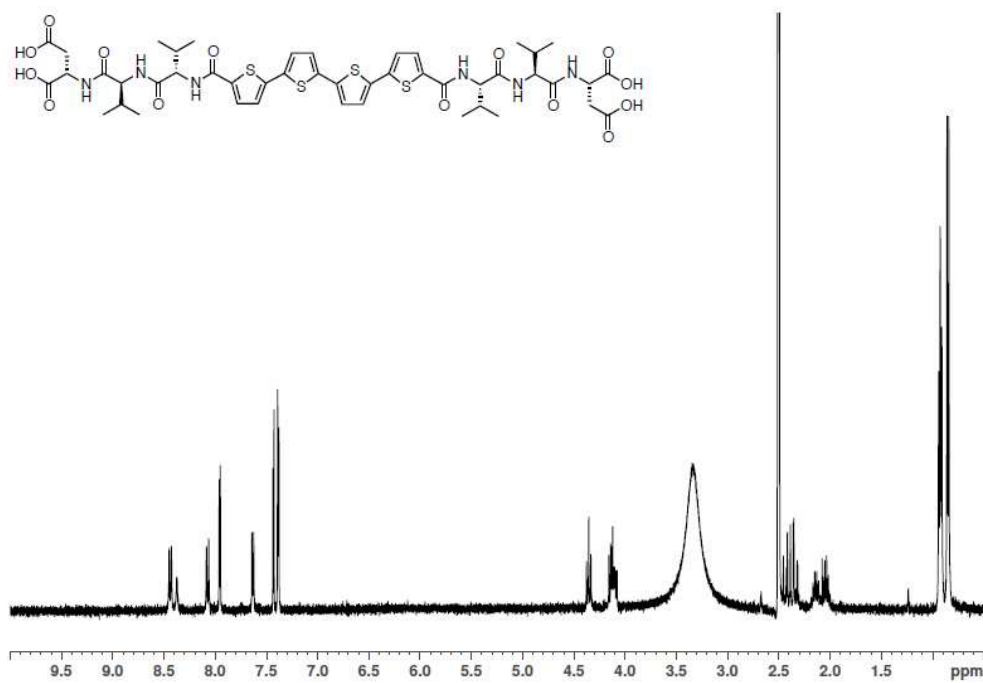


Figure A2.2. ¹H (400 MHz, d₆-DMSO) NMR spectrum of **DVV OT4** peptide.

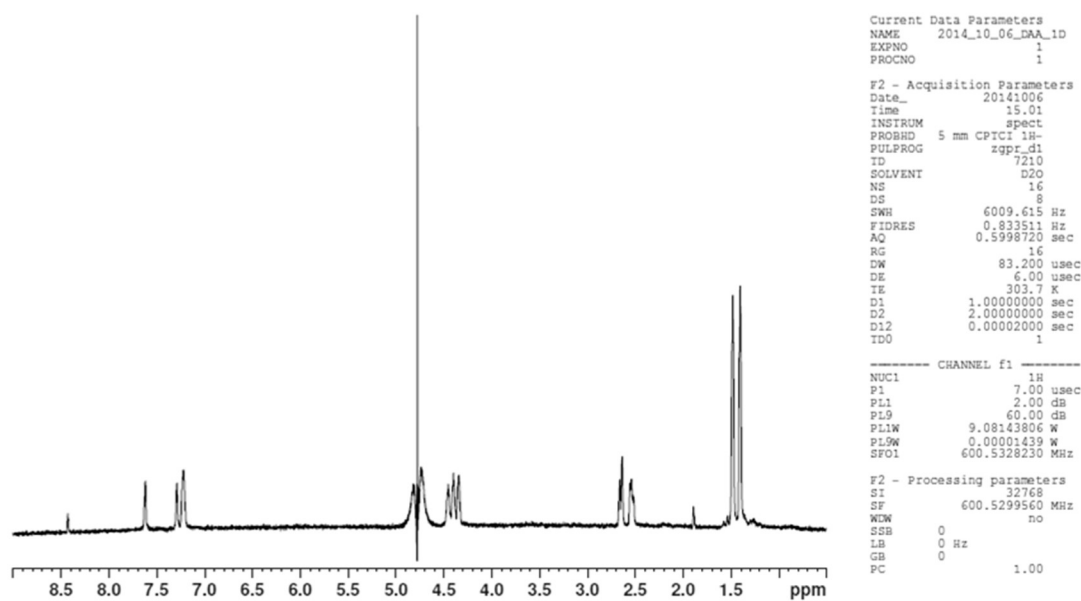
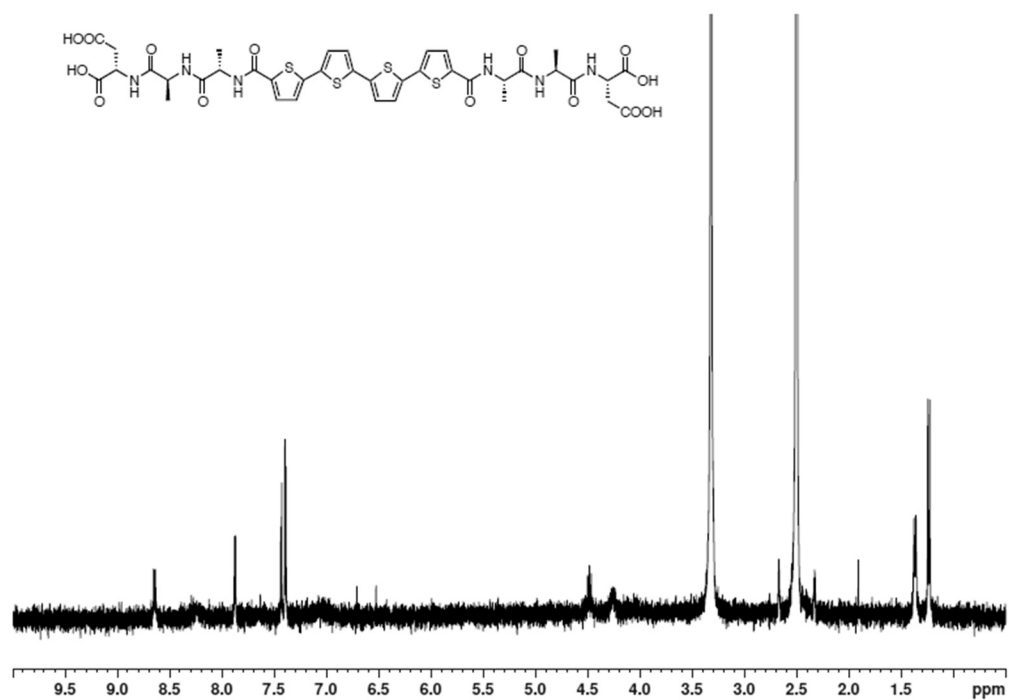


Figure A2.3. ^1H (400 MHz, d_6 -DMSO) NMR spectrum (*top*) and ^1H (600 MHz, D_2O) NMR spectrum (*bottom*) of **DAA OT4** peptide.

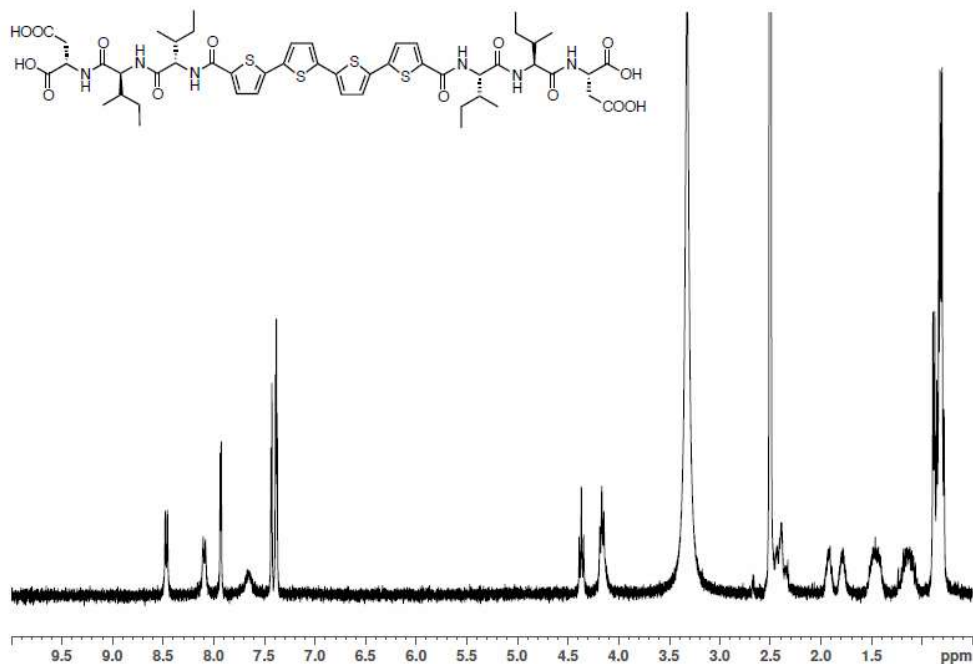


Figure A2.4. ^1H (400 MHz, d_6 -DMSO) NMR spectrum of **DII OT4** peptide.

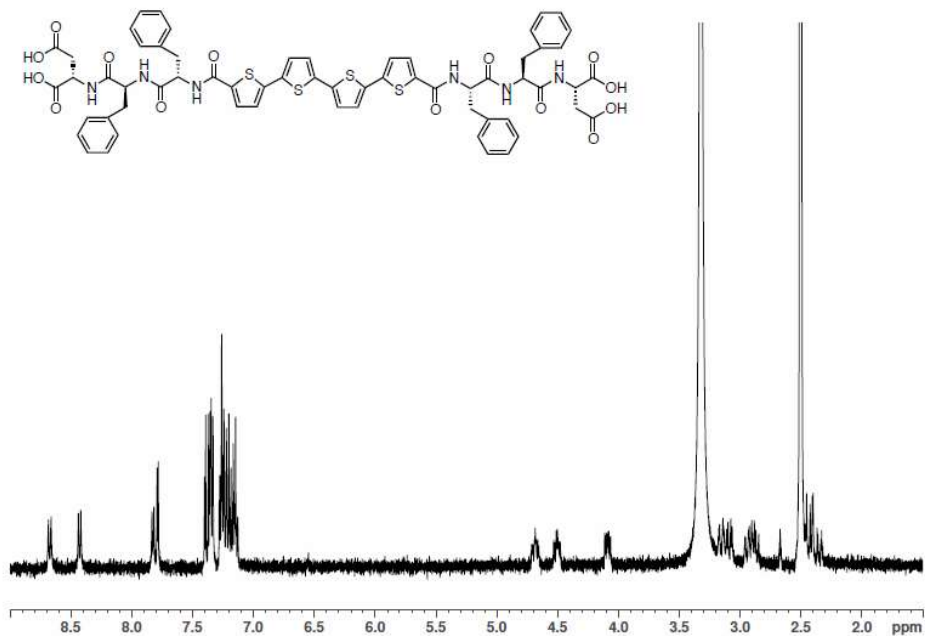


Figure A2.5. ^1H (400 MHz, d_6 -DMSO) NMR spectrum of **DFF OT4** peptide.

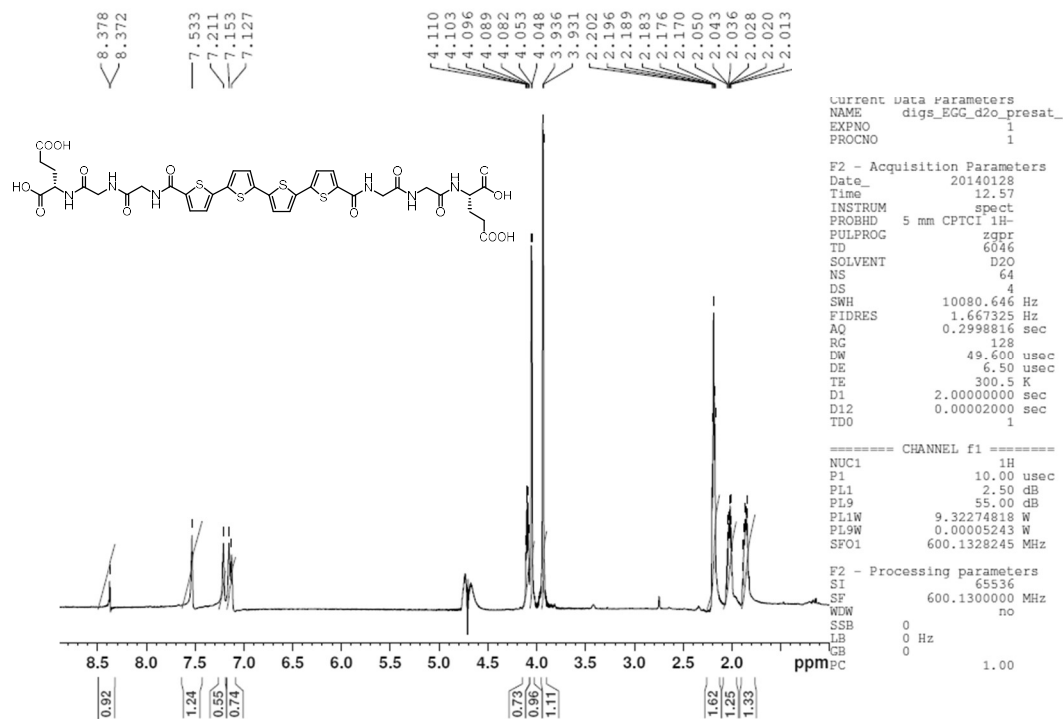


Figure A2.6. ^1H (600 MHz, D_2O) NMR spectrum of EGG OT4 peptide.

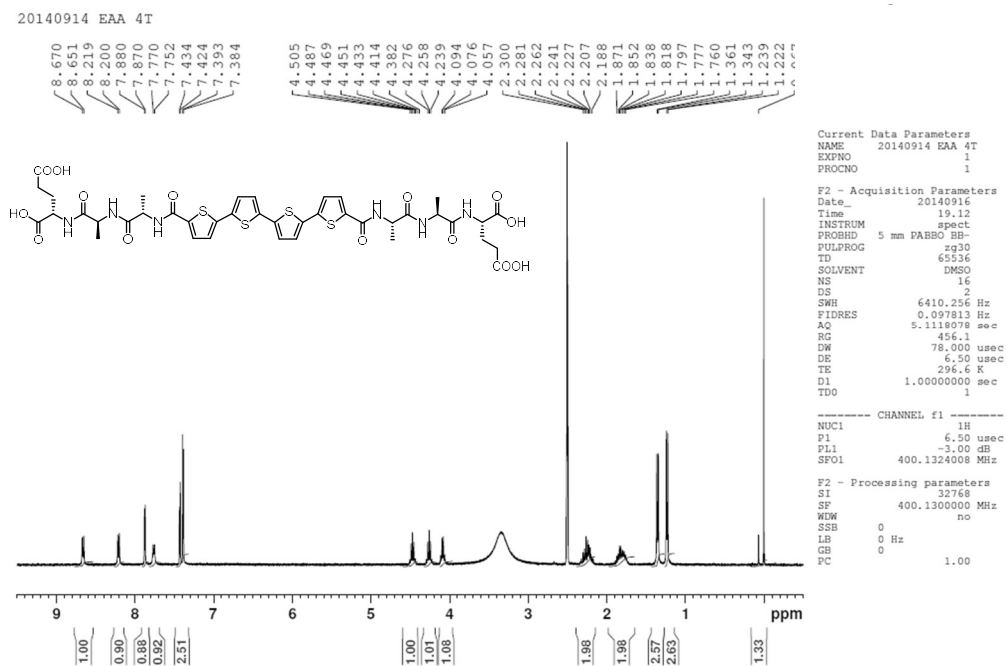


Figure A2.7. ^1H (400 MHz, d_6 -DMSO) NMR spectrum of EAA OT4 peptide.

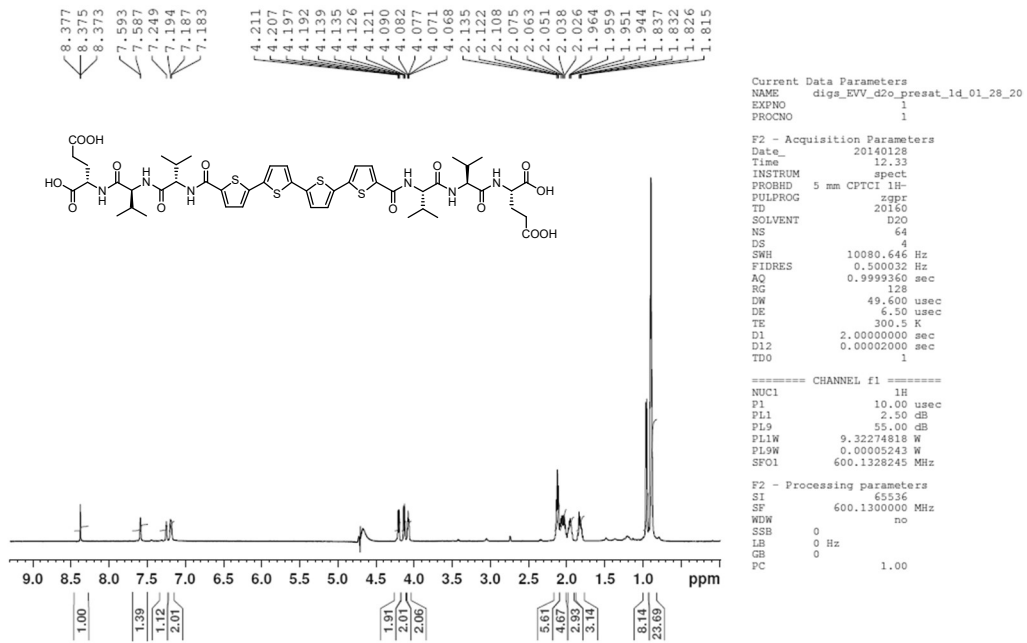


Figure A2.8. ¹H (600 MHz, D₂O) NMR spectrum of EVV OT4 peptide.

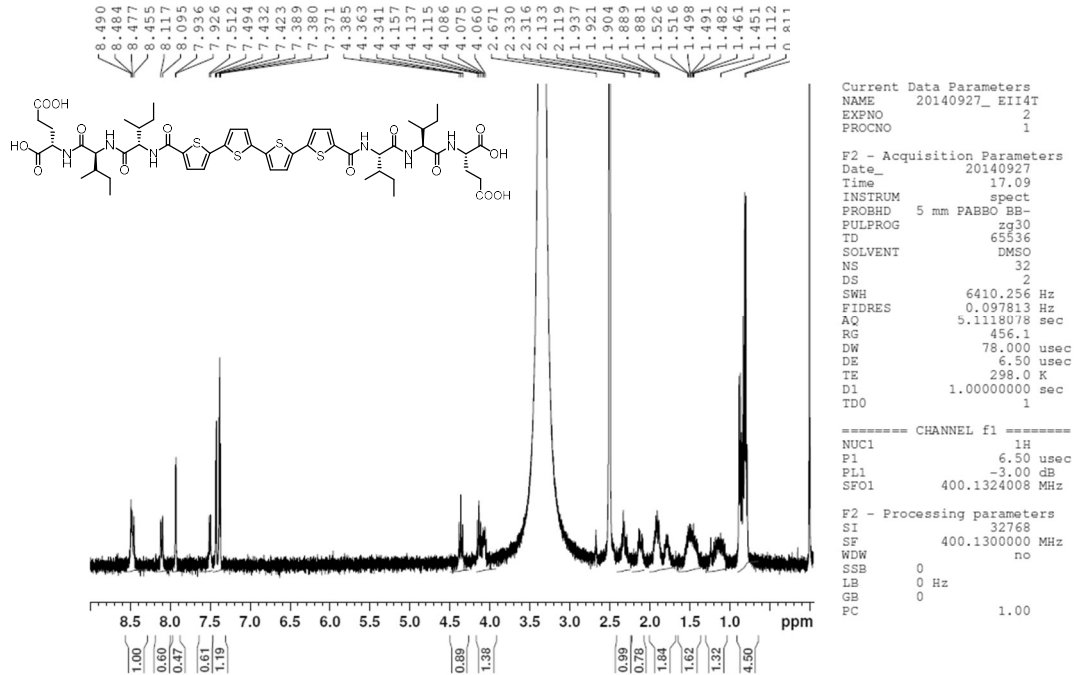


Figure A2.9. ¹H (400 MHz, d₆-DMSO) NMR spectrum of EII OT4 peptide.

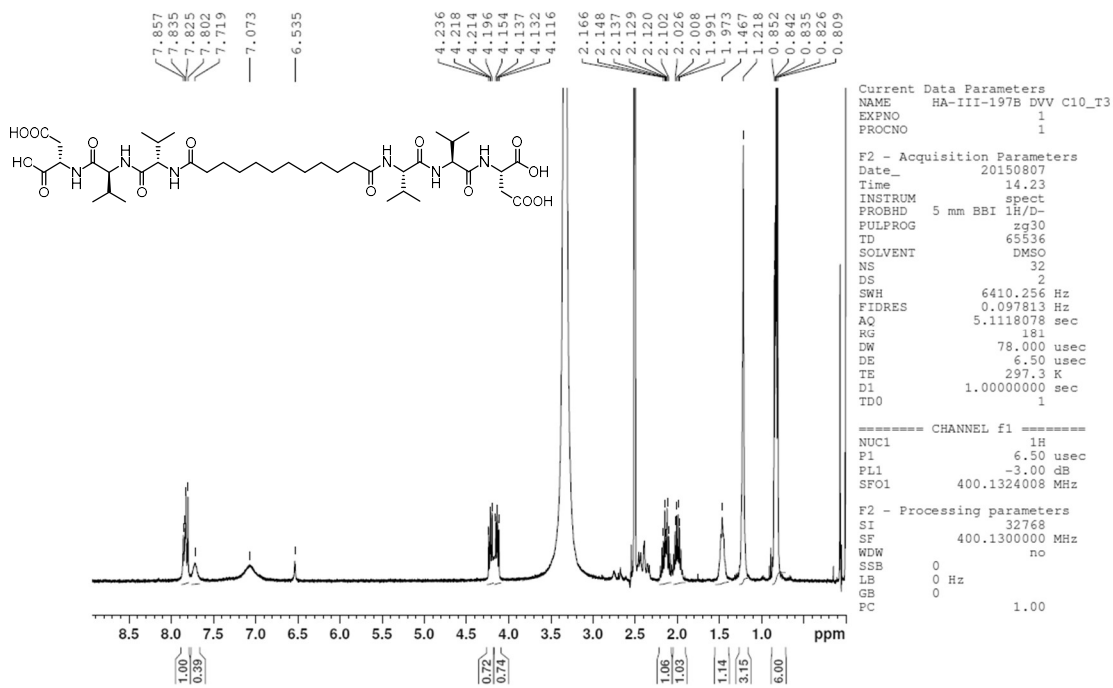


Figure A2.10. ^1H (400 MHz, d_6 -DMSO) NMR spectrum of DVV C10 peptide.

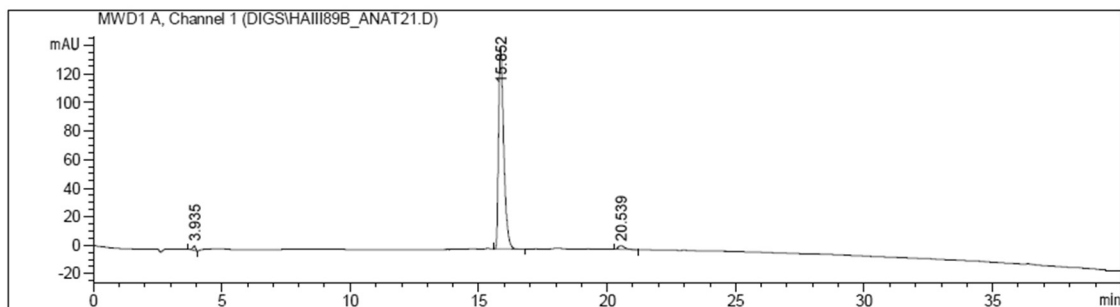


Figure A2.11. Analytical HPLC trace of DGG OT4, monitoring at 400 nm.

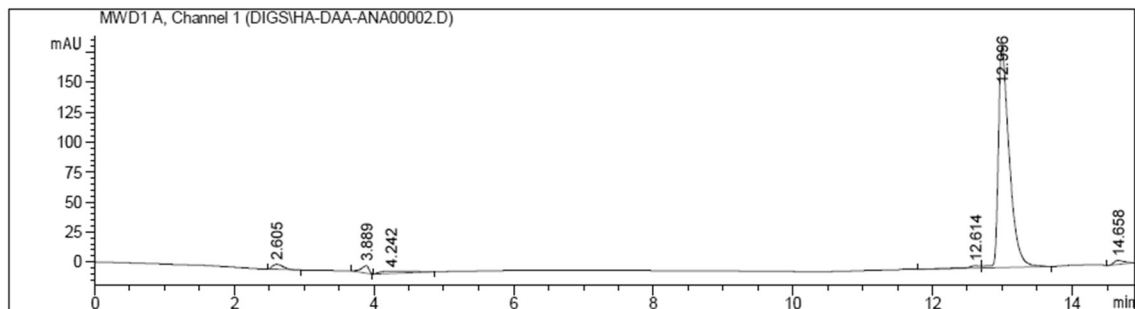


Figure A2.12. Analytical HPLC trace of DAA OT4, monitoring at 400 nm.

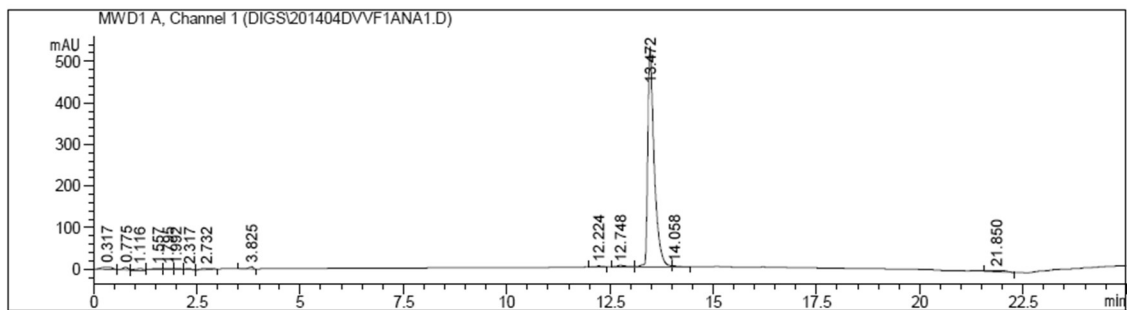


Figure A2.13. Analytical HPLC trace of **DVV OT4**, monitoring at 400 nm.

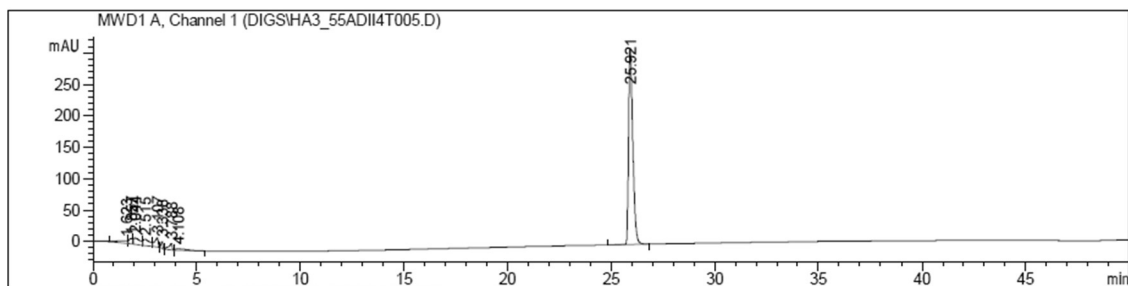


Figure A2.14. Analytical HPLC trace of **DII OT4**, monitoring at 400 nm.

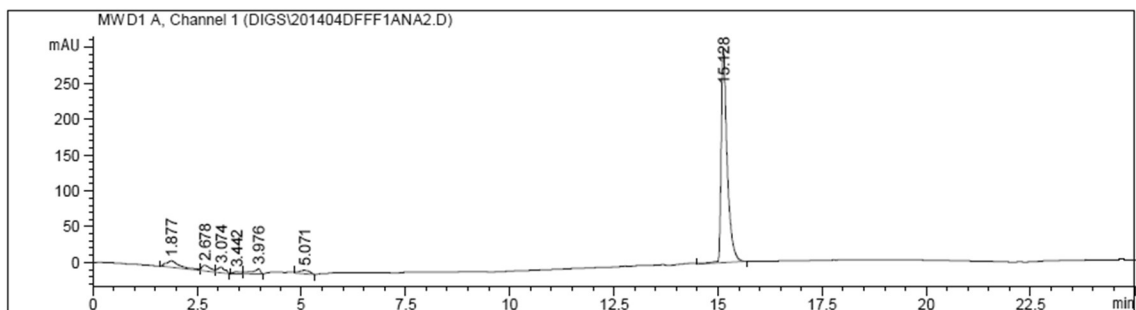


Figure A2.15. Analytical HPLC trace of **DFF OT4**, monitoring at 400 nm.

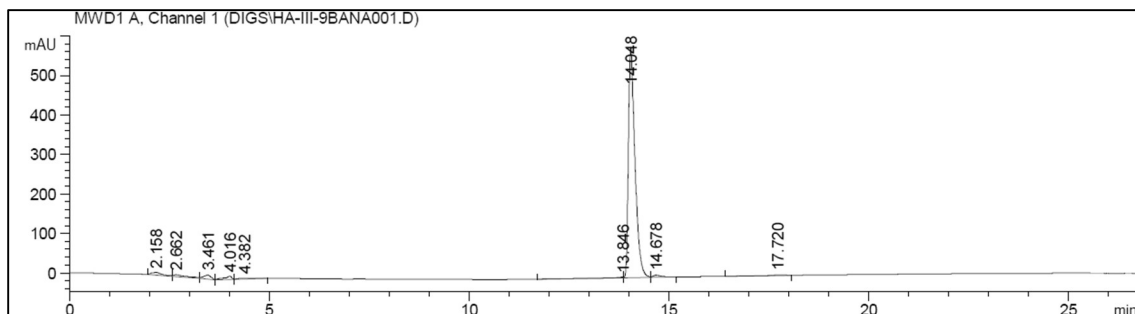


Figure A2.16. Analytical HPLC trace of **EGG OT4** peptide, monitoring at 400 nm.

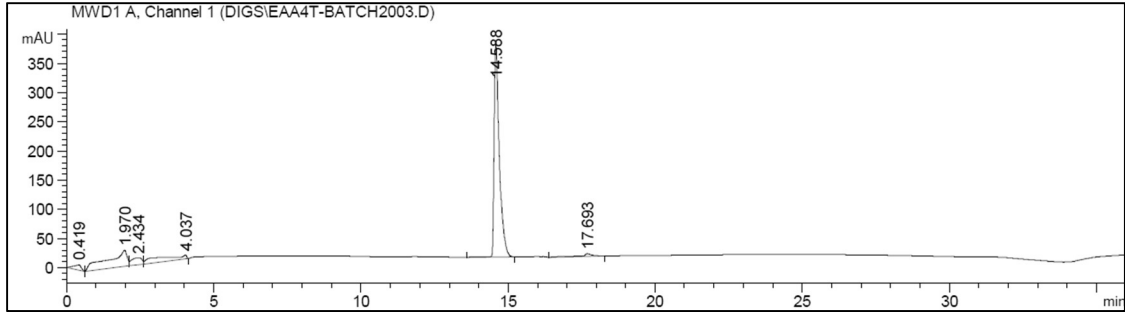


Figure A2.17. Analytical HPLC trace of **EAA OT4** peptide, monitoring at 400 nm.

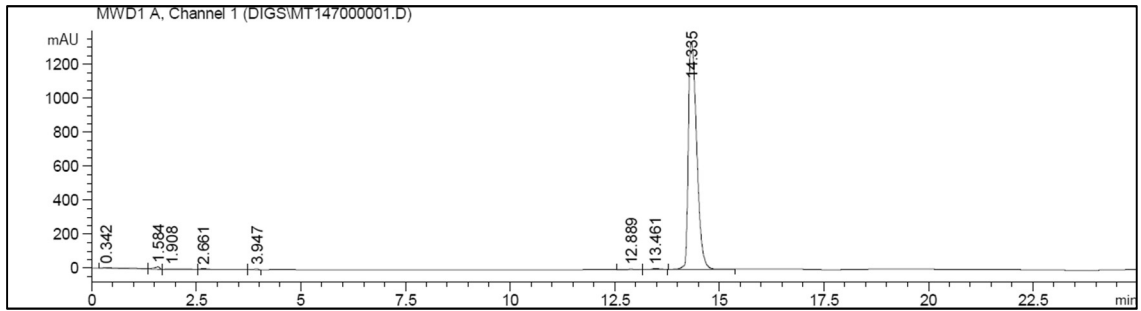


Figure A2.18. Analytical HPLC trace of **EVV OT4** peptide, monitoring at 400 nm.

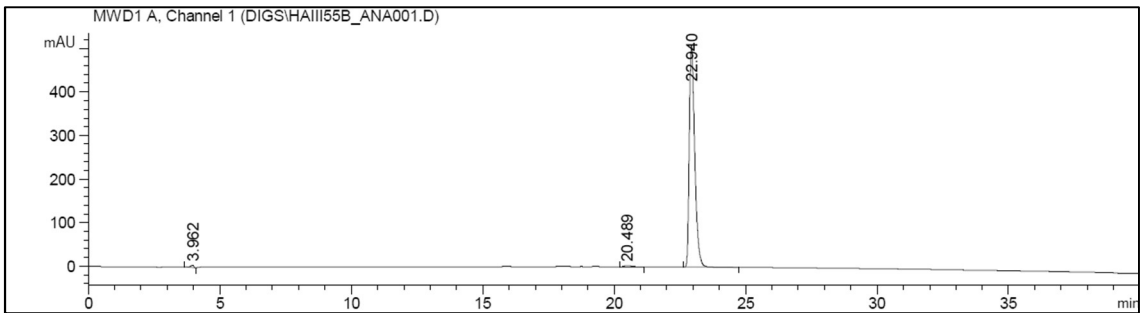


Figure A2.19. Analytical HPLC trace of **EII OT4** peptide, monitoring at 400 nm.

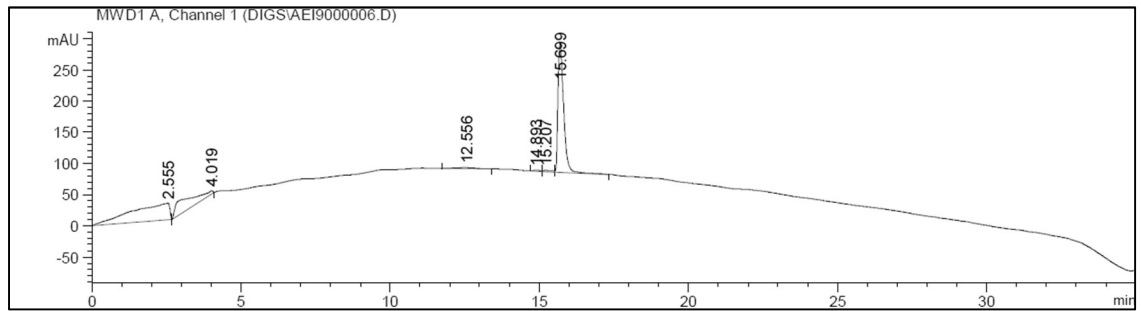


Figure A2.20. Analytical HPLC trace of **DVV C10** peptide, monitoring at 220 nm.

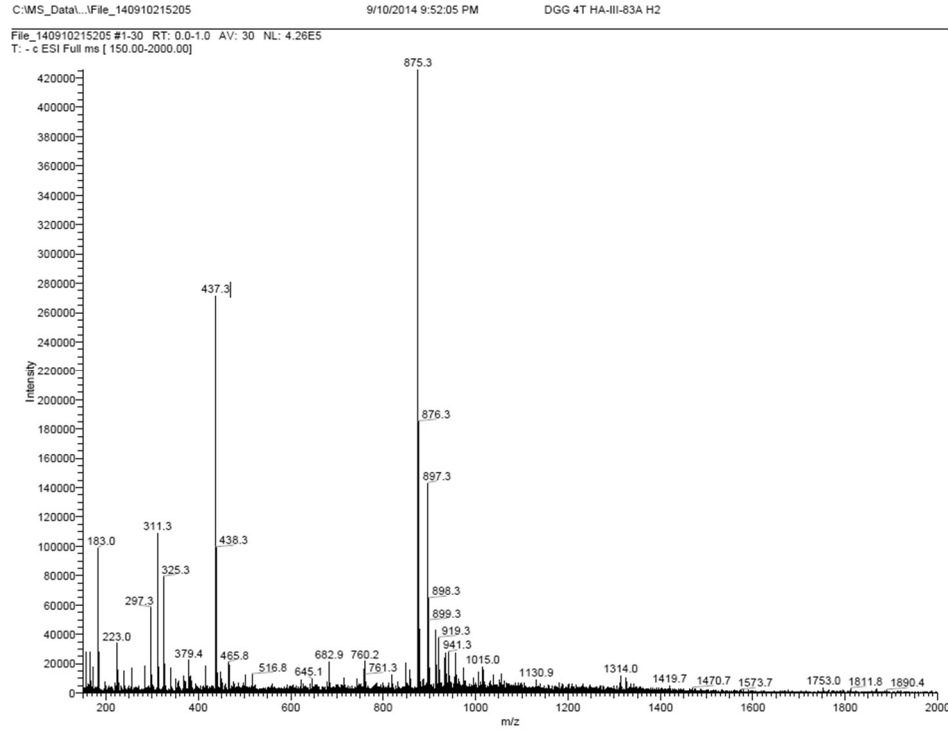


Figure A2.21. ESI-MS spectrum of DGG OT4 peptide.

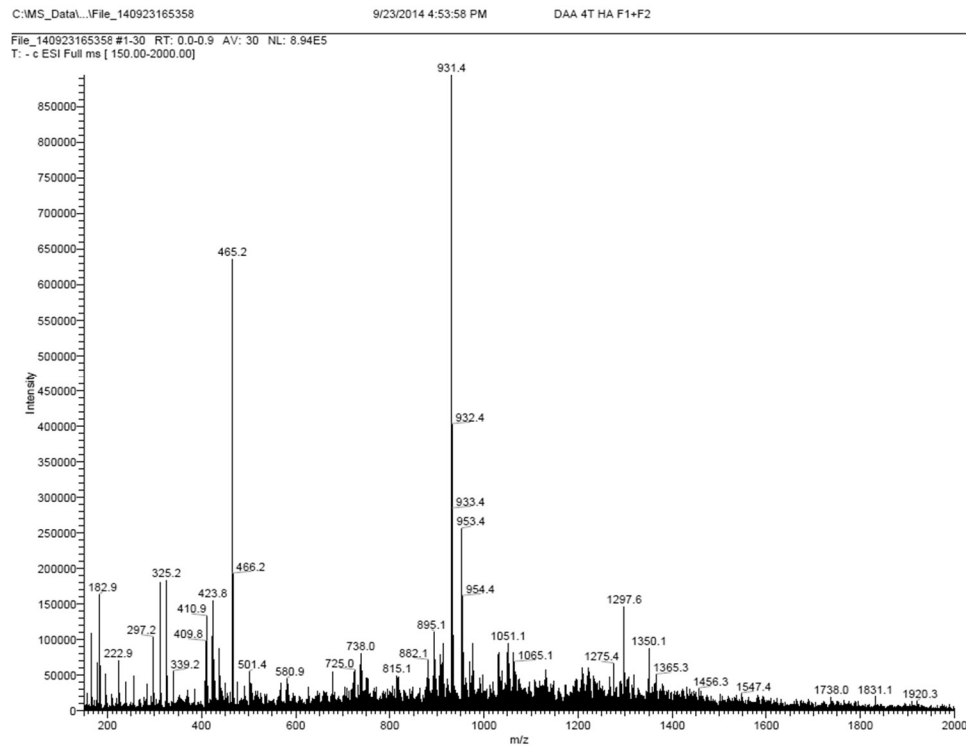


Figure A2.22. ESI-MS spectrum of DAA OT4 peptide.

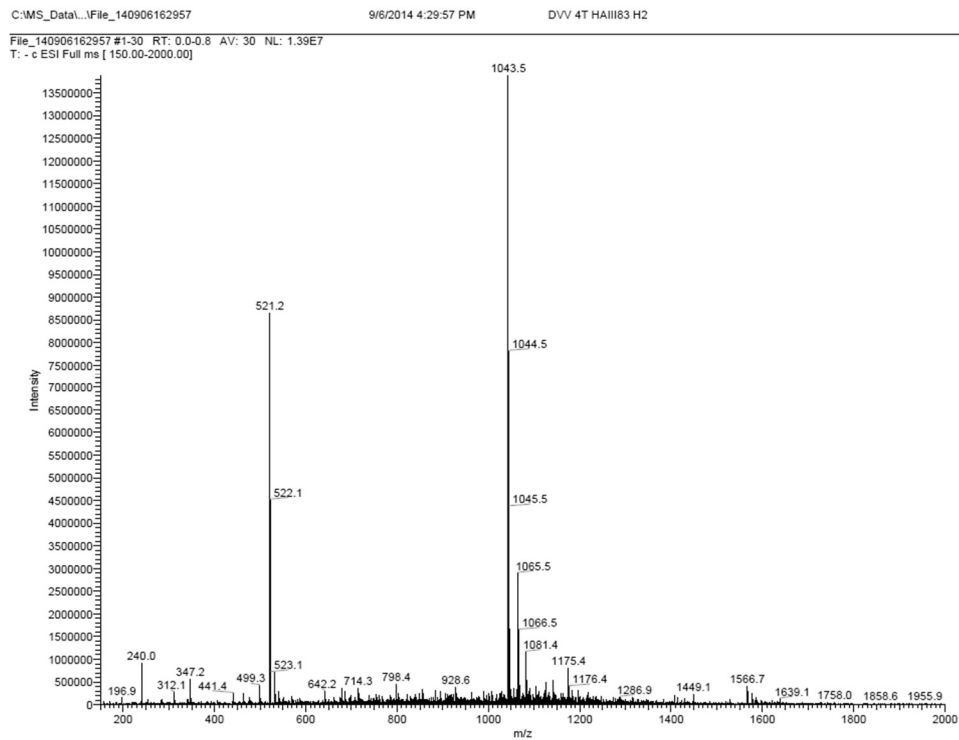


Figure A2.23. ESI-MS spectrum of DVV OT4 peptide.

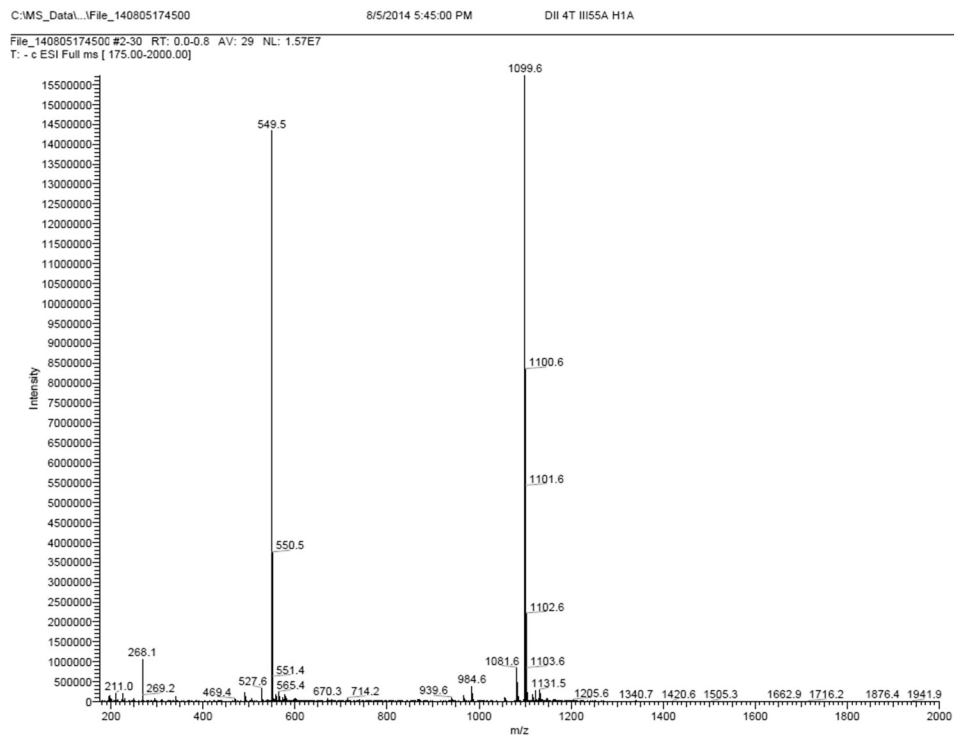


Figure A2.24. ESI-MS spectrum of DII OT4 peptide.

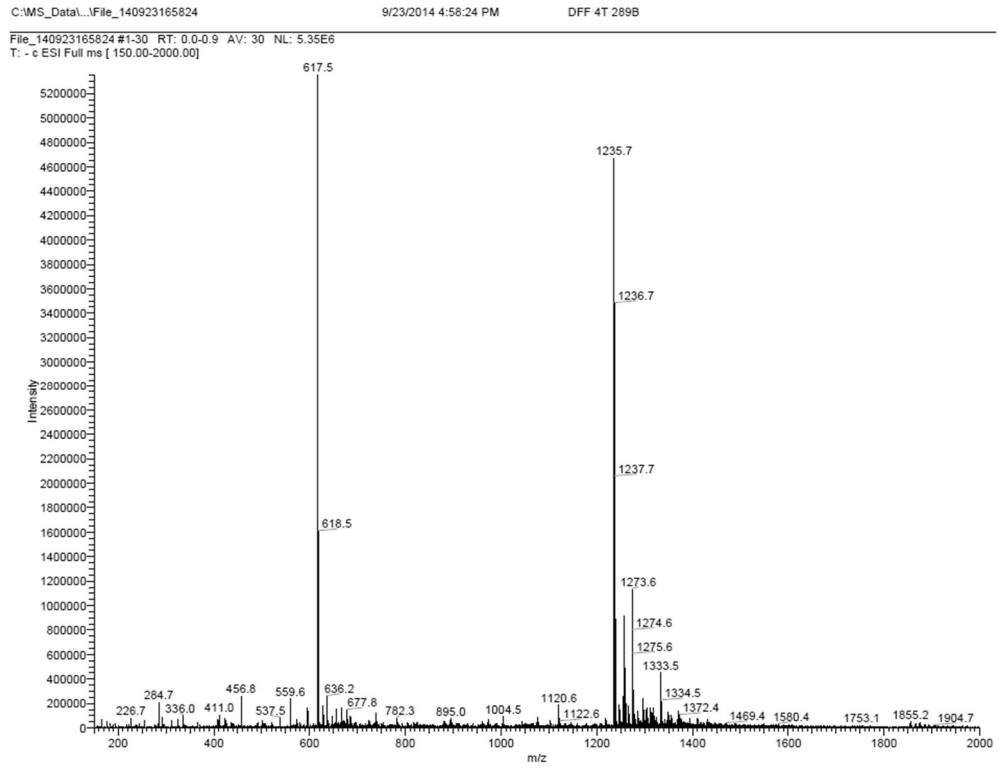


Figure A2.25. ESI-MS spectrum of **DFF OT4** peptide.

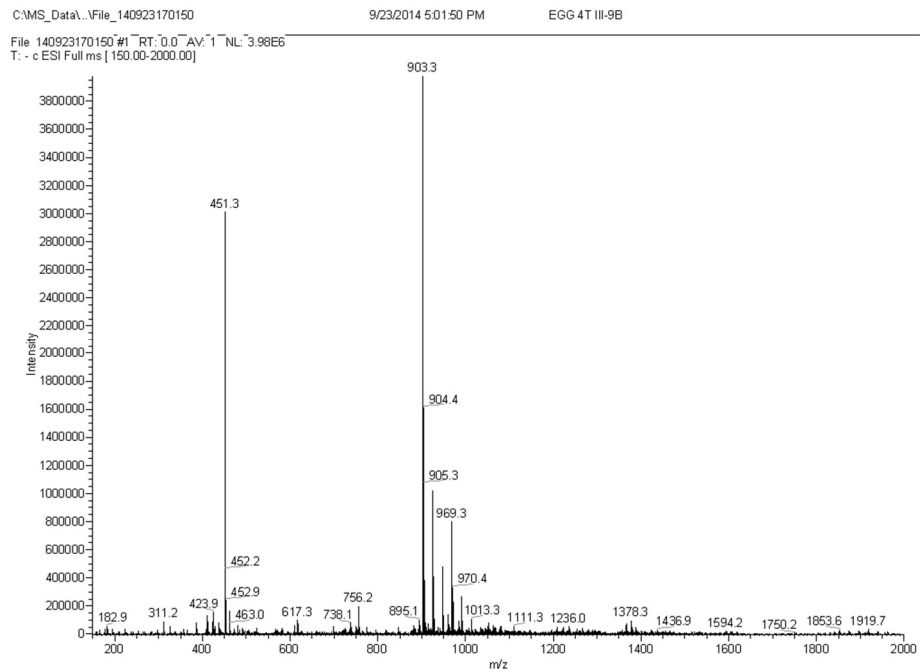


Figure A2.26. ESI-MS spectrum of **EGG OT4** peptide.

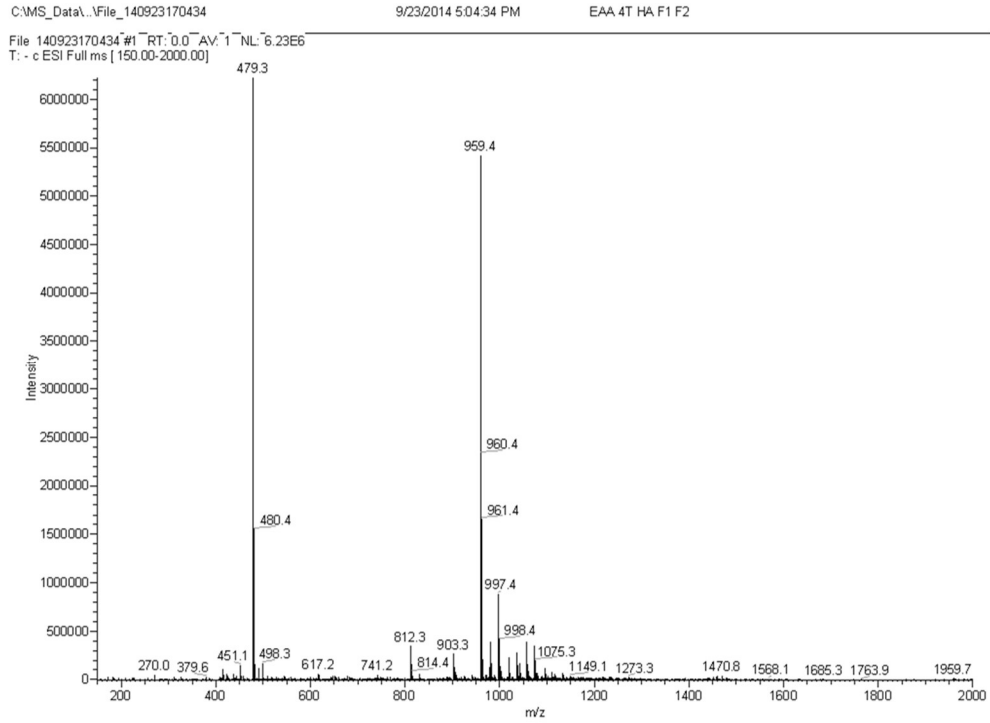


Figure A2.27. ESI-MS spectrum of EAA OT4 peptide.

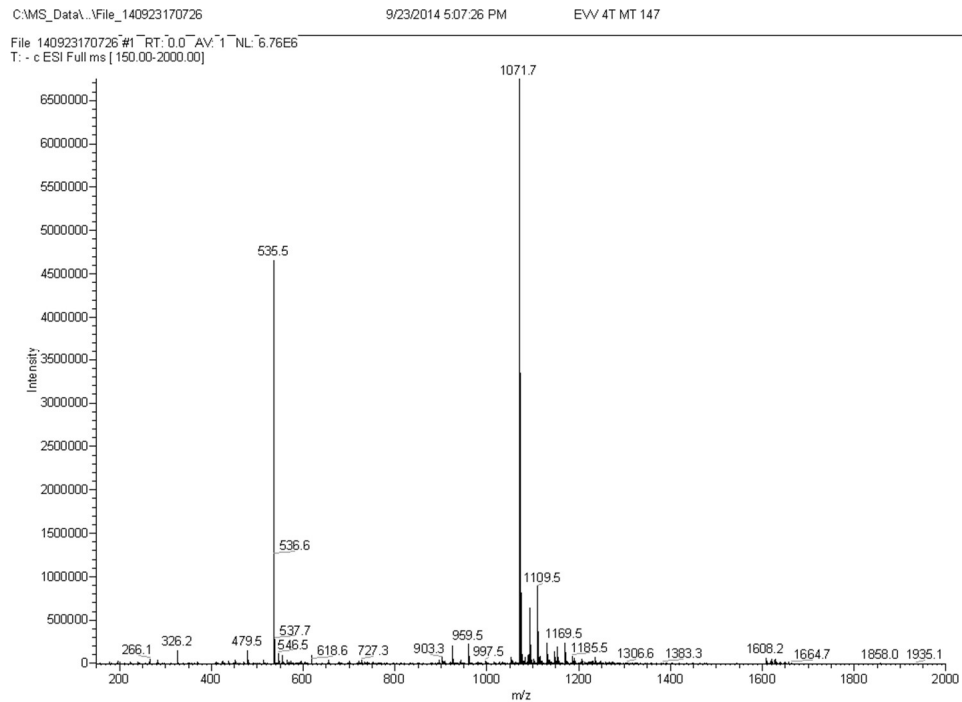


Figure A2.28. ESI-MS spectrum of EVV OT4 peptide.

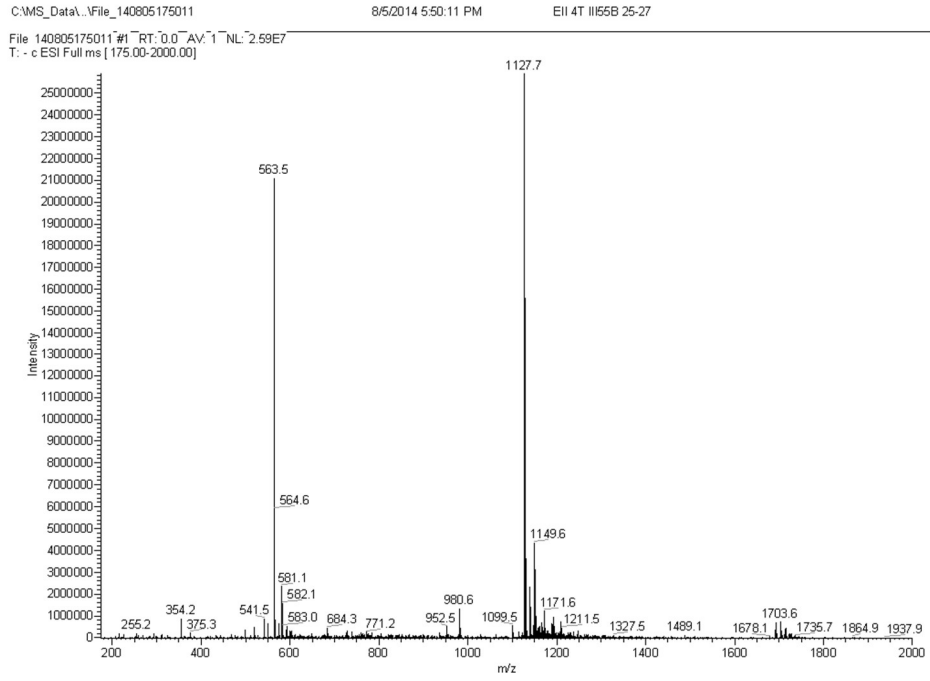


Figure A2.29. ESI-MS spectrum of EII OT4 peptide.

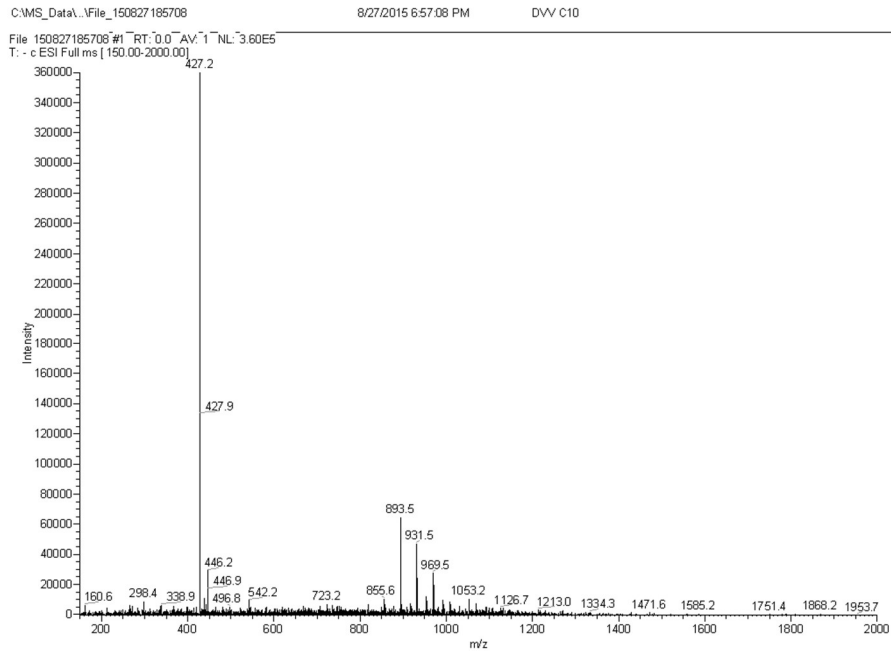


Figure A2.30. ESI-MS spectrum of DVV-C10 peptide.

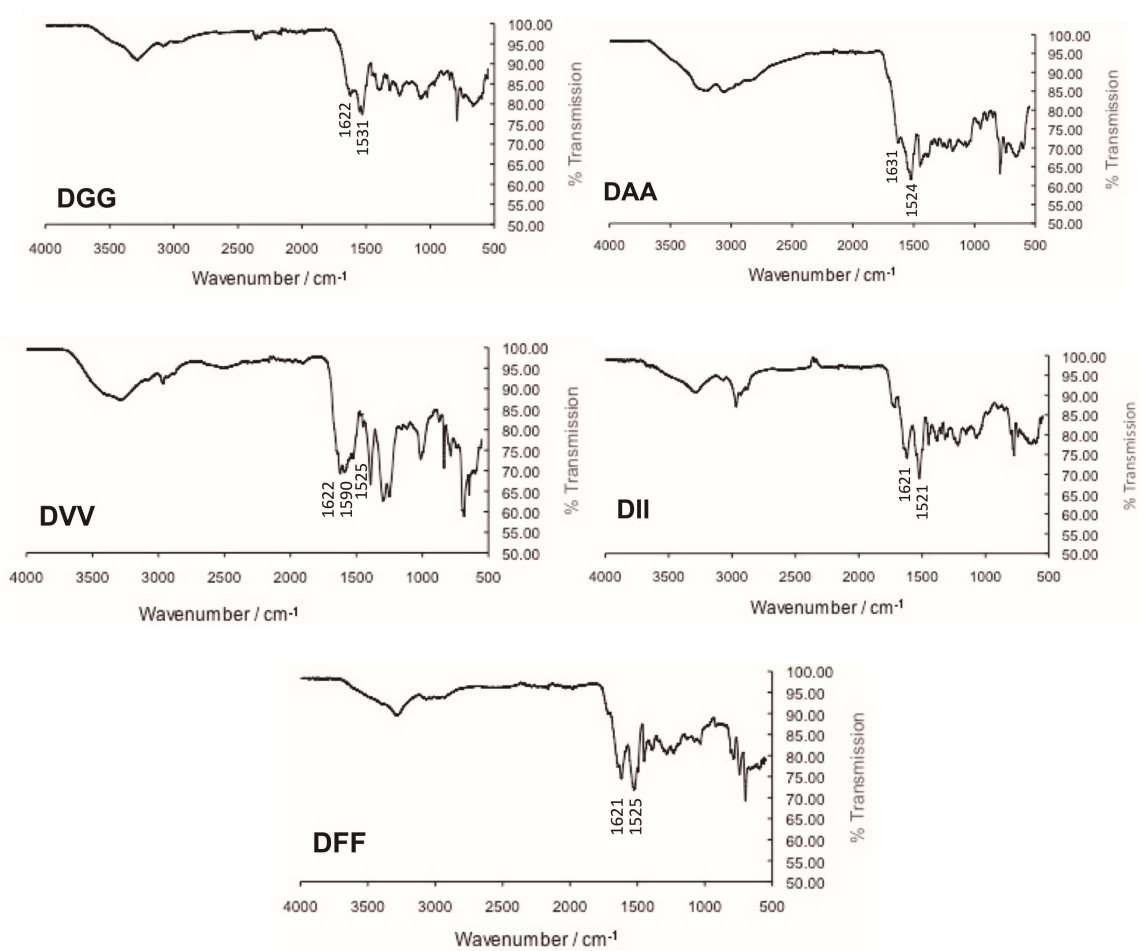


Figure A2.31. Attenuated total reflectance IR spectra of **DGG, DAA, DVV, DII, and DFF** OT4 peptides in solid state.

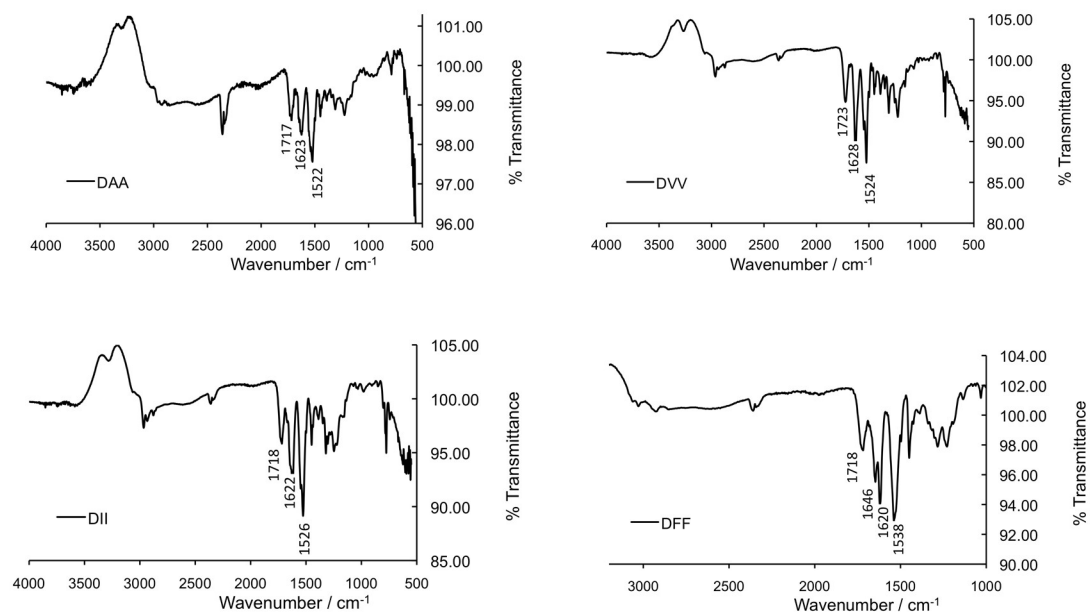


Figure A2.32. Attenuated total reflectance IR spectra of **DAA**, **DVV**, **DII** and **DFF** OT4 peptides in gel state.

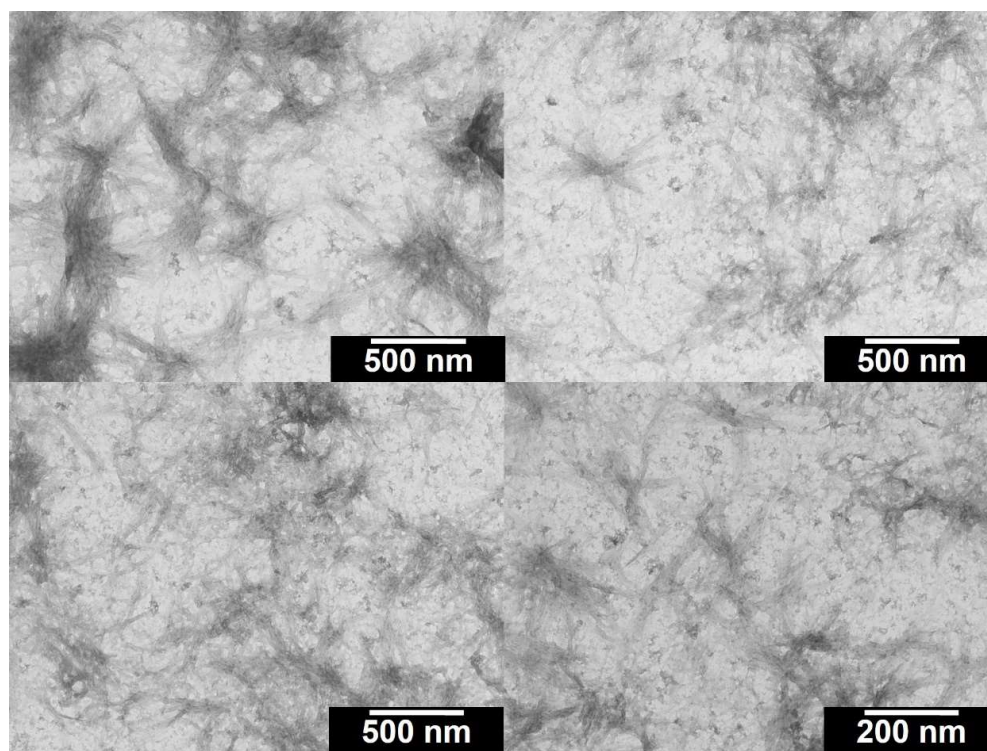


Figure A2.33. TEM images of 1 wt% **DGG-OT4** peptide gel.

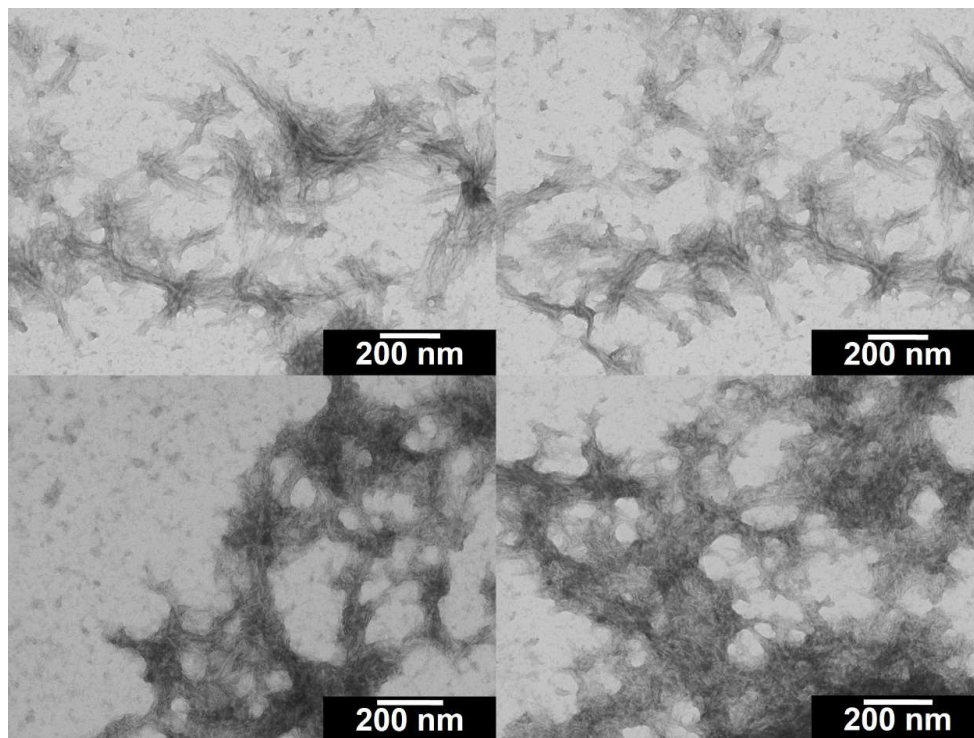


Figure A2.34. TEM images of 1 wt% **DAA-OT4** peptide gel.

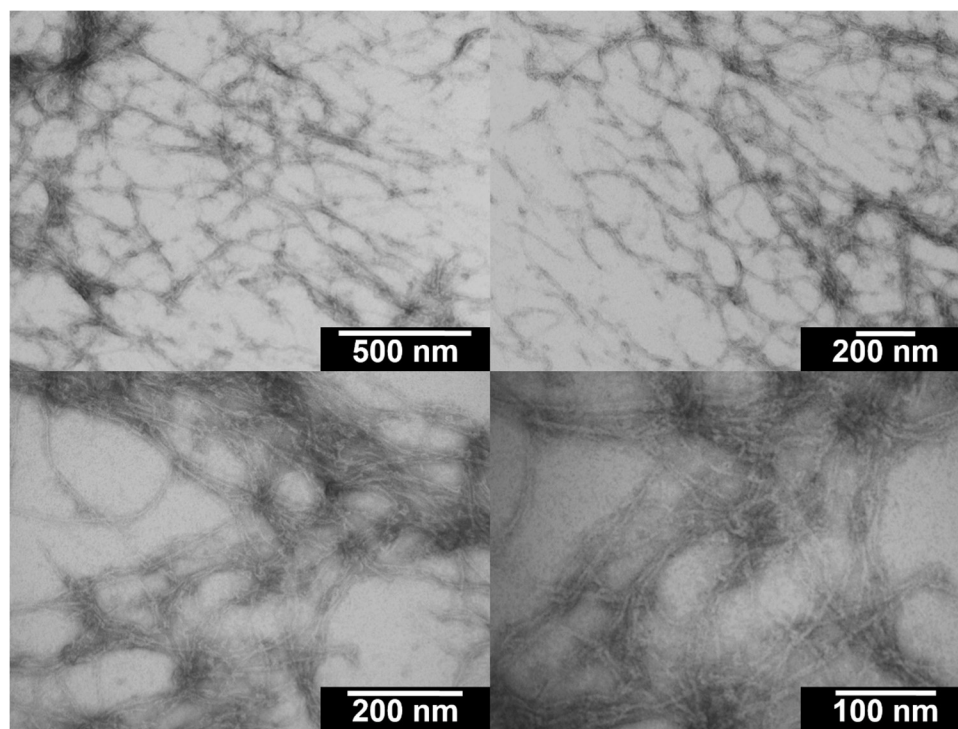


Figure A2.35. TEM images of 1 wt% **DVV-OT4** peptide gel.

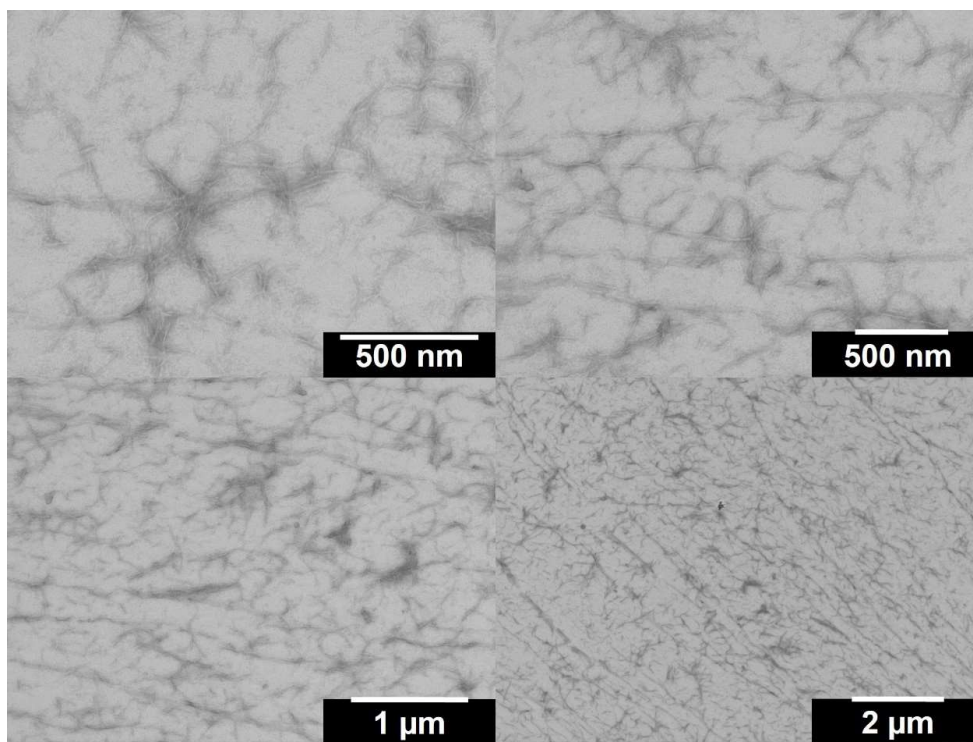


Figure A2.36. TEM images of 1 wt% **DII-OT4** peptide gel.

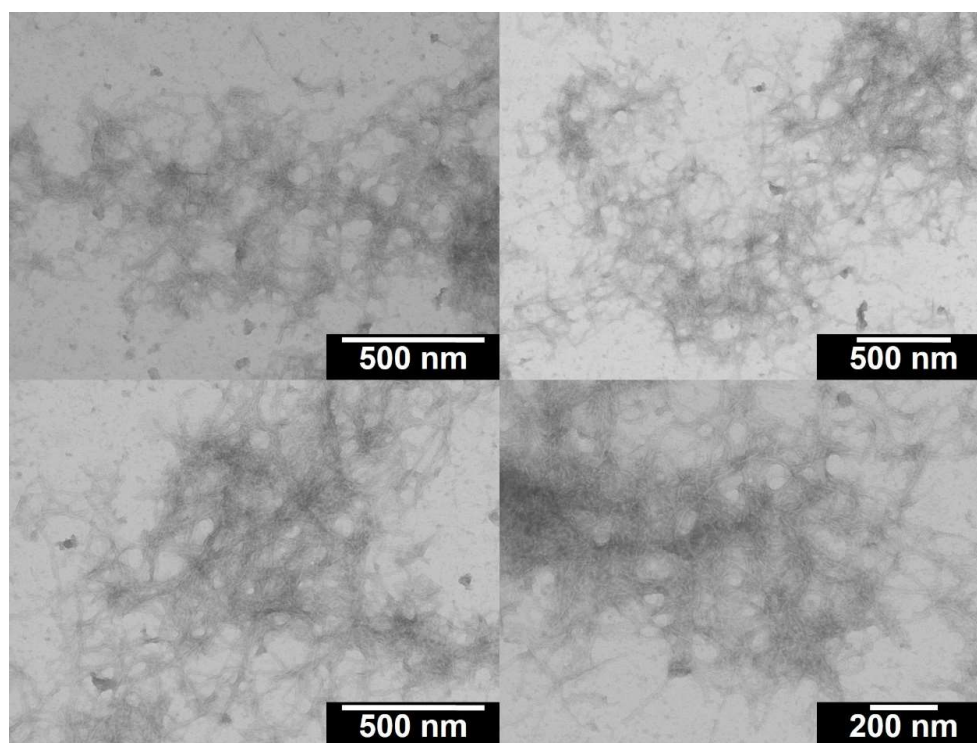


Figure A2.37. TEM images of 1 wt% **EGG-OT4** peptide gel.

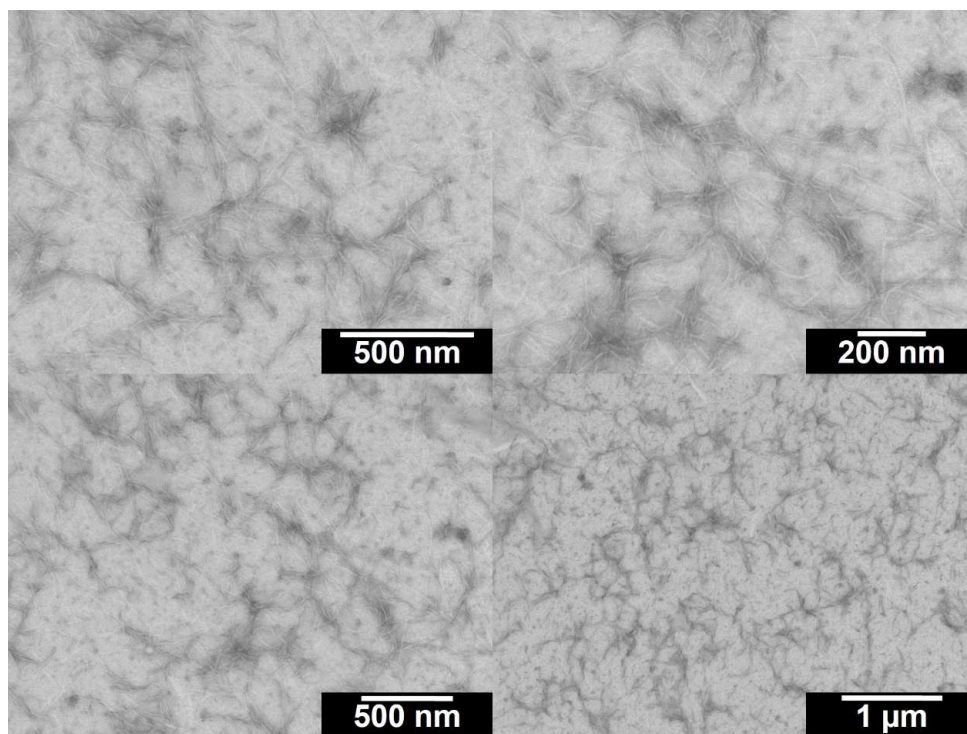


Figure A2.38. TEM images of 1 wt% EAA-OT4 peptide gel.

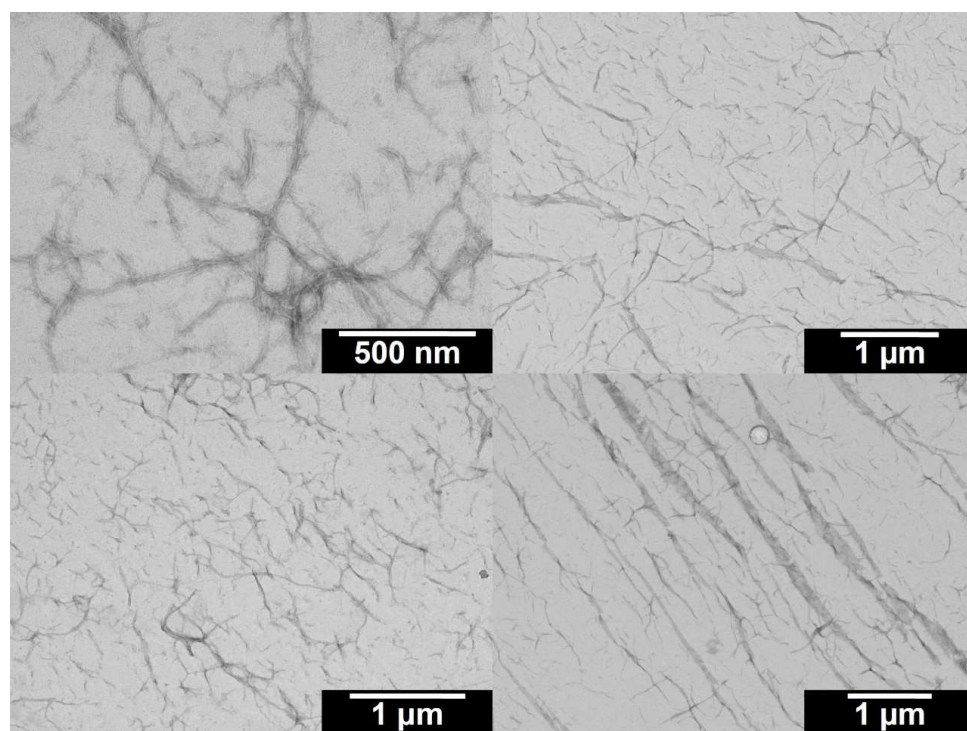


Figure A2.39. TEM images of 1 wt% EVV-OT4 peptide gel.

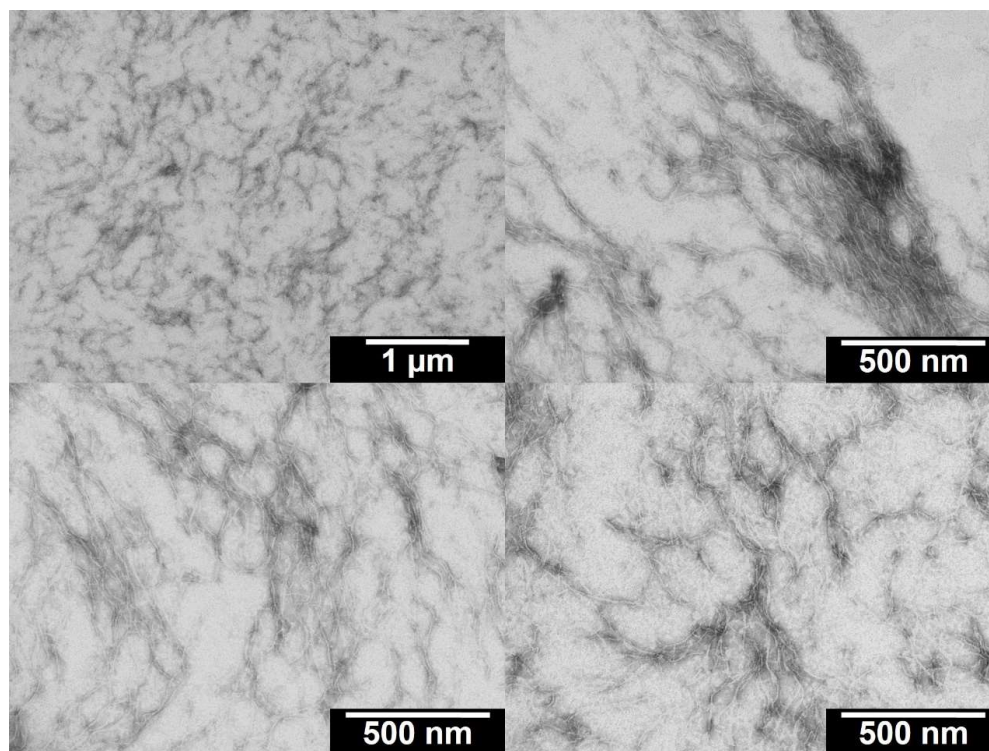


Figure A2.40. TEM images of 1 wt% EII-OT4 peptide gel.

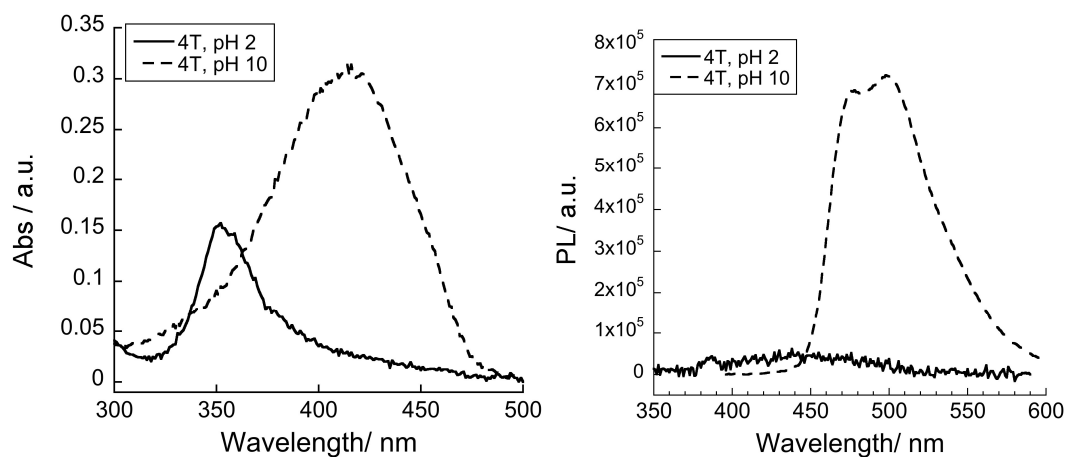


Figure A2.41. Absorption (*left*) and photoluminescence (*right*) spectra for HOOC-(quaterthiophene)-COOH (OT4) under basic (---) and acidic (—) conditions, for reference; $\lambda_{\text{exc}} = 380$ and 340 for PL, respectively.

Chapter 3

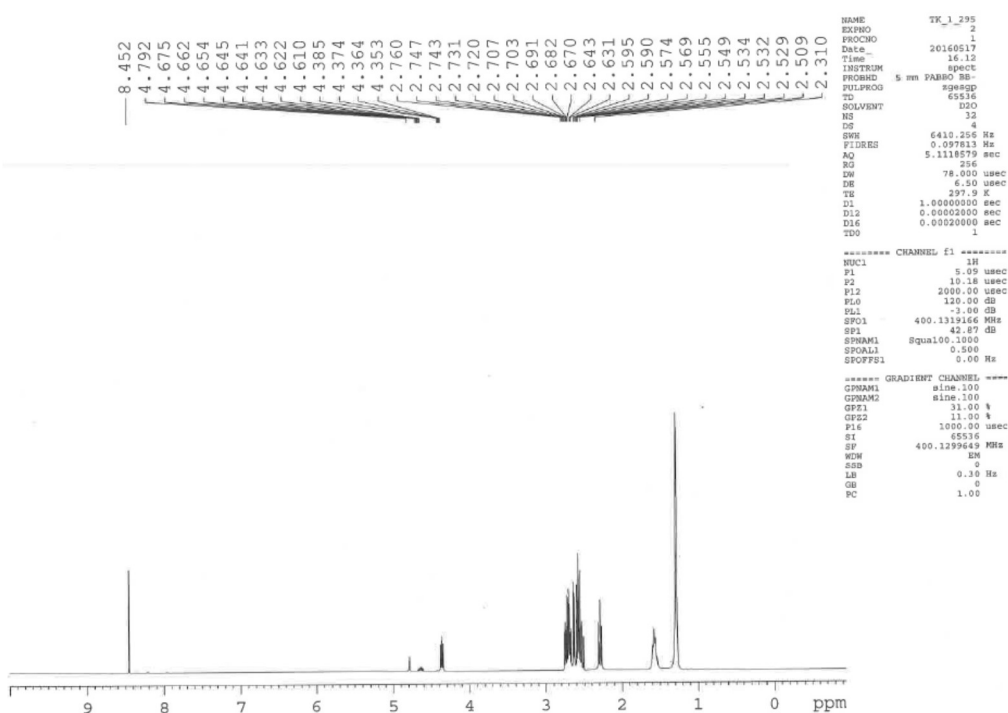


Figure A3.1. ¹H NMR (D₂O) spectrum of peptide **DDD C10**.

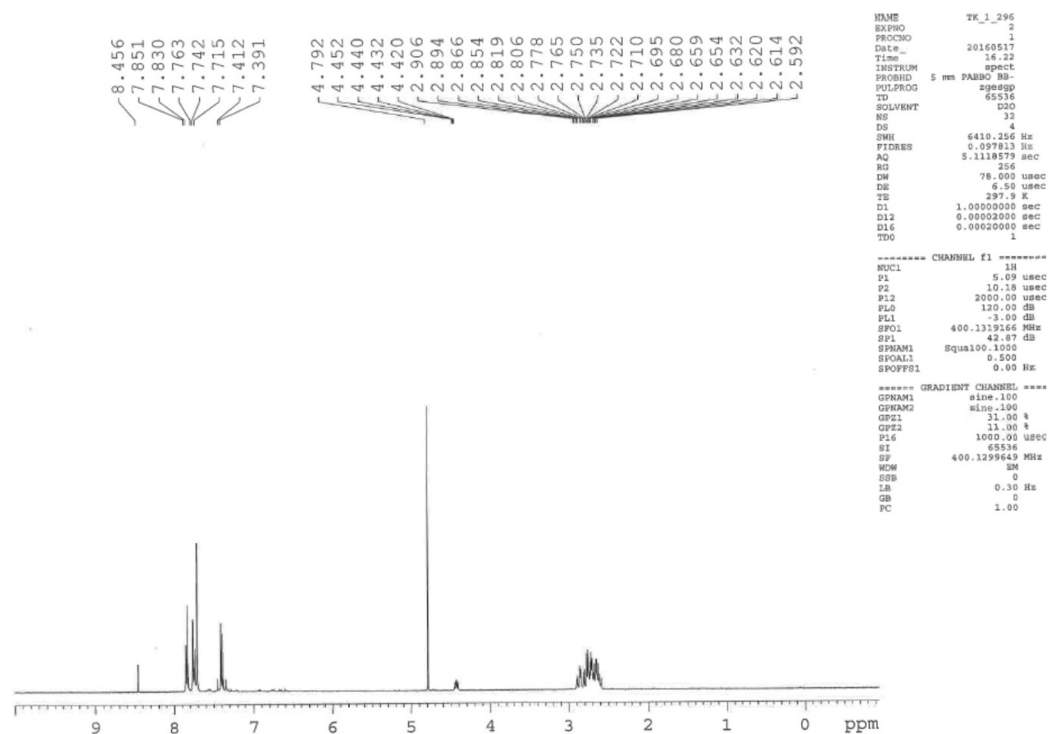


Figure A3.2. ¹H NMR (D₂O) spectrum of peptide **DDD OPV3**.

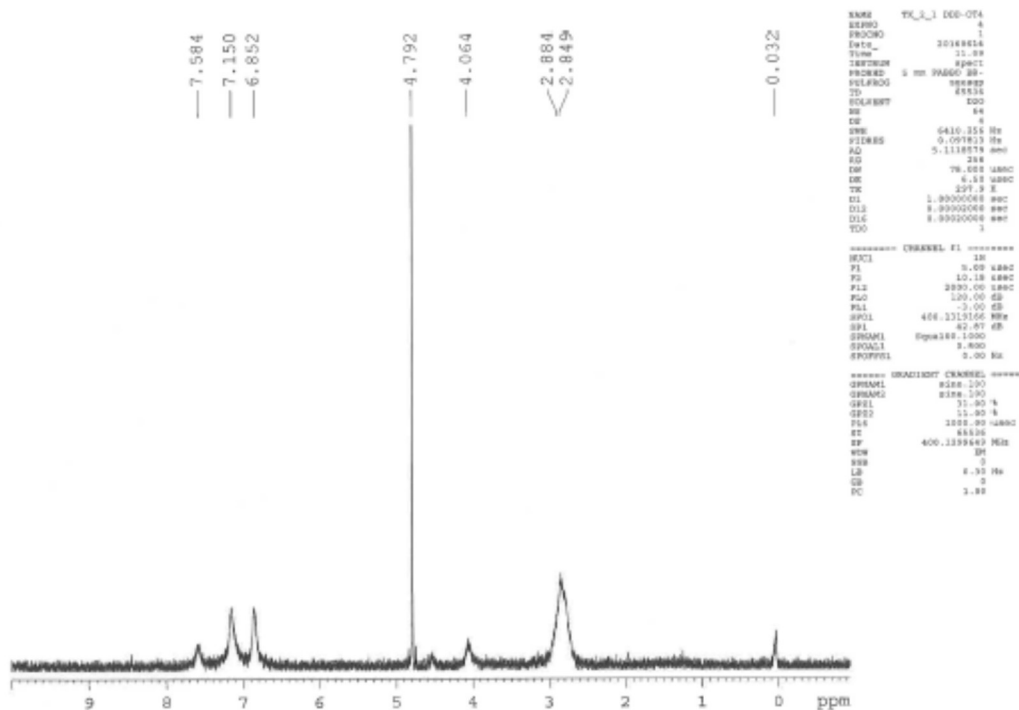


Figure A3.3. ¹H NMR (D₂O) spectrum of peptide **DDD OT4**.

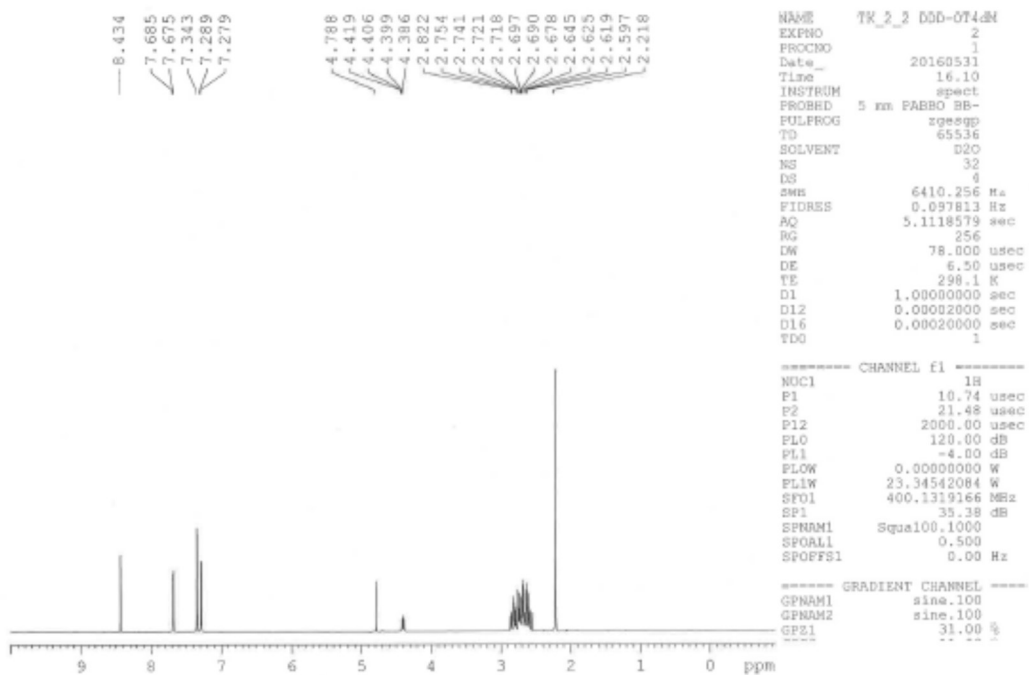


Figure A3.4. ¹H NMR (D₂O) spectrum of peptide **DDD OT4dM**.

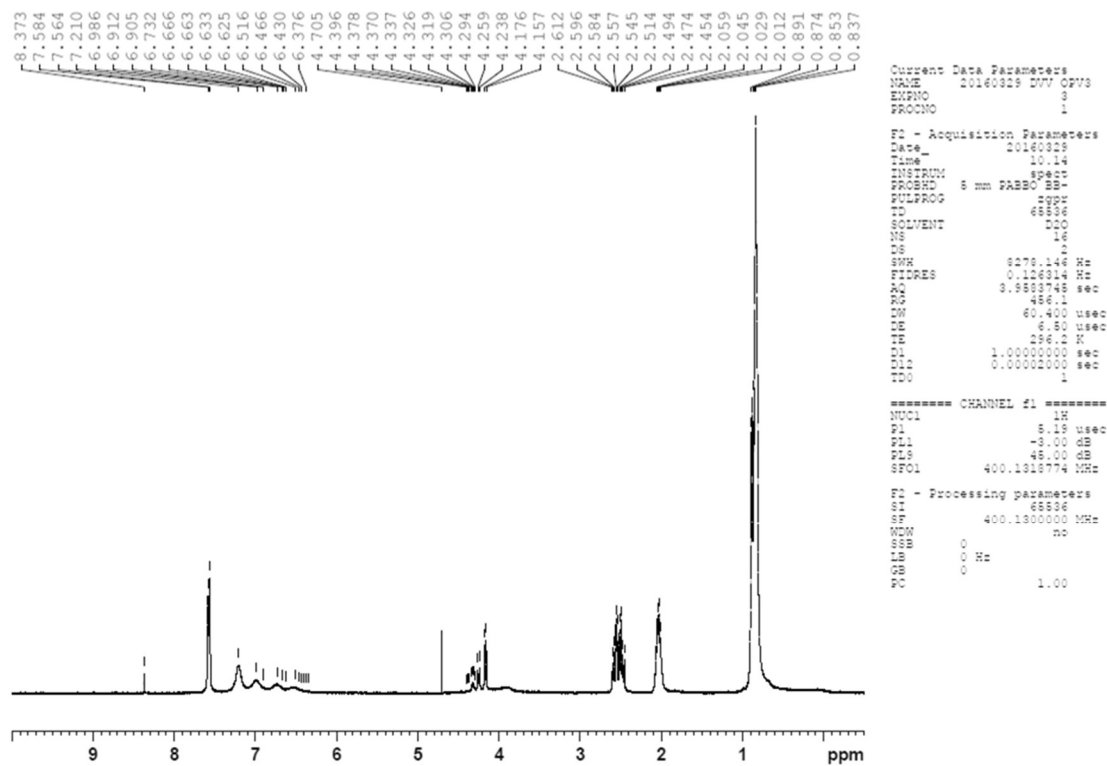


Figure A3.5. ¹H NMR (D₂O) spectrum of peptide DVV OPV3.

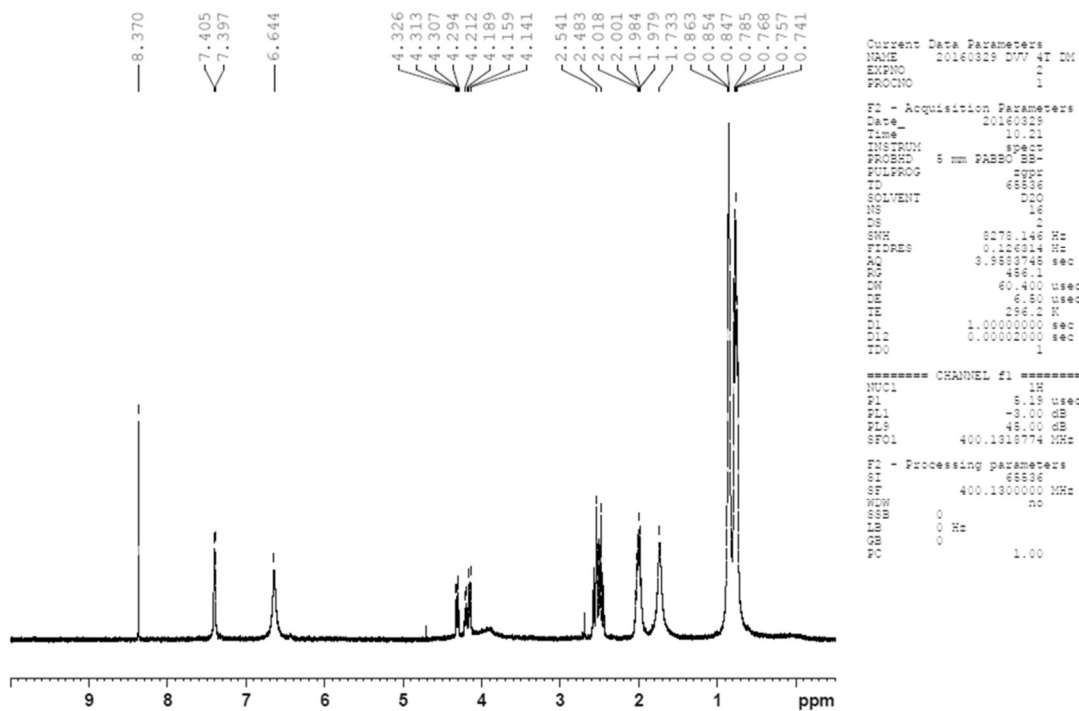


Figure A3.6. ¹H NMR (D₂O) spectrum of peptide DVV OT4dM.

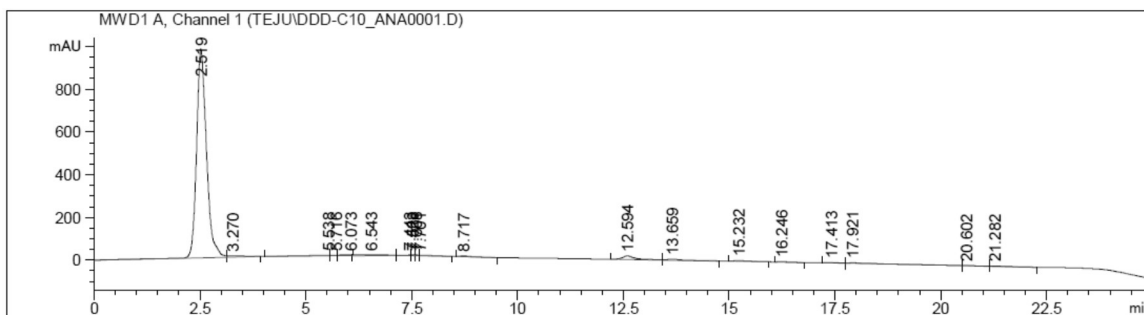


Figure A3.7. Analytical HPLC trace of **DDD C10** peptide, monitoring at 220 nm.

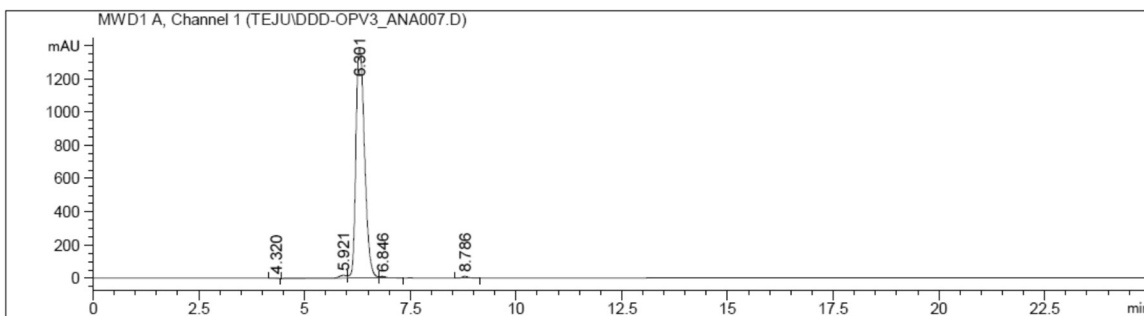


Figure A3.8. Analytical HPLC trace of **DDD OPV3** peptide, monitoring at 400 nm.

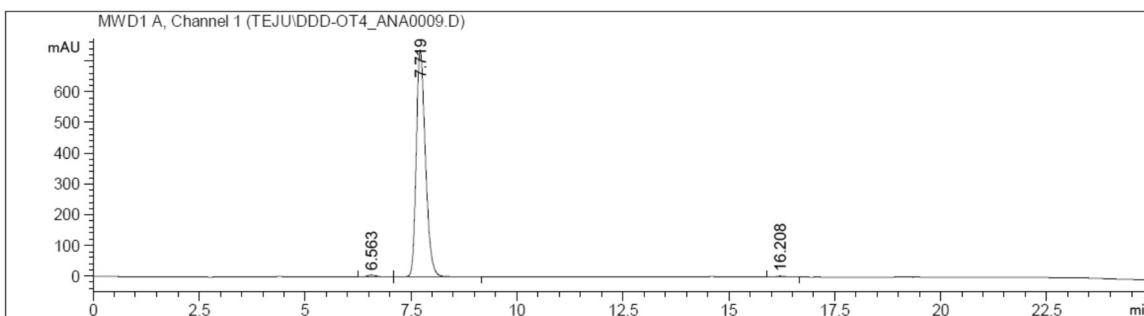


Figure A3.9. Analytical HPLC trace of **DDD OT4** peptide, monitoring at 400 nm.

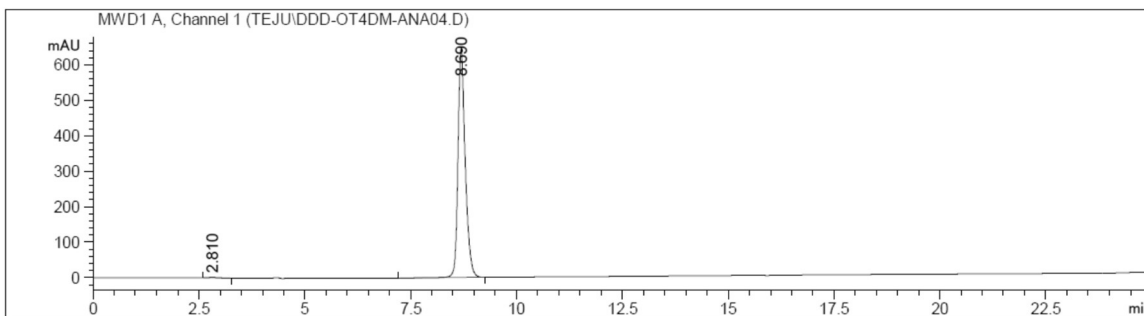


Figure A3.10. Analytical HPLC trace of **DDD OT4dM** peptide, monitoring at 400 nm.

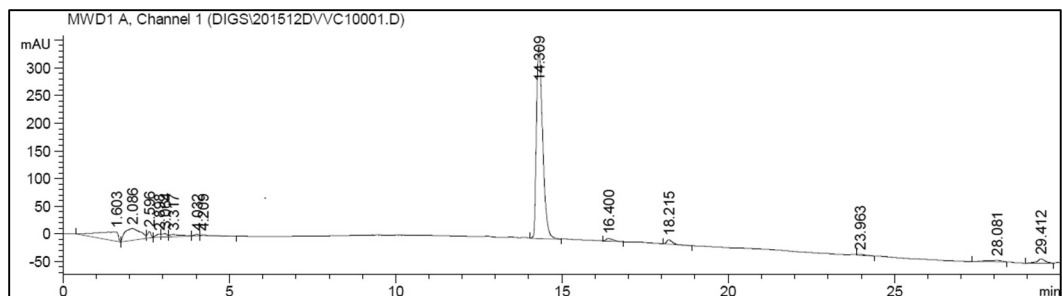


Figure A3.11. Analytical HPLC trace of DVV C10 peptide, monitoring at 220 nm.

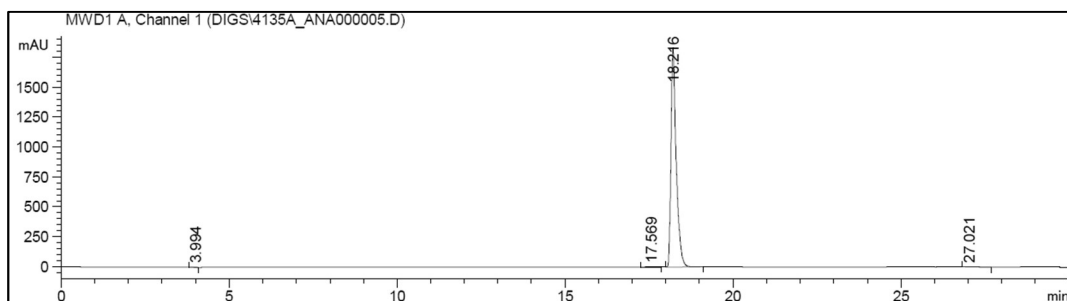


Figure A3.12. Analytical HPLC trace of DVV OPV3 peptide, monitoring at 365 nm.

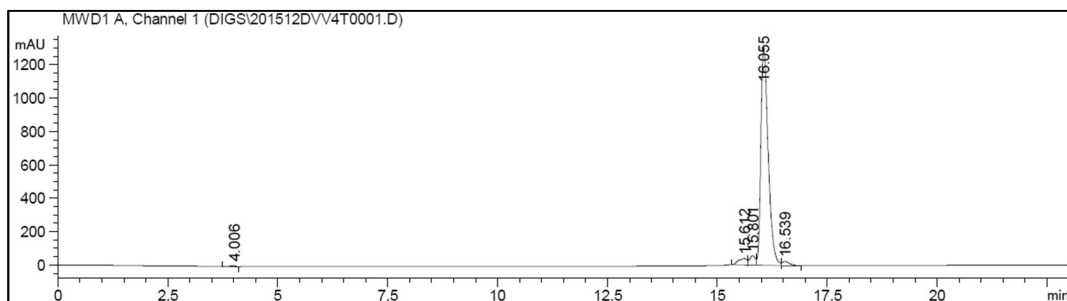


Figure A3.13. Analytical HPLC trace of DVV OT4 peptide, monitoring at 400 nm.

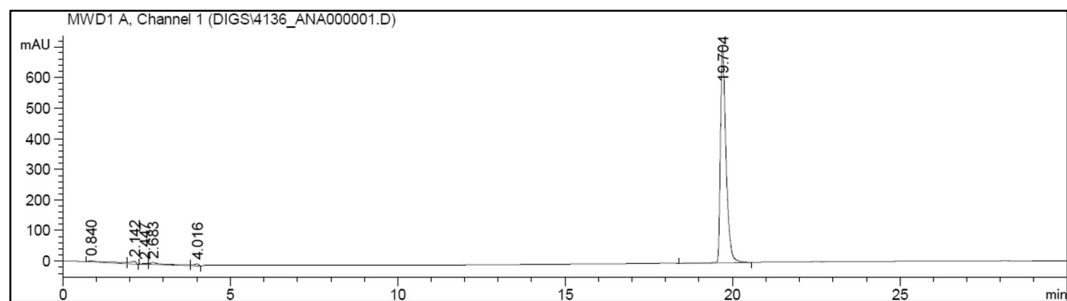


Figure A3.14. Analytical HPLC trace of DVV OT4dM peptide, monitoring at 400 nm.

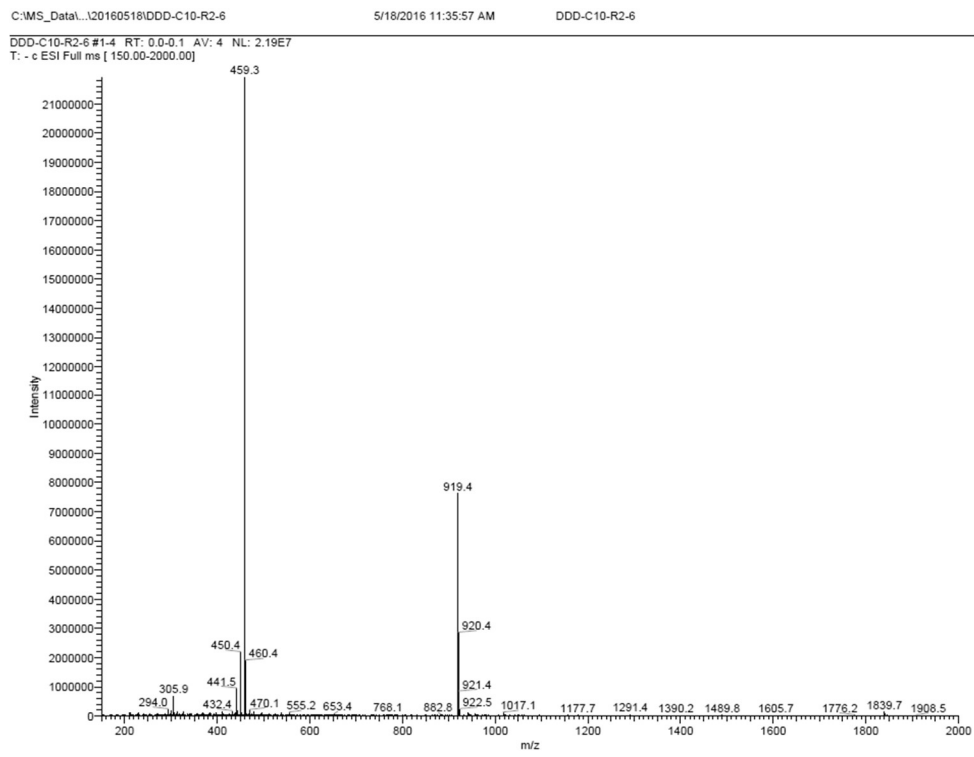


Figure A3.15. ESI-MS spectrum of peptide **DDD C10**.

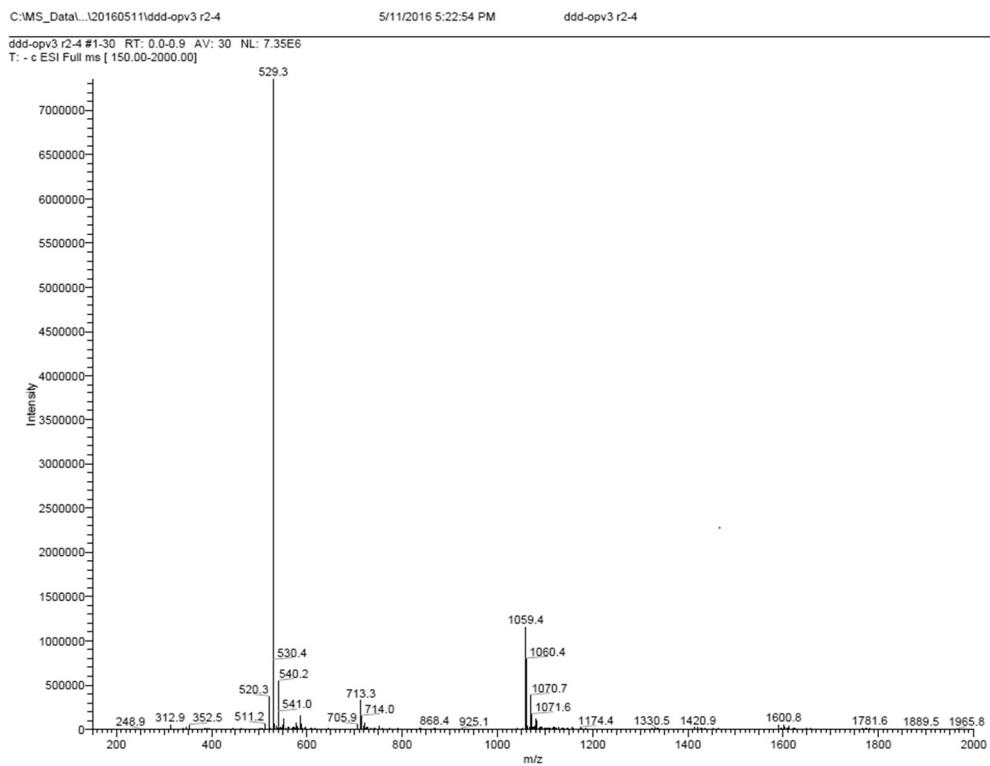


Figure A3.16. ESI-MS spectrum of peptide **DDD OPV3**.

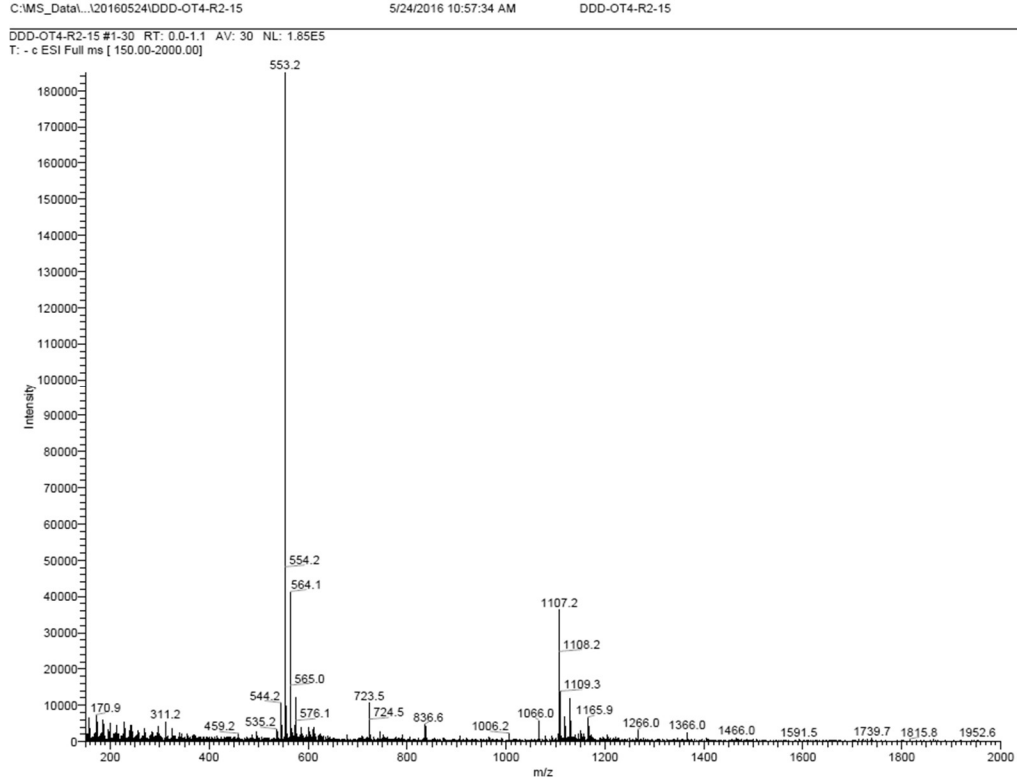


Figure A3.17. ESI-MS spectrum of peptide **DDD OT4**.

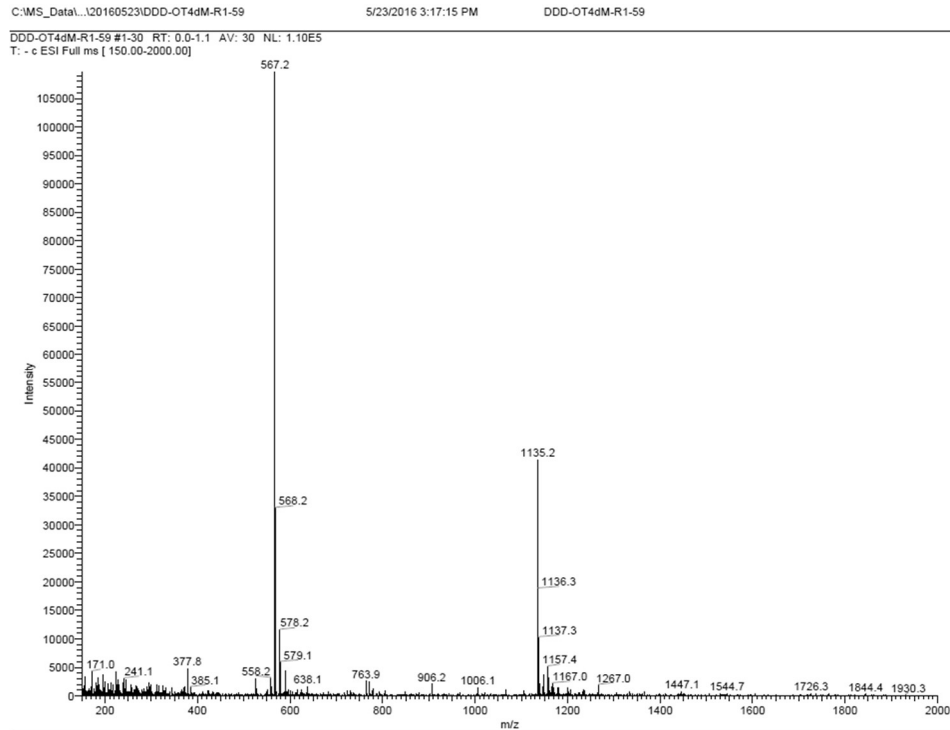


Figure A3.18. ESI-MS spectrum of peptide **DDD OT4dM**.

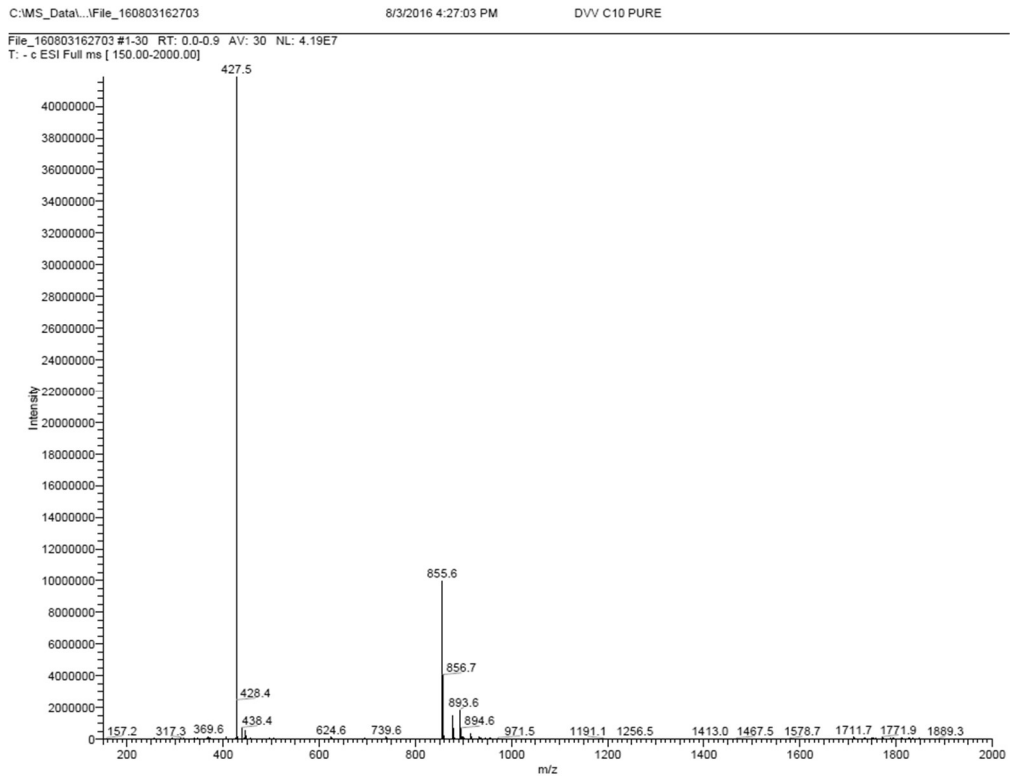


Figure A3.19. ESI-MS spectrum of peptide DVV C10.

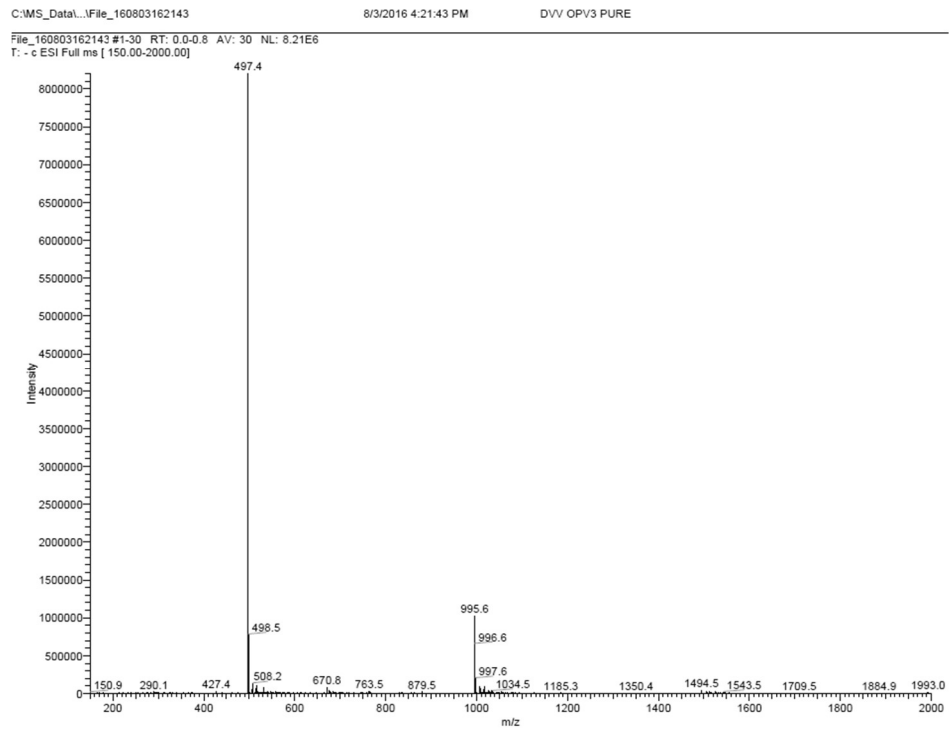


Figure A3.20. ESI-MS spectrum of peptide DVV OPV3.

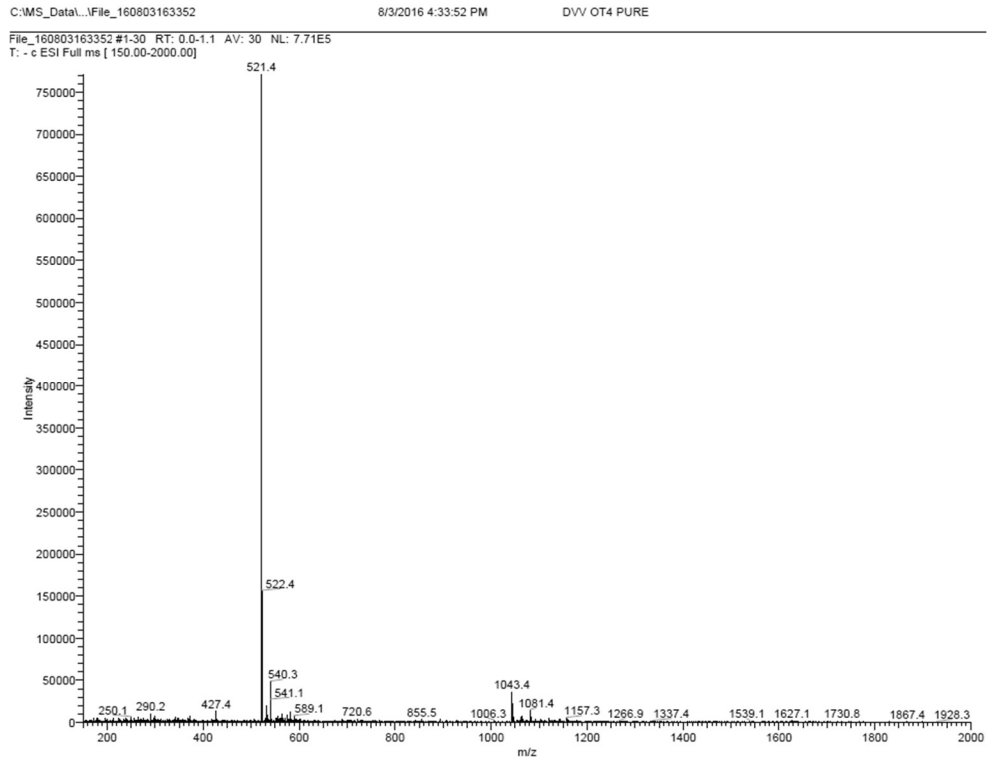


Figure A3.21. ESI-MS spectrum of peptide DVV OT4.

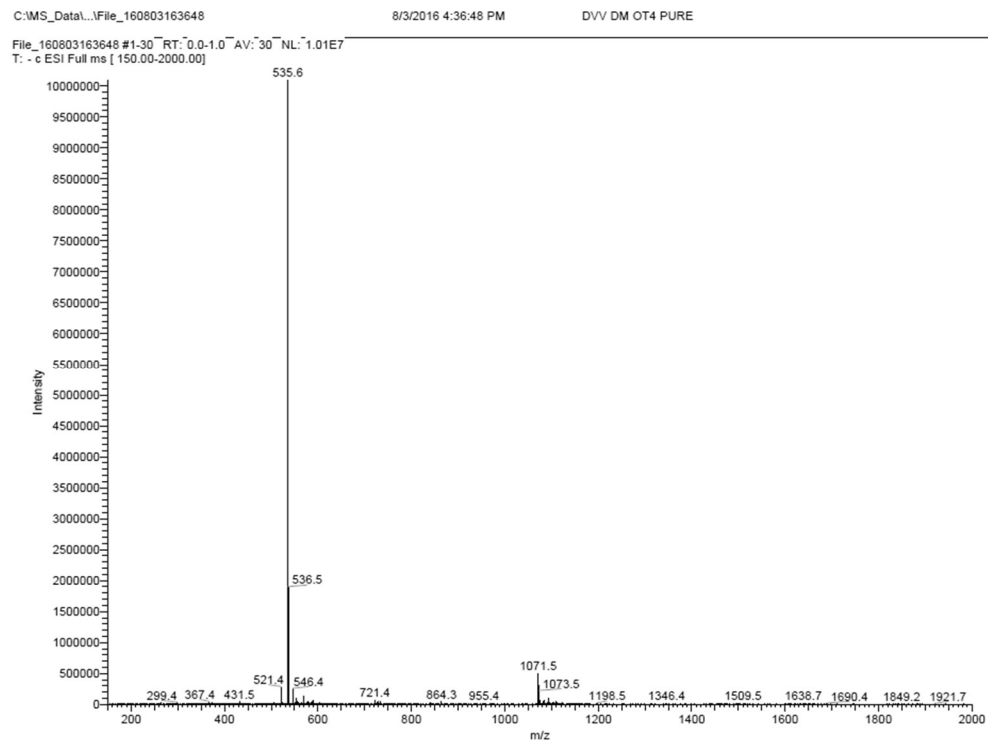


Figure A3.22. ESI-MS spectrum of peptide DVV OT4dM.

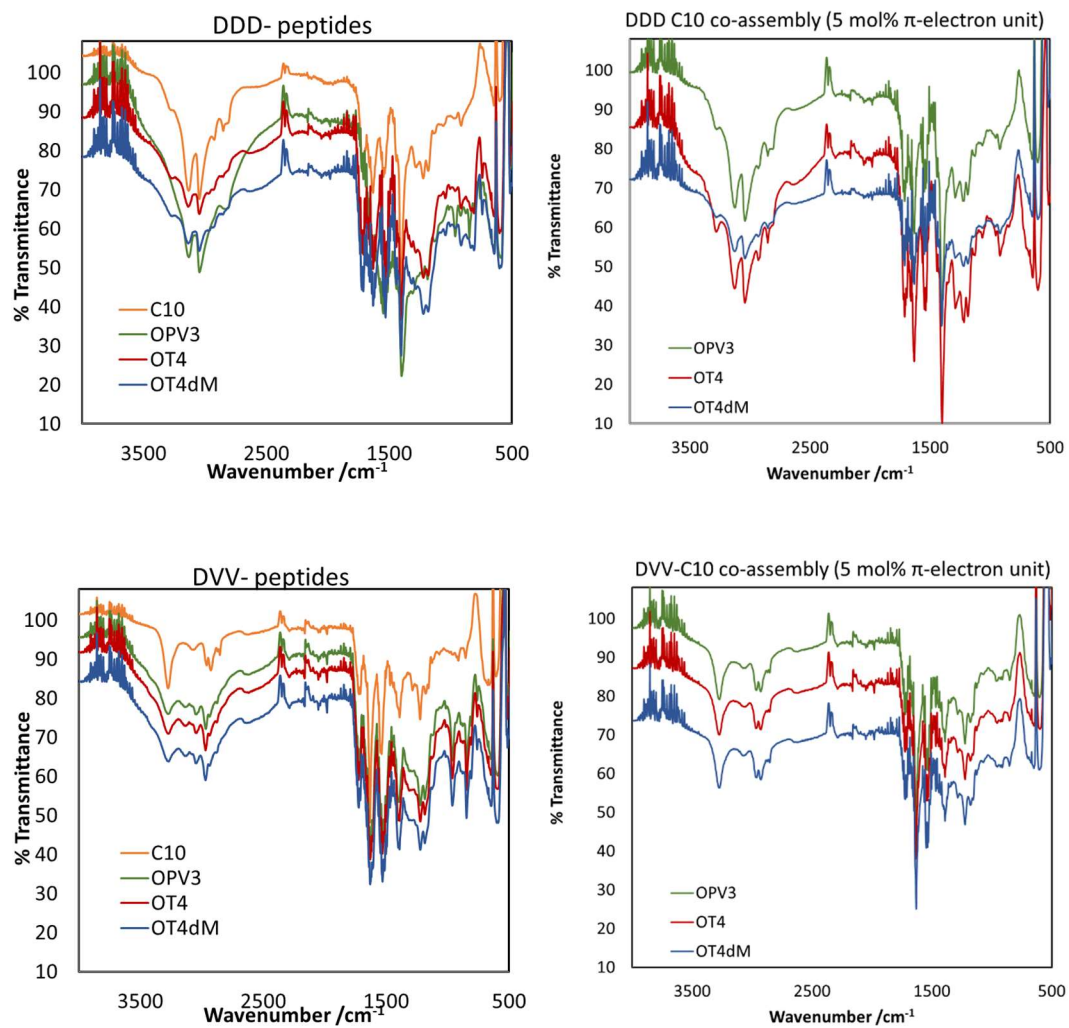


Figure A3.23. FT-IR spectra of DDD peptides (*top, left*) and co-assemblies thereof with **DDD C10** peptide (*top, right*) and DVV peptides (*bottom, left*) and co-assemblies thereof with **DVV C10** peptide (*bottom, right*).

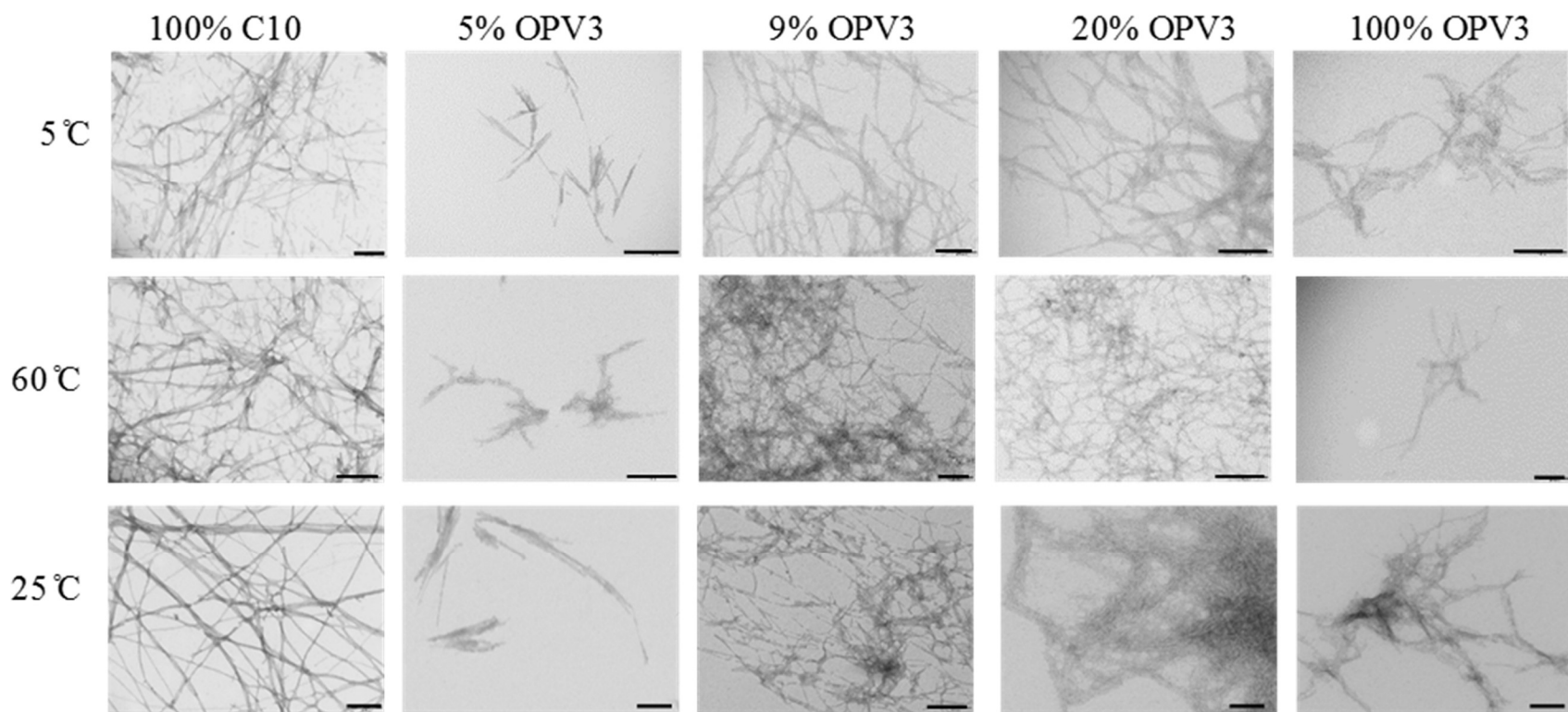


Figure A3.24. TEM images of **DDD OPV3/ DDD C10** co-assembled nanostructures obtained at 5 °C (top) and 60 °C (bottom). All scale bars are 200 nm.

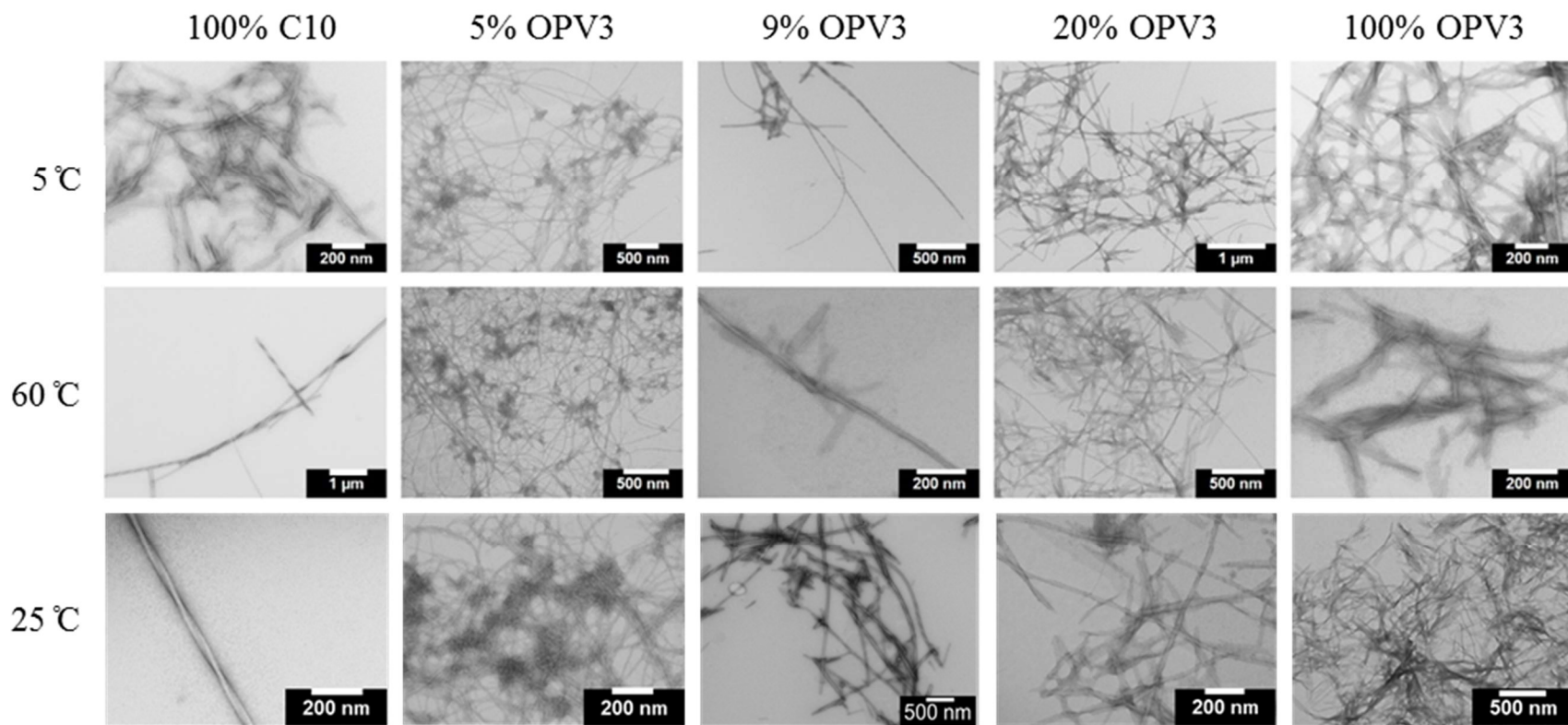


Figure A3.25. TEM images of DVV OPV3/ DVV C10 co-assembled nanostructures obtained at 5 °C (top) and 60 °C (bottom).

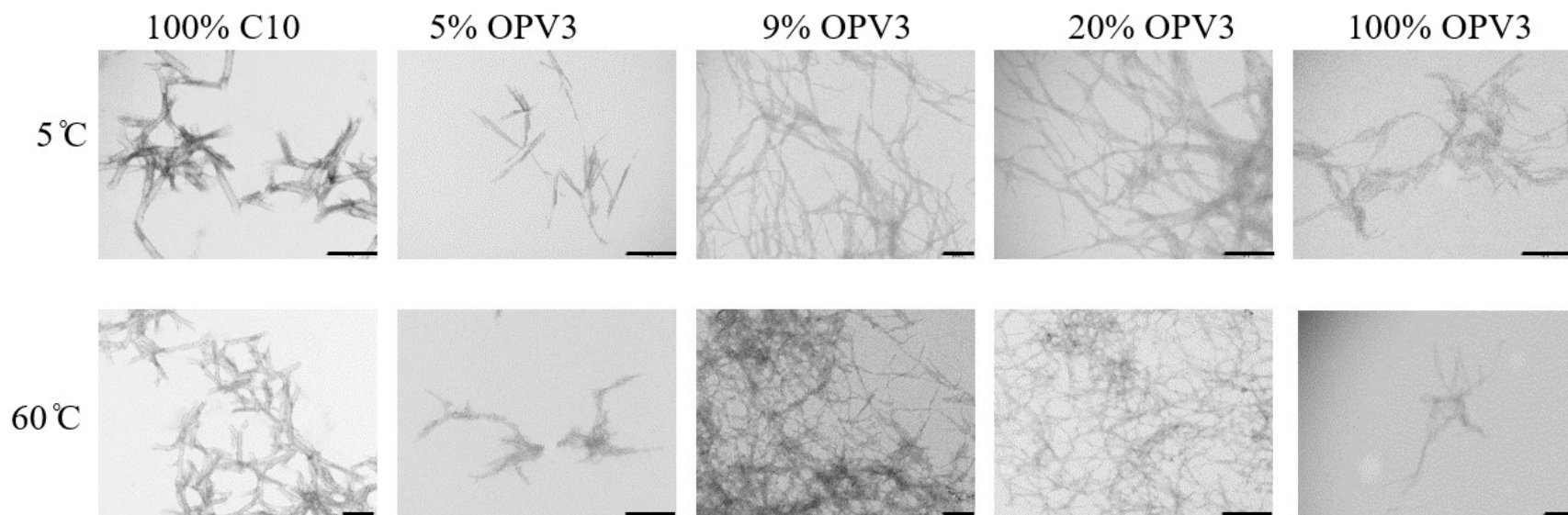


Figure A3.26. TEM images of **DDD OT4/ DDD-C10** co-assembled nanostructures obtained at 5 °C (top) and 60 °C (bottom). All scale bars are 200 nm.

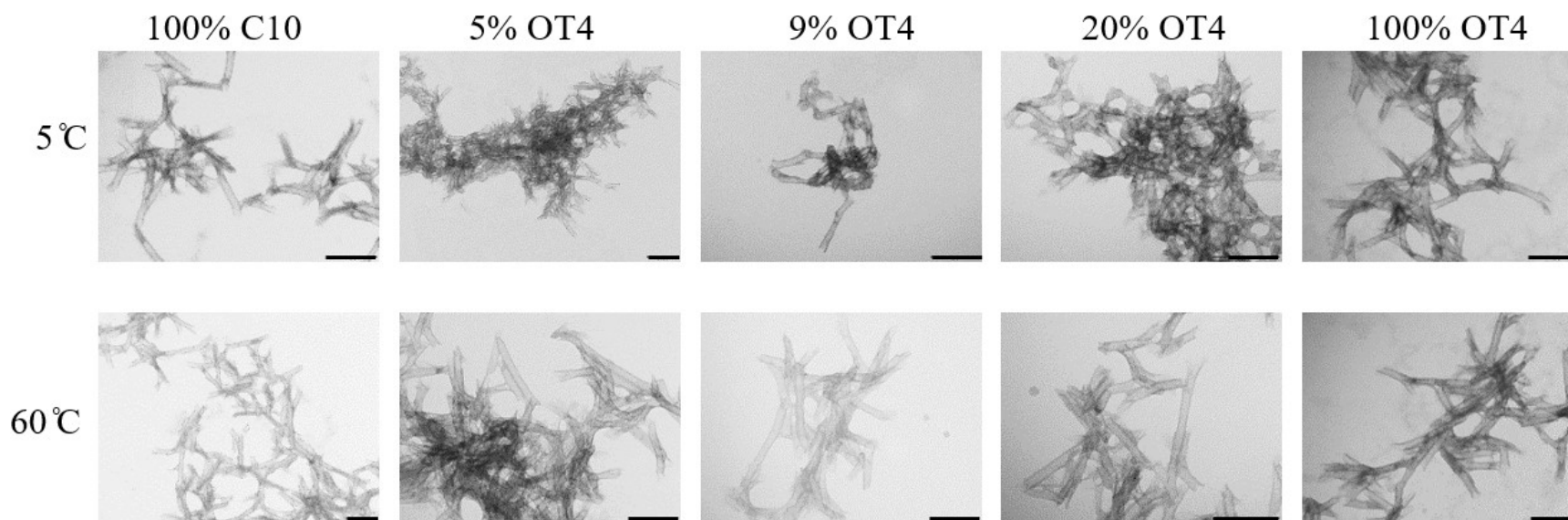


Figure A3.27. TEM images of **DDD OT4dM/ DDD C10** co-assembled nanostructures obtained at 5 °C (top) and 60 °C (bottom). All scale bars are 200 nm.

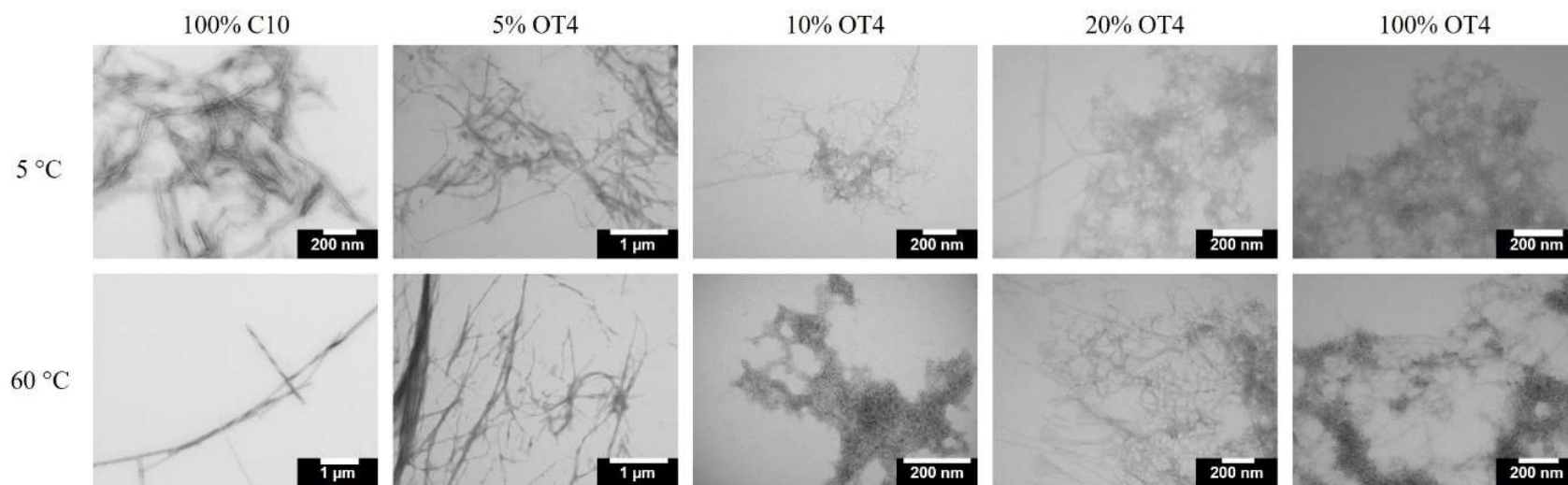


Figure A3.28. TEM images of DVV OT4/ DVV C10 co-assembled nanostructures obtained at 5 °C (top) and 60 °C (bottom).

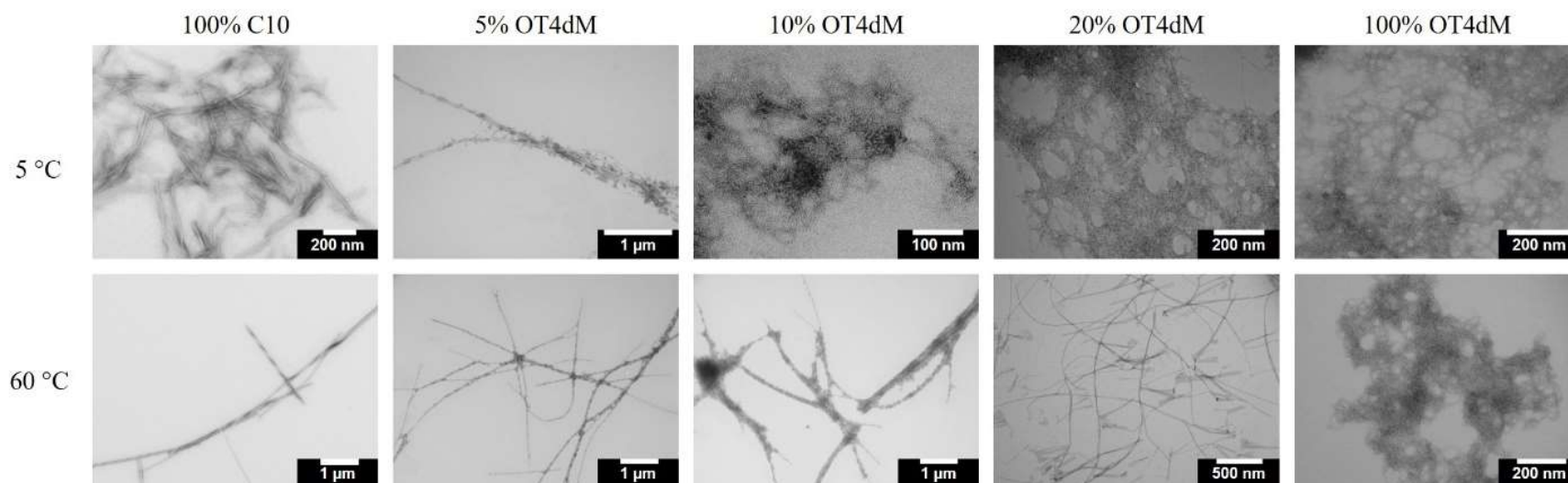


Figure A3.29. TEM images of DVV OT4dM/ DVV C10 co-assembled nanostructures obtained at 5 °C (top) and 60 °C (bottom).

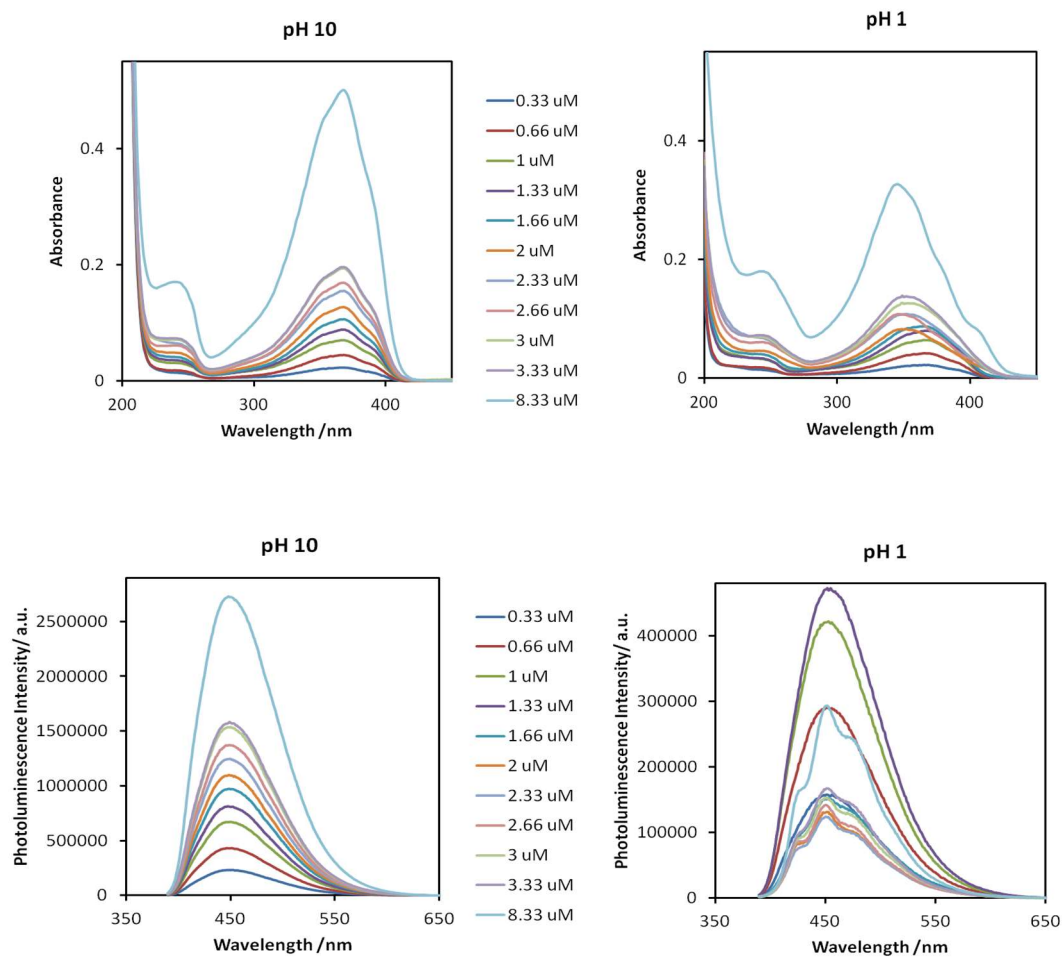


Figure A3.30. UV-Vis absorption (*top*) and PL (*bottom*) data of different concentrations of DDD OPV3 peptide homo-assemblies in aqueous media; recorded at room temperature.

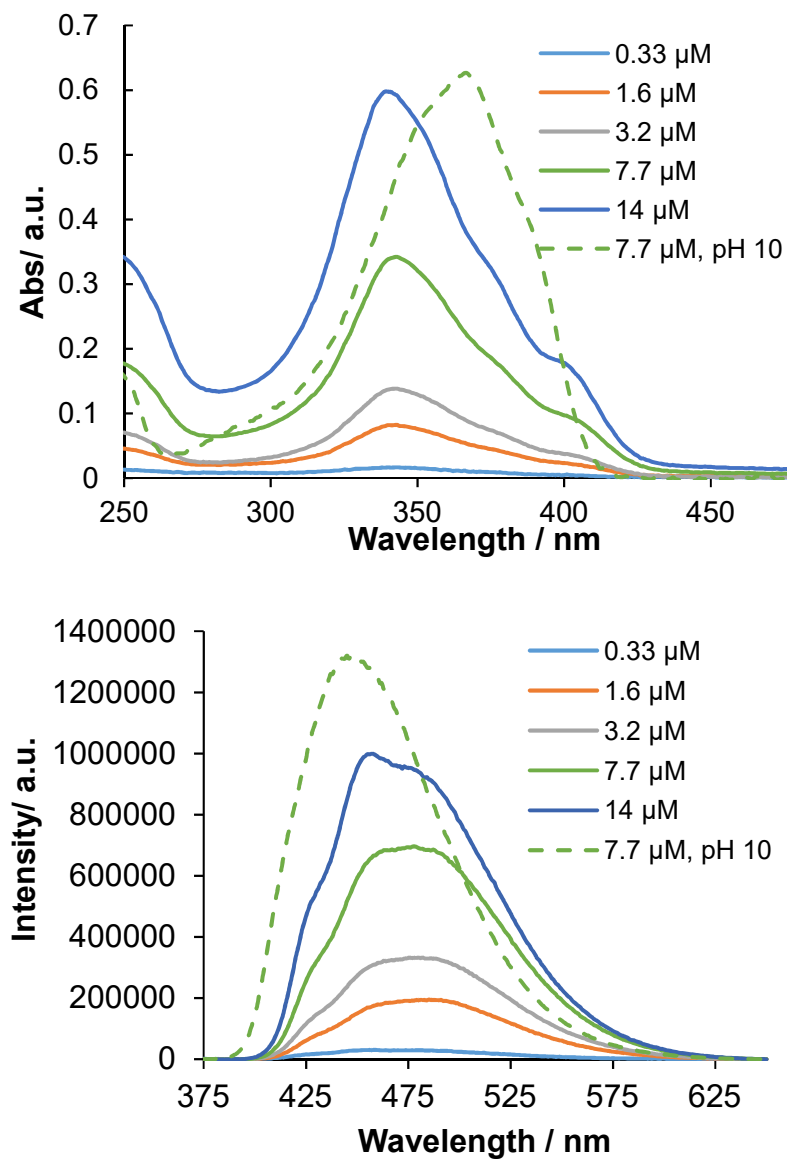


Figure A3.31. UV-Vis absorption (*top*) and PL (*bottom*) data of different concentrations of DVV OPV3 peptide homo-assemblies in aqueous media; recorded at room temperature.

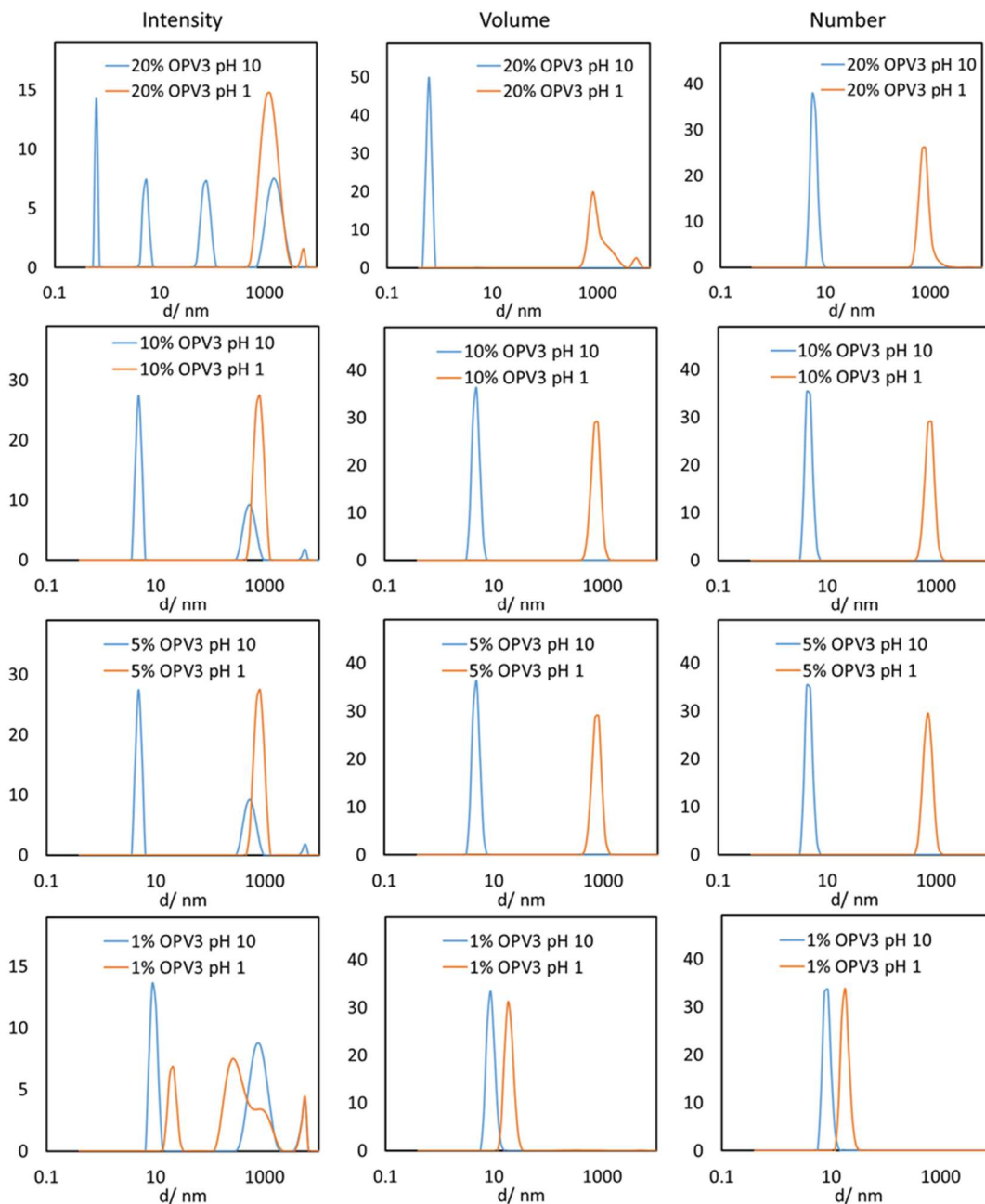


Figure A3.32. DLS data of **DDD OPV3/ DDD C10** co-assembled nanostructures generated at 25°C displayed as intensity (*left*), number (*center*) and volume (*right*) averages.

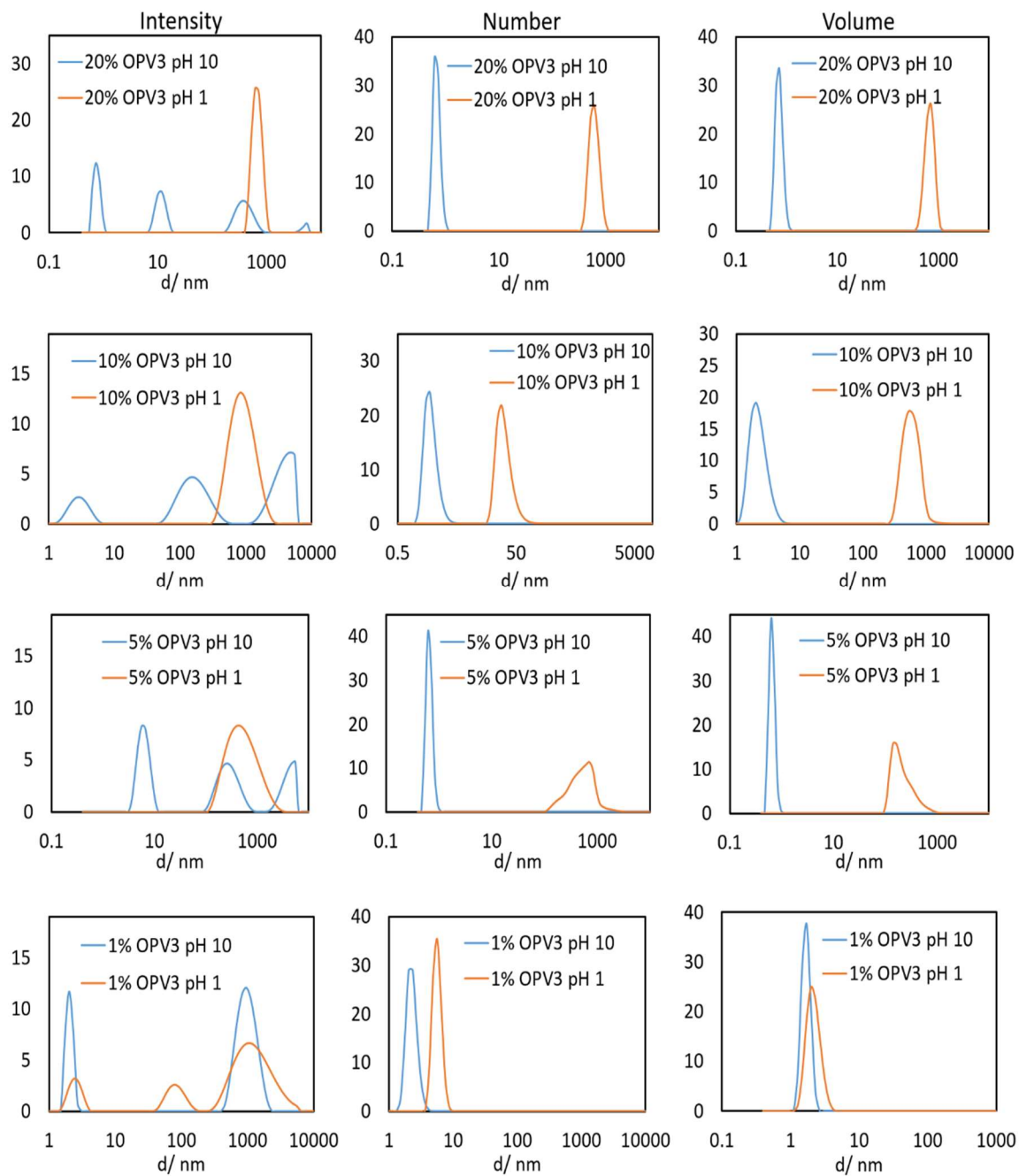


Figure A3.33. DLS data of DVV OPV3/ DVV C10 co-assembled nanostructures generated at 25°C displayed as intensity (*left*), number (*center*) and volume (*right*) averages.

Table A3.1. Relative quantum yields for co-assemblies of **DDD OPV3/ DDD C10** and **DVV OPV3/ DVV C10** with respect to the respective pure, acidic OPV3 peptide.

DDD OPV3, pH 1	1
5% Co-assembled	4.2
20% Co-assembled	0.8
5% Separate	0.5
20% Separate	0.9
DVV OPV3, pH 1	1
5% Co-assembled	1.8
20% Co-assembled	1.3
5% Separate	1.7
20% Separate	1.4

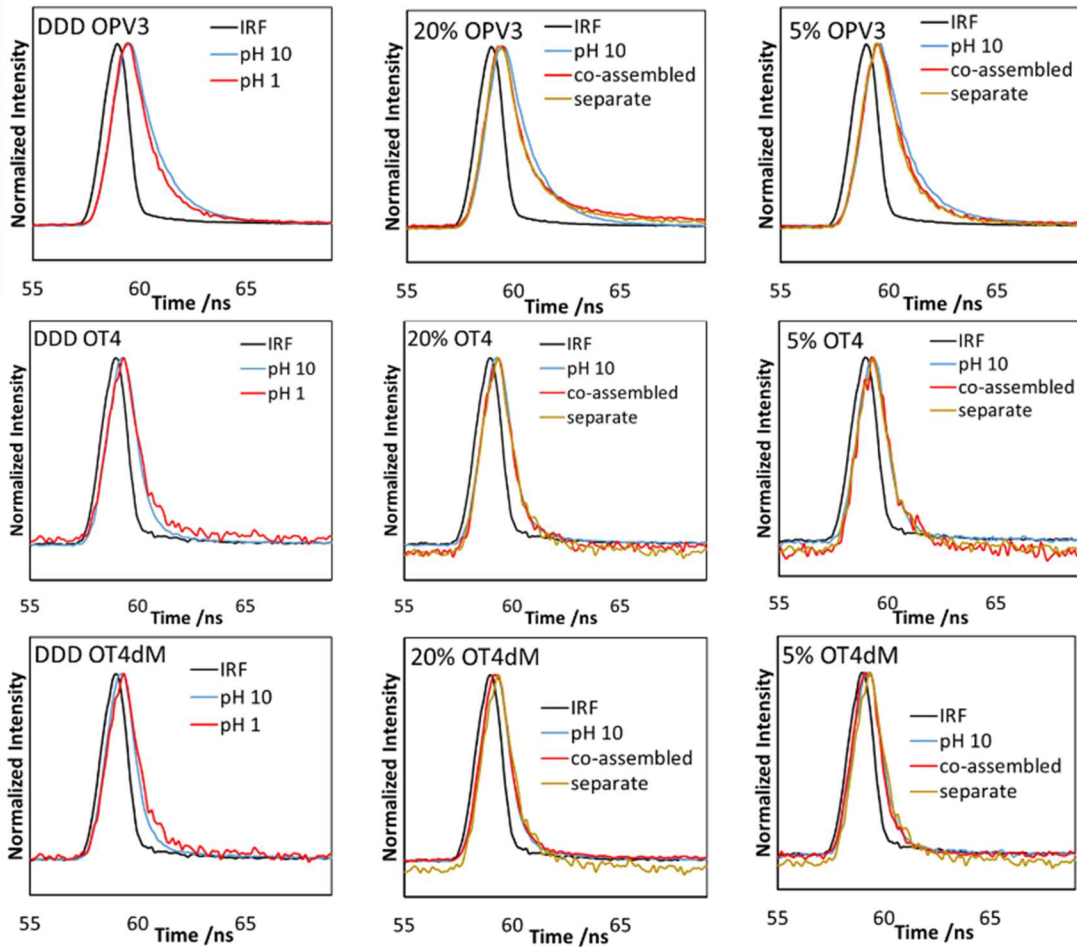


Figure A3.34. PL lifetime measurements recorded for DDD peptides.

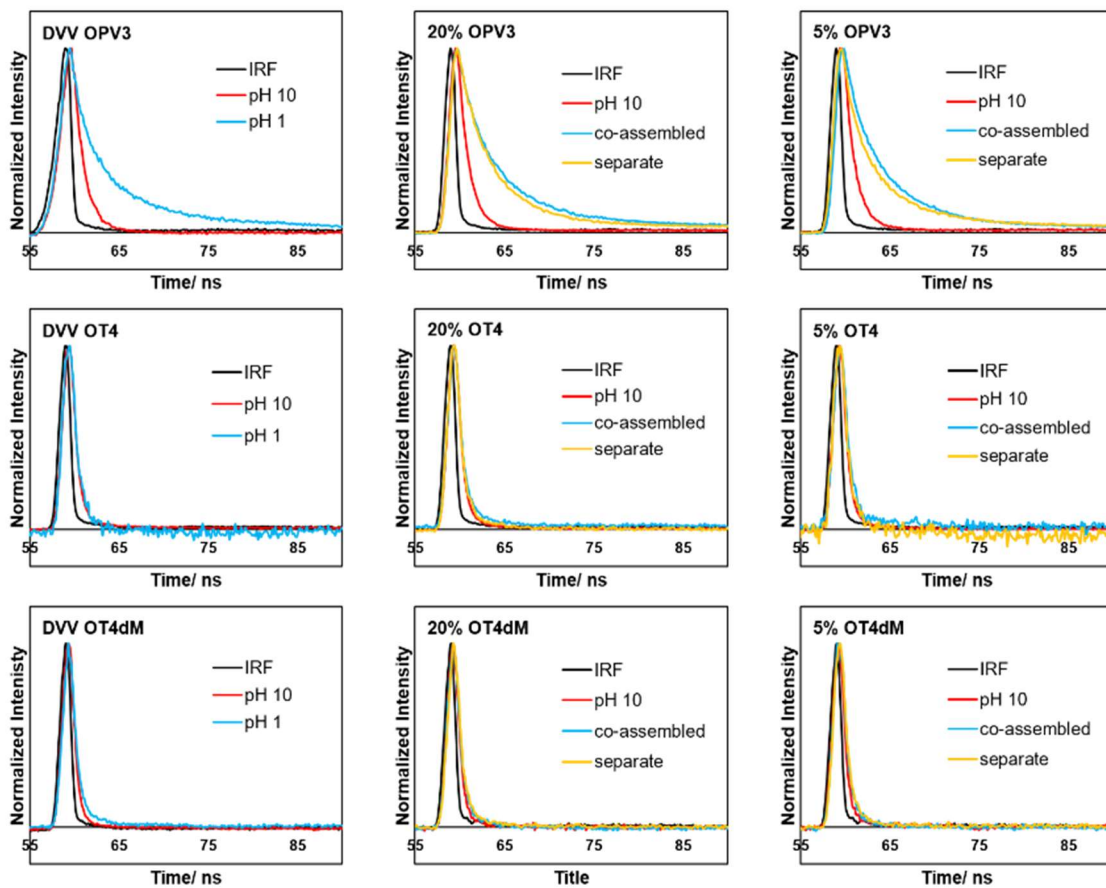


Figure A3.35. PL lifetime measurements recorded at room temperature for DVV peptides.

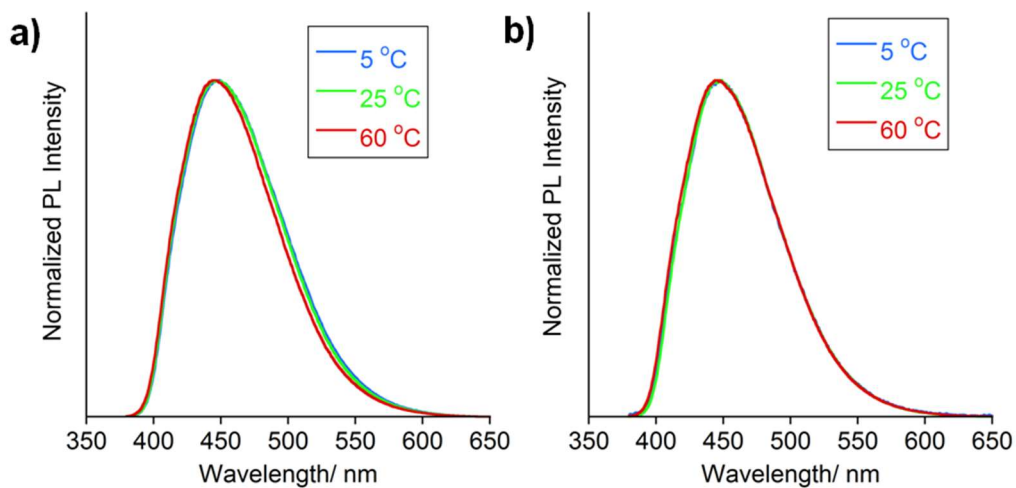


Figure A3.36. Normalized PL spectra of (a) **DDD OPV3** and (b) **DVV OPV3** peptides in molecularly dissolved state (pH 10) at various temperatures; [OPV3]= 8 μ M.

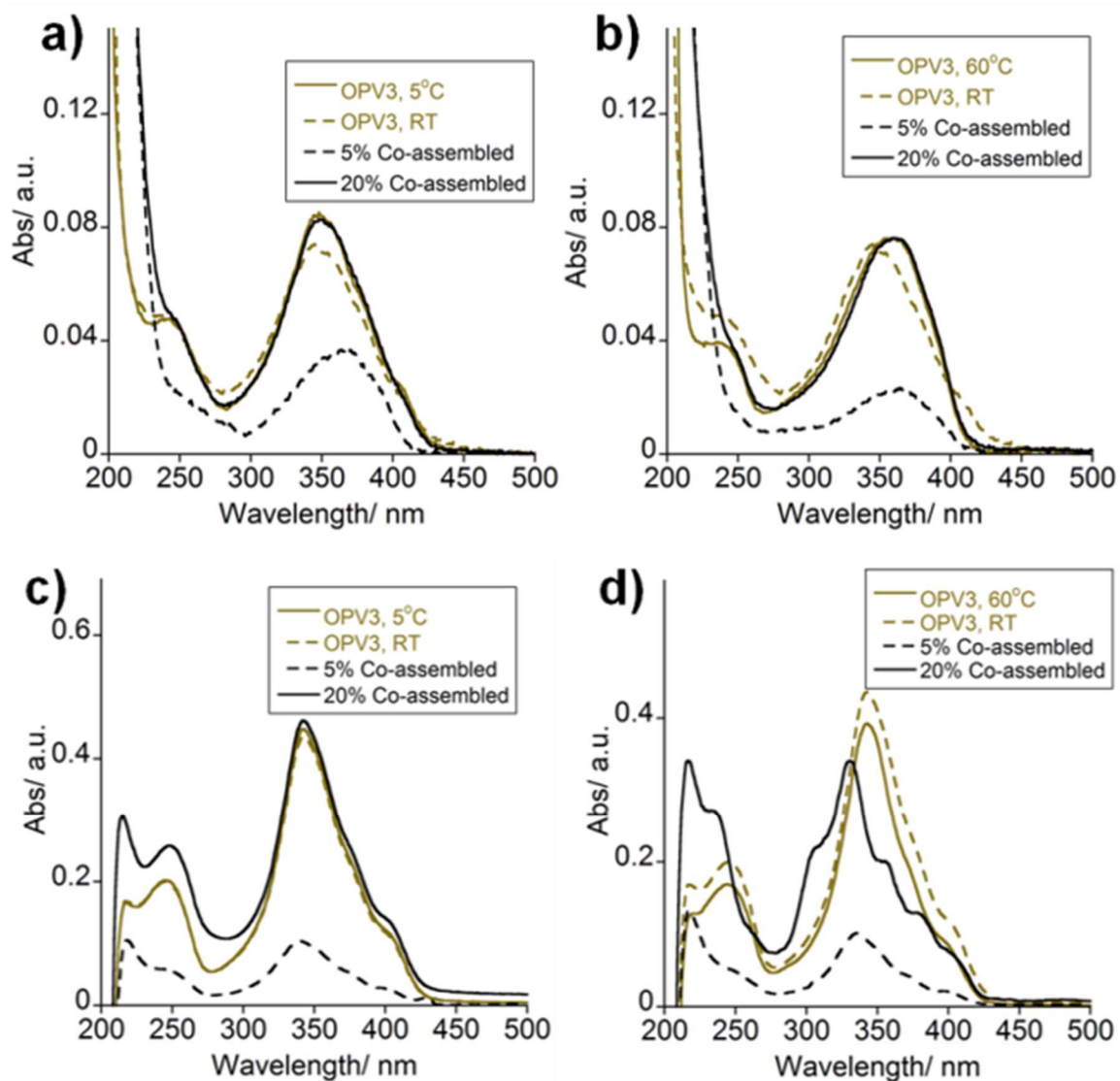


Figure A3.37. Absorption spectra recorded at 5 °C (a,c) and 60 °C (b,d) spectra of **DDD OPV3** (a,b) and **DVV OPV3** (c,d) homo-assemblies, and co-assemblies with their respective C10 peptide equivalents.

Chapter 4; Part I

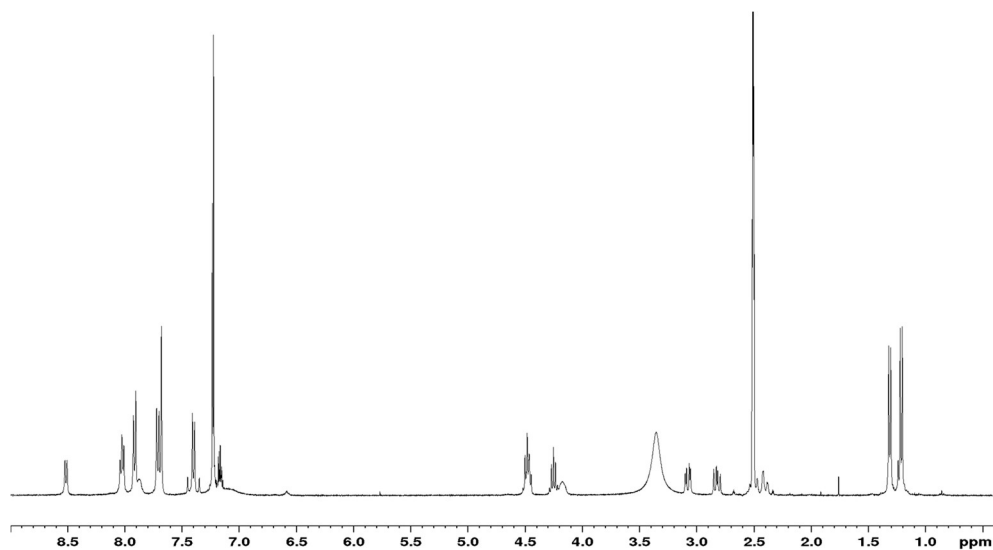


Figure A4.1. ^1H (400 MHz, $\text{d}_6\text{-DMSO}$) NMR of **DFAA-OPV3** peptide.

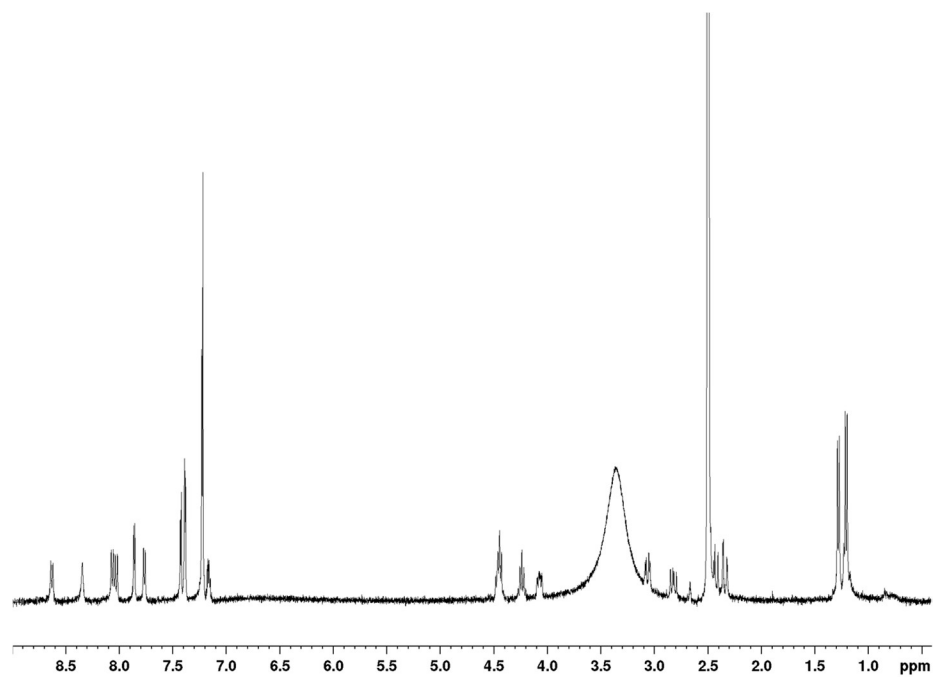


Figure A4.2. ^1H (400 MHz, $\text{d}_6\text{-DMSO}$) NMR of **DFAA-OT4** peptide.

File_140403174623 #1-30 RT: 0.0-0.9 AV: 30 NL: 6.45E5
T: - c ESI Full ms [100.00-2000.00]

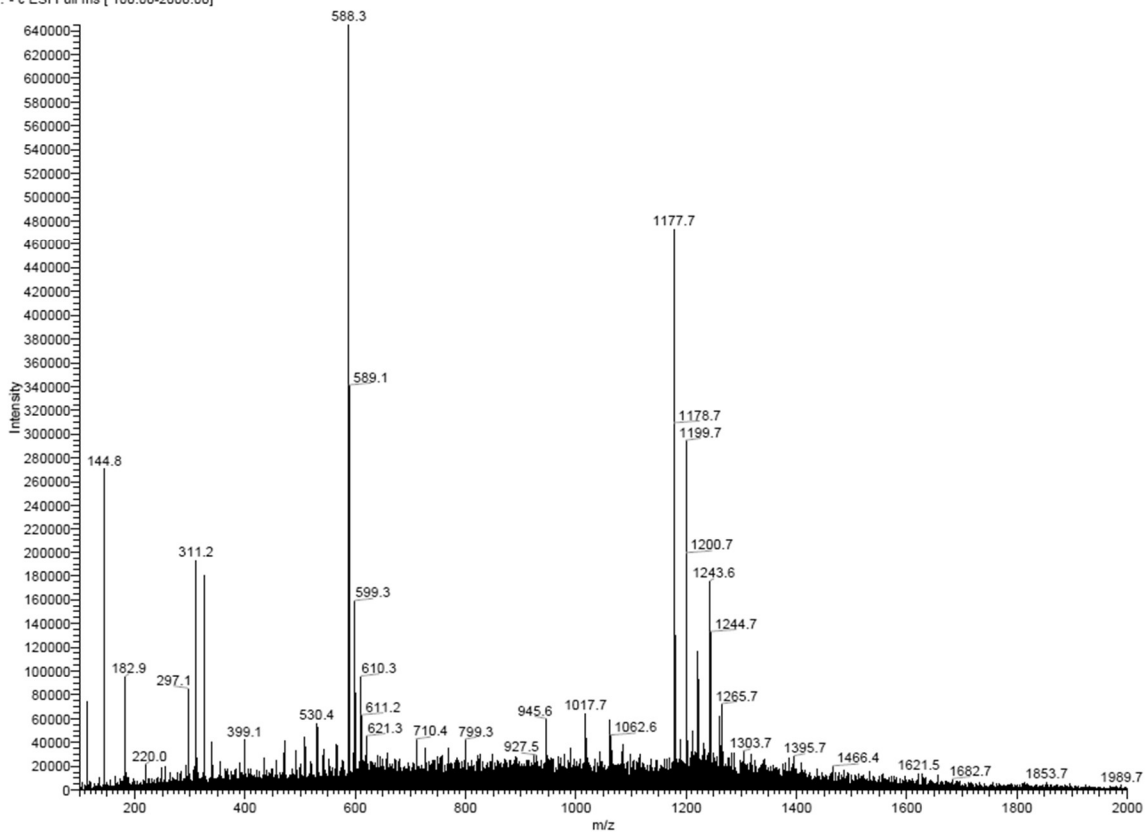


Figure A4.3. ESI-MS spectrum of DFAA-OPV3 peptide.

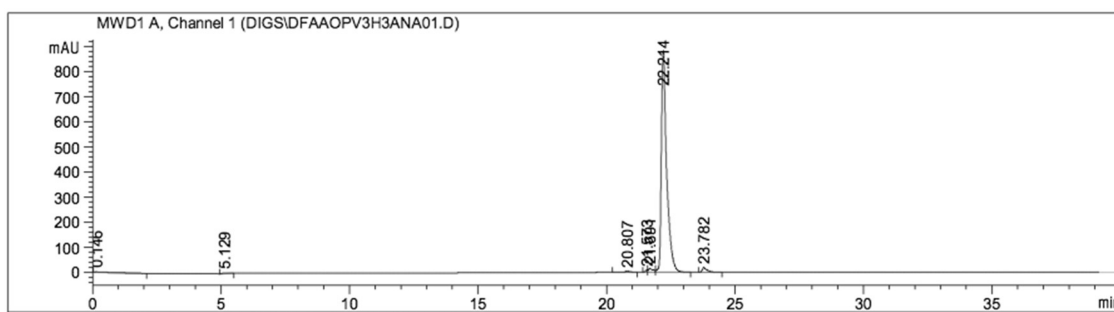


Figure A4.4. Analytical HPLC trace of DFAA-OPV3, monitoring at 365 nm.

File_140403175235 #1-30 RT: 0.0-0.9 AV: 30 NL: 9.83E5
T: - c ESI Full ms [100.00-2000.00]

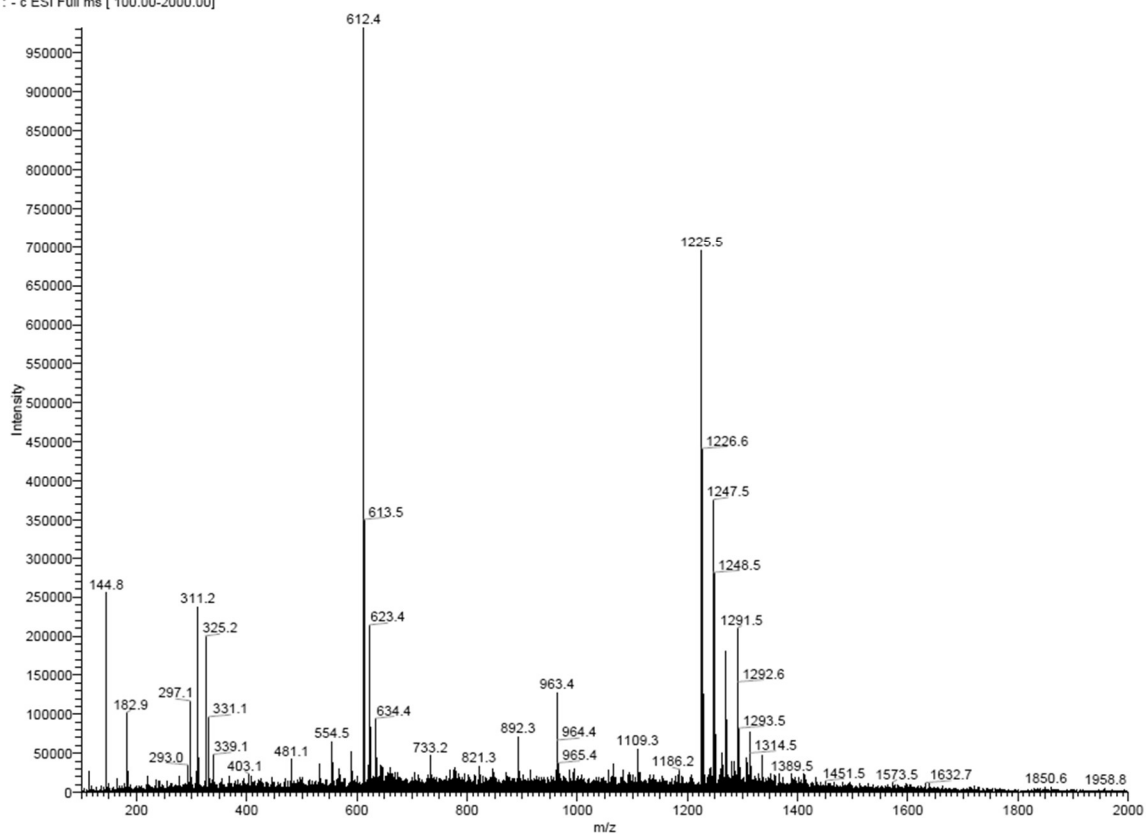


Figure A4.5. ESI-MS spectrum of DFAA-OT4 peptide.

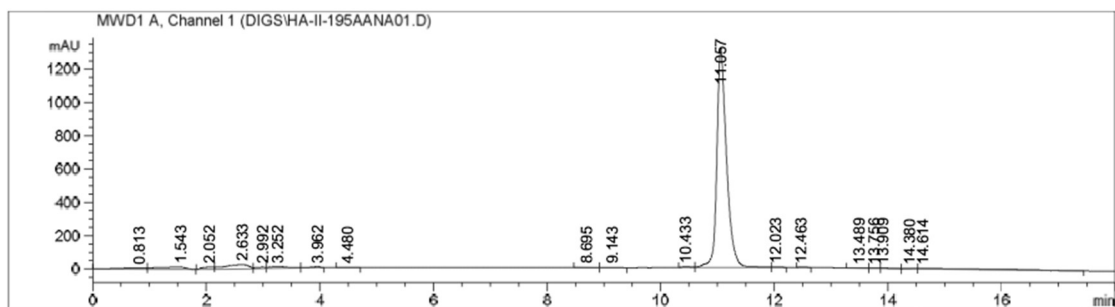


Figure A4.6. Analytical HPLC trace of DFAA-OT4, monitoring at 400 nm.

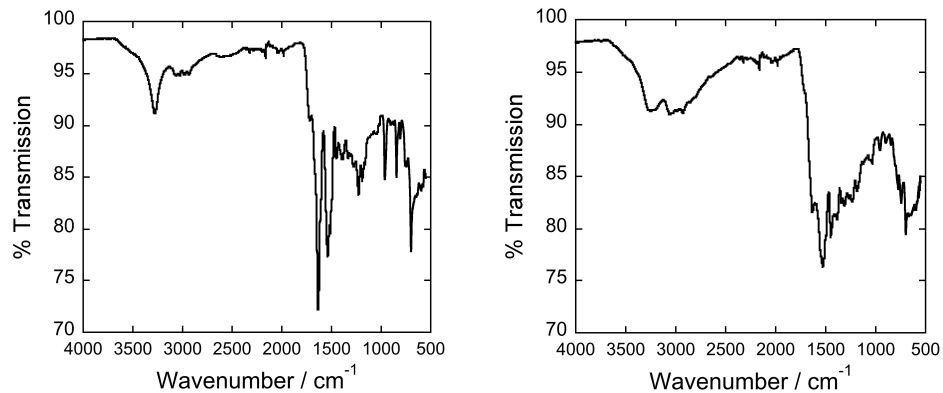


Figure A4.7. Attenuated total reflectance (ATR)-IR spectra of **DFAA-OPV3** (left) and **DFAA-OT4** (right) in solid state.

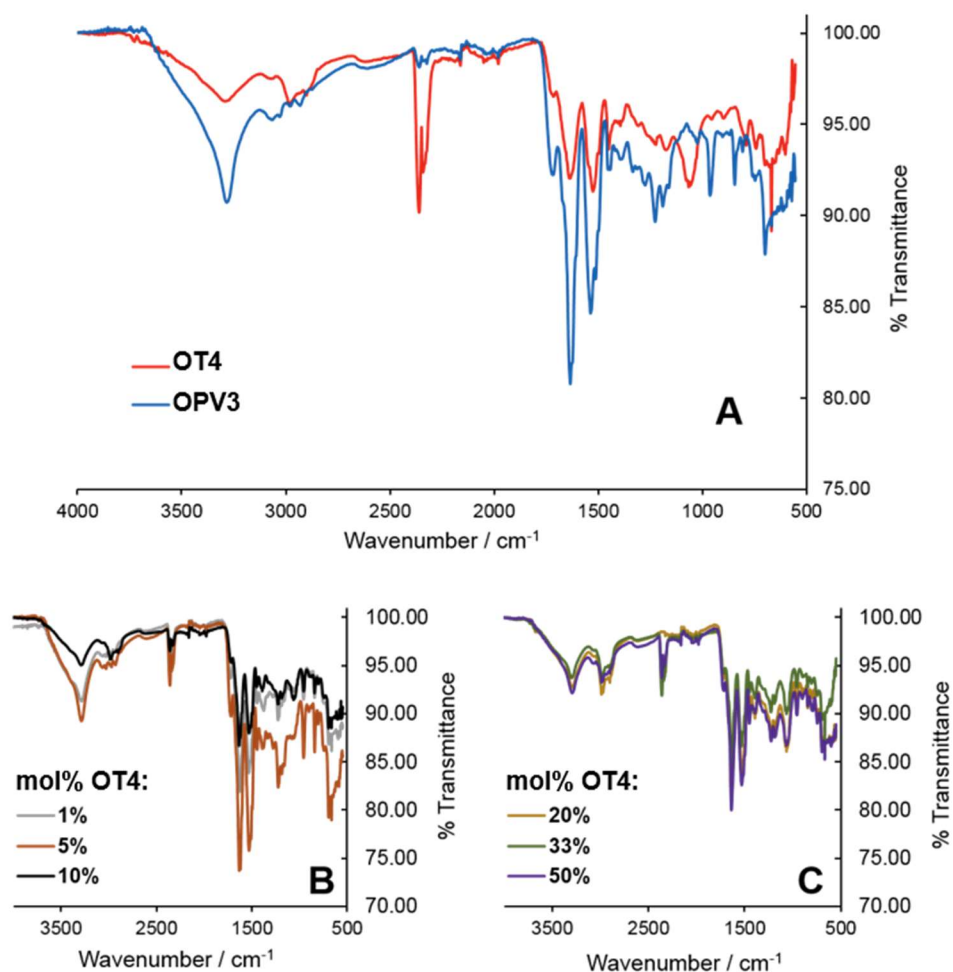


Figure A4.8. ATR-IR spectra of lyophilized acidic solutions of **DFAA-** (a) **OPV3**, **OT4**, and (b,c) coassemblies.

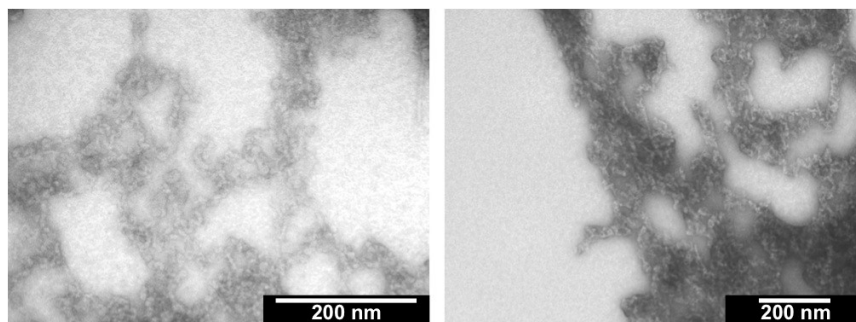


Figure A4.9. Representative TEM images showing the nanostructures from a 0.1 wt% acidic solution of **DFAA-OT4**.

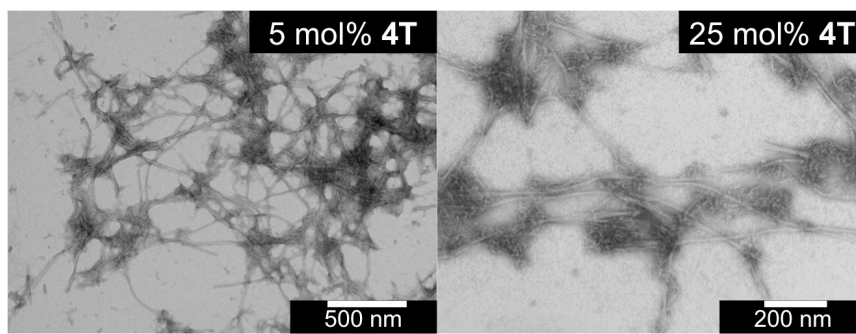


Figure A4.10. Representative TEM images of the nanostructures from a 0.1 wt% acidic solution of coassembled **DFAA-OPV3/-OT4** at different mol% **DFAA-OT4** (widths/ nm: 5 mol%= 10.8 ± 1.6 ; 25 mol%= 13.0 ± 2.3).

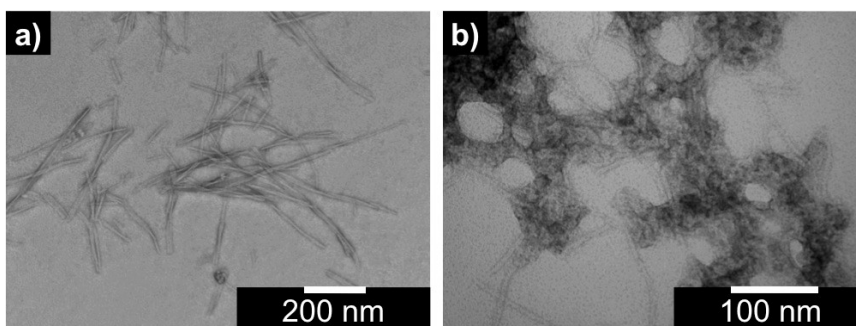


Figure A4.11. Representative TEM images of the nanostructures from a 0.1 wt% acidic solution of (a) coassembled **DFAA-OPV3/-OT4** (1:1) and a solution wherein (b) **DFAA-OT4** was added to pre-assembled **DFAA-OPV3** solution (1:1).

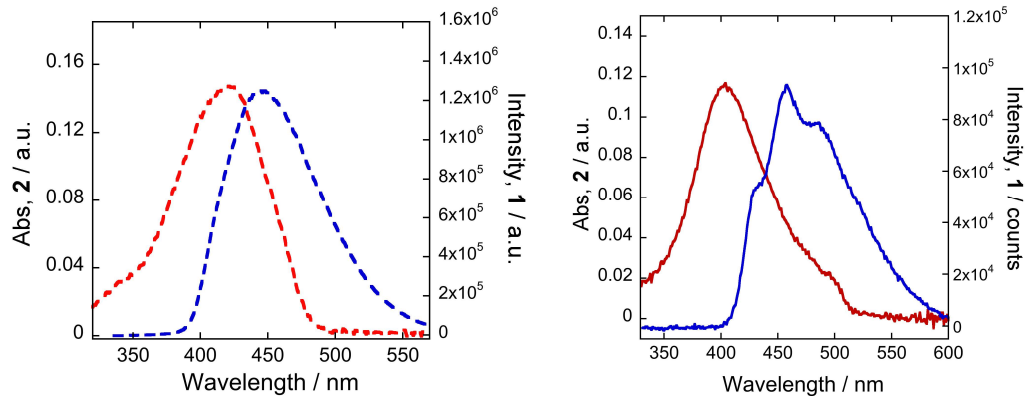


Figure A4.12. Plots showing the spectral overlap between the DF_AA-OPV3 donor emission and DF_AA-OT4 acceptor absorbance for basic (left) and (right) acidic solutions.

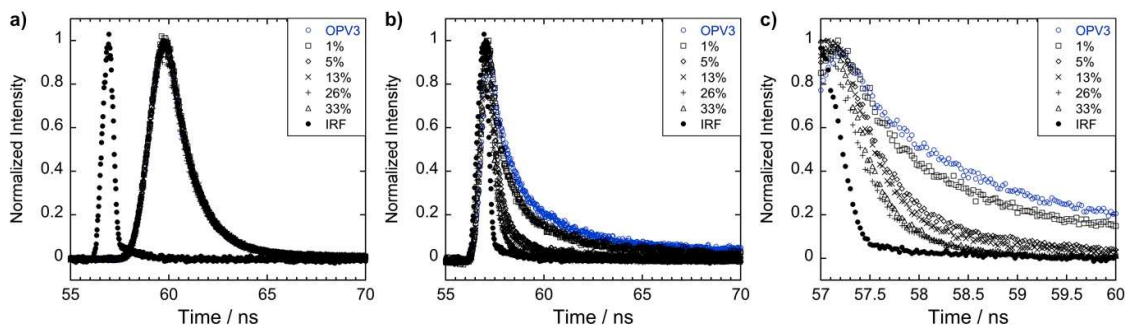


Figure A4.13. Lifetime decay profiles ($\lambda_{exc}= 375$ nm) of pure donor and coassemblies under (a) basic (ca. pH 10) and (b,c) acidic (ca. pH 2) conditions.

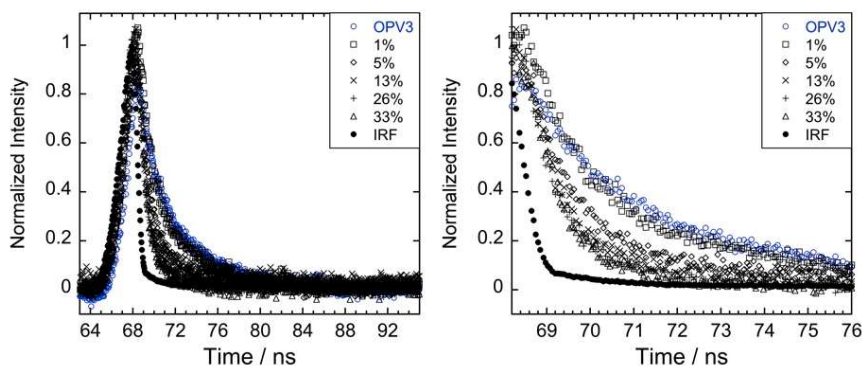


Figure A4.14. Lifetime decay profiles ($\lambda_{exc}= 340$ nm) of pure donor and coassemblies under acidic (ca. pH 2) conditions.

Chapter 4; Part II

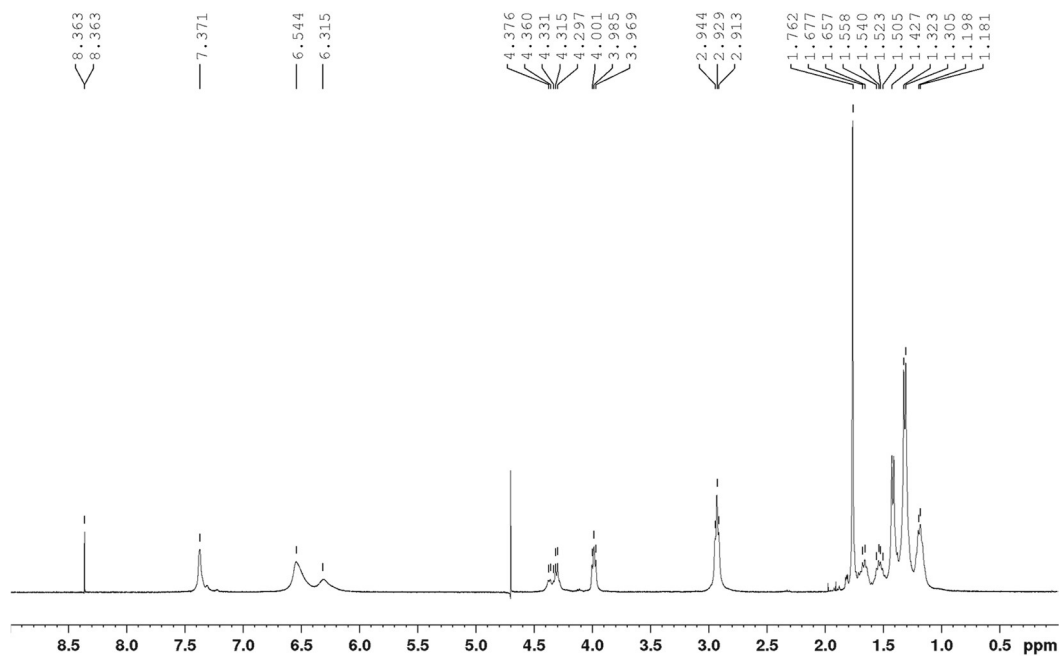


Figure A4.15. ^1H (400 MHz, D_2O) NMR spectrum of OT4-Ac peptide.

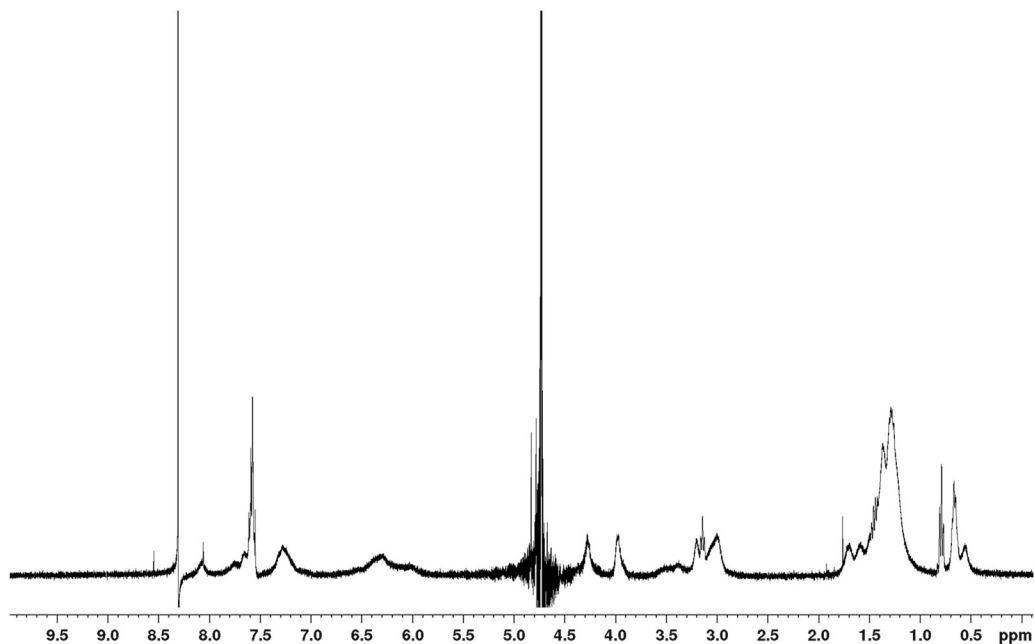


Figure A4.16. ^1H (400 MHz, D_2O) NMR spectrum of OT4-NDI peptide. Peak broadness can be attributed to the aggregation of the material even at high pH. A presaturation pulse was applied during spectrum acquisition to suppress water.

File_160927192427 #1-25 RT: 0.0-0.9 AV: 25 NL: 2.98E5
T: - c ESI Full ms [150.00-2000.00]

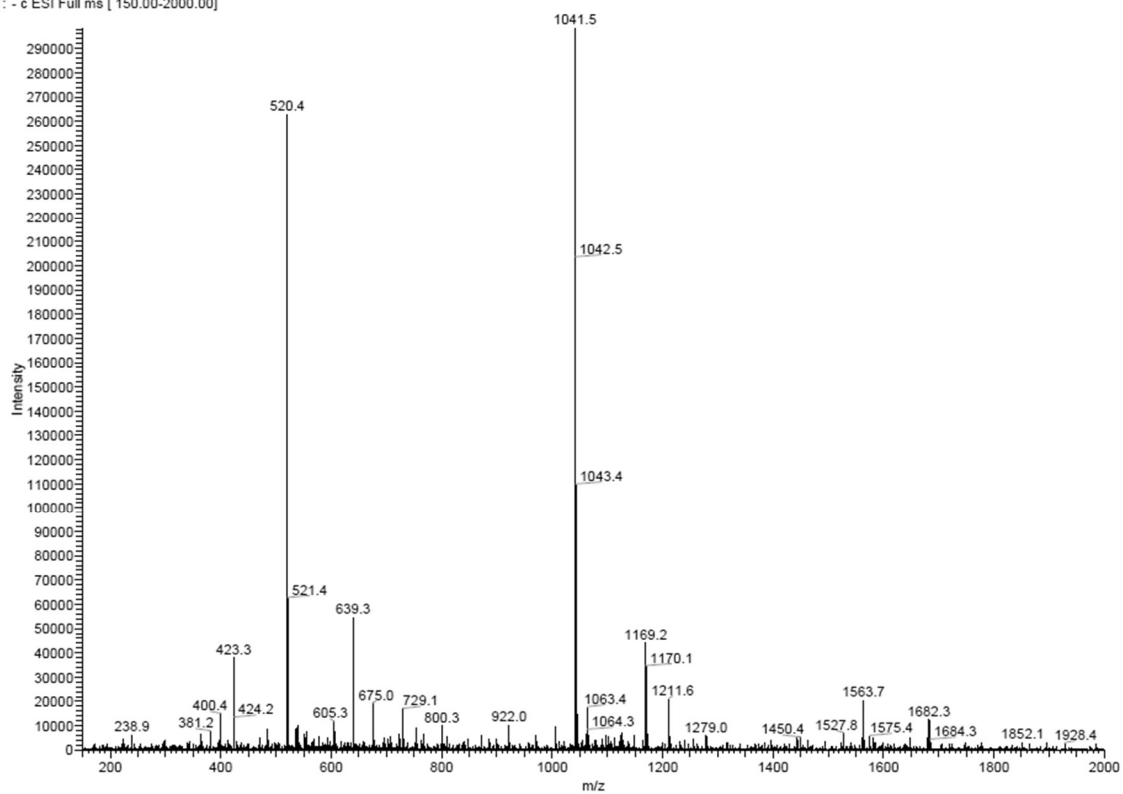


Figure A4.17. ESI-MS spectrum of OT4-Ac peptide.

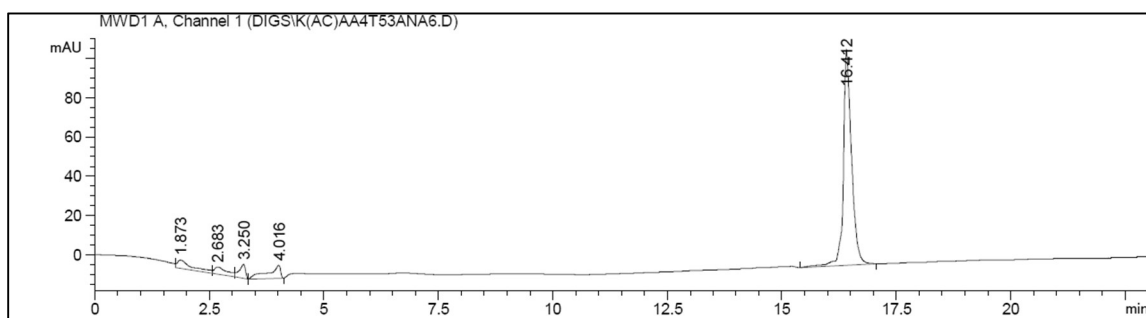


Figure A4.18. Analytical HPLC trace of OT4-Ac, monitoring at 400 nm.

File_160327193005 #1-30 RT: 0.0-0.9 AV: 30 NL: 4.74E5
T: - c ESI Full ms [150.00-2000.00]

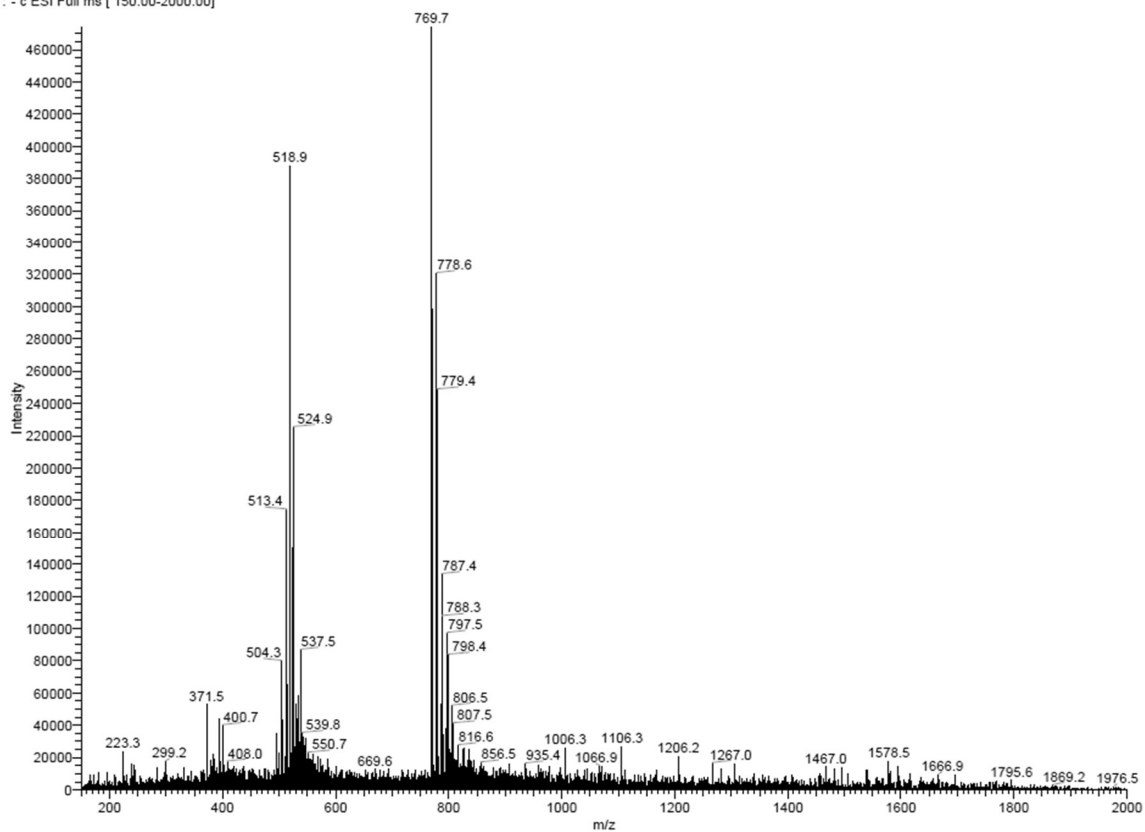


Figure A4.19. ESI-MS spectrum of OT4-NDI peptide.

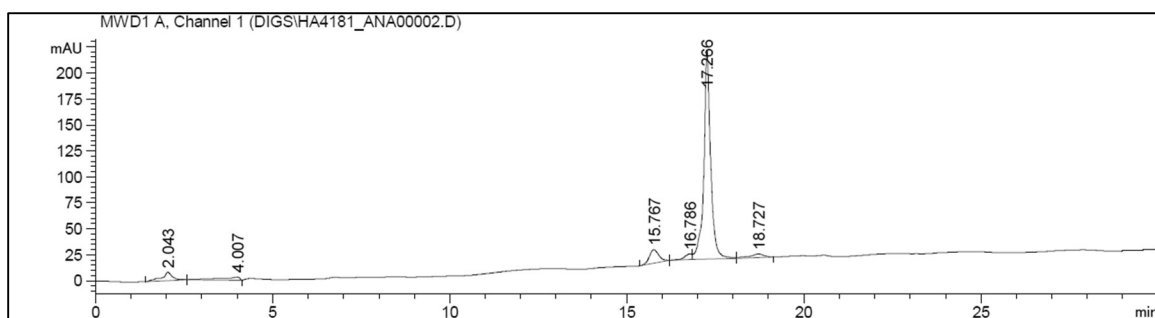


Figure A4.20. Analytical HPLC trace of OT4-NDI, monitoring at 400 nm.

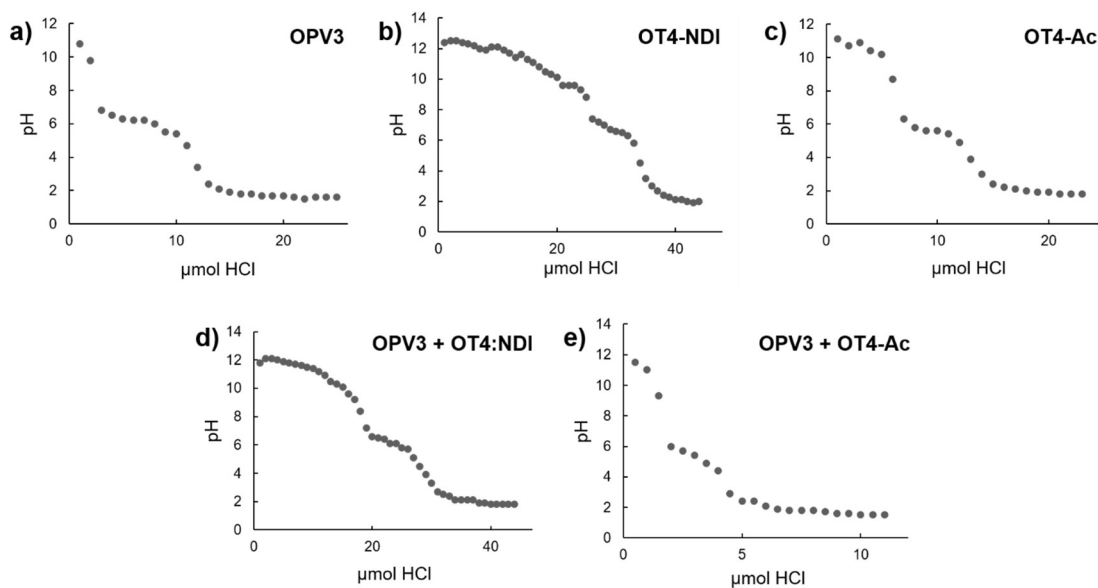


Figure A4.21. pH titration curves for the homoassemblies of **OPV3**, **OT4-NDI** and **OT4-Ac**, and co-assemblies of **OPV3** with **OT4-Ac** and with **OT4-NDI** (1:1 mixture). Plateaus on the curve indicate the apparent pK_a of the gelators.

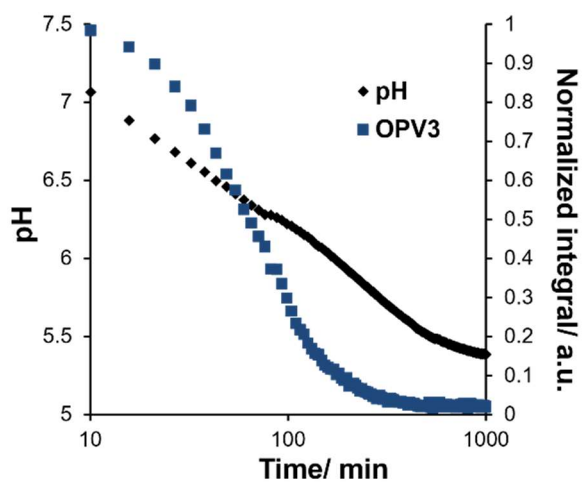


Figure A4.22. Monitoring of GdL-triggered gelation *via* ^1H NMR for **OT4-NDI** and **OPV3** mixed sample; final concentration of each peptide component is 5 mg/mL; prepared with 30 mg/mL GdL [no resonances were observed for pure *OT4-NDI* solutions even at high pH].

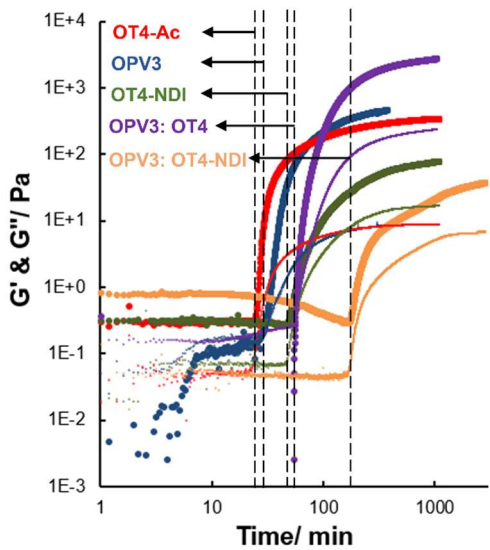


Figure A4.23. Rheology plots (G' = solid circles; G'' =smaller circles) for peptide homoassemblies and mixed assemblies prepared with 30 mg/mL of GdL. Each peptide component is at 5 mg/mL (total of 10 mg/mL peptides for the 1:1 mixed samples; 5 mg/mL for the pure peptide samples).

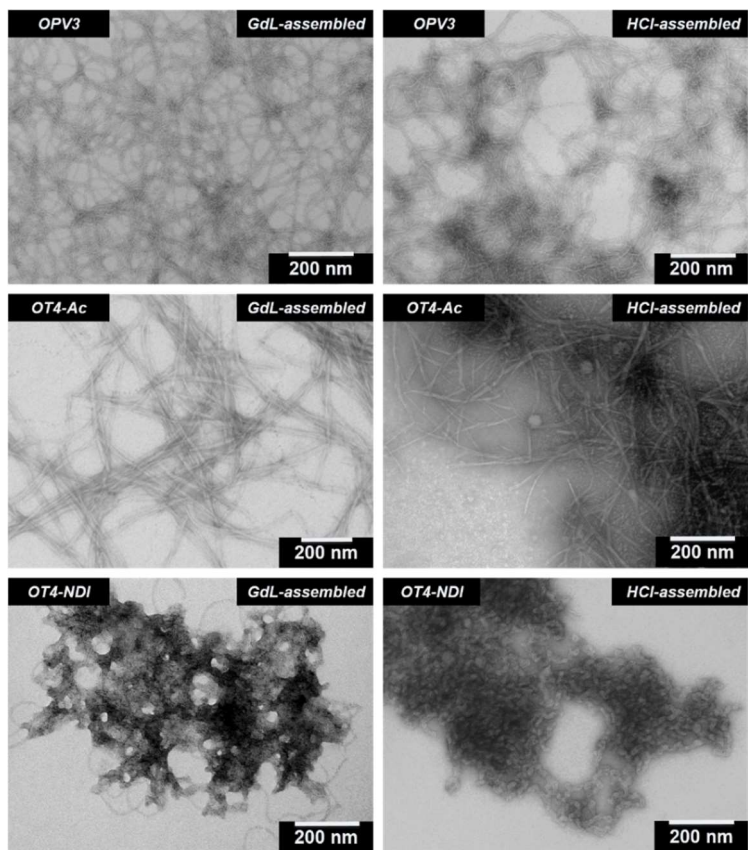


Figure A4.24. TEM images of OPV3, OT4-Ac, OT4-NDI homoassemblies ($[\text{peptide}] = 3 \mu\text{M}$) prepared with HCl addition and GdL (10 mg/mL).

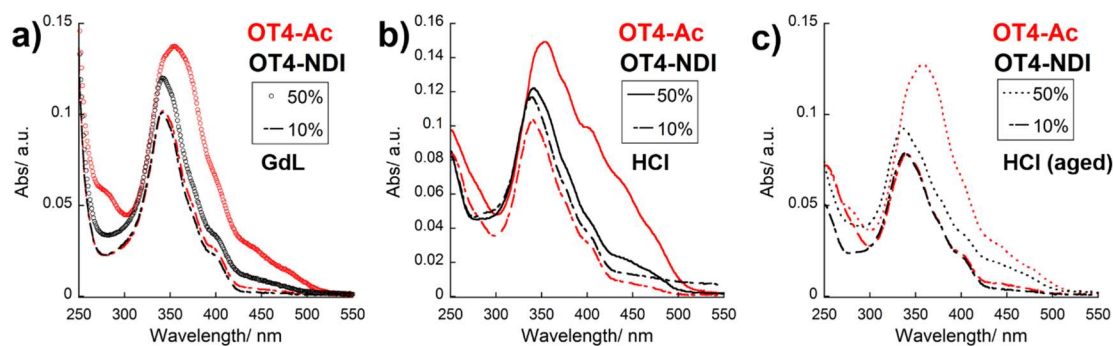


Figure A4.25. UV-vis absorption spectra for GdL- (10 mg/mL) and HCl-coassembled peptide structures of **OPV3** with **OT4-Ac** (red) and with **OT4-NDI** (black); measured under different conditions: a) with GdL (empty circles), b) with HCl (—), and c) with HCl, aged (...); [OPV3]= 3 μ M.

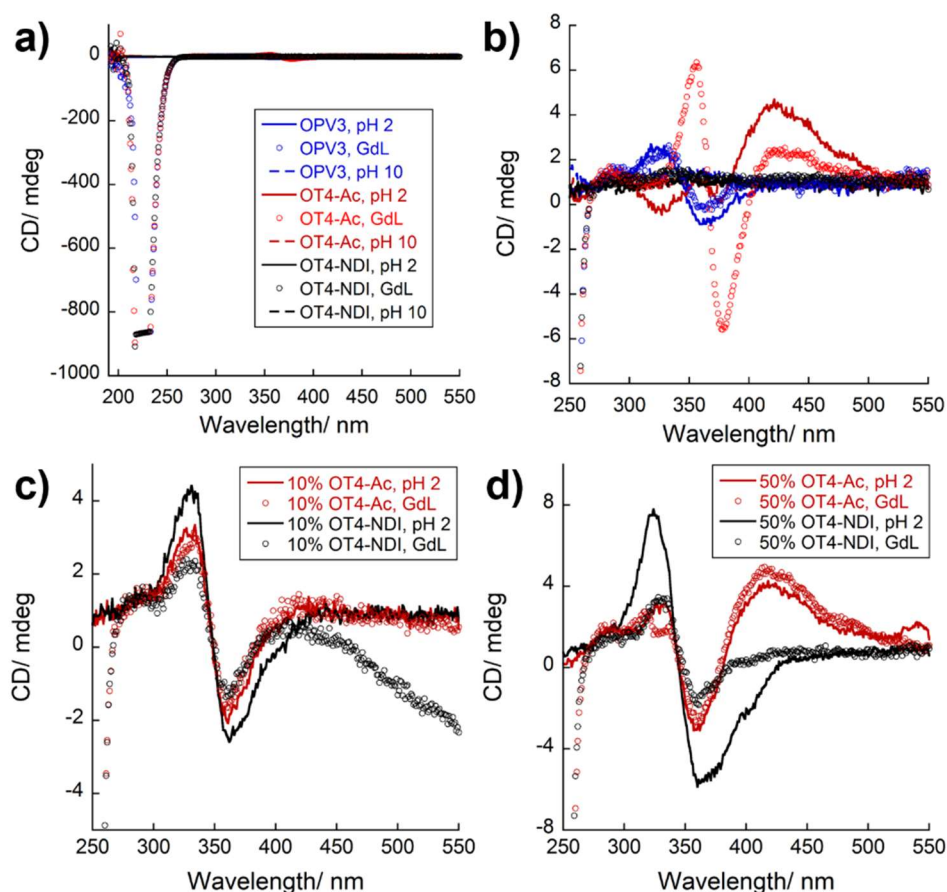


Figure A4.26. Circular dichroism spectra for GdL- (10 mg/mL) and HCl- assembled peptide structures with a,b) one-component/ homo-assemblies, [peptide]= 3 μ M; c) 10 mol% and d) 50 mol% **OT4-Ac** and **OT4-NDI** in **OPV3**, [OPV3]= 3 μ M.

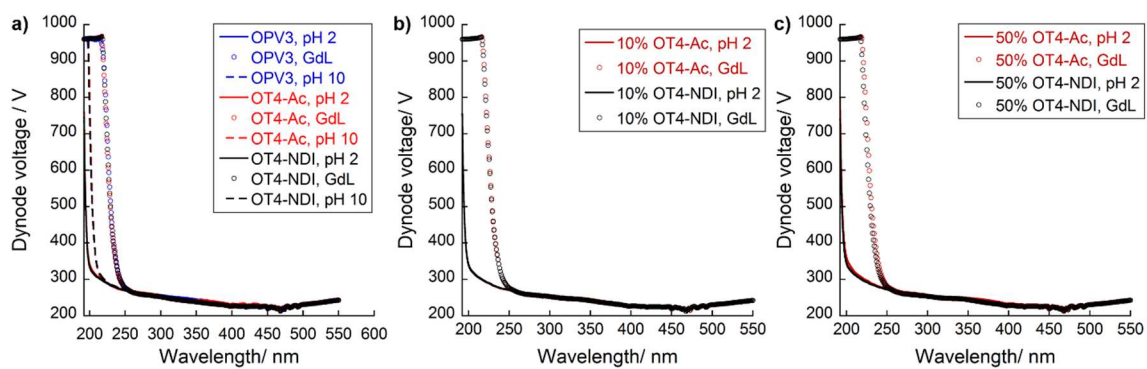


Figure A4.27. Dynode voltage vs. wavelength plots for the CD spectra in Figure A4.26; GdL- (10 mg/mL) and HCl- assembled peptide structures with a,b) one-component/ homo-assemblies; c) 10 mol% and d) 50 mol% **OT4-Ac** and **OT4-NDI** in **OPV3**; [OPV3]= 3 μ M.

Chapter 5

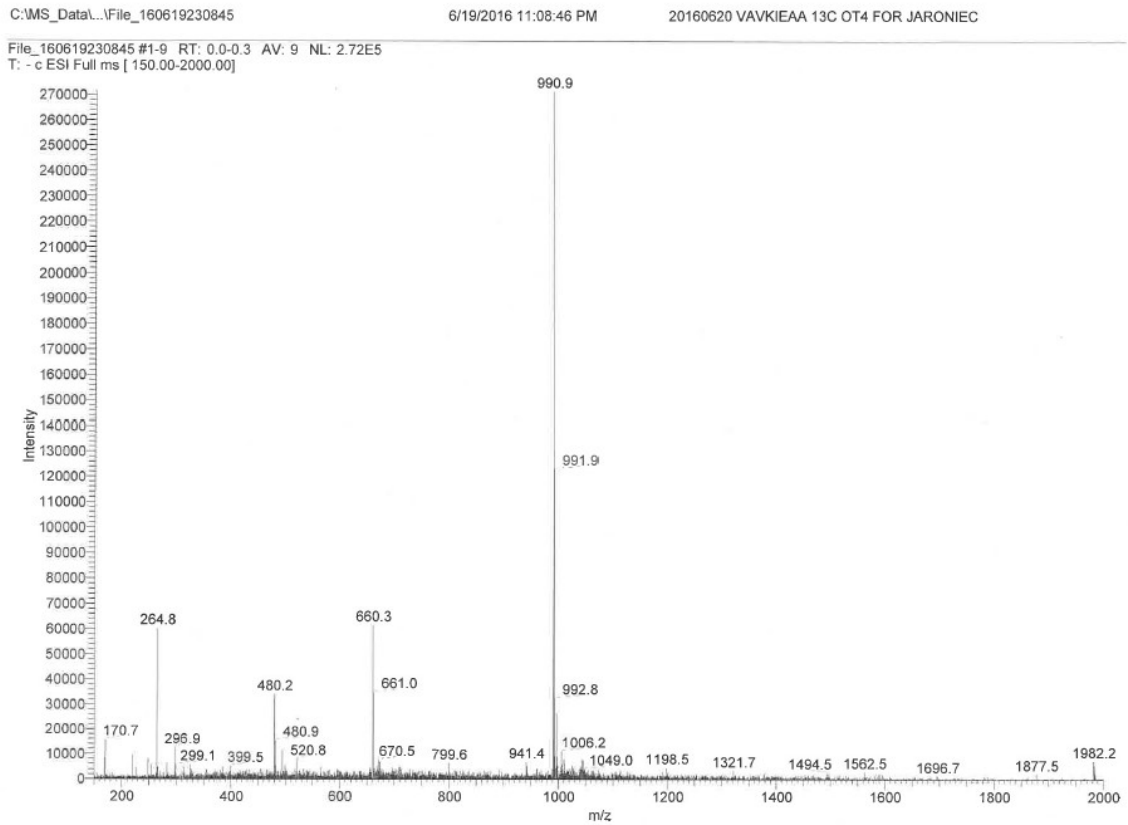


Figure A5.1. ESI-MS spectrum of HO-(A1-¹³C-VAVKIEAA)₂-OT4.

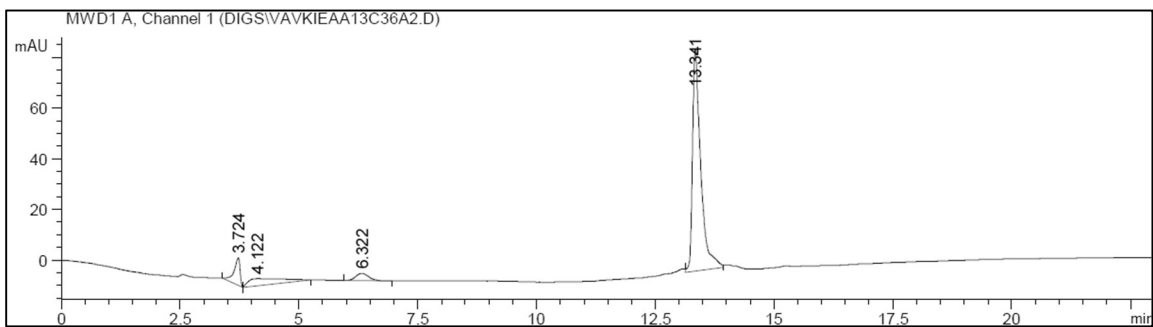


Figure A5.2. Analytical HPLC trace of HO-(A1-¹³C-VAVKIEAA)₂-OT4, monitoring at 400 nm.

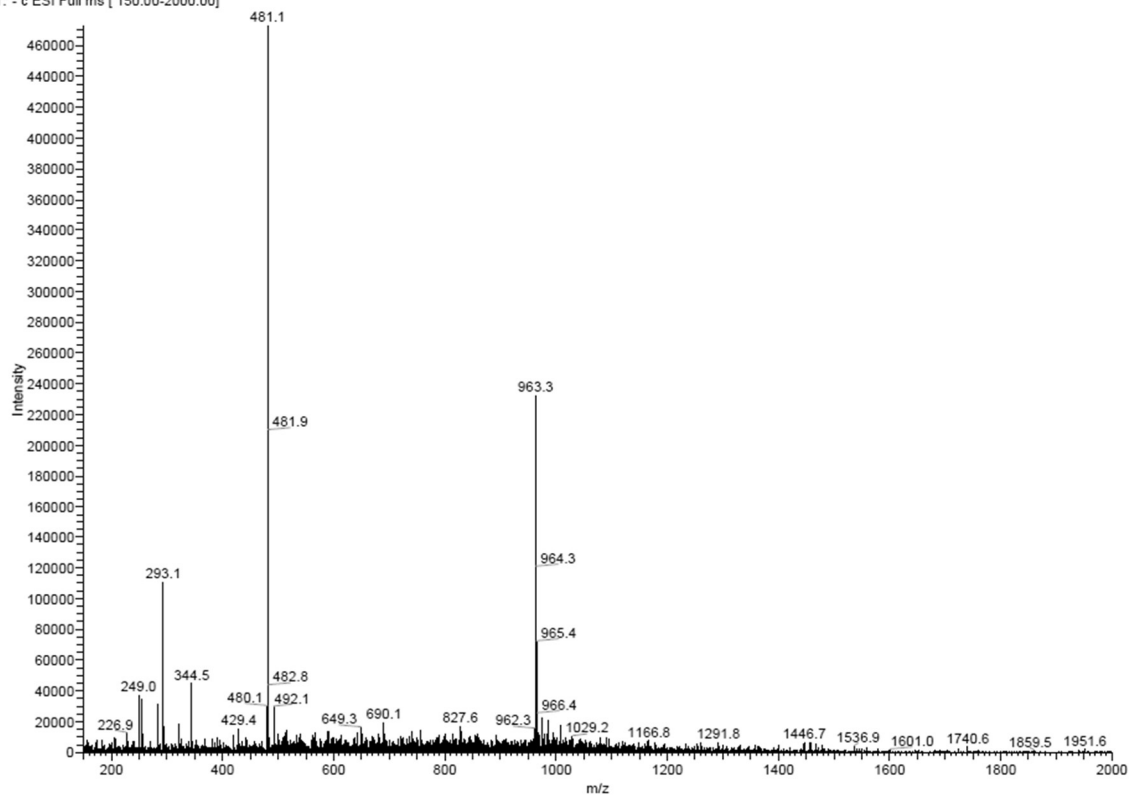
MeOH after_151107164957 #1-30 RT: 0.0-1.1 AV: 30 NL: 4.73E5
T: -c ESI Full ms [150.00-2000.00]

Figure A5.3. ESI-MS spectrum of HO-(A1-¹³C-A2-¹⁵N-EAA)₂-OT4.

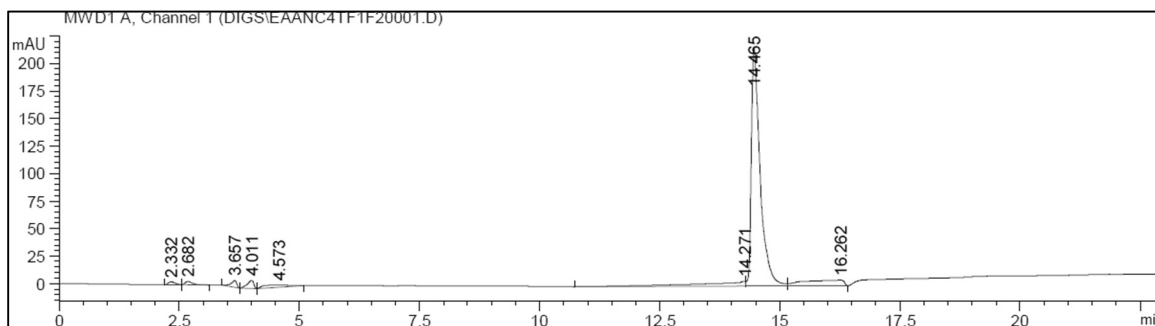


Figure A5.4. Analytical HPLC trace of HO-(A1-¹³C-A2-¹⁵N-EAA)₂-OT4, monitoring at 400 nm.

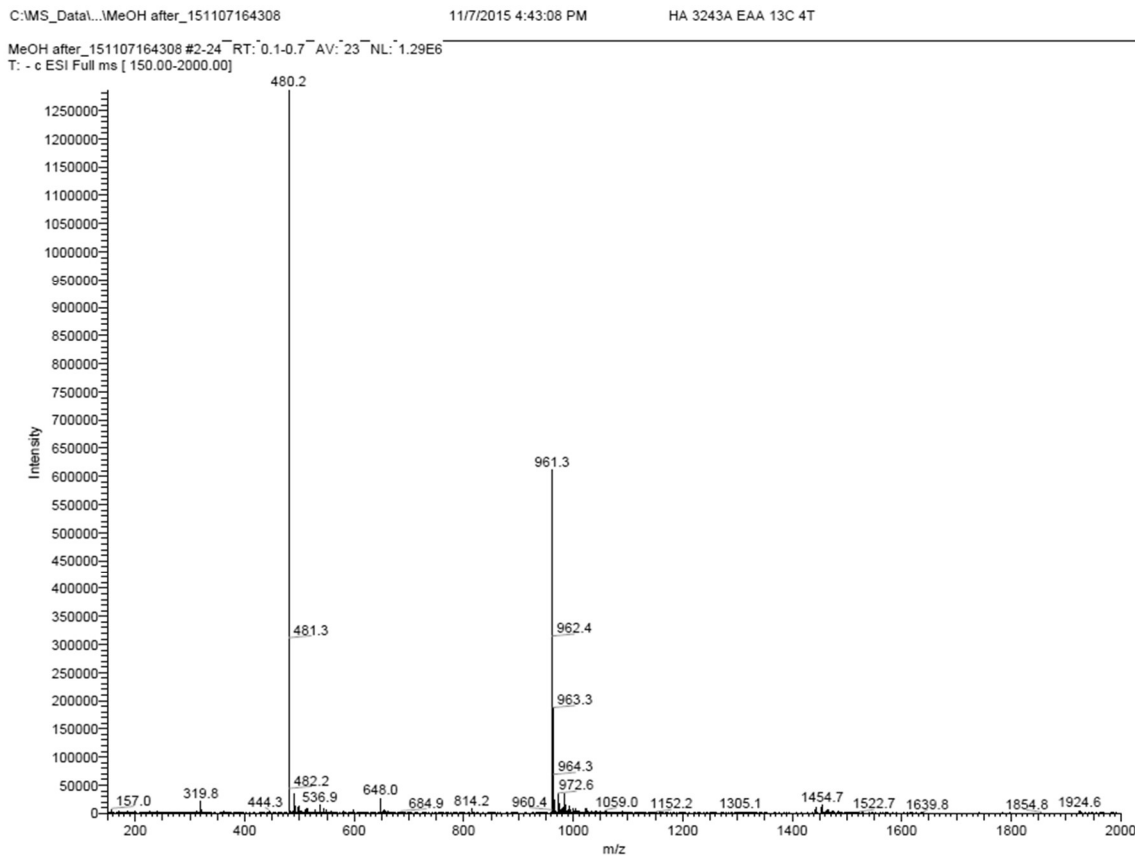


Figure A5.5. ESI-MS spectrum of HO-(A1-¹³C-EAA)₂-OT4.

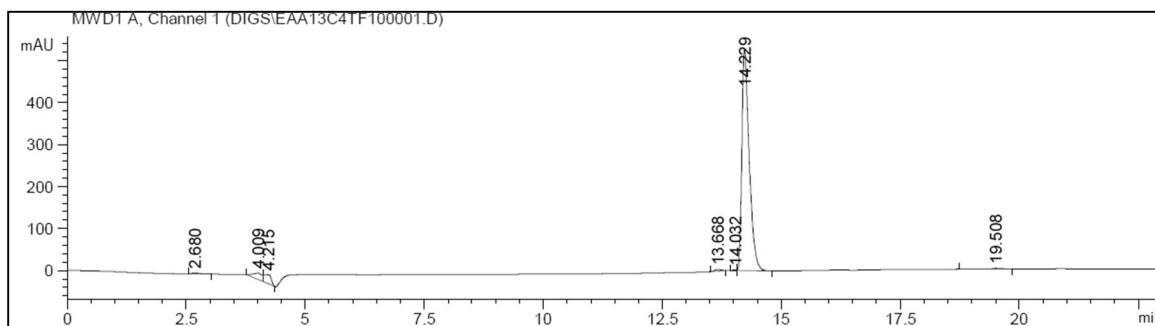


Figure A5.6. Analytical HPLC trace of HO-(A1-¹³C-EAA)₂-OT4, monitoring at 400 nm.

MeOH after_151107164742 #1-29 RT: 0.0-1.1 AV: 29 NL: 5.58E5
T: - c ESI Full ms [150.00-2000.00]

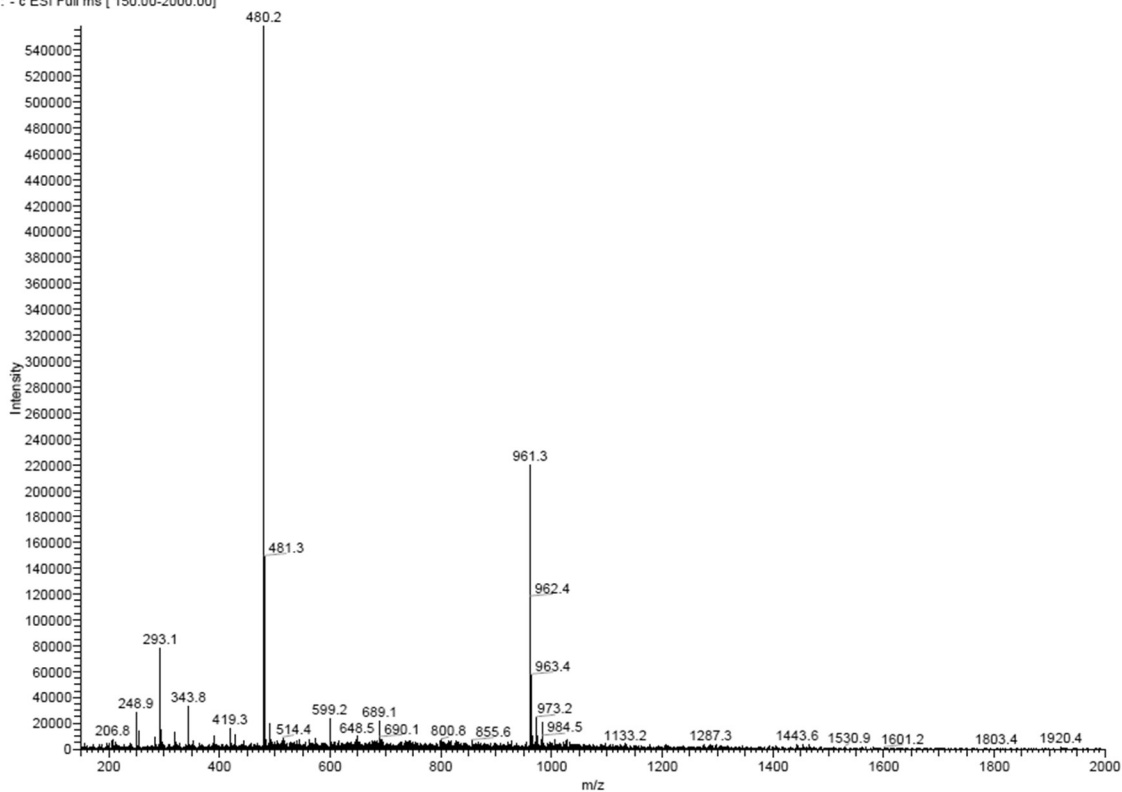


Figure A5.7. ESI-MS spectrum of HO-(A2-¹⁵N-EAA)₂-OT4.

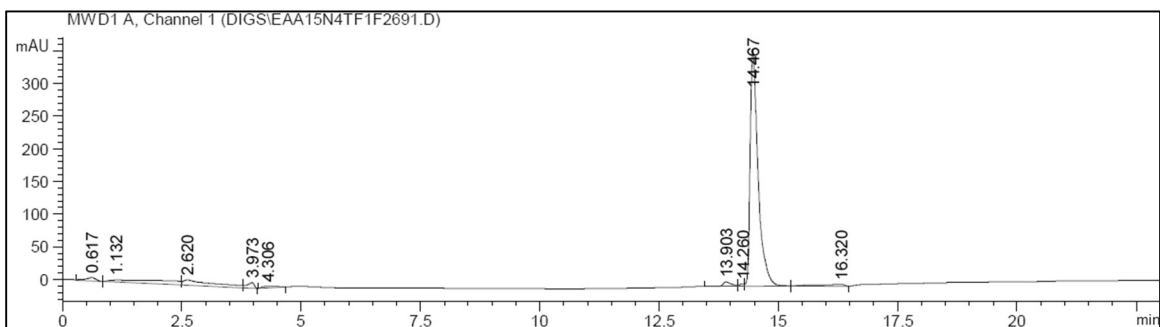


Figure A5.8. Analytical HPLC trace of HO-(A2-¹⁵N-EAA)₂-OT4, monitoring at 400 nm.

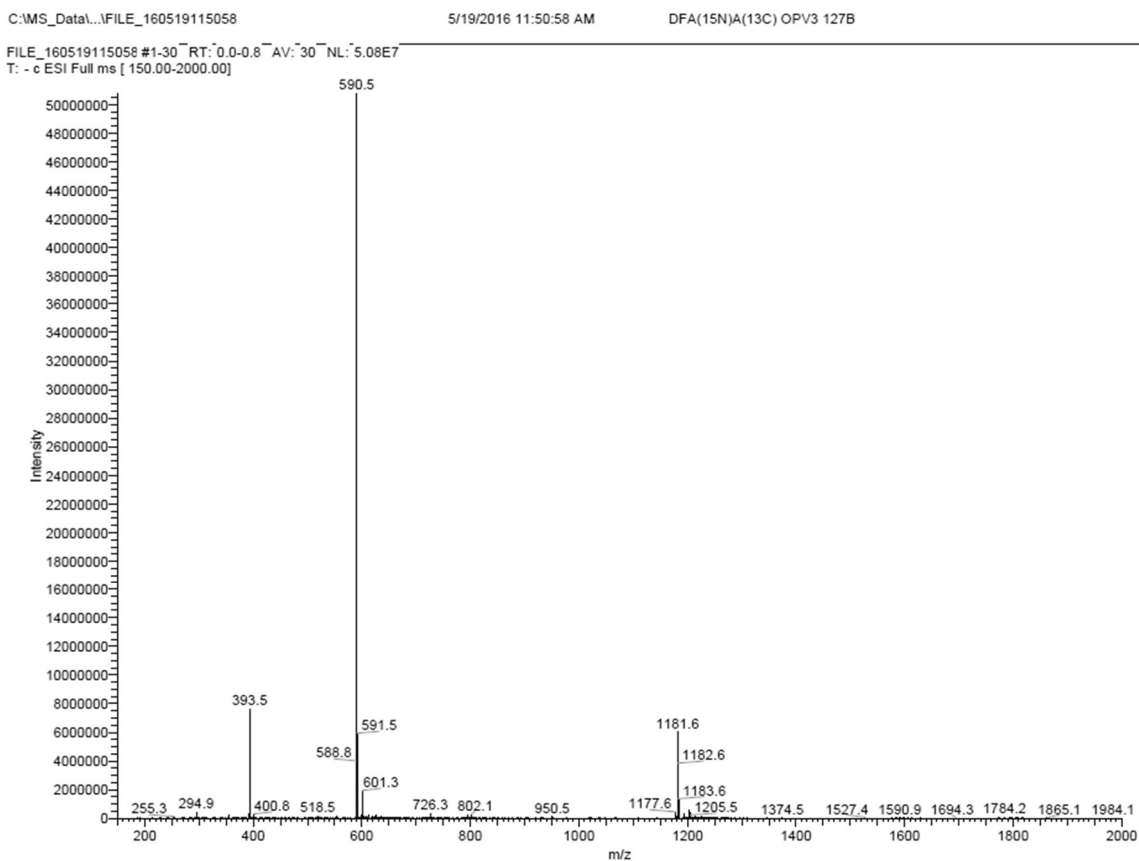


Figure A5.9. ESI-MS spectrum of HO-(A1-¹³C-A2-¹⁵N-DFAA)₂-OPV3.

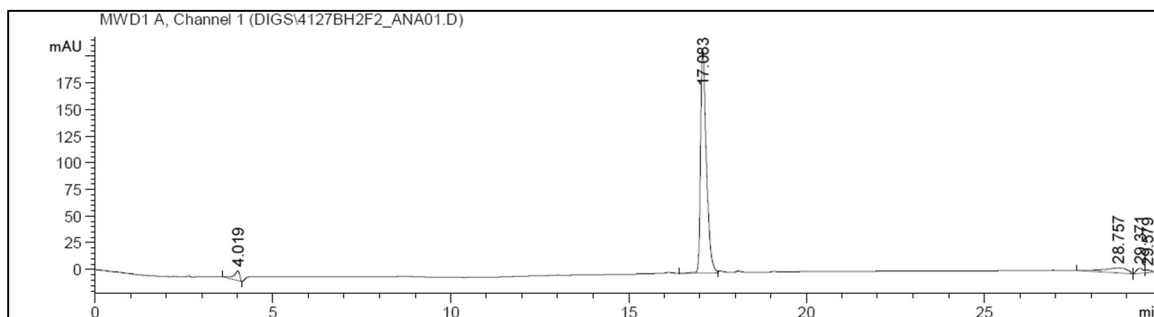


Figure A5.10. Analytical HPLC trace of HO-(A1-¹³C-A2-¹⁵N-DFAA)₂-OPV3, monitoring at 365 nm.

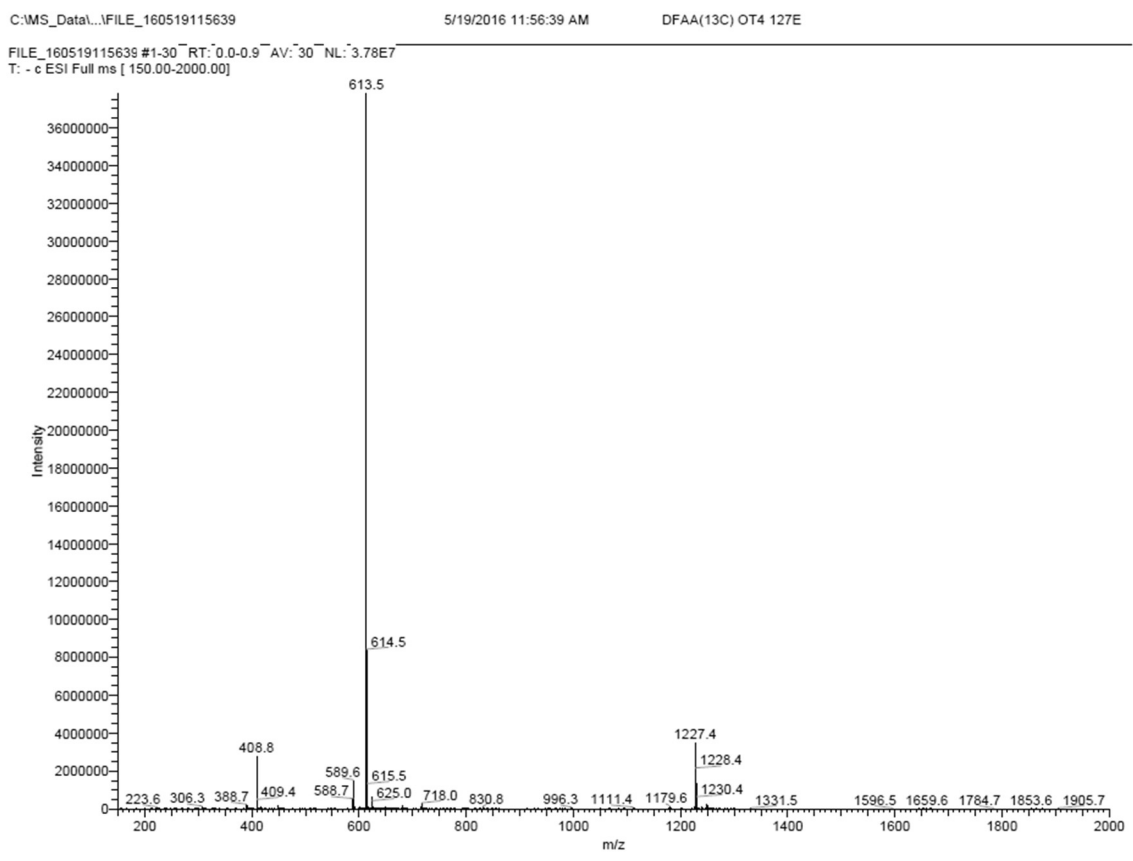


Figure A5.11. ESI-MS spectrum of HO-(A1-¹³C-DFAA)₂-OT4.

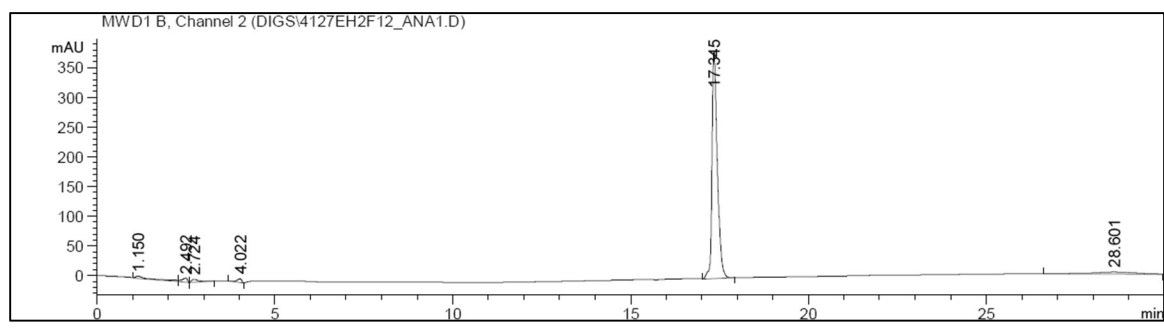


Figure A5.12. Analytical HPLC trace of HO-(A1-¹³C-DFAA)₂-OT4, monitoring at 400 nm.

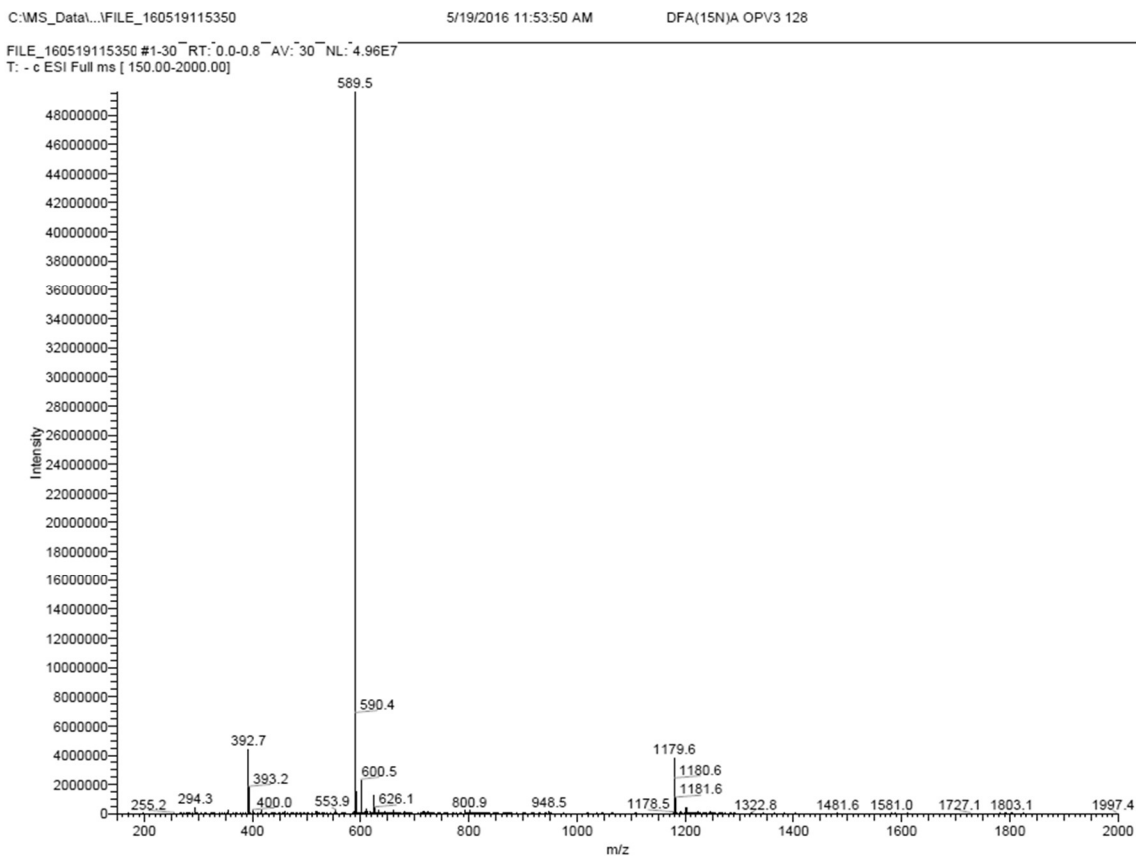


Figure A5.13. ESI-MS spectrum of HO-(A2-¹⁵N-DFAA)₂-OPV3.

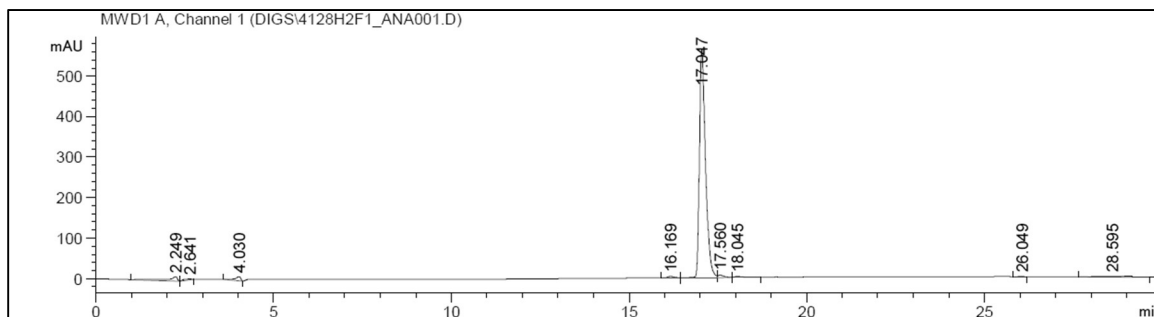


Figure A5.14. Analytical HPLC trace of HO-(A2-¹⁵N-DFAA)₂-OPV3, monitoring at 365 nm.

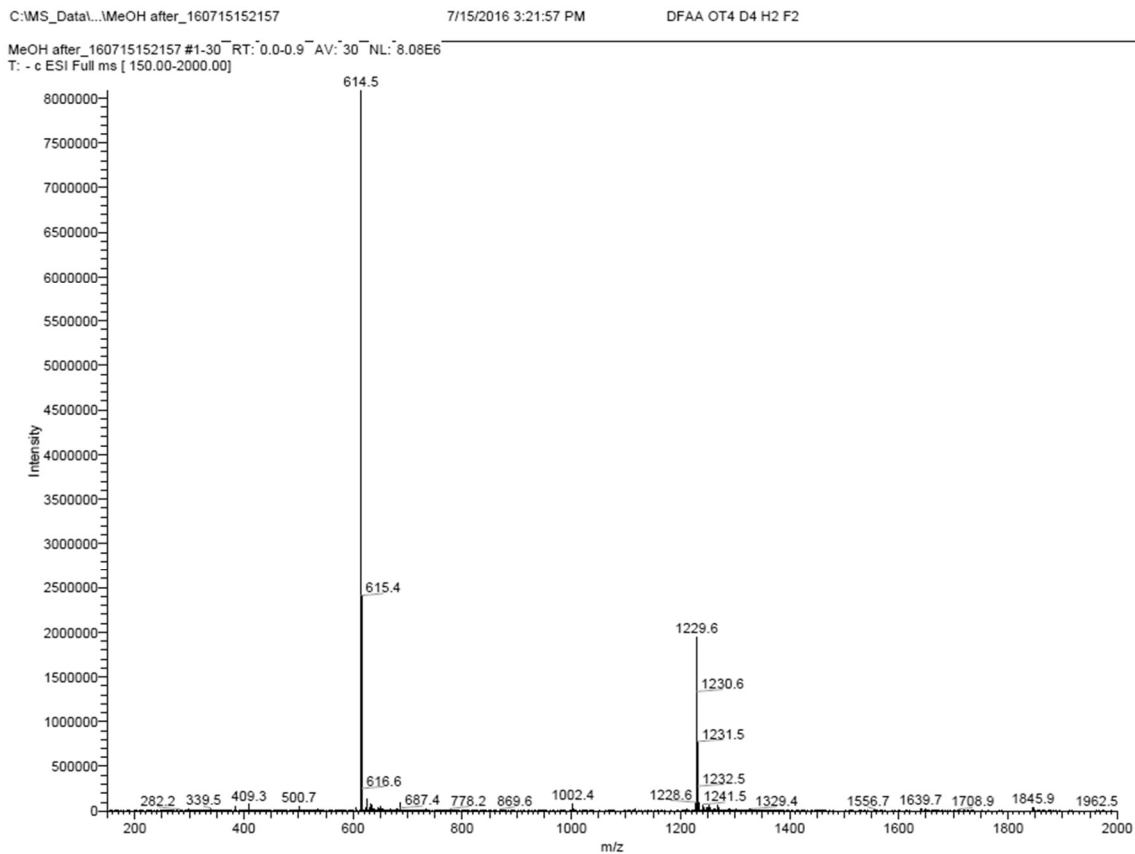


Figure A5.15. ESI-MS spectrum of HO-(DFAA-d₄)₂-OT4.

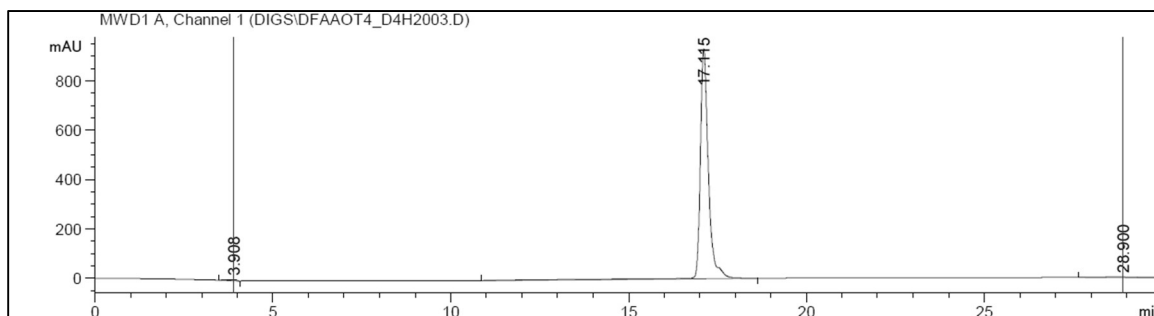


Figure A5.16. Analytical HPLC trace of HO-(DFAA-d₄)₂-OT4, monitoring at 400 nm.

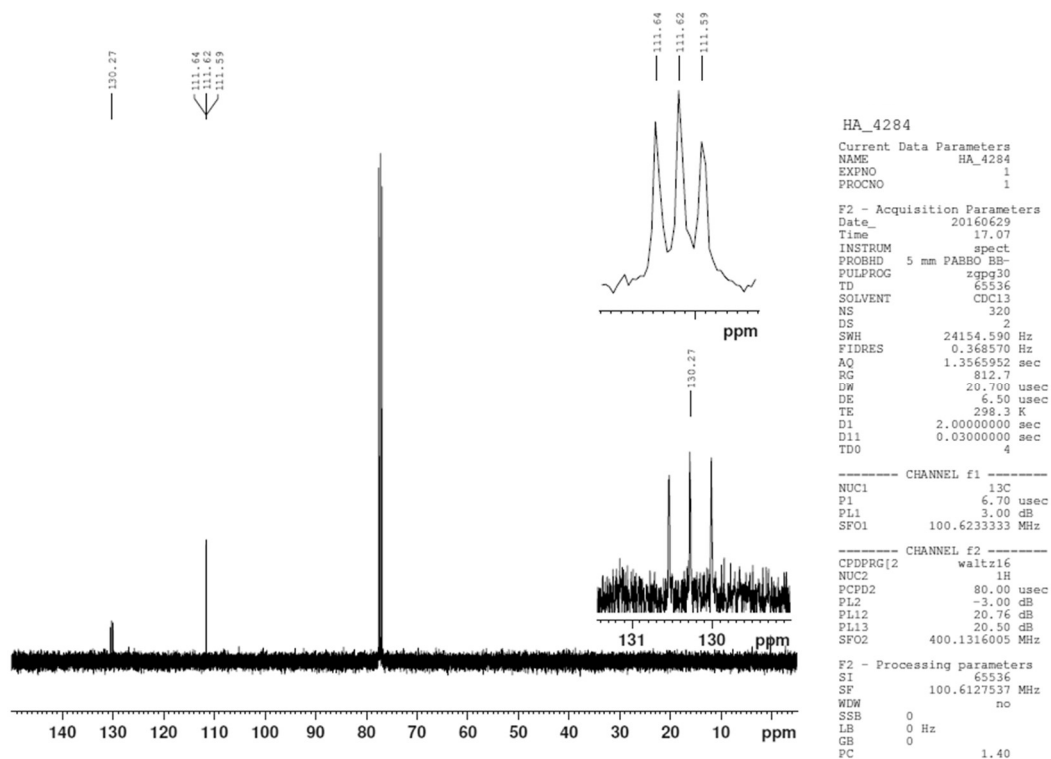


Figure A5.17. ^{13}C (400 MHz, CDCl_3) NMR spectrum of 2,5-dibromothiophene (d_2).

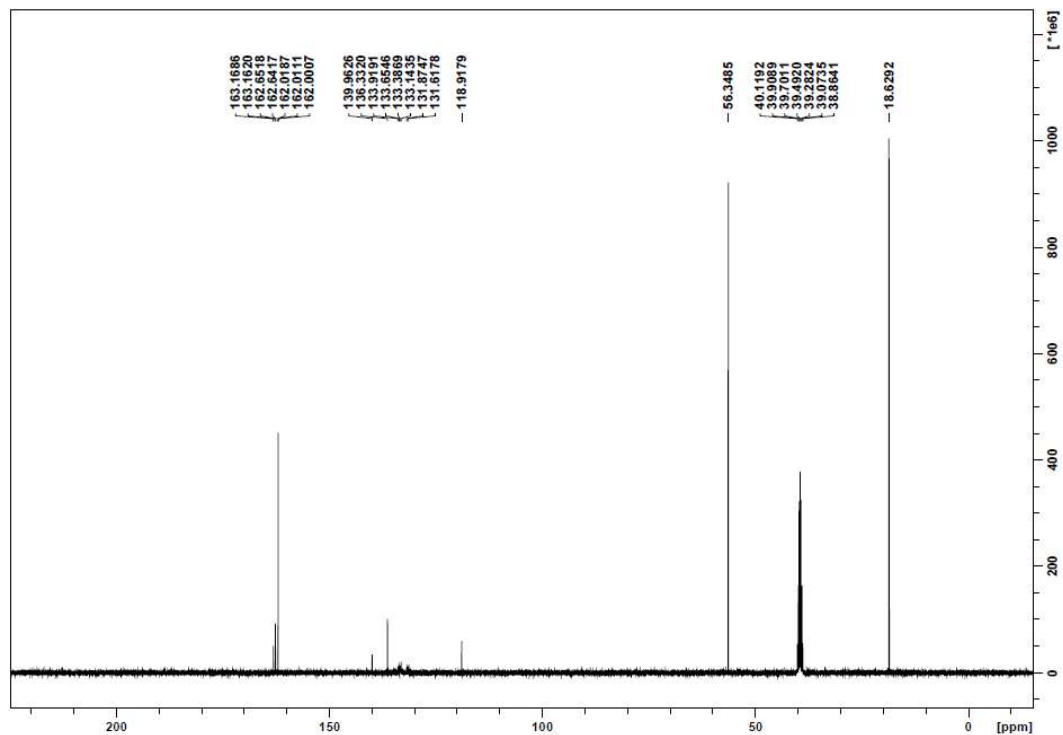


Figure A5.18. ^{13}C (400 MHz, d_6 -DMSO) NMR spectrum of 5-bromothiophene-2-carboxylic acid (d_2); peaks at 56 and 19 ppm are from tetrahydrofuran.

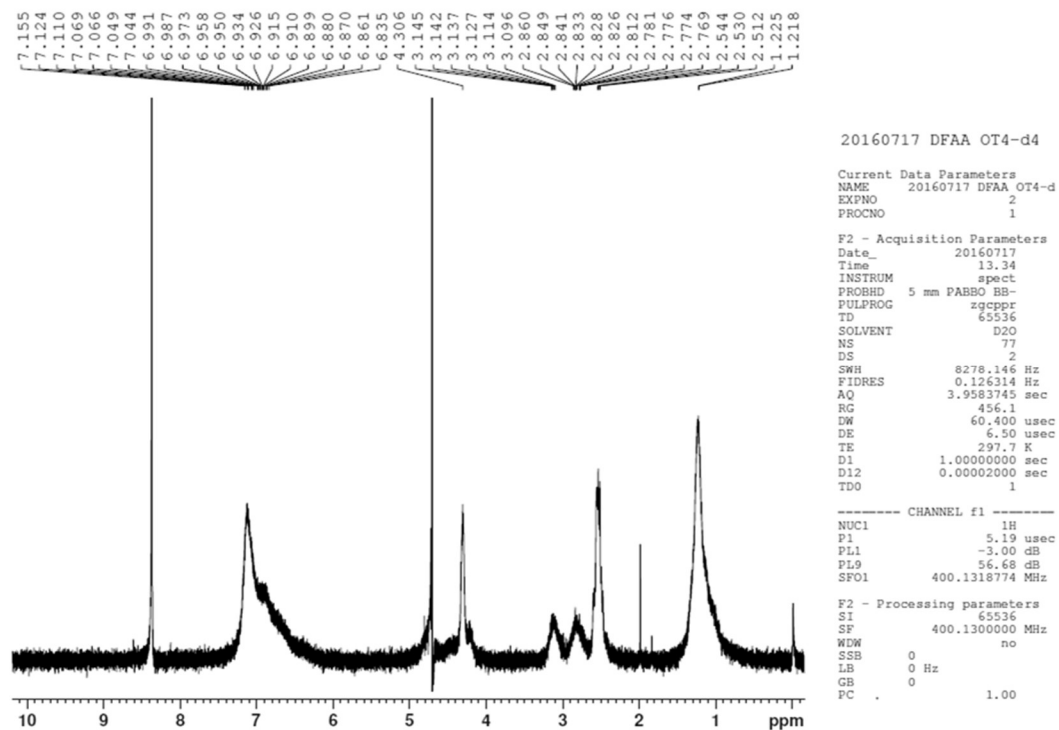


Figure A5.19. ^1H (400 MHz, D_2O) NMR spectrum of DFAA-OT4 (d4) peptide.

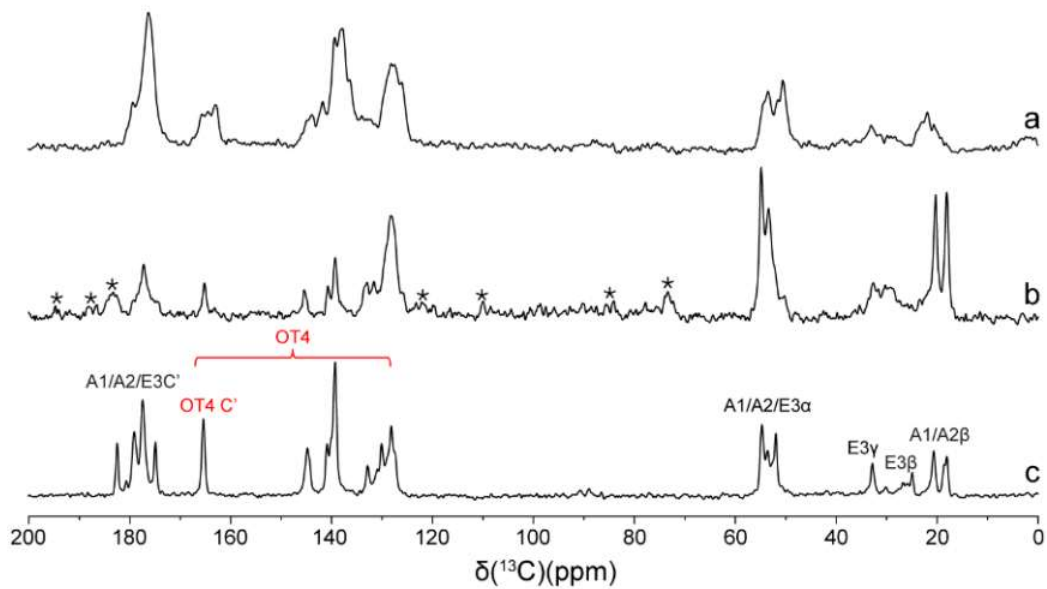


Figure A5.20. 1-D ^{13}C cross polarization spectra of N. A. EAA-OT4. (a) N. A. EAA-OT4 on 500 MHz spectrometer; (b) N. A. EAA-OT4 on 800 MHz spectrometer.; (c) A2- ^{15}N -EAA-OT4 on 500 MHz spectrometer; Integrals in (a): 6.2 (183.0-170.0 ppm), 2.0 (170.0-160.0 ppm), 14.8 (146.5-118.0 ppm), 5.6 (58.5-43.0 ppm), 8.0 (35.0-14.0 ppm).

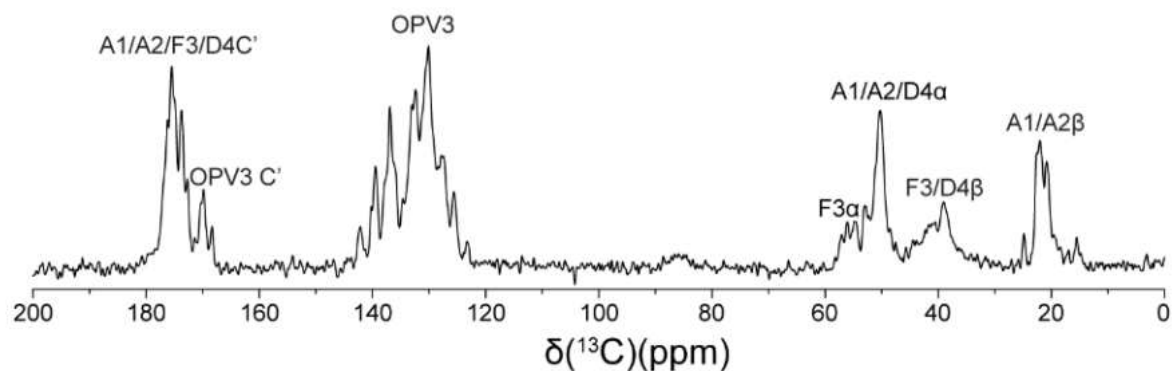


Figure A5.21. 1-D ^{13}C cross polarization of N.A. DFAA-OPV3. Integrals: 10.0 (182.0-167.0 ppm), 20.4 (144.0-122.0 ppm), and 16.2 (60.0-14.0 ppm).

Table A5.1. List peaks in the NCO spectrum of A1- ^{13}C -A2- ^{15}N -EAA-OT4.

$\delta(^{13}\text{C})$, ppm	$\delta(^{15}\text{N})$, ppm	$\Delta\delta(^{13}\text{C})$, ppm*	Ratio, %
175.6	116.9	-2.2	23.9
175.1	114.7	-2.7	40.8
175.9	121.2	-1.9	12.8
176.2	122.9	-1.6	14.5
174.0	122.1	-3.8	8.0

*Secondary chemical shifts as compared to a random coil structure.

Table A5.2. List peaks in the NCO spectrum of A1- ^{13}C -A2- ^{15}N -DFAA-OPV3.

$\delta(^{13}\text{C})$, ppm	$\delta(^{15}\text{N})$, ppm	$\Delta\delta(^{13}\text{C})$, ppm*	Ratio, %
175.8	126.8	-2.0	9.2
175.1	126.0	-2.7	22.8
174.1	125.1	-3.7	19.5
175.7	119.8	-2.1	16.9
174.1	119.5	-3.7	16.7
173.7	117.3	-4.1	14.8

*Secondary chemical shifts as compared to a random coil structure.



Figure A5.22. Mapping of DRAWS signal contribution. Red: ^{13}C nucleus; Gray: ^{12}C nucleus. Considering three neighboring carbon nuclei in a row, if the middle one is ^{13}C , the two peripheral ones can be both ^{13}C (case *a*, 25% probability), one ^{13}C and one ^{12}C (cases *b* and *c*, 25% probability each), or both ^{12}C (case *d*, 25% probability). Considering that ^{13}C - ^{13}C interaction should occur, only case *d* doesn't contribute to the DRAWS signal.

Table A5.3. Nominal and actual* ratios for EAA-OT4 control samples.

Sample Components	Nominal Ratio	Actual Ratio	DQE**, if fully mixed
A1- ^{13}C -EAA-OT4:A2- ^{15}N -EAA-OT4	50:50	44:56	68%
A1- ^{13}C -A2- ^{15}N -EAA-OT4: N. A. ** EAA-OT4	15:85	14:86	26%

*Estimated from 1-D $^{13}\text{C}/^{15}\text{N}$ cross polarization integrals; **calculated double quantum efficiency (DQE).

Table A5.4. Nominal and actual* ratios for the mixed samples.

Sample Components	Nominal Ratio	Actual Ratio	DQE**, if fully mixed
A2- ^{15}N -EAA-OT4: A1- ^{13}C -VAVKIEAA-OT4	75:25	71:29	50%
	85:15	83:17	32%
	90:10	88:12	22%
A2- ^{15}N -DFAA-OPV3: A1- ^{13}C -DFAA-OT4	75:25	77:23	41%
	90:10	91:9	18%

*Estimated from 1-D $^{13}\text{C}/^{15}\text{N}$ cross polarization integrals; **calculated double quantum efficiency (DQE).

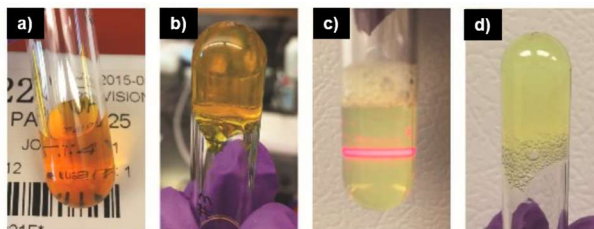


Figure A5.23. Representative images of 1 wt% peptide solutions and hydrogels. (a) EAA-OT4 in basic solution; (b) self-supporting EAA-OT4 hydrogel after HCl addition; (c) DFAA-OPV3 in basic solution; and (d) self-supporting DFAA-OPV3 hydrogel after HCl addition. Tyndall effect was observed when irradiated with a laser beam, suggesting a colloidal suspension rather than a homogenous solution. Colloidal aggregation in the basic state was not investigated in these studies.

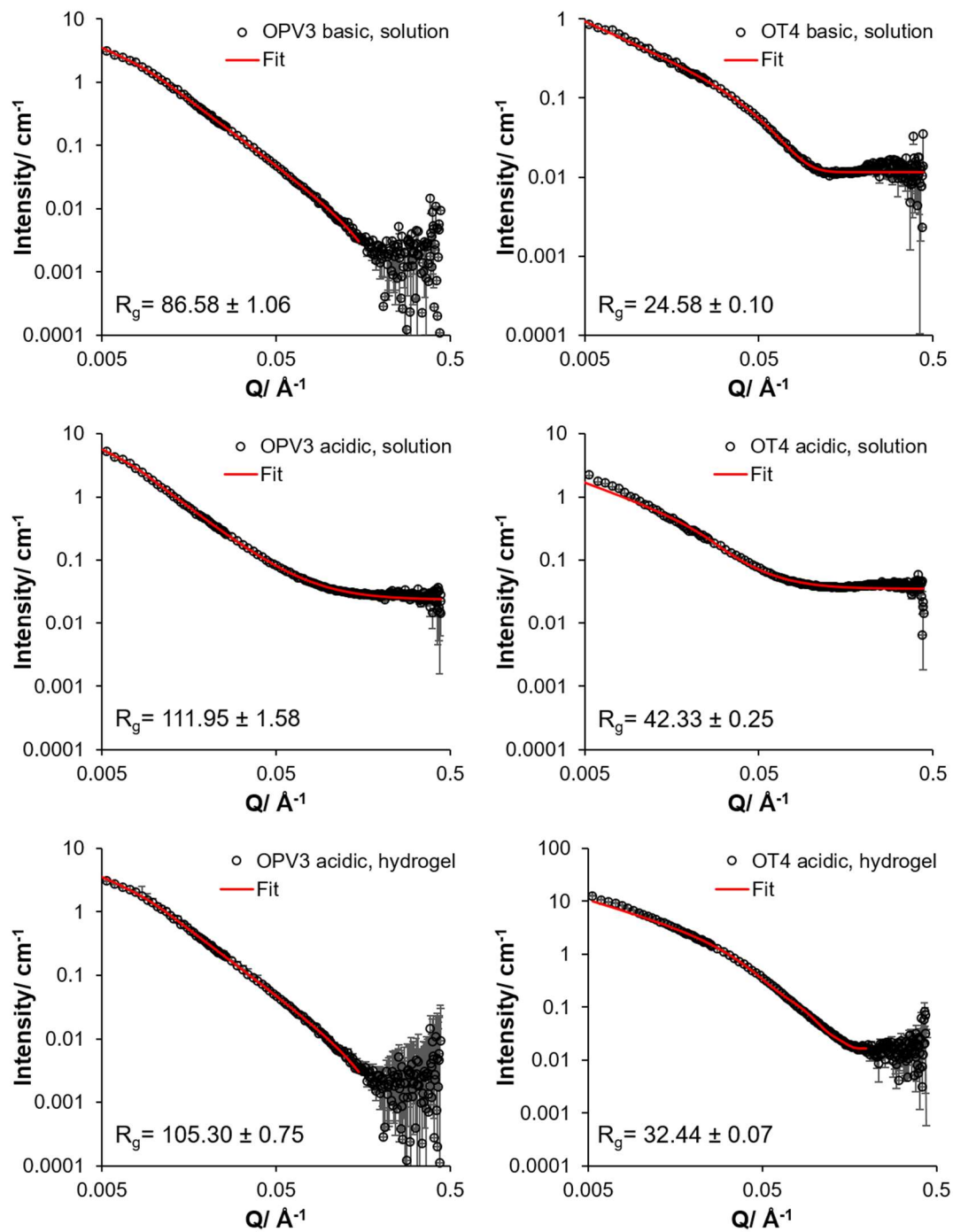


Figure A5.24. SANS curves for DFSA-OPV3 and DFSA-OT4 at 0.2 wt% solutions in D₂O. Data fitting was done with a Guinier-Porod model.

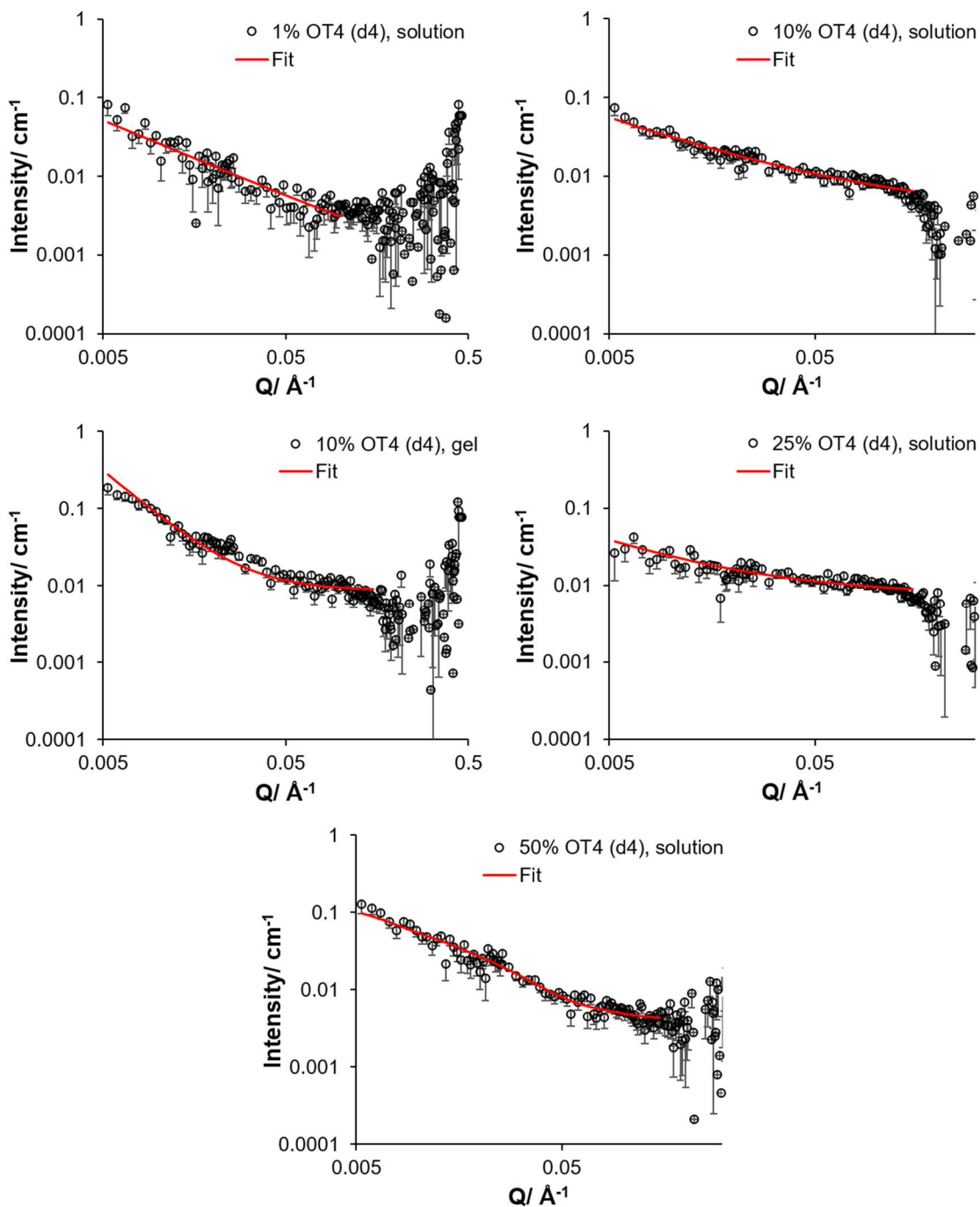


Figure A5.25. SANS curves for mixed DFAA (d₄) OT4 and OPV3 (mol% of OT4 indicated) in 40% D₂O in H₂O. Data fitting was done with a parallelepiped model.

Table A5.5. Calculated parameters from parallelepiped model fits for SANS data for one-component samples; the longest axis dimension was fixed to 4000 Å (*a* and *b* represent the shorter dimensions).

Sample	Relative Scale	<i>a</i> / Å	<i>b</i> / Å
0.2 wt% OPV3, acidic	0.169	29.768 ± 0.33448	417.55 ± 3.5395
0.2 wt% OPV3, basic	0.160	25.045 ± 0.5318	307.93 ± 2.1695
1 wt% OPV3, acidic	1.000	30.388 ± 0.13215	391.73 ± 1.5782
0.2 wt% OT4, acidic	0.093	37.079 ± 0.43734	155.66 ± 0.99828
0.2 wt% OT4, basic	0.090	43.005 ± 0.66499	71.078 ± 0.76818
1 wt% OT4, acidic	0.903	32.687 ± 0.14743	113.21 ± 0.27061

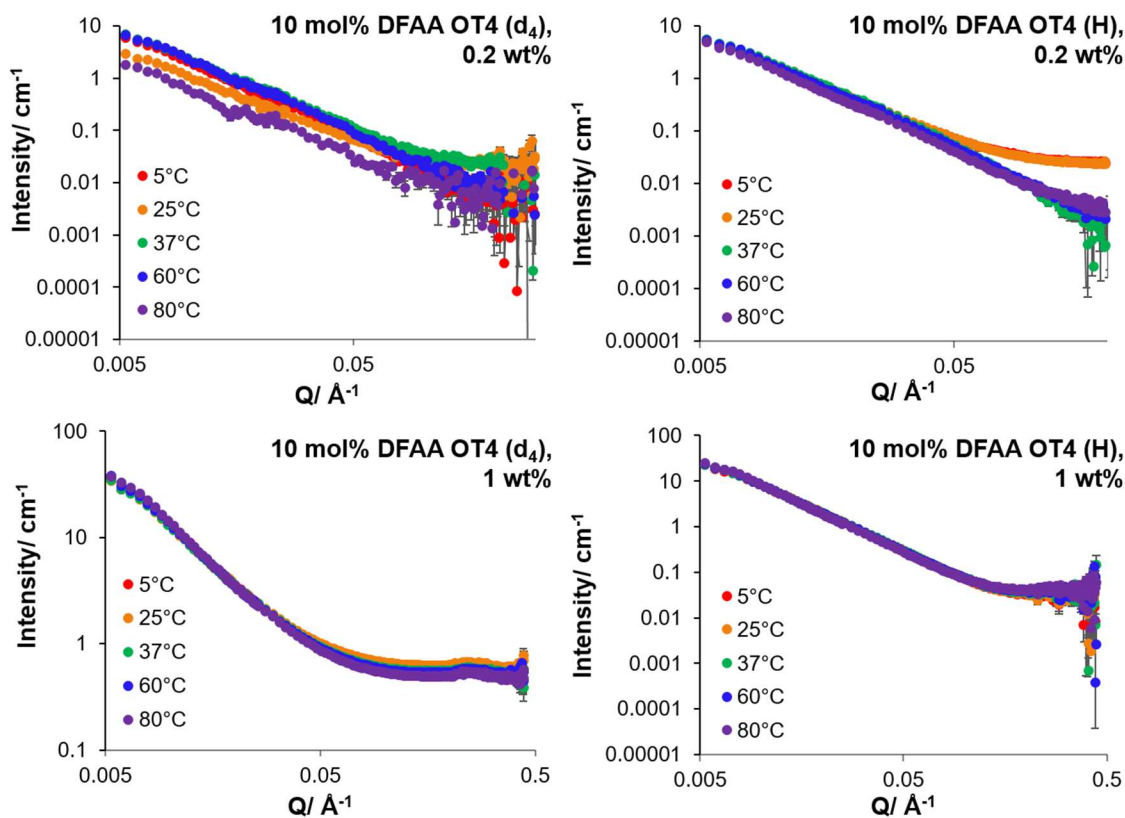


Figure A5.26. SANS curves for 10:90 (DFAA OT4 d₄: DFAA OPV3) at 0.2 wt% and 1 wt%, in different temperatures.

Chapter 6

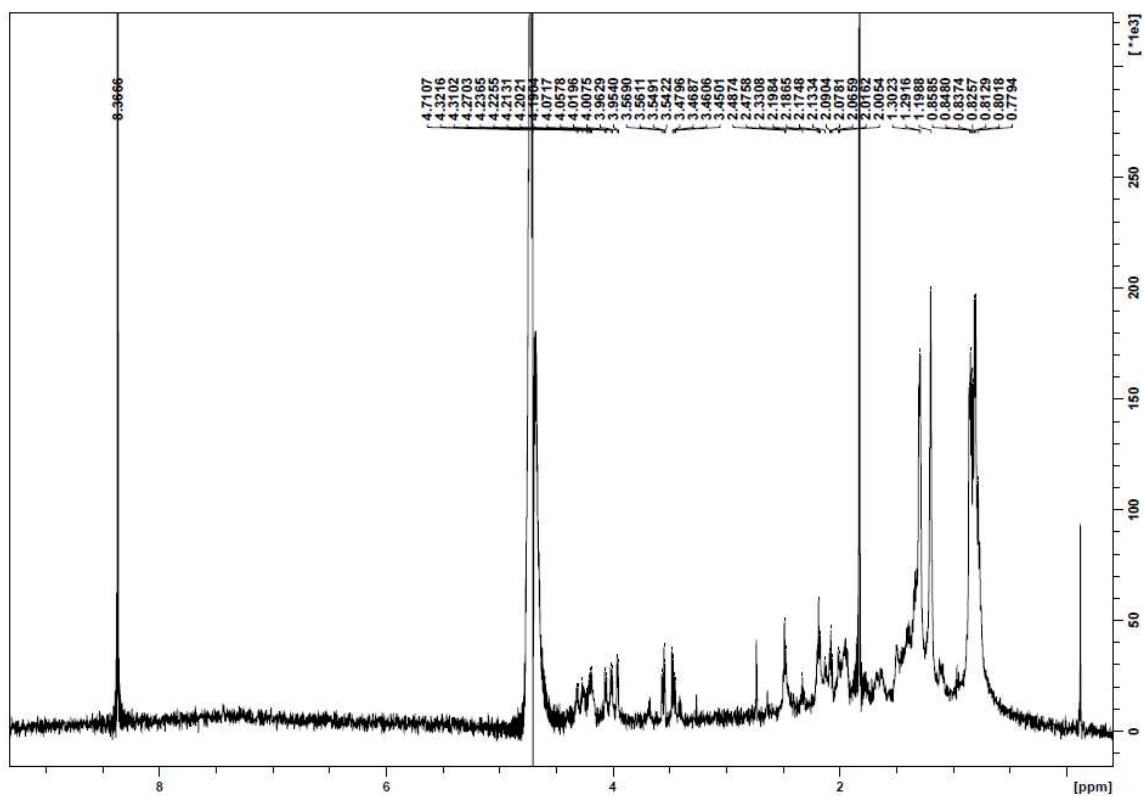


Figure A6.1. ^1H (600 MHz, D_2O) NMR spectrum of VAVKIEAA-OT4 peptide. Peak broadness in the aromatic region can be attributed to the aggregation of the material even at high pH. A presaturation pulse was applied during spectrum acquisition to suppress water.

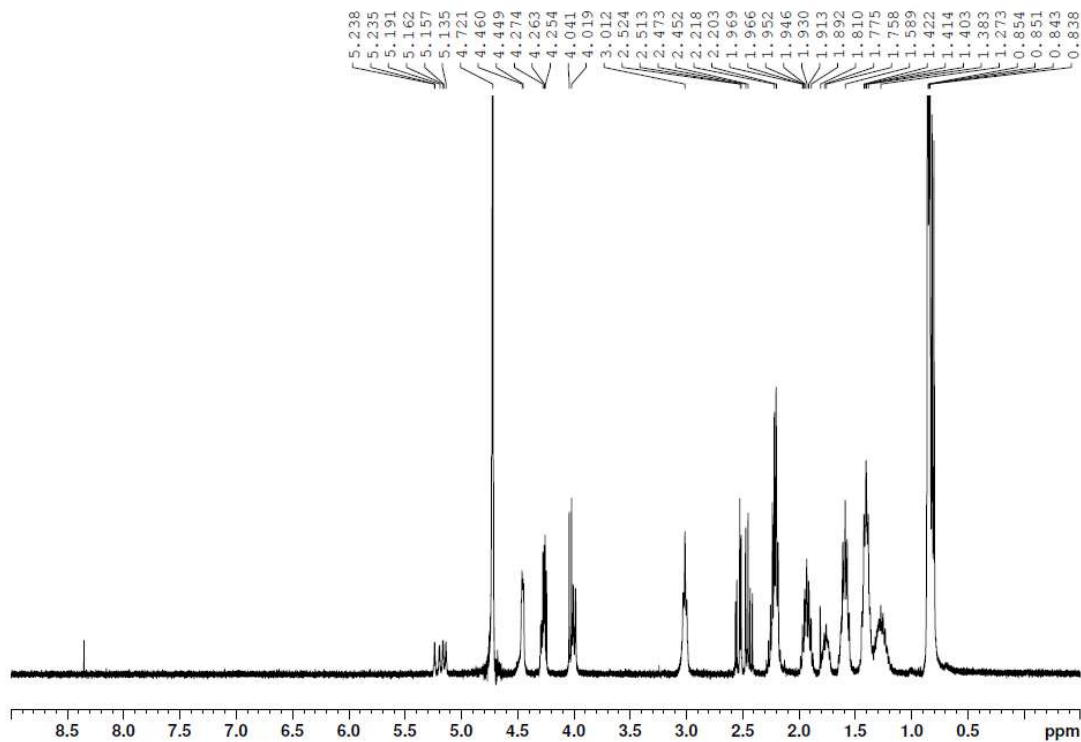


Figure A6.2. ^1H (400 MHz, D_2O) NMR spectrum of DK(Alloc)VV-diacetylene peptide.

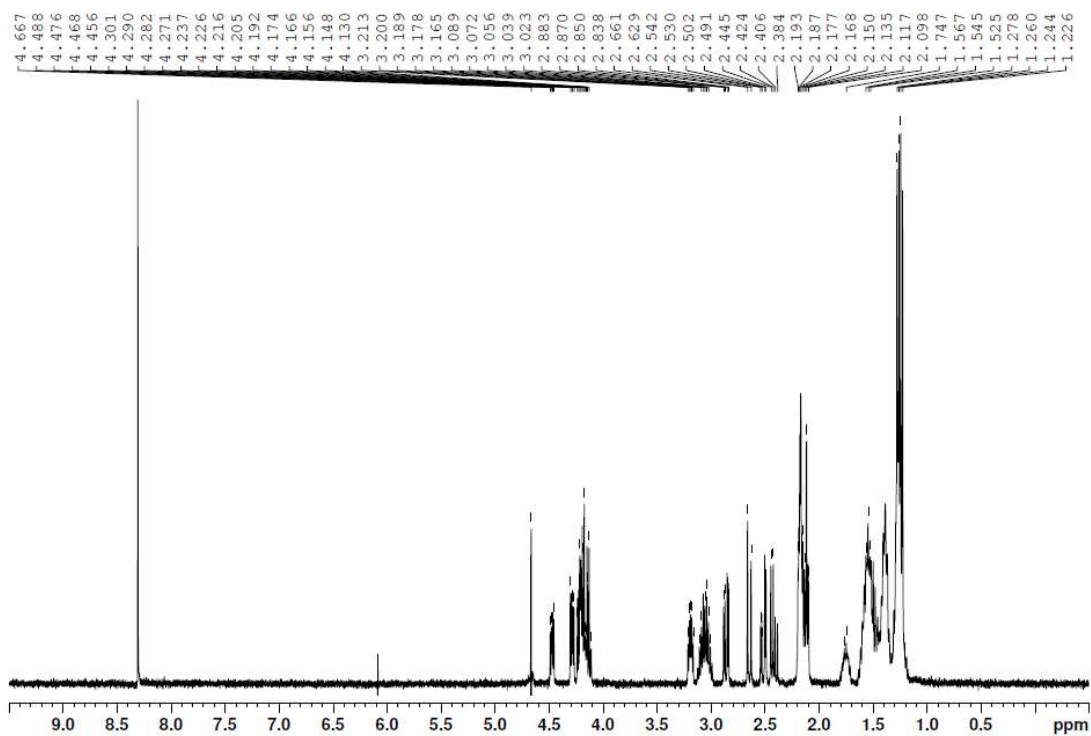


Figure A6.3. ^1H (400 MHz, D_2O) NMR spectrum of DK(biotin)VV-diacetylene peptide.

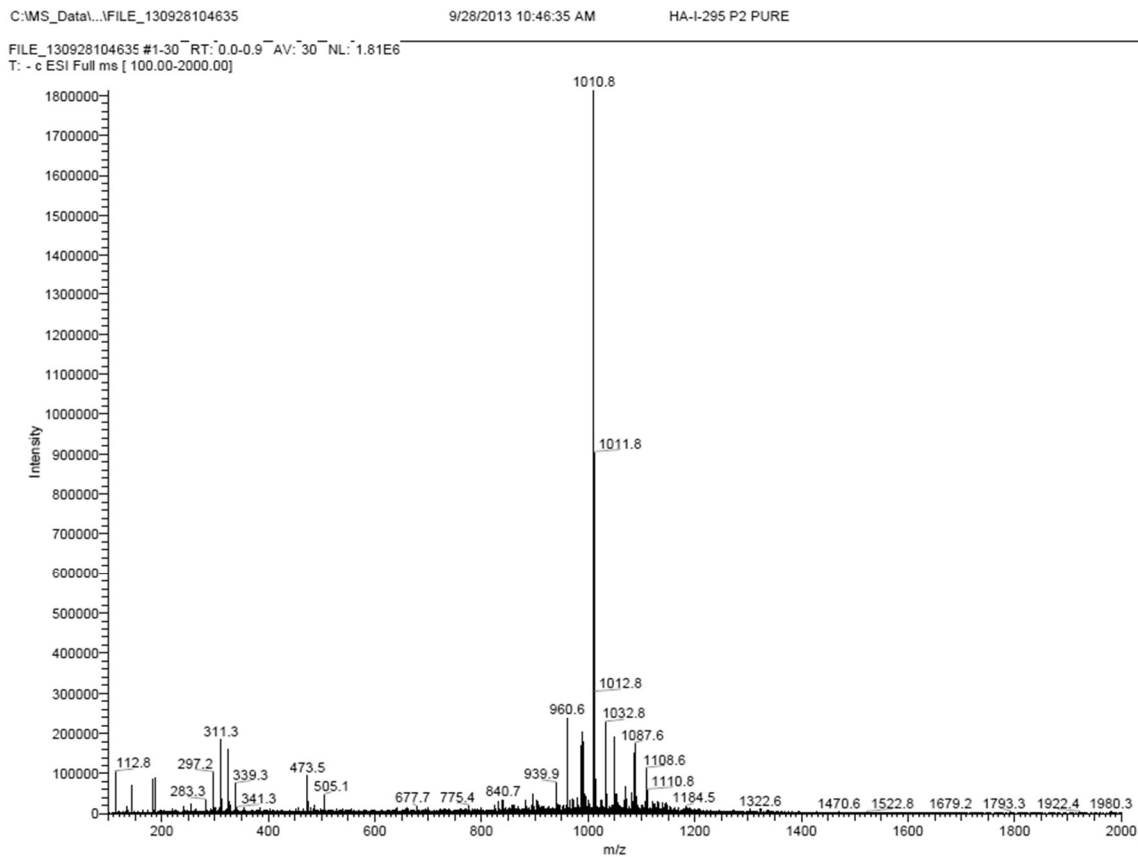


Figure A6.4. ESI-MS spectrum of **HO-(VAVKIEAA)₂-OT4**.

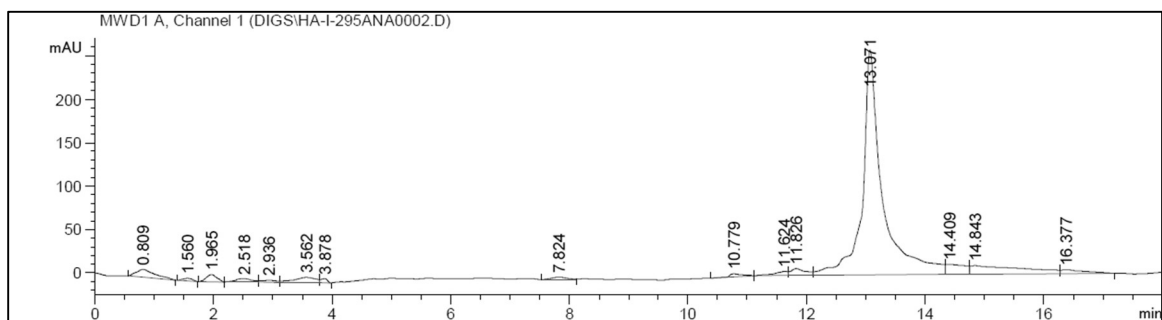


Figure A6.5. Analytical HPLC trace of **HO-(VAVKIEAA)₂-OT4**, monitoring at 400 nm.

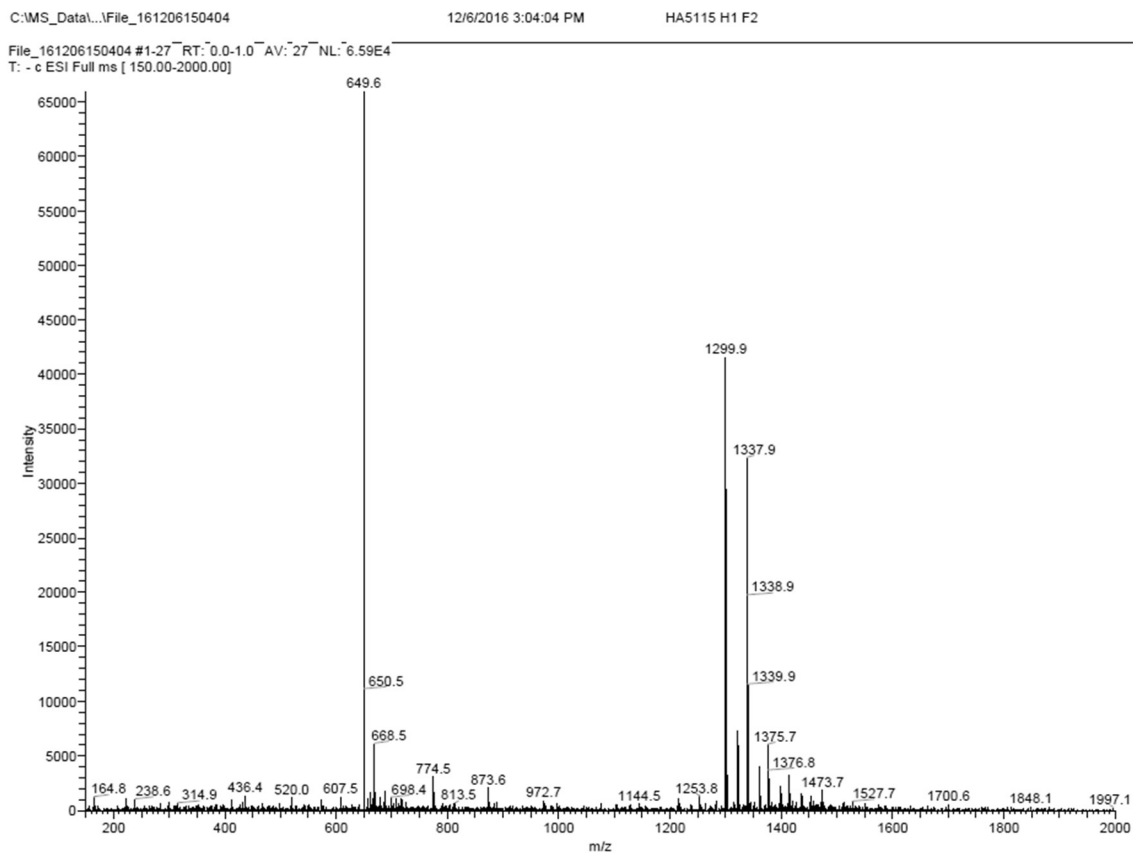


Figure A6.6. ESI-MS spectrum of **HO-(DK(Alloc))₂-diacetylene** peptide.

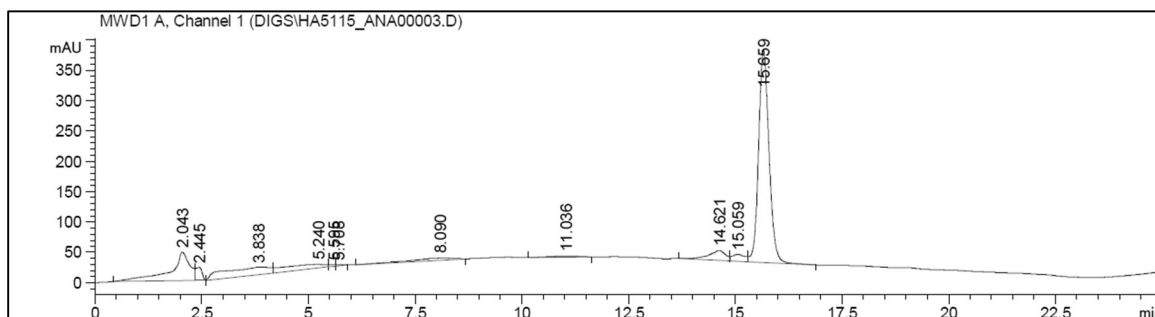


Figure A6.7. Analytical HPLC trace of **HO-(DK(Alloc))₂-diacetylene** peptide, monitoring at 260 nm.

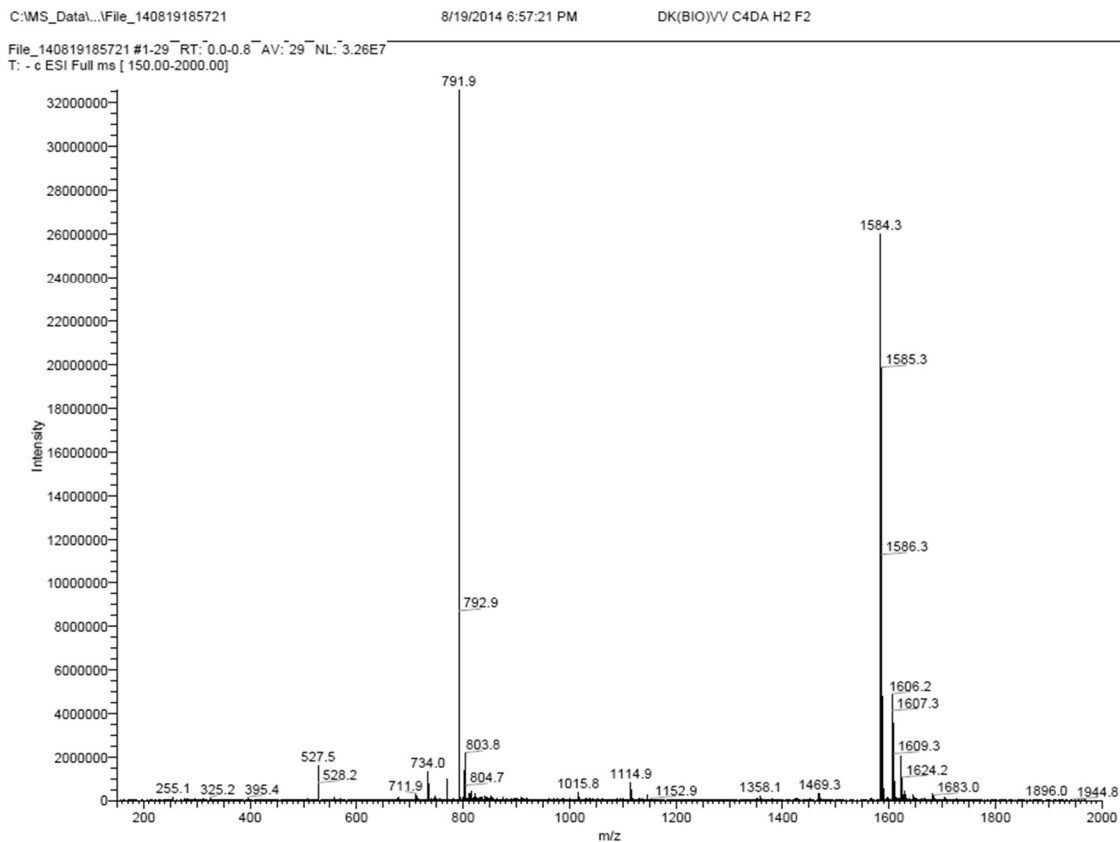


Figure A6.8. ESI-MS spectrum of **HO-(DK(biotin))₂-diacetylene** peptide.

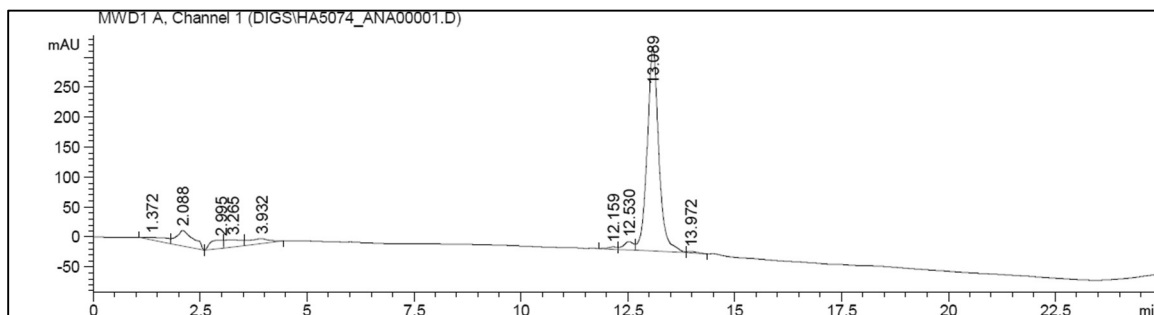


Figure A6.9. Analytical HPLC trace of **HO-(DK(biotin))₂-diacetylene** peptide, monitoring at 260 nm.

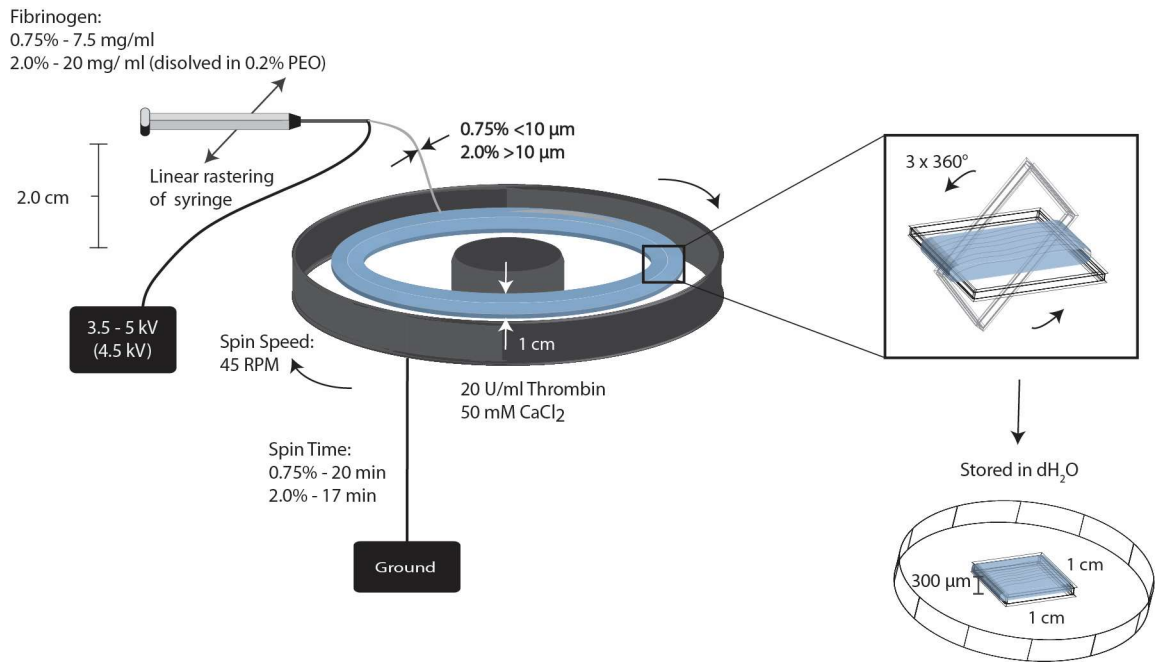


Figure A6.10. Modified electrospinning setup for fiber hydrogel processing. Figure courtesy of Justin Morrissette-McAlmon.

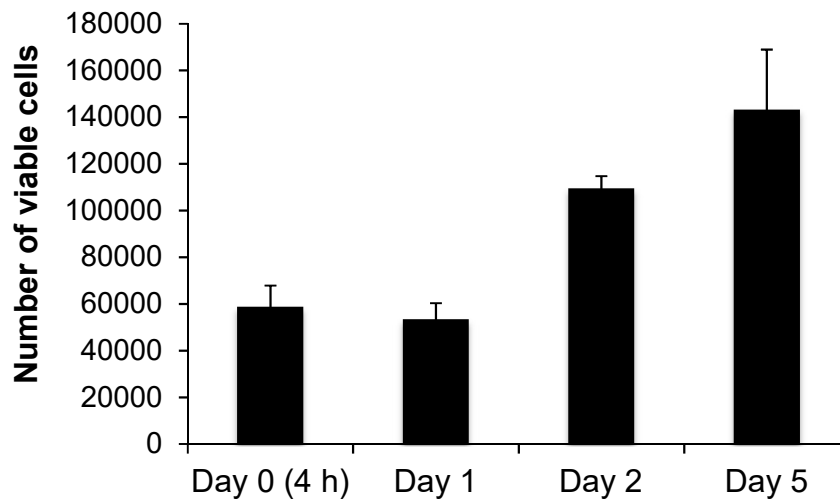


Figure A6.11. WST-1 proliferation assay, data within five days of Schwann cell culture with the hybrid fiber (alginate + VAVKIEAA-OT4).

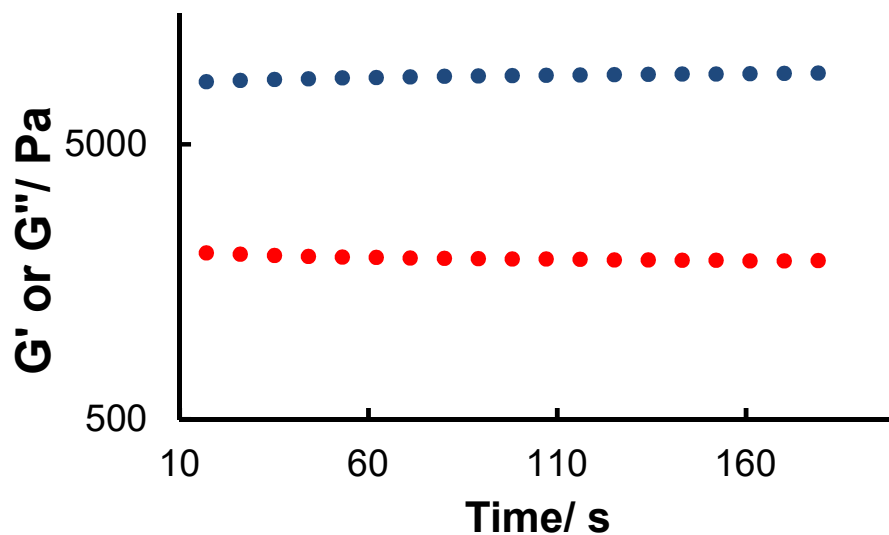


Figure A6.12. Representative rheology plot for co-spun fiber bundles of alginate and VAVKIEAA-OT4 at 1 Hz and 5% oscillation strain; Averaging with two other runs, G' (blue circles)= 8420.41 ± 32.28 Pa and G'' (red circles)= 1939.68 ± 3.49 .

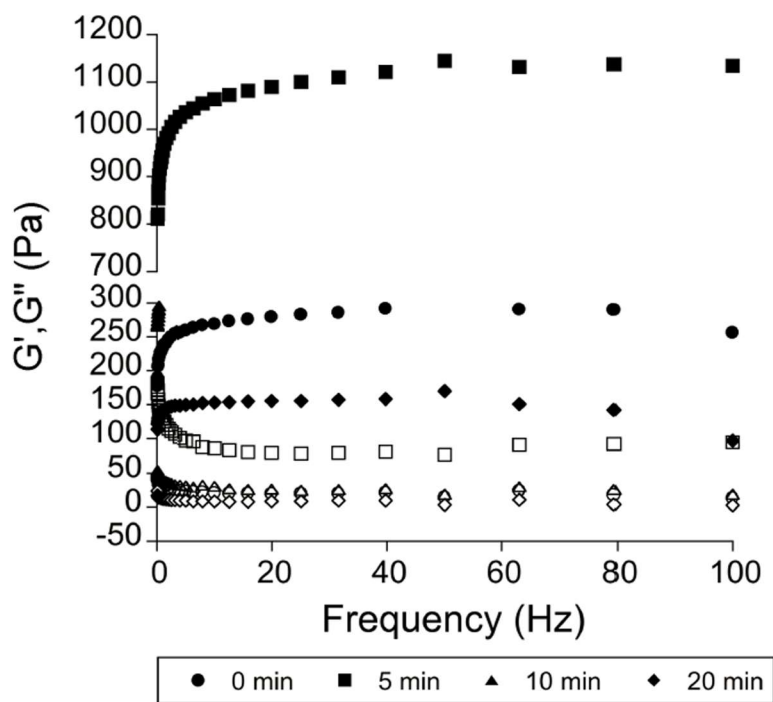


Figure A6.13. Bulk rheology measurements (dynamic oscillatory frequency sweep) for 2 wt% DK(bio)VV-diacetylene hydrogels under different irradiation times with a 4-W 254 nm source. Solid and empty shapes represent storage (G') and loss moduli (G''), respectively.

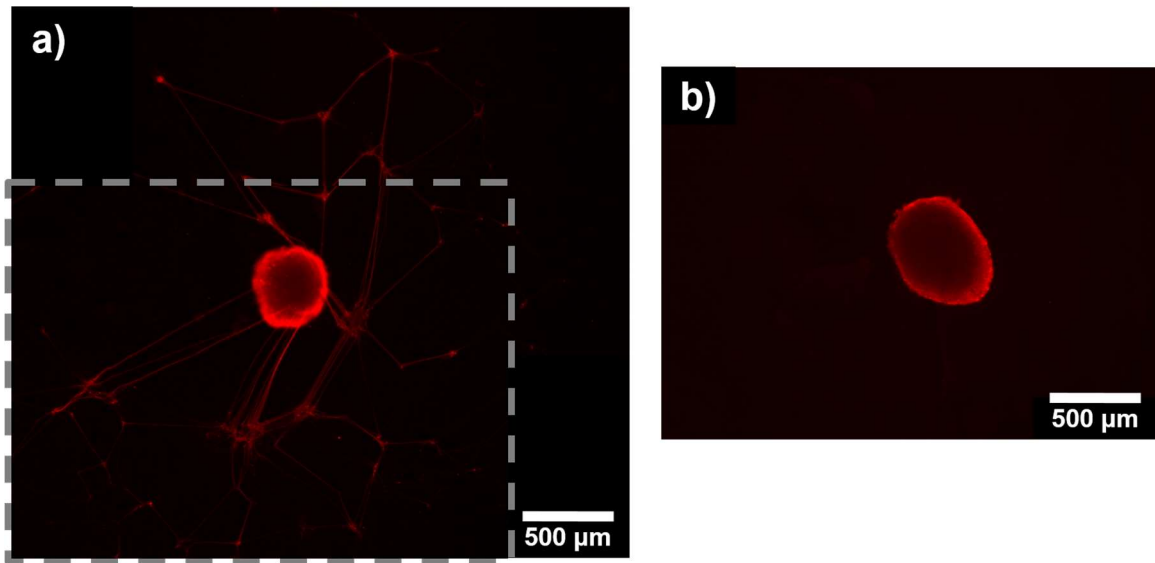


Figure A6.14. (a) Stitched images showing a Day 8-DRG explant in culture on TCPS substrate and (b) a Day 1-DRG explant on **DK(Alloc)VV-polydiacetylene**; The stitched region is indicated by the dashed lines in (a); immunostained images against **neurofilament**.

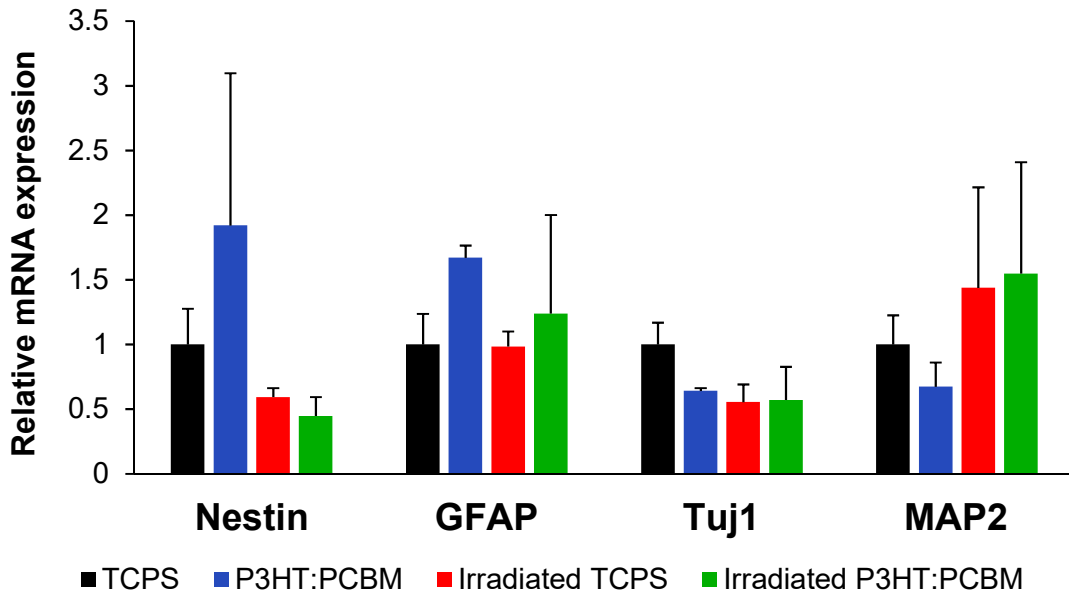


Figure A6.15. Relative mRNA expression of hNSCs seeded on P3HT/PCBM films after 11 days in culture. All results were normalized with respect to non-irradiated TCPS samples.

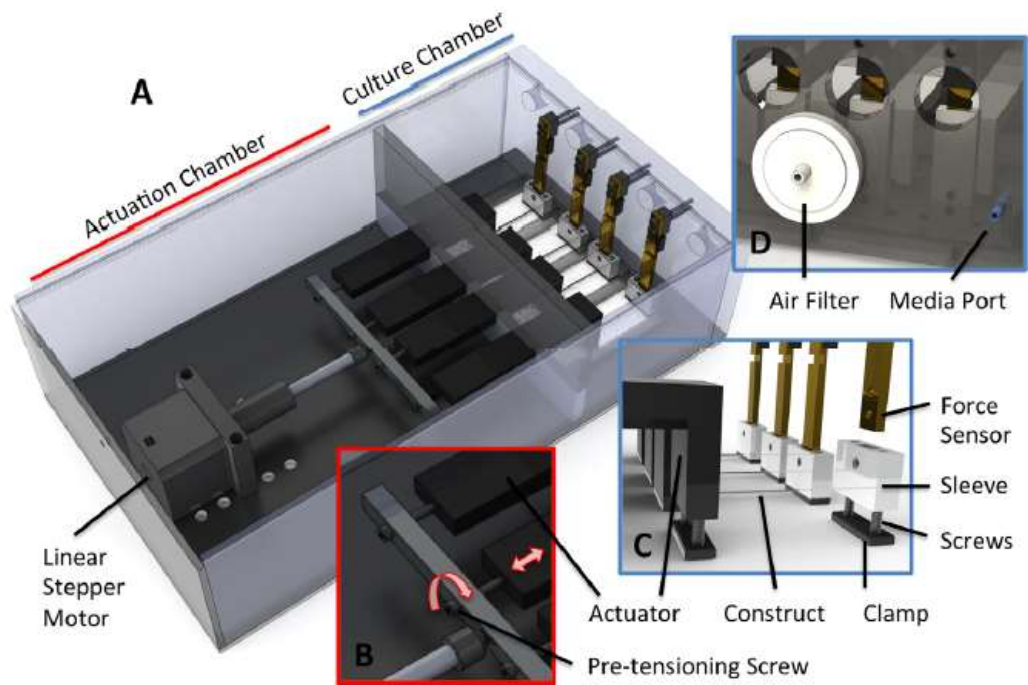


Figure A6.16. Bioreactor setup used to apply 10% strain to fibrin and fibrin-PPy for current vs. time recordings and *in vitro* NRVM culture. Adapted from Ref. 5.

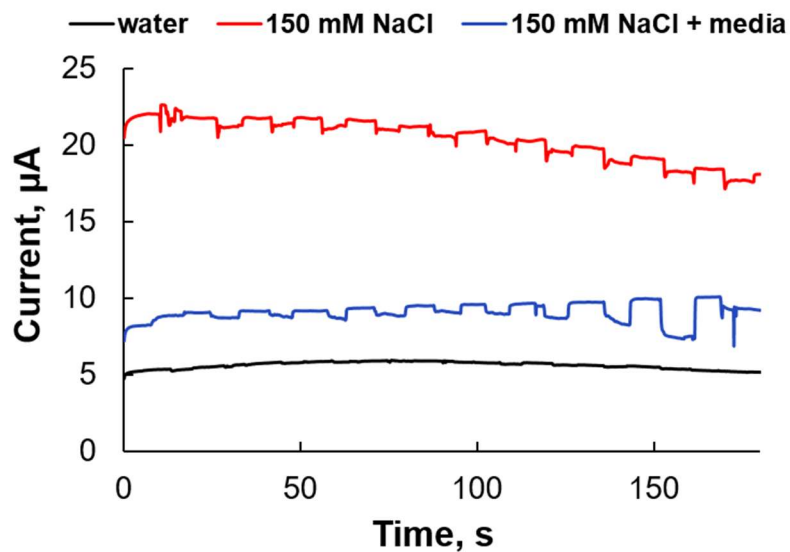


Figure A6.17. Current response over time for fibrin-PPy bundles. The material was strained manually (~10%), for every 10 s.

References

- (1) Sanders, A. M., Dawidczyk, T. J., Katz, H. E., and Tovar, J. D. (2012) Peptide-based supramolecular semiconductor nanomaterials *via* Pd- catalyzed solid-phase “dimerizations.” *ACS Macro Lett.* *1*, 1326–1329.
- (2) Guo, X., and Watson, M. D. (2008) Conjugated polymers from naphthalene bisimide. *Org. Lett.* *10*, 5333-5336.
- (3) Vadehra, G. S., Wall, B. D., Diegelmann, S. R., and Tovar, J. D. (2010) On-resin dimerization incorporates a diverse array of p-conjugated functionality within aqueous self-assembling peptide backbones. *Chem. Commun.* *46*, 3947–3949.
- (4) Aoki, K., Kudo, M., and Tamaoki, N. (2004) Novel odd/even effect of alkylene chain length on the photopolymerizability of organogelators. *Org. Lett.* *6*, 4009-4012.
- (5) Cook, C. A., Huri, P. Y., Ginn, B. P., Gilbert-Honick, J., Somers, S. M., Temple, J. P., Mao, H.-Q., and Grayson, W. L. (2016) Characterization of a novel bioreactor system for 3D cellular mechanobiology studies. *Biotechnol. Bioeng.* *113*, 1825-1837.

BIOGRAPHICAL SKETCH

Herdeline Ann M. Ardoña (Digs) was born in Quezon City, Metro Manila in Philippines on October 11th, 1991. She studied in Our Lady of Lourdes College in Valenzuela City, Metro Manila for her primary and secondary education (1997-2007). She then attended University of the Philippines-Diliman in 2007 as a Chemistry major. Her undergraduate research with Prof. Susan D. Arco focused on the development of quantum dots capped by ionic liquids and dispersed on electrospun polymer fibers that can be useful for wastewater pollutant degradation. After graduating from UP Diliman in 2011, she served as a junior faculty member in the same university for undergraduate General Chemistry and Organic Chemistry laboratory classes. In 2012, she began her Ph.D. studies in the Department of Chemistry and Institute for Nanobiotechnology at Johns Hopkins University. Her graduate dissertation research, under the guidance of Prof. John D. Tovar and co-supervision of Prof. Hai-Quan Mao, involves the development and biophysical characterization of peptidic nanomaterials with optoelectronic function as bioscaffolds that can influence the cellular growth and behavior.

HERDELINE ANN M. ARDOÑA

3400 N. Charles St., New Chemistry Building, Baltimore MD, 21218
hardoaa1@jhu.edu | (443) 721-8724

RESEARCH INTERESTS

Organic materials chemistry, bioelectronics, mechanistic bioengineering, nanotechnology

EDUCATION

2012-2017 Johns Hopkins University (JHU)

Ph.D. Chemistry

(*M.A. Chemistry, 2014; Certificate for Advanced Studies in Nanobiotechnology, 2016*)

Advisors: Prof. John D. Tovar and Prof. Hai-Quan Mao

2007-2011 University of the Philippines-Diliman (UP Diliman)

B.S. Chemistry, *Summa Cum Laude*

Advisor: Prof. Susan D. Arco

AWARDS AND HONORS

Howard Hughes Medical Institute (HHMI)-International Student Research Fellowship (2015-2017)

Schlumberger Foundation-Faculty for the Future Fellowship (2014-2017)

Emmett and Elsie Buhle Fellowship Award, JHU (2014):

In acknowledgement of excellent academic performance

Leticia Shahani Award for Best Undergraduate Thesis, UP Diliman (2011)

Bank of the Philippine Islands-Department of Science and Technology: Science Award (2010):

Annually given to students in the nation that excel in science and engineering

Baldomero M. Olivera, Jr. and Lourdes J. Cruz Award, UP Diliman (2010):

Annually given to two top-ranking incoming B.S. Chemistry seniors of Institute of Chemistry, UP Diliman

National Scholarship Program, Commission on Higher Education, Philippines (2007-2011)

University Scholar (7 consecutive semesters), UP Diliman (2007-2010)

PUBLICATIONS

- [1] Y. Zhou, B. Li, S. Li, **H.A.M. Ardoña**, W. L. Wilson, J. D. Tovar, C. M. Schroeder "Sol-gel transition of π -conjugated oligopeptides," *submitted*.
- [2] **H.A.M. Ardoña**,* T.S. Kale,* A. Ertel and J.D. Tovar (*equal contribution), "Non-resonant and local field effects on the photophysics of oligo(*p*-phenylenevinylene) segments within peptidic nanostructures," *Langmuir*, **2017**, *in press*.
- [3] **H.A.M. Ardoña**, E. R. Draper, F. Citossi, M. Wallace, L. Serpell, D.J. Adams, and J.D. Tovar "Kinetically controlled coassembly of multichromophoric peptide hydrogelators and the impacts on energy transport," *J. Am. Chem. Soc.*, **2017**, *in press*.
- [4] B. Li, S. Li, Y. Zhou, **H.A.M. Ardoña**, L. R. Valverde, W. L. Wilson, J. D. Tovar, C. M. Schroeder "Non-equilibrium self-assembly of π -conjugated oligopeptides in solution," *ACS Appl. Mater. & Interfaces*, **2017**, *9*, 3977-3984.
- [5] W. Liyanage, **H.A.M. Ardoña**, H.-Q. Mao, and J.D. Tovar "Cross-linking approaches to tune the mechanical properties of peptide π -electron hydrogels," *Bioconjugate Chem.* (part of the *Peptide Conjugates for Biological Applications* special issue), **2017**, *28*, 751-759.
- [6] **H.A.M. Ardoña** and J.D. Tovar, "Peptide pi-electron conjugates: organic electronics for biology?" *Bioconjugate Chem.* (featured as *cover article*), **2015**, *26*, 2290-2302.
- [7] K. Besar,* **H.A.M. Ardoña**,* J.D. Tovar and H.E. Katz (*equal contribution), "Demonstration of hole transport and voltage equilibration in self-assembled pi-conjugated

- peptide nanostructures using field-effect transistor architectures.” *ACS Nano*, **2015**, 9, 12401–12409.
- [8] **H.A.M. Ardoña**, K. Besar, M. Togninalli, H.E. Katz and J.D. Tovar, “Sequence-dependent mechanical, photophysical and electrical transport properties of pi-conjugated peptide hydrogelators.” *J. Mater. Chem. C* (part of a special themed collection: *Bioelectronics and 2015 Journal of Materials Chemistry C Hot Papers*), **2015**, 3, 6505-6514.
- [9] **H.A.M. Ardoña** and J.D. Tovar, “Energy transfer within pi-conjugated peptide heterostructures in aqueous environments” *Chem. Sci.*, **2015**, 6, 1474-1484.
- [10] B.D. Wall, Y. Zhou, S. Mei, **H.A.M. Ardoña**, A.L. Ferguson and J.D. Tovar, “Variation of formal hydrogen bonding networks within electronically delocalized pi-conjugated oligopeptide nanostructures” *Langmuir*, **2014**, 30, 11375-11385.
- [11] **H.A.M. Ardoña**, F.U. Paredes, I.H.J. Arellano and S.D. Arco, “Electrospun PET supported-ionic liquid-stabilized CdS catalyst for the photodegradation of Rhodamine B under visible light” *Mater. Lett.*, **2013**, 91, 96-99.

MANUSCRIPTS IN PREPARATION

- [1] T.S. Kale*, **H.A.M. Ardoña***, A. Ertel and J.D. Tovar (*equal contribution), “Torsional demands of quaterthiophene segments imposed within peptidic nanostructures,” *in preparation*.
- [2] **H.A.M. Ardoña***, Z. Qi,* C. B. Stanley, C. Jaroniec and J.D. Tovar (*equal contribution) “Probing the local nanostructures of energy transporting peptide heterostructures,” *in preparation*.
- [3] **H.A.M. Ardoña**, H.-Q. Mao and J.D. Tovar “Topochemically polymerized peptide bioscaffolds for electrosensitive cells,” *in preparation*.

PATENT

- [1] J.D. Tovar, H.E. Katz, **H.A.M. Ardoña**, A.M. Sanders, K. Besar, “Energy transporting pi-conjugated peptide nanomaterials” U.S. Provisional Patent Appl., **2015**.

SELECTED PRESENTATIONS

- [1] Oral/Poster Presentation in GRS (and Selected Short Talk from Poster Presenters in GRC): “Molecular Engineering Approaches for the Development of Pi-Conjugated Peptides Towards Bioelectronics.” Physical Organic Chemistry-Gordon Research Conference (GRC)/ Seminar (GRS), Holderness, NH. June 2017.
- [2] Poster Presentation: “Energy-Transporting Peptide Assemblies for Bioelectronics.” HHMI Science Meeting, Janelia Research Campus, VA. September 2016.
- [3] Oral Presentation (and Session Moderator): “Self-Assembling Bioelectronic Peptide Hydrogels.” Oral Presentation (and Session Moderator): 34th Annual Chemistry Graduate Student Symposium, University at Buffalo-The State University of New York, NY. May 2016.
- [4] Oral Presentation: “Energy Transfer Within Self-Assembling Bioelectronic Hydrogelators With Tunable Properties” Macro Group UK, Young Researchers Meeting, University of Liverpool, UK. April 2016.
- [5] Oral Presentation: “Demonstration of Energy Transfer within Self-Assembling Bioelectronic Hydrogelators with Tunable Properties.” Institute for Nanobiotechnology Mini-Graduate Symposium, JHU, Baltimore, MD. March 2016.
- [6] Poster Presentation: “Self-Assembling Bioelectronic Peptide Hydrogels.” Active and Adaptive Materials Symposium, City University of New York- Advanced Science Research Center, NY. October 2015.
- [7] Oral Presentation: “Energy Transfer within Pi-Conjugated Peptide Hydrogelators with Sequence-Dependent Properties.” 12th International Symposium on Functional π -Electron Systems, University of Washington, Seattle, WA. July 2015.

- [8] Poster Presentation (Best Poster Award): “Self-Assembling Bioelectronic Peptide Hydrogels” 44th National Organic Symposium, American Chemical Society, University of Maryland, College Park, MD. June 2015.
- [9] Poster Presentation: “Self-Assembling π -Conjugated Peptides as Bioelectronic Nanomaterials” Faculty for the Future Forum, Schlumberger Foundation, Cambridge, MA. November 2014.
- [10] Poster Presentation (2nd Prize, Poster Pitching Competition): “Synthesis, Characterization and Application of Imidazolium Ionic Liquid-Capped Photocatalytic Quantum Dots in Polymer Fibers for Pollutant Degradation in Wastewaters.” 31st Philippine-American Academy of Science and Engineering Symposium, Quezon City, Philippines. June 2011.

RESEARCH AND TEACHING EXPERIENCE

Graduate Student/Research Assistant, JHU (2013-2017)

- Tovar Research Group and Mao Research Group (*co-advised*): Department of Chemistry; Institute for Nanobiotechnology; and Translational Tissue Engineering Center-Johns Hopkins School of Medicine
- Thesis: “Molecular Engineering Strategies for the Development of Energy-Transporting Conjugated Systems Towards Bioelectronics”

Honorary Research Associate, University of Liverpool (April 2016)

- Prof. Dave J. Adams Research Group: Department of Chemistry

Participant, 17th National School on Neutron and X-ray Scattering (June 2015)

- Argonne National Laboratory, IL and Oak Ridge National Laboratory, TN

Teaching Assistant, Johns Hopkins University (2012-2014)

- for Introductory Chemistry Laboratory and Organic Chemistry Lecture

Instructor 5, Institute of Chemistry, UP Diliman (2011-2012)

- for General Chemistry Laboratory and Organic Chemistry Laboratory

Intern, Avon Products Manufacturing Inc., Laguna, Philippines (April-May 2010)

Undergraduate Researcher, UP Diliman (2009-2011)

- Arco Research Group, Institute of Chemistry
- Thesis: “Synthesis, Characterization and Application of Imidazolium Ionic Liquid-Capped Photocatalytic Quantum Dots in Recycled Polymer Fibers for Pollutant Degradation in Wastewaters”

MEMBERSHIPS AND PROFESSIONAL ACTIVITIES

Chemistry Department Representative, Graduate Representative Organization, JHU (Spring 2017)

Chemistry Diversity Committee (ChemDNA), Department of Chemistry, JHU (2016-2017)

Roseman Lecture Planning Committee, Department of Chemistry, JHU (2016)

Member, American Chemical Society (2016-present)

Associate Member, Royal Society of Chemistry (2016-present)

Mentor, STEM Achievement in Baltimore Elementary Schools, JHU (2015-2017)

Mentor, Women in Science and Engineering (WISE), JHU (2015-2016)

Member, American Association for the Advancement of Science (2013-present)

Mentor, Thread Inc., Baltimore, MD (2012-2017)

Member, Integrated Chemists of the Philippines (2011-present)

Licensed Chemist, Professional Regulation Commission, Philippines (2011)

Chapter Life Member, International Honor Society of Phi Kappa Phi, Chapter 045 (2010-present)

Staff/Illustrator, Scientia: Student Publication of College of Science, UP Diliman (2008-2010)

Children’s Rights Advocates’ League, UP Diliman (2008-2011)

Red Cross Youth, Philippine National Red Cross (2006-2008)